Durham University

Durham E-Theses

Early compaction history of marine siliciclastic sediments.

Allsop, Timothy

How to cite:

Allsop, Timothy (1994) *Early compaction history of marine siliciclastic sediments.*, Durham theses, Durham University. Available at Durham E-Theses Online: http://etheses.dur.ac.uk/5675/

Use policy

The full-text may be used and/or reproduced, and given to third parties in any format or medium, without prior permission or charge, for personal research or study, educational, or not-for-profit purposes provided that:

- a full bibliographic reference is made to the original source
- a link is made to the metadata record in Durham E-Theses
- the full-text is not changed in any way

The full-text must not be sold in any format or medium without the formal permission of the copyright holders.

Please consult the full Durham E-Theses policy for further details.

Academic Support Office, The Palatine Centre, Durham University, Stockton Road, Durham, DH1 3LE
e-mail: e-theses.admin@durham.ac.uk Tel: +44 0191 334 6107
http://etheses.dur.ac.uk

Early Compaction History of Marine Siliciclastic Sediments.

Timothy Allsop BSc. (Hons) Dunelm.
(Graduate Society)

The copyright of this thesis rests with the author.
No quotation from it should be published without
his prior written consent and information derived
from it should be acknowledged.

A thesis submitted to the University of Durham
for the Degree of Doctor of Philosophy.

September, 1994.

UNIV DURHAM

28 SEP 1995

This Thesis is dedicated to **Mum and Dad, Simon and Christine,** a very special family.
Thanks for everything.

Declaration.

The contents of this thesis are the original work of the author, and have not been previously published for a degree at this University or any other institution. The work of others is acknowledged throughout this thesis through reference.

Timothy Allsop BSc. (Hons) Dunelm.
Department of Geological Sciences,
University of Durham,
U.K.

Copyright.

The copyright of this thesis rests with the author. Any information taken from it should be acknowledged. No quotation should be published without prior written permission from the author.

Abstract.

Differential compaction occurs within many sedimentary settings, such as alluvial and deltaic deposition, but it is within the submarine fan environment where the process is most effective due to the very high depositional porosities of the muds found there. Additionally the grain size of siliciclastic sediments within the submarine fan environment varies rapidly both horizontally and vertically, and hence the effect of differential compaction control on the depositional geometry and arrangement needs to be examined and modelled. It is also important to ascertain the rate at which sediments compact when buried, and whether compaction is complete at the end of deposition or whether it requires additional time to achieve this state. Sea-floor topography can be created if the latter case is true, and could influence subsequent deposition. Alternatively, if sea-floor topography is not created, the major control upon subsequent deposition may be the compactibility of the underlying section. Both controls will favour deposition of successive coarse clastic units above areas of fine-grained sediments, i.e. sand above shale rather than sand above sand.

The Palaeocene sediments of the Central North Sea in the Montrose - Arbroath area (Blocks 22/17 and 22/18) combined with outcrop studies in southern California and New Mexico, have been used to assess the control of differential compaction on sediment distribution in a deep-sea fan setting. Differential compaction affects the Montrose - Arbroath area on a variety of scales. Firstly, differential compaction of the entire Palaeocene section across the underlying Forties - Montrose High induces structure. At a smaller scale, differential compaction may form a considerable control upon the spatial distribution of submarine fan channels and lobes that form the reservoir section throughout the area, and therefore the areal distribution of the oilfields themselves. Finally differential compaction may effect the distribution pattern of individual turbidites within such channel systems, thus forming a fine control upon the distribution of sands and shales within the reservoir.

Fieldwork on submarine fan deposits in southern California has highlighted further complications to differential compaction that need to be addressed during the modelling process. Sedimentary processes such as basal loading and slumping are highly common in such deposits, and both can effect the compactional process to differing degrees. Results obtained from the modelling of stratal patterns observed in New Mexico provide information on the timing of differential compaction. It is suggested that compaction of sediments, even during early burial, requires a time interval often greater than the period of deposition, resulting in post-depositional compaction and the production of near-surface overpressure.

Acknowledgments

Firstly I would like to thank my supervisor, Dr. R. E. Swarbrick, for introducing me to North Sea oil geology, and for his guidance throughout the research. I must also thank Amoco (U.K.) Exploration Company for their sponsorship of the research project, and for the data and help they have provided throughout my period of study. A few Amoco people I would especially like to thank are Andy Griffin for the initial data and core logging, Reg Littlefair for his help with the geophysics, Warren Birch for the discussions concerning well correlation and Montrose - Arbroath geology, and finally Philip Farfan for his assistance and discussions about compaction throughout my period of sentence.

There are many people in Durham who I would like to thank, and I only hope I leave no-one out. Most of them are reprobates from the post-graduate fraternity, always an enigmatic group!! In this list comes the post-grads that started with me, Stevie 'the bald pecten' Edwards, Paul, Jane, John Bole, Guy and Kate. Further to this list come the post-grads with all this yet to come....you lucky people...including Charlotte, Jipper, Jon Booler, Sarah, Pete, Sue, Adam, Zoë, Roberto, Wayne and Alun. Special mention for Billy 'he's a nutter' Butler needs to be added for keeping me sane throughout my writing up period (it seemed like a decade!), and for keeping the office 223 not only the funniest and most entertaining place within the department, but for also providing us with insights into some of the stranger human parasites, and the complex workings of the human brain. Unfortunately some of the brains of 223 do not appear to conform to the normal complexity!! Both Bob and Michele Holdsworth also deserve a large "thank you" for many different reasons. For everything they have done I am extremely grateful, I cannot thank them enough.

Continuing the Durham theme there are many members of the technical staff who deserve a mention. Carol and Lynn for numerous secretarial-type reasons, Jerry, George 'The Babe' Ruth, Ron and Alan, and not forgetting Karen and Julie for endless drawing stuff plus interesting conversations to listen to when using the Kroy machine and the guillotine. Finally, the head Honcho, who makes the department tick, Dave Asbery, the fix it man with numerous talents....stand-up comedy being a lesser one of these! Only kidding Dave.

A final couple of post-grads I need to thank are Marc Audet from Oxford who helped with many aspects of compaction, and Dave Hunt, who provided many convincing stories to not only fix one more field trip, but also pull off

another one. Dave's help throughout the study turned up many important results and points of discussion, and I am very grateful for all he did.

To finish, I must thank my family for many years of support (including financial) plus the encouragement and loyalty to allow me to take the opportunities I wanted. Thanks go to Mum and Dad, Simon and Christine. And to end, Cath requires a huge acknowledgment for a multitude of reasons, too many to list in this thesis, but of which I am sure she is aware.

CONTENTS

Title Page.

Declaration and Copyright. I.

Abstract. II.

Acknowledgments. III.

Contents. V.

PAGE.

Chapter 1: Introduction. 1-6

Chapter 2: Compaction. 7-92

2.1 Theory of Compaction. 7

2.2 Depositional Porosities, Porosity-Depth Relationships, Autocompaction and Differential Compaction. 11

2.2.1 Compaction of Argillaceous Sediments. 14

Early Compaction Theory. 16

Porosity-Depth Curves From Empirical and Mathematical Datasets. 23

Recent Compaction Studies. 31

2.2.2 Compaction of Coarse-Grained Sediments. 37

Near-Surface Textural Parameters. 38

The Effect of Time and Temperature. 45

Empirically Derived Porosity-Depth Relationships. 49

Cementation Versus Compaction. 59

Recent Compaction Modelling. 66

2.2.3 Compaction of Carbonate Sediment. 67

2.2.4 Autocompaction. 72

2.2.5 Differential Compaction. 72

Differential Compaction Models. 73

Differential Compaction and Coal Geology. 79

2.3 Compaction as a Temporal Process. 82

2.4 Simple Modelling of Compaction. 87

Chapter 3: Fieldwork - Southern California. 93-163

3.1 Introduction. 93

3.2 Ridge Basin. 93

3.2.1 Introduction. 93

3.2.2 Tectonics. 96

3.2.3 Stratigraphy. 102

3.2.4 Depositional Model for the Castaic Formation. 104

3.2.5 Exposure Within Ridge Basin. 106

3.2.5.1 Castaic Lake Exposures. 106

Section 1. 108

Section 2. 112

Section 3. 113

Section 4. 117

3.2.5.2 Ridge Route and Templin Highway Exposures. 117

3.2.6 Discussion of Slumped and Brecciated Horizons. 122

3.2.7 Compactional Modelling of Outcrop Data. 124

Example 1. 124

Example 2. 132

Example 3. 137

Other Important Processes. 139

Summary Conclusions. 139

3.3 La Jolla, San Diego. 142

3.3.1 Introduction. 142

3.3.2 Stratigraphy. 146

3.3.3 Section Description. 146

3.3.4 Compaction Modelling. 149

3.4 Wheeler Gorge, Santa Ynez Mountains. 152

3.4.1 Introduction. 152

3.4.2 Section Description. 152

3.4.3 Compaction Modelling of the Wheeler Gorge Section. 157

3.5 Conclusions. 160

Chapter 4: Sacramento Mountains - New Mexico. 164-266

4.1 Introduction. 164

4.1.1 Siliciclastic Environments Versus Carbonate Environments. 164

4.2 Porosity and Compaction of Carbonate Strata. 167

4.3 Location and Geological Setting. 168

4.4 Stratigraphy. 170

4.4.1 Mississippian Formations. 170

4.4.1.1 The Lake Valley Formation. 173

Pre-Biohermal Strata. 173

Biohermal Strata. 174

Post-Biohermal Strata. 175

4.4.1.2 The Rancheria Formation 181
4.5 Depositional Model. 184
Biohermal Formation. 186
Post-Biohermal Sediment Deposition. 187
4.6 Stratal Patterns. 189
4.6.1 Muleshoe Mound: Southeastern Flank. 191
Arcente. 192
Dona Ana. 195
Rancheria. 197
4.6.2 Sugarloaf Mound: Southeastern Flank. 198
Alamogordo - Tierra Blanca. 198
Arcente. 198
Dona Ana. 200
Rancheria. 203
4.6.3 Dog Canyon. 205
Arcente - Dona Ana. 205
Rancheria. 206
Northern Cliffs of Dog Canyon. 209
Southern Cliffs of Dog Canyon. 212
4.7 Compaction Phenomena. 219
4.7.1 Differential Compaction Around Muleshoe Mound. 221
A. Introduction. 221
B. Qualitative Data. 222
C. Methodology. 227
D. Calculations. 231
E. Results and Implications. 236
4.7.2 Differential Compaction Around Sugarloaf Mound. 248
4.7.3 Differential Compaction Above Dona Ana Channels - Dog Canyon. 251
A. Introduction. 251
B. Qualitative Data. 251
C. Methodology. 252
D. Calculations. 254
E. Results and Implications. 254
4.8 Conclusions. 258
Sea-Level Effects on Near-Surface Compaction. 260
4.9 Summary. 265

Chapter 5: North Sea - Montrose and Arbroath Oilfields. 267-363
5.1 Introduction. 267
5.2 Field Stratigraphy. 267

5.3 Geophysics. 273
5.4 Oilfields. 275
5.4.1 Trap. 275
5.4.2 Reservoir. 275
5.4.3 Source. 281
5.5 Depositional Model. 283
5.5.1 General Submarine Fan Models. 285
5.5.2 Submarine Fan Processes. 291
5.5.3 Similar Field Models. 299
5.5.3.1 North Sea Sequence Stratigraphy. 302
5.5.3.2 North Sea Oil and Gas Fields. 317
The Frigg Field 317
The Forties Field. 320
The Nelson Field. 320
The Balder Formation, Quadrant 9. 322
5.5.4 Montrose - Arbroath Model. 331
5.5.4.1 Geological Model. 331
5.5.4.2 Seismic Data. 333
5.5.4.3 Well Correlation. 335
5.6 Modelling. 340
5.6.1 Mega-Scale Compaction Effects. 340
5.6.2 Meso-Scale Compaction Effects. 342
Results. 347
Arbroath Depositional Development. 349
5.6.3 Small-Scale Compaction Effects. 355
5.7 Conclusions. 356

Chapter 6: Conclusions. 364-368

References. 369-398

Appendix 1.

Appendix 2.

Chapter 1:- Introduction.

The purpose of this study is to assess the role of compaction on the deposition of deep-marine submarine fan sediments. Particular interest is aimed at facies development, stacking patterns and geometry of depositional units.

The objectives of this study are:-

1. A detailed understanding of sediment compaction, particularly near-surface compaction of submarine fan deposits.
2. A clearer definition of the timing and rate of compaction at shallow burial depths, coupled with the implications such as near-surface overpressure of pore fluids, and the stratal relationships produced.
3. An assessment of compaction effects and possible control upon deposition in a submarine fan depositional setting.
4. An assessment of the depositional characteristics of Palaeocene rocks of the Montrose Arbroath area of the North Sea, followed by an assessment of the role played by differential compaction during/upon the fields' depositional development.

There are various scales at which compactional effects can be viewed, and each will be dealt with in the following chapters.

Modelling of sedimentary basins primarily aims to simulate the geometric deformations caused by compaction during geological time, often coupled with fluid flow (water and hydrocarbons). However, compaction is a dynamic process and is the result of various mechanisms which are not yet well understood. Therefore, the wide-ranging topic of compaction forms an important area of research. Differential compaction, as part of this category, is equally poorly studied, although it can be interpreted to provide possible controls and influences on deposition throughout many sedimentary environments.

The present study concentrates on deposition within the submarine fan environment, particularly dealing with channelised, mid-fan deposits for the reasons outlined in greater detail in Chapter 2. There is a focus on near-surface effects of compaction, as it will be shown (Chapter 2) that within the early burial (0-300m) of siliciclastic sediments the greatest bed thickness reductions occur, and, therefore, the effects of compaction are at their maximum. Accordingly, the difference between the compaction of different sediment types and facies is also greatest during early burial, meaning the effects of differential compaction are at their most noticeable. However, as depths of burial increase, the porosity-depth

relationships, which define a sediment's compaction history, begin to converge, and the amount of differential compaction markedly decreases.

Near-surface compactional processes are poorly understood, both in qualitative and quantitative terms, mainly due to the lack of porosity data from shallow buried sediments. Defining a sediments compaction history during burial is the first step in the modelling process, and is therefore of fundamental importance. Figure 1.1 illustrates possible sources of near-surface porosity data, although the quality of data provided varies greatly. The drilling process disturbs most of the surface sediment, resulting in porosity data provided by the Deep Sea Drilling Project (DSDP) having a wide spread of values. However, Stacor, a piston coring device devised by the French Institute of Petroleum, can provide porosity-depth data for shallow buried sediments (Truyol, 1989), with minimal disturbance effects. Quality of porosity measurements from this source is therefore high, exhibiting little scatter of data. Bottom Shear Modulus Profiling (BSMP) uses geophysical techniques to assess sediment porosity, but is still at an early stage in its development (Yamamoto et al., 1989). Finally, observations and modelling of bedding/stratal patterns of outcrop can provide verification of near-surface porosity-depth data, with few, minor assumptions.

To achieve an understanding of the processes involved during early burial, an extensive summary of previous published research was undertaken (Chapter 2). Geological and engineering literature provided the basic understanding of the fundamentals of the compaction process. Important to the study is a definition of a porosity-depth profile for the early burial of submarine fan sediments, principally sand and mud. The starting points of depositional porosities for such sediments are relatively well documented (e.g. Hamilton, 1976; Truyol, 1989), however, the following destruction of porosity during burial to approximately 300m is poorly understood. Porosity-depth equations and compaction curves have been proposed by various authors, generally falling into two categories:-

- Mathematically derived porosity-depth relationships, based on soil mechanics theories and engineering test results.
- Porosity-depth relationships based on curve fitting techniques to empirical datasets.

Some of these curves and equations have been interpreted for deep-water, submarine fan sediments, and may therefore be suitable for the modelling of the present work.

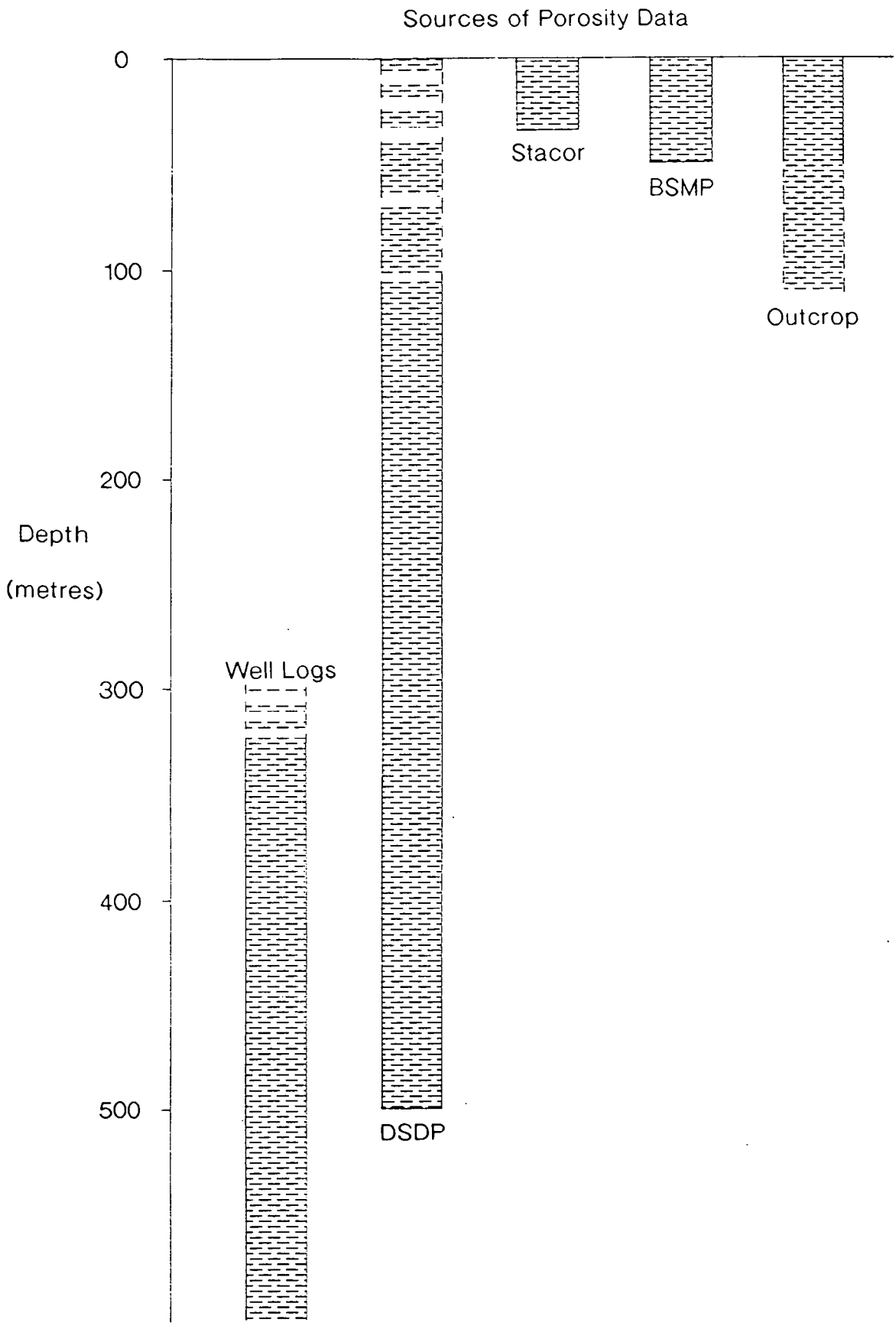

Figure 1.1 Graph to illustrate possible sources of porosity-depth data. DSDP = Deep Sea Drilling Project, Stacor is a piston corer developed by the French Institut of Petroleum (IFP), and BSMP = Bottom Shear Modulus Profiler (see Yamamoto et al., 1989).
Well logs = Oil Co. BOREHOLE LOGS.

Models of compactional control upon deposition are mainly qualitative, especially those concerned with coal deposition. However, a few are quantitative (e.g. Bridge & Leeder, 1979; Collier, 1989; Anderson, 1991; Bridge & Mackey, 1993), but mainly deal with deposition in the alluvial environment. These models provide information on the techniques involved in modelling depositional environments, along with information concerning the problems and assumptions required.

The present study focussed on field based data to define the near-surface depositional processes that occur, and to attempt to constrain the amount of compaction occurring during early burial. Field data also enable the testing of the previously published porosity-depth relationships outlined in Chapter 2. As the present study was primarily interested in submarine fan deposition, a field area consisting of an identical depositional environment was chosen. Large amounts of both vertical and lateral exposure were required, to show not only the stratigraphy and growth of the fan deposits, but also the lateral changes of the facies, along with the stacking patterns of the depositional units. Ridge Basin in Southern California was chosen (Chapter 3). Along with providing information on compactional processes occurring within such a depositional environment, these field studies also provided information concerning depositional and post-depositional processes that occur within submarine fan settings, and that may effect the compaction of the sediments involved.

The regional changes in facies, and hence lithology, are not well matched to the outcrop scale in siliciclastic environments. Consequently, the effects of compaction produce bedding patterns and stratal relationships from which it is extremely difficult to appreciate the contribution of compaction. Gradual change in facies occurs over great distances, thus making measurement of the effects of differential compaction extremely difficult. Rapid facies changes in carbonate environments, however, offer the opportunity for the effects of differential compaction to be studied more easily at outcrop scale. The presence of large, early-cemented carbonate buildups provides a clear reference frame about which the effects of compaction can be measured and modelled. An area of the Sacramento Mountains of New Mexico was chosen to fulfil this purpose, as giant carbonate mounds, consisting of an incompressible framework and having excellent lateral exposure, are present here (Chapter 4).

With a much clearer fundamental understanding of near-surface compaction provided by field data, the compactional control upon deposition was assessed

for the Montrose and Arbroath oilfields of the North Sea (Chapter 5). With the development of a depositional model for the oilfields, a detailed correlation of facies units is proposed, breaking down the depositional model into its component parts. Forward modelling of each chronostratigraphic unit allowed the assessment of compactional control upon deposition at each time stage, aided by data from fieldwork.

Finally, Chapter 6 outlines the conclusions to the present work. These conclusions basically fall into two categories:-

- Conclusions relating to the process of compaction, particularly during early burial (0-300m), combined with the effects of differential compaction. Also the effects created by varying rates of compaction and deposition, and the implications involved.
- Conclusions relating to deposition within the submarine fan environment, with respect to facies development, stacking of depositional units, and the geometry of facies packages and the entire depositional system.

Figure 1.2 illustrates a flow diagram of how the present study set about the objectives, indicating where various aspects of the work inter-relate. Importantly, it shows how the two basic fundamentals (double outline on Fig. 1.2; i.e. understanding of near-surface compaction and the depositional model of the Montrose - Arbroath area), are finally brought together in order to assess the precise role of compaction in the depositional process of the study area.

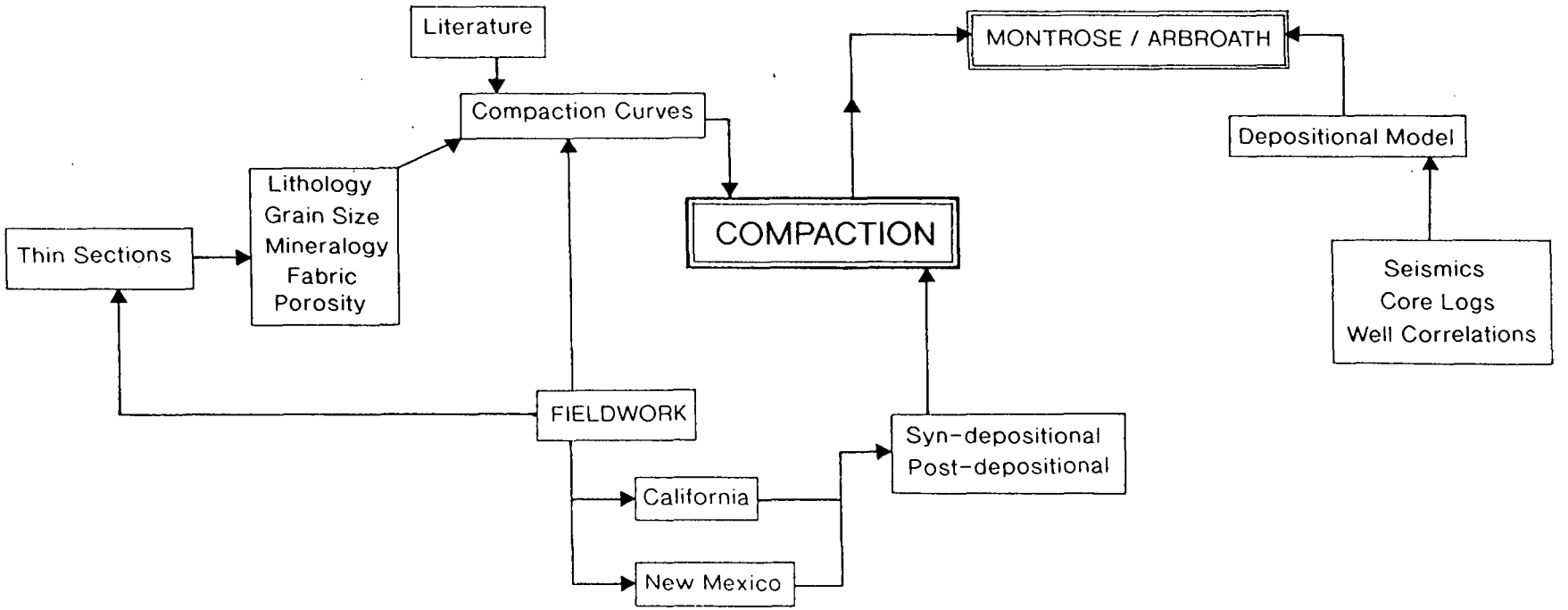

Figure 1.2 Flow diagram illustrating the structure of the present study.

CHAPTER 2:- COMPACTION.

2.1 Theory of Compaction.

The process of sediment compaction, due to the gravitational pressure resulting from the weight of the sediment unit and the weight of the overlying strata, has long been recognised as a geological phenomenon. However, a clear understanding of the overall process is still lacking, and indeed a consensus of opinion has not yet been achieved for over a century of research and study. Early compaction studies showed how the porosity of a sediment decreased with age, and that this decrease in pore space was the primary result of compaction (Sorby, 1908). The idea that the compaction of sediments may have played an important part in the origin of oilfield structures promoted compaction studies by Shaw (1918), Mehl (1919) and McCoy (1934). Early geological explanations on the settling of sediments, and on the gravitational compaction of sediments, along with more specialised compaction theories, have been presented by Blackwelder (1920), Monnett (1922), Teas (1923), Terzaghi (1925), Hedberg (1926, 1936), Athy (1930), Parasnis (1960), and Skempton (1970). Athy's (1930) study presented the results of some 2200 density determinations and 200 porosity determinations of well samples from a depth range of 700 to 5,000ft (210 to 1525m) from wells in Oklahoma and Texas. His was the first research to definitively confirm a direct relationship between depth of burial and rock density, and an inverse relationship between depth of burial and porosity for fine-grained, argillaceous sediments. This also resulted in the first porosity-depth profiles for differing lithologies (sand and shale), and their associated mathematical formulae representing the trends of the curves seen. The generation of porosity-depth profiles for differing lithologies has since been a very active area of research but with much disagreement between workers, and will be expanded upon later within this chapter.

Hedberg's (1936) research concerning gravitational compaction extended the work of Athy, showing how sediments evolved through differing stages of compaction as depth of burial, and therefore pressure, increases. Since Hedberg's work there appears to be a scarcity of compaction work within the geologic literature for around thirty years (1936-1966). However, many important contributions were made during this period by civil engineers investigating soil mechanics. These studies were begun by Terzaghi (1925), whose work summed up the results of engineering investigations on the effect of pressure on clays and soils.

At this stage it is important to clear up the definition of the terms **compaction** and **consolidation**, because they tend to be used in differing ways by geologists and engineers respectively. The basic laws covering consolidation are those of soil mechanics, and engineers do not use the term compaction as a synonym for the consolidation process. The Dictionary of Geology (Whitten & Brooks, 1987) provides the following definitions, and these will be adopted in the present work:-

1) CONSOLIDATION. The process of conversion of a loose or soft material to a compact, harder material - e.g. sand to sandstone (by cementation), mud to clay (by de-watering).

2) COMPACTION. In the diagenetic formation of massive rock from loose sediment, the close-packing of the individual grains mainly by the elimination of pore-space and the expulsion of entrapped water, normally brought about by the weight of the overlying sediments.

Within the engineering literature compaction is considered as a man-made process in which a soil is strengthened due to loading by construction projects. Consolidation is the naturally occurring process of settlement of sediments and soils. This is the fundamental difference in the use of the two terms by engineers and geologists. However, this study will use the term compaction throughout, meaning the closer packing of sediment grains due to their own weight and the weight of overburden, with the associated reduction of pore-space and fluid expulsion. The term consolidation will not be used because consolidation is often understood by many geologists to include other diagenetic processes such as cementation.

In order to understand the theory of compaction, the theory of consolidation from soil mechanics must be taken in hand. From a geological point of view they are essentially the same process. Therefore, the theory of compaction involves a two phase system, a sediment matrix and a pore fluid. During compaction, due to an increase of overburden pressure, for example, pore fluid will be squeezed out of the sediment as the pore volume of the sediment is reduced, and a closer packing of the sediment matrix is attained. In a coarse-grained, free draining sediment the fluid escape may be very rapid. However, in a fine-grained clay, where the permeability is appreciably lower, this drainage of pore fluid may take a considerable time. Therefore, grain size distribution and drainage pathways play a very important role in early sediment compaction.

In nature the support of the overburden load is divided between the sediment matrix and the interstitial pore fluid, so that the total vertical stress at any point within the sediment column consists of the sum of the two components: the intergranular stress (P_e), and the pore fluid stress (P_w). The "effective pressure" (P_e) is the difference between the total overburden pressure (P_t) and the pore pressure (P_p) (i.e. $P_e = P_t - P_p$) (Terzaghi & Peck, 1948). If the vertical permeability of the sediment allows pore water to escape when loaded, then the pressure distribution in the pore fluids is the same as that of a continuous column of water extending to the water table surface (i.e. hydrostatic pressure).

The concept of compaction can therefore be described by the mechanical model shown in Figure 2.1 (Terzaghi & Peck, 1948). This model consists of a perforated, round metal plate and an enclosing cylinder, which contains a metal spring and water. In this analogy the spring represents the compressible clay particles, the water represents the pore fluid which is regarded as incompressible, and the size of the perforations in the metal plate represents the permeability of the sediment (i.e. the smaller the holes the less the permeability). At the initial stage the perforations are sealed and there is no applied load on the sediment, so that both the effective stress and the pore fluid stress are zero. Subsequently a 25psi overburden pressure is introduced to the system while the perforations are closed. In this scenario the entire load is carried by the pore water, which is incompressible, with the effective stress (carried by the spring) still equal to zero. Now, as the perforations are opened, pore fluid will begin to flow out of the system and the perforated plate will begin to descend. During this stage the total stress is carried by both the spring and the pore water, with progressive transfer of the stress from the pore fluid to the spring. As time continues pore fluid will cease to be expelled from the system once the pore-water stress is equal to zero, and the entire overburden load is carried by the spring. The perforated plate will descend no lower at this equilibrium stage. The length of time required for the spring to pass from one state of compaction to another depends on how rapidly the pore water can escape from the system, which is determined by the size of the perforations in the plate (i.e. the permeability of the sediment). This illustrates a very important point when dealing with sediment compaction, in that the time required for a state of equilibrium compaction to be attained depends on the permeability of the sediment. This point has been an underevaluated aspect of the modelling concerning compactional

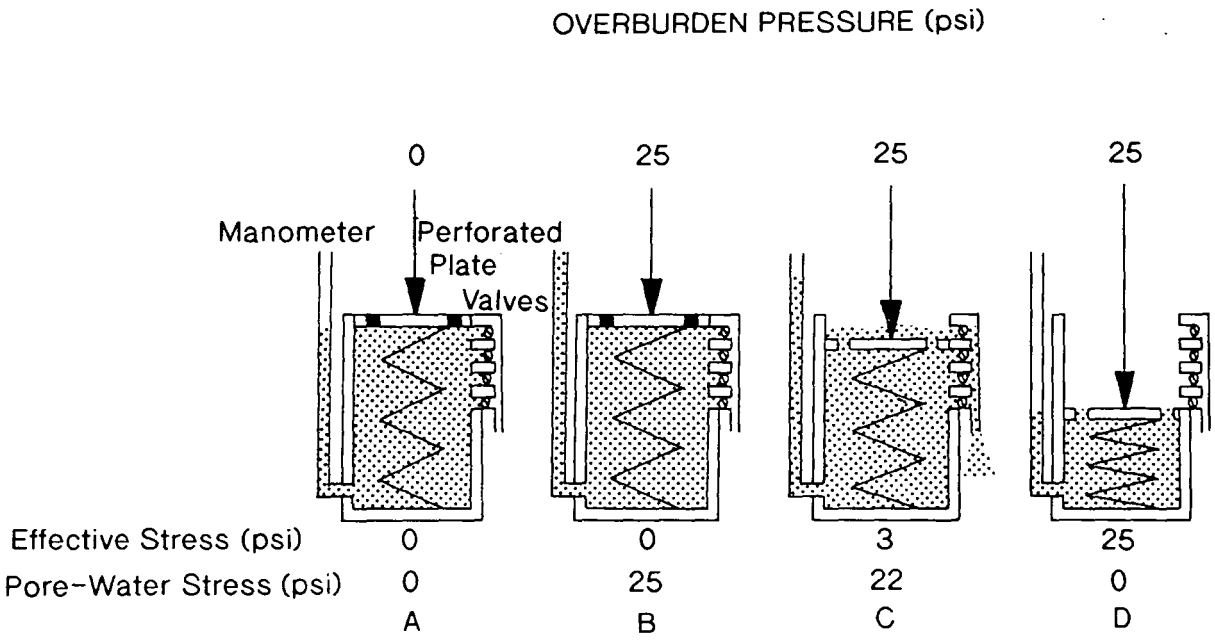

Figure 2.1 Mechanical model used to describe the process of compaction (Terzaghi & Peck, 1948).

processes and will be dealt with in greater detail at a later stage in this, and subsequent chapters (see section 2.3).

We therefore have a very basic model of additional sediment being added on top of a sedimentary column with the associated stress initially being carried by the pore fluid as excess pore water pressure. This excess pressure causes pore water to bleed off at speeds depending on the permeability of the sediment being compressed, and the load is gradually transferred to the sediment matrix. The difference between the total applied stress (σ), and the pore water pressure (σ_w) at any instant is known as the effective stress (σ_1), and is approximately the same stress as carried by the sediment skeleton (Simons & Menzies, 1977). Hence, we can write:-

$$\sigma_1 = \sigma - \sigma_w \qquad \text{(equation 2.1)}$$

which is a fundamental equation in soil mechanics (Terzaghi, 1925). As the stress is gradually transferred to the sediment matrix a closer packing of the individual matrix grains, along with some grain deformation, is induced.

2.2 Depositional Porosities, Porosity-Depth Relationships, Autocompaction and Differential Compaction.

As explained in the previous section, compaction of sediments occurs due to overburden pressure which induces a closer packing arrangement in the underlying sediments, with associated dewatering and porosity destruction. It therefore follows that the higher the initial, depositional porosity of the sediment being loaded the greater the amount of pore fluid which can be expelled, thus leading to greater compaction and bed thickness reduction. Attempts have been made to measure near-surface porosities for differing sedimentary facies, however, there are numerous problems in collecting near-surface data due to the great instability, and high water content of the sediments within the first few metres below the sediment - water interface. This phenomenon can clearly be seen when looking at the majority of porosity data collected by the Deep Sea Drilling Project (DSDP), where the first twenty to thirty metres of core are highly disturbed due to the drilling and coring process (e.g. porosity data collected by *Glomar Challenger*, leg 18, von Huene et al., 1973). Hamilton (1976) used specifically selected DSDP core data taken from the least disturbed sediment cores to produce porosity-depth and density-depth profiles for various deep-sea sediments. For deep-sea pelagic clays he demonstrated a surface, depositional porosity of 81.2%. Recent studies have been carried out by a French group using a newly designed drilling tool called *Stacor*. This coring device creates very little

disturbance in the near-surface sediment and, therefore, porosity determinations can be made with a great degree of confidence in their accuracy. Their data show that pelagic deep-sea muds at the depositional surface have an initial porosity averaging 80% (Truyol, 1989). For non-calcareous muds this appears to be the accepted value for the depositional porosity used in forward modelling and back-stripping procedures, and there tends to be a consensus for this value throughout the literature (e.g. Hamilton, 1976; Baldwin & Butler, 1985; Truyol, 1989; Anderson, 1991).

It has also been shown by various researchers (e.g. Hedberg, 1936; Rieke & Chilingarian, 1974; Hamilton, 1976; Anderson, 1991), that deep-sea muds have the highest depositional porosities (80%) when compared to muds from other depositional environments, and when compared to different lithologies (e.g. sandstone). Alluvial muds have depositional porosities averaging 55% (Anderson, 1991), and deltaic muds average 60% (Brown, 1975). Lower initial porosities in these environments, relative to undisturbed deep-sea sediments, are due to other processes such as sub-areal exposure of fluvial sediments, combined with the effects of groundwater lowering, evaporation and transpiration (Komornik et al., 1970; Anderson, 1991).

Sandstones, because of their coarser grain size, sorting, grain shape (sphericity) and roundness (angularity) have original depositional porosities of only 40 to 45% (Pryor, 1973). It is therefore apparent that the greatest effects of compaction will be seen in deep-sea pelagic muds as shown in Figure 2.2 (curves are based on the porosity-depth relationship of Sclater & Christie (1980) as explained in the following section 2.2.1). These sediments will undergo the greatest bed thickness reduction during compaction, and as will be shown later, this thickness reduction will occur at a greater rate during burial if equilibrium compaction is maintained.

As muds and sands are buried compaction will reduce pore volume. The decrease in porosity can be used as a convenient measure of the amount of compaction a sediment has undergone since deposition. Plots of porosity versus depth can therefore be produced to show the evolution of porosity in a sedimentary unit as it is progressively buried, thus producing a porosity-depth profile. These porosity-depth profiles (or compaction profiles) vary for differing lithologies (i.e. between muds and sands), and therefore, are often treated separately within the geological literature, and during the modelling process.

Fine-grained sediment density also increases rapidly during the first few hundred metres of the burial process, and can therefore also be used as a

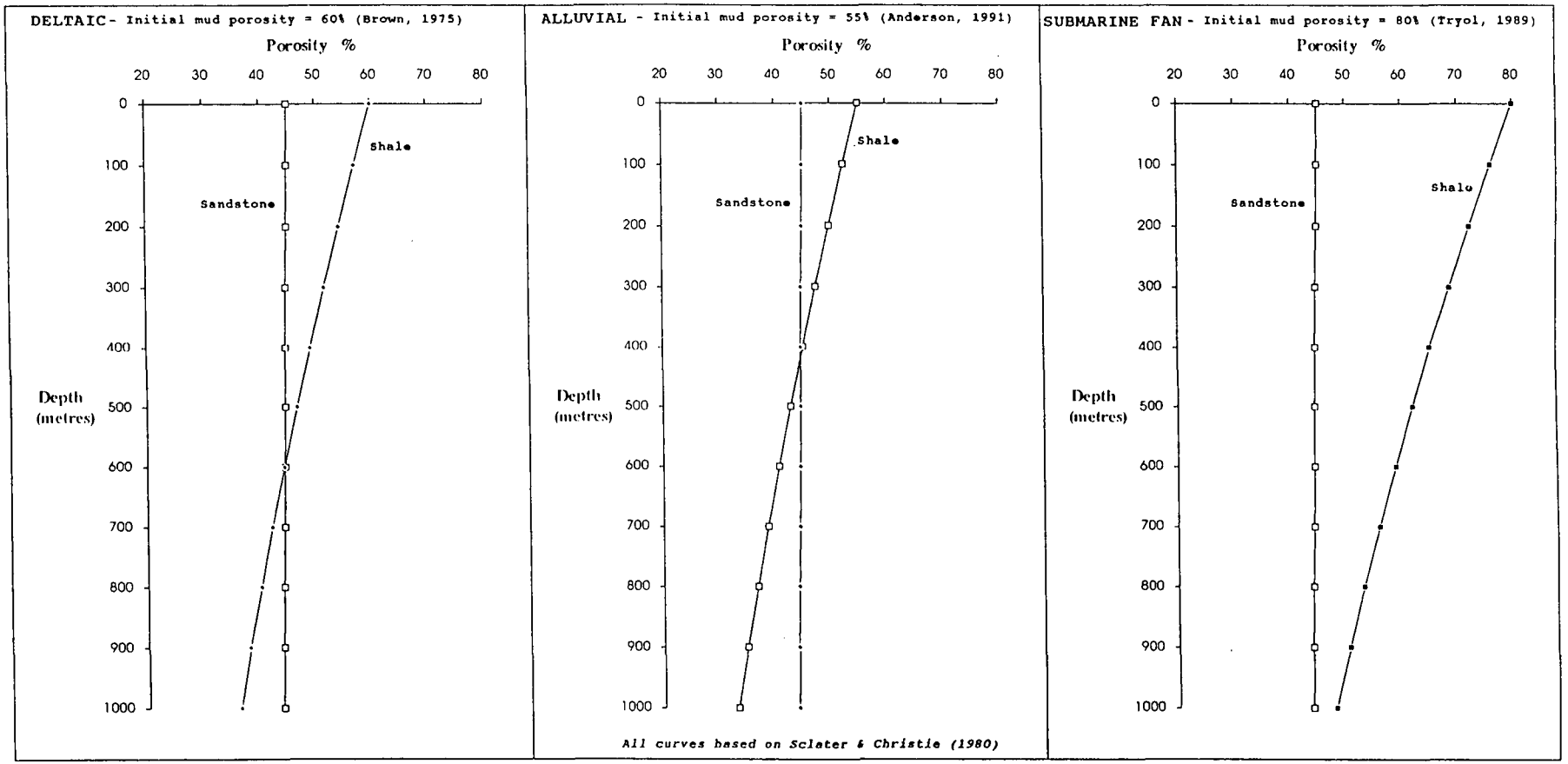

Figure 2.2 Porosity-Depth curves for three different environments of deposition. Depositional porosities vary for shale in each environment, meaning the amount of differential compaction, and the depth to which it occurs, varies accordingly.

gauge of compaction (e.g. Athy, 1930). The increase in density is a function of overburden and tectonic stresses, temperature, time, loading rate, and in part, of grain-size distribution, secondary cementing material, trapped salts in the pores, and mineralogy of the non-clay fraction (Rieke & Chilingarian, 1974). Morgan (1969) observed from data on fresh-water clayey sediments in Lake Erie that there was no simple, clear correlation between the median diameter of grains and bulk density. Bulk density of argillaceous sediments and rocks can vary extensively with depth from one region to another and even within the same stratigraphic unit in a depositional basin. Dana (1967) investigated the lateral and vertical variations of bulk density within a Miocene sandstone and shale sequence in the San Bernadino Mountains in California. He did not find any noticeable systematic variation in bulk densities, but this study did highlight the problem of considerable variation in bulk density within only a short distance in rock units. For these reasons, no universal bulk shale density curve can be constructed to characterise a specific type of argillaceous sediment or rock. Although there is scatter in porosity-depth relationships, there tends not to be such a wide variation of porosity values within individual rock units. It is therefore believed that porosity-depth profiles provide a better guide to the compactional history of argillaceous sediments (Buryakovskiy et al., 1991), and the present work deals exclusively with such profiles.

Many simple porosity-depth relationships for muds have been published, and will be explained in the following section 2.2.1. This will be followed by sections on the compaction of coarse-grained sediments (2.2.2), and the compaction of carbonate sediments (2.2.3). However, these relationships, mathematical equations and models, often fail to take into account the effects of deposition rates and compaction rates. These are highly important variables within compaction modelling, and are explained in section 2.3 of this chapter.

2.2.1 Compaction of Argillaceous Sediments.

Porosity decreases with depth, and as shown in Figure 2.3 shows a marked decrease at shallow depths of burial. This curve is based on a 'best-fit' relationship of various empirically derived porosity-depth relationships. It demonstrates that the greatest porosity loss in argillaceous sediments occurs in the first few hundred metres of burial, with the loss becoming less significant at depths below 300m, if compaction is considered as the only process occurring (i.e. no cementation) (Baldwin & Butler, 1985; Weaver,

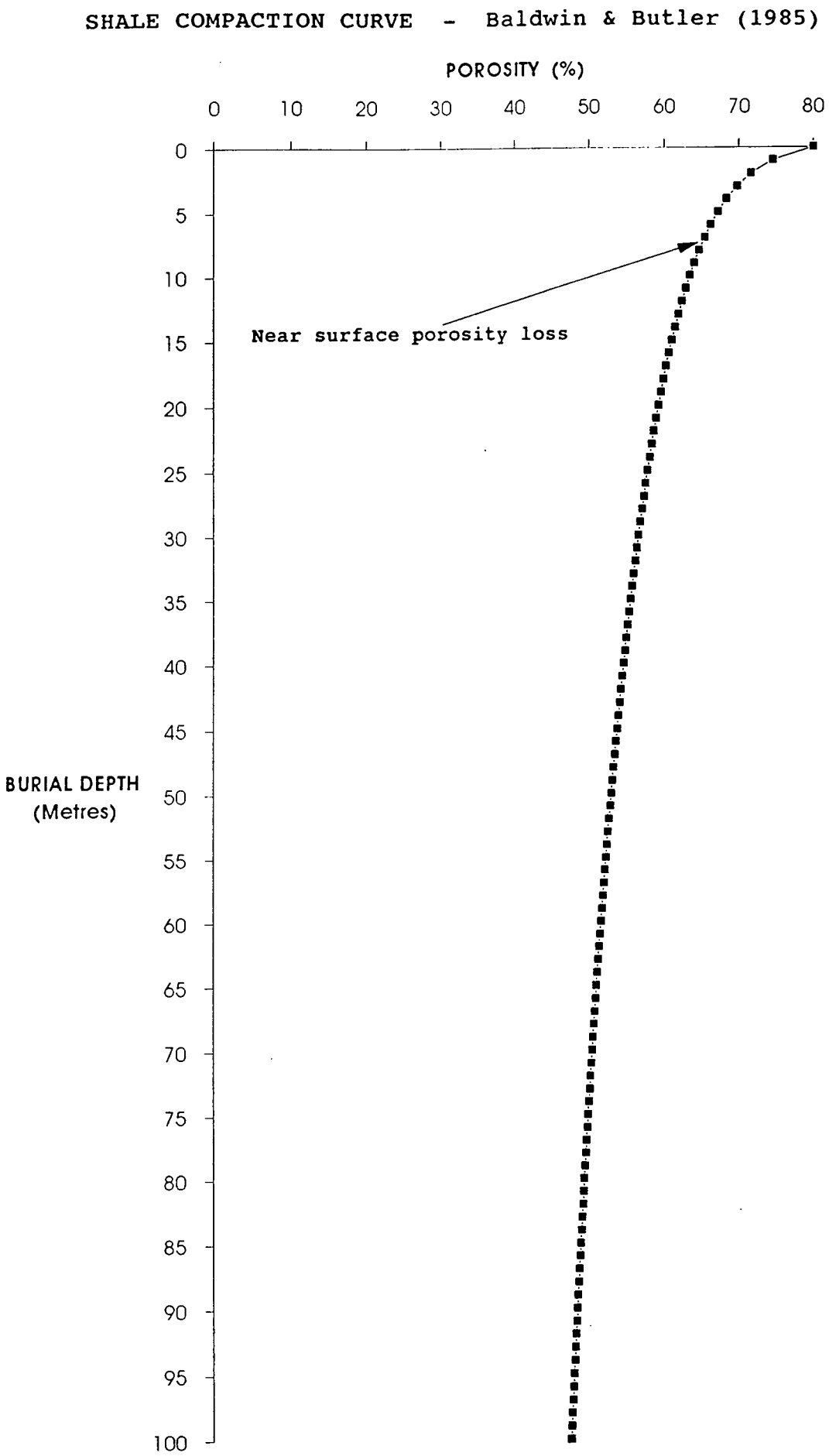

Figure 2.3 Porosity-Depth curve for shallow burial, based on the equation of Baldwin & Butler (1985).

1989). The present study is concentrating on the near-surface compaction behaviour of sediments, and it is therefore important to understand near-surface porosity-depth profiles and compaction processes, such as mechanical rearrangement of grains, which is the dominant process in the near-surface environment (e.g. Hedberg, 1936; Rieke & Chilingarian, 1974; Hinch, 1978; Smosna, 1989; Luo et al., 1993; Waples & Kamata, 1993; Bryant et al., 1993). Mechanical compaction of muds may occur in geologically short periods of time if fluid expulsion occurs as porosity decreases (Magara, 1968). The following section will explain some of the better known compaction theories, curves, and models for argillaceous sediments and how subsurface data from well logs, core samples and outcrop studies have been linked with the depositional porosities explained above to produce a porosity-depth relationship.

Figure 2.4 illustrates the possible sources of porosity data, and how, through the combination of these studies it is possible to assimilate a porosity-depth profile for the entire depth range. Electric well logs and core samples, combined with DSDP data, provide porosity information mainly for the deeper sections of study. However, the *Stacor* coring device and the *Bottom Shear Modulus Profiler* (BSMP; Yamamoto et al.,1989) provide near-surface porosity information. Near-surface porosity data is also available from studies of the literature of both the geological journals, and the research dealing with soil Mechanics and laboratory testing of sediments. Outcrop data enable extra insights into the process of compaction providing some basic assumptions are made, mainly dealing with depositional porosities.

Early Compaction Theory.

Athy(1930) built the first simple compaction model for muds. He was the first to show a definite relationship between porosity and depth of burial for relatively pure shales, producing some early porosity-depth curves, such as the one shown in Figure 2.5. Hedberg (1936) realised that because compaction was a combination of numerous processes which are often dependant upon time, permeability of the loaded sediment, the presence or absence of flow pathways and cements, it is not possible to express satisfactorily pressure-porosity relationships for clays and shales throughout the entire depth range by any one, simple equation.

From well data, Hedberg (1936) proposed a compaction model for clays and shale which basically consisted of three stages (Fig. 2.6). The stages are defined by pressure intervals (i.e. discrete intervals of overburden stress).

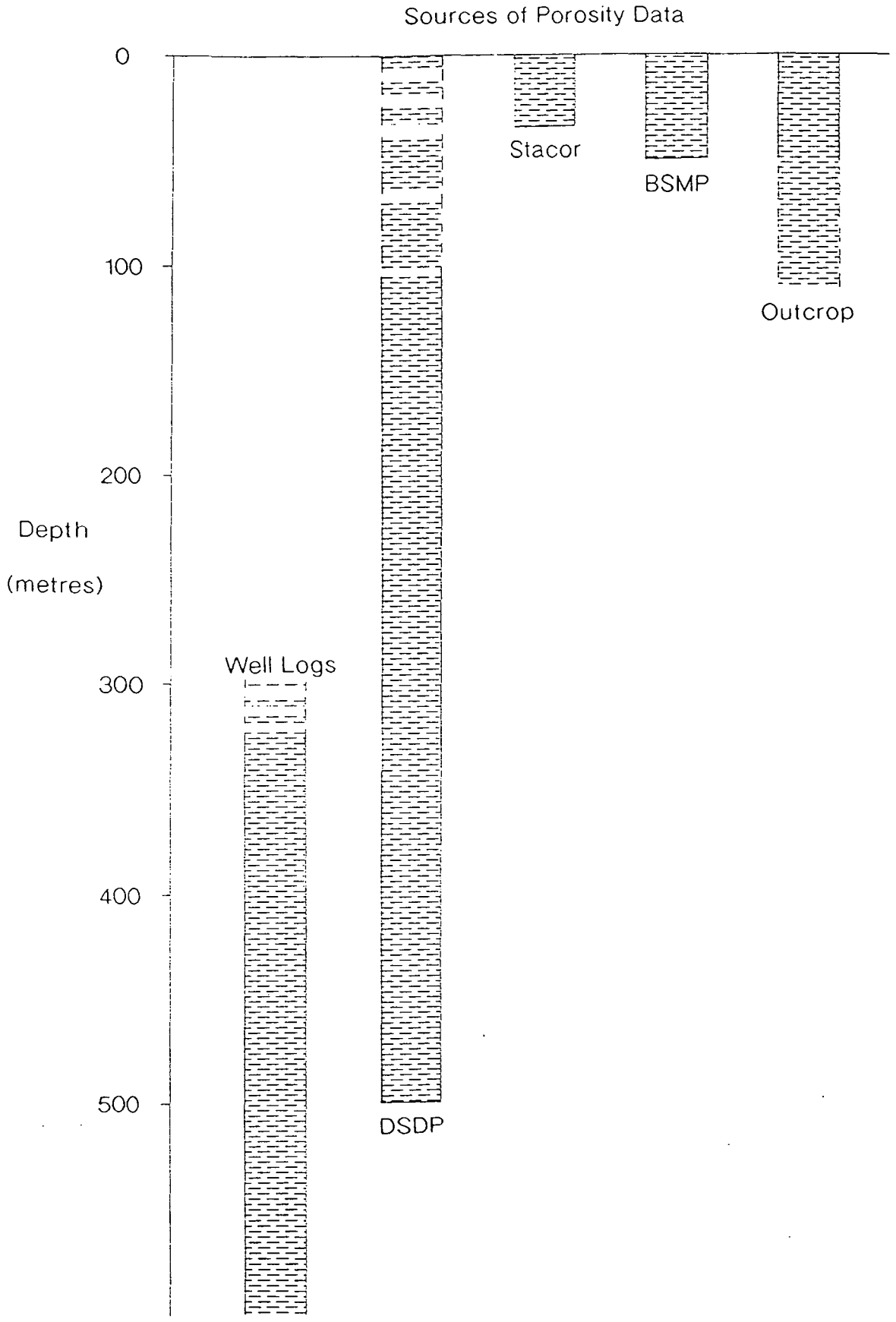

Figure 2.4 Graph to illustrate possible sources of porosity-depth data. DSDP = Deep Sea Drilling Project, Stacor is a piston corer developed by the French Institut of Petroleum (IFP), and BSMP = Bottom Shear Modulus Profiler (see Yamamoto et al., 1989).

Well logs = Oil Co. borehole logs.

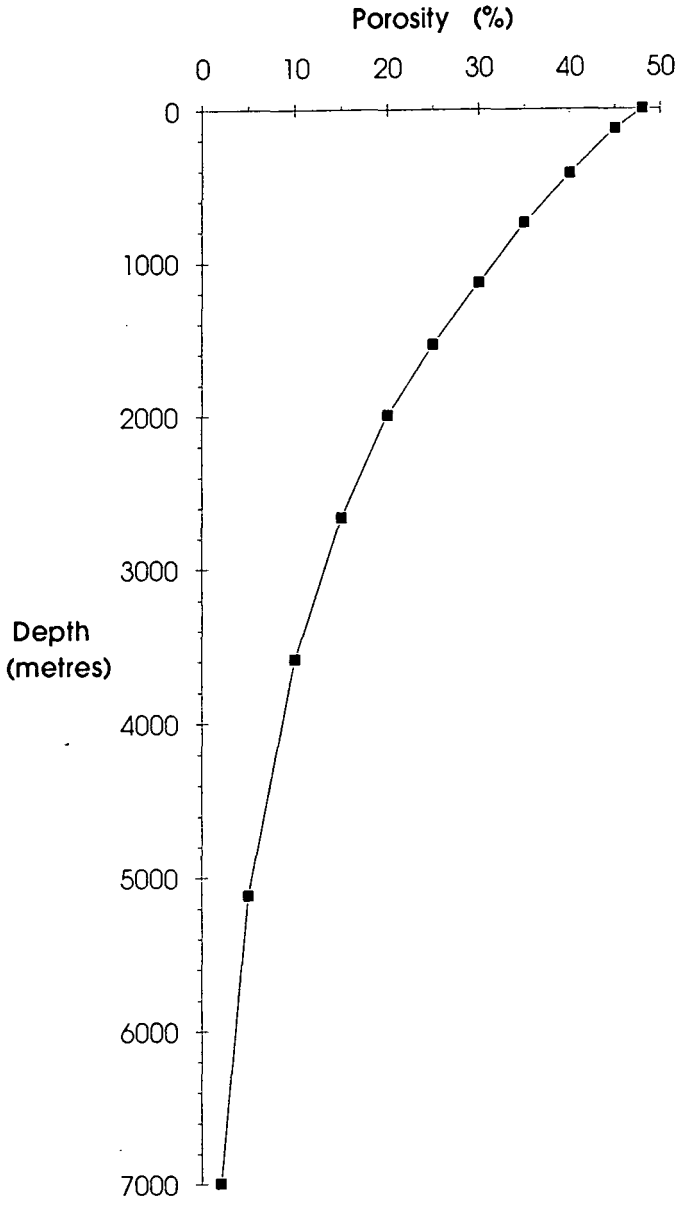

Figure 2.5 Porosity-Depth curve defined by Athy (1930).

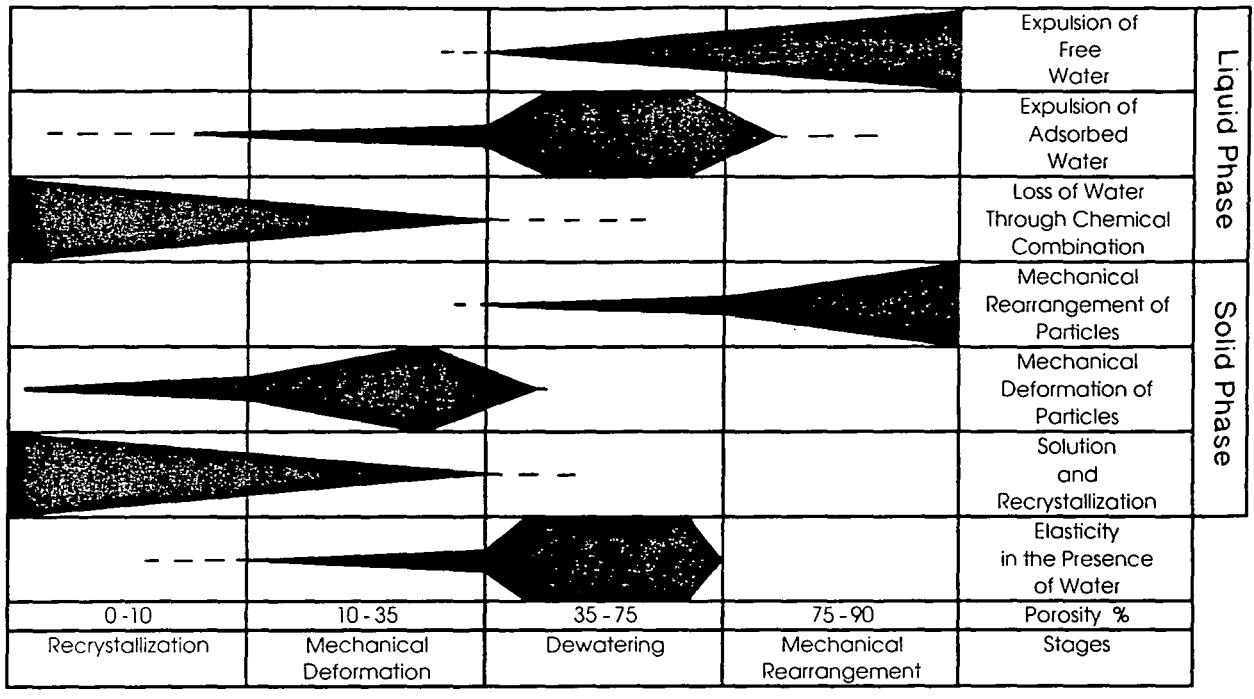

Figure 2.6 Relative importance of different processes in the compaction of clay and shale (modified from Hedberg, 1936).

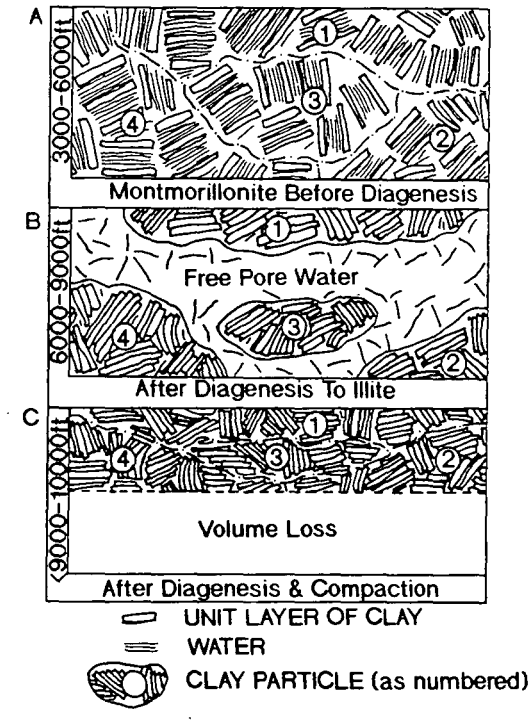

Figure 2.7 Effect of clay diagenesis on compaction of water from mudrocks. It is assumed that same number of particles, "books", and unit layers of clay occur in each compaction stage represented. A - No effective porosity or permeability; virtually all water is "bound" water. B - Most "bound" water becomes free water; effective porosity and permeability thereby produced. C - Free water squeezed out; effective porosity, permeability, and original volume are greatly reduced (from Powers 1967).

The first stage consists of dominantly mechanical rearrangement and dewatering of the clay in a pressure interval from 0 to 800psi (an equivalent depth range of 0 to 544m). This is the stage when there is a rapid decrease in the porosity for relatively small amounts of overburden pressure. The dewatering process also occurs in stages where free water is the first to be expelled, followed by adsorbed water (e.g. bound to clays), mainly between a porosity of 75% and 35%. In the second stage of this compaction model, between a pressure of 800 and 6,000psi (i.e. at a depth between 544m and 4082m), mechanical deformation and further expulsion of adsorbed water reduces the sediment volume. Recrystallization of the clay particles may also occur during this stage. The final stage of compaction occurs at very high pressure once the porosity has been reduced below 10%, and is termed the recrystallization phase by Hedberg (1936). Reduction of pore volume by recrystallization occurs at a very slow rate with large increases in pressure needed. Large crystals may grow during this stage at the expense of smaller ones, and there is a gradual transition from shale to slate and, ultimately phyllite.

Hedberg's (1936) model was adapted by Weller (1959), who produced a porosity-depth curve based on the data of Terzaghi, Athy and Hedberg. However, problems arise from this curve, firstly from applying laboratory soil-compression data to buried sediments, and secondly by failing to account for the occurrence of carbonates, sands and abnormal pressure zones within the well data used.

Powers (1967) produced a fluid-release theory for compacting marine mudrocks, based on changes in clay mineralogy and other bulk properties correlated against depth of burial. This model introduced the fact that when montmorillonite is deeply buried (6,000ft (1830m) and deeper) it changes to illite, which involves the transfer of large amounts of bound water from montmorillonite surfaces to interparticle areas where it becomes interstitial water.

The theoretical model of Powers (1967) basically shows that when dealing with marine montmorillonite, after an initial stage of compaction an equilibrium is reached within a few hundred feet of burial between the water retained in the sediment, and the water-retaining properties of montmorillonite. Little pore fluid can now be squeezed out by an increase in the overburden pressure. This is due to the fact that between depths of 1,500 - 3,000 feet (460 - 910m) most of the water within the sediment exists as water of hydration, and is stacked at least four monomolecular layers thick

between the unit layers of montmorillonite (Powers, 1967). Between 3,000 and 6,000 feet (910 - 1830m) only minimal amounts of oriented water (i.e. water occurring between the crystals and particles of montmorillonite) exists within the sediment (Fig. 2.7). Within this particular study Powers (1967) found that at burial depths below 6,000 feet (1830m), montmorillonite is altered to illite and the bound water is desorbed and becomes free pore water (Fig. 2.7). Due to the decrease in clay-particle size after this alteration, and a corresponding increase in the effective porosity and permeability of the sediment, further compaction occurs until a new equilibrium balance is established, based upon the water-retaining properties of illite (Fig. 2.7).

Figure 2.8 shows the relationship between water escape and clay type, against depth of burial. Powers (1967) stated that the water-escape curves are diagnostic of the porosity, permeability, and bulk density of compacting argillaceous sediments. He also stated that the compaction history of mudrocks depends largely on their original clay composition and the diagenesis which they undergo after burial. The figure also shows that as montmorillonite alters to illite water is forced out, and this can provide a flushing mechanism for any trapped hydrocarbons which are formed at this depth of burial, i.e. the montmorillonite rich shale is acting as a source rock. However, there is no such flushing effect produced during the burial of illite and kaolinite rich shales, and therefore, if these deposits are rich in the organic raw materials for forming hydrocarbons, they may compact to oil shales rather than to source rocks (Powers, 1967).

The compaction theory of Teodorovich & Chernov (1968) consists of three stages of compaction, related to depth of burial. They, like Hedberg (1936), identified an initial rapid compaction within the first 8 to 10 metres of burial based on observations from the hydrocarbon productive Apsheron horizons of Azerbayjan. Large amounts of water are lost during this stage as porosity is destroyed, and this is followed by a stage during which the rate of compaction slows down, between the depths 10 metres to approximately 1,200 to 1,400 metres. The final stage of compaction from 1,400 to 6,000 metres is characterised by very slow sediment compaction, and only small changes in shale porosity.

Burst (1969) also produced a three-stage compaction model for Gulf Coast clayey sediments. His basic conclusion was that the initial dehydration of the sediment is completed in the first few thousand feet of burial, as the interstitial water content is reduced from 70-80% water by volume, to approximately 30% (20-25% interlayer water and 5-10% residual pore water).

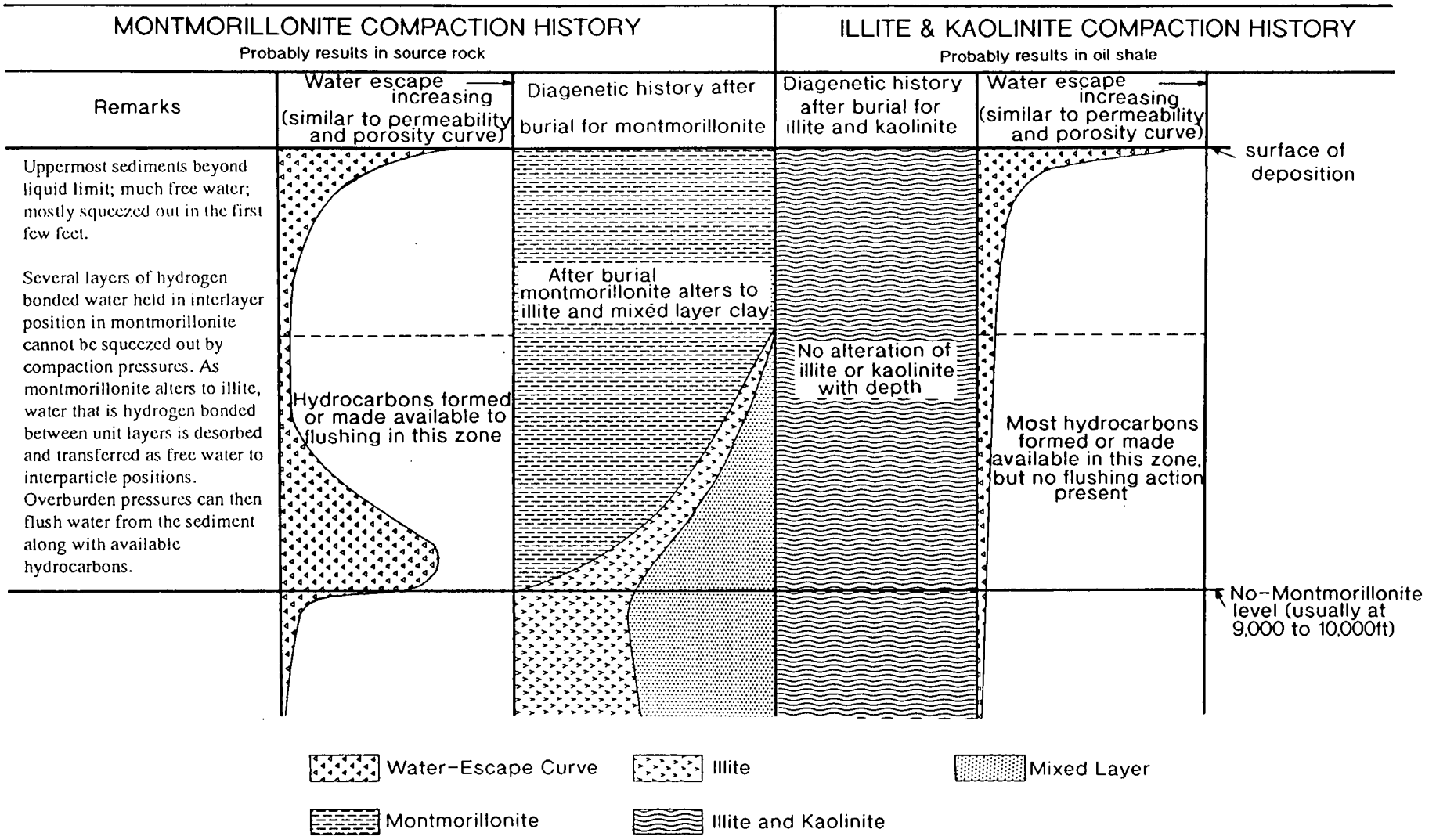

Figure 2.8 Compaction history of different clay minerals when deposited in marine environment and its probable relation to release of hydrocarbons from shale (modified from Powers, 1967).

A further compaction model proposed by Beall, and reported in Rieke & Chilingarian (1974), envisioned an early stage of rapid compaction which primarily involves expulsion of pore fluid by mechanical processes. He stated that approximately 50% of the total consolidation is reached at a very shallow depth of burial.

Porosity-Depth Curves From Empirical and Mathematical Datasets.

Since 1970, after the publication of Gretener & Labute's (1969) discussion of compaction, interest in the process, its controls and effects grew, with the publication of many papers concerning shale, sandstone and carbonate sediment compaction. With reference to the compaction theories and models for muds, Hamilton (1976) produced *in-situ* porosity and density-depth profiles for calcareous ooze, siliceous oozes (diatomaceous and radiolarian), pelagic clay, and terrigenous sediments. The profiles were based on data from the Deep Sea Drilling Project (DSDP). Results of laboratory consolidation tests were also used to estimate the amount of elastic rebound (increase in volume) which has occurred after removal of the samples from overburden pressure in the boreholes. These results were used to correct porosity and density data measured from core samples to produce *in-situ* porosity and density-depth profiles. Hamilton's (1976) curves are shown in Figure 2.9, with their associated regression equations. For the present study we are essentially interested in curve 2 of Figure 2.9, dealing with the early compaction of deep-sea pelagic clay. There is very little scatter in these porosity-depth curves due to the homogeneity of the sediment cored (Hamilton, 1976). This fact shows the dependence of porosity-depth trends on the grain size distribution and the composition of the muds being investigated. Deep-sea pelagic clays tend to be homogenous (Weaver, 1989), an important fact in future chapters concerning the modelling of submarine fan deposits.

Baldwin & Butler (1985) attempted to define the porosity-depth trend for sands and muds utilising the vast majority of previously published data. They argued that solidity (S), the volume of solid grains as a percentage of total volume of sediment, should be used as a reference for the pore space reduction due to compaction, instead of porosity. Solidity is the compliment of porosity. Their reasoning for this is simply the fact that the thickness of solid grains is constant when compaction is the only process occurring, so that the relationship between solidity and length reduction of sediment is linear,

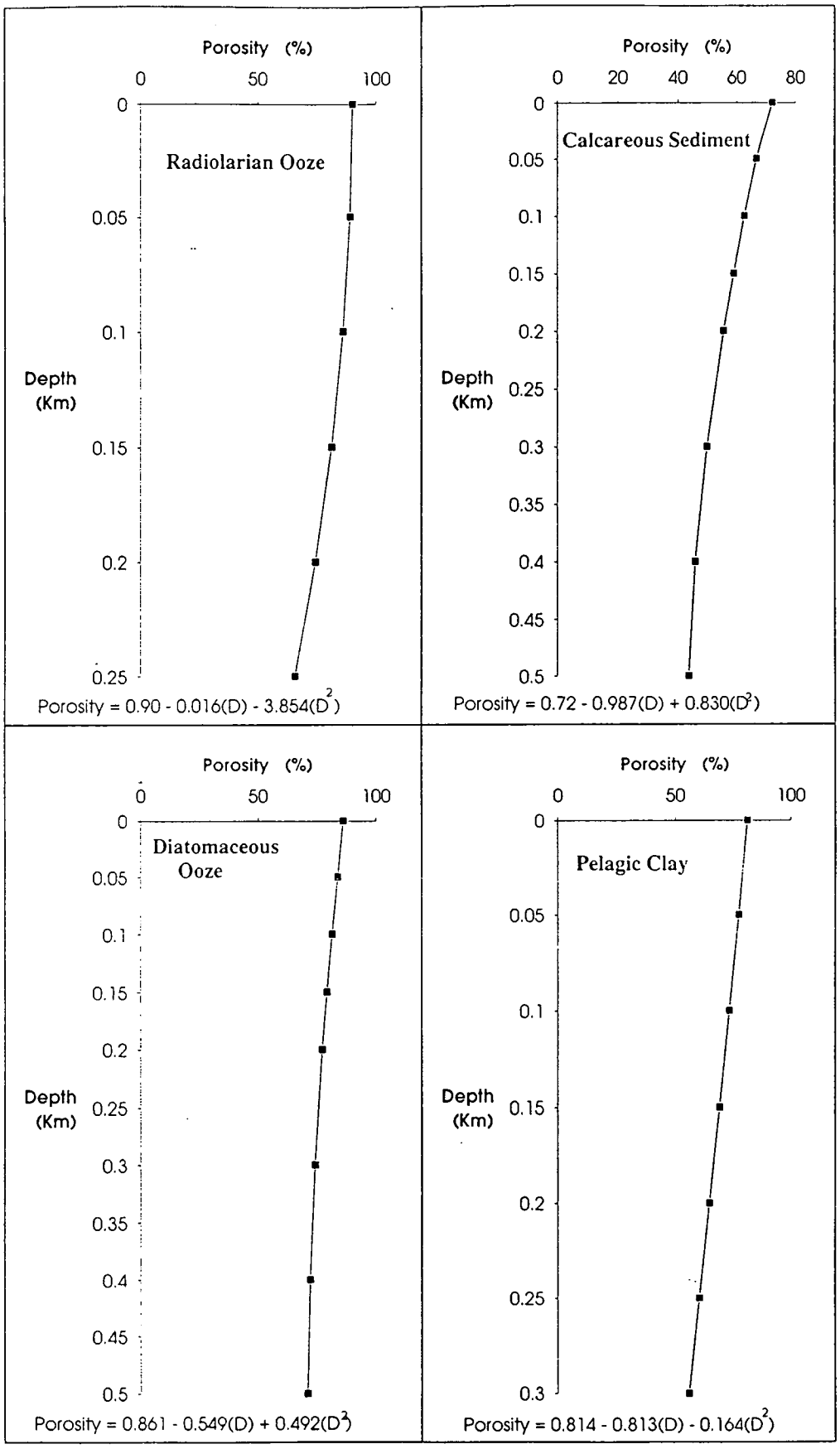

Figure 2.9 Porosity-Depth relationships for deep-sea sediments, based on data from Hamilton (1976).

whereas the relationship is non-linear between porosity and length reduction (Shinn & Robbin, 1983) (Fig. 2.10).

Baldwin & Butler (1985) plotted a number of published porosity-depth curves on a single graph (Fig. 2.11), and attempted to produce a best-fit curve through the data. Their results show that for normally pressured shales (i.e. shales where pore fluid pressure is hydrostatic throughout the unit which they define as shales less than 200m (660ft) thick), the porosity-depth curve can be represented by a power-law equation of the form:-

$$Z = Z_{max}.S^{\alpha} \qquad \text{(equation 2.2)}$$

where S^{α} is the solidity raised to the power α, and Z is the burial depth. The power-law equation plots as a straight line on log-log graph paper (Fig. 2.12), using values of α = 6.35 and Z_{max} = 6.02, and provides a mathematical solution for burial depth (Z) in kilometres and porosity (1 - solidity). These values predict the solidity of the mud to within 2% of Baldwin's (1971) empirical curve which is based on published data compiled from compaction tests, drill cores, and unlithified clay cores, throughout the depth range from 0.5m (20 inches) to 6km (20,000ft)(Fig. 2.12). They noted that for single shales units that are 200m (660ft) thick and greater, pore water is not easily lost, and therefore undercompaction and overpressure tends to occur, especially in young strata (e.g. the Gulf Coast Tertiary muds). Baldwin & Butler (1985) also fitted the same power-law equation to a porosity-depth curve produced by Dickinson (1953) for the Tertiary muds of the Gulf Coast. The values for the proposed "Dickinson equation" for burial depths in kilometres are α = 8 and Z_{max} = 15. This fits Dickinson's curve to within 1% solidity from 300m (1,000ft) to 7.3km (24,000ft) (Fig. 2.12).

The point is made that the form of these power-law equations may not be significant in describing the mechanics of compaction. All the published curves show scatter of porosity versus depth, and therefore the curves on which the equations are based are not necessarily unique. Hedberg (1936) concluded that compaction is a response to a series of discrete processes and no universal porosity-depth profile will be possible due to the large number of variables. This fact was also a conclusion of Gretener & Labute (1969), and Equation 3 of Bridge & Leeder (1979) also implies more than one process occurs during compaction. However, the curve of Baldwin & Butler (1985) implies that compaction is a continuous process and is not segmented during sediment burial. This will be discussed in later chapters dealing with the modelling of compaction, and in section 2.3 of this chapter.

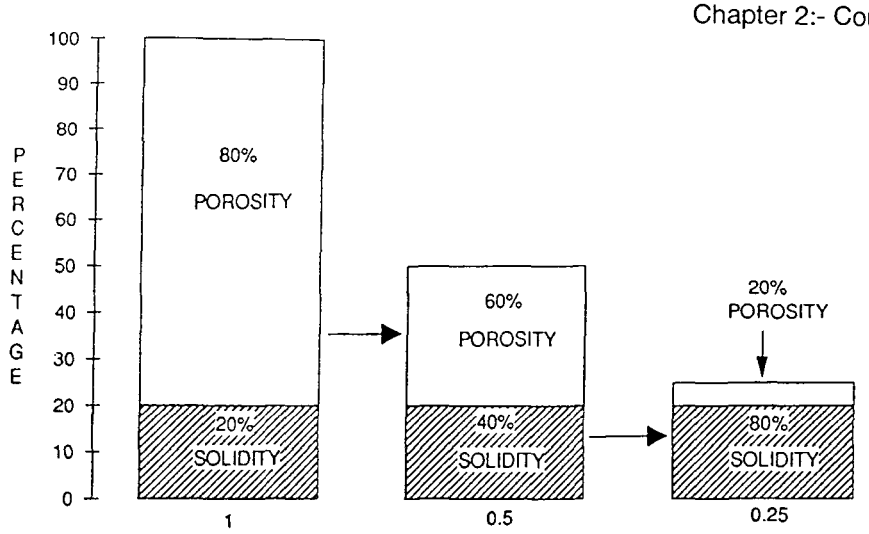

Figure 2.10 Solidity versus porosity. Percentages in clear blocks are porosity, percentages in shaded areas are solidity, and bottom ratios are length reductions (modified from Shinn & Robbin, 1983).

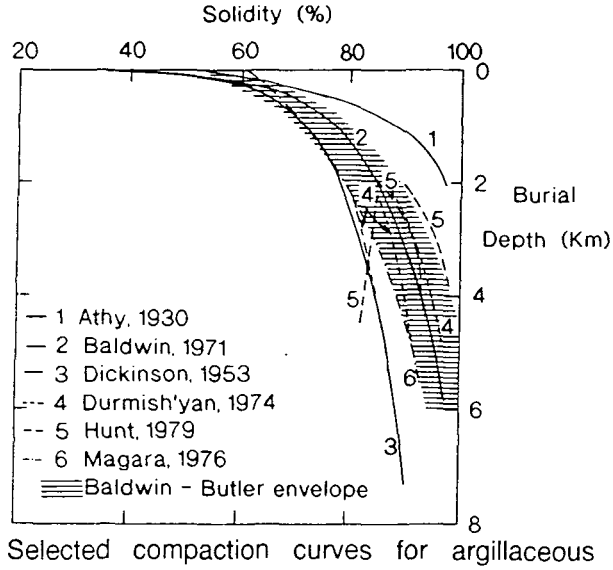

Figure 2.11 Selected compaction curves for argillaceous sediments, and best-fit envelope (modified from Baldwin & Butler, 1985).

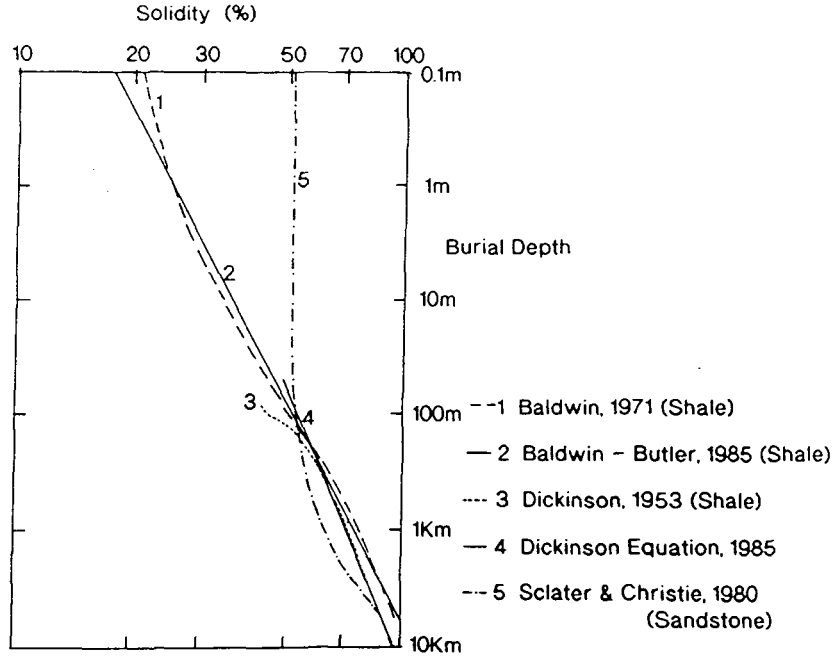

Figure 2.12 Log-log plot of compaction curves. 1, 3, and 5 are empirical; 2 and 4 represent equations (modified from Baldwin & Butler, 1985).

From a mathematical point of view there has long been a debate as to the form of the porosity-depth curve, ranging from an exponential curve, a straight line, or a power-law curve. Athy's (1930) law proposed an exponential curve for the porosity-depth trend, and this has certainly been widely accepted by the vast majority of subsequent researchers. His equation, providing an answer for porosity (P), takes the form:-

$$P = P_0.e^{-bz} \qquad \text{(equation 2.3)}$$

where P_0 is the average porosity of clays at the depositional surface, b is a constant, and z is burial depth. Problems have since arisen in Athy's work as he used a surface porosity for his muds of 48%, a value that is much lower than those obtained from modern coring (Truyol, 1989). Athy also estimated 425m (1,400ft) of beds had been eroded before coring, and questions have been raised about the structural deformation of the study area (Rieke & Chilingarian, 1974). Both Korvin (1984) and Bayer & Wetzel (1989) pointed out that Athy's law is only applicable to thick, homogeneous mudstone sequences. Both sets of workers have since published slight variations on Athy's law for their compaction laws concerning muds.

Utilising standard methods of statistical physics, Korvin (1984) attempted to mathematically prove the empirical exponential compaction law of Athy (1930), which has been widely accepted and confirmed by many examples (Hedberg, 1926, 1936; Athy, 1930; Dickinson, 1953; Maxwell, 1964; McCulloch, 1965; Watts, 1981; Luo et al., 1993 etc.). Some workers, however, have questioned the exponential law for porosity versus depth (Baldwin & Butler, 1985), and have instead favoured straight line or power law curves. Korvin (1984) points out that the reason for this apparent discrepancy is that the Athy compaction law describes the final equilibrium state of shales after part of the pore water content has been expelled vertically upwards. In the case of sand - shale interbedding there is the distinct possibility of significant horizontal migration of pore fluid, as modelled by Magara (1976), so that the exponential compaction law should not strictly apply.

Korvin (1984) produced a modified version of Athy's formula:-

$$\phi(z) = \frac{\phi_0.\exp[-(1+\phi_0)Z]}{Z_0} \qquad \text{(equation 2.4)}$$

where $\phi(z)$ is the porosity at depth Z, ϕ_0 is the surface porosity, and Z_0 is the depth of the basement. Working on the principle that the evolution of closed systems always proceed towards the maximal entropy, Korvin (1984)

proceeded to prove that Athy's empirically derived exponential compaction law is mathematically correct. This simply means that the exponential compaction law expresses the maximum entropy equilibrium state of the pores in the rock; that is compaction is an irreversible process where clay particles tend towards a statistically defined final equilibrium. The modified equation (2.4) also qualitatively expresses the inverse dependence of compaction rate on basin depth, reported by Nafe & Drake (1957). Within the equation (2.4) the surface porosity, $\varnothing_0$, and the average porosity $\varnothing$ are both functions of the total amount of water squeezed out of the shale, which are in turn linked to geological time, temperature, granulometry and possibly depth. However, if the surface porosity, $\varnothing_0$, of the shale is known and is fairly constant, the inverse relation of compaction rate to basin depth appears to be an exact law (Korvin, 1984).

Korvin (1984) noted that the principle of maximum entropy only determines the final, asymptotic state of the system studied as the time, t, tends to infinity. It does not, however, provide the time - history of the evolution towards this final state. His equation therefore cannot be used to provide a porosity-depth curve for compactional modelling, such as estimating shale thickness during various stages of burial (Anderson, 1991). Furthermore, any large deviation from the maximal entropy state (i.e. from Athy's law) reflects some discrepancy (sand - shale interbedding, recent tectonic movements, or sediment heterogeneity), or it simply refers to the fact that the shale column is too young and the equilibrium state has not yet been achieved. In the latter case one would expect some quantitative relationship between the deviation of the porosity-depth curve from Athy's law and the age of the shale (Korvin, 1984).

From the mid 1980's there appears to have been a growing trend of defining porosity-depth curves using theories once again developed from soil mechanics, and laboratory tests on argillaceous sediments. Jones & Addis (1985) utilised clay stress paths, as defined by Atkinson & Bransby (1978), and critical state diagrams to investigate the range of porosities possible in argillaceous sediment as the effective stress increases. They showed how the porosity of argillaceous sediments is determined by the magnitude of the effective stress acting within the sediment, the previous stress history and, especially at shallow burial depths, the mineralogy and nature of the depositional environment. Because of the dependency of porosity on the mean effective stress, no simple relationship exists between porosity and depth of burial but in the absence of overpressured pore fluids, and assuming

the sediment is not overconsolidated, it is possible to contour the porosity/effective stress diagram in terms of burial depths (Jones & Addis, 1985). Figure 2.13 shows the range of possible burial stress paths for clay for the first 100m of burial as defined by Jones & Addis (1985), using data on naturally occurring clays. The actual stress path followed by a particular clay is likely to lie somewhere within this envelope and depends on the actual clay mineralogy and depositional environment rather than the exact nature of the stress system. The authors' note, however, that the data used in their research is not complete, and it is possible that some clays, especially those with large concentrations of montmorillonite or quartz, may lie outside the envelope outlined in Figure 2.13.

It becomes very clear from the literature that porosity-depth curves for argillaceous sediments vary greatly, and this variety probably reflects numerous factors which are often superimposed on each other. Dzevanshir et al. (1986) lists these factors as: 1) geological age; 2) effective stress; 3) lithology; 4) mineralogy; 5) tectonic stresses; 6) speed of deposition; 7) thickness of sedimentary formations; 8) sorting; 9) amount and nature of cementing material; and 10) chemistry of interstitial solutions. They also suggested that perhaps one method of solving the problem of the porosity-depth relationship is to establish the dependence of porosity on the most important natural factors such as depth of burial, geological age and lithology, whose influence greatly overshadows (or incorporates) the influence of other factors. Utilising an Athy-type formula based on published data and developed by Dobrynin (1970):-

$$\varnothing = \varnothing_0 . e^{-0.014\beta D} \qquad \text{(equation 2.5)}$$

where $\varnothing_0$ = initial porosity of clays, $\varnothing$ = porosity of clays at burial depth D (in metres) and β = coefficient of irreversible compaction (MPa^{-1}), Dzevanshir et al. (1986) produced an equation (see below) which reflects porosity ($\varnothing$) to depth of burial (D, in metres), geologic age (A, in millions of years), and lithology (R = rate of thickness of shale/total thickness of terrigenous deposits).

The value of the coefficient of irreversible compaction, β, in equation 2.5 includes all the previous mentioned variables apart from depth of burial. Dzevanshir et al. (1986) correlated β with geological age and lithology of the terrigenous complex by comparing published porosity-depth curves, first of differing geological ages, and secondly of the same age but different lithologies. From this comparison the authors managed to relate β to geological age and lithology of the terrigenous complex as follows:-

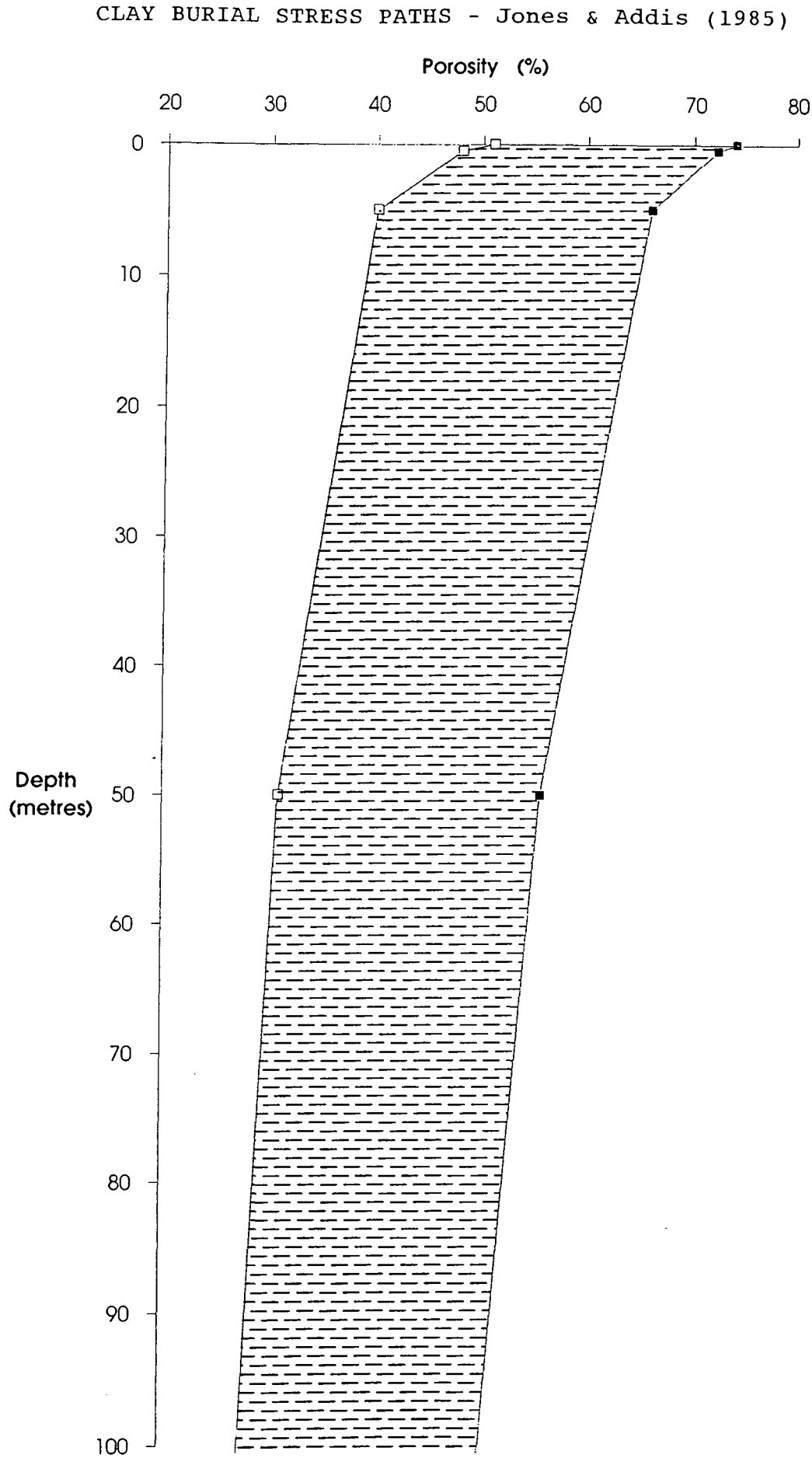

Figure 2.13 Porosity-Depth relationship for shallow burial, based on data from Jones & Addis (1985).

$$\beta = (26.62 \log A - 8.42) \times 10^{-3} \qquad \text{(equation 2.6)}$$

$$\beta = (14.0 - 166.6 \log R) \times 10^{-3} \qquad \text{(equation 2.7)}$$

Combining these two equations, equation 2.8 is derived. A nonogram, illustrated in Figure 2.14, enables rapid solution of equation 2.8.

$$\varnothing = \varnothing_0.\exp[-0.014(13.3 \log A - 83.25 \log R + 2.79) \times 10^{-3} D] \qquad \text{(equation 2.8)}$$

Utilising statistical analysis of DSDP data, laboratory experiments and theoretical models, Bayer & Wetzel (1989) attempted to derive standard compaction curves for various deep-sea, argillaceous sediments that are in compaction equilibrium with their overburden. They essentially follow the work of Hamilton (1976), separating the core data into five lithologies: 1) terrigenous mud; 2) pelagic clay; 3) carbonate ooze; 4) radiolarian ooze; and 5) diatomaceous ooze. Samples were selected carefully so that they were not taken from overpressured zones, but they were taken from sections that had accumulated continuously so that ageing effects (Dzevanshir et al., 1986) could be ignored. Like Hamilton (1976), they corrected the data for elastic rebound after removal from the borehole using laboratory investigations of the samples. Using Athy's exponential compaction law (1930), and Hamilton's (1976) data, Bayer & Wetzel (1989) show how there is a clear relationship between depth of burial and porosity (Fig. 2.15), which is an exponential relationship for terrigenous mud and pelagic clay. However, Athy's law appears to break down when dealing with radiolarian and diatomaceous ooze. Bayer & Wetzel (1989) conclude that Athy's law is only applicable to homogenous sediment (as stated by Korvin (1984)), and, that it may be restricted to certain sediment types, such as shales, or perhaps certain porosity intervals. Compaction occurring at greater depths and in 'abnormal' sediments does not follow Athy's law because this equation can only handle a single parameter for compaction, there is no possibility to take account of the interaction of multiple processes (Bayer & Wetzel, 1989). The authors proceed to modify Athy's equation to encompass all sediment types, not just clays, so that secondary effects of grain modification, which they state as being the primary cause for these sediments not obeying Athy's law, are also taken into account. They also show how the empirical data of Hamilton (1976) correlates closely to their modified Athy equation.

Recent Compaction Studies

Luo et al. (1993) addressed the problem of the spatial variability of the compaction coefficients of argillaceous sediments used within Athy's porosity-

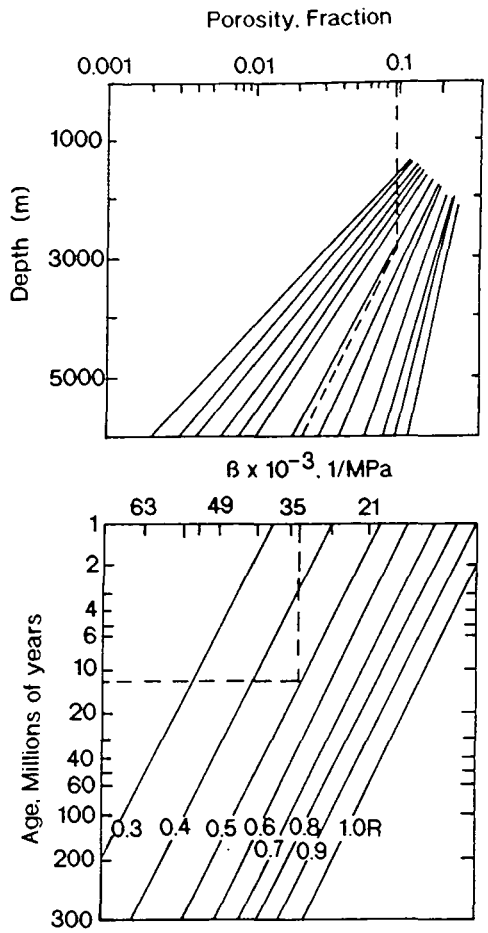

Figure 2.14 Nonogram for determining porosity at a particular depth of burial using geological age and lithology (ratio of thickness of shales/total thickness of terrigenous complex) as controlling factors. Enables the solving of equation 2.8 (after Dzevanshir et al., 1986).

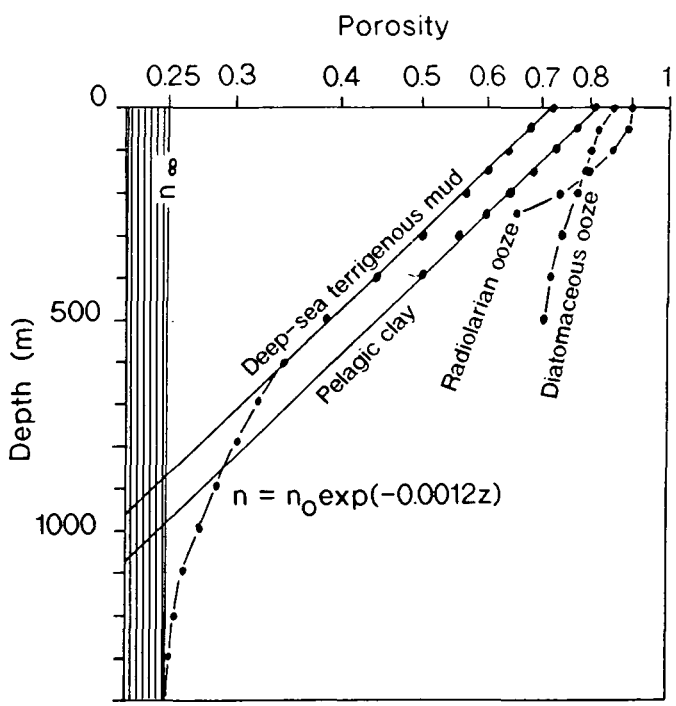

Figure 2.15 Semilogarithmic porosity-depth relationship for various sediments for which the data have been taken from Hamilton (1976). Clay rich sediments follow a simple exponential equation over a sufficiently long depth interval. Within this interval they can be approximated by a common regression function, as indicated. The regression function was derived from data of DSDP site 511, indicating that some general "laws" may exist for clay-rich sediments (modified from Bayer & Wetzel, 1989).

depth equation (the variable b in equation 2.3). They suggest that the main control upon the compaction coefficients is the microfabric of argillaceous sediments inherited from the environmental factors at the time of their deposition, and the depositional process of the sediment itself. Variations in the compaction coefficients therefore dictate the compactional behaviour of the sediment, and thus effect the production of overpressure within shale sequences. However, difficulties still exist in accurately measuring the compaction coefficients of argillaceous sediments, and Luo et al. (1993) propose the use of *in-situ* values obtained from geophysical well logs. Such geophysical well logs have been widely and successfully used in compaction studies (e.g. Hottman & Johnson, 1965; Ham, 1966; Fertl, 1976; Magara, 1978; Serra, 1984; Chen & Luo, 1988) to define a normal, characteristic compaction trend for each well. This method is not only beset with empirical corrections which cast doubt on its accuracy, but it also requires that density, neutron and sonic logs are run throughout the formation in question. These logs are usually confined to reservoir formations only. Therefore this method is impossible to apply to near-surface compaction phenomena, and is probably of only limited value to studies aimed at deeper burial of reservoir formations.

The final compaction theory and model for argillaceous sediments once again returned to the principles of soil mechanics theory. It was also the first research to recognise, and model, the interrelationship between the **rate of compaction** of the sediment being loaded and the **sedimentation rate** (i.e. the rate of addition of load). Audet & McConnell (1992) presented a mathematical model for one-dimensional compaction of an accreting layer of argillaceous sediment. Additional theoretical details of their mathematical modelling are given in Audet & Fowler (1992). They showed how the extent of abnormal pore fluid pressure (overpressure) develops depending on the sedimentation parameter, λ, which is a dimensionless group representing the ratio of the sediment's hydraulic conductivity to the sediment accumulation rate. It is defined by:-

$$\lambda = \frac{k_1}{V_0}\left(\frac{\rho_s}{\rho_f - 1}\right) \qquad \text{(equation 2.9)}$$

where k_1 is the hydraulic conductivity of the sediments, V_0 is the time-averaged sedimentation rate, ρ_s and ρ_f are the mass densities of the sediment grains and the pore fluid, respectively. The sedimentation parameter, λ, represents the ratio of the rate at which pore fluid moves

through the porous sediments versus the rate of overburden accumulation at the depositional surface (Audet & McConnell, 1992). When $\lambda >> 1$, fluid is expelled from the compacting sediments sufficiently fast that the pore fluid pressure is normal or hydrostatic. Conversely, when $\lambda << 1$, corresponding to relatively fast sedimentation rates, pore fluid is retained within the sediments with the consequence that the pore fluid pressure is abnormally high (Audet & McConnell, 1992). Figures 2.16 and 2.17 graphically show the results of this modelling, firstly using porosity versus depth (Fig. 2.16), and secondly pore pressure versus depth (Fig. 2.17) at different geological times (t), to show how appreciable amounts of overpressure may be achieved if the sedimentation rate is high (i.e. $\lambda << 1$).

The initial porosity of the sediments was taken by the authors as being 50% (0.5 on Figure 2.16) because their studies were primarily interested in the mechanical behaviour of the sediments once they have developed an appreciable fabric and microscopic structure. When the initial porosity, $\varnothing_0$, is greater than 0.5 (50%), the sediment volume consists mostly of pore fluid, and the clay particle - pore fluid mixture behaves essentially like a concentrated suspension. Therefore, for mixtures with $\varnothing_0 > 0.5$, the compaction process is best described as hindered sedimentation and the concept of effective stress is not strictly valid (Audet & McConnell, 1992). However, the graphs shown in Figures 2.16 and 2.17 clearly show the important relationship between sedimentation rate, compaction rate (combined in the sedimentation parameter, λ), and time.

The work of Audet & McConnell (1992) also highlighted some other important factors that were previously glossed over or completely forgotten by previous researchers. Firstly Audet & McConnell (1992), with the use of compression indices (C_C) (Lambe & Whitman, 1979; Burland, 1990), showed how slight compositional variation in argillaceous lithologies compact differently as they are loaded (Fig. 2.18). The porosity-depth curve of Figure 2.18 show that for a clay sediment of $C_C=1$, comparable to the value for a plastic clay like montmorillonite or illite, the porosity profile shows a significant loss of porosity near the basement. In contrast, for $C_C=0.25$, a value typical for silt-rich clays, total porosity loss is less, but most of this porosity loss is in the upper region of the basin near d=0.

Finally, Audet & McConnell (1992) showed the effects of changes in permeability on one-dimensional compaction (Fig. 2.19). The parameter α is used to describe how quickly the permeability of the clay decreases as the porosity is reduced, and it is therefore used by the authors to model changes

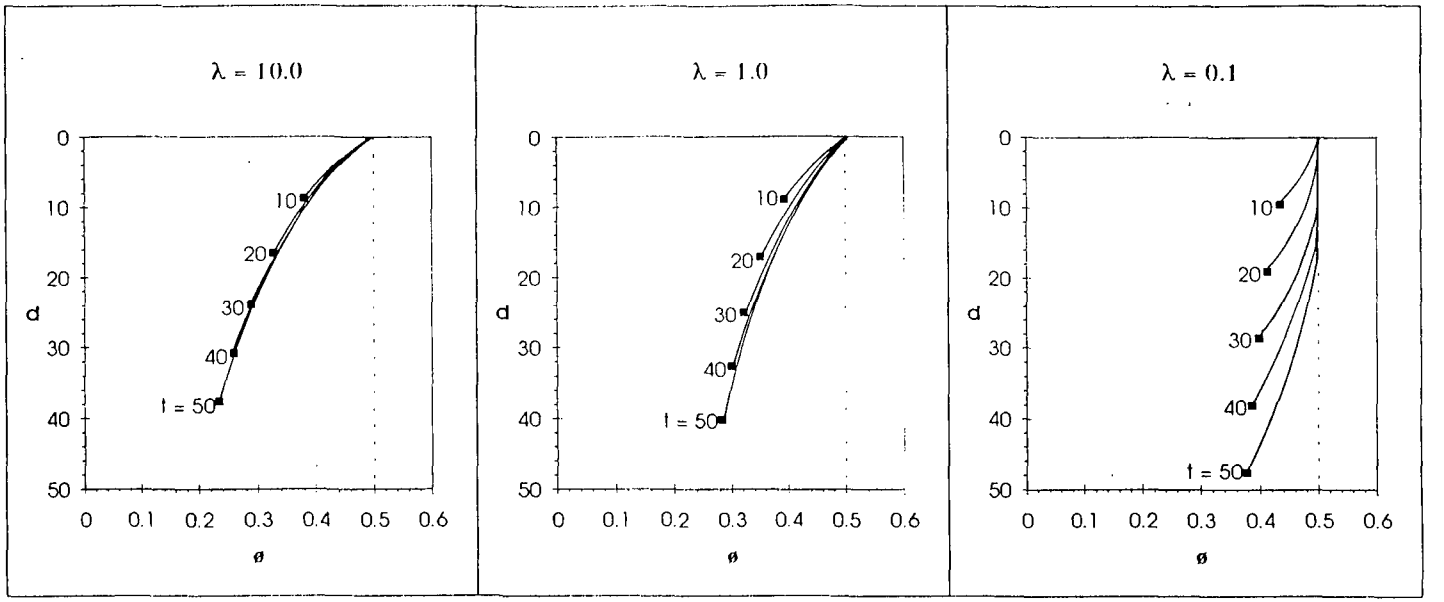

Figure 2.16 Porosity (ø) versus depth (d), for different times; t=10, 20, 30, 40, 50. The vertical dotted line at ø=0.5 is a reference line through the initial porosity value (modified from Audet & McConnell, 1992).

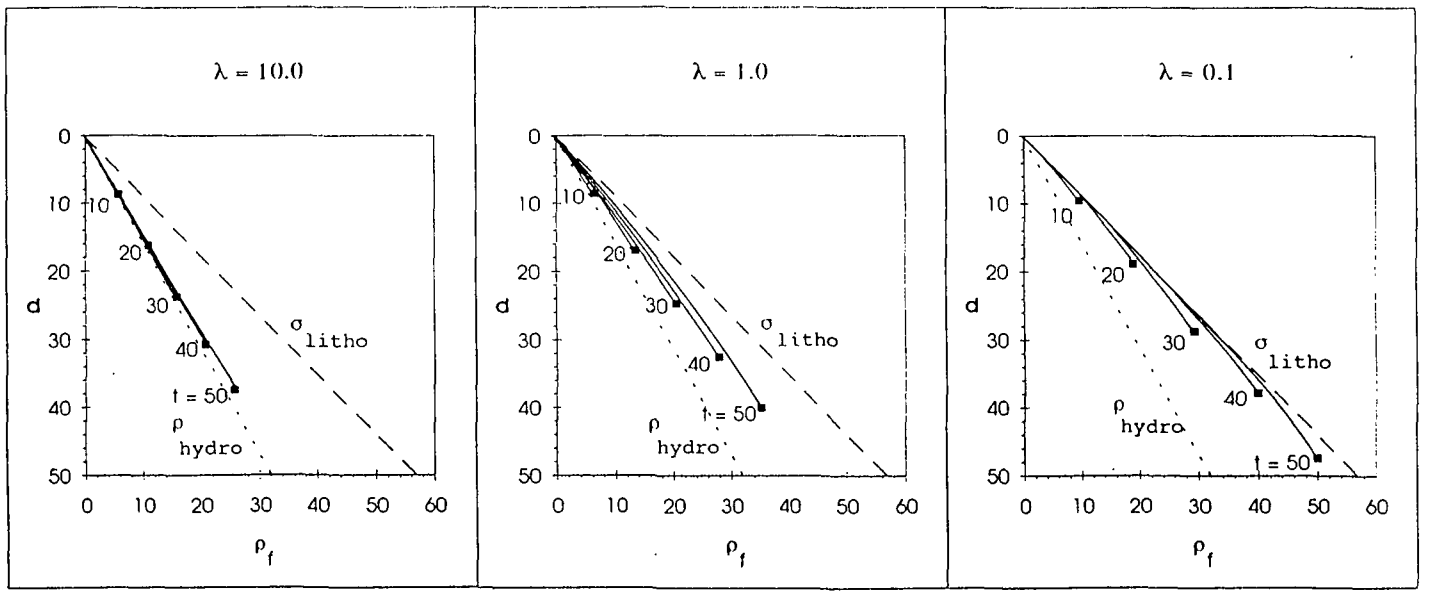

Figure 2.17 Pore pressure (ρ_f) versus depth (d), for different times; t=10, 20, 30, 40, 50. The dotted line represents the hydrostatic pressure, ρ_{hydro}, and the dashed line represents the lithostatic stress, σ_{litho} (modified from Audet & McConnell, 1992).

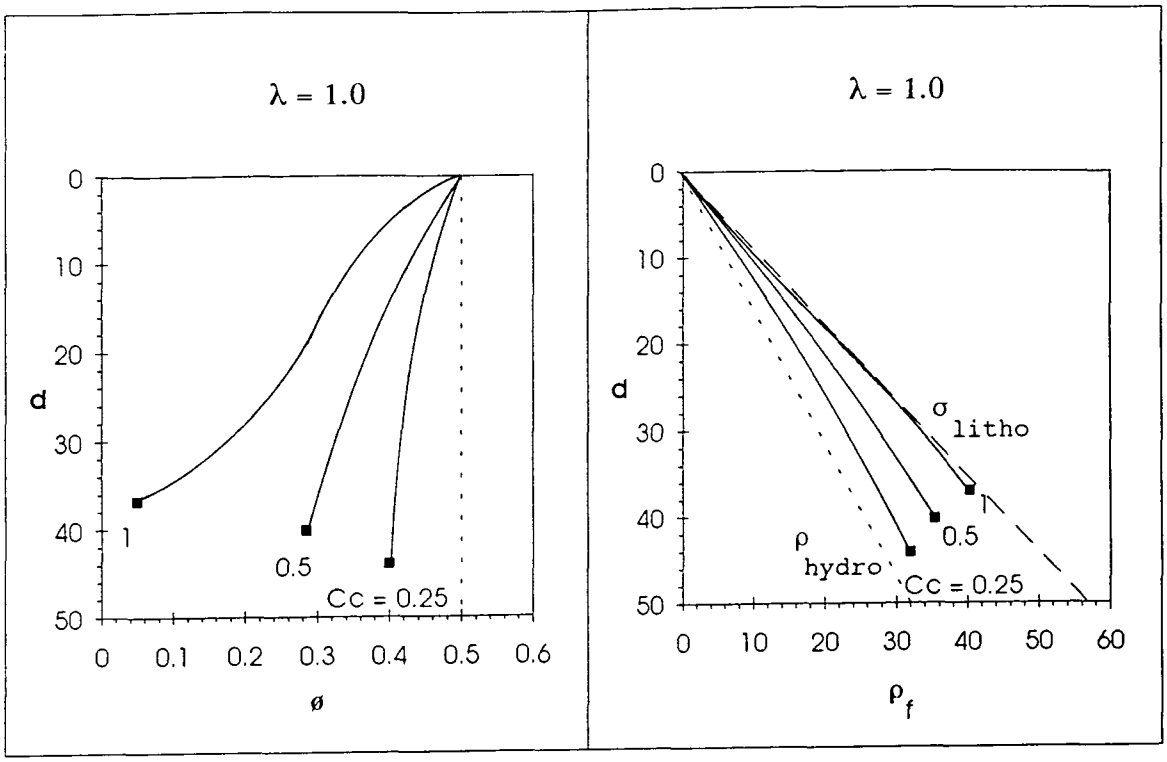

Figure 2.18 Porosity (ø) versus depth (d), and the pore pressure (ρ_f) versus depth (d) plots for λ=1 at t=50, and different values of the compression index: C_c=o.25, 0.5, 1 (modified from Audet & McConnell, 1992).

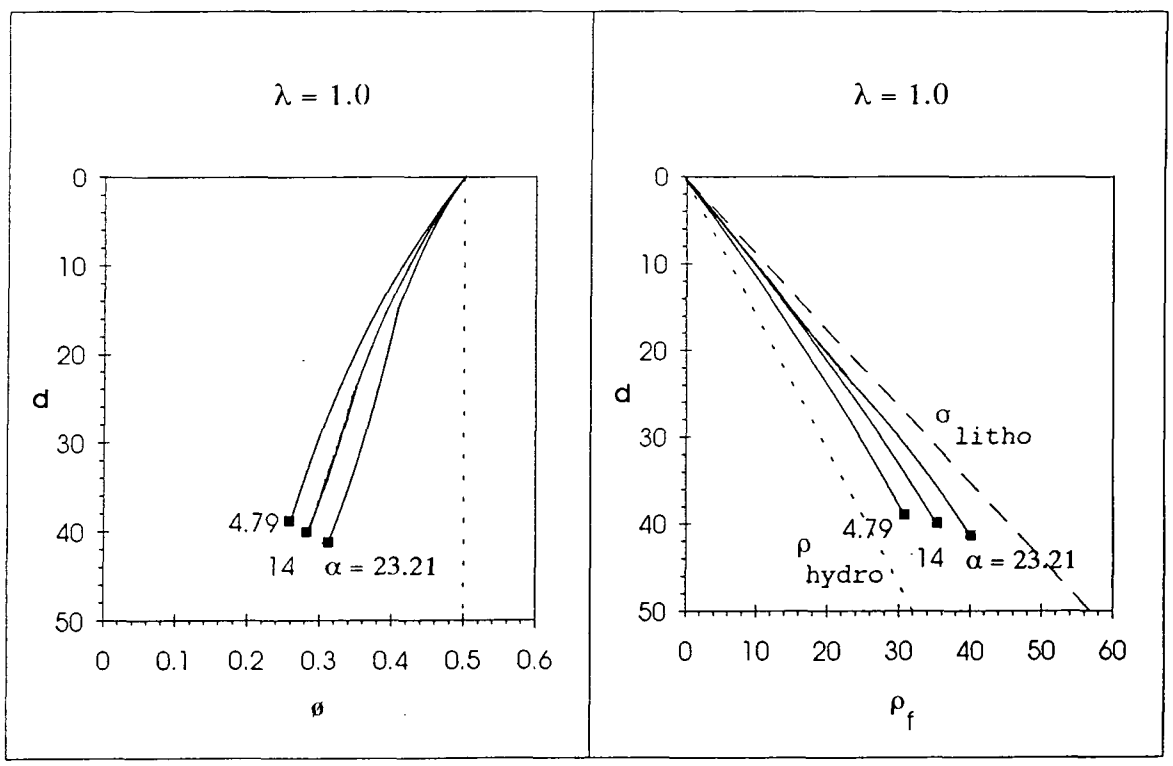

Figure 2.19 Porosity (ø) versus depth (d), and the pore pressure (ρ_f) versus depth (d) plots for λ=1 at t=50, and different values of α=4.79, 14.0, and 23.21 (modified from Audet & McConnell, 1992).

in clay permeability. The porosity-depth curve on Figure 2.19 shows that near the depositional surface the porosity profiles do not depend significantly on the permeability. In contrast, for d>6, the porosity-depth profiles show that when the permeability decreases slowly with porosity, the case of α=4.79, there is a greater porosity loss than when the permeability decreases rapidly with porosity, α=23.21.

It becomes clear from this work that the compaction of argillaceous sediments is extremely complex and depends on many variables, firstly dealing with the depositional environment of the clay (i.e. the exact lithology and compression index, C_C, and the initial porosity and permeability of the sediment), and secondly, dealing with the rate of loading compared to the rate of compaction of the sediment. All these variables and the interaction between them need to be understood for compactional modelling of a depositional system. Later chapters of this work will show how this present study has addressed these variables, mainly through field observations and modelling, and how the knowledge gained may be applied to the modelling of early compaction within the siliciclastic submarine fan depositional environment.

Conclusions Concerning the Compaction of Argillaceous Sediments.

1. Deep marine muds have the greatest depositional porosity of ~80 %.
2. The compaction process is extremely complex, and the porosity evolution is probably best summarised by the porosity-depth profile of Baldwin & Butler (1985).
3. The aspect of timing is very important indeed in the compaction process of deep-sea muds. i.e. Rate of compaction versus rate of deposition (see section 2.3). This is primarily due to the low permeabilities of muds produced by shallow burial.

2.2.2 Compaction of Coarse-Grained Sediments.

As explained in section 2.2, the original depositional porosity of the sediment is a major control on the compactional response of the sedimentary unit to overburden pressure. The previous section also shows how argillaceous sediments, especially deep marine pelagic clays, have the highest original, depositional porosities, averaging around 80%. For coarse-grained sediments, exclusively sands in this study, original depositional porosities are significantly lower than their fine-grained counterparts. Estimates of porosity vary from author to author, and there is the difficulty of

measuring near-surface porosities, due to the tendency of the coring technique disturbing the sediment, and rendering measured porosity/permeability values questionable. Coring disturbance is particularly common in unconsolidated sands. Early porosity measurements from naturally occurring sands range between 34% to 39% (Terzaghi, 1925; Trask, 1931; Fraser, 1935). In contrast, work carried out using artificially generated sands, give estimates of depositional porosities for such sediments ranging between 35% and 43% (Gaither, 1953; Ludwick, 1956; Scott, 1960: Bernal & Mason, 1960; Rogers & Head, 1961, Bernal & Finney, 1967; Morrow et al., 1969).

Near-Surface Textural Parameters.

Some recent works (Pryor, 1973; Beard & Weyl, 1973; Scherer, 1987) collectively provide a sizeable dataset for near-surface sand porosities and permeabilities, and also summarise most of the earlier works cited above. The first study primarily focused on depositional porosities was carried out by Pryor (1973), who studied 922 oriented and undisturbed sand samples from river bars, beaches, and dunes undergoing active sedimentation. From these three environments Pryor (1973) determined porosity and permeability values for his samples to provide a dataset concerning the reservoir characteristics of freshly deposited sands. The knowledge of sandstone depositional characteristics combined with a knowledge of the modifications impressed upon them by post-depositional processes is required to give a clearer understanding of the heterogeneous character of sandstone reservoirs, and some of the possible controls on the heterogeneity. Pryor (1973) collected samples using an aluminium tube pushed carefully into the unconsolidated sediment, avoiding the effects of aeolian reworking by taking measurements from the samples at six inches burial depth. Table 2.1 shows the data collected by Pryor (1973), with the result that mean porosities determined by him for the differing environments average slightly higher than 45%. His results also show that the permeability of recent sandstone bodies varies greatly, illustrating the heterogeneity of flow pathways of equivalent reservoir sands, an important observation when dealing with compaction and fluid flow through sedimentary units.

Trench sections provided Pryor (1973) with a vertical face to measure the porosity and permeability distributions of river bar, beach, and dune sands. These sections should therefore show the porosity and permeability-depth relationships for the first few feet of burial, as measured by Pryor (1973)

SAMPLE LOCATION	PERMEABILITY Means (Darcys)	POROSITY Means (%)
Wabash River Bar		
Total	77.86	44.95
Profile	79.21	44.85
Grid	77.4	44.41
Trench	78.88	45.22
Whitewater River Bar		
Total	94.74	36.92
Profile	81.95	33.76
Grid	50.55	40.78
Trench	124.95	38.57
Mississippi River Bar		
Total	6.39	44.98
Bedding Units	9.77	45.62
Boundary Units	3.02	44.35
Ship Island Beach		
Total	60.82	45.94
Profile	62.82	46.11
Grid	80.29	47.14
Trench	52.21	45.41
Santa Rosa Island Beach		
Total	75.34	49.61
Profile	76.62	48.24
Grid I	73.48	51.29
Grid II	72.42	48.26
Trench	75.61	50.75
Sabine Pass Beach		
Total	6.88	45.08
Grid	5.27	44.57
Trench	8.49	45.59
Santa Rosa Island Dune		
Trench	71.59	47.9
St. Andrew Park Dunes		
Total	36.17	50.82
Profile	35.89	49.07
Trench	36.58	52.83

Table 2.1 Permeability and porosity data for Holocene sand bodies (data from Pryor, 1973).

directly from the field. Figure 2.20 shows the vertical trench section through the Wabash River bar, illustrating the porosity-depth relationship for the first three feet (1 metre) of burial. It can be seen from this section that there is very little systematic change in a sand porosity over this depth of burial, and perhaps individual sand units, separated by bedding surfaces, each have their own unique porosity-depth profile, which vary slightly from one unit to another depending on depositional and textural variations within these units.

Research into the effect of petrological and geochemical factors influencing the porosity and permeability of shallow buried clays and sands was carried out by Meade (1966), prior to Pryor's (1973) study. This work was then followed later by Beard & Weyl (1973) who documented the influence of texture on the porosity and permeability of unconsolidated sand. Meade (1966) showed that the porosity of sands is not uniquely related to increases in overburden load, but it is also related to texture, composition and the depositional history. Studying the early stages of compaction using laboratory techniques, Meade (1966) was able to show that for overburden loads between 0 and 100Kg per cm^2 (approximately 0 - 500m depth of burial) different factors influenced the porosity evolution of sand. From initial depositional porosities varying from 30% to 50%, Meade (1966) showed that the major factors influencing porosity are the textural characteristics of the constituent particles: size, sorting, roundness, shape, and flexibility. Well sorted sands have greater porosities than poorly sorted sands of equivalent grain size (Rogers & Head, 1961), and experimental results of Meade (1966) showed how this differential persists during burial (Fig. 2.21a). These experimental results also showed how angular sands have greater initial porosities, reflecting the instability of the initial packing of the angular particles, and are therefore more compressible than rounded sands during early burial (Fig. 2.21b). This latter relationship was also observed in low-pressure experiments on sandstones by Fatt (1958), who noted that sandstones consisting of poorly sorted angular grains were more compressible than sandstones whose grains were well sorted and rounded.

Beard & Weyl (1973) investigated the relations between porosity, permeability, and texture of artificially mixed and packed sands, to determine the approximate porosity and permeability values to be expected for unconsolidated sand of eight grain-size subclasses and six sorting groups. Porosity values were determined for two packings, designated as "dry loose" and "wet-packed". Porosity data for "wet-packed" sand samples remains about the same for changes in grain size of a given sorting, but decrease

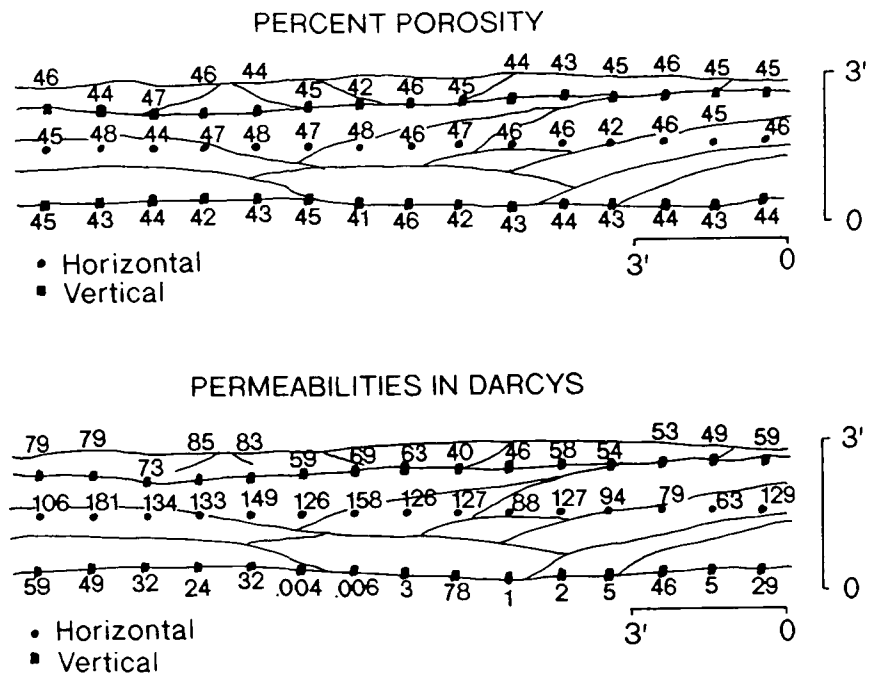

Figure 2.20 Trench sections through sand-scale front on Wabash River bar. Sections are taken parallel to the front (modified after Pryor, 1973).

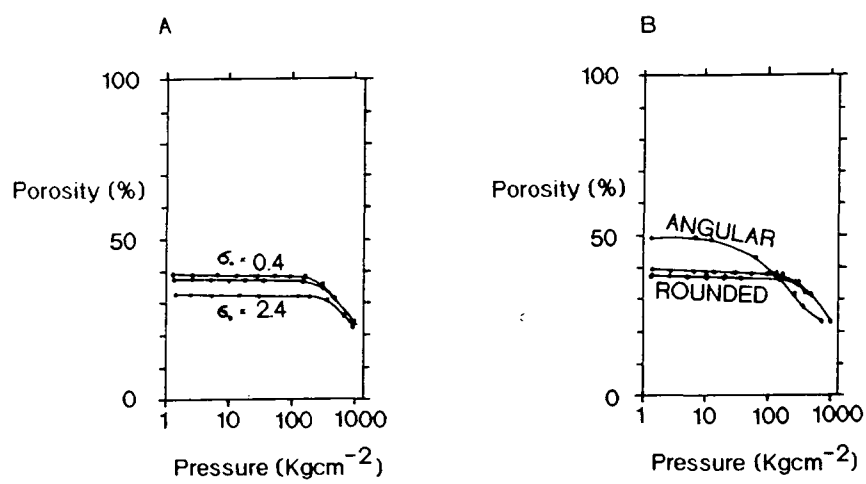

Figure 2.21 (A) Influence of sorting in well rounded quartz grains. Sorting index (σ_0) defined by Inman (1952); median diameter of the two better sorted sands, 0.60mm; median diameter of sand with poorer sorting, 0.48mm. (B) Influence of rounding of quartz sands, 0.42 to 0.84mm in size (modified form Meade, 1966).

from an average of 42.4% for extremely well-sorted sand to 27.9% for very poorly sorted sand (Table 2.2) (Beard & Weyl, 1973). Beard & Weyl (1973) concluded that grain size is not a major control on sand porosity for sands of similar sorting, but permeability increases with increasing grain size. Sorting, however, is a very important variable when considering the porosity and permeability characteristics of unconsolidated sand. Here the work of Beard & Weyl (1973) agrees with Fraser (1935), Graton & Fraser (1935), Meade (1966) and Morrow et al. (1969), i.e. both porosity and permeability decrease as sorting becomes poorer, but both porosity and permeability increases as grain roundness decreases, and the sand is mainly composed of angular grains (Fig. 2.21b). These conclusions are confirmed by Coskun et al. (1993) using well samples, and investigated the effects of depositional texture, composition and diagenesis on the porosity and permeability of reservoir sands from undisclosed hydrocarbon areas of North America. This study illustrates the importance of understanding the depositional and early diagenetic history of sediments when modelling and assessing potential reservoir sands.

The basic conclusions of these essentially near-surface studies show that the consensus of opinion is that sands have depositional porosities averaging somewhere between 40% and 45%, and during early burial and compaction there is very little change in the porosity characteristics of sand. It also appears from these works that sorting is of first-order importance when investigating the porosity and permeability characteristics of sands. Due to the fact that sands form the majority of the world's hydrocarbon reservoirs there are many recent published studies concerning the parameters influencing the porosity and permeability characteristics of sand, and thus their reservoir potential. The following discussion summarises some of the important papers within this group, the conclusions drawn from these studies, and the importance these might have on the present study of early compaction.

Continuing on from the earlier work of Maxwell (1964), who basically investigated the influence of depth, temperature and geological age on the porosity of quartzose sandstones, Scherer (1987) reviewed thirteen parameters to determine their influence on the porosity of sandstones undergoing compaction. Scherer (1987) concluded that for basins of average geothermal gradients the first-order parameters are age (time of burial), detrital-quartz content, maximum depth of burial, and sorting. Second-order

SIZE →	COARSE		MEDIUM		FINE		VERY FINE		AVERAGE	S.D.
SORTING ↓	Upper	Lower	Upper	Lower	Upper	Lower	Upper	Lower	POROSITY	percent
Extremely Well Sorted	43.1	42.8	41.7	41.3	41.3	43.5	42.3	43	42.4	0.8
Very Well Sorted	40.8	41.5	40.2	40.2	39.8	40.8	41.2	41.8	40.8	0.6
Well Sorted	38	38.4	38.1	38.8	39.1	39.7	40.2	39.8	39	0.8
Moderately Sorted	32.4	33.3	34.2	34.9	33.9	34.3	35.6	33.1	34	1
Poorly Sorted	27.1	29.8	31.5	31.3	30.4	31	30.5	34.2	30.7	1.8
Very Poorly Sorted	28.6	25.2	25.8	23.4	28.5	29	30.1	32.6	27.9	2.8
Average Porosity	35	35.2	35.3	35	35.5	36.4	36.7	37.4		
Standard Deviation, percent	6	6.3	5.5	6.2	4.9	5.3	5	4.2		

Table 2.2 Porosity (%) of artificially mixed and wet-packed sand (data from Beard & Weyl, 1973).

parameters include depth-related temperature and median grain size, a conclusion agreeing with the experimental work of Beard & Weyl (1973).

To enable porosity prediction for quartz sands, Scherer (1987) calculated function coefficients for the relationship between porosity and the first-order parameters for 428 cases. This enabled the production of an equation which is valid for sandstones older than 3Ma with little or no cement, no leaching, depth of burial in excess of 500m, and little or no shear stresses:-

$$\text{Porosity} = 18.60 + (4.73 \times \ln \text{Quartz}) + (17.37 / \text{sorting}) - (3.8 \times \text{depth} \times 10^{-3}) - (4.65 \times \ln \text{age}) \qquad \text{(equation 2.10)}$$

where porosity is in percent of bulk volume, detrital quartz in percent of solid-rock volume, depth in metres, age in million years, and sorting is the Trask sorting coefficient.

As a small sideline to the study, Scherer (1987) also investigated the effect of pressure on compaction of sands, noting a positive correlation between pressure and porosity, as pointed out by Selley (1978) and others. For a general guide, it appears that sandstones retain approximately 1.9% more porosity for every 1,000 psi (6.9 MPa) overpressure during compaction (Scherer, 1987). However, care must be taken when applying this rule because the influence of pressure upon porosity also depends on the stage of compaction at which the overpressure developed. Compaction still appears to occur during periods of overpressure, albeit at a much slower rate (Scherer, 1987).

Cementation also plays a very important role in sandstone diagenesis, and will be dealt with in more detail in a following section. Scherer (1987) noted that cementation may play a very important role in sandstone compaction, its effects being quite different depending on the timing of the onset of sediment cementation. Cementation will of course reduce sandstone porosity along with compaction, but it may also stabilise the sandstone fabric thus inhibiting compaction and complicating porosity prediction. Near-surface cementation can sometimes be extremely good at reducing all the sandstone porosity, thus making compaction of the strata impossible during normal burial processes.

A short discussion of Scherer's (1987) paper is presented by Shanmugam & Alhilali (1988), who basically criticise Scherer's model on three points. Firstly that the importance of leaching and secondary porosity formation was ignored, secondly that the inter-relationship of variables had not been recognised, and thirdly that the data were biased. Scherer (1988) replied that his equation (2.10, in the present work) is a model that predicts

the compaction-related porosity of sandstones, according to his restrictions, and that if other local processes, such as secondary porosity or blanketing authigenic clay mineral coatings form around grains, then porosity estimates should be adjusted according to local conditions. This statement agrees with the observation of the early compaction work by Gretener & Labute (1969) who concluded that unique porosity-depth relationships probably do not exist, and local processes overprint general trends and thus need to be accounted for when predicting porosity.

The Effect of Time And Temperature.

In 1988, after studying some of the earlier conclusions of Maxwell (1964) and Scherer (1987), Schmoker & Gautier (1988) proposed that sandstone porosity should be considered in terms of its time-temperature history, a method first proposed by Van de Kamp (1976) as a better alternative to depth. Depth is merely a position co-ordinate specifying the present day location of a formation within a well. This approach uses the assumption that subsurface reactions proceed linearly with time and exponentially with temperature, i.e. chemical processes affecting sandstone burial diagenesis are considered to be dependent on the time-temperature exposure of the formation. Viewing the work of previous authors such as Baldwin & Butler (1985), and working with the fact that a linear porosity-depth model will predict a defined depth at which zero porosity exists, which in general is not observed in well data, Schmoker & Gautier (1988) concluded that sandstone porosity decreases exponentially with increasing depth of burial (i.e. in agreement with Athy (1930)). They proposed that the loss of sandstone porosity in the subsurface can be represented as a power function of time-temperature exposure:-

$$\text{Porosity } (\varnothing) = A\,(M)^{B} \qquad \text{(equation 2.11)}$$

where A and B are constants, and M is integrated time-temperature history. It is suggested that M can be approximated by a measure of thermal maturity such as Lopatin's Time-temperature index (TTI) or vitrinite reflectance (R_o).

The use of an exponential equation, rather than a linear equation to describe the porosity-depth relation is questioned by Ehrenberg (1989a) in his later comment on the paper, stating that the question of an exponential or linear trend is far from being resolved. However, it is the opinion of the present author that porosity-depth trends for sands are exponential once the whole depth range for a sedimentary unit is plotted, a view that is supported by a large amount of soil mechanics theory and experimentation. Schmoker &

Gautier (1988) do however conclude that this common observance of an exponential decrease of sandstone porosity with depth follows as a special case from their power function, a case where temperature increases linearly with depth (e.g. 34°C/Km in the North Sea, Burley et al., 1989). This situation is approximately correct for most sedimentary basins (Naeser & McCulloh, 1989; Brigaud et al., 1990).

Schmoker & Gautier (1988) proposed three advantages of their method over the traditional porosity-depth theories used in modelling processes. These were that firstly thermal maturity is a useful independent variable by which to compare sets of porosity data from differing basins around the world which have undergone different sedimentary and diagenetic histories. Secondly, they believe that plots of porosity versus a measure of thermal maturity establish norms by which unusual porosities within a sandstone sequence can be recognised. Thirdly, porosity prediction will be possible using their equation. However, Ehrenberg (1989a) pointed out that the latter two advantages can also be recognised or modelled using traditional porosity-depth methods without the use of a measure of thermal maturity. He also showed some disadvantages to Schmoker & Gautiers (1988) method, firstly that depth is a precisely measured parameter whereas measurements or calculations of maturity indices is beset with a range of uncertainties and assumptions. Secondly, Ehrenberg (1989a) pointed out that vitrinite data tend to vary depending upon who prepares and measures the sample, and that TTI values vary depending upon whose method used. The TTI calculation of Waples (1980) does not take into account the effect of compaction during burial, and it appears that the Arrhenius TTI is preferred to Lopatin TTI if comparison of sediments with variations in heating rate is desired (Wood, 1988). Schmoker & Gautier (1989a) reply that although depth is more easily and accurately determined than indices of thermal maturity, for predicting porosity or for developing models of diagenetic processes that affect porosity, time-temperature exposure is the more fundamental variable. Dykstra (1987) illustrates a method for correcting Lopatin's (1971) TTI values for sediment compaction. These CTTI values are possibly the correct variables to use in the equations of Schmoker & Gautier (1988, 1989b).

Following an identical theme Schmoker & Gautier (1989b) expanded their earlier model to encompass not only sandstone, but carbonates and shales too. The authors basically reintroduced their model as before but suggested that their data plotted for carbonates and sandstone fall in quite a narrow band, and therefore a general porosity-thermal maturity curve can be plotted

for both these sediment types, taking modal values for the constants A and B in equation 2.11 equal to 30 and -0.33, respectively i.e. for carbonates and sandstones:-

$$\varnothing = 30\ (TTI)^{-0.33} \qquad \text{(equation 2.12)}$$

This curve is analogous to a traditional porosity-depth curve, but it has the advantage of describing a temporal model for the compaction of basin sediments (Schmoker & Gautier, 1989b). As stated earlier, if temperature increases linearly with depth, exponential porosity-depth curves or curve segments follow from the more general dependence of porosity upon integrated time-temperature history (Ray, 1985; Schmoker, 1985). Using equation 2.12 Schmoker & Gautier (1989b) produced five exponential porosity-depth curves as shown in Figure 2.22a, which differ significantly because they represent porosity evolution in basins with different time-temperature histories (Fig. 2.22b). The decrease of porosity with TTI is identical in each basin (equation 2.12), but the decrease of porosity with depth varies considerably which shows that any number of porosity-depth curves can result from a single porosity-TTI function. The shaded area of Figure 2.22a represents the shale compaction envelope of Baldwin & Butler (1985). The various sandstone and limestone curves plotted encompass this shaded area, leading Schmoker & Gautier (1989b) to conclude that as long as near-surface shale compaction is ignored, the loss of shale porosity with burial can be treated analogously to that of sandstones and carbonates. In a more theoretical sense, chemical compaction laws for sandstones, carbonates and shales must all reflect processes that are dependant upon time and temperature. Schmoker & Gautier (1989b) stated that, in effect, porosity-depth curves are artefacts of burial and thermal histories, and do not characterise particular rock types or petrographic facies. The present work would tend to disagree with this statement, as here the belief is that differing lithologies, especially sand and mud, compact at much different rates and amounts in the first few hundred metres of burial. It is only when burial approaches a depth of approximately 3 to 3.5Km where exponential compaction curves for pure sands and muds appear to approximate each other, as shown by Figure 2.22a of Schmoker & Gautier (1989b). Because the present study is specifically dealing with near-surface compaction the influence of lithology is extremely important. The time factor used in Schmoker & Gautier's (1988, 1989b) work plays an important role in near-surface compaction, however, temperature will probably have little effect until burial depths increase to 100-200m.

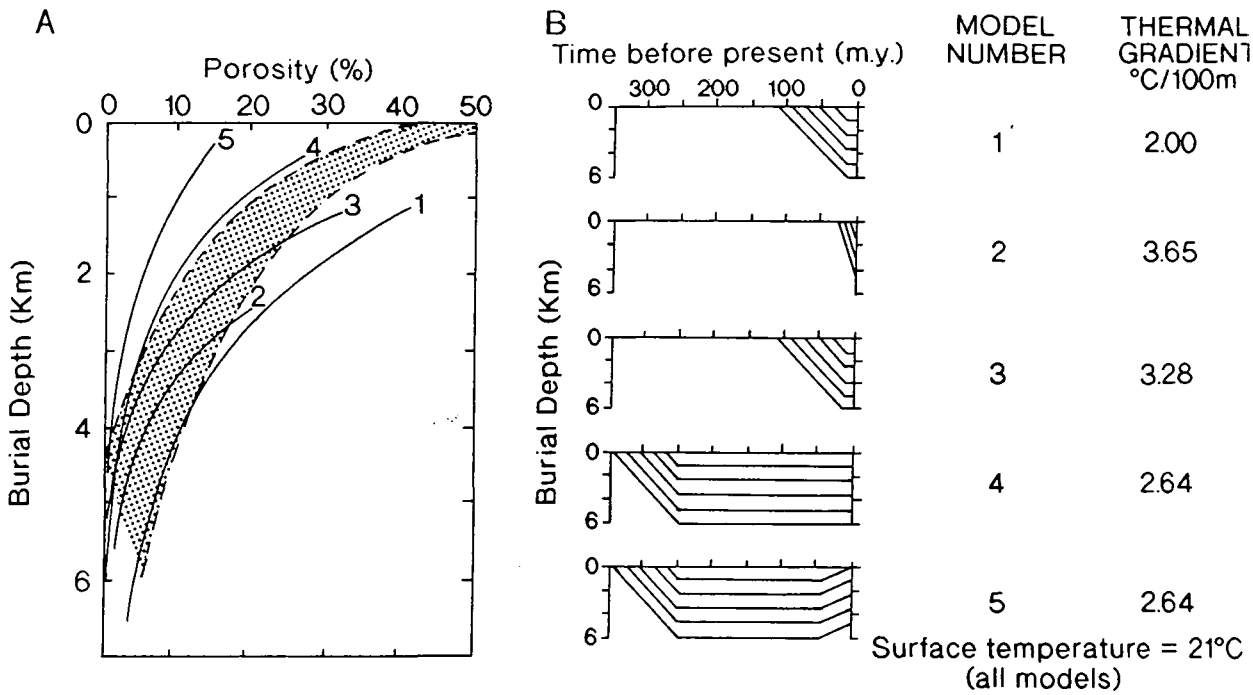

Figure 2.22 (A) Exponential porosity-depth curves derived from type curve $\phi=30(TTI)^{-0.33}$ but representing different (hypothetical) basins. Depending on time-temperature history, a wide variety of porosity-depth curves can result from a single porosity-TTI function. Porosity-depth curves encompass shale compaction envelope (shaded) of Baldwin & Butler (1985). (B) Basin models corresponding to five porosity-depth curves of 2.22a. Parallel lines of each model depict sedimentary horizons (modified from Schmoker & Gautier, 1989b).

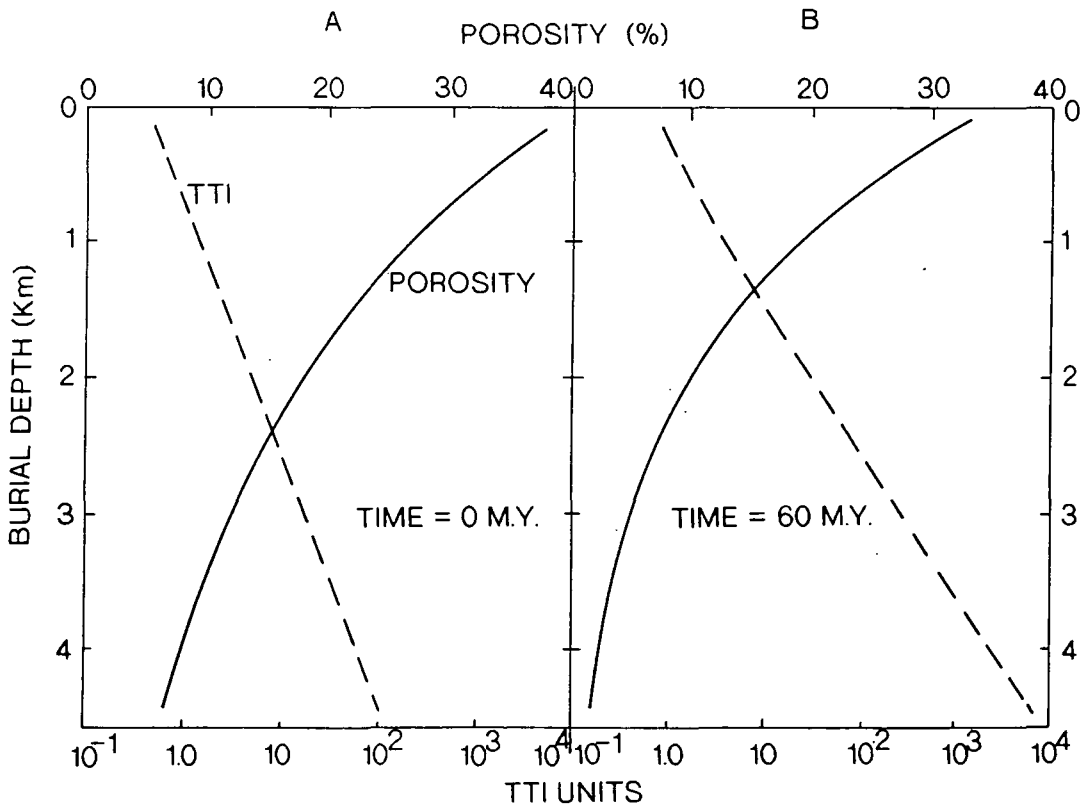

Figure 2.23 (A & B) Plots of porosity and Lopatin's time-temperature index versus depth, showing increase in TTI during a 60m.y. time span and the concomitant decrease in porosity as predicted by the equation $\phi=30(TTI)^{-0.33}$ (modified from Schmoker & Gautier, 1989b).

An important aspect modelled in Schmoker & Gautier's (1989b) paper is the effect of time and temperature on a quiescent basin. They showed that basin sediments continue to compact through geological time in response to increasing time-temperature exposure, even if the basin is quiescent. If porosity is modelled as a function of depth, porosity would not change through time in a static basin. However, when modelled as a function of integrated time-temperature history (equation 2.12), porosity decreases with the passage of time as shown in Figure 2.23a and b, at t=0 m.y. and t=60 m.y. respectively. At t=60 m.y. (Fig. 2.23b), porosity at a depth of 900m has decreased from 28 to 20%, and porosity at a depth of 4000m has decreased from 8 to 2.5%, all without the addition of extra sedimentary load.

The time for this porosity destruction, and therefore associated surface subsidence, requires tens of millions of years (Fig. 2.23). This time span also characterises tectonic driving forces of basin formations, and this model therefore shows that passive subsidence of the sediment - water interface can thus mimic tectonic processes of basin formation (Schmoker & Gautier, 1989b). If no sediment is added to this secondary, passively formed basin, no isostatic adjustment is required. However, if new sediments are deposited as the original surface subsides, isostatic adjustment to the added sediment load amplifies the total basin subsidence by a factor of roughly 2.5 (Steckler & Watts, 1978). Figure 2.24 compares the subsidence through time in the deepest part of the basin, shown in Figure 2.25, for the cases of no sediment influx, and of sediment influx keeping pace with subsidence. it shows that with continuous sediment influx approximately a thickness of 1Km can accumulate, solely dependant on the increasing time-temperature exposure of the underlying sedimentary rocks, rather than on dynamic processes of basin development.

Empirically Derived Porosity-Depth Relationships.

Hsü (1977) derived an empirical relation relating permeability to lithology and compaction from sedimentological data (grain size and sorting) and reservoir-engineering data (porosity and permeability) from the producing zones of the Ventura field, California. His empirical relation is :-

$$k = C.\ d_m 2.\mathbf{e}^{-1.31\sigma\text{ø}} \qquad \text{(equation 2.13)}$$

where k is permeability in millidarcys, C an empirical number, d_m the medium grain size in millimetres, and σø the sorting expressed in ø - standard deviation. Hsü (1977) believed that his equation, which can give an insight into the degree of compaction, coupled with a knowledge of the nature of the

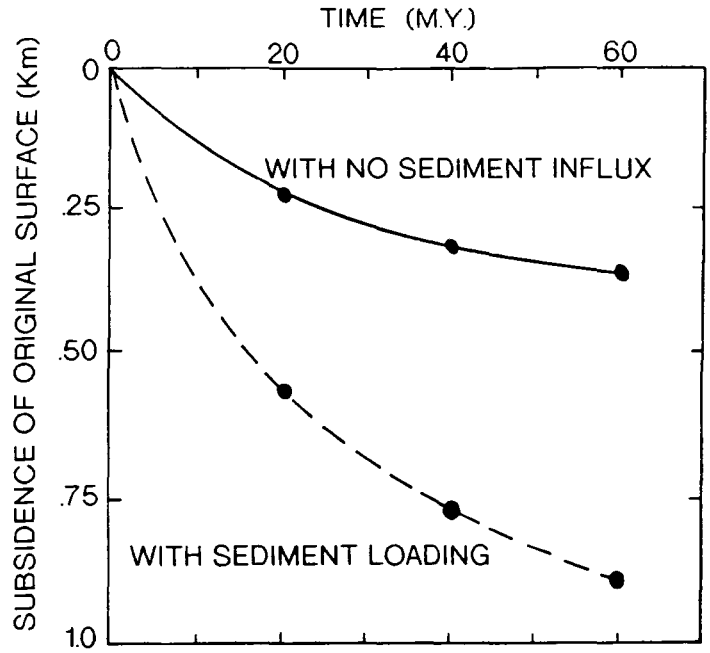

Figure 2.24 Subsidence of original surface as a function of time for deepest part of sedimentary-basin model (Fig. 2.25). Subsidence is caused by increase of TTI with time and the concomitant porosity decrease of basin sediments as predicted by the equation $\varnothing=30(TTI)^{-0.33}$. Solid curve represents sediment starved basin. Dashed curve represents case of sediment influx keeping pace with subsidence and isostatic adjustment to added sediment load (modified from Schmoker & Gautier, 1989b).

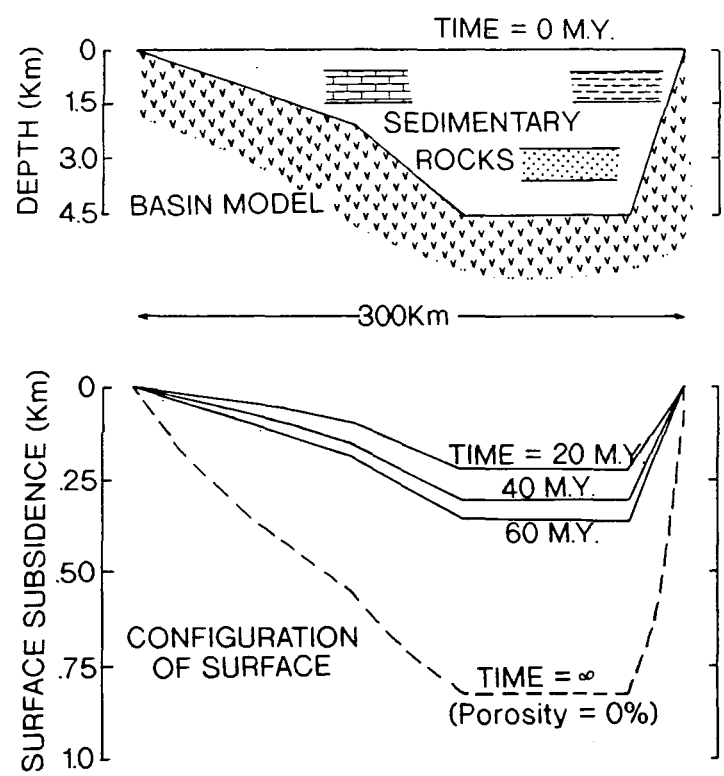

Figure 2.25 Surface subsidence of hypothetical, static, sedimentary basin caused by increase of TTI with time and the concomitant porosity decrease of basin sediments as predicted by the equation $\varnothing=30(TTI)^{-0.33}$ (modified from Schmoker & Gautier, 1989b).

sedimentary facies may determine whether development of a deep-seated reservoir will be profitable.

Leder & Park (1986) modelled the reduction of porosity in sandstones by quartz overgrowth. However, they totally ignored the effects of compaction on porosity reduction throughout the burial history of the sediments, producing 'porosity history' curves which only take the deposition of quartz overgrowth cements as the agent of porosity destruction. As stated earlier, mechanical rearrangement of grains during early compaction greatly reduces sandstone porosity from an initial depositional porosity, which as shown by Pryor (1973) and Beard & Weyl (1973) is mainly dependant on sorting. Leder & Park (1986) provided a diagram for determining the initial porosity of sands based on these earlier works (Fig. 2.26). The research of Leder & Park (1986) is very important for the modelling of sandstone porosity and permeability during burial, however, it is the opinion of this work that ignoring the effects of compaction, especially during early burial, introduces significant errors into the prediction of sandstone porosity at depth.

Three sandstone compaction studies are worthy of note at this stage. They all investigated the compaction and porosity evolution of specific sandstone horizons within hydrocarbon reservoirs, producing their own compaction laws and equations. The first study, by Wilson & McBride (1988), investigated the compaction and porosity evolution of the Pico and Repetto sandstone formations from the Ventura basin in California. The authors used the concept of contact index (CI = average number of contacts per grain) and tight packing index (TPI = average number of long, sutured, and embayed contacts per grain) for assessing the closer packing of sedimentary grains by compaction, measured from thin section analysis. This method was first proposed by Taylor (1950) in her study of fabric changes with depth in the Mesozoic sandstones of Wyoming, and was later defined by Pettijohn et al. (1972). Wilson & McBride (1988) concluded that compaction of the Pico and Repetto sandstones was more or less entirely the result of overburden pressure, with tectonic stresses only contributing to a minor degree within local areas. Temperature also appeared to play only a minor role in their study of the Pico sandstone, probably enhancing pressure solution by mainly increasing the solubility of quartz and feldspar. Their results showed that mechanical grain rearrangement of the grains as they slip past one another to achieve a closer packing relationship was the major process of porosity loss, which achieves its greatest effect at shallow depths, but continues at greater depths when projecting corners of grains are removed by pressure solution.

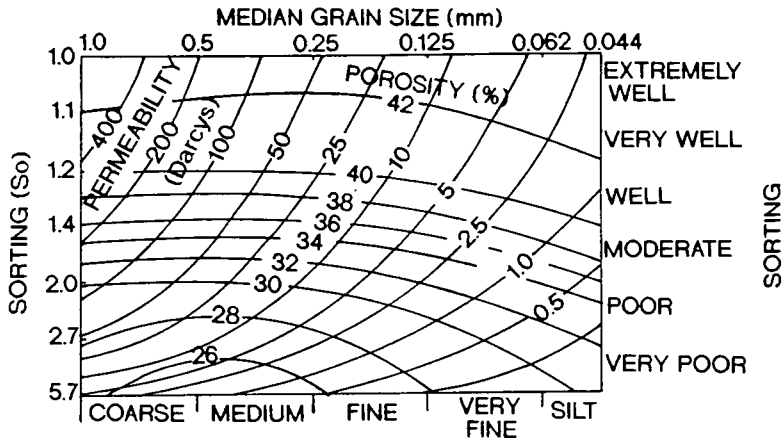

Figure 2.26 Porosity and permeability of artificially mixed and wet-packed natural sands from Brazos River, Texas. S_0 is the sorting coefficient of Trask (modified from Beard & Weyl, 1973).

Calculations by Wilson & McBride (1988) showed that in the deepest samples studied, approximately 53% of the initial porosity lost by compaction was by grain rearrangement. Equal amounts of porosity (24% of initial porosity) were lost by pressure solution and ductile grain deformation, including bending of micas. Sandstones at depths between 11,300 and 13,000ft (3,444 and 3,962m) lost a total porosity of 26% by all compactional processes, 14% by grain rearrangement, and 6% each by pressure solution and ductile grain deformation. An important conclusion of Wilson & McBride's (1988) is that within their study simple grain rearrangement was complete by a depth of 4,940ft (1,506m), but pressure solution, it's associated grain rearrangement, and ductile grain deformation continued at greater depths. They also concluded that sands which contained the greatest amounts of micas and ductile rock fragments underwent the most compaction. Their derived relationship of CI to depth for samples with less than 10% cement is:-

$$CI = 2.05 \times 10^{-4} \times \text{Depth (in feet)} + 2.87 \qquad \text{(equation 2.14)}$$

and means that the sandstone samples from the Montrose and Arbroath oilfields examined in the present work should have a CI averaging around 4.5 (see Chapter 5).

Smosna (1989) used the concept of grain fraction to derive a compaction law for Cretaceous lithic arenites and wackes of Alaska's North Slope. He defines grain fraction as the volume of constituent grains in a sandstone as a percentage of total rock volume, i.e. this is almost the same as solidity, explained earlier, except that the latter also includes cement within its calculation. The initial porosities of these sands ranges between 35 and 40%, approaching an ultimate value of 41%, i.e. equivalent to an initial grain fraction of 59% when no matrix or cement is present. There is also no evidence of pressure solution or stylolitization, and therefore, all of the observed compaction resulted from mechanical processes (Smosna, 1989). Results from thin section analysis showed that a burial depth of 550 to 800m appears to mark a crossover from mechanical compaction by simple grain rearrangement to that of ductile deformation. Grain rearrangement during the initial shallow burial increases the grain fraction from its initial value of 59% to 83-85%, i.e. a 25% increase (Smosna, 1989). Grain fraction is then further increased due to plastic grain rearrangement (i.e. bending of mica grains, and deformation of lithics such as shale, phyllite and coal), by an additional 2 to 13% during further burial below 800m, and the variation in this increase is primarily a factor of ductile grain content. Plastic deformation falls off significantly below 1,000m, resulting in the fact that 75% of total compaction

occurs due to simple grain rearrangement in the first 550 - 800m of burial. The overall increase in grain fraction appears to be linear with depth, but the increase may be logarithmic at shallow depths, although Smosna (1989) based this conclusion on very few data points.

Smosna (1989) also found that for sandstone samples with 15% or more matrix, grain fraction never exceeds 83% due to the stabilising effect of the cement (also see Scherer, 1987). He also pointed out that microporosity exists between clay-sized particles of the matrix, which is also destroyed due to compaction with increasing depth. The conclusion follows, therefore, that variations in sandstone composition greatly effect the compaction and porosity history of the sediments, as illustrated in Figure 2.27. Figure 2.28 summarises the post-depositional history of the sediments used in Smosna's study, emphasising the importance of early compaction, which is dominantly mechanical grain rearrangement. From his modelling Smosna (1989) proposed the following formula for the prediction of grain fraction (GF):-

$$GF = 90 + 0.23P - 0.72M + 0.0018d \qquad \text{(equation 2.15)}$$

where P is the volume percent of phyllite rock fragments, M the thin section point count of matrix, and d the maximum burial depth in metres.

The final work continuing this theme is the study of McBride et al. (1991), where the conclusions from their research into the compaction of the Wilcox and Carrizo sandstones of the Texas Gulf Coast basically agreed with those of Smosna's (1989) earlier work. They noted that by studying the packing indices (i.e. CI and TPI) and the porosity changes, that sands compact rapidly to a depth of approximately 1,200m, and then more slowly and variably at greater depths. The total rock porosity lost by compaction for individual samples ranges from 9 to 31%. In concordance with Smosna's (1989) data, McBride et al. (1991) noted that porosity lost by simple grain rearrangement amounts to 9 to 27%, a value greater than twice the amount of porosity lost by either ductile grain deformation (0 to 8.3%) or pressure solution (0 to 7.3%).

Pre-Cement porosity (PCP) is used in the study of McBride et al. (1991) as an independent gauge of compaction. It is defined as the sum of intergranular pores (exclusive of oversize grain dissolution pores) plus the volume of all cements. To quantitatively assess compaction McBride et al. (1991) used the formula of Ehrenberg (1989b):-

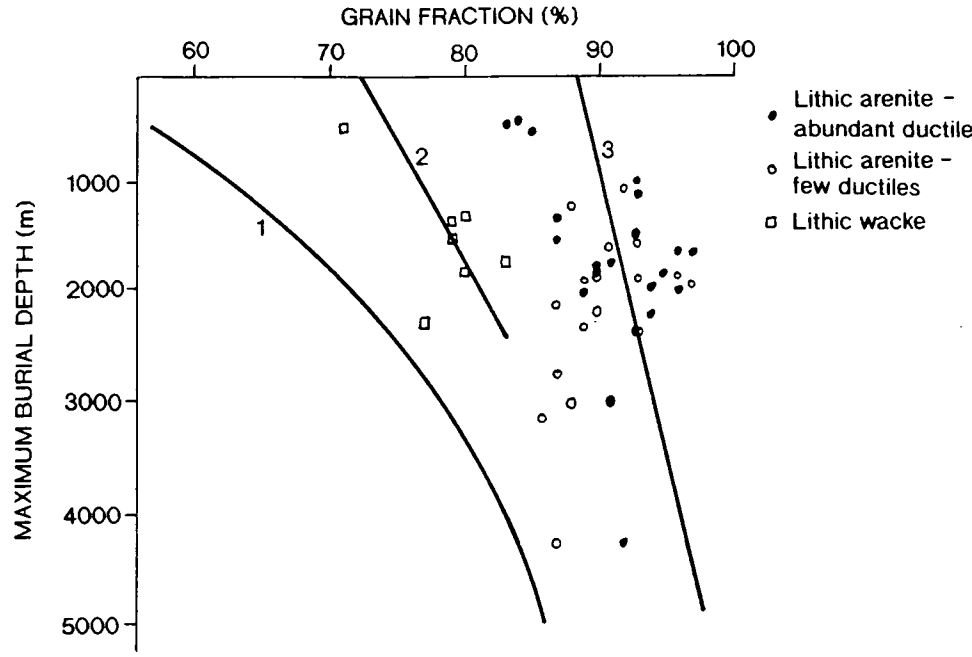

Figure 2.27 The curve relating grain fraction to maximum burial depth is horizontally translated toward a higher grain fraction as a function of sandstone composition. Curve 1, for mature sandstones with little or no matrix and cement, is taken from Sclater & Christie (1980) and Baldwin & Butler (1985). Curve 2 is for lithic wackes of Smosna (1989), and curve 3 represents lithic arenites with abundant ductile grains (solid circle only) (modified from Smosna, 1989).

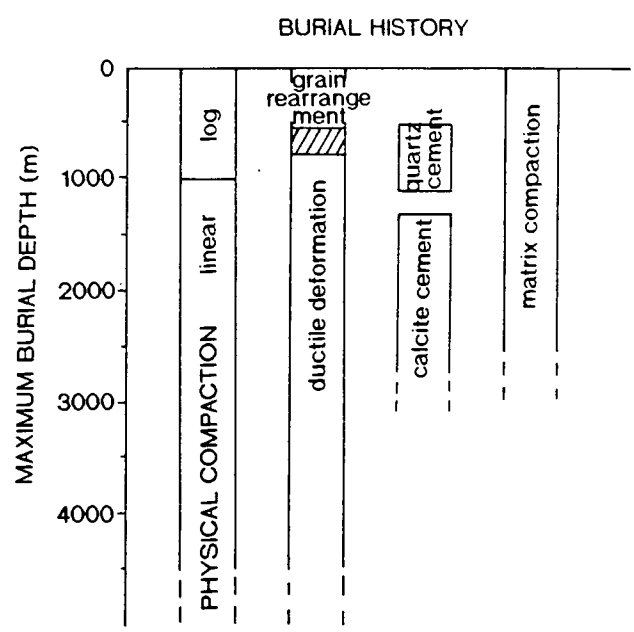

Figure 2.28 Summary diagram of post-depositional compaction and cementation events that affected grain fraction and porosity of Cretaceous sandstones in the NPRA (modified from Smosna, 1989).

$$\phi \text{ lost by compaction} = \text{initial } \phi - \frac{\left((100 \times \text{PCP}) - (\text{initial } \phi \times \text{PCP})\right)}{(100 - \text{PCP})}$$

(equation 2.16)

To estimate initial porosities, McBride et al. (1991) used two methods. Firstly, they assumed a constant 45% initial porosity for all sand samples. The second method involved using the work of Beard & Weyl (1973) to estimate sorting, converting Trask sorting values into phi units, and using the nomograph in Leder & Park (1986) (Fig. 2.26) to obtain porosity values. The latter method yielded initial porosity values ranging from 36 to 42%, averaging 41%.

Bloch (1991) argued that although empirically derived porosity prediction models have their limitations, they are still the only feasible approach available to predict reservoir quality (porosity and permeability) at the predrill stage. This technique is identical to that used by Scherer (1987) and Smosna (1989), namely the use of multivariate regression equations derived from calibration datasets. According to Bloch (1991), the most important parameters controlling sandstone porosity are composition, sorting, temperature history (expressed as vitrinite reflectance or TTI), and pressure history. These parameters are in general agreement with those used by Scherer (1987), described earlier. Providing that reservoir quality predictions are made using a calibration data set with more or less identical sedimentological and diagenetic parameters (i.e. based on samples from wells within the close vicinity) then the empirical approach can provide accurate estimates of porosity and permeability of buried sandstone units (Bloch, 1991). Empirical predictions, therefore, are usually basin specific, or even play specific, and require at least some understanding of fundamental processes affecting reservoir quality of a given sandstone target (Bloch, 1991). This point is illustrated when looking at the porosity versus thermal maturity indicators (e.g. TTI) as proposed by Schmoker & Gautier (1988). Bloch (1991) showed how vitrinite reflectance values of 0.53% taken at 15% porosity in Taranaki basin (New Zealand) vary greatly at the corresponding 15% porosity in the Yacheng field (People's Republic of China) where vitrinite reflectance is of the order of 0.95%. This observation, therefore, is in contrary to the conclusion of Schmoker & Gautier (1988) who propose a world-wide correlation. It also emphasises the point that empirically derived models are, in general, basin specific, a conclusion mentioned in the much earlier work of Gretener & Labute (1969).

Pittman & Larese (1991) investigated the important question of the effect sandstone composition, specifically the amount of lithic fragments, has on the compactional behaviour of sands. As shown earlier, lithic fragments are often more ductile than quartz or feldspar, and can therefore deform under shallow burial pressure, reducing porosities earlier than expected if no lithics are present (e.g. Rittenhouse, 1971; Nagtegaal, 1978). Nagtegaal (1978) observed that quartz arenites show the highest framework stability, and that coarse-grained, well sorted pure quartz arenites have the optimal potential of preserving high porosity and permeability during burial diagenesis. Arkosic arenites show a similar behaviour to quartz arenites down to a depth of at least 3352m (11,000ft) under the influence of basic saline solutions. Lithic arenites (those with soft and volcanic lithics) range lowest in framework stability because of their susceptibility to plastic deformation and mineralogical alteration of the framework constituents, in addition to the mechanical compaction and pressure solution potentially operative in nearly all sandstones. It follows, therefore, that lithic sandstones have the least chances of retaining porosity and permeability at depth (Nagtegaal, 1978).

Pittman & Larese (1991) used experimental sands, with differing percentages of lithic fragments added. They outlined three classes of ductile fragments; moderately ductile material (slate), highly ductile shale fragments, and extremely ductile weathered basalt material, which they added in measured quantities to sand, so that the ratio of sand to lithics is known. Experimental compaction of these sediments was then carried out and the results of this study are summarised in Figure 2.29. From this figure it can be seen that lithic sands which contain weathered basalt loose large amounts of porosity during early burial, whereas lithic sands containing slate (a less ductile material) compact at a much slower rate, and hence, porosity is preserved to a greater depth for such sediments.

The conclusion follows therefore, that the amount of compaction a lithic sand undergoes is related to the volume and type of lithic material (Pittman & Larese, 1991). The experimental work carried out by Pittman & Larese (1991) also showed how the timing of cementation is important when dealing with the compactional behaviour of sands. They noted, in concordance with earlier work, that early cement often preserves sandstone porosity due to its stabilising effect upon the sand pack. They also noted that the early development of overpressure produces the same effect, because it reduces the effective stress due to the overburden load.

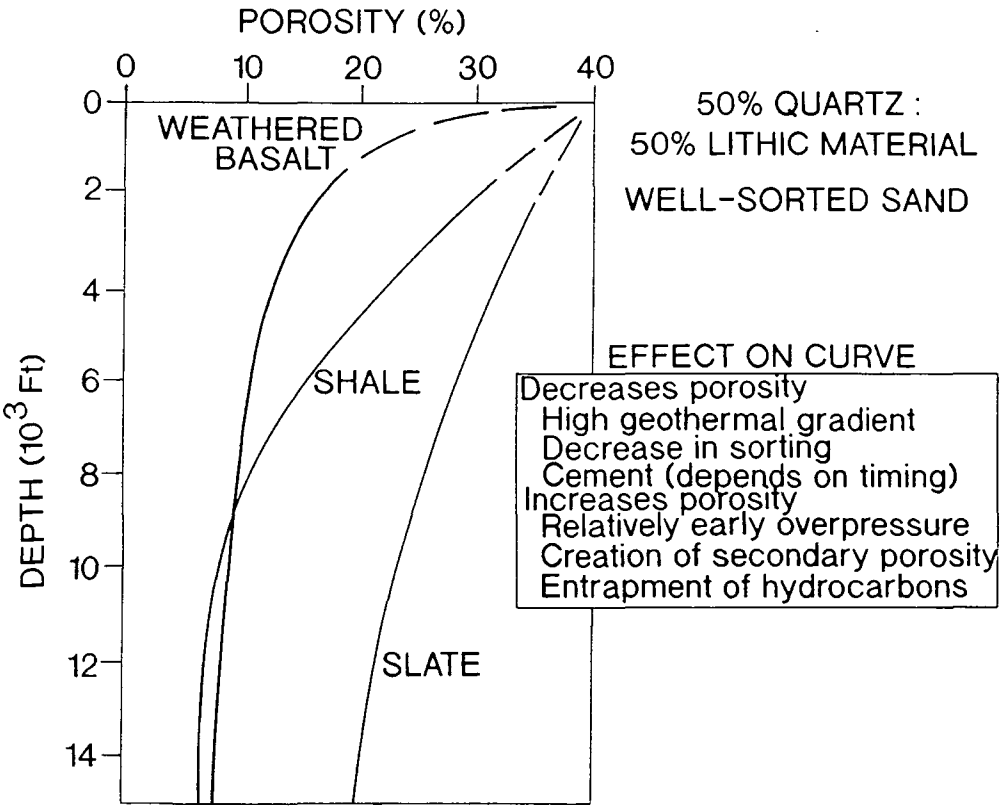

Figure 2.29 Compaction model with 50% quartz: 50% lithic well-sorted sands for slate, shale, and weathered basalt for comparison. The slate-bearing sand apparently was still compacting at the limit of the plot (15,000ft or 4572m). The shale-rich and weathered basalt-rich sands ended up with about the same loss of porosity, although the weathered basalt-rich sand lost the porosity at shallower depth (modified from Pittman & Larese, 1991).

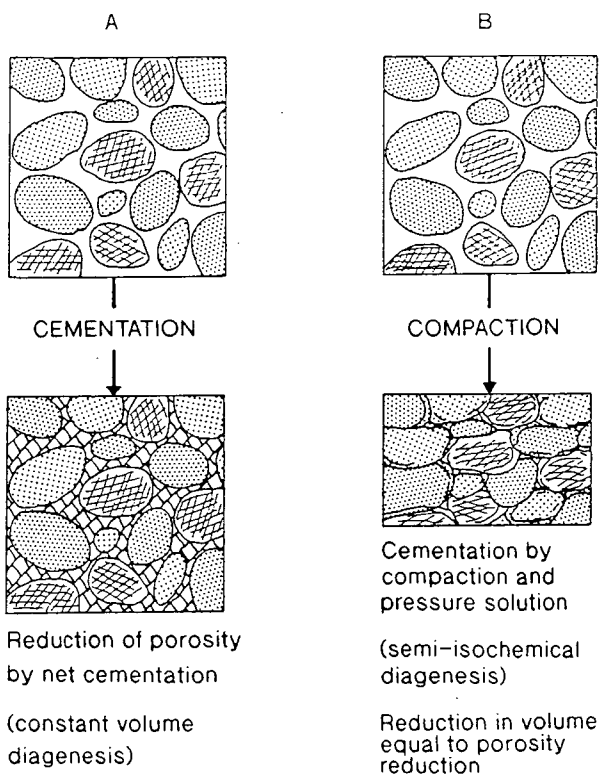

Figure 2.30 Reduction of sandstone porosity by (A) cementation (constant volume diagenesis), and (B) compaction (volume loss equals the porosity reduction) (modified from Bjørlykke, 1988).

Cementation Versus Compaction.

The primary porosity of sandstones can be reduced from 35-45% by two methods during burial (Fig. 2.30). Firstly it can be reduced by mechanical compaction, pressure solution and isochemical diagenesis as described in the previous section. Here the loss of porosity is accompanied by a corresponding loss in rock volume and stratigraphic thickness (Manus & Coogan, 1974). The second method of porosity reduction in sandstones is by cementation, as touched on earlier, precipitated from solutions brought from outside the sandstone and precipitated in the available pore space (allochemical diagenesis). This scenario requires a very high flux of porewater which is supersaturated with respect to a mineral phase (Bjørlykke, 1988). In this case the volume of the sandstone remains unchanged.

Precipitation of cement requires, 1) a flow of porewater from an area of higher solubility with respect to the cementing mineral, or 2) transportation of ions by diffusion in stationary porewater due to concentration gradients, or 3) dissolution of the locally stable minerals. Diffusion is most important in short-distance transport (<100m) in near-surface sediments where sandstone porosities are higher, whereas flow overshadows diffusion for longer transport distances. As burial depths increase and compaction reduces the average porosity, fluid flow becomes more difficult due to the increase in the specific surface area of the sediment, and thus the percentage of water influenced by mineral surfaces increases. Diffusion is still important at depth in the process of pressure solution where short-distance transport of ions from mineral surfaces occurs, and are precipitated on surrounding grains. A further problem encountered when dealing with cemented sandstones is the source of the cementing material. Do sandstones act as chemically open systems during burial diagenesis? i.e. are the cementing materials derived from within or outside these sandstones? Immediately after deposition these sandstones may be subjected to through-flow or percolation of porewater at a relatively high rate, and may, therefore, be subjected to early cementation or leaching, depending on whether the porewater is supersaturated or undersaturated with respect to the most common silicate or carbonate minerals present (Bjørlykke, 1988). Early cementation often occurs this way in shallow-marine environments, with the precipitation of calcite cements commonly.

In the porosity-loss model of Robinson & Gluyas (1992a) they used the assumption that sandstones act as open systems with respect to silica. This means that the silica incorporated in the quartz cement has been imported

from an external source. Evidence for this assumption comes from the research of Gluyas & Coleman (1992) who looked at the chemistry and petrography of early diagenetic calcite nodules which have escaped quartz cementation compared to the surrounding quartz-cemented sandstones. The model of Robinson & Gluyas (1992a) incorporated three general features:-

1) The amount of quartz cement increases with depth. This is a general trend seen in most sedimentary basins.

2) Compaction reduces sandstone porosity **before** cementation. This can be argued by looking at minus-cement porosities, determined petrographically, and seeing that they are characteristically less than the initial depositional sandstone porosity of 40-50% (e.g. Bloch et al., 1990).

3) Cementation occurs over a restricted time interval, of the order of 10Ma (Robinson & Gluyas, 1992b), so that quartz grows in a sandstone unit over a range of temperatures and depths. Evidence for this often comes from fluid inclusion studies (e.g. Burley et al., 1989).

Calculations and equations within this model are then based on a dipping sand bed, where water saturated with respect to quartz enters and moves upwards thus crossing isotherms and cooling, leading to supersaturation of quartz and eventually precipitation. Robinson & Gluyas (1992a) also assumed that once cementation begins compaction is effectively halted, and subsequent porosity loss is only by the precipitation of quartz in the available pore space.

The results from this model highlight some interesting observations and predictions. Important to the present study is the observation that very little quartz cement is precipitated at depths of less than about 1-2Km, even if the flow rates or bed dip are extreme (Robinson & Gluyas, 1992a). The other predictions are that there should be a relationship between bed dip and porosity gradient, as yet unstudied. A more problematic prediction is that for beds which dip at shallow angles, characteristic of the majority of sedimentary basins, average flow rates of the order of several metres per year to tens of metres per year must be sustained over 10Ma if significant amounts of quartz are to be precipitated (Robinson & Gluyas, 1992a). Such flow rates are only characteristic of artesian flow through an aquifer with a connection to the surface (Giles, 1987), whereas quartz cementation appears to occur in sandstones which are at depths of several kilometres within sedimentary basins, where a connection to the surface is highly unlikely. As pointed out by Robinson & Gluyas (1992a), this problem may be due to the fact that the present understanding of water flow within sedimentary basins is poorly

understood, and that focused flow through more permeable horizons, such as sand units, may play an important role in increasing flow rates.

It is important, therefore, when assessing the modification of sandstone porosity during burial diagenesis to separate the effects of compaction and cementation, to deduce how much each individual process contributes to porosity destruction. This assessment is made possible by using a diagram devised by Houseknecht (1987), which plots the intergranular volume (IGV) of samples against cement (Fig. 2.31). From this diagram it is then possible to graphically show the relative amounts of porosity destroyed by mechanical compaction and cementation respectively. However, constraints are placed on the results achieved using this diagram as an original depositional porosity for sands is plotted as the maximum IGV (synonymous with minus-cement porosity). Houseknecht (1987) choose a value of 40% for sands with few ductile grains, and composed of spherical, well-rounded and well sorted grains. As shown earlier in this section there are many factors that effect initial sandstone porosity, one of the most important being sorting (Pryor, 1973; Beard & Weyl, 1973). Therefore, Houseknecht's (1987) diagram requires some modification if local initial porosity values are known to differ from a general average of 40%. This requires some simple rescaling of the diagrams axes, and the substitution of the locally derived initial porosity value into the governing equations (e.g. Anderson, 1991).

The vertical axis of Figure 2.31 represents the IGV of the sample (presuming an original porosity of 40%), and it can also be used to quantify the percentage of original porosity that has been destroyed by mechanical and chemical compaction. This value can be quantified using the equation:-

$$\text{Percentage of original porosity destroyed by compaction} = \frac{(40 - \text{IGV})}{40} \times 100$$

(equation 2.17)

where IGV is expressed as a percentage of whole rock.

The horizontal axis of Figure 2.31 represents the percentage of cement present within a sample, and can also be used to show the percentage of original porosity destroyed by cementation. This value is quantified by a similar governing equation:-

$$\text{Percentage of original porosity destroyed by cementation} = \frac{\text{cement}}{40} \times 100$$

(equation 2.18)

where cement is the volume of cement present expressed as a percentage of whole rock.

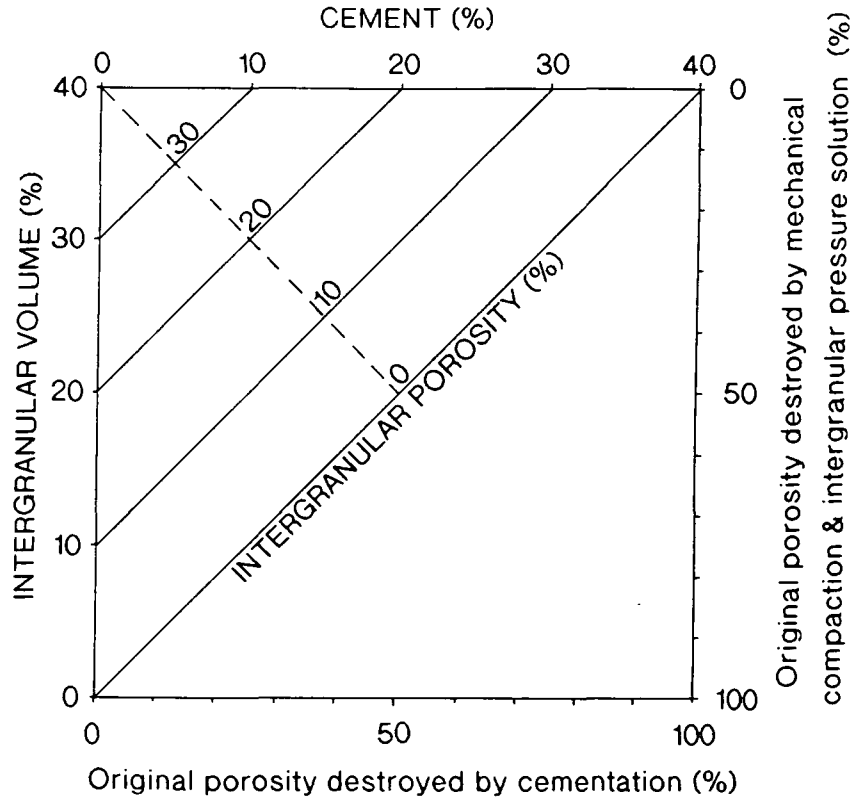

Figure 2.31 Intergranular volume versus cement (IGV/cement) diagram. Designed to enable the assessment of compaction and cementation volume loss in sandstones (after Houseknecht, 1987).

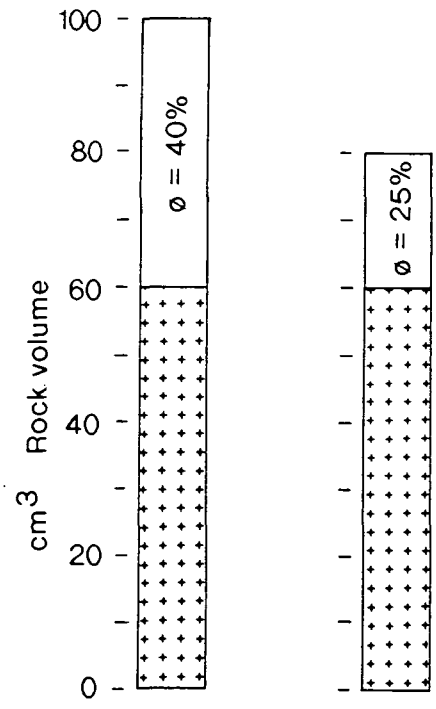

Figure 2.32 Bar diagrams representing change in total rock volume and porosity attending compaction of given volume of sandstone. Each sample consists of solid grains (represented by shaded region) and intergranular porosity (unshaded). Before compaction (left), rock comprises 60cm^3 grains and 40cm^3 of pore space. After compaction (right) rock has same grain volume, but less total volume, pore volume, and percent porosity (ø) (after Ehrenberg, 1989b)

The respective effects of compaction and cementation are separated by the dashed line on Figure 2.31, which enables a rapid assessment of the relative importance of the two processes in porosity reduction. Samples that plot to the lower left of this line have been effected to a greater degree by compaction, whereas those samples effected by cementation to a greater degree than compaction plot to the upper right of the dashed line.

Both Pate (1989) and Ehrenberg (1989b) observed that Houseknecht's (1987) and Wilson & McBride's (1988) method of calculating the percentage of original porosity destroyed by compaction and cementation are in error, because they ignored the fact that bulk sediment volume is dynamically reduced as compaction proceeds (Fig. 2.32). Pate (1989) used the fact that when dealing with compaction it is easier to refer to the amounts of solids and pore fluids as fractions of the total thickness of a given layer, as proposed by Perrier & Quiblier (1974). With the derivation of such equations, Pate (1989) redrew Houseknecht's (1987) original figure (Fig. 2.31), and produced two similar graphs to determine the amounts of porosity destroyed by compaction and cementation (Fig. 2.33a and b). These modified figures incorporate the reduction in a sediments bulk volume during compaction, and actually illustrate that compaction has a greater effect in porosity reduction than would be predicted by Houseknecht's (1987) original figure.

Ehrenberg (1989b) provided the correct formula for calculation of the compactional porosity loss of a sandstone:-

$$\mathrm{COPL} = \mathrm{OP} - \frac{((100 \times \mathrm{IGV}) - (\mathrm{OP} \times \mathrm{IGV}))}{(100 - \mathrm{IGV})} \quad \text{(equation 2.19)}$$

where COPL is the amount of original porosity lost by compactional processes (expressed as a percentage of the original rock volume), and OP is the original porosity after minor compactional rearrangement, equivalent to the wet packing technique of Beard & Weyl (1973).

The amount of original porosity destroyed by cementation, the cementation porosity loss (CEPL), is derived by Ehrenberg (1989b) in a similar way:-

$$\mathrm{CEPL} = (\mathrm{OP} - \mathrm{COPL}) \times \left(\frac{\mathrm{CEM}}{\mathrm{IGV}}\right) \quad \text{(equation 2.20)}$$

where CEM is the present volume of cement.

Using these equations, Ehrenberg (1989b) suggested some simple modifications to Houseknecht's (1987) original diagram (Fig. 2.31), shown in Figure 2.34. Again this improved figure showed that the dividing line between

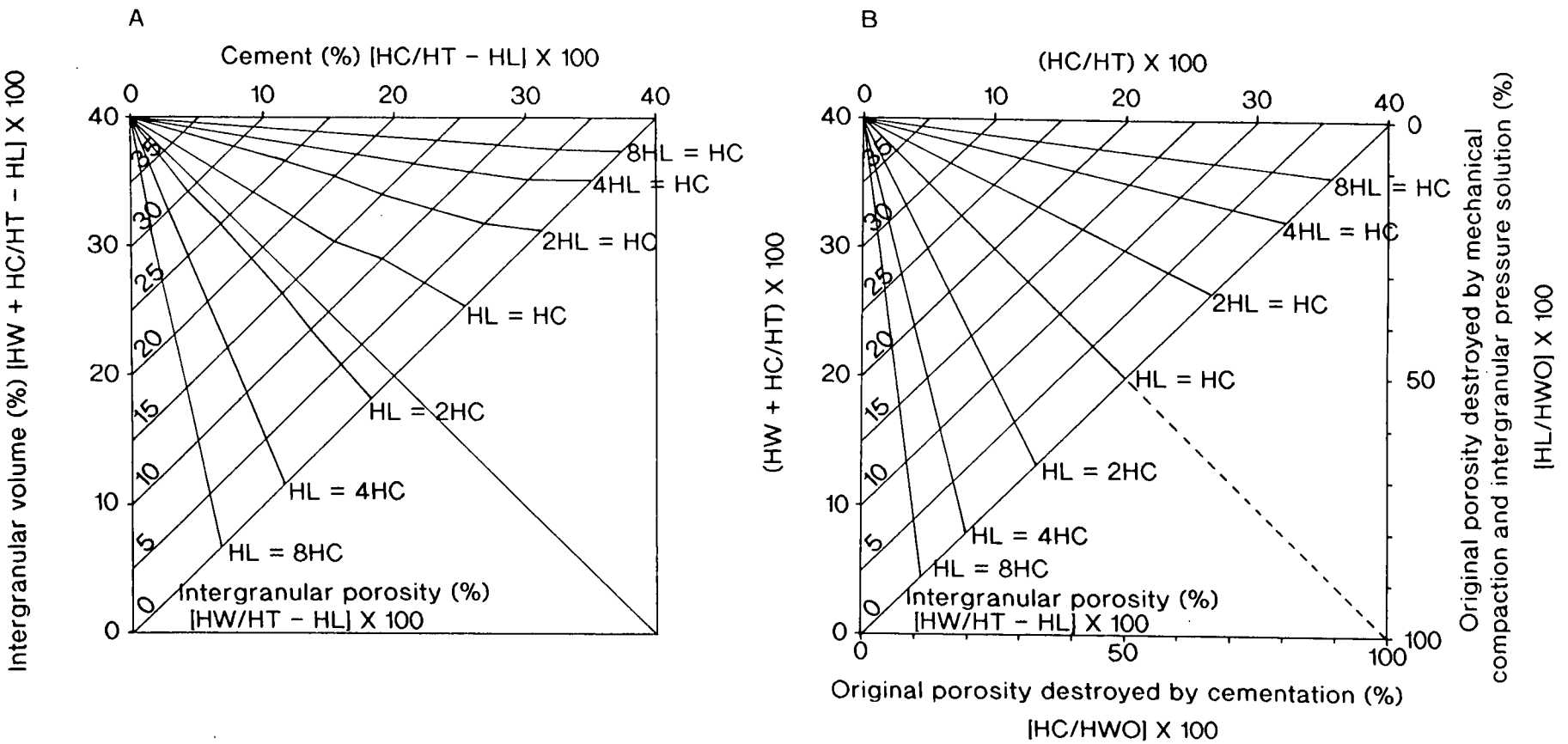

Figure 2.33 (A) Corrected and expanded version of Houseknechts (1987) diagram (Fig. 2.31). Lines radiating outward from upper left corner join points at which HL and HC are related by some value (N). For example, where N=1, HL=HC; pore thickness lost to compaction is equal to pore thickness lost by filling with cement.

(B) Plot of cement and pore volume expressed as ratios of initial total thickness. Notice that radiating HL/HC lines are now straight, and the HL=HC line is parallel to the diagonal line bisecting the diagram (after Pate, 1989).

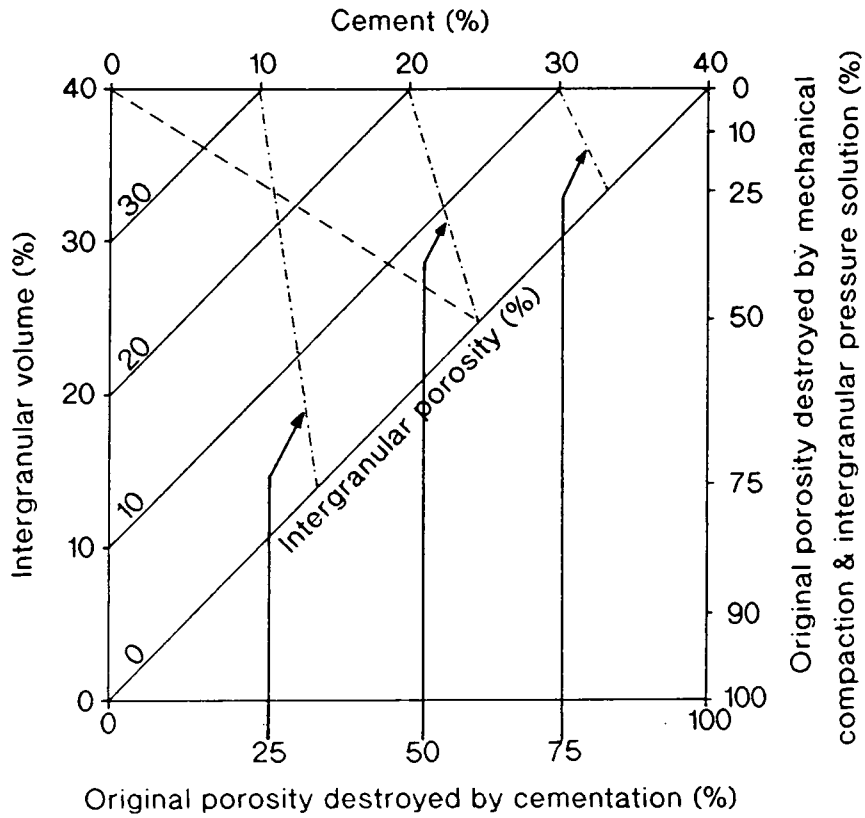

Figure 2.34 Suggested modification of volume-cement diagram proposed by Houseknecht (1987) (Fig. 2.31). Amount of original porosity destroyed by cementation is not a fixed function of percent cement only, but varies with percent intergranular volume as indicated by dotted lines (after Ehrenberg, 1989b).

equal amounts of porosity destroyed by compaction and cementation moves towards the upper cement axis, resulting in the suggestion that compaction is a more important process in porosity destruction. It must be noted however, that Ehrenberg (1989b) calculated IGV and CEM as percentages of the present rock volume, unlike Pate (1989) who uses original rock volume. Secondly, Ehrenberg (1989b) used original porosities that are slightly compacted. Both these reasons will mean that Ehrenberg's (1989b) diagram (Fig. 2.34) will slightly underestimate the amount of porosity destroyed by compaction.

Houseknecht (1989) and Wilson & McBride (1989) replied to these discussions of their work, admitting that they ignored the fact of dynamic reduction in bulk volume during compaction. However, Houseknecht (1989) believed that his original diagram, although slightly incorrect, is still superior to those proposed by Pate (1989) and Ehrenberg (1989b), for a number of reasons. Pate's (1989) method requires the data collected by the petrographers to be processed through a series of equations before plotting. These equations all implicitly assume 40% initial IGV, a problem discussed earlier, and introducing possible errors into Pate's (1989) method. The ease of plotting IGV versus cement on Houseknecht's (1987) original diagram is preserved in Ehrenberg's (1989b) method, but Houseknecht (1989) argued that his equations, as like those of Pate (1989), do not allow IGV to be reduced below 30%, and are therefore only correct for sands that have undergone purely mechanical compaction. Neither method takes chemical compaction into account (i.e. sandstones with IGV less than 30%). Houseknecht (1989) also pointed out that the error incurred in ignoring bulk volume reduction is probably small in comparison to the natural variation in sandstone porosity values, as illustrated by the work of Pryor (1973).

Recent Compaction Modelling.

As an aside, Waples & Kamata (1993) take a different approach to the modelling of porosity reduction in all the rock types discussed in the previous two sections, i.e. shale and sandstone, and they also look at the porosity reduction in carbonates, explained in the following section. Instead of using depth of burial as a function of porosity which lumps together several different porosity-reducing processes, some of which require additional factors such as time and temperature, they developed an empirical set of equations which expresses the reduction of porosity as a function of seven different processes. These processes are; repacking of grains from the original

inefficient packing mode, crushing of microfossils, ductile flow and deformation of grains, pressure solution, welding following pressure solution, clay diagenesis (including formation of authigenic clays), and cementation by minerals precipitated from moving fluids. For the modelling Waples & Kamata (1993) used six of the above processes in the porosity reduction of limestones, chalks, and sandstones, and three in shales. Figure 2.35 graphically shows how each of these processes effects sediment porosity as time elapses. The important point to note from this study is that for sandstone and shale, the most effective porosity reducing process during the early history of the sediment is mechanical rearrangement of the grains and subsequent repacking. This supports the earlier conclusions of Wilson & McBride (1988), Smosna (1989), and McBride et al. (1991) (see section 2.2.2). Apart from this the work of Waples & Kamata (1993) relied on previously produced porosity-depth models such as Sclater & Christie (1980) or Falvey & Middleton (1981), used within existing computer programs. Both these models require depth of burial as a factor, just like other models explained above. Therefore it still appears that for the porosity evolution of sediments to be modelled during burial, depth is the fundamental aspect to be included in model equations, and that porosity reduction at specific depths is a function of different processes as modelled by Waples & Kamata (1993), and the relative importance of these processes changes as depth of burial increases.

Conclusions Concerning the Compaction of Coarse-Grained Sediments.

1. The average depositional porosity of sand is ~40-45%.
2. The near-surface compaction process is not as complex as that for argillaceous sediments, mainly because of the better permeability and drainage of such deposits.
3. Grain rearrangement is the dominant porosity destruction process during shallow burial.
4. Cementation is an important process in compactional studies, both as a method of porosity reduction, and as a stabiliser of the sand framework.

2.2.3 Compaction of Carbonate Sediment.

Compactional studies in the field of carbonate sediments has, in general, been concerned with the mechanical and chemical compaction effects of overburden pressure seen on a grain to grain, microscopic scale (e.g.

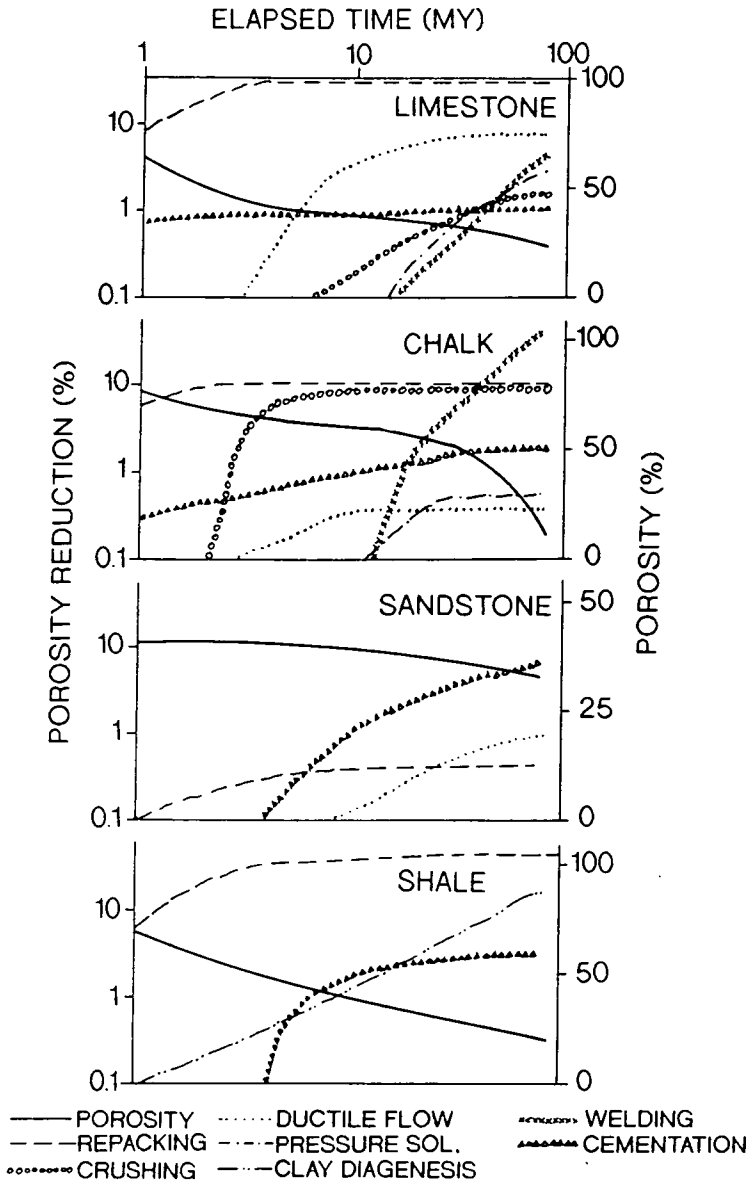

Figure 2.35 Porosity reduction by each of seven processes for limestone, chalk, sandstone, and shale. All rocks are buried to 2000m at a constant rate for 80m.y., with a geothermal gradient of 2°C/100m. Porosity reduction and time are plotted on log scales for better resolution. Also shown is total porosity, plotted on a linear scale at the right (modified after Waples & Kamata, 1993).

Meyers, 1980; Meyers & Hill, 1983; Shinn & Robbin, 1983; Shinn et al., 1983: Bhattacharyya & Freidmann, 1984). There has been rather less interest in the production of porosity-depth curves for differing carbonate facies, some notable exceptions being Fruth et al. (1966), Schmoker & Halley (1982), and Halley & Schmoker (1983).

Meyers (1980) and Meyers & Hill (1983) attempted to quantify the amount of compaction that has occurred in Mississippian coarse-grained skeletal grainstones and cement-rich packstones, exposed in southwestern New Mexico. Petrographic analysis showed that compaction plays an important role in the destruction of intergranular pore space in skeletal limestones, and that most of the compaction occurs under shallow burial. Meyers (1980) suggested that it is likely that the compactional features within the Mississippian strata were formed under less than 30m (100ft) of burial, and perhaps as little as a few tens of feet of overburden.

The mechanical and chemical compaction of fine-grained limestones has been studied by Shinn & Robbin (1983), who artificially compacted *in-situ* cores of modern sediment. Their experimental work followed on from theoretical work of Enos & Sawatsky (1981) who suggested that due to the shape of carbonate mud particles (i.e. being elongate, compared to equant particles as found in pelagic ooze) dewatering in the first 100m of burial is the most important compactional process reducing mud porosity to approximately 40% from an initial depositional porosity of 70%. Shinn & Robbin (1983) also observed a reduction in porosity from an initial value of 65 to 75% to a value of 35 to 45% porosity, along with a 50% and greater reduction in core thickness for depths of burial as little as 100m (328ft). With further experiments they predicted that significant mechanical compaction results from pressures simulating less than 305m (1000ft) of burial. As the load is increased to an equivalent depth of more than 3,400m (10,000ft) no significant increase in compaction was observed. Chemical compaction (pressure dissolution) was detected only in sediment cores compacted to pressures greater than 3,400m (10,000ft) of burial. Similar conclusions had been made by the earlier work of Fruth et al. (1966) who showed that for mud facies, which in concordance with siliciclastic mud has the greatest depositional porosity, averaging around 70%, nearly 40% compaction occurs for only 100 bars of pressure, a depth equivalent of approximately 1000m. However, 30% compaction occurs for less than 50 bars of pressure, i.e. less than 500m of burial.

Schmoker & Halley (1982) attempted to produce a porosity-depth curve for carbonate rocks producing a relationship of:-

$$\text{porosity } (\varnothing) = 41.73.e^{-z/2498} \qquad \text{(equation 2.21)}$$

where z is burial depth measured in metres. This produces a surface porosity of only 41.73%, a value only really valid for coarse-grained carbonates, and therefore does not accurately predict the porosity evolution of lime mud with a surface porosity of 70% (as measured by the DSDP in the Western Pacific (Schlanger & Douglas, 1974). Better curves to describe lime mud porosity evolution have been proposed by Hardenbol et al. (1981) (Fig. 2.36). Figure 2.36 is a summary diagram of porosity-depth trends for differing carbonate facies, used in the research of Campbell & Stafleu (1992).

Recent studies by Doglioni & Goldhammer (1988) and Campbell & Stafleu (1992) are the first to investigate how compaction has influenced depositional patterns in carbonate platform successions. Doglioni & Goldhammer (1988) proposed that syn-depositional compaction of an underlying formation (San Cassiano Formation) produced the wedge-shaped geometry of the overlying Raibl Formation. Because the San Cassiano Formation changes thickness as it is traced laterally into the basin, differential compaction (see section 2.2.5) has occurred to produce an areal variation in the basin subsidence during the deposition of the Raibl Formation, and thus influencing its stratal geometry. Campbell & Stafleu (1992) reconstructed the Djebel Bou Dahar carbonate platform from the High Atlas Mountains of Morocco to produce a seismic model of a carbonate succession. Decompaction was carried out using the curves shown in Figure 2.36 to produce a seismic model for carbonate platforms that have not been deeply buried.

Conclusions Concerning the Compaction of Carbonate Sediment.

1. Carbonate muds tend to have depositional porosities of 70%, slightly less than that of siliciclastic mud.
2. Carbonate sands have more or less identical depositional porosities to siliciclastic sand of 45%.
3. Near-surface compaction, and the problems of timing are identical in carbonate sediments as in their siliciclastic counterparts.
4. Near-surface cementation can be extremely important, and care is needed when assessing the process of compaction and its timing.

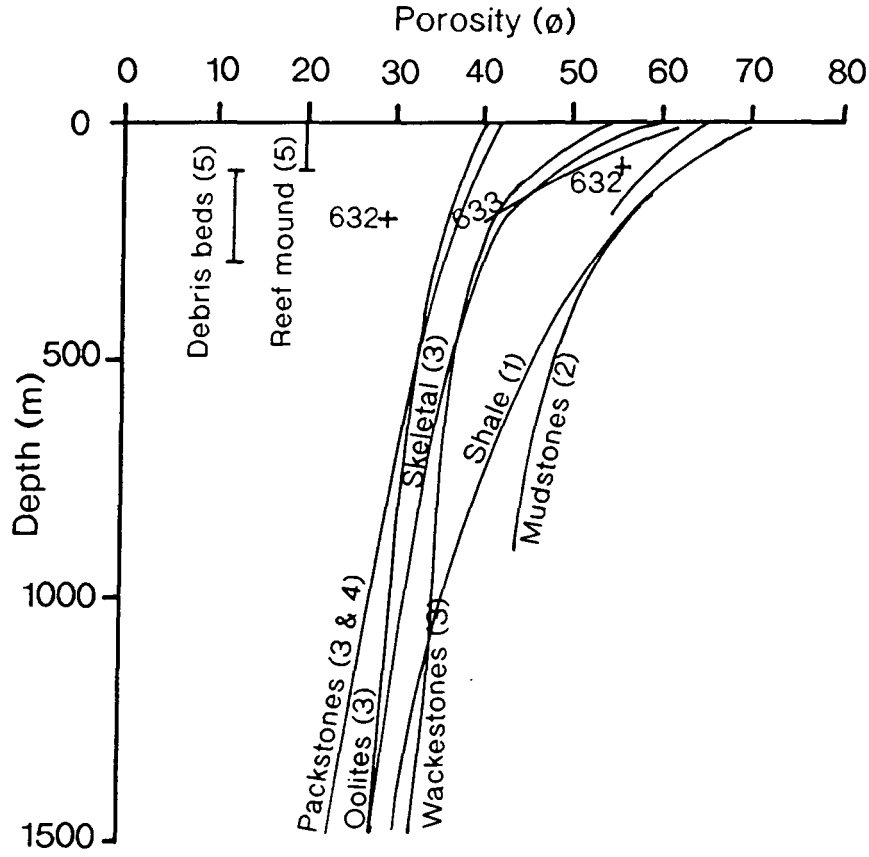

Figure 2.36 Plots of porosity versus depth for the lithologic cross-section. Muds and finer grained sediments have the highest initial porosities. Porosity rapidly decreases during the first 500m of burial. Shales and lime mud follow the same compaction curve over the first 450m. Porosities in the debris beds and reef mounds are the result of early sea-floor diagenesis and are based on measurements from thin sections and photomicrographs. Burial curves for other lithologies are based on compaction experiments by (1) Hardenbol et al. (1981), (2) Schlanger & Douglas (1974), (3) Fruth et al. (1966), and (4) Schmoker & Halley (1982). Also plotted are values of porosity versus depth for ODP leg 101, sites 630, 632, and 633 (after Campbell & Stafleu, 1992).

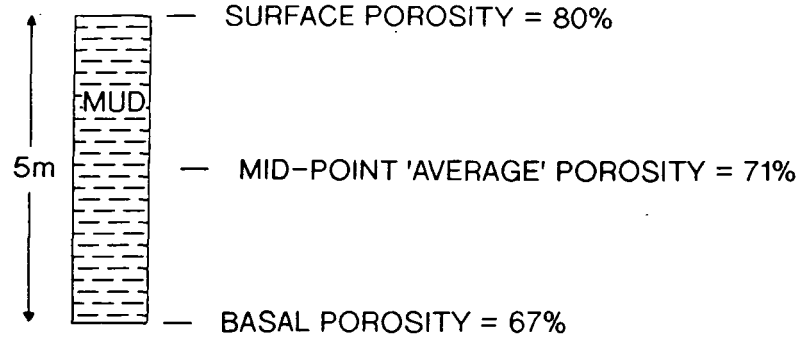

Figure 2.37 Diagram representing autocompaction of mud. Porosities vary throughout the 5m section, with the average porosity taken at the mid-point thickness.

2.2.4 Autocompaction.

The previous sections have discussed the depositional porosities of argillaceous and coarse-grained sediments, which are encountered at the sediment - water interface, immediately after the sediment has come to rest from suspension. Section 2.1 has also shown that with the increase of overburden pressure, compaction occurs, and that this process is dynamic throughout sediment burial. It follows therefore, that as soon as a freshly deposited sediment is buried slightly, compaction will occur, exclusively by grain rearrangement in the first metre of burial, and the porosity of the sediment will be reduced. It has been shown that the porosity reduction during this very early burial will be more apparent in deep-marine muds than in sandstones. Therefore, if we imagine a 5m thick unit of mud (Fig. 2.37), the very top of this unit will have a porosity of 80%, but the base will have a lower porosity due to compaction by its own overburden. Using the equation of Baldwin & Butler (1985), the porosity at the base of the mud unit will be 67% (Fig. 2.37). This compaction due to a units own overburden is termed **autocompaction** throughout the present study, and it means that an individual unit of sediment has its own porosity-depth profile within it, as shown in Figure 2.37.

At first glance the observation of autocompaction appears relatively unimportant, however, the process can drastically reduce the **average porosity** of a sedimentary unit, and this reduction in average porosity plays an important role in compactional modelling. Figure 2.37 shows that the average porosity taken at a units mid-point for a freshly deposited mud which is 5m thick is 71% using the equation of Baldwin & Butler (1985). It should also be noted that because the porosity depth profiles for muds are curves, the mid-point porosity of a sedimentary unit is not strictly the true average porosity for that layer. The true average porosity will be slightly higher than the mid-point porosity, however, for thin units (<10m) the errors are very slight (<1% difference) and are therefore regarded as negligible. Average porosities are required for many of the modelling equations used in backstripping and geohistory analysis explained in section 2.4.

2.2.5 Differential Compaction.

The previous sections have illustrated that differing lithologies are deposited with different initial porosities, dependant upon many factors, but primarily grain size and sorting. Likewise the compaction curves used to describe the changes in porosity with depth vary widely for different

sediments, especially during early burial (e.g. between sands and muds (Fig. 2.38)). Therefore, if sand and mud are deposited juxtaposed in any geologic setting (e.g. in a channel and interchannel area), upon burial compaction will occur. From the compaction curves shown in Figure 2.38 it is apparent that during early burial (the first 100m) the muds will loose a greater amount of porosity and, therefore, the subsequent bed thickness reduction will be greater. This will cause the production of topography upon the depositional surface (Fig. 2.39a), with the topographic high over the sand and the low over the muds. This difference in compactional behaviour is defined as **differential compaction**, and this process is extremely important in compactional and facies modelling, along with the production of structure and topography upon the depositional surface. It also forms one of the fundamental considerations of the present work. Maillart (1991) has shown that the amount of deformation of many sedimentary features (e.g. bed dips, bed and fault geometries) by differential compaction approaches the scale of deformations caused by syn-sedimentary tectonics.

Differential Compaction Models.

Collier (1989) modelled differential compaction and its influence upon the facies architecture of coal deposits within the Northumberland Basin. He pointed out that there are basically two methods by which differential compaction may be produced, shown in Figure 2.39a and b. The first method is as described in the previous paragraph, namely facies-dependant differential compaction governed by the porosity-depth curves of the lithologies involved (Fig. 2.39a). The second method that may produce differential compaction is by a lateral change in the a sedimentary units thickness. This is usually achieved by the deposition of a sedimentary unit over an incompactible underlying topography (Fig 2.39b). The thicker section of sediment will compact and undergo a greater thickness reduction than the thinner section, again producing topography on the depositional surface. Labute & Gretener (1969) described differential compaction around a Leduc reef, where an essentially incompactible reef is surrounded and covered by compactible sedimentary layers (Fig. 2.40). From their work they showed how structures formed by differential compaction decrease in amplitude upwards through the sedimentary section, and there comes a limit to where no structure is seen in the overlying strata. An identical phenomena is also described by Parker Gay (1989), who also introduced the timing aspect of compaction. This aspect will be dealt with in section 2.3, but for now the

BALDWIN & BUTLER, 1985

Burial Depth (Km) = $6.02\ (1 - \phi)^{6.35}$

SCLATER & CHRISTIE, 1980

$\phi = \phi_{o.} e^{-cz}$

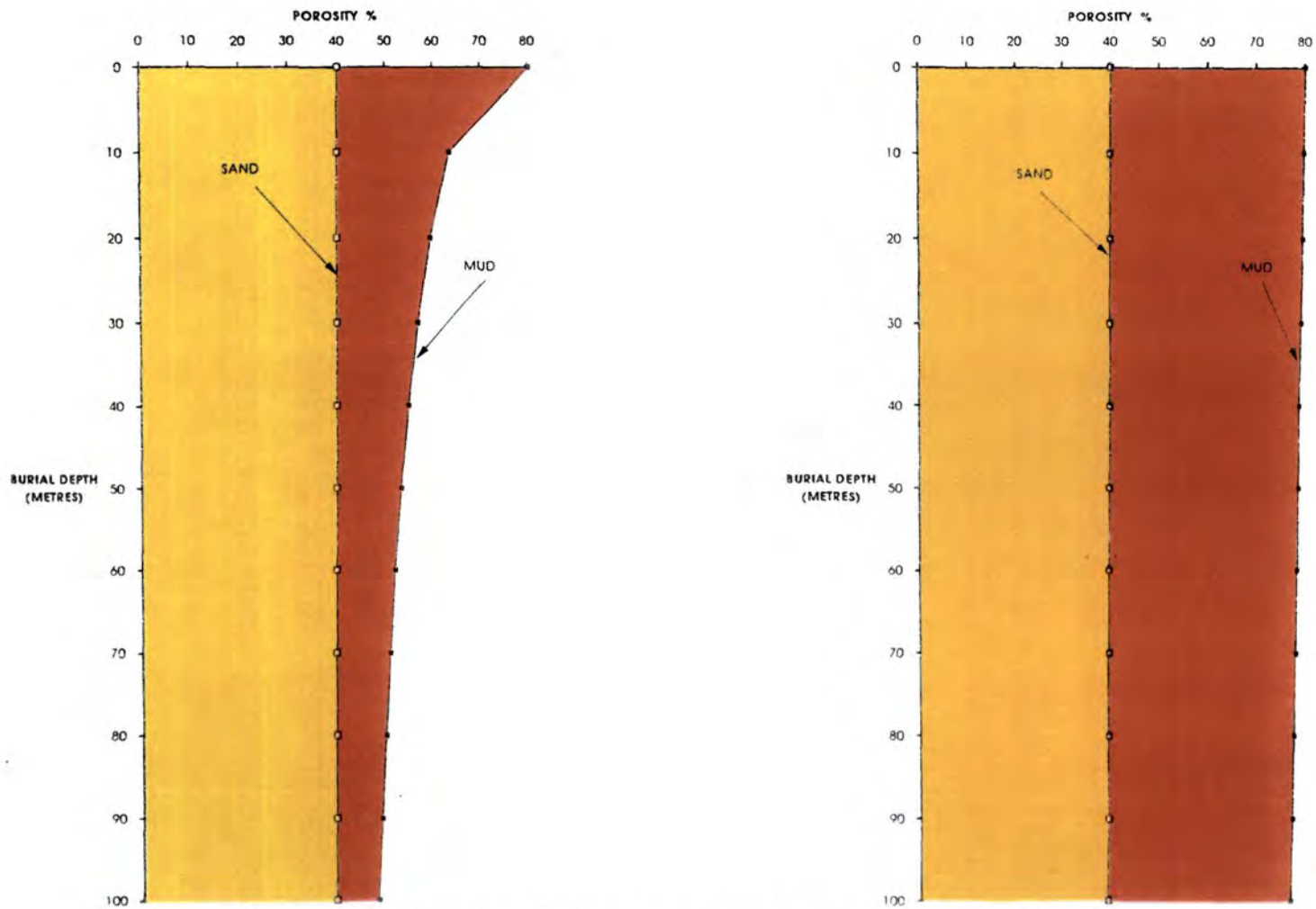

Figure 2.38 Porosity-depth curves for shallow burial, illustrating differential compaction between sand and mud. Left-hand diagram is based on the equations of Baldwin & Butler (1985), right-hand diagram based on the equations of Sclater & Christie (1980).

DIFFERENTIAL COMPACTION

1. HORIZONTAL CHANGES IN SEDIMENT COMPRESSIBILITY i.e. Change in Facies

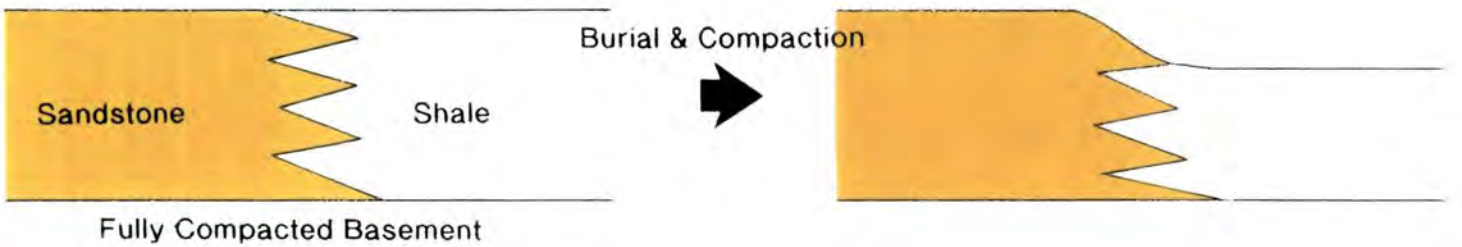

2. UNDERLYING TOPOGRAPHY

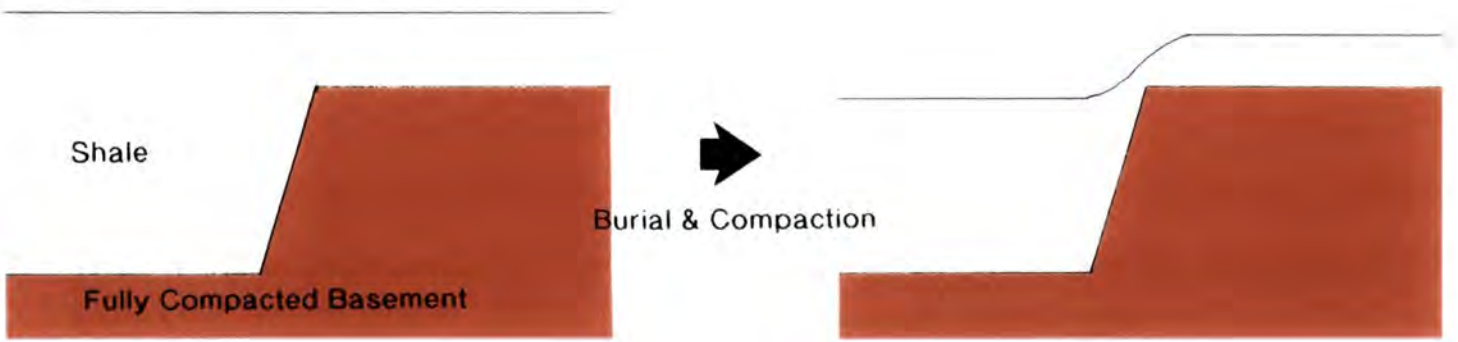

Figure 2.39 Two methods for the production of differential compaction.

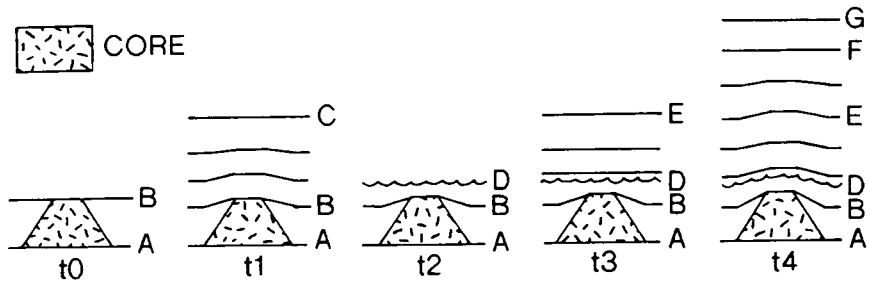

Figure 2.40 Schematic presentation of the development of a differential-compaction structure in the presence of an unconformity (after Labute & Gretener, 1969).

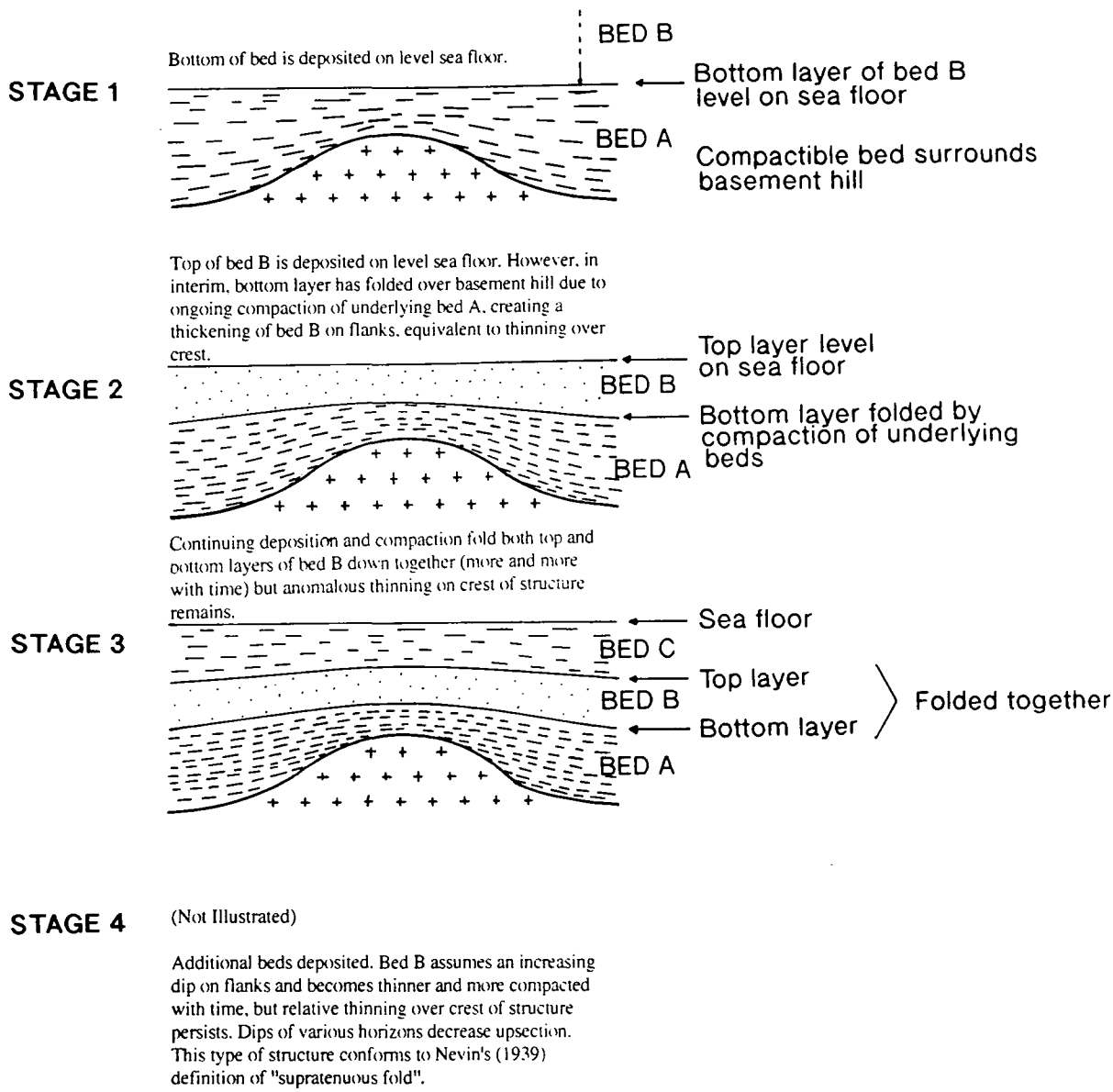

Figure 2.41 Thinning of strata over structural highs - usually explained by nondeposition, erosion, slumping, drape, or dissolution of thinned beds - is shown to be logical and expected consequence of compaction of underlying beds contemporaneous with deposition of thinned bed (modified from Parker Gay, 1989).

question to be asked is does compaction occur during deposition (i.e. syn-depositionally), or is there a time lag between deposition of a unit and the occurrence of compaction (both autocompaction and compaction of the underlying sequence)? Parker Gay (1989) reported the thinning of beds across incompactible basement topographic highs, and therefore concluded that compaction may be occurring syn-depositionally. The thinning may also be attributed to other processes such as nondeposition, erosion, slumping, drape, or dissolution of beds on the crest of a "growing" structural high (Parker Gay, 1989). Figure 2.41 illustrates how syn-depositional compaction can account for the thinning of beds across a topographic high.

Collier's (1989) work described how computer modelling can be used to show how differential compaction, produced by both methods described earlier, may occur and what effect this differential compaction may have on subsequent deposition. His modelling used Westphalian coal deposits of the Northumberland Basin to illustrate the theoretical computer models, whereas the present study is primarily interested in the differential compaction occurring in submarine fan deposits. The models of Collier (1989) assumed that deposition is periodic and is followed by a period of compaction of the underlying mud sequence. Therefore, a sand unit is instantaneously deposited in the topographically lowest area of the model, with mud deposited in the intervening areas. Compaction of the underlying sequences is then calculated and modelled, with bed thicknesses being reduced accordingly. A new topography is thus produced at the depositional surface and the modelling process begins again. Facies patterns and geometries are therefore controlled by compaction-induced topography upon the depositional surface, with early compaction in the first hundred metres of burial being the prime control upon the production of topography. As shown earlier, it is here where the greatest porosity reduction and subsequent bed thickness reduction occurs in argillaceous sediments, whereas sandstone see very little change in porosity and therefore bed thickness throughout this interval. Within the submarine fan environment deposition of sandstone bodies is geologically instantaneous, as sands are deposited from turbidity currents which may last a matter of days or even hours (Reading, 1986).

The basic concept dealt with throughout this study therefore, consists of the instantaneous deposition of sandstone bodies within a mud rich section. Upon compaction of the units within the section, topography can be produced upon the depositional surface, and this may directly influence the subsequent deposition of a turbidite sand by concentrating the flow within the

topographically lowest point on the depositional surface. This general process has been modelled by previous researchers working within the alluvial environment (Allen, 1978; Bridge & Leeder, 1979; Anderson, 1991). However, it is believed that the effect of compactionally produced topography will be greater within the submarine fan environment due to the much higher initial porosities of the muds found there (Fig. 2.2), and therefore, the greater amount of bed thickness reduction occurring during early burial.

The model of Allen (1978) essentially dealt with the stacking pattern of channel sand bodies in a zone of influence within which a river may cross a coastal plain. The river builds up a suite of alluvium deposits over a series of equal time steps, each of which begins with an avulsion. The choice of the new site for the river after an avulsion is governed by random number tables combined with the rules of avoidance of older, relief-creating sand bodies. The relief is caused by two methods, firstly by differential compaction between channel sands and overbank argillaceous sediment of buried channels, and secondly by the fact that the last channel will have built levee deposits to form an alluvial ridge. The new river will tend to avoid areas of inherited relief. Within the model the effect of older, buried sand bodies creating relief by differential compaction is incorporated by assuming a rule that a given sand body may not overlap (i.e. erode) any earlier body whose top lies less than a calculated depth below the surface of the alluvial plain. This depth depends on the subsidence rate and the period of avulsion chosen by the modeller. Apart from this simple rule, Allen (1978) ignored compaction within the model, suggesting that this restricts his model to alluvial deposition occurring during geologically short periods of time (10^5 to 10^6 years). It is the belief of the present work however, that compaction is a dynamic process, which will still have a great effect on the surface topography even during geologically short time periods. The omission by Allen (1978) of the modelling of compaction using porosity-depth relationships flaws the model somewhat, as early compaction of overbank muds would drastically reduce the bed thickness within this area, and hence greatly change the surface topography and subsequent channel position.

Bridge & Leeder (1979) attempted to address the importance of compaction within the models of alluvial deposition, refining earlier models of Leeder (1978) and Allen (1978), described above. Using Baldwin's (1971) composite curve to define a porosity-depth function for clay-rich sediments, and assuming no change in sand porosity for the first 500m of burial, Bridge & Leeder (1979) modelled alluvial deposition in a similar way to Allen (1978).

However, immediately before avulsion occurs all the layers of sediment below the newly deposited horizon are compacted to produce a new topography upon the surface of the flood plain. The newly deposited horizon is not compacted until it has been loaded. The subsequent channel is then positioned in the lowermost area of the flood plain, and if there are more than one equally low positions, the channel is placed in the one nearest the previous channel. Therefore, stacking patterns can be built up sequentially to estimate sand body density, and the interconnectedness of sand deposits. Further refinement of the model has been carried out by Bridge & Mackey (1993) to more accurately simulate alluvial depositional processes, and to predict more aspects of alluvial architecture.

Differential Compaction and Coal Geology.

Differential compaction has for a long time been a recognised process within coal geology, operative during coal deposition, and producing such effects as seam splitting (Fielding, 1984). Many researchers have proposed that differential compaction across a delta plain controls sedimentation patterns due to the topography produced (e.g. Fielding, 1982, 1984, 1986; Ferm & Staub, 1984; Weisenfluh & Ferm, 1984; Harper & Olyphant, 1991; Demko & Gastaldo, 1992). The work of Fielding (1982, 1984, 1986) goes into slightly more detail than most of these studies, showing how an interplay of compactionally controlled subsidence and regional structural development may influence channel geometries and coal depositional models. Topographic variations of up to 8m are believed to be produced by rapid differential compaction of peat, clay and sand-dominated sequences (Fielding, 1984). Evidence for this is the presence of thick sedimentary sequences directly overlying thick coal and claystone dominated units, with only thin subsequent sedimentary sequences found overlying major channel sandstones. The combined effect of rapid vertical accretion of channel deposits compared to that of the interchannel areas, and the slower rate of compactional subsidence of the channel sandstones causes the topography of the depositional surface to be such that subsequent sandstone channel deposits will be situated above previous, more compactible, muddy interchannel deposits. This process produces characteristically diagonally offset, vertical stacking patterns of channel sandstone bodies (Fig. 2.42), identical to those formed by the alluvial models of Allen (1978) who ignored the modelling of compactional effects, and Bridge & Leeder (1979) who incorporated compaction into their modelling process. Problems arise with

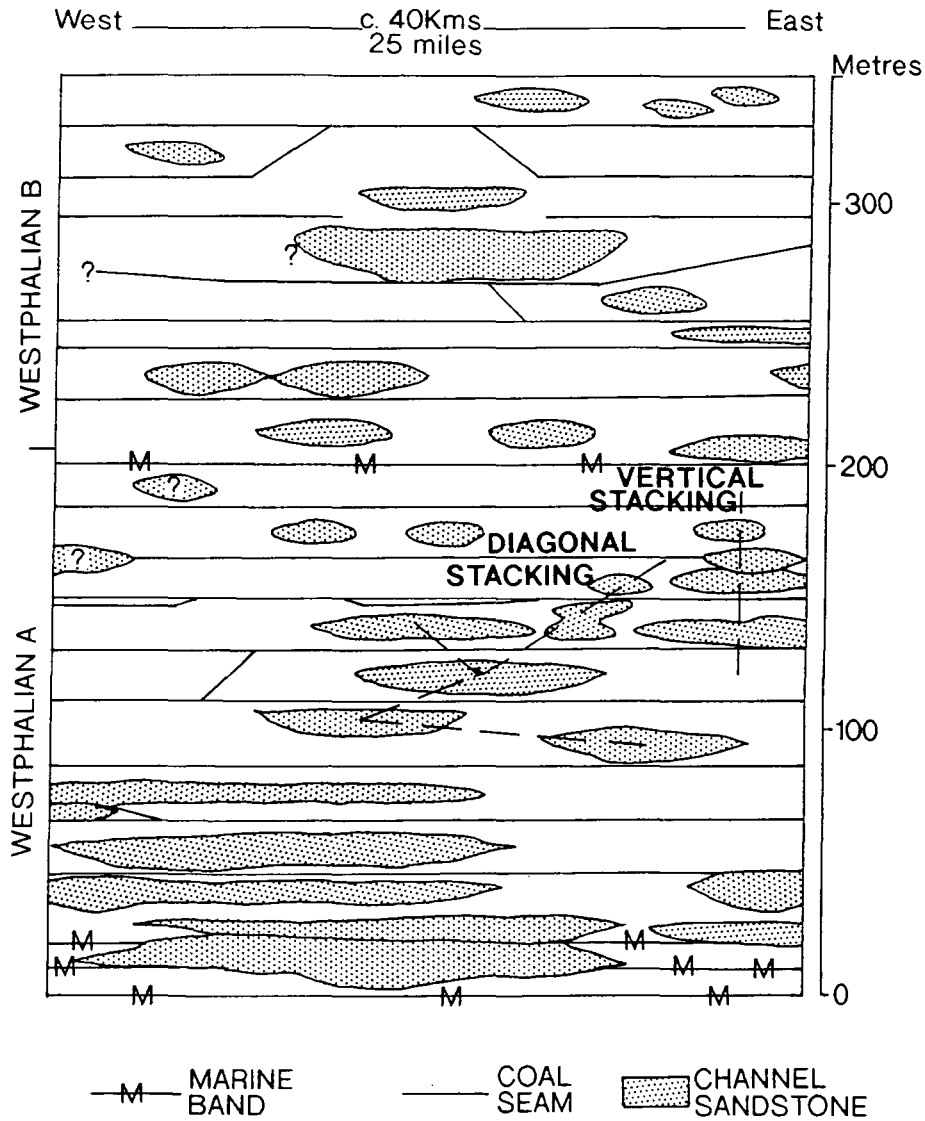

Figure 2.42 East-West section across the Durham coalfield, showing major channel belt sandstone architecture (after Fielding, 1986).

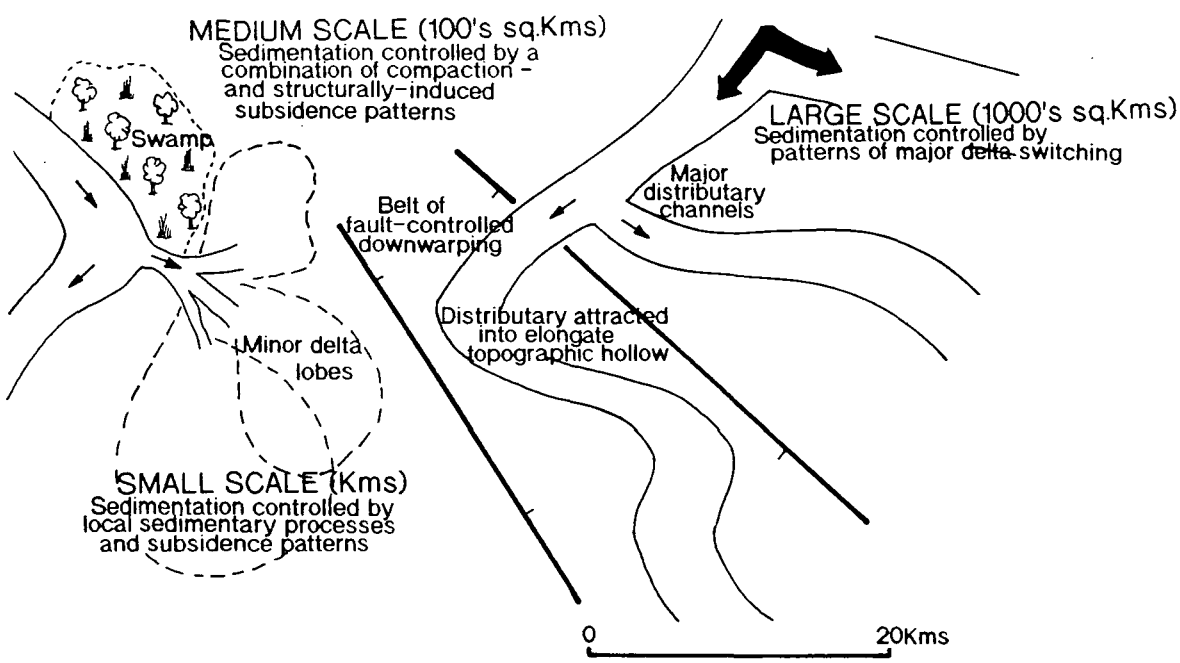

Figure 2.43 Schematic reconstruction of the Coal Measures plain, showing controls on sedimentation (after Fielding, 1984).

these models however, as mature meandering rivers which have built a flood plain will not avulse in such a way to make these models feasible.

Fielding (1984) pointed out that vertically stacked channel sandstones can also be seen on a profile through coal field sequences (Fig. 2.42), thus contradicting the compactional model for the build-up of sequences. It is believed that in such areas of vertically stacked channels, a structural control influences channel deposition, producing structural depressions of less than 5m relief upon the depositional surface. Fielding (1984), therefore, divided the depositional model of coal into three scales, and assesses the controls upon sedimentation in each of these:-

1. Large Scale (1000's Km^2) - Sedimentation controlled by the patterns of delta switching.
2. Medium Scale (100's Km^2) - Sedimentation controlled by structurally and compactionally induced subsidence patterns.
3. Small Scale (Km^2) - Sedimentation controlled by local sedimentary processes, and subsidence patterns.

(see Figure 2.43).

These scales provide a valuable way of dividing up large depositional systems into units where compactional effects can be recognised, and the possible depositional control they exert can be assessed in all scales of facies geometry and build-up.

A similar compactionally controlled depositional arrangement is described by Demko & Gastaldo (1992), where thickness changes in the Jagger coal seam of approximately 2.3m occur, with the thick coal sections overlying the topographic lows of the underlying "Jagger Bedrock" sandstone. These topographic lows also appear to influence the thickness of the Blue Creek coal, and the siting of thin (<2m) channel sands, approximately 8m higher up within the stratigraphic column. Demko & Gastaldo (1992) described a depositional model where accommodation space is provided by short-term compaction of buried peat bodies, creating topographic lows which allow continued accumulation of catastrophic flood deposits that buried the clastic swamp vegetation. This process of punctuated loading, compaction and subsidence, and recolonization by clastic swamp vegetation continued until the buried peat body reached relative compactional stability.

Thickness changes, and the distribution pattern of the Survant, Springfield, and Hymera coals are believed by Harper & Olyphant (1991) to reflect the differential compaction of sediments around the underlying Survant

sandstone, with thick coals occurring within the compactionally produced lows across this sandstone. They also postulated that the deposition of the Survant sandstone was influenced by the underlying Silurian reefs present within this area of the Illinois Basin. Differential subsidence around the Silurian reefs may have been due to differential compaction, as the reefs are relatively incompactible compared to the surrounding sediments, or it may have been due to differential diagenesis of the rocks (Harper & Olyphant, 1991). However, the important observation in this part of the study is that the volumetric change in the Silurian beds surrounding the reefs, by whatever process, is not instantaneous, and it may continue under the influence of previously added sediments, even during hiatal periods. Harper & Olyphant (1991) noted that during hiatal periods (and in the absence of tectonic movement), land subsidence would have been caused by the cumulative compaction and diagenesis of every underlying Palaeozoic unit. Initially during such hiatal periods, compaction of shallow, more compactible, recently deposited units (such as muds that flanked Pennsylvanian sandstones) would contribute most to subsidence of the land surface. But given the passage of time and the rapid physical compaction of shallow buried muds, the thinning of deeper older units (such as Silurian rocks around reefs) might have become significant again. Such differential thinning of Silurian rocks during long hiatuses could have been subtly expressed in the topography of the land surface or the sea floor, and areas with the greatest subsidence would have captured drainage ways. Chapter 4 of the present work will describe field observations and interpretations of differential compaction occurring during hiatal periods. The main conclusion to be reached from the work of Harper & Olyphant (1991) and the fieldwork described in Chapter 4, is that compaction is a temporal process, a fact ignored by most, if not all models that incorporate compaction into their calculations. This conclusion therefore raises the important question of the timing and the rate of compaction compared to the timing and rate of deposition (i.e. addition of overburden).

2.3 Compaction as a Temporal Process.

Many authors point out that compaction is a dynamic process (Athy, 1930; Hedberg, 1936; Gretener & Labute, 1969; Desmaison & Beaudoin, 1989; Buryakovskiy et al., 1991), but with the exception of the work by Audet & McConnell (1992), described in section 2.2.1, the aspect of time in compaction studies is mostly ignored. This is probably due to a number of reasons, but mainly because it is a difficult concept to incorporate into

mathematical compactional models, and it makes formulae complicated and difficult to use. On a large scale (observations at the scale of >1Km) the final result is probably more or less identical whether the aspect of time it taken into account or not during compactional modelling. However, as the scale of observation decreases below 1Km, then the aspect of time becomes a very important variable to consider when looking at the compactional history of a sedimentary sequence.

The two important variables to consider are the deposition rate of the sediment (i.e. the rate of addition of overburden), and the compaction rate of the sediment being deposited (i.e. Autocompaction, as explained in section 2.2.3), and the underlying sedimentary strata being loaded. Figure 2.44a and b shows the two possible relationships between the rate of deposition and the rate of compaction. The first scenario, shown in Figure 2.44a, illustrates the situation that arises when the rate of autocompaction and compaction of the underlying sequence is equal to the rate of deposition. This means that as a sediment is being deposited pore fluid escapes at such a rate that the pore fluid pressure is not raised above hydrostatic pressure. This is never strictly true as pore fluid pressure must be raised slightly at the initial period of loading to start the dewatering process. But providing the equilibration of fluid pressure back to hydrostatic is geologically instantaneous, then the rate of compaction is essentially equal to the rate of deposition. Therefore, within this scenario **equilibrium compaction** is maintained at all times. This also means that the depositional surface remains essentially flat, as the flow of deposition will tend to fill any topographic lows, even if they are produced by differential compaction of the underlying sedimentary strata.

Figure 2.44b illustrates the alternative scenario where the rate of deposition is greater than the rate of autocompaction, and the compaction of the underlying strata. Here sediment is deposited at such a rate that pore fluid cannot escape from the underlying sedimentary rocks, possibly due to low permeability and lack of flow pathways, causing pore fluid pressure to increase to a value above normal hydrostatic pressure for the depth of burial, where the sediment is said to be **overpressured**. If deposition is halted for any reason compaction can still occur as pore fluid slowly bleeds out of buried strata, as the pore fluid pressure tries to achieve hydrostatic pressure. Because no further sediment is being added, as **post-depositional compaction** occurs, any bed thickness reduction in the sedimentary sequence will be expressed at the depositional surface. Therefore, if differential compaction occurs at this stage, topography will be produced at

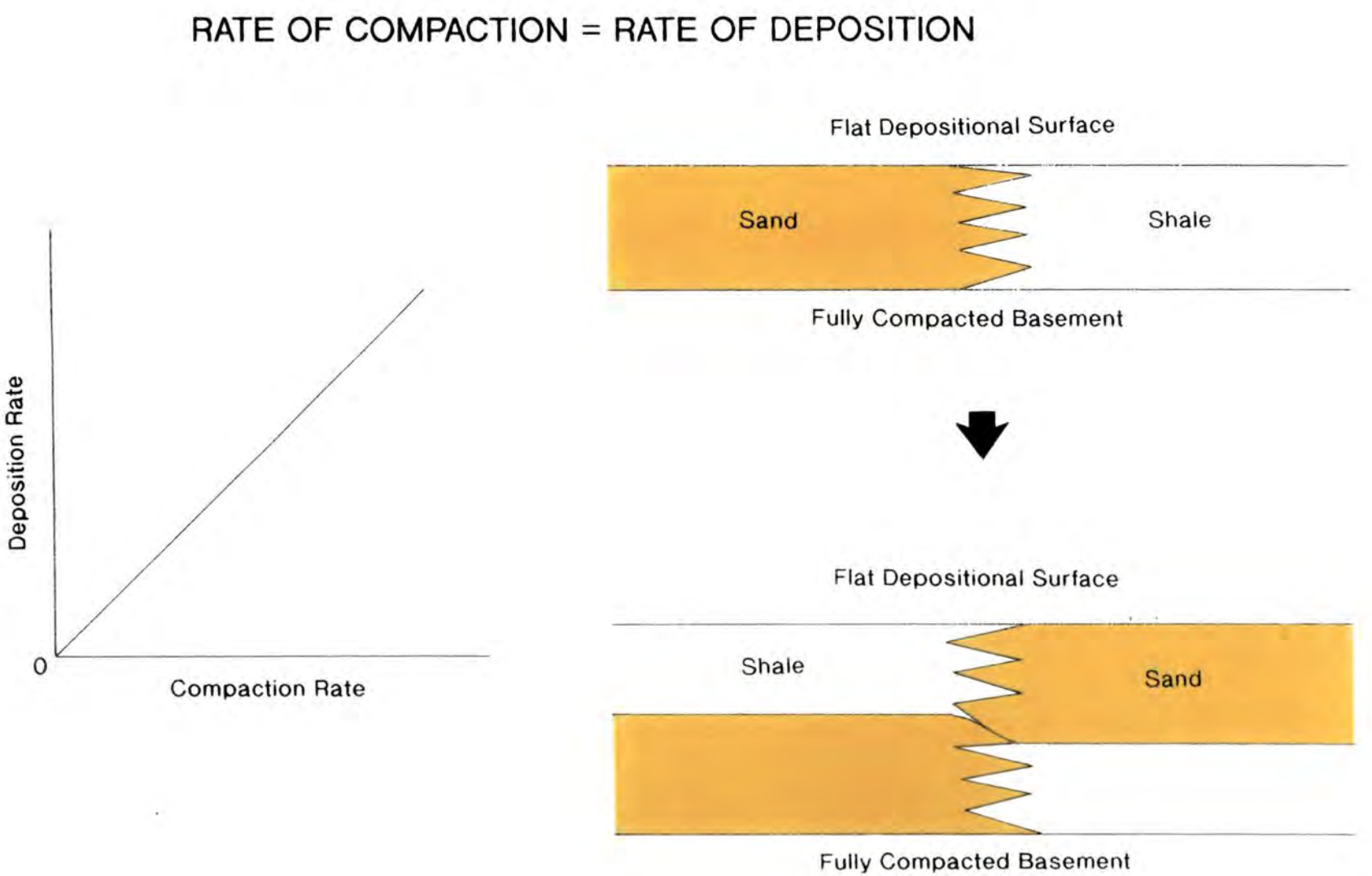

Figure 2.44 (A) Rate of compaction equal to the rate of deposition. The depositional surface remains flat, and underlying compactibility may form a control upon sedimentation

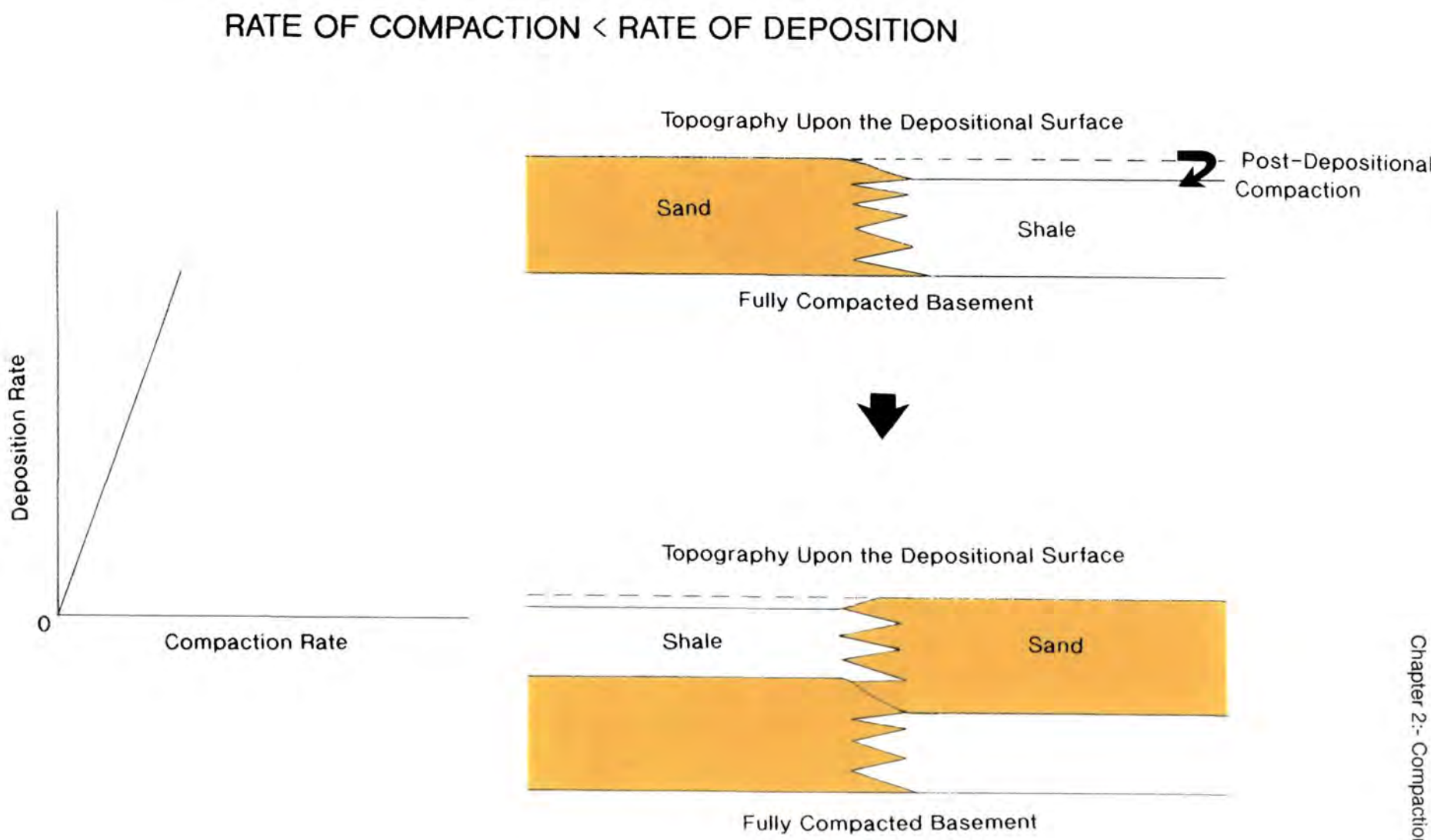

Figure 2.44 (B) Rate of compaction less than the rate of deposition. Topography formed on the depositional surface with the lows over the shales. Topography may control subsequent deposition.

the depositional surface. The scale of this topography depends on exactly how much overpressure has built up during deposition, and remains just after deposition has ceased. The greater the amount of overpressure the greater the post-depositional compaction, and therefore topography produced, providing the hiatus in sedimentation is long enough to allow all the remaining overpressure to dissipate, and a state of equilibrium compaction to be achieved. Overpressure from the shallow buried section will be the first to bleed off, followed by that which has built up in the more deeply buried sediment as more time passes. This is the basic process by which Harper & Olyphant (1991) believed subsidence occurs in coal swamp deposits during hiatal periods, outlined in the previous section.

Sediment permeability is a major factor in this process, as this dictates the speed at which a sediment can dewater. Fine-grained sediments have considerably lower permeabilities than coarse-grained sands and will therefore take a relatively longer time to dewater and compact (Rubey & Hubbert, 1959; Ebhardt, 1968; Magara, 1968, 1976; Bredehoeft & Hanshaw, 1968; Einsele, 1977; Bishop, 1979; Buryakovskiy et al. 1991). Therefore, in environments where sand and shale are juxtaposed the relative speeds of compaction will vary as well as the amounts of bed thickness reduction. When this effect occurs in geologic environments where deposition is episodic, the process of post-depositional compaction can play an important role in modifying the topography of the depositional surface during hiatal periods.

The modelling of Einsele (1977) showed how the rate of deposition also plays an important role in the production of overpressure within loaded sediment. Using experimental sedimentation of kaolinite Einsele (1977) demonstrated that during rapid sedimentation (2cm / day), conditions of under-consolidation (and overpressure) can be generated due to insufficient permeability. Earlier research of Bredehoeft & Hanshaw (1968) showed that during continuous sedimentation negligible excess pore pressure can be created in sediments having a permeability of 1mD or higher. However, if the loaded sediment has a permeability of 10^{-2}mD or lower, then pore pressures can be raised to a value approaching lithostatic during continuous sedimentation. Further modelling by Bishop (1979) demonstrated that **near-surface overpressure** within shale beds could be produced by rapid burial even at shallow depths. Slow burial also produces similar amounts of initial overpressure at depth, due to the poor drainage of mud sequences. Rapid shale burial also produces an inversion in the density profile throughout the

section, meaning that the section has a high density 'cap' which may effect the compaction of the less dense sequence beneath, as vertical fluid flow will be impeded.

To summarise, the fact that the quicker the rate of deposition of sediment the greater the potential for overpressure to develop, combined with episodic deposition which allows overpressure to dissipate during hiatal periods, the ideal depositional environment for this process to be occurring and therefore modelled, is that of the submarine fan. Within the submarine fan depositional environment there is not only the high initial mudstone porosities to allow large amounts of differential compaction to occur, but there is also very rapid deposition of turbidity flows, a matter of hours or days (Reading, 1986). By definition turbidite deposition is episodic, with flows being deposited within submarine channel systems and depositional lobes geologically instantaneously, followed by relatively long periods of negligible sedimentation, perhaps a fine pelagic rain of mud. Therefore, all the ingredients for a differential compactional control upon the topography of the depositional surface within the submarine fan environment are present, and its possible control upon deposition of flows requires assessing and modelling.

2.4 Simple Modelling of Compaction.

This section describes the technique used to model the effects of compaction upon sedimentary sequences. The first stage of this process usually takes a sequence of sediments that requires the removal of layers of sediment from the top downwards and the associated decompaction of the underlying units. This is then followed by the reverse process of forward modelling and re-compaction, to assess if compactional effects of the underlying strata directly influence deposition of subsequent sedimentary packages. Compaction is one of the processes that requires modelling along with other processes such as heat and fluid flow, hydrocarbon generation and expulsion, and secondary migration, to allow an entire model of a basin to be developed, and thus the potential of hydrocarbon exploration within that basin to be assessed. Hermanrud (1993) provided an excellent review of most of the historical research into these topics, and how they have provided a more complete understanding into the evolution of basins and their hydrocarbon potential.

The process of decompaction (Watts & Ryan, 1976; Steckler & Watts, 1978), diagrammatically shown in Figure 2.45, is most usually described and

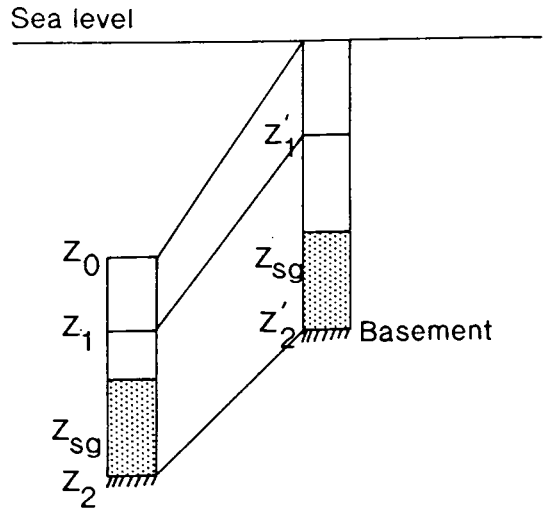

Figure 2.45 A schematic diagram outlining the decompaction as a layer of sediment is removed (after Sclater & Christie, 1980).

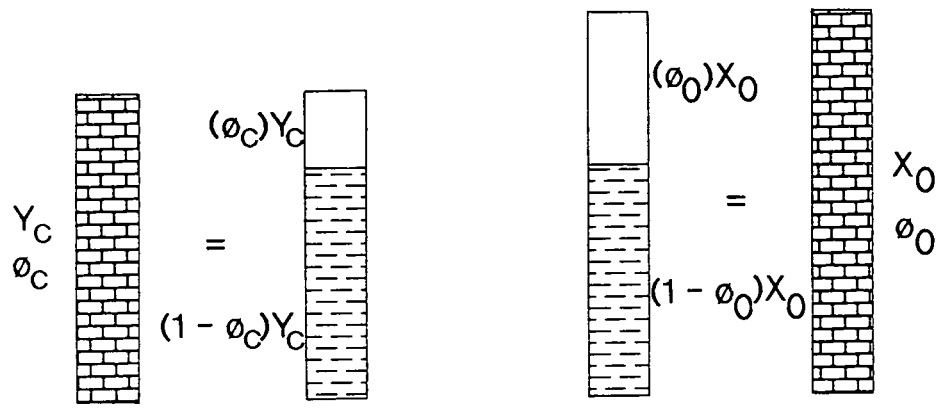

Since $(1 - ø_C)Y_C = (1 - ø_0)X_0$

$$X_o = \frac{(1-\phi_c)Y_c}{(1-\phi_0)}$$

e.g. Yc = 100m
øo = 0.50
øc = 0.20

(1 - øc)Yc = 0.8(100) = 80m of sediment

$$X_o = \frac{(1-\phi_c)Y_c}{(1-\phi_0)} = \frac{80}{0.5} = 160m$$

Figure 2.46 Theory and example of compaction correction following the approach of Van Hinte (1978)

utilised in the production of burial history curves (geohistory analysis), which essentially graphically shows the accumulation of sediment within a basin, and the inferred subsidence of the basin floor. Production of burial history curves requires various types of data such as sediment thicknesses, lithology, age information and palaeowater depth. Once a sedimentary sequence has been divided into its constituent layers a simple stratigraphic accumulation curve can be drawn. The layers are usually based on changes in lithology which require different compaction corrections, or on the amount of age control data for the section, since burial histories are plotted versus time. For the present work the modelling consists of dividing a section into separate lithologic slices to assess the impact of differential compaction on deposition. Therefore, the variable of age can be ignored as the intent is not to construct a burial history curve, however, the process is very similar.

Van Hinte (1978) described a method to decompact a section which then allows the construction of the initial thicknesses of the units, providing porosity data are known, or can be estimated using porosity-depth relationships. The method of Van Hinte (1978) showed that the thickness of a unit at the time of deposition (T_0) and any time thereafter is related to the change in porosity of the sediment during burial (Fig. 2.46). In the derivation it is pointed out that the volume of grains does not change during burial (assuming no significant diagenesis), but that the volume of the pore space decreases during burial. Therefore, the original thickness is related to the present-day thickness as follows:-

$$T_0 = \frac{(1-\phi_N)T_N}{(1-\phi_0)} \qquad \text{(equation 2.22)}$$

where ϕ_0 is the original porosity at the time of deposition, and allowing for autocompaction, and T_N and ϕ_N are the present-day thickness and porosity of the unit respectively.

Initial thicknesses can now be approximately calculated if a porosity-depth function, such as those of Baldwin & Butler (1985), or Sclater & Christie (1980) are used to predict the porosity of the unit at depth. Since the units present thickness is known, and a depositional porosity can be assumed depending on lithology, then once the porosity at depth is calculated, the initial thickness of the unit can also be calculated using equation 2.22. This approach assumes that all the reduction in a units porosity is due to compaction, and the effects of cementation are completely ignored. Petrographic work may suggest the amount of porosity destroyed by cement,

especially when used in conjunction with the graphs of Houseknecht (1987), or the later corrected graphs of Pate (1989) and Ehrenberg (1989b). Petrographic work may also show evidence of the timing of cement deposition. Thus improvements in calculations, and therefore modelling, can be achieved using thin section analysis. Models proposed by Gallagher (1989) also allow some correction of burial histories where both compaction and cementation are taken into account.

Using a chosen porosity-depth function and equation 2.22 the thicknesses of the units at successive stages of burial can be restored. For convenience, the porosity for the middle of each unit is calculated, and this is assumed to represent the average porosity of the entire unit. It must also be noted that the depth to the middle of a unit changes during burial, and therefore requires recalculation at every stage of unloading and decompaction. Figure 2.47 shows an example table used to calculate the compaction correction during the unloading of a sedimentary pile. The present porosities for the units midpoints can be calculated using the suitable porosity-depth relationship for each lithologic unit. In the second column from the left the uppermost sedimentary unit (unit 7) has been removed, and hence, represents the sedimentary sequence just after unit 6 was deposited. It is now possible to calculate the average porosity of unit 6, and thus its initial thickness using equation 2.22. Working down successively through the units it is possible to determine the new average porosities, and therefore their thicknesses prior to deposition of unit 7. This process is repeated for each unit down the column to determine the total thickness (ΣT) of the stratigraphic section after the deposition of unit 6. The entire process is then repeated for each column across the table, starting with the original column every time. The original column is used instead of the immediate preceding one as the latter will contain small errors due to the use of an approximate porosity-depth function, and it is important to lessen the effects of cumulative errors. Therefore, to calculate the effects of compaction on unit 5, the next step is to go back to the original column and remove units 6 and 7 to calculate the original porosity and thickness of unit 5.

The method described above only provides an approximate answer for the amounts of compaction occurring, dependant on the porosity-depth function chosen. The accurate method is described by Angevine et al. (1990) assuming that porosity decreases exponentially with depth (i.e. the porosity-depth function of Sclater & Christie, 1980), and that the volume of rock grains within the unit never changes. If a unit of thickness T_N is buried to a depth of

		Mid-Point (m)							
Unit 7	Limestone	500	1000 35%	Thickness Porosity					
Unit 6	Shale	1400	800 25%	1017 41%	Thickness Porosity				
Unit 5	Sandstone	1850	100 23%	108 29%	126 39%	Thickness Porosity			
Unit 4	Hiatus		0	0	0	0	Thickness Porosity		
Unit 3	Limestone	2350	900 10%	976 17%	1209 33%	1209 33%	1209 33%	Thickness Porosity	
Unit 2	Shale	2850	100 12%	106 17%	117 25%	120 27%	120 27%	172 49%	Thickness Porosity
Unit 1	Sandstone	4000	2200 12%	2278 15%	2361 18%	2390 19%	2390 19%	2652 27%	2652 27%	Thickness Porosity
	Sum of Thickness		5100	4485	3813	3719	3719	2824	2652	0

Figure 2.47 Example table for carrying out compaction corrections.

d_N, then its thickness (T_0) at some earlier time when the unit was buried to a depth of do can be found using the following relationship:-

$$\int_{d_0}^{d_0+T_0}(1-\phi)dz = \int_{d_N}^{d_N+T_N}(1-\phi)dz \qquad \text{(equation 2.23)}$$

Analytical evaluation of these two integrals is possible, to produce a transcendental equation which can only be solved using an iteration process (Angevine et al., 1990). This produces a very clumsy equation which essentially requires a computer to provide a solution, and only improves the compaction correction by 3% from the approximate method described above, when dealing with units thicker than 100m. As the present work is more or less completely dealing with units thinner than 100m, the approximate method will be used throughout the compaction modelling process in Chapters 3, 4 and 5.

Both Perrier & Quiblier (1974) and Collier (1989) presented formulae to model compaction of sedimentary sequences. However, both these methods use an exponential porosity-depth function of the form calculated by Sclater & Christie (1980), which requires a variable dependant upon the lithologic character of the sediment. The present work will show in the later chapters that for early compaction this relationship does not appear to be correct and, accordingly, these formulae derived will not correctly model near-surface compactional processes.

Conclusions Concerning the Near-Surface Compaction of Sediments.

1. Near-surface compaction is much greater in muds (especially those with the highest depositional porosities) than in sands, where it is more or less absent for depths less than 100m of burial.
2. Environments where sand and shale are juxtaposed are areas where differential compaction can occur, creating a possible topographic control on the subsequent facies development and geometry.
3. Equilibrium compaction of muds requires a considerable amount of time. Therefore, environments where deposition is episodic possibly show the greatest effects of differential compaction, as hiatal periods and breaks within sedimentation allow further compaction of muds to occur while no further sediment load is added. Thus the topography produced on the depositional surface by this process will be greater than if only a short time span of mud compaction is allowed.

CHAPTER 3:- FIELDWORK - SOUTHERN CALIFORNIA.

3.1 Introduction.

This chapter deals with the field data collected during April and May 1991, in Southern California, during the first year of study. Essentially three areas were studied during this period, namely Ridge Basin, within the central Transverse Ranges; La Jolla, San Diego, and Wheeler Gorge within the Santa Ynez Mountains. The majority of the study was concentrated in Ridge Basin because of the excellent exposure within the region, and therefore forms the main part of the data within this chapter. However, the latter two areas also provide valuable observations and insights into the process of early compaction within the submarine environment.

The basis of the field study was to provide outcrop data of submarine fan deposition, comparable in depositional setting to the geophysical data and well data from the Montrose and Arbroath oilfields in the North Sea, described in Chapter 5. Field data enables an insight into the early compactional process within the submarine environment which can then be built into the depositional model for the Montrose - Arbroath area (see Chapter 5). This allows a greater refinement of the syn-depositional compactional process described in Chapter 2, providing valuable information on the timing, amount, and possible control upon the depositional arrangement and geometry within such environments.

Section 3.5 concludes the chapter showing how field data have been interpreted and used to assess the process of early compaction within the submarine fan environment, and how this may affect the depositional model for the Montrose - Arbroath area. It outlines possible theories for deposition of sediments within the submarine setting and also possible problems that can be superimposed upon a model of simple turbidite deposition.

3.2 Ridge Basin.

3.2.1 Introduction.

Ridge Basin is a narrow, fault controlled basin lying forty miles north of Los Angeles in the central Transverse Ranges of Southern California, U.S.A. (Figs. 3.1 & 3.2). During the late Miocene, and lasting into the Pliocene, an extremely thick stratigraphic section, exceeding 13,500m (44,000ft) was laid down within the narrow basin as the depocentre migrated northwards. Sedimentary facies within the basin are unusually well exposed and document a change through time from a marine embayment to a lacustrine

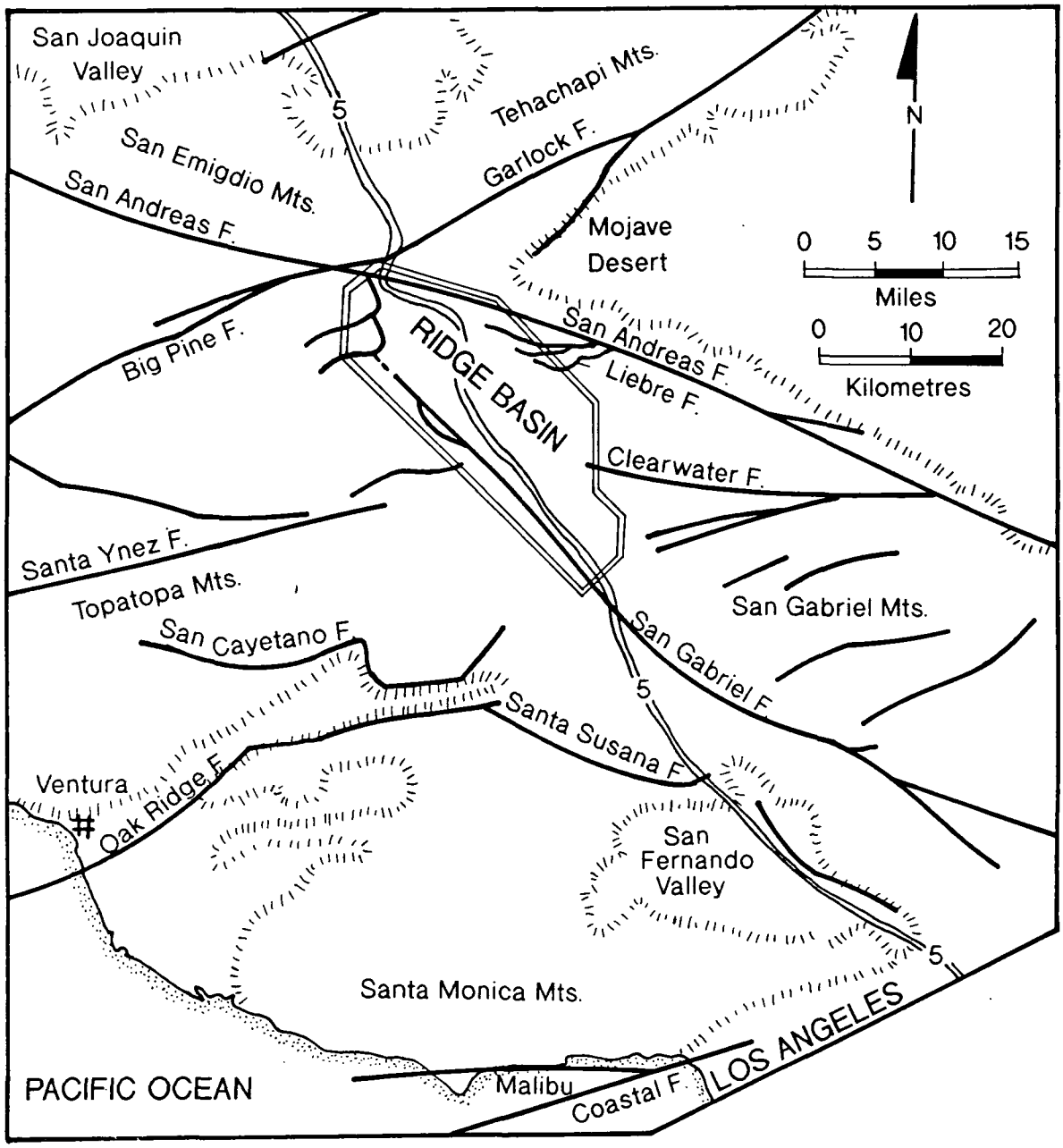

Figure 3.1 Ridge Basin location map.

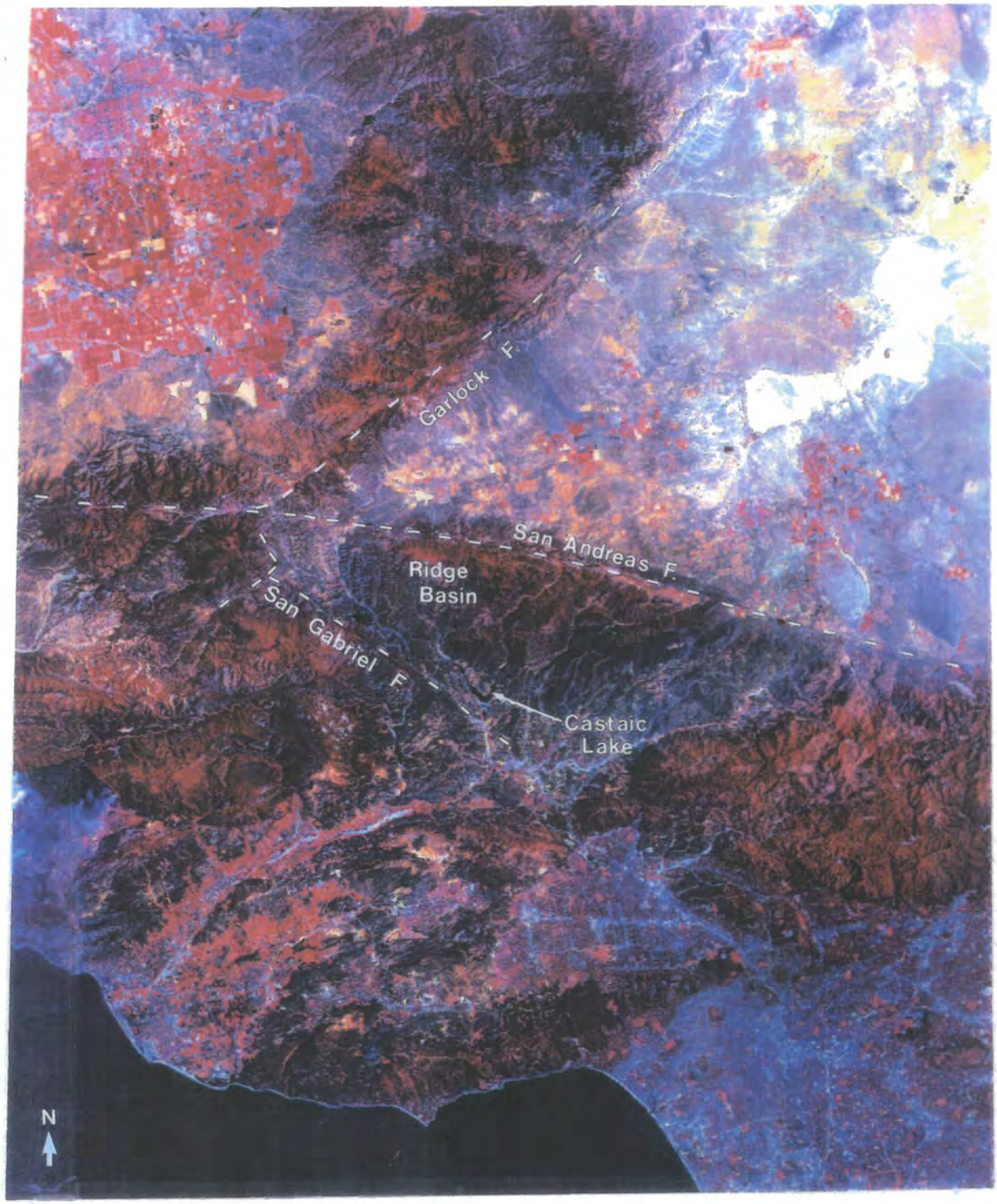

Figure 3.2 Satellite image of Ridge Basin, showing Castaic Lake, and northern Los Angeles.

and alluvial environment. The region is situated between the complex faulted transform margin of the Pacific and North American lithospheric plates, and therefore allows a good insight into the interplay between sedimentation and tectonics. The sedimentary fill of the basin has been extensively studied by numerous workers, especially Crowell and Link, who edited the 1982 geological history of the basin, which forms a comprehensive text book and field guide to the area. Other studies have been carried out concerning the tectonics, palaeontology, palaeoecology and diagenesis of the region, and are all contained within the guide book.

3.2.2 Tectonics.

Ridge Basin originated during the Miocene epoch as a stretched and sagged crustal wedge within the complex boundary between the Pacific and North American plates. The ages of fault movements surrounding the basin can be well documented by the overlapping relationships of the sedimentary fill. The San Gabriel Fault (Fig. 3.1), forming the southwest edge of the basin, began its activity about 12m.y. ago, when it formed an early strand of the San Andreas transform system, and ceased its displacement 5m.y. ago. On the eastern edge of the basin the Clearwater Fault was active around the same time ceasing its displacement slightly earlier, approximately 8m.y. ago. This activity was followed by successive strands of the Liebre Fault Zone which migrated northeastwards, ceasing displacement slightly earlier than the San Gabriel Fault, between 6 and 5m.y. ago. At the termination of San Gabriel Fault displacement all transform movement was taken over by the present day San Andreas Fault system. The switch in active fault traces created the 'Big Bend' within the San Andreas Fault, forming the northern end of Ridge Basin, with the Frazier Mountain Thrust (Fig. 3.3) forming the northwest boundary, due to later crustal shortening south of the 'Big Bend'. Uplift and erosion in the Pleistocene, continuing to this day, have exposed geological relations that allow an unusual documentation of the interplay between tectonics and sedimentation, including the timing of fault movements (Crowell, 1982a).

The San Gabriel Fault developed in late Miocene times, approximately 12m.y. ago and possibly as early as 14m. y. ago, forming the plate boundary within the region. The fault is extremely long and can be traced for 130Km (80 miles) on the surface, with the type of the displacement varying along its length. Throughout the central part of Ridge Basin the fault dips 70° to the northeast, whereas at the southern end of the basin, around the town of

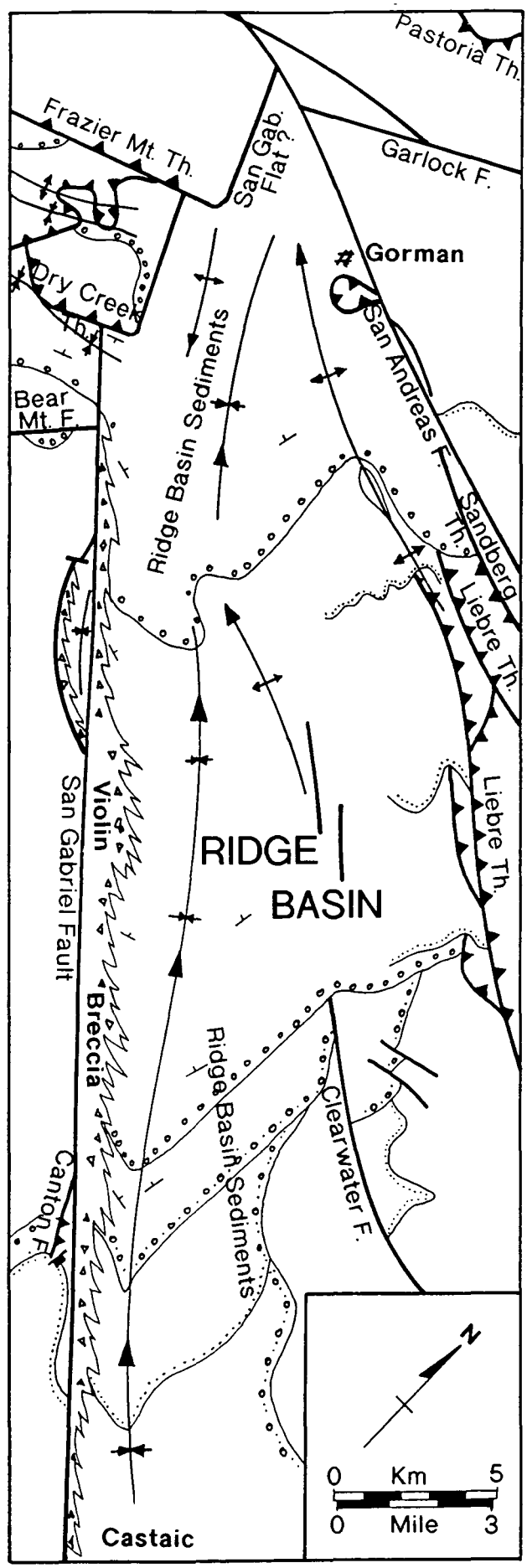

Figure 3.3 Simplified structural map of Ridge Basin (modified from Crowell, 1982a).

Castaic, the fault dips nearly vertically. The amount of displacement along the fault is one of controversy, but it appears to amount to at least 35km (22 miles) of essentially right (dextral) slip, and possibly as much as 56km (35 miles). There is also evidence for a low angle of oblique slip apparent in some regions along the fault trace (Crowell, 1982a). Due to the fact that the trace of the fault is not perfectly straight around the northern region of Ridge Basin, having a gentle eastward arc around a restraining bend bounding the Frazier Mountain region, when movement of the fault occurred, it caused the squeezing and uplifting of the Frazier Mountain terrane, providing a sediment source along the southwest edge of the basin. At the same time, the movement of the terrane on the northeast side of the fault trace caused stretching of the area around the outside of the bend, causing the plate to sag and form the floor of Ridge Basin itself. The mountains to the north of this 'sag' provided the majority of the sedimentary input for Ridge Basin, and the relationship between their deposition and the tectonic activity will be described in more detail in the following section. To summarise, Ridge Basin originated as a tectonically controlled basin, produced by crustal stretching around a releasing bend of a dextral strike-slip fault.

For 35km (22 miles) along the San Gabriel Fault there is a strip of sedimentary breccia forming the southwest edge of Ridge Basin (Fig. 3.3). This formation was named the Violin Breccia by Crowell (1954) due to its exposure within Violin Canyon. The strip reveals considerable information on the nature of the fault's history of displacement, as well as on the origin of Ridge Basin itself. The breccia unit is over 11,000m (36,000ft) thick stratigraphically, and it changes facies within a kilometre or so from coarse gneissic rubble, into finer beds within the central trough of Ridge Basin (Crowell, 1982b). The nature and distribution pattern of Violin Breccia reveals that there was continuous, or closely spaced intermittent, rejuvenation of the San Gabriel Fault scarp throughout the time of its deposition, i.e. from 12 to 5m.y. ago. Throughout this period the fault movement was essentially right slip with concurrent uplift along the southwest edge of a restraining bend, as described above. Sediment was shed from this uplifted region, which was intermittently elevated during fault activity, forming talus and small alluvial cones passing into the basin over a very short horizontal distance from the active fault, accumulating on the North American plate as it moved southwards. Therefore, a 'conveyor-belt' mechanism can be imagined, controlling not only the deposition of the Violin Breccia but also the major

sedimentary fill of the basin, sourced from the mountains to the north and northeast (Fig. 3.4) (Crowell, 1982).

The 'conveyor-belt' system was active during faulting, causing right-lateral (dextral) movement of the basin towards the southeast, and with associated uplift and rejuvenation of the sedimentary source area each time an earthquake occurred. Slow creep may also have occurred along the fault trace. As fault movement continuously occurred, deposits of breccia were transported on the American plate towards the southeast, creating 'new' regions of basin floor, which provided accommodation space for further deposits of breccia from the relatively uplifted fault scarp region. The combined mechanism of slow creep and active fault displacement accounts for the total of more than 11,000m (36,000ft) of Violin Breccia, and the northwestwards overlap of the sedimentary units within Ridge Basin. Modern day analogies to this mechanism can be described, showing that major earthquakes probably accompanied horizontal displacements along the faults (e.g. the San Andreas Fault).

Two major fault systems enter Ridge Basin from the east, the Clearwater and the Liebre (Figs. 3.1 & 3.3). The Clearwater Fault can be traced for 43Km (27 miles) from a western point where it is overlapped by sediments within Ridge Basin, eastwards to where it joins the San Andreas Fault. The fault is believed to be an oblique and right-slip fault, which is more or less vertical, accounting for its straight trace across rugged mountain terrain. Several episodes of displacement occurred along the Clearwater Fault, before, during, and after deposition of sediments within Ridge Basin itself, which overlap the fault at the western end. Fault movement after the deposition of the overlapping sediments did not completely cut the thick mass deposited within the central part of the basin, and it is represented as local folds and minor faults in the sediments (Crowell, 1982a).

Bordering Ridge Basin on the northwest at least four strands of the Liebre Fault Zone are overlapped by successively younger beds of the basin sequence (Crowell, 1982a). Individual fault strands within the area were therefore active at different times during deposition of Ridge Basin sediments, and the coarse conglomerates proximal to the fault show that the fault zone played a role in forming the basin margin (Fig. 3.5). Displacement along this fault is less well known and documented, although Crowell (1982a) proposes a right slip of the order of 8Km (5 miles). The four episodes of sedimentary overlap of the fault strands document the northeastern migration

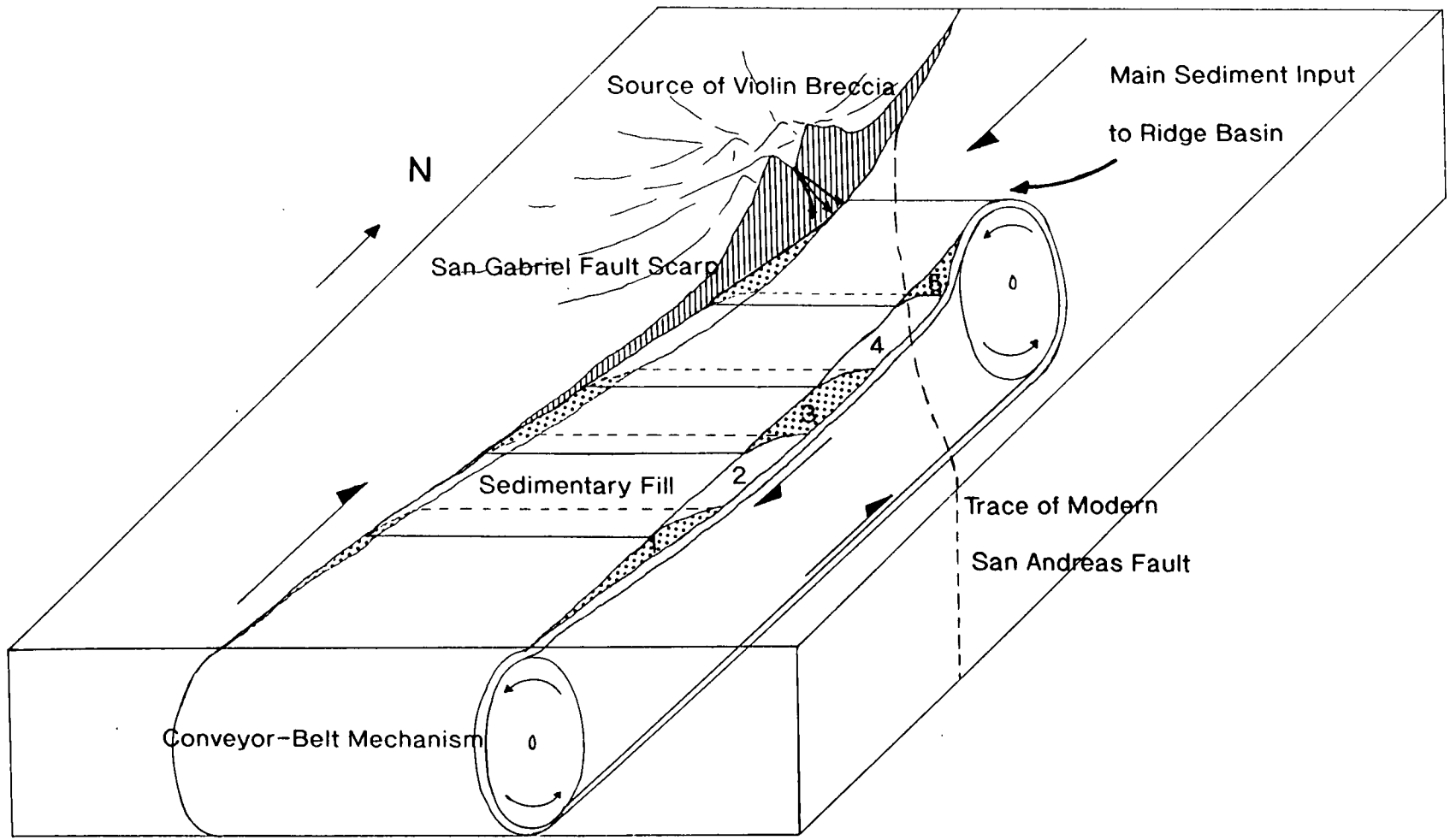

Figure 3.4 Diagram illustrating conveyor-belt mechanism for deposition of sedimentary units in Ridge Basin, including the Violin Breccia (modified from Crowell, 1982a).

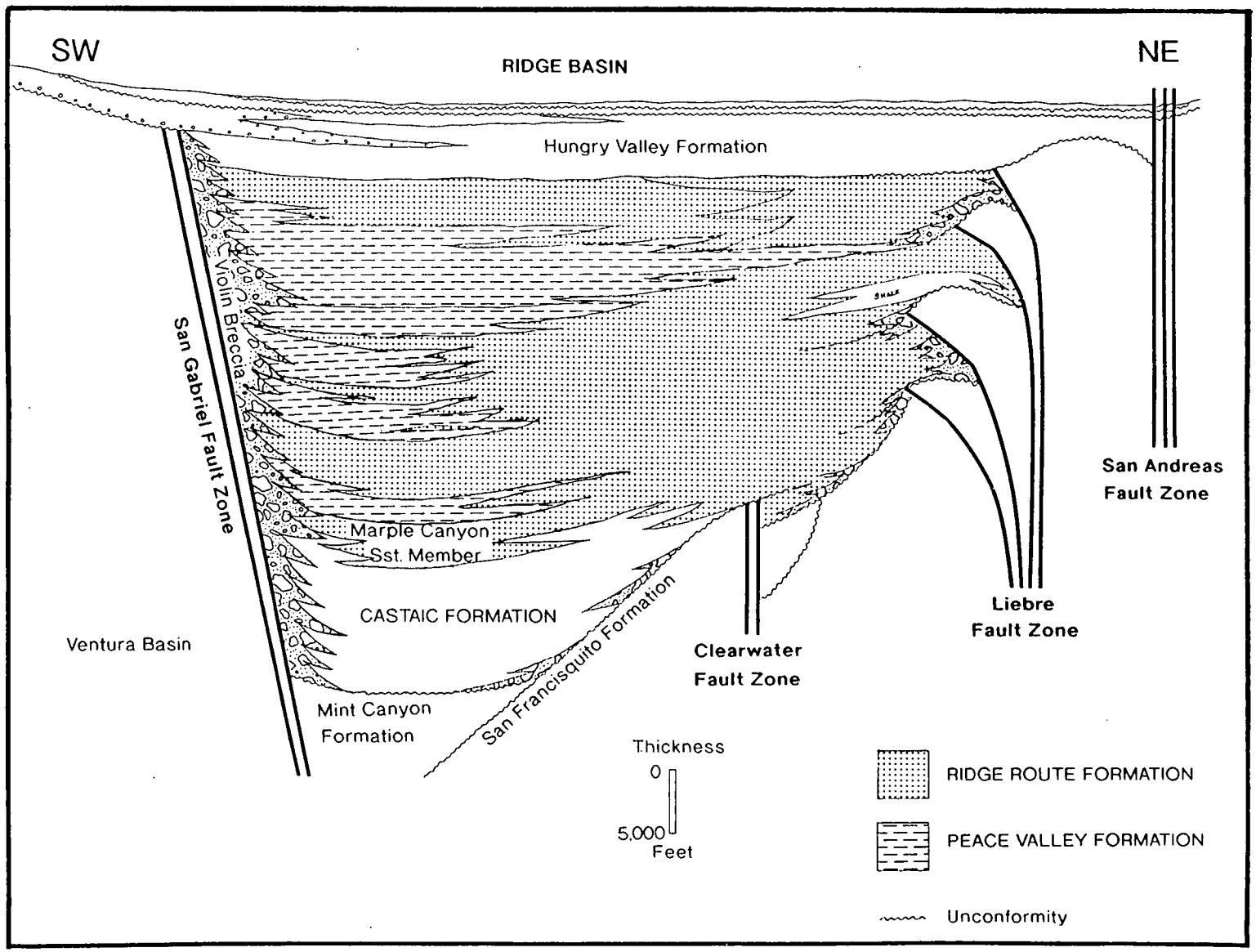

Figure 3.5 Stratigraphic arrangement, Ridge Basin, southern California (Redrawn from Link, 1982a).

of the principal strand of movement on the fault system during the time of Ridge Basin sedimentation (Fig. 3.5).

The Frazier Mountain Thrust System forms the northwestern corner of Ridge Basin (Fig. 3.3). This system is made up of a series of thrusts, the most conspicuous of these being the Dry Creek Thrust and the Frazier Mountain Thrust. Precambrian basement rocks are thrust over Ridge Basin sediments by this system, and Crowell (1982a) interprets that the thrusts have originated from north-south shortening that has telescoped the rocks to the south of the San Andreas. From the map shown in Figure 3.3 it can be seen that both the Dry Creek and Frazier Mountain Thrusts have straight faults along their eastern edges, and these are believed to be uplifted and rotated segments of the San Gabriel Fault (Crowell, 1982a). This would mean that the displacement on the system need not exceed 6Km (3 miles). It therefore appears that this thrust system originated and grew as the 'Big Bend' in the San Andreas developed during the Pliocene and Pleistocene.

Ridge Basin is sharply truncated on the north by the active San Andreas Fault (Fig. 3.3). The timing and amount of displacement along this fault within the area is still poorly constrained. However, it is believed that the fault originated around 5 to 6m.y. ago as transform movement upon the San Gabriel Fault weakened and died. Therefore, the San Andreas formed the northern edge of Ridge Basin during the final stages of sedimentary deposition within the basin.

The Sandberg Thrust (Fig. 3.3) is of little consequence to the overall tectonic framework of Ridge Basin. It is poorly exposed, and hence poorly studied and understood. It can be traced laterally for 4Km (2.6 miles) and is interpreted as a high angle thrust fault which dips steeply to the south at depth, beneath Liebre Mountain (Crowell, 1982a). Strands of the San Andreas have since dismembered the Sandberg Thrust.

The Ridge Basin Syncline runs along the axis of the basin, plunging to the northwest (Fig. 3.3). Major folding, along with other minor folds and faults primarily occurred during the Pleistocene, and was associated with compression and uplift of the central Transverse Ranges.

3.2.3 Stratigraphy.

The oldest rocks within the Ridge Basin area are Precambrian gneisses, diorites, gabbros, amphibolites and anorthosites, which are intruded by Cretaceous granitic rocks. These are unconformably overlain by Cretaceous and Palaeocene marine sedimentary rocks of the San Francisquito Formation

which formed the basement to much of Ridge Basin. Unconformably overlying these sequences there is a 13,000 to 14,000m (42,650 to 46,000ft) thick section of Miocene to Pliocene, marine and nonmarine sedimentary rocks (Fig. 3.5). These units are from oldest to youngest; Mint Canyon Formation, Castaic Formation, and the Ridge Basin Group. The Mint Canyon Formation is a small tongue of fresh/brackish water sandstones and conglomerates that unconformably overlies the San Francisquito Formation in the extreme southeast region of Ridge Basin, representing an early phase of subsidence. The Castaic Formation unconformably overlies the Mint Canyon Formation, and marks the beginning of marine sedimentation within Ridge Basin itself. The Ridge Basin Group consists of the Violin Breccia, Ridge Route Formation, and the Hungry Valley Formation, and the Ridge Route Formation fills the thickest central part of the basin, where it interfingers with the laterally equivalent, Peace Valley Formation (Fig. 3.5).

For this study interest is focused on the Castaic Formation and the overlying Marple Canyon Sandstone Member, which is the lowermost member of the Ridge Route Formation. The Marple Canyon Sandstone is transitional with the Castaic Formation below. The Castaic Formation ranges from 520 to 2800m (1700 to 9200ft) thick, and is a late Miocene sequence of mudstones interbedded with siltstone, sandstone, and conglomerates, containing marine molluscs and foraminifera. The formation is exposed in the southern end of Ridge Basin, with a maximum lateral extent of about 10Km (6 miles) measured on a northeast - southwest section. It has an average dip of 20° to the west, and is contemporaneous with the Modelo Formation of the neighbouring Ventura Basin. Thus early workers named the formation Modelo, but slight variations of the lithologic character between the two formations exist, and hence separate names are now used (Link, 1982a).

Stanton (1960, 1966) indicates that the basal portion of the Castaic Formation in the east of the basin was deposited during a transgressive marine event, whereas deposits in the middle part of the basin were deposited at water depths between 45 to 90m (150 to 300ft). Benthic foraminiferal assemblages suggest moderately deep water and restricted circulation (Skolnick & Arnal, 1959).

Ridge Basin was born in Castaic Formation times, forming a restricted marine basin behind the San Gabriel Fault scarp. The deep end of the basin was to the south where it opened into Ventura Basin. Link (1982b, 1983) interprets the formation as consisting of slope facies and basin axis turbidites, being transitional with the Marple Canyon Sandstone Member above, and

laterally interfingering with the Violin Breccia to the southwest (Fig. 3.6). Slope facies consist of mudstone interbedded with laterally discontinuous sandstone, conglomerate and coquina deposits, interpreted as turbidite-filled channels. Slope deposits follow the northwest trend of the basin, and were predominant on the northeast and southwest sides of the basin. The turbidite-filled channels locally meander, and exhibit laterally adjacent levee deposits (Link, 1982b). Large slide blocks, slump folded strata and breccia beds are common within the slope facies.

Basin axis deposits consist of major channel and interchannel facies plus depositional lobe sequences. These deposits are confined to the centre of the basin and interfinger laterally with slope deposits to the northeast and southwest (Fig. 3.6). Link (1982b) interprets the channel deposits as thinning and fining upward sequences that are laterally discontinuous, with the interchannel deposits forming inclined wedges of slump-folded strata. Depositional lobe sequences are laterally continuous with minor channelling and slumping. Palaeocurrent directions to the south and southeast indicate that sediment dispersal was along the axis of the basin derived from elevated terranes in the north and northeast (Link, 1982b).

With Ridge Basin being a relatively shallow-marine and symmetrical basin, typical submarine fans, such as those described by the models of Mutti & Ricci Lucchi (1972), Normark (1978), and Walker(1978), having typical upper, middle, and lower regions, did not form during Castaic Formation times. Instead, a simple division of slope facies developed around the basin margins, with turbidite-filled channels and depositional lobes forming within the axis of the basin.

3.2.4 Depositional Model for the Castaic Formation.

Link (1982b, 1983) has extensively studied the Castaic Formation, proposing the depositional model which forms the basis of the present study. His observations and interpretations are often used and corroborated by the present work, enabling a full understanding of the depositional history and overall geometry of the system to be achieved.

Castaic Formation and the lower units of the Marple Canyon Sandstone Member were deposited in a narrow northwest trending, linear trough (Link, 1982b). Shallow-marine sedimentation was confined to the margins of the basin, and deeper-marine sedimentation occurred on the slopes and in the axis of the basin (Fig. 3.6). Slope facies deposits formed along the northeast and southwest margins of the basin, across which sediment from the eroded

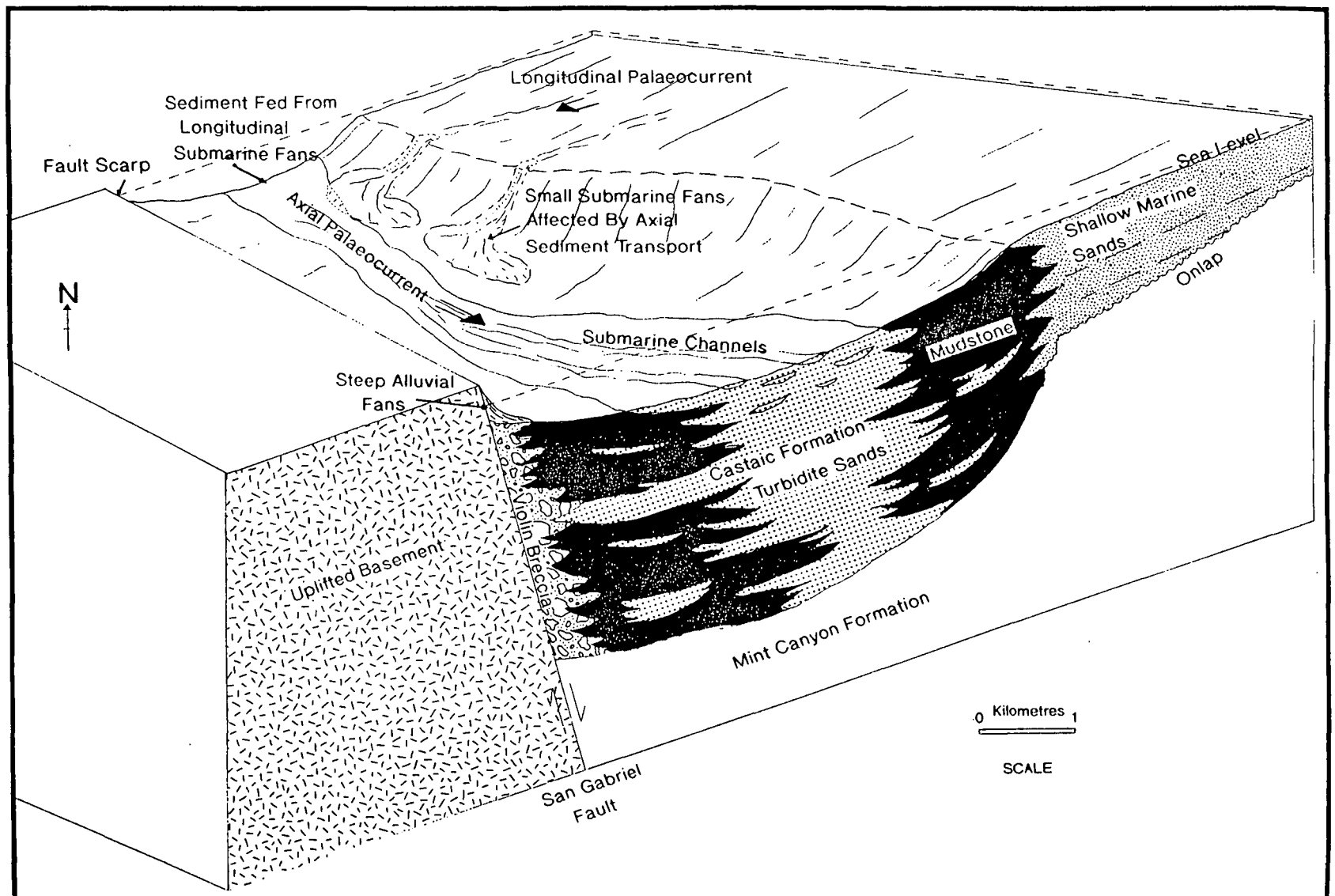

Figure 3.6 Depositional model for the Castaic Formation and the lower Marple Canyon Sandstone Member.

uplands was transported within meandering channel systems, to be deposited as thick channel deposits, or depositional lobes within the deeper water basin axis (Fig. 3.6). Slope deposits therefore, consist of muddy sediments interbedded with turbidite-filled channels, associated slumped levee deposits, and thin laterally continuous turbidites produced by over banking of the channel system. The slope channels coalesce in the basin axis forming major distributary channels that funnelled the sediment south-southeastwards along the basin axis to form depositional lobes where sediment spread out and became unchannelised. A major progradational sequence is preserved in the axis of the basin (Link, 1982b). Depositional lobes were overlain by channel and interchannel facies, which were in turn eventually overlain by nonmarine fluvial-deltaic sequences as the basin filled.

To summarise, the depositional model as proposed by Link (1982b, 1983) for the Castaic Formation and the lower marine section of the Marple Canyon Sandstone, consists of a simple two-fold division of facies associations. Firstly, slope facies consisting of generally mud-dominated sediment, interbedded with turbidite-filled channels occurs around the basin margins. Secondly, the basin axis consists of generally sand-dominated deposits, in a sequence of depositional lobes overlain by major distributary, turbidite channel systems. The following descriptions of measured sections will provide greater detail of the facies involved, and illustrates all the aspects of the depositional model described.

3.2.5 Exposure Within Ridge Basin.

In general, exposure and access of all formations within Ridge Basin is excellent. However, although Castaic Lake now covers part of the type area of the Castaic Formation (Fig. 3.2), access to good continuous exposures along the lakeside cliffs is still possible. Other good exposures of Castaic Formation and the Marple Canyon Sandstone Member occur in roadcuts along the Old Ridge Route, which runs sub-parallel to the axis of the basin, and the Templin Highway which generally runs perpendicular to the basin (Fig. 3.7).

3.2.5.1 Castaic Lake Exposures.

Four sections were measured from the cliff exposures on the southwest shores of Castaic Lake (Fig. 3.7), starting from the southern end of the lake by the coastguard station and moving north for approximately 2km (1.25 miles). These exposures show the general upward progradation from

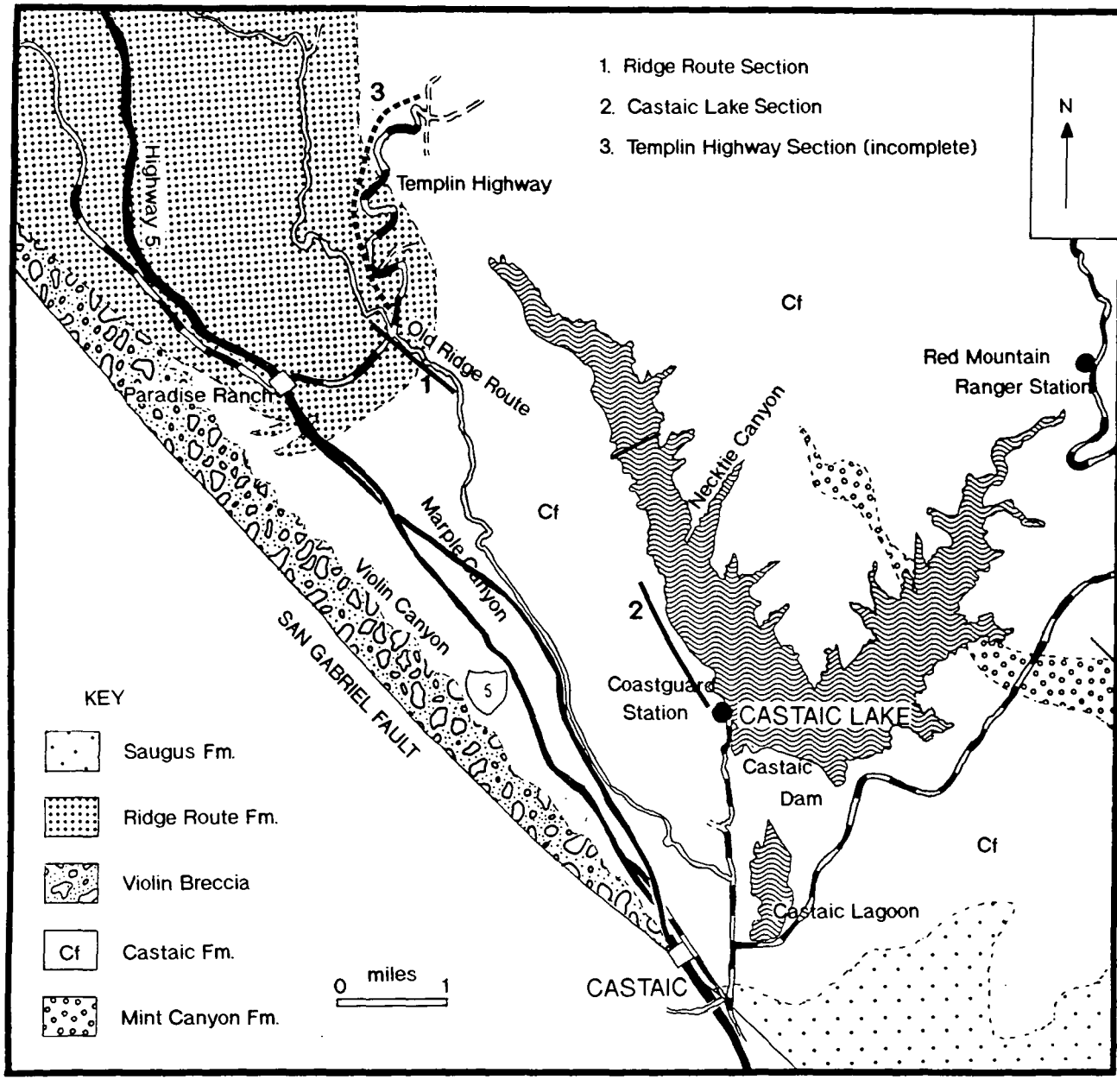

Figure 3.7 Location map of measured sections of the Castaic Formation in Ridge Basin.

depositional lobe to submarine fan distributary channel deposition a number of times throughout the sections (Figs. 3.8 & 3.9). Sections 3 and 4 form the most complete exposure of the Castaic Formation within the entire basin, showing good examples of both depositional lobe sequences which are laterally continuous, and distributary channel and levee deposits which pinch out along strike within the outcrop.

Section 1.

Section 1 crops out at the southern-most shores of the lake, just north of Castaic Dam and the lifeguard station. The section consists of a sequence of interbedded sandstones and shales (Fig. 3.8 & Plate 3.1).

Sandstone beds range from 0.1 to 4m (0.3-13ft) thick, averaging 1.2m (4ft). The mudstone is massive and completely envelops this predominantly sandstone sequence. Mudstone interbeds are up to 1.5m (5ft) thick, averaging 0.3m (1ft) (Fig. 3.8). The sands are generally coarse to medium grained, moderately sorted, consisting of a graded and loaded basal section, with rare parallel laminations above. Cross lamination is extremely rare, and occurs on the top of thin sand beds. Shale rip-up clasts are common throughout the sand units, along with dish structures and pipe dewatering phenomenon. Bouma sequences (Fig. 3.10) are also present, most commonly represented by the T_{ab} division (Fig. 3.8), and the beds show extreme lateral continuity. Individual beds can be traced along the shores of Castaic Lake from section 1, cropping out again at the base of section 2, approximately 400m (0.25 miles) away, before they disappear below the water line of the lake. Some evidence for small scale channelling occurs at the top of the section, with small scours down-cutting up to approximately 1m (3.3ft) into the underlying shale and sandstone sequence. On detailed graphic logs, the exposure shows two sequences of thickening and coarsening upward packages, although Figure 3.8 does not give a clear representation of this.
Sandstone deposits are interpreted by Link (1982b, 1983) to be turbidites, consisting of facies associations B, C, and D, according to the nomenclature of Mutti & Ricci Lucchi (1972) (Table 3.1). They can be traced laterally for distances greater than 1Km (Link, 1982b). Due to their location within the centre of the basin, and more importantly, palaeocurrents to the south-southeast combined with the facies patterns, Link (1982b, 1983) interprets these deposits as depositional lobes which formed along the axis of the basin. They differ from the channel and interchannel facies (see descriptions of sections 3 and 4) by having beds which are more laterally persistent,

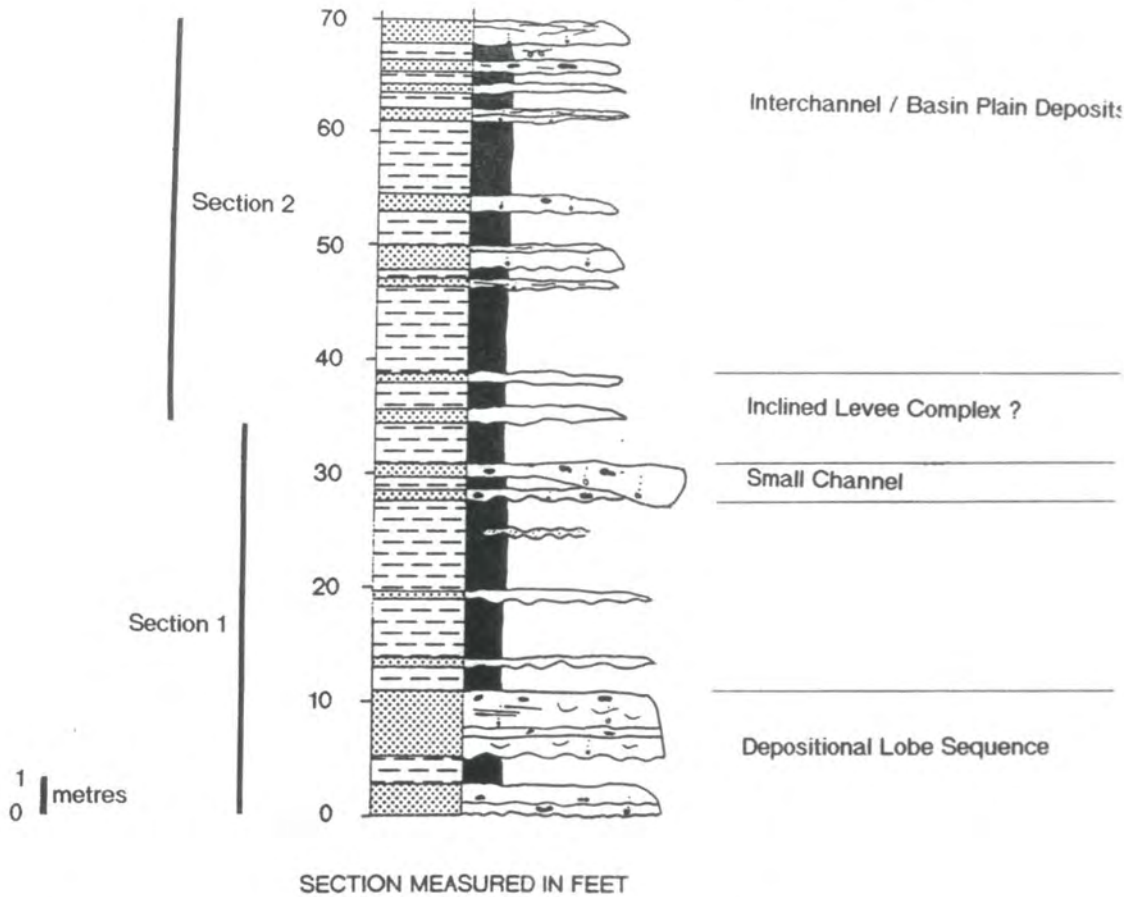

Figure 3.8 Measured sections 1 and 2, Castaic Lake.

Plate 3.1 Section 1, Castaic Lake.

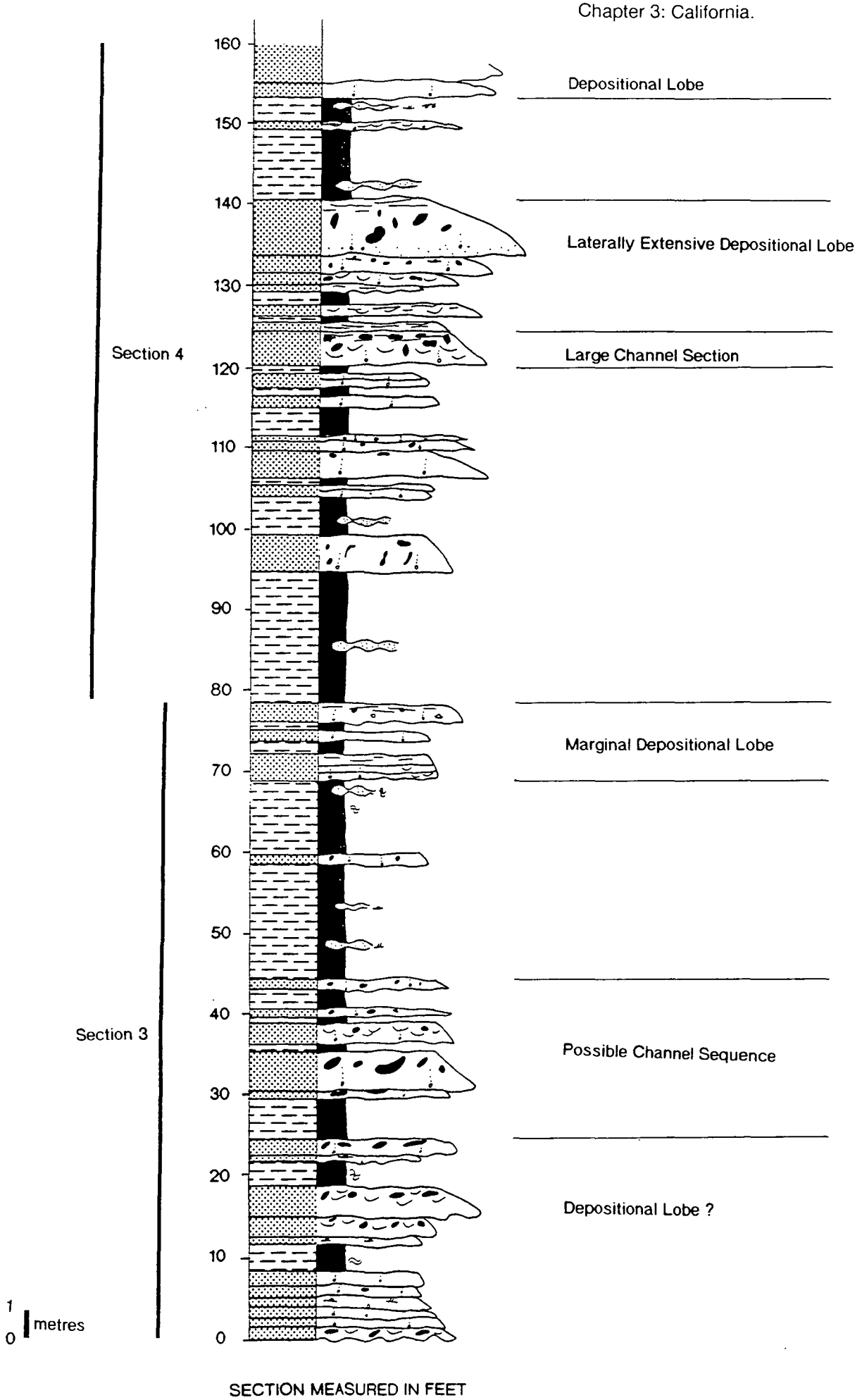

Figure 3.9 Measured sections 3 and 4, Castaic Lake.

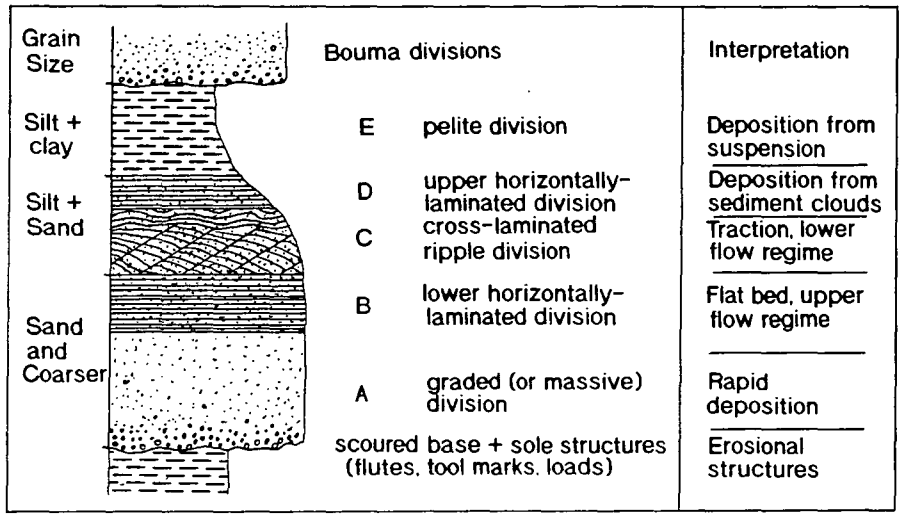

Figure 3.10 Sequences of structures and Bouma divisions of a siliciclastic turbidite bed. Turbidites range in thickness from several centimetres to a metre or more (After Tucker, 1981).

higher percentages of facies C and D turbidites in contrast to facies B turbidites (Table 3.1), and show fewer slump-folded strata and channels.

Facies	Lithology	Bedding	Features
A	Conglomerate Coarse Sandstone	Thick, Irregular, Amalgamated	Channel Fill, Shale Clasts, Poor Sorting
B	Coarse to Medium Sandstone	Thick, Lenticular	Channel Fill, Shale Clasts, Dish Structures
C	Medium to Fine Sandstone, Minor Shale	Medium, Continuous	Complete Bouma Sequence
D	Fine to Very Fine Sandstone, Siltstone, Shale	Thin, Remarkably Continuous, Parallel	Bouma Sequence with Base Missing
E	Sandstone, Siltstone	Thin to Medium, Irregular, Discontinuous	Beds with Sharp Upper Contacts
F	Complex	Chaotic	Slumps
G	Shale, Marl	Laminated, Remarkably Continuous, Parallel	Homogeneous Texture

Table 3.1 Turbidite facies associations (according to Mutti & Ricci Lucchi, 1972)

Section 2.

Moving northwest approximately 400m (0.25 miles) around the shores of Castaic Lake, section 2 crops out in a rocky point on the north side of a small inlet, and forms the upward continuation of section 1 (Plate 3.2). The section also consists of interbedded sandstones and shales, although the sands are generally thinner than those seen at section 1 (Fig. 3.8). The sandstones of section 1 can be seen cropping out at the water-line, forming the base to section 2. Exposure above this is quite poor, being covered, although one small exposure shows that most of the section is extremely slumped and contorted. Above the slumped horizon comes a well exposed section of laterally continuous thin, interbedded sandstones and shales,

which are in turn covered by another highly slumped and chaotically bedded sandstone-shale section (Plate 3.2).

The sands exposed in this section are identical in composition and texture to those of section 1, being buff coloured, medium grained, moderately sorted, and exhibiting graded bases with some parallel lamination apparent. Slumping is much more common in this section than in the first, and appears restricted to certain horizons within the section. This phenomenon is quite abundant throughout the field area, and will be expanded upon later (see section 3.2.6).

Interpretation of the sediments, facies and overall sequence of sections 1 and 2 points to the lowest sands being deposited within a depositional lobe setting, and above this the turbidites tend to be considerably thinner, with thicker interbedded shale sections (section 2). This area possibly represents an interlobe depositional environment, with only thin sands deposited at the very fringe of a depositional lobe off-set from the lower lobe that produced the sands seen in section 1.

Section 3.

Moving further northwest about 800m (0.5 miles) around the shores of Castaic Lake an extremely well exposed section of cliff face provides excellent exposure of the Castaic Formation, over a large lateral distance of around 2.4Km (1.5 miles). Approximately 800m (0.5 miles) of this exposure is accessible by foot along the shore of the lake, whereas the rest of the exposure, which is slightly poorer due to scree, can only be reached by boat. Numerous sections were measured here to provide a thorough overview of the depositional setting of the sediments (Fig. 3.9). Essentially the sediments are identical to those seen at previous sections to the southeast of the lake, however, there is a general overall trend for the sands to become coarser up through the section, becoming pebbly and conglomeratic. Dish structures are extremely common along with slumped horizons (Plate 3.3). The turbidites around the base of the section are generally facies B and C (Table 3.1) showing Bouma sequences (Fig. 3.10) of T_{ab} and T_{abc}. Moving up section the turbidites tend to be of facies A and B (Table 3.1).

The base of section 3 shows sandstone beds that are laterally discontinuous and wedge out along strike. Adjacent to these beds are inclined strata of thin bedded sands, silts and muds. These are interpreted to be channel-fill deposits with associated inclined levee facies, with palaeocurrents indicated to the southeast. The stacking arrangement of the

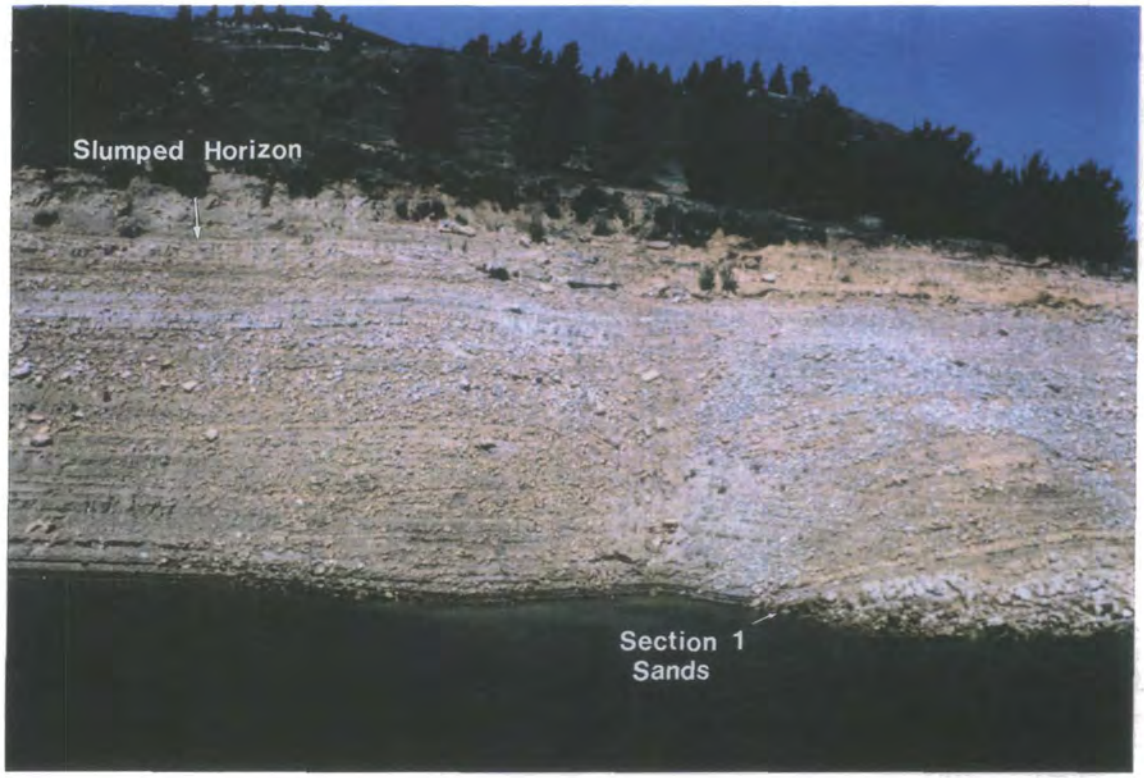

Plate 3.2 Section 2, Castaic Lake. Note slumped horizon at top of section.

Plate 3.3 Dish structures within a turbidite bed, Castaic Lake.

channel-levee complexes is interesting as a diagonal off-set pattern is clearly visible from section photographs (Plate 3.4). Similar patterns were observed by Fielding (1982, 1984), when dealing with the depositional arrangement of distributary channels within a coastal/deltaic environment, with associated coal deposition. The stacking pattern is interpreted to have resulted from the influence of differential compaction upon the depositional arrangement, and is further developed in section 3.2.7. The channel-levee complexes could either represent small distributary channels within the basin axis, or crevasse splay deposits from a larger channel. However, the presence of associated levee deposits, and the abundance of at least three channel complexes seems to suggest that these deposits are more likely to be small distributary channels that crossed the floor of the basin axis depositing small sands lobes at their distal ends. Above this section laterally persistent turbidites occur, which form regular, horizontally bedded sandstone units averaging 1m (3.3ft) thick with thin shale beds between. These shale beds are sometimes loaded into and completely cut out in places as the overlying sandstone loads down, and through the underlying shale, to rest on the previous sandstone bed, creating amalgamation through loading. The section here is interpreted to represent a small depositional lobe deposit forming at the end of the small distributary channels, similar to those described above.

The section above the small lobe sequence contains many examples of laterally discontinuous sand bodies that exhibit frequent scours and amalgamation (Plate 3.5), reaching a maximum thickness of 2m (6.6ft) for an individual amalgamated sand section. Plotted on the graphic log the entire section appears to thin and fine upwards (Fig. 3.9) suggesting that these sands are channel turbidites, forming in a larger channel than those previously seen lower in the section. This section is overlain by a thick (7.3m) mud section containing a few interbedded, cross-laminated silts and fine sands exhibiting Bouma divisions T_{c-e}, interpreted to represent an interchannel environment, associated with channel deposition situated somewhere to the northeast or southwest of the area. Near the top of the interbedded mud and thin sandstone section the deposits become slumped, and most likely form a levee deposit with the associated channel section or marginal depositional lobe deposit apparent above. This sand section is quite thin, being only 2.5m (8ft) thick. There is some suggestion of the beds thinning along the outcrop which would indicate that these sands could be interpreted as a channel deposit with some scouring apparent in a few exposures. However, the thinning of the beds can only be seen in one

Plate 3.4 Off-set channel deposits, exposed in Section 3, Castaic Lake.

Plate 3.5 Amalgamation of turbidite beds, Castaic Lake.

direction (to the south) and therefore the sands could also be interpreted as the distal edge of a small depositional lobe deposit.

Section 4.

The sequence exposed here is the upward continuation of section 3, measured slightly further around the lake shores (300m). The section exhibits excellent lateral exposure, with numerous graphic logs taken to illustrate the frequent lateral facies changes, and bed thickness variations within such a depositional setting (Fig. 3.9). Turbidites exposed in the cliffs here are generally much coarser and conglomeratic than those seen in the lower section 3, consisting almost exclusively of facies A with some interbedded facies B turbidites (Table 3.1). The lower half of the section forms a continuation of the facies architecture seen around the top of section 3, consisting of laterally discontinuous sandstone beds that exhibit scouring, numerous large rip-up clasts and pebble lag deposits. The sands also show amalgamation, and local down-cutting in the order of a few centimetres.

Above this section numerous thick (5m) sandstone units are viewed in the cliff face, which are highly laterally persistent and crop out for distances greater than 100m, until their dip takes them under the water-line of the lake. These sands are generally flat based and topped, possessing graded bases and some parallel lamination. Plotted on the graphic log (Fig. 3.9) the sequence appears to show a cycle of thickening and coarsening upward, and combined with the lateral exposure, these deposits are interpreted as representing large depositional lobe deposits. Access around the lake further north of this point becomes impossible by foot, however photographs of further exposures have been taken and clearly show large, major channel deposits, that can be seen to wedge out in the outcrop. Such channel deposits and their associated levee deposits have been described by Link (1982b, 1983), and represent the large basin axis channels that funnelled the sediment in a south-southeasterly direction down the length of the basin.

3.2.5.2 Ridge Route and Templin Highway Exposures.

Large roadcut sections along the Old Ridge Route and Templin Highway expose excellent sections of the Castaic Formation, and the basal portion of the Marple Canyon Sandstone Member of the Ridge Route Formation (Fig. 3.11). Old Ridge Route generally runs along the axis of sedimentation within Ridge Basin, lying closer to the proposed slope deposit of Link's (1982b, 1983) depositional model than Castaic Lake, which is located in the central,

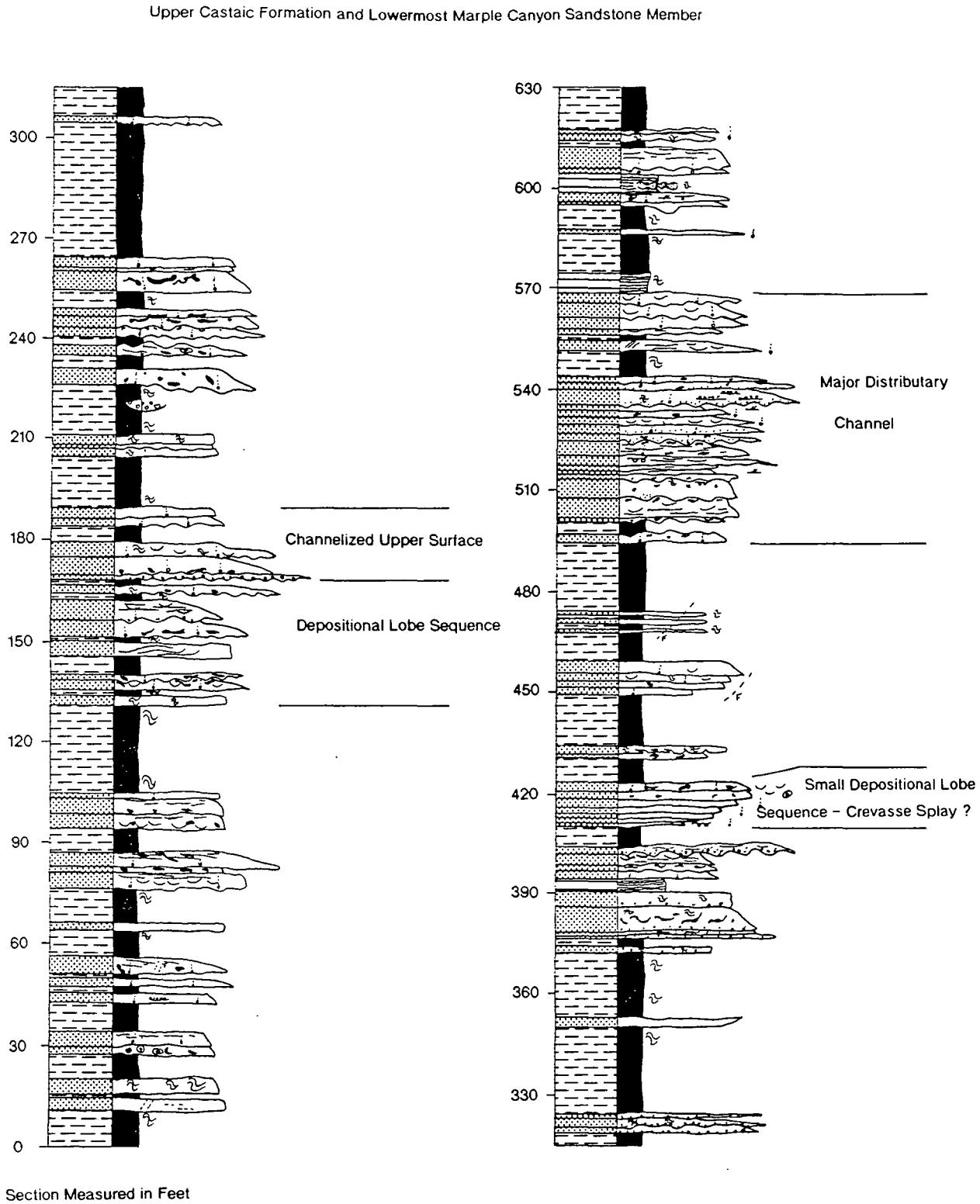

Figure 3.11 Measured section, Old Ridge Route.

deeper-water region of the basin. However, Templin Highway runs more or less perpendicular to this (i.e. sub-parallel to the strike direction), and exposes the progradational sequence from basin axis, through to slope facies, as interpreted by Link (1982b, 1983) (Fig 3.7).

The section exposed along Old Ridge Route shows a change from thin (1m) bedded turbidites at its base, up to thicker (2-3m) bedded and channelised turbidites within the Marple Canyon Sandstone at the top (Fig. 3.11). The sediments involved are more or less identical to those exposed at Castaic Lake. However, Link (1982b, 1983) interprets them as being slightly more marginal in their depositional setting, i.e. consisting more of a slope facies compared to basin axis sediments seen along the shores of Castaic Lake.

Turbidites along Old Ridge Route fall into two categories :-

i. Thin bedded, laterally continuous, medium to fine grained sandstone units, exhibiting some Bouma divisions (T_{a-c}) (Fig. 3.10), interpreted as facies C turbidites (Table 3.1). These units are around 10cm to 1m in thickness and have sole marks, dish structures and soft-sediment deformation structures.

ii. Thick bedded, coarse to medium grained sandstone turbidites, forming thicker sandstone sections due to amalgamation, and often showing cycles of thinning and fining upwards in some parts of the sequence. These sandstone beds tend not to be laterally persistent and can be seen in places to wedge out along strike (Plate 3.6). The sands themselves are generally coarse grained with pebble lag deposits at their bases, and showing Bouma divisions T_a and T_{ab}, being of facies A and B (Table 3.1). The units also contain numerous mudstone rip-up clasts, groove marks, small scale scouring of the order of 1 to 1.5m (3.3 to 5ft), and amalgamation creating thick sand sections around 10m (33ft) thick, as seen exposed along a section of Old Ridge Route (Plates 3.7 & 3.8). These sands can be interpreted a number of ways, such as submarine channel deposits that carried the sediment across a short muddy slope into the basin axis, the marginal edge of a lobe deposit, or a large crevasse channel. Depositional lobe sandstones tend to be regularly bedded, possessing fairly flat bases and tops (Mutti & Ricci Lucchi, 1972). The sands exposed near the top of the Old Ridge Route section however are not regularly bedded as seen in the depositional lobe deposits exposed in the cliffs of Castaic Lake. As described above there are numerous sandstone beds that pinch out within the section, and they contain numerous scours and coarse pebble lag deposits, with a general overall

Plate 3.6 Major channel exposed along Old Ridge Route. Note how turbidite beds thin and pinch-out towards the left of the section.

Plate 3.7 Basal groove marks of a turbidite bed, Old Ridge Route.

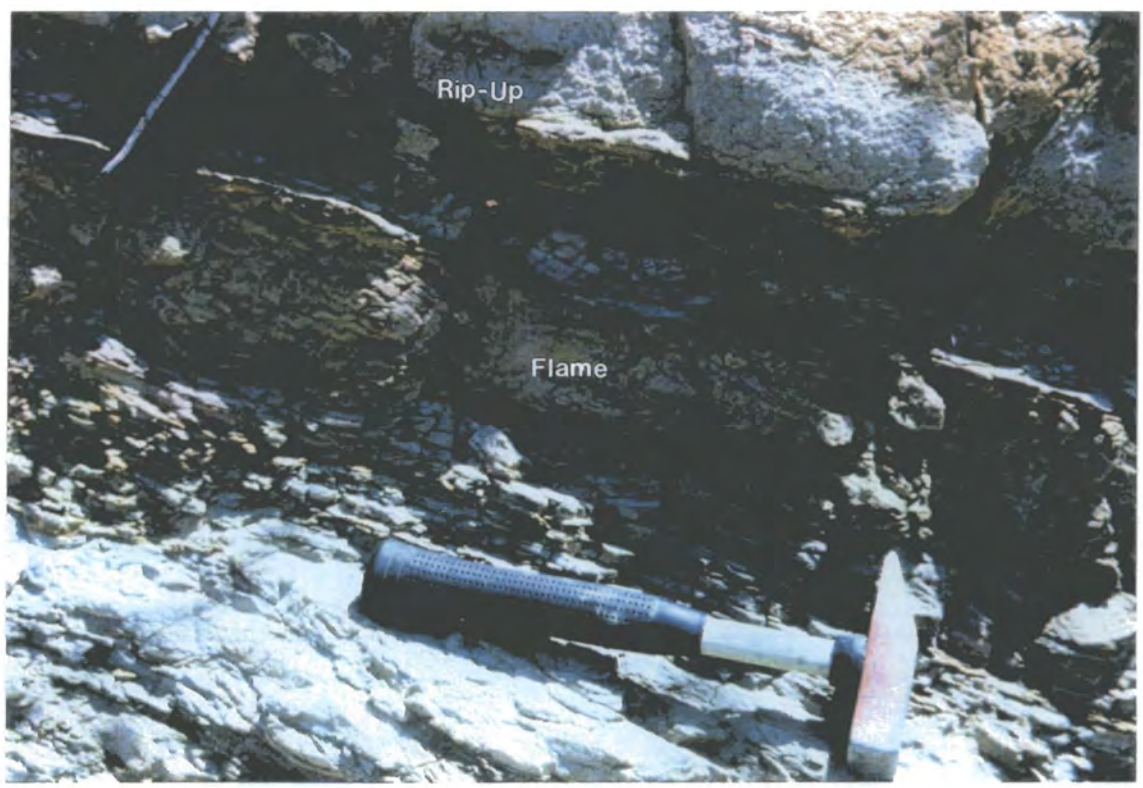

Plate 3.8 Flame structures and rip-up clasts in a sandstone turbidite bed, Old Ridge Route.

trend for the beds to thin and fine upwards. Therefore, the sands are interpreted to represent channel deposition, within a slope environment. Because of the greater proportion of facies B turbidites (Table 3.1), the lateral pinch-out of beds, and the overall sedimentology and bedding patterns (Fig. 3.11), Link (1982b, 1983) interprets these sands as being part of the major channels that transported the sediment across the muddy slope deposits into Ridge Basin. Once they reached the axis of the basin they were affected by the primary axial transport direction, forming depositional lobes at their distal terminations, as seen along the shores of Castaic Lake. Some levee deposits formed along these channel margins, with overbanking occurring to deposit the thinner bedded and laterally persistent turbidites (Facies C and D).

Templin Highway has numerous isolated roadcuts, and therefore forms a discontinuous section up through the Castaic Formation and the Marple Canyon Sandstone. The section shows a general transition from thin-bedded and fine-grained turbidites of the order of a few centimetres thick, through thicker depositional lobe deposits where individual turbidites are of the order of 1m (3.3ft) thick, up to thick distributary channel turbidites. This illustrates not only a vertical sequence through the basal sedimentary fill of Ridge Basin, but also a section running from basin axis deposits southwestwards to slope facies deposits at the intersection with Old Ridge Route.

3.2.6 Discussion of Slumped and Brecciated Horizons.

Within the Castaic Formation and the Marple Canyon Sandstone, numerous intensely folded slump horizons occur which have flat bases and tops (Plate 3.9). These were termed "intestinoform folds" by early workers within Ridge Basin, notably Crowell (1954) (Fig. 3.12). A few brecciated horizons also occur, again with flat bases and tops. These horizons are interpreted as being situated at the sediment-water interface at the time of an earthquake either on the San Gabriel Fault, or the Clearwater and Liebre Fault System (Sylvester, pers. comm., 1991). Similar phenomena have been viewed at times when man-made lakes have been drained after an earthquake, and the sediment at the water interface has shown intense folding and contortion. This similarity in deformation, and the fact that later erosion by following turbidite flows would lead to these units possessing flat tops as now viewed in outcrop, seems to suggest that this process of 'seismic shock deformation' is the driving process in producing such units.

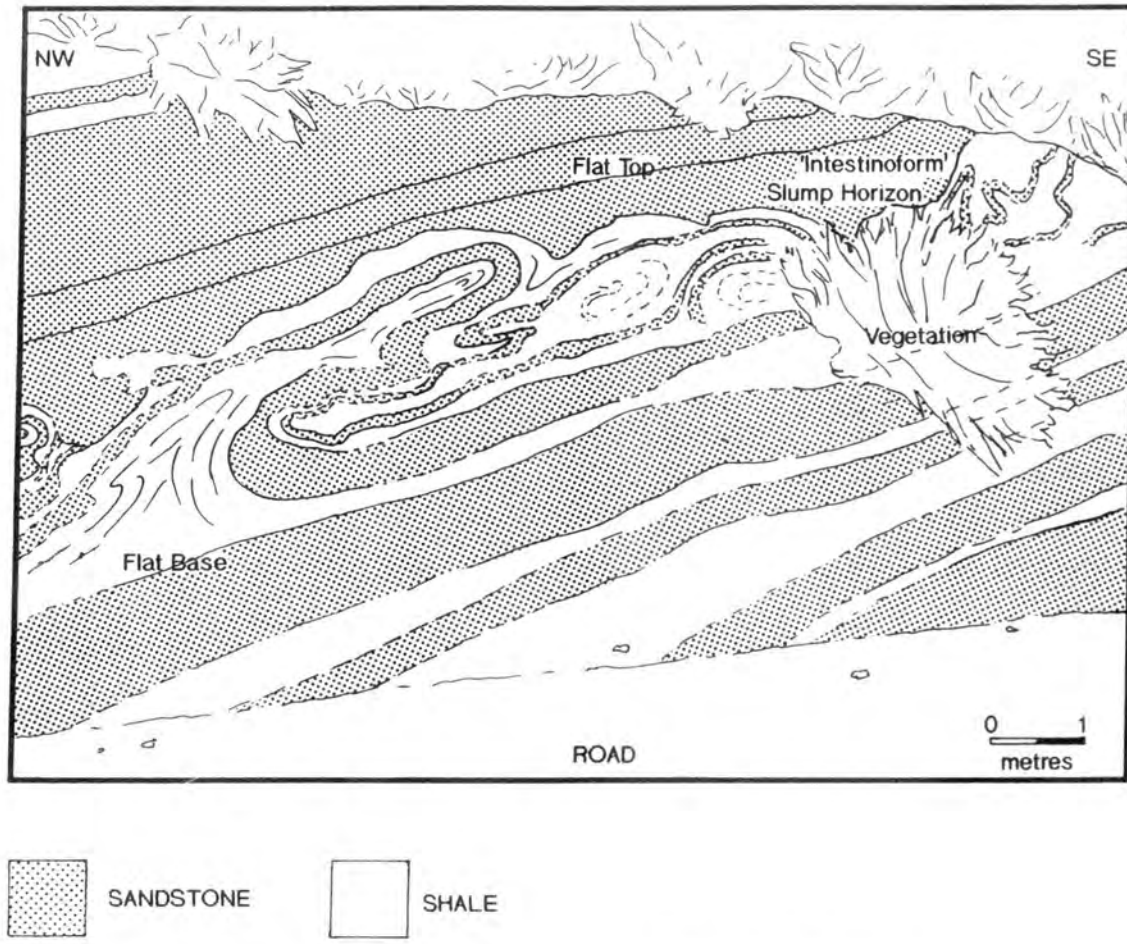

Figure 3.12 "Intestinoform" slump horizon, Old Ridge Route.

Plate 3.9 "Intestinoform" slumped horizon, Old Ridge Route. Note flat base and top to slumped section.

3.2.7 Compactional Modelling of Outcrop Data.

The objective of the present work was to assess the early compaction of submarine fan deposits, attempting to provide quantitative data, test published porosity-depth curves/equations, and build a model of deposition in which differential compaction may form a control upon facies location, based upon field observations. Throughout the sections of study within Ridge Basin various examples of compaction and compaction-related phenomenon were viewed and measured. Modelling of these examples would allow an insight into the compactional processes involved during their deposition, and provide data on the early compaction behaviour of submarine fan sediments.

Three outcrop examples where the process of compaction can be interpreted as playing an important role in deposition were viewed within the Castaic and Ridge Route Formations of Ridge Basin. These are:

- Depositional thickening of sandstone beds across a small, shale-filled 'graben' feature - Templin Highway.
- Off-set stacking of distributary channel deposits - Castaic Lake.
- Depositional thickening of sandstone beds above a shale-filled slump scar - Old Ridge Route.

Example 1.

The first, and best, example occurs in a small roadcut on Templin Highway (Fig. 3.7) shown in Plate 3.10, and diagrammatically in Figure 3.13.

Bed relationships at this outcrop suggest that differential compaction above a small fault 'graben' has caused some thickening of the beds in the region directly above the 'graben', which is predominantly filled by shale. The bed relationships show that the 'graben' was forming primarily during the deposition of shale (shale "a"), and thus received a thicker section (i.e. 2m (6.6ft) of shale "a" within the 'graben' equates to 0.5m (1.6ft) either side). The subsequent sandstone beds thicken above the greater shale section, showing that compaction of the shale was occurring during the deposition of the immediately overlying sandstone bed (sand "A") (i.e. within the very first few metres of burial). Two further sandstone - shale cycles (shale "b"-sand "B"; and shale "c") show depositional thickening above the shale "a" 'graben', making a thickness of 2.5m (8.2ft) above the top of the 'graben'. Above this no further thickening of beds can be seen in the outcrop (e.g. sand "C"), and overlying sand and shale beds have flat bases and tops. This observation essentially shows that differential compaction appears to have ceased after only 33% thickness reduction within the shale unit, which would appear less

Plate 3.10 'Graben' example of differential compaction, exposed along Old Ridge Route/Templin Highway section.

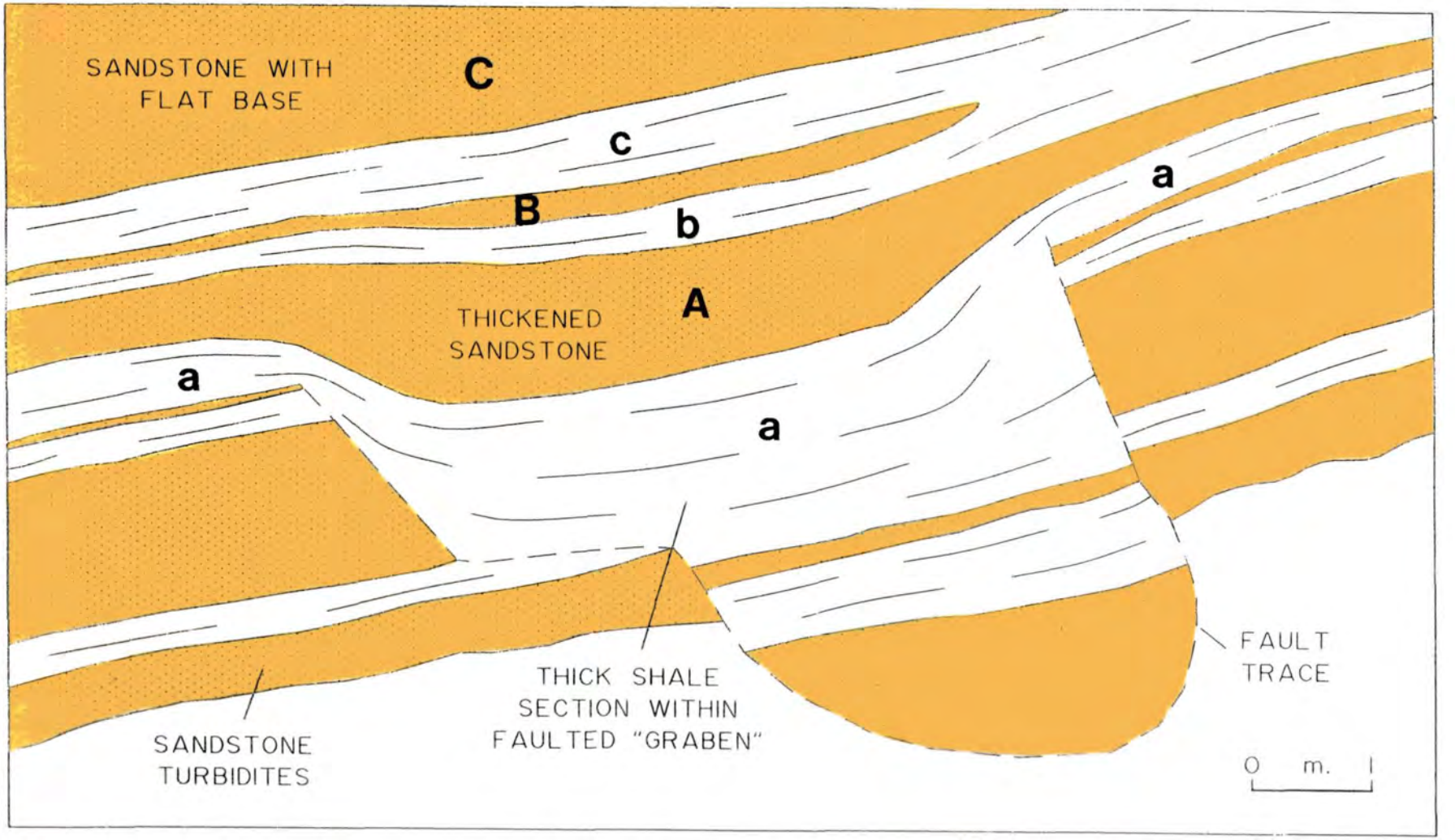

Figure 3.13 Compactional thickening of turbidite beds above small fault 'graben'.

than expected. However, the scale of the example may need to be taken into account here.

Compactional modelling of this outcrop has allowed some insight into the very early compactional behaviour of this interbedded sandstone/shale unit. Assuming that immediately after deposition, all the beds filling the 'graben' feature had flat tops, it is possible to backstrip the beds and then forward model them again to observe how much compaction has occurred during the early burial to produce the geometry seen in outcrop today. Due to the extremely high depositional porosities of submarine deposits (see Chapter 2) it is interpreted that depositional slope angles can only be of the order of a few degrees (i.e. $<5^{\circ}$) before the angle of slope fails and is subsequently reduced (e.g. Pickering et al., 1989; Kenter, 1990). Therefore an approximate flat depositional surface is maintained at all times. Modelling also allows a porosity-depth relationship to be plotted directly from the outcrop observations and measurements.

Backstripping allows the calculation of the true depositional thicknesses of the beds, and therefore the amount of loading that occurs during early burial (see Chapter 2). However, to perform backstripping three variables are needed:-

1) Present day thickness.
2) Present day porosity.
3) Initial porosity.

The present day thickness of the beds is simply measured in the field, or from scaled field photographs. Due to deep weathering of the sediment, the present day porosity is more accurately estimated from published porosity-depth equations, provided an estimate of maximum burial depth is possible. The initial porosity of the bed can also be estimated from published porosity-depth equations, and is measured at the half height of the present day thickness of the bed in question, as if the bed had just been deposited at the surface, and accounting for autocompaction. Published data on modern near-surface submarine fan sediments also aid in the estimation of initial sediment porosities (e.g. Hamilton, 1976; Truyol, 1989). However, to perform backstripping on a sequence, a knowledge of the total depth of burial is required, not only for porosity estimation but to allow the correct amount of sedimentary overburden to be removed. Vitrinite reflectance data published in the field guide to the area (Crowell & Link, 1982), is interpreted to show that the Castaic Formation and the Marple Canyon Sandstone Member were buried to maximum depths of 2 to 3km (Link & Smith, 1982). For this example, therefore, modelling was carried out for a total burial depth of firstly

3Km, and secondly 2Km, thus also enabling a comparison of the results, to see if an extra kilometre of burial had any great effect on the **near-surface** porosity-depth profile.

The first stage of the modelling consisted of measuring the bed thicknesses of the present day outcrop. These thicknesses were tabulated (Table 3.2a & b), one for the bed measurements from the graben centre, and another table for the bed measurements from the graben edge. A simple routine of backstripping is then carried out using Baldwin & Butler's (1985) power law for shale compaction, and Sclater & Christie's (1980) exponential law for sandstone compaction (see Chapter 2). Results from this modelling provide the approximate thicknesses of the beds at the time of their deposition. The tables also provide the complete evolution of all the bed thicknesses and porosities during their burial to the present day.

However, it was found that if the values provided by these calculations were plotted for the graben centre and the graben edge, and the throw on the bounding faults is kept constant, then the beds filling the graben are not deposited with flat tops, one of the assumptions of our modelling. It was therefore decided that the values calculated for the graben edge would be used as these would contain less error than those calculated for the graben centre, because the beds involved are thinner. Taking these values, and assuming a constant throw on the faults the history of deposition within the graben was constructed for each stage of bed deposition (Fig. 3.14). At each stage the porosity of the mid-point of each bed was calculated using the bed thickness relations and equation 2.22 (see Chapter 2). Porosities were plotted on a porosity-depth plot to produce a porosity-depth profile as described in Chapter 2, constructed from field data. Both profiles calculated for 2Km and 3Km total burial more or less agree with each other, showing that 1Km greater burial has very little effect on the near-surface porosity development of a section. This also illustrates that the estimation of the total burial depth need not be precisely accurate to provide good answers which still carry a large degree of confidence in their accuracy.

Porosity-depth profiles plotted for the 'graben' example show a very large decrease in the near-surface porosity of the fine-grained muds filling the graben (Fig. 3.15). For the first three metres of burial, this decrease is slightly greater than that predicted by the Baldwin & Butler (1985) curve. However, the decrease in porosity is considerably greater for subsequent burial below three metres.

A Graben Decompaction - 3 Kilometre Burial.

3Km Sediments	3000	Thickness					
	??	Porosity					
Shale unit "c"	0.48	2.12	Thickness				
	10.40%	79.70%	Porosity				
Sandstone unit "B"	0.1	0.14	0.14	Thickness			
	17.80%	40.00%	40.00%	Porosity			
Shale unit "b"	0.23	0.71	1.04	1.04	Thickness		
	10.40%	70.90%	77.30%	77.30%	Porosity		
Sandstone unit "A"	0.5	0.68	0.68	0.68	0.68	Thickness	
	17.80%	40.00%	40.00%	40.00%	40.00%	Porosity	
Shale unit "a"	0.55	1.56	1.66	1.68	1.82	1.97	Thickness
	10.40%	68.50%	70.40%	70.60%	72.90%	75.00%	Porosity

A Graben Decompaction - 2 Kilometre Burial.

2Km Sediments	2000	Thickness					
	??	Porosity					
Shale unit "c"	0.48	1.99	Thickness				
	15.90%	79.70%	Porosity				
Sandstone unit "B"	0.1	0.13	0.13	Thickness			
	23.30%	40.00%	40.00%	Porosity			
Shale unit "b"	0.23	0.67	0.86	0.87	Thickness		
	15.90%	71.20%	77.50%	77.80%	Porosity		
Sandstone unit "A"	0.5	0.64	0.64	0.64	0.64	Thickness	
	23.30%	40.00%	40.00%	40.00%	40.00%	Porosity	
Shale unit "a"	0.55	1.48	1.59	1.6	1.72	1.87	Thickness
	15.90%	68.80%	70.90%	71.00%	73.10%	75.20%	Porosity

B Edge Decompaction - 3 Kilometre Burial.

3Km Sediments	3000	Thickness					
	??	Porosity					
Shale unit "c"	0.48	2.16	Thickness				
	10.40%	79.80%	Porosity				
Sandstone unit "B"	0.1	0.14	0.14	Thickness			
	17.80%	40.00%	40.00%	Porosity			
Shale unit "b"	0.23	0.71	1.04	1.04	Thickness		
	10.40%	70.90%	77.30%	77.30%	Porosity		
Sandstone unit "A"	0.5	0.68	0.68	0.68	0.68	Thickness	
	17.80%	40.00%	40.00%	40.00%	40.00%	Porosity	
Shale unit "a"	0.55	1.6	1.71	1.77	1.98	2.36	Thickness
	10.40%	69.00%	70.70%	71.80%	75.00%	78.80%	Porosity

B Edge Decompaction - 2 Kilometre Burial.

3Km Sediments	2000	Thickness					
	??	Porosity					
Shale unit "c"	0.48	1.99	Thickness				
	15.90%	79.70%	Porosity				
Sandstone unit "B"	0.1	0.13	0.13	Thickness			
	23.30%	40.00%	40.00%	Porosity			
Shale unit "b"	0.23	0.67	0.86	0.87	Thickness		
	15.90%	71.20%	77.50%	77.80%	Porosity		
Sandstone unit "A"	0.5	0.64	0.64	0.64	0.64	Thickness	
	23.30%	40.00%	40.00%	40.00%	40.00%	Porosity	
Shale unit "a"	0.55	1.48	1.59	1.6	1.72	1.87	Thickness
	15.90%	68.80%	70.90%	71.00%	73.10%	75.20%	Porosity

Table 3.2 Decompaction table for (A) 'graben' centre, and (B) 'graben' edge.

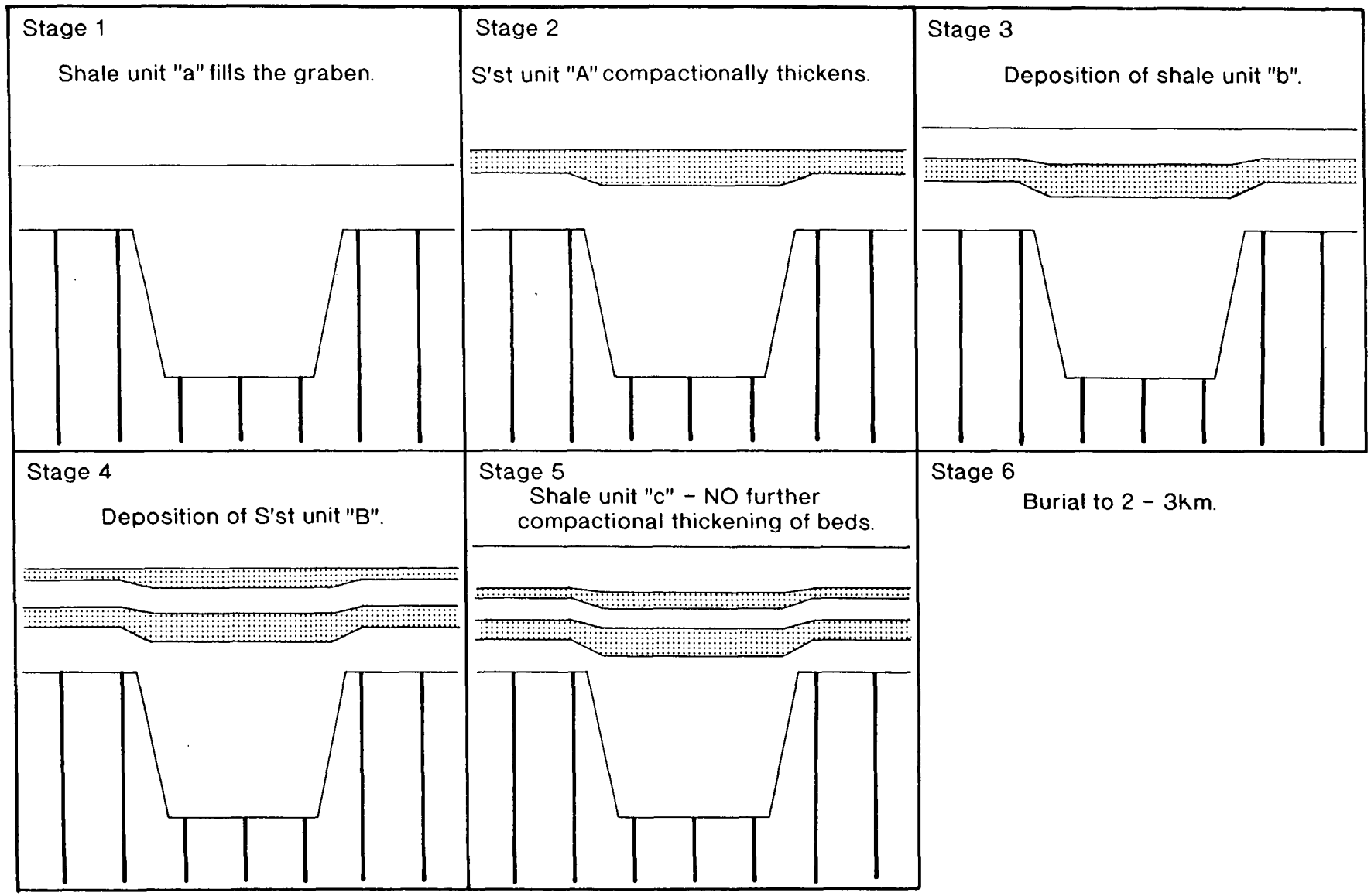

Figure 3.14 History of depositional fill and compaction within fault 'graben'.

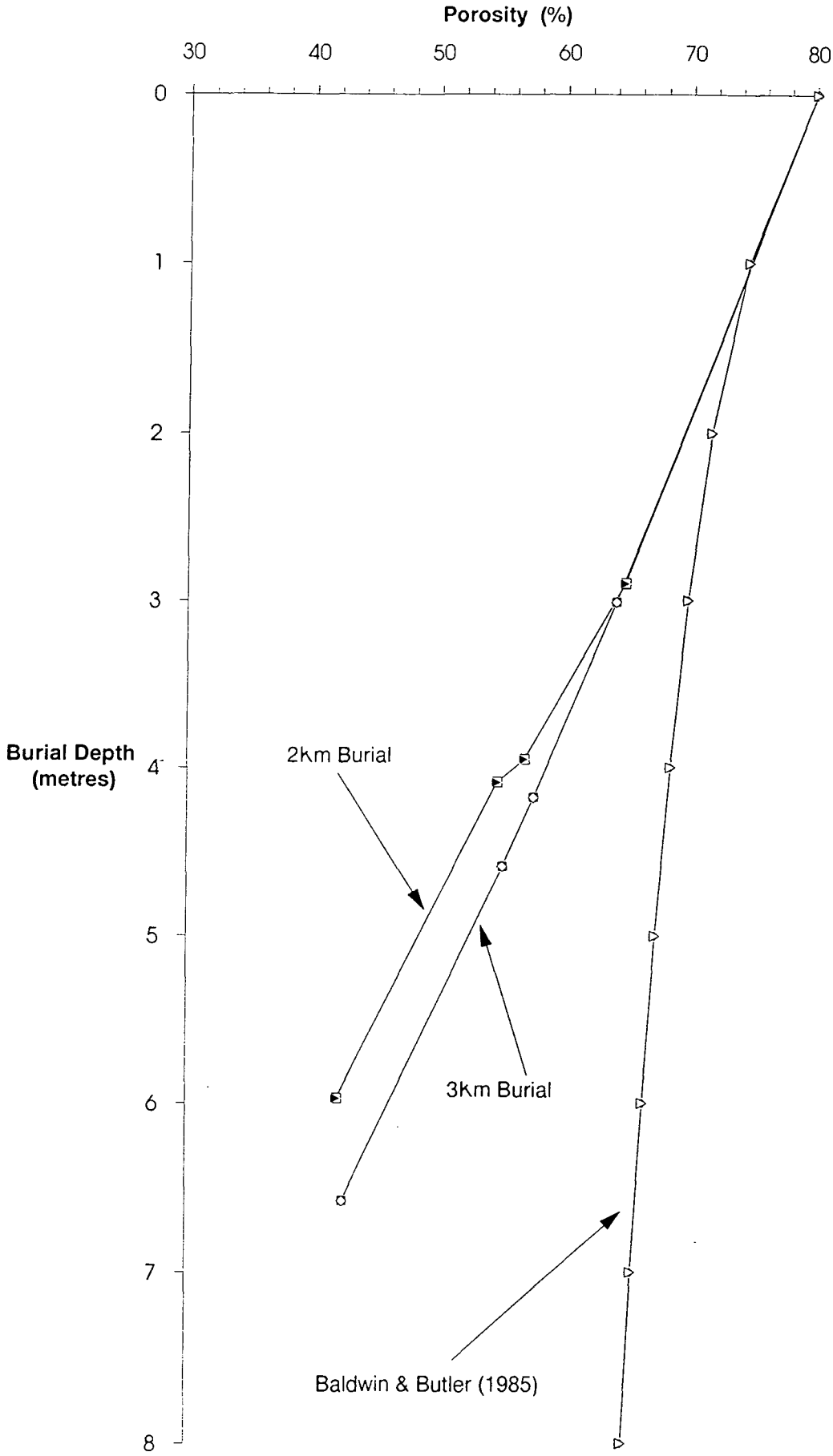

Figure 3.15 Porosity-depth profile calculated for fault 'graben', illustrating the difference between 2 and 3km of burial. Note the significant difference between the calculated curves and the Baldwin & Butler (1985) curve during shallow burial (2-7m).

It is important to remember that these results reflect the assumption that compaction was the only process occurring during the deposition of the sediments filling the graben. Movement/growth on the faults may have occurred during deposition of the sediments, hence effecting bed thicknesses, and model results. This may be the reason why there is quite a large change in the gradient of the porosity-depth profile around three metres burial depth. Separation of the contribution to bed thickness by further fault displacement or compaction is extremely difficult, due to the lack of specific knowledge of when fault displacement occurred. However, bearing these limitations in mind, the overall conclusion from the modelling is that the near-surface porosity development of fine-grained argillaceous sediments is one of rapid decrease, slightly greater than that predicted by the published porosity-depth profiles of Baldwin & Butler (1985), and other examples described previously in Chapter 2. It also highlights the effects of syn-depositional compaction in contrast to the bedding arrangements that would be formed by post-depositional compaction (see Chapter 5), where onlap patterns of bedding onto a pre-existing topography should be seen.

Example 2.

The cliffs at Castaic Lake provide excellent lateral exposures of submarine channel and depositional lobe deposits. Plate 3.4 shows one particular outcrop where diagonally off-set channel sandstones are exposed near the base of measured section 3 (Fig. 3.9). It is possible to model compaction in such an environment, and to see the effects and controls upon sedimentation due to the process of differential compaction. Figure 3.16 and Table 3.3a & b show the backstripping and forward modelling of such an arrangement, using the modelling parameters of 80% and 40% for the original depositional porosities for shale and sand respectively, and taking into account the effects of autocompaction. Equilibrium compaction is presumed to be achieved at the time of deposition of the first channel deposit. This means that the mud beneath compacts at the same rate of deposition and that simple grain packing and rearrangement occurs in the basal section of the channel sand itself, also at the same rate of deposition.

Modelling shows that only a very slight topography (less than 5cm of relief) can be produced upon the depositional surface after shallow burial of the area, and this topography may then influence subsequent turbidite deposition. However, this topography is only very slight and flow velocities of turbidites may be too great (from 50 to 250cms^{-1} (Reading, 1986)) to be influenced by such small slopes of less than 1°. It appears therefore that it is

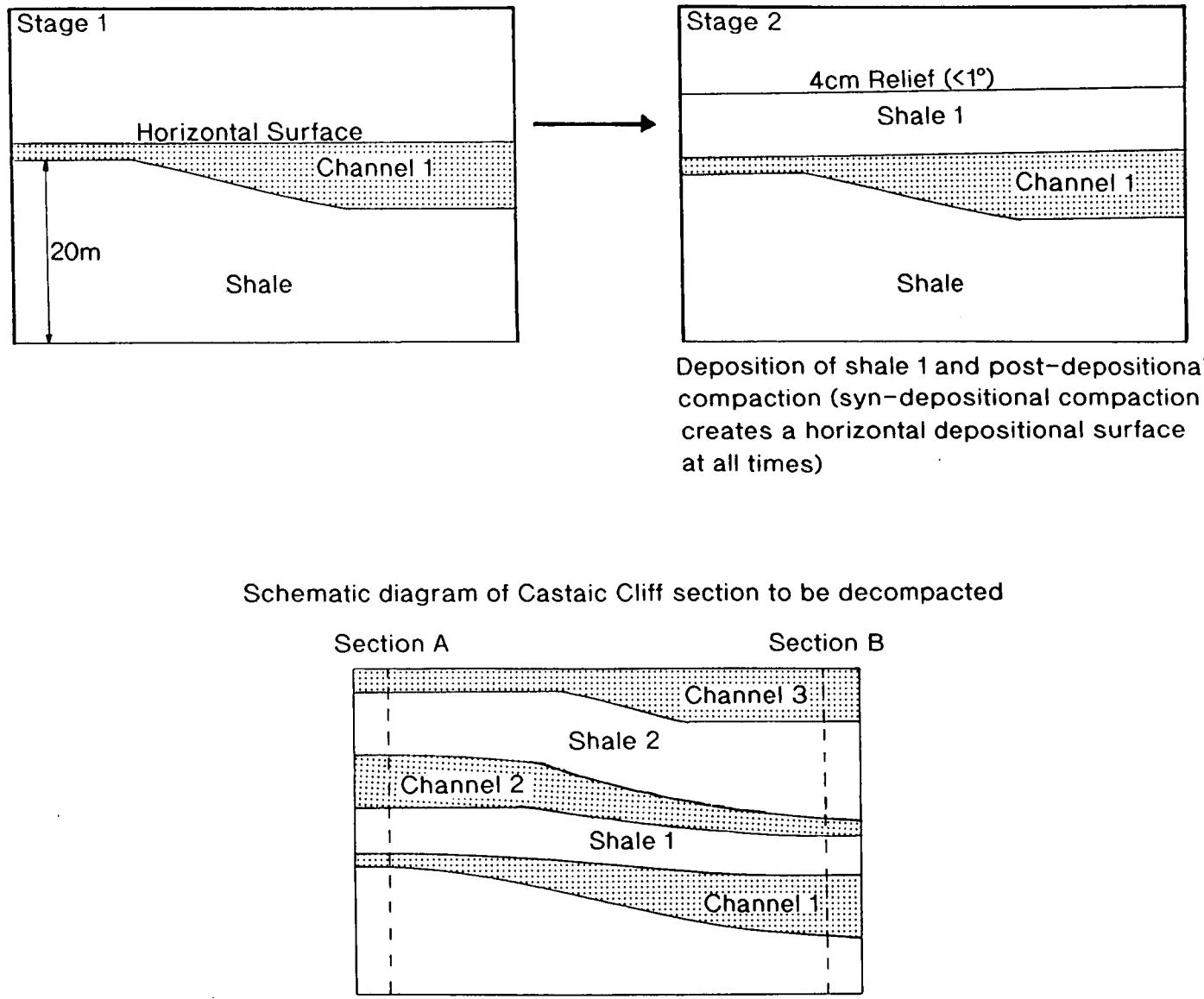

Figure 3.16 Compactional modelling of minor turbidite channels, Castaic Lake. Note small topographic variation above Channel 1, created by differential compaction.

A Castaic Cliffs, Channel Section - Section A

2Km Sediments	2000	Thickness					
	??	Porosity					
Channel 3	0.35	0.45	Thickness				
	23.30%	40.00%	Porosity				
Shale 2	0.53	1.85	1.85	Thickness			
	15.90%	75.90%	75.90%	Porosity			
Channel 2	1.05	1.34	1.34	1.34	Thickness		
	23.30%	40.00%	40.00%	40.00%	Porosity		
Shale 1	0.7	1.86	1.86	2.04	2.31	Thickness	
	15.90%	68.40%	68.40%	71.10%	74.50%	Porosity	
Channel 1	0.21	0.27	0.27	0.27	0.27	0.27	Thickness
	23.30%	39.90%	39.90%	40.00%	40.00%	40.00%	Porosity

B Castaic Cliffs, Channel Section - Section B

2Km Sediments	2000	Thickness					
	??	Porosity					
Channel 3	0.7	0.89	Thickness				
	23.30%	40.00%	Porosity				
Shale 2	0.63	2.02	2.09	Thickness			
	15.90%	73.80%	74.60%	Porosity			
Channel 2	0.14	0.18	0.18	0.18	Thickness		
	23.30%	40.00%	40.00%	40.00%	Porosity		
Shale 1	0.7	1.91	1.93	2.27	2.27	Thickness	
	15.90%	69.10%	69.50%	74.10%	74.10%	Porosity	
Channel 1	0.77	0.98	0.98	0.98	0.98	0.98	Thickness
	23.30%	39.90%	39.90%	40.00%	40.00%	40.00%	Porosity

Table 3.3 Decompaction table for (A) Section A channel section , Castaic Lake Cliffs, and (B) Section B channel section , Castaic Lake Cliffs.

possible that relief upon the depositional surface, as produced by differential compaction, may only be a minor influence on subsequent deposition within a submarine setting, and that the major driving force to the off-set pattern of sandstone bodies is the fact that the area with the thickest underlying shale section will compact at a considerably greater rate than the neighbouring area with a thinner shale section, and a greater percentage of less compactible sandstone. From Figure 3.16 it can be seen that there is a 0.71m difference in the thickness of underlying shale beneath the first channel sandstone. The second channel deposit forms directly above the thicker underlying shale section (Plate 3.4). It is quite probable that the small amount of relief (4cm) created on the depositional surface by differential compaction of the underlying section, forms a small but considerable trigger to the deposition of channel deposits upon the thicker shale section.

It is also possible that the scale of the example needs to be taken into account here. Increasing the scale enables a better visualisation of the differential compaction process, as the reductions in bed thicknesses are greater, although the resultant bed geometries are similar. The channels exposed at Castaic Lake are on average only 1m (3.3ft) thick. If they were 20m (66ft) thick then the topographic difference produced by differential compaction can be in the order of metres. Figure 3.17 shows a similar depositional arrangement of a theoretical channel sandstone deposited within basinal shale, with a larger scale used here than in Figure 3.16. The scale in this example is more relevant to the submarine channels found within the Montrose - Arbroath oilfields of the North Sea (see Chapter 5). The diagram illustrates that an area underlain by 100m of shale is 3 times more compactible than the neighbouring area with 50m of shale overlain by 50m of channel sandstone.

Vertically off-set depositional patterns of channel sands have been described in many papers concerning the deltaic environment and associated coal deposits (e.g. Brown, 1975; Fielding, 1984; 1986). However, most studies do not quantify the differential compaction across such depositional environments to reproduce these stacking arrangements in models. Depositional porosities are considerably lower in such environments when compared with the submarine environment (see Chapter 2), and the differential between sand and shale depositional porosities are far less, thus producing less differential compaction.

The argument described above requires compaction to occur almost instantaneously with respect to deposition of the overlying sediments, i.e.

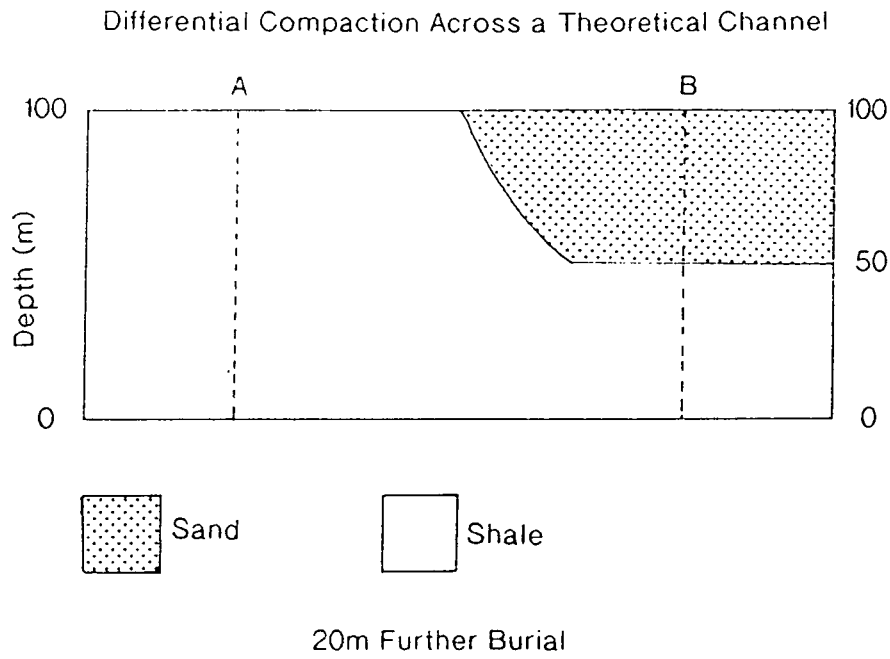

Section A

100m Shale now buried by 20m

$\phi_o = 53\%$ $\phi_c = 51.5\%$

Compacted Thickness $(1 - \phi_o)X_o = (1 - \phi_c)Y_c$

$(0.47)100 = (0.485)Y_c$

$Y_c = 96.9m$

Section B

50m Shale already buried by 50m Plus an extra 20m

$\phi_o = 50\%$ $\phi_c = 49\%$

Compacted Thickness $(0.5)50 = (0.51)Y_c$

$Y_c = 49.0m$

Plus 50m of Sand Channel. Thickness = 99.0m

Section A Compacts 3.1m
Section B Compacts 1.0m
With 20m further burial section A compacts greater than section B, producing 2.1m of relief upon the depositional surface.

Figure 3.17 Compactional modelling of a theoretical, 50m thick channel, illustrating the scale of relief created by differential compaction.

equilibrium compaction is maintained when dealing with near-surface compaction related phenomena in a submarine environment. This requirement appears to be reasonably feasible when the depositional porosities of shale and sandstone within the submarine environment are taken into account (80% and 40% respectively at the depositional surface). However, the permeability of the sediment is the major control on the rate of sediment dewatering. A possible interpretation is that permeabilities are great enough to maintain equilibrium compaction at the near surface. However, as greater burial occurs, the permeability of shales in particular, is reduced by such an amount that equilibrium compaction cannot be maintained during the deposition of a turbidite, as pore fluid cannot be expelled at a sufficient rate. This results in a time lag between deposition and equilibrium compaction, producing topography upon the depositional surface. However, the topography will be produced without the addition of overlying sediment, i.e. no loading of the section is required for the production of sea-floor topography if syn-depositional equilibrium compaction is not maintained. Therefore, we are concerned with the balance of two rates; the sedimentation rate and the compaction rate of the sediment being loaded and the sediment being deposited. As shown in Chapter 2, it is the balance between these rates that dictates whether topography upon the depositional surface is created or not.

Example 3.

The final compaction-related example of outcrop from Ridge Basin occurs on Templin Highway near the very top of the marine section within the Marple Canyon Sandstone Member. This example again shows the depositional thickening of subsequent sandstone beds above a thicker shale section that fills an underlying slump scar on the top of a lower sandstone bed (Plate 3.11). The model here is essentially identical to that of the graben example explained in the earlier part of this section, showing that thicker sands are deposited above the thicker shale sections, due to the greater compaction in this region.

Each of these three examples of compaction-related phenomenon viewed in the field illustrate both the methods of differential compaction, which are interpreted by Collier (1989) to control depositional arrangements. The methods being facies dependant compaction curves, and differential compaction induced by underlying topography. Facies dependant porosity-depth curves provide the controlling process in the diagonally off-set channel sandstone deposits, whereas underlying topography is the controlling factor

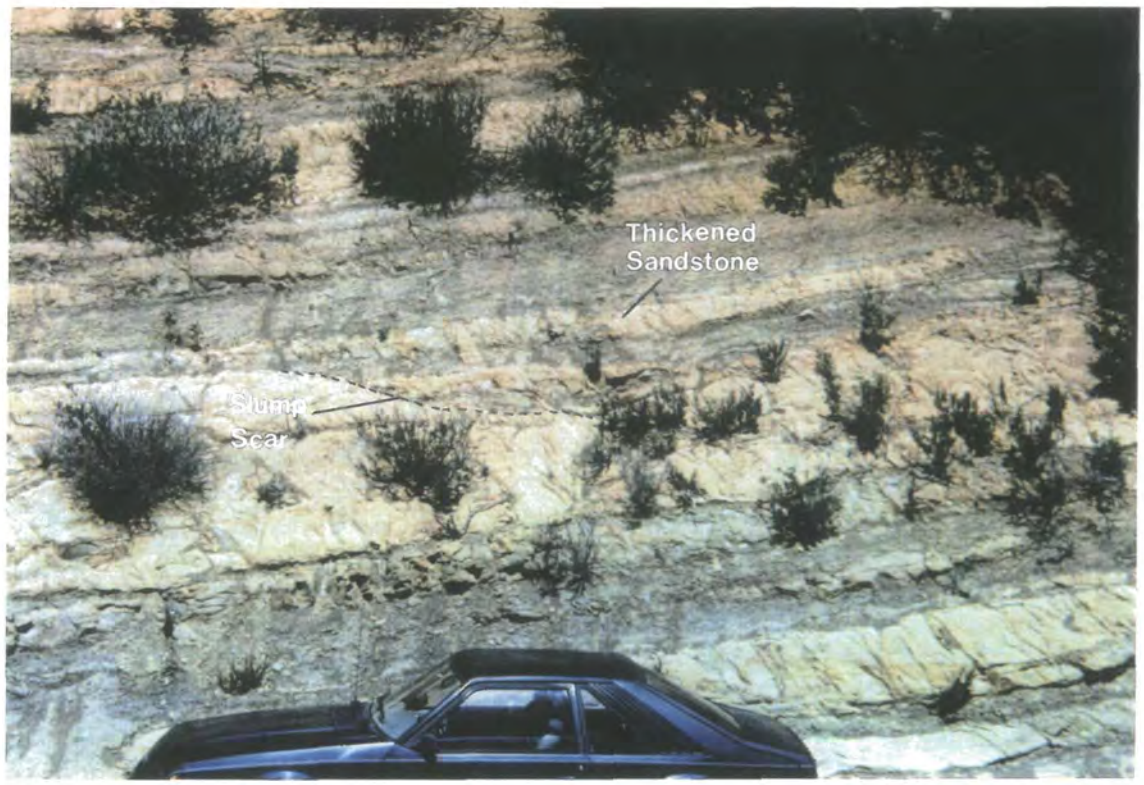

Plate 3.11 Thickening of sandstone turbidite bed above a minor slump scar filled by a thicker shale section, illustrating syn-depositional differential compaction.

in both the graben example and the depositional thickening of sandstone beds above a slump scar.

Other Important Processes.

Throughout the submarine fan deposits viewed in the field it is very apparent that loading of sands into the underlying muds is an important and widespread process (Plate 3.12). Numerous exposures show how loading of overlying sand totally cuts out underlying shale sections, thus creating isolated shale units in thick sand sections, with sand loaded down onto the tops of previous, underlying sandstone turbidite deposits (Plate 3.13). This illustrates that sandstone amalgamation can occur due to large scale loading of the underlying shale horizon, as well as by erosion of the overlying shale bed during turbidite deposition. If this is the case in all deep sea fan deposits then discontinuous shale horizons may be common within thick amalgamated sandstone deposits, possibly having implications for reservoir porosity and the extent of reservoir connectivity in oil producing basins.

'Loading out' of shale horizons also greatly reduces the compaction potential of the section, replacing a more compactible strata with less compactible sand. However, at the same time, it also creates areas where differential compaction can occur, as the sections with shale will compact at greater rates than the now amalgamated sandstone section. These sections may be too small though to affect the depositional arrangement, and the scale of the loading may be the controlling factor in the production of a compaction differential.

Slumping is another very important process within the submarine environment, and undoubtedly occurs within all tectonic settings whether they be strike-slip, passive continental margin, or extensional basin settings. Ridge Basin is slightly unique due to its close proximity to a major strike-slip system, and was therefore, presumably regularly affected by seismic shocks during Castaic Formation and Ridge Route Formation deposition, producing slumped horizons such as those examined in section 3.2.6 (Plate 3.9). Slumping (Plate 3.14) will cause rapid dewatering of sediment, probably reducing porosities to lower values than expected for the present burial depths. A subsequent reduction in the potential for differential compaction will result.

Summary Conclusions.

A general observation of the submarine fan deposits of Ridge Basin illustrates that siliciclastic environments offer a scale at which the assessment of compactional control upon depositional arrangement and

Plate 3.12 Basal loading structures of sandstone turbidite bed, Old Ridge Route.

Plate 3.13 Basal loading of sandstone turbidite bed, cutting out a continuous shale bed and creating amalgamated units.

Plate 3.14 Panorama of large slumped horizon exposed along Templin Highway.

geometry is difficult to measure and quantify. Differential compaction control of major distributary channels is extremely difficult to assess due to the vast amount of exposure, both lateral and vertical, that would be required. Often, areas with excellent exposure only show one major channel system, and not the full stacking geometries. However, insights into the compaction process within the submarine environment can be gleaned from smaller scale outcrops, as described above.

The overall view from field outcrops within Ridge Basin appears to show that near-surface compaction has the ability of controlling the depositional thickness of turbidite units. If it is assumed that the depositional surface remains flat, the requirement is that compaction occurs syn-depositionally. However, the observations made here do not enable the differentiation between a flat or undulating depositional surface to be made. The second example of differential compaction across small distributary channels suggests that the depositional surface may exhibit topographic variations. Scaling-up the example to major channel systems, it may be presumed that the topography can be in the order of several metres, and therefore, has the ability to control deposition of subsequent turbidity currents. The timing of when one channel ceases to be active and deposition switches to another area may rely on a large volume turbidity current breaching the levees, if present, and creating a crevasse splay onto interchannel muds. Channel switching may now occur at this point, partly due to topographic differences in the depositional surface, and enhanced due to the greater compaction potential of the interchannel area, as explained in earlier sections.

In summary, Ridge Basin offers the opportunity to assess the development of sub-surface structure, and its influence on deposition in deep water siliciclastics, by careful analysis and reconstruction of small-scale phenomenon involving rapid changes in lithology.

3.3 La Jolla, San Diego.

3.3.1 Introduction.

Eocene rocks in the San Diego area form an eastward thinning wedge of continental margin deposits extending from Oceanside, California southward to the Mexican Border (Lohmar et al., 1979) (Fig. 3.18). The northwest trending palaeoshoreline, which marks the featheredge of this wedge, is located 20 to 30km east of the present coastline. With deep basins located immediately offshore at this time, the rocks were deposited on a narrow shelf with a steep slope into the basin. They grade rapidly westward from non-

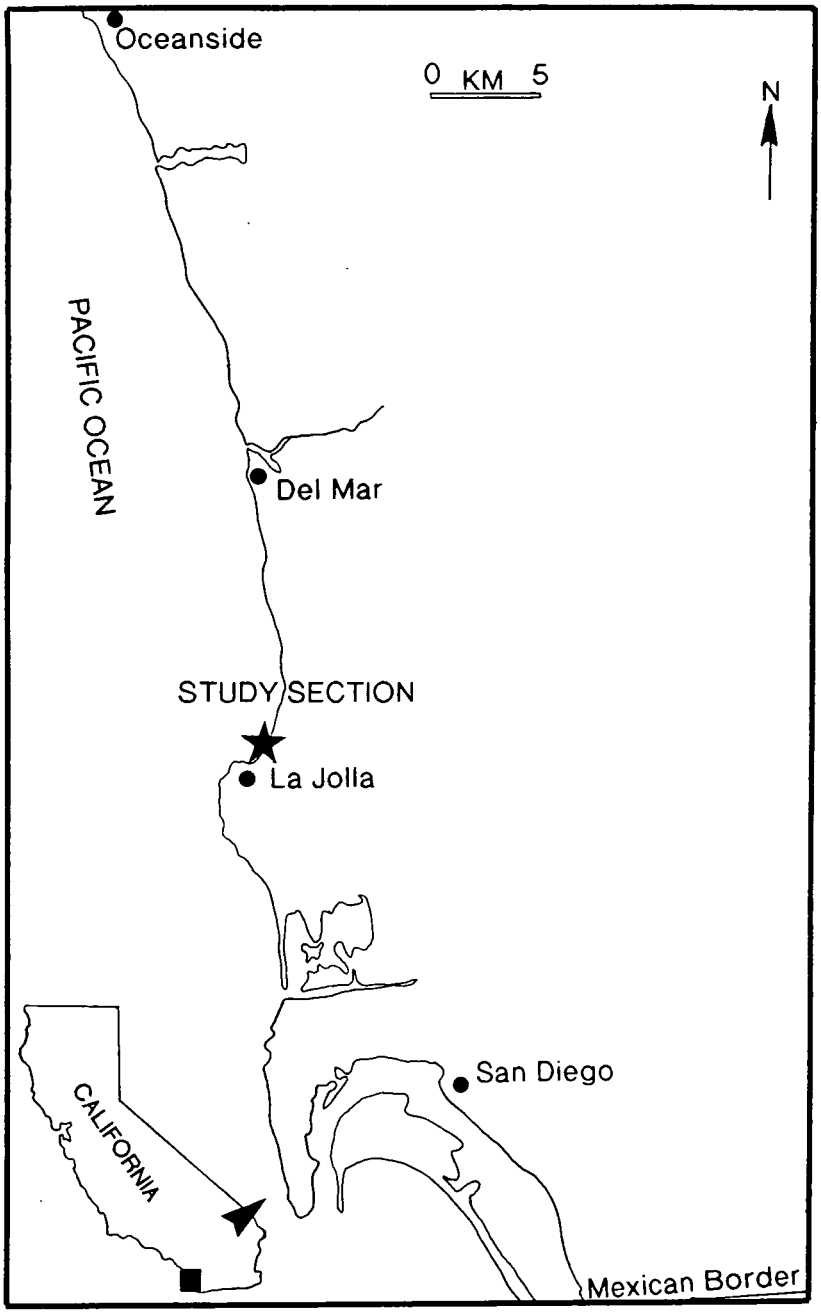

Figure 3.18 Location map of La Jolla, southern California, and Black's Beach (marked as Study Section).

marine strata into mudstones with bathyal assemblages of benthonic foraminifera (Lohmar et al., 1979).

The north - south oriented sea cliffs between Torrey Pines State Reserve and Scripps pier, marked as study section on Figure 3.18, form an oblique section through an Eocene submarine canyon and the apex of the associated fan, according to the interpretation of Lohmar et al. (1979). Shelf edge deposits exposed along the cliffs represent five different sedimentary environments:

1. submarine canyon head,
2. lower slope,
3. inner fan channel,
4. channel margin, and
5. inner fan.

Exposures further inland expose slope deposits which accumulated adjacent to this channel system.

Lohmar et al. (1979) suggest that the canyon was probably cut into the shelf edge during a lowstand in global sea level in early Eocene times. During a rapid marine transgression, beginning in the late early Eocene, the canyon eroded headward into the drowned shelf deposits. Fine-grained deep water deposits filled the canyon as sea level reached a high stand in middle Eocene times. At the equivalent time a small delta began to prograde across the shelf from which conglomeratic sands were shed from the delta front as sea level began to fall again at the end of the middle Eocene. These deposits were funnelled into the canyon where they scoured into the earlier deep water canyon fill.

The canyon itself enclosed an anastomosing network of large channels which emptied into a deep ocean basin at the edge of a very narrow shelf. According to Lohmar et al. (1979), regional facies relationships, sedimentary environments interpreted along the sea cliffs, and palaeobathymetries of foraminifera faunas suggest that the continental slope was located 20 to 30Km from the middle Eocene shoreline, at water depths ranging from 200 to 1500m.

The objective of the present study was to examine the northern submarine canyon wall, which is exposed south of the glider port forming the back of Black's Beach (Fig. 3.19), where post-depositional modification of the stratal relationship of the sediments has occurred.

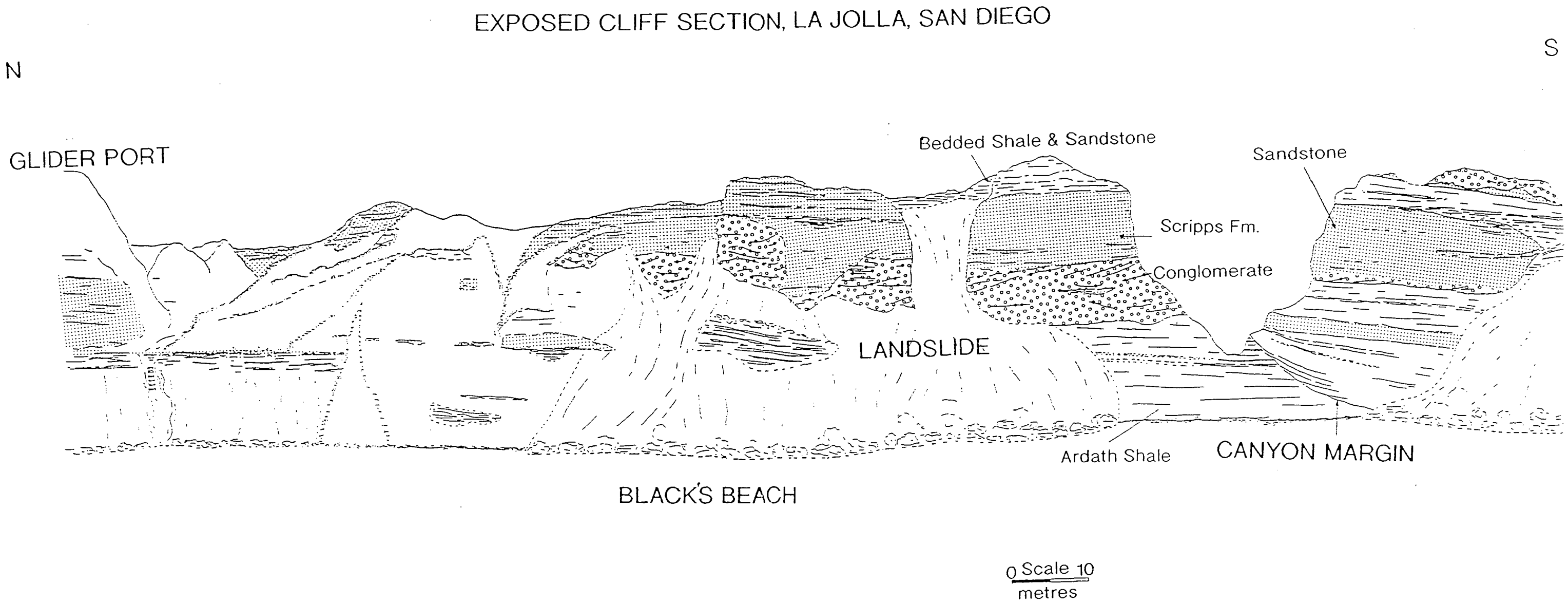

Figure 3.19 Panorama of cliff section, Black's Beach.

3.3.2 Stratigraphy.

Within the present study area, outlined above, there are only two main facies recognised (Fig. 3.20) :-

i. the Ardath Shale, and
ii. the Scripps Formation.

The Ardath Shale is a heterogeneous unit, that is characterised by channel-fill deposits of mudstone, siltstone, shale, and some fine-grained sandstone. It forms a wedge shaped deposit that wedges out to the northern end of the section, and thickens to the south. The Scripps Formation is a channelised, conglomeratic, coarse sandstone unit that forms the majority of the fill of the canyon. The sands within the deposit are coarse-grained and amalgamated, commonly possessing conglomeratic basal lag deposits. This formation has been interpreted by Lohmar et al. (1979) as being deposited at the apex of an inner fan channel, and reaches a maximum outcrop thickness of 100m towards the southern end of the cliff section, where the erosive base enters the subsurface.

3.3.3 Section Description.

The present study concentrates on the northern canyon wall, exposed in the cliffs immediately behind Black's Beach, because the submarine canyon edge is exposed here, and post depositional rotation of beds is interpreted to have occurred. Throughout the exposed cliff section, approximately 6,000m (20,000ft) long, the Ardath Shale has a regional dip of 4° to the south (Fig. 3.19). Immediately south of the northern canyon edge at beach level, a small outcrop of Ardath Shale can be seen within the canyon itself, with the coarse sandstone and conglomerate canyon fill of the Scripps Formation above. The angle of dip within this area of Ardath Shale is extremely variable, but is considerably greater than that of the regional dip of the area as described above, averaging around 15°, with a maximum approaching 30° towards the south (Plate 3.15).

Due to the very high initial porosities of deep sea muds it is interpreted that this greater angle of dip is not produced by depositional processes, as slumping would reduce the angle of slope (Kenter, 1990). If the shale was deposited within the canyon after its initial incision, then the angle of dip would be expected to be very shallow at the time of deposition (e.g. 0 - 4°). Therefore, post-depositional changes in dip must have occurred by some process (or processes) to account for the current situation viewed in outcrop. There are a few possibilities that account for the increased dip, such as, (1) compaction of

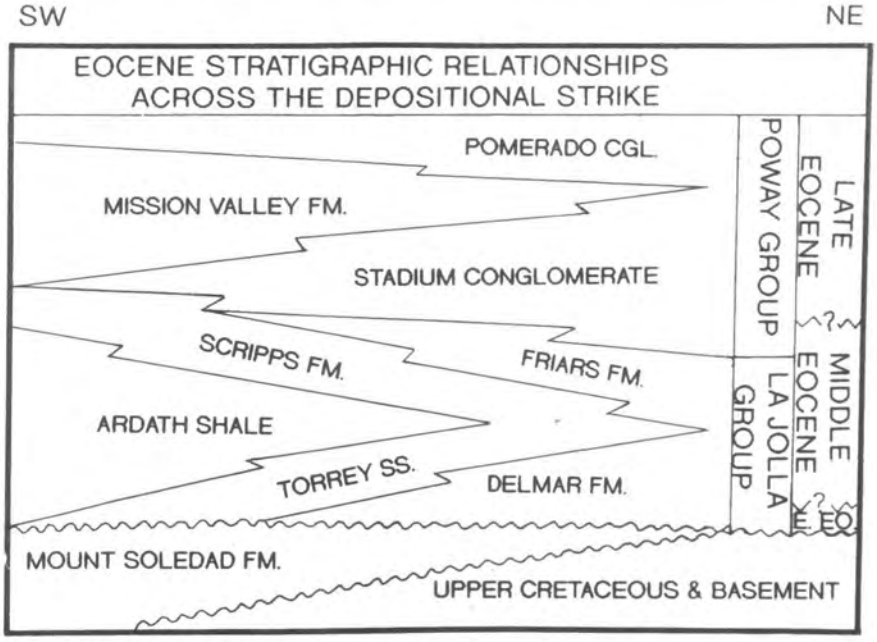

Figure 3.20 Regional stratigraphic relationships of the Eocene units along a southwest to northeast transect across the San Diego Embayment (After May & Warme, 1987).

Plate 3.15 Close-up of northern canyon edge, Black's Beach, La Jolla. Note area of mud with increased dip, immediately to the south of the canyon edge.

the shale, induced by the overlying canyon fill, (2) post-depositional rotation of the sediments, or (3) slumping and sliding of the canyon wall down onto the canyon floor.

Post-depositional rotation of the sediments appears improbable, as it is unlikely to produce the present day configuration of the sediments viewed in outcrop. For the shale mass to rotate a large bulk of sediment would be required to be displaced from beneath thus allowing the shale to 'slump' into the hollow below. The displaced sediment would, therefore, have slumped or slid by some mechanism to the south of the section, into the slightly deeper part of the canyon. It should also be possible to view these sediments in their present position, approximately 100m (330ft) further south of the exposed cliff shown in Figure 3.19. This area is unfortunately badly exposed and masked by landslide debris, however, there appears to be very little evidence of sediment slumping within the canyon to support such a theory of post-depositional rotation. Post-depositional slumping would also induce a variety of tectonic structures such as minor folding and faulting within the sediment, of which there is no evidence. The mechanism of such an evacuation of a mass of sediment from beneath a shale deposit also seems highly problematical, and therefore improbable.

Alternatively, it is possible that this area of shale with an increased angle of dip may simply be a slide block of former canyon wall sediment, slid from the north into the canyon once it has been incised. This theory requires a mass of canyon wall to have slid more or less intact down into a pre-existing valley. Throughout the mass of steeply dipping shale there are numerous small scale extensional faults with an offset of approximately 10cm each, but there is little conclusive evidence to suggest that this area of mud has slid into its present position. A slide block would be expected to show evidence of some sort of break up and dislocation of beds within its mass, especially along its basal contact, and it is apparent from the outcrop that this does not exist. The bedding pattern also appears not to conform to such a pattern that would be produced by a large slide block. A block of canyon wall sediment would tend to rotate backwards as it slid into the canyon, so that the beds would dip down to the north, a situation completely different from that which is seen in outcrop at the present day. It is highly likely that this shale was deposited within the canyon during the highstand of sea level in middle Eocene times (Lohmar et al., 1979) (see section 3.3.1).

An alternative interpretation is that the area of mud is in its original depositional position, and post-depositional compaction induced by the

overlying sedimentary deposits results in the present angle of dip viewed in the field today.

3.3.4 Compaction Modelling.

Mathematically modelling mud compaction within the canyon is possible if an original depositional porosity for the mud is assumed, and equilibrium compaction occurs throughout the section, i.e. compaction is complete at the end of deposition. The mud is loaded only by the canyon fill above, dewatering it and compacting the sediment beneath. The angle of bedding and thickness reduction of the mud from horizontal to its present position within the canyon is easily measurable in the field or from scaled photographs of the exposures.

As can be seen from Figure 3.21 the mud contained within the canyon has undergone a thickness reduction of 3.90m to 1.65m (i.e. 58% reduction). Putting these values into the equation 2.22 (see Chapter 2):-

$$(1-\phi_0)T_0 = (1-\phi_c)T_c$$

along with an estimate of the original depositional porosity of the mud, accounting for autocompaction, a value can be calculated for the present day compacted porosity. This value is 33.3% compacted porosity and can now be used in a porosity-depth equation to estimate the maximum burial depth of the mud within the canyon wall. Taking the compacted porosity value and placing it into Baldwin & Butler's (1985) power law equation for shale compaction (see equation 2.2 in Chapter 2) a value of 460m for the maximum burial depth is calculated. However, using exactly the same values in Sclater & Christie's (1980) porosity-depth equation for shale:-

$$z = \frac{-\ln\left(\phi_c / \phi_0\right)}{c} \qquad \text{(equation 3.1)}$$

where c = 5 x 10^{-4} m^{-1}, a maximum burial depth slightly in excess of 1.5Km is obtained.

According to May & Warme's (1987) figure 2-6 a burial depth of approximately 160 to 180m for the outer shelf/slope environment of the Scripps Formation is shown, based upon stratigraphic patterns from 2 well exposed dip sections and other exposures of the area. This diagram however, is a representation of the present day situation, and therefore does not reflect the maximum burial depth of the Scripps Formation. Thus, the complete thickness of the blanketing Stadium Conglomerate is not shown, and we can therefore only estimate a minimum depth of burial (160-180m) for

the sediments within the canyon. The estimation of minimum burial depth however does appear to suggest that the maximum burial depth estimate calculated using the Baldwin & Butler (1985) porosity-depth equation is probably closer to the true figure than the 1.5km of burial predicted by the Sclater & Christie (1980) equation. The latter estimate would require over a kilometre of erosion and uplift to produce the outcrop pattern of the present day, which appears unreasonable due to the lack of deposits derived from the area.

To test the calculations thin sections from the vicinity have been examined to provide an estimate of the compacted porosity. Due to the impossibility of point counting mud porosity, samples from the adjacent sands were taken and point counted to provide an estimate of the compacted porosity of the sand which has been buried to the equivalent depth (Plate 3.16). A consistent porosity of approximately 33% was calculated for these sands, some of which is presently filled by authigenic and pore filling clay deposits. Sclater & Christie's (1980) equation (3.1 above) appears to work very well for the compaction of sands as there is no large decrease in sand porosity at the near-surface (see Chapter 2). Therefore using this equation, with $c = 3x10^{-4}$ for sands, a maximum burial depth of 630m is calculated. This figure is considerably closer to that of the one calculated using Baldwin & Butler's (1985) porosity-depth equation for the mud within the canyon.

Calculations carried out here, therefore, appear to reinforce the arguments of Chapter 2. That is that mud porosity is destroyed very early during burial, and that Baldwin & Butler's (1985) power law curve describes this porosity evolution much better than that of other published porosity-depth equations, such as Sclater & Christie (1980). Modelling here also assumes that the mud through which the canyon is cut has already fully compacted before the deposition of the mud, sandstone and conglomerate within the canyon itself. This basic assumption makes the modelling much simpler as it means that the point of intersection on the canyon wall where the mud was initially deposited is fixed, and the bed 'rotates' around this point upon compaction (Fig. 3.21). Small errors within the calculations will be introduced due to this presumption, and the true thickness reduction of the mud within the canyon will be very slightly under estimated. However, the amount of differential compaction between the basal part of the canyon wall and the point at which the mud within the canyon intercepts the canyon wall will be so slight and insignificant, the errors introduced by ignoring this fact will not greatly effect the final results.

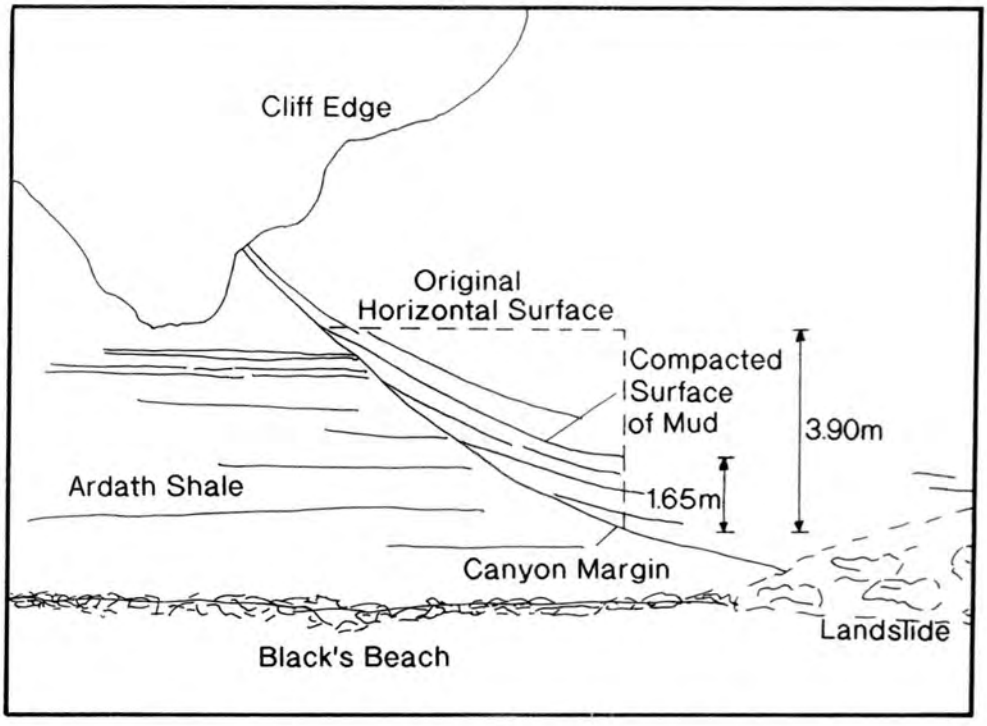

Figure 3.21 Close-up of northern edge of the submarine canyon, and mud compaction, Black's Beach, La Jolla.

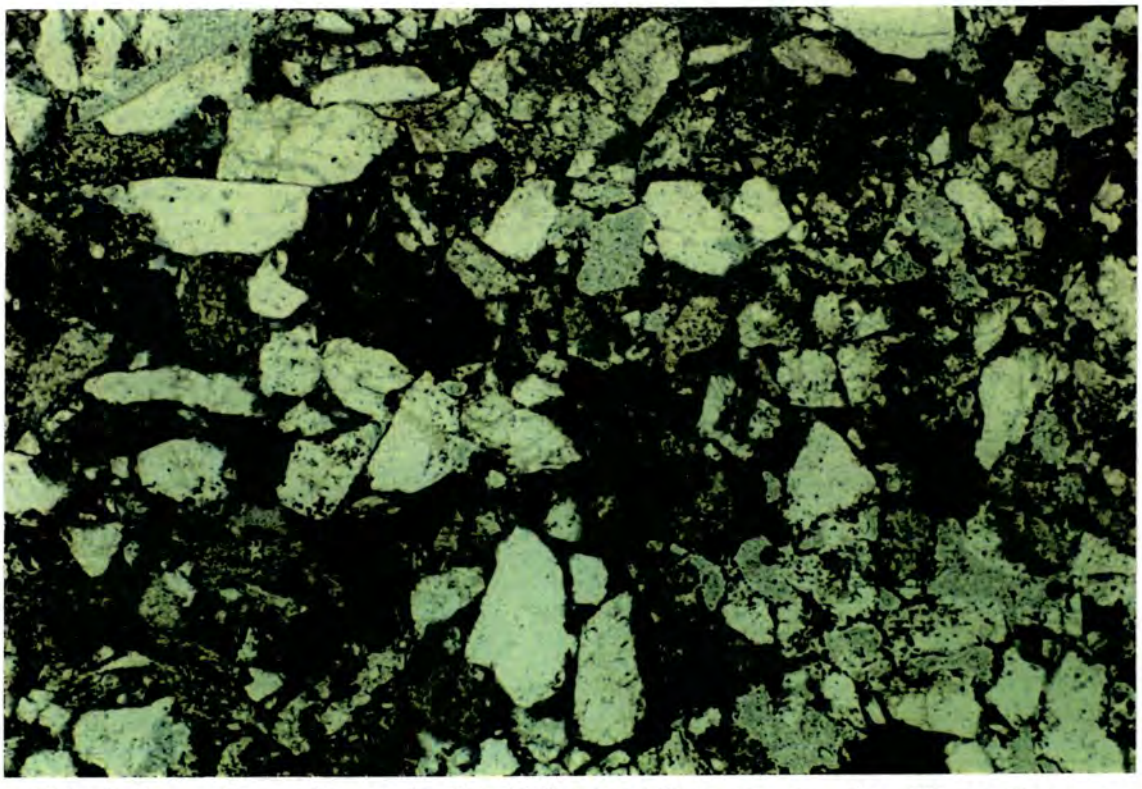

Plate 3.16 Photomicrograph of turbidite sand from canyon edge, Black's Beach, La Jolla. Field of view 3.3mm.

3.4 Wheeler Gorge, Santa Ynez Mountains.

3.4.1 Introduction.

Wheeler Gorge is situated between the Santa Ynez and Topatopa Mountains, seven miles north of Ojai, in Ventura County, California (Fig. 3.22). Upper Cretaceous rocks are exposed within the gorge below Highway 33, forming a continuous section of 475m running north - south. These rocks are more or less vertically bedded, and young to the southwest, consisting of black shale, thin arkosic sandstones/siltstones, with thick conglomeratic units and classic turbidites in the middle of the section (Fig. 3.23). Since deposition the rocks of this area have undergone a complex tectonic history, accounting for their vertical bedding at present, and they have also been metamorphosed to quite a high degree (greenschist facies), rendering porosity and permeability measurements meaningless.

3.4.2 Section Description.

Various authors have interpreted this sequence as consisting of submarine channel deposits and basin plain muds (Walker, 1975, 1985; Nelson et al., 1977). Walker (1975, 1985) published geological maps and graphic logs of the entire exposed section within the area, and in the latter paper proposed a channel - levee - interchannel model for the deposition of the sediments within Wheeler Gorge (Fig. 3.24). Walker's (1985) model proposes that the lower mudstone sequence is probably basin plain, or possibly interchannel deposition laterally far removed from any channel influence. This is followed by a gradual incision and lengthening towards the west of a coarse clastic channel into the basin plain environment, producing the coarse conglomerates at the start of the northern road tunnel. Two further conglomerate and coarse sandstone deposits are found moving up the section, which generally thin and fine upwards, representing episodes of channel cutting and filling (Plate 3.17). Within this general channel dominated sequence Walker (1985) proposes lateral channel migration superimposed upon the overall aggradation pattern of the channel - levee profiles, producing a vertical pattern of channel - levee complexes with the main channel systems offset from previous channels below (Fig. 3.24). Such offset produces the thick mud deposits on top of the conglomerates, interpreted as a levee deposit associated with a channel somewhere to the east of Wheeler Gorge.

Channel - levee - interchannel complexes provide excellent analogues for the Palaeocene submarine channels of the Montrose and Arbroath

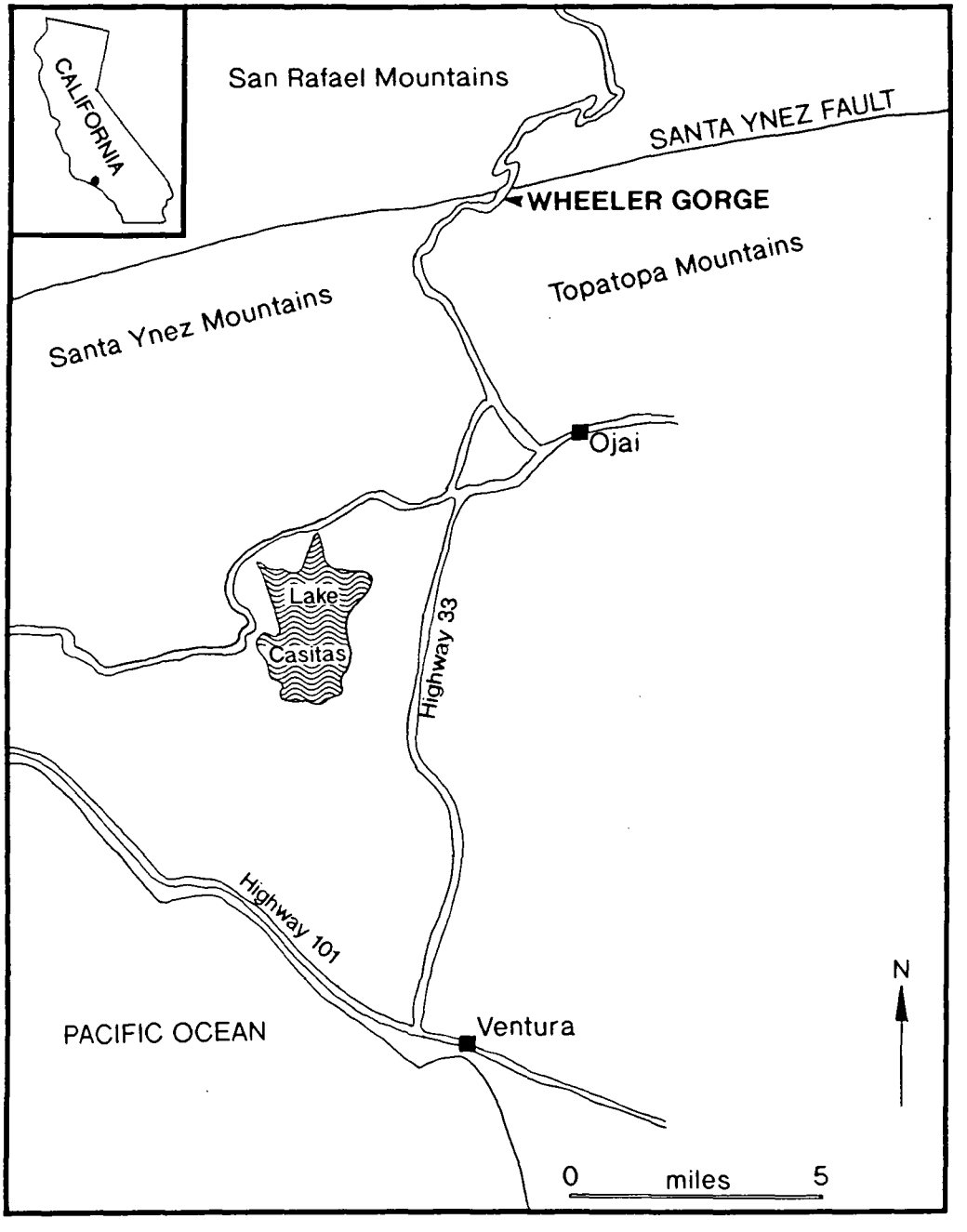

Figure 3.22 Location map of Wheeler Gorge, southern California.

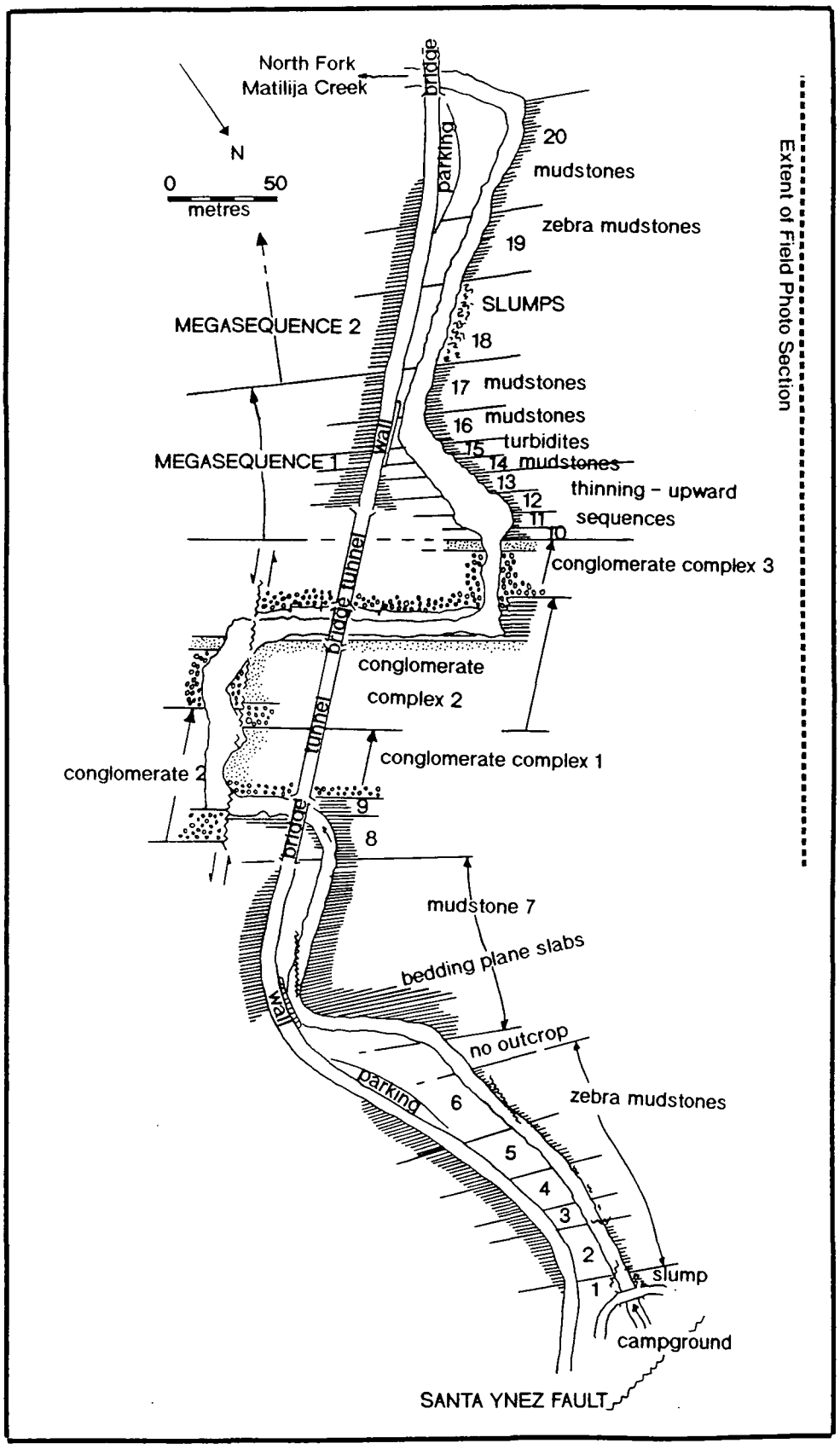

Figure 3.23 Map of sedimentary sequence exposed along Wheeler Gorge. Note map orientation (Redrawn and Modified from Walker, 1985).

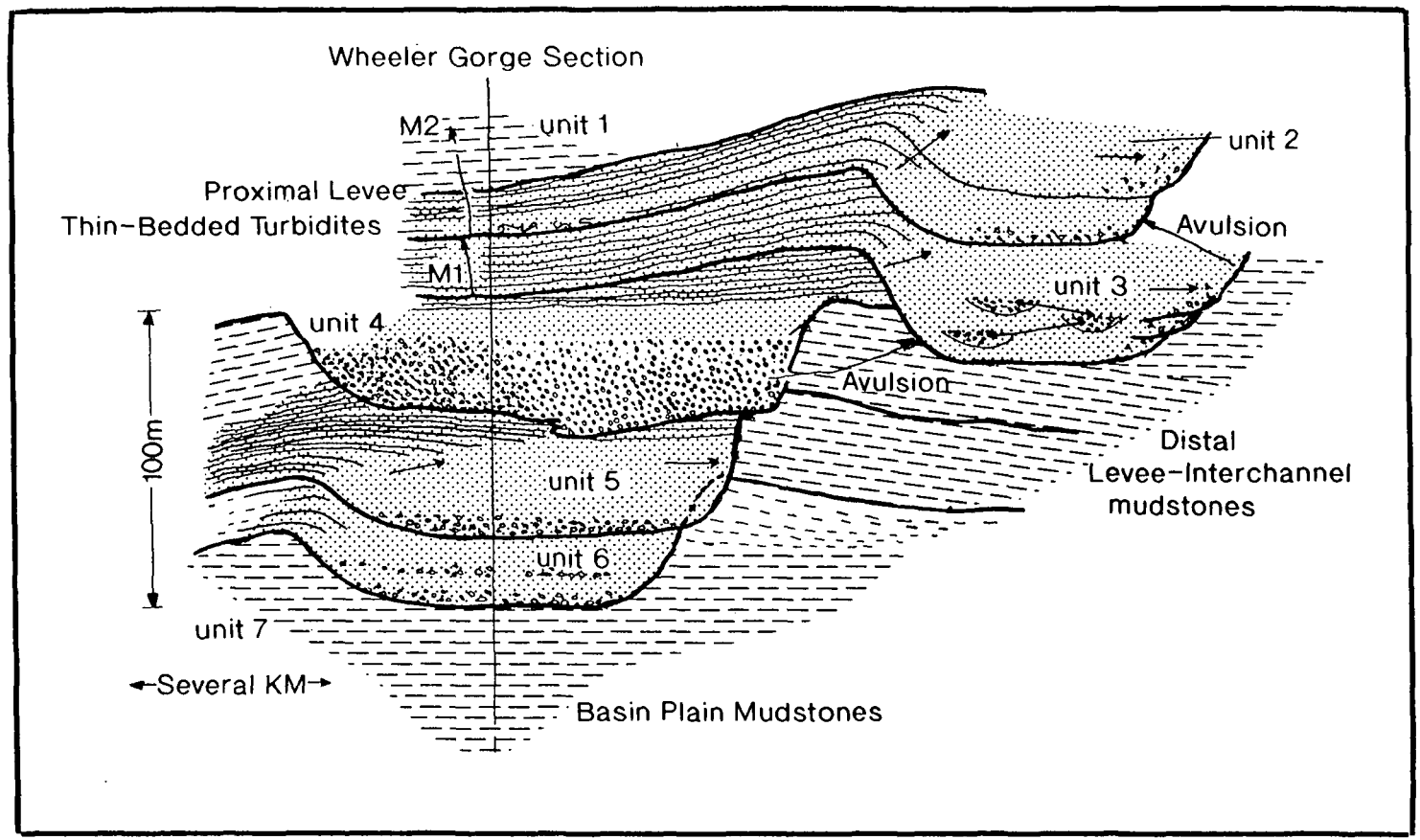

Figure 3.24 Diagram of channel-levee-interchannel complexes, based upon Wheeler Gorge and the Newport channel data of Graham & Bachman (1983). It is interpreted that the channels switched position by avulsion after the deposition of Unit 4, resulting in the deposition of the thinning-upward levee facies above the channels, exposed in Wheeler Gorge (Redrawn and Modified from Walker, 1985).

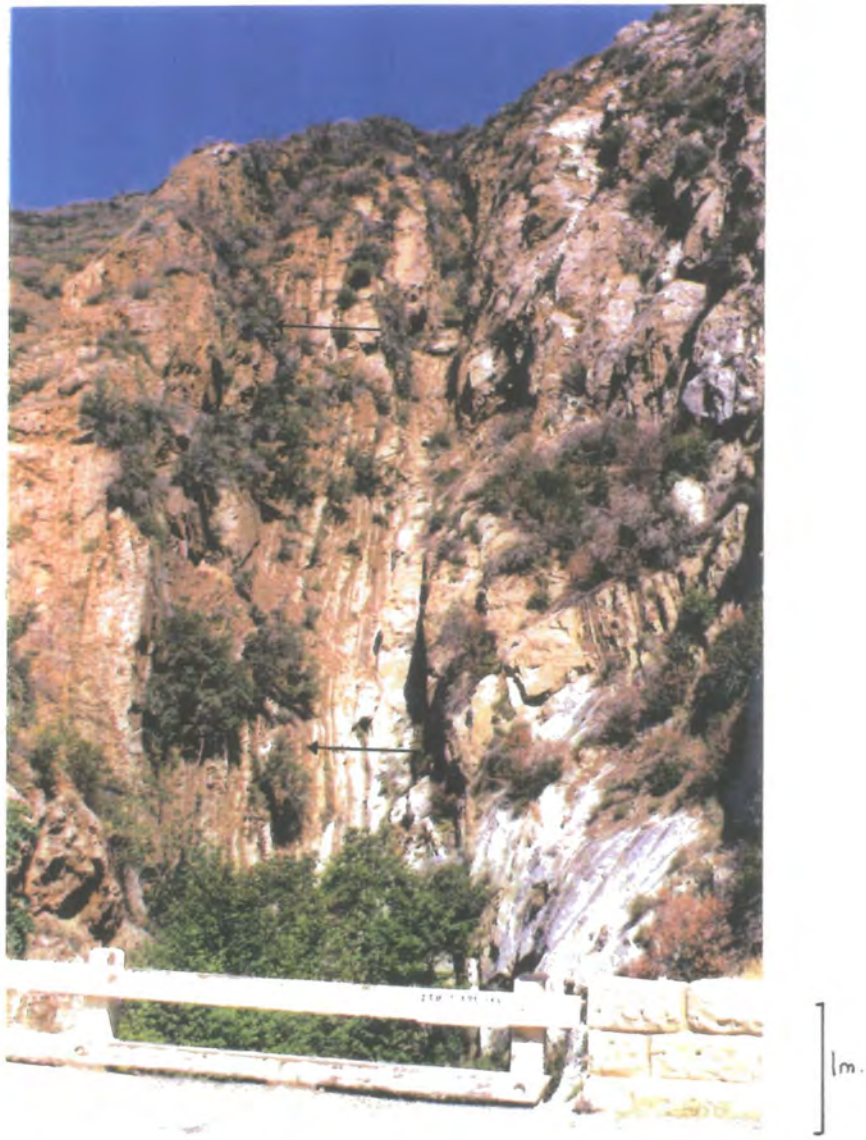

Plate 3.17 Thinning and fining upward channel sections within Unit 3, Wheeler Gorge.

oilfields (see Chapter 5). Forward modelling of the depositional arrangements of these complexes can provide valuable information on the influence of differential compaction on the geometry and spatial distribution of facies. A model can then be developed utilising these principles for the Palaeocene section of the Montrose - Arbroath area of the North Sea. The following section illustrates how modelling of a depositional arrangement such as that seen at Wheeler Gorge can be used to provide data on the influence of differential compaction. Other examples are contained in Chapter 5.

3.4.3 Compaction Modelling of the Wheeler Gorge Section.

Simple backstripping of Walker's (1985) channel - levee - interchannel model for Wheeler Gorge deposition (Fig. 3.24) has been performed in an identical manner to the 'graben' example in Ridge Basin (see section 3.2.7). This modelling demonstrates how differential compaction of the sediments may cause the major avulsion after the deposition of the first three coarse channel sections, accounting for the lateral channel migration proposed by Walker (1985).

Figure 3.24 was divided into 4 vertical sections evenly spaced across the model, and each section was accurately measured and divided into individual sedimentary units. Simple decompaction of each section was then carried out using the exponential relationship for the change in unit porosity with depth for sands and sand/shale units:-

$$\phi = \phi_o . \exp^{-cz} \qquad \text{(equation 3.2)}$$

where $c=3x10^{-4}$ for sands and $4x10^{-4}$ for sand/shale units. The depositional porosity for sands ($\varnothing_0$) is taken as 40%, and for sand/shale units 60%. Shale units were decompacted using the Baldwin & Butler (1985) power law equation (equation 2.2, Chapter 2). Once the thickness of each section was ascertained using the various decompaction methods described, forward modelling of the entire section was carried out, showing how the model builds up in time, and thus estimating topography immediately before deposition of the following channel - levee complex. Results of the decompaction are shown in Table 3.4, and the forward modelling is shown in Figure 3.25.

Burial greater than that shown in the section is ignored at this stage, and it is assumed that the model, as drawn by Walker (1985), represents the depositional arrangement immediately after deposition of the capping mudstone unit. Figure 3.25 shows that after deposition of the channel complex number 4, avulsion of the channel system to the right-hand side occurs. This avulsion appears to be partly controlled by topography as this

A

SECTION 1

Units 1,2,3	Shale	85					
		54%					
Unit 4	Shale	31	41.6				
		48%	61%				
Unit 5	Sh/S'st	28	29.2	29.9			
		57%	59%	60%			
Unit 6	Sh/S'st	18	18.7	19.2	19.5		
		56%	58%	59%	60%		
Unit 7	Shale	58	62.5	66.5	71.1	75.6	
		42%	46%	49%	53%	55%	
Sum of Thickness		220	152	115.6	90.6	75.6	0

B

SECTION 2

Unit 1	Shale	33							
		61%							
Unit 2	Sh/S'st	19	19.4						
		59%	60%						
Unit 3	Sh/S'st	24	24.5	24.7					
		59%	59%	60%					
Unit 4	Sandstone	37	37.2	37.4	37.6				
		39%	39%	40%	40%				
Unit 5	Sandstone	43	43.3	43.4	43.6	43.9			
		38%	39%	39%	39%	40%			
Unit 6	Sandstone	24	24.2	24.2	24.4	24.5	24.8		
		38%	38%	39%	39%	39%	40%		
Unit 7	Shale	40	41.1	41.9	43	45.3	50.2	55.5	
		42%	43%	44%	46%	48%	53%	58%	
Sum of Thickness		220	189.7	171.6	148.6	113.7	75	55.5	0

C

SECTION 3

Unit 1	Shale	11							
		67%							
Unit 2	Sh/S'st	22	22.1						
		60%	60%						
Unit 3	Sh/S'st	38	38.2	38.7					
		59%	59%	60%					
Unit 4	Sandstone	28	28	28.2	28.4				
		39%	39%	39%	40%				
Unit 5	Shale	4	4.1	4.2	4.8	7.2			
		48%	48%	51%	57%	71%			
Unit 6	Shale	36	36.5	37.7	41.1	45.3	46.8		
		46%	47%	49%	53%	57%	59%		
Unit 7	Shale	81	81.7	83.3	86.7	89.4	90.1	100.6	
		43%	43%	44%	46%	48%	48%	54%	
Sum of Thickness		220	210.6	192.1	161	141.9	136.9	100.6	0

D

SECTION 4

Unit 1	Shale	10						
		67%						
Unit 2	Sandstone	43	43.1					
		40%	40%					
Unit 3	Sandstone	42	42.1	42.4				
		39%	39%	40%				
Unit 5	Shale	23	23.4	25.6	32.2			
		47%	48%	52%	62%			
Unit 6	Shale	32	32.4	34.4	37.5	43.6		
		45%	46%	49%	53%	60%		
Unit 7	Shale	70	70.6	73.3	76.3	79.6	89.1	
		42%	43%	45%	47%	49%	55%	
Sum of Thickness		220	211.6	175.7	146	123.2	89.1	0

Table 3.4a-d Decompaction tables for Wheeler Gorge depositional model.

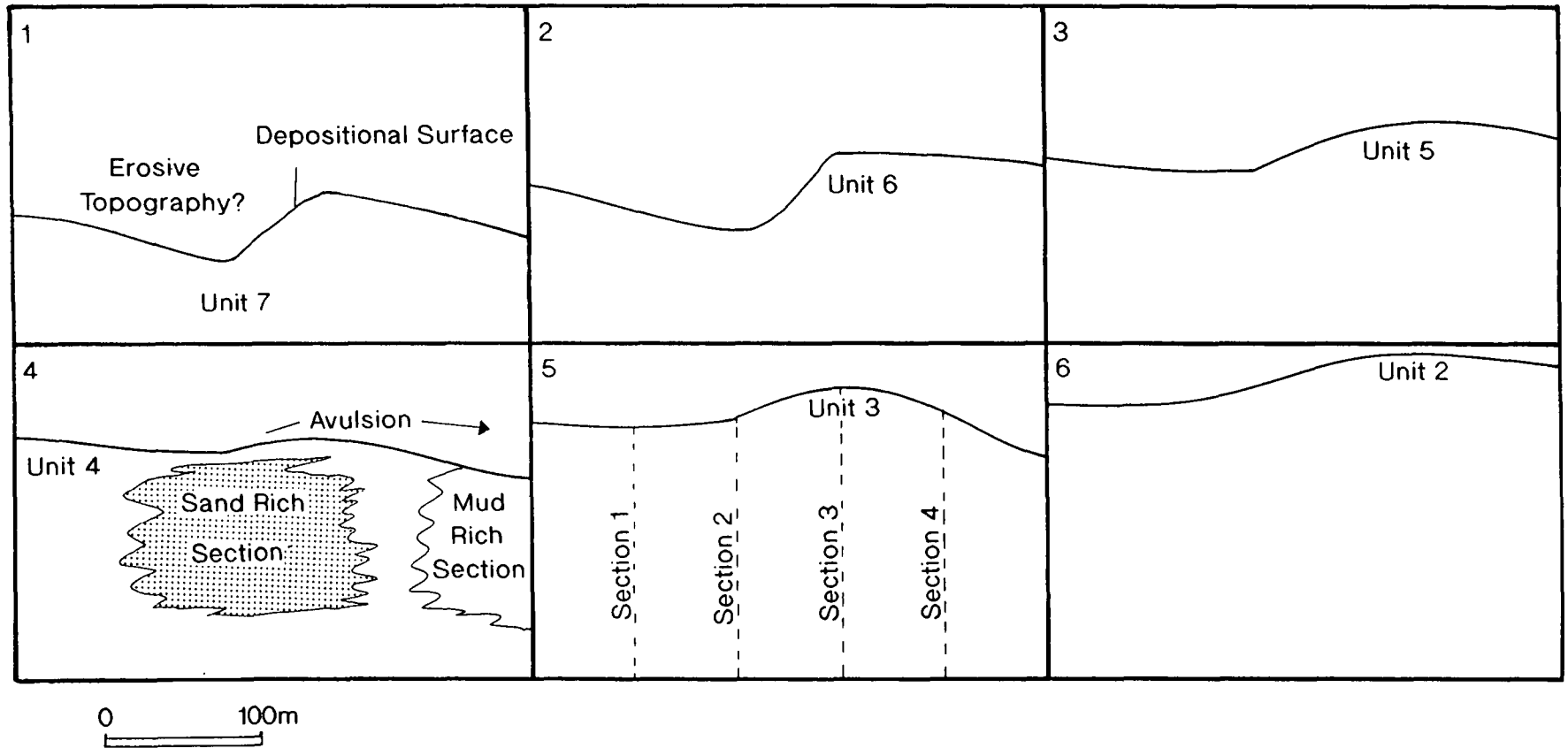

Figure 3.25 Forward modelling of the decompacted Walker model. Note the avulsion occurring after Unit 4 deposition switches channel deposition away from an area underlain by a sand-rich sequence, to an area underlain primarily by muddy levee and interchannel facies.

area forms a slight topographic low within the section (Fig. 3.25). Thickness measurements originate from the base of the diagram, a practise that will induce errors in calculations, as a thicker mudstone basal section will form greater topography after deposition of section 4, and thus a greater control upon the successive channel deposition. A second, major driving factor of the avulsion however, is that the right-hand side of the section is entirely underlain by highly compactible muds compared with the stacked channel section to the left, which will be significantly less compactible. Any deposition upon this mudstone will induce a greater percentage of compaction in this section, and a greater amount of relief will therefore be produced at a quick rate, thus perpetuating deposition of coarse-grained channel sediments in this area.

The modelling has not taken into account any erosion at the base of the channel sections, although this undoubtedly does occur (e.g. deposition of the initial channel sequences). However, erosion seems to have little effect on the overall compactionally produced relief. Indeed, the only effect erosion does have is to introduce greater quantities of sand into the certain sections, and thus enhances the differential compaction between channel and levee/interchannel area, because of increased loading and the addition of more incompactible sediment to certain areas. Erosion probably enables the onset of the major avulsion to occur, thus activating the greater compaction of the mud section and preferred deposition in this area.

This simple modelling of a schematic depositional model therefore illustrates how differential compaction has the capability of controlling facies geometries and distributions, and can thus be used as a predictive tool to locate possible other coarse-grained channel deposits.

3.5 Conclusions.

Field data and subsequent modelling have allowed many important insights into the near-surface compactional process, and the effects the process has on further deposition. Unfortunately, the scale at which observations of compactional processes in a submarine fan environment could be made was significantly less than had first been anticipated. Stacking patterns of major distributary channels were not evident, even though exposure in Ridge Basin was excellent. However, observations and measurements were possible from smaller examples of differential compaction, allowing a certain degree of assessment of the influence of compaction on submarine fan deposition. Fieldwork also highlighted the

extreme variability of near-surface processes within the submarine fan depositional environment, and the problems these may introduce into the future modelling of the Montrose and Arbroath oilfields (Chapter 5).

For modelling of outcrop data to be carried out, various assumptions had to be made:

- The porosity-depth curves of Baldwin & Butler (1985), and Sclater & Christie (1980) are adequate for describing the porosity evolution of muds and sands, respectively, at depths greater than approximately 500m.
- Immediately after deposition in a submarine fan environment, tops of beds are horizontal.

The first assumption is discussed in detail in Chapter 2. The latter assumption is likely to be true, as sea-floor topography will be subdued by deposition, and the high initial porosities of the sediments are unable to maintain any appreciable slope (i.e. $<5^{\circ}$) (Kenter, 1990).

Field exposures show the extreme importance of an understanding of the compaction rate when considered against the rate of deposition and loading within the modelling process. This is the most fundamental question within the present study, as it controls the topography of the sea-floor, and any depositional influence that this might have. Exposures within Ridge Basin illustrated that differential compaction occurred syn-depositionally, producing thickened sandstone beds where greater amounts of compaction had occurred in the underlying sequence.

One of the implications of syn-depositional compaction is that pore fluid is lost from the underlying sediment at the same rate of loading. Once deposition has ceased, pore fluid pressure in the underlying section has already attained an equilibrium state with the amount of overburden, resulting in the depositional surface (sea-floor) remaining flat. With a flat sea-floor, the major control on subsequent deposition may be the underlying compactibility of the sediment, maintaining the likelihood of future channel deposits upon underlying shale sections and producing off-set channel sand bodies.

However, the exposures used in the modelling were relatively small when compared to the size of submarine fan channels, which range from tens of metres in width up to a kilometre in scale. Therefore, the question of scale needs to be developed and understood. It is possible that thin beds viewed in outcrop have the ability to dewater and compact syn-depositionally because of their high initial porosities, combined with the short distances over which pore fluid must be expelled, so that pore fluid pressure remains in equilibrium

with the amount of overburden. Also aiding pore fluid expulsion is the frequent interbedding of sandstone beds, which, due to their higher porosity and permeability with respect to the muds, can act as carrier beds for expelled pore fluids. This may not follow for larger depositional episodes, especially where sand-rich, submarine channels are adjacent to laterally equivalent, thick, mud-rich, overbank sediments. Due to the thickness of the mud, and the inherent low permeability, accentuated because of the absence of regularly interbedded sands, pore fluid may require a longer period of time to equilibrate to the amount of loading, and will not reach an equilibrium state during the period of loading. Therefore, once deposition has ceased, post-depositional compaction will occur, resulting in topography on the depositional surface, due to differential compaction between the channel and overbank facies.

However, although the argument between syn- or post-depositional compaction cannot be adequately resolved using the scale of observations of the fieldwork described, bed relationships within the Castaic Formation of Ridge Basin have shown that large amounts of near-surface compaction occur in the submarine environment. The amount of compaction appears to be greater than that proposed by most of the published porosity-depth curves and equations, mainly because these are based on data from deeper buried sediments. Near-surface compactional behaviour of sediments is important however, when considering the creation of a control for the subsequent distribution of facies. Knowledge of near-surface processes is required if compactional control on sediment distribution is to be modelled. This knowledge can be best obtained from fieldwork specifically looking at the bedding relationships.

More generally, it appears that both slumping and basal loading are widespread processes throughout submarine deposition, and these can effect the near-surface compactional behaviour of the sediments, as explained in section 3.2.7. These processes also need to be taken into account therefore, within any modelling of submarine fan deposition. Fieldwork and subsequent compaction modelling at Wheeler Gorge also illustrates that erosion at the base of a submarine channel is another important factor to consider when assessing sediment deposition and distribution. However, sediments exposed at Wheeler Gorge are interpreted to be proximal in composition with respect to those of the Castaic Formation of Ridge Basin (see section 3.2.5). Higher flow velocities, and associated greater erosion effects, are more likely in a proximal setting compared to a distal environment. Exposures of turbidites in

Ridge Basin show evidence of only little basal erosion occurring, with only minor shale rip-up clasts being present towards the bases of these beds.

Fieldwork has therefore highlighted many important aspects of the submarine depositional process, and near-surface differential compactional phenomenon, such as instantaneous compaction and sedimentation, off-setting of sand bodies due to the relative compactability of the underlying sequence, sedimentary loading within a sand/shale dominated sequence, and the problem of erosion at the base of submarine channel deposits. Much of the data collected, and ideas formulated, are taken forward and are combined into the model for submarine channel deposition within the Palaeocene section of the Montrose - Arbroath area of the North Sea (Chapter 5).

Chapter 4:- Sacramento Mountains - New Mexico.

4.1 Introduction.

The following sections deal with the fieldwork, and subsequent modelling of differential compaction occurring around carbonate buildups, and over submarine channels, within the Sacramento Mountains of south-central New Mexico. At first glance this appears to be a strange choice of field area for the present research, which is primarily interested in siliciclastic depositional systems. However, the carbonate systems provide a complimentary dataset to that of the Californian fieldwork of Chapter 3. In particular, information concerning the timing and rate of compaction has been accumulated from this work.

Section 4.1.1 summarises the background of compaction modelling in a channelised geological setting, and then outlines the advantages and objectives of studying compaction of a carbonate system. Further sections deal with the descriptions of stratal patterns, the implications these patterns have concerning compaction, and the modelling of compaction and pore pressure within the present study area (Fig. 4.1).

4.1.1 Siliciclastic Environments Versus Carbonate Environments.

Research into differential compaction and its control upon depositional architecture within siliciclastic systems has been an area of study for some years (e.g. Brown, 1975; Bridge & Leeder, 1979; Parker Gay, 1989; Anderson, 1991)(see Chapter 2). This research has basically looked at channel stacking patterns, especially within the alluvial environment (e.g. Anderson, 1991). The present research has focused on submarine fan systems due to the greater potential for differential compaction to occur because of the higher mudstone depositional porosities present in marine environments (see Chapters 2 & 3). However, theoretical modelling of differential compaction is limited by two fundamental problems: (1) very little data concerning the near-surface porosity - depth profile, and (2) a poor understanding of the exact timing and rates of compaction with respect to the rate of deposition (see sections 2.2.5 and 2.3).

Attempts to isolate the effects, processes and possible role of differential compaction within a submarine fan system at outcrop are hindered by some major practical problems. Specifically these are: (1) the extremely large scale of submarine channel bodies (around 1km in width) compared to that of decent exposure (a few hundred metres at best), and (2) the relatively low

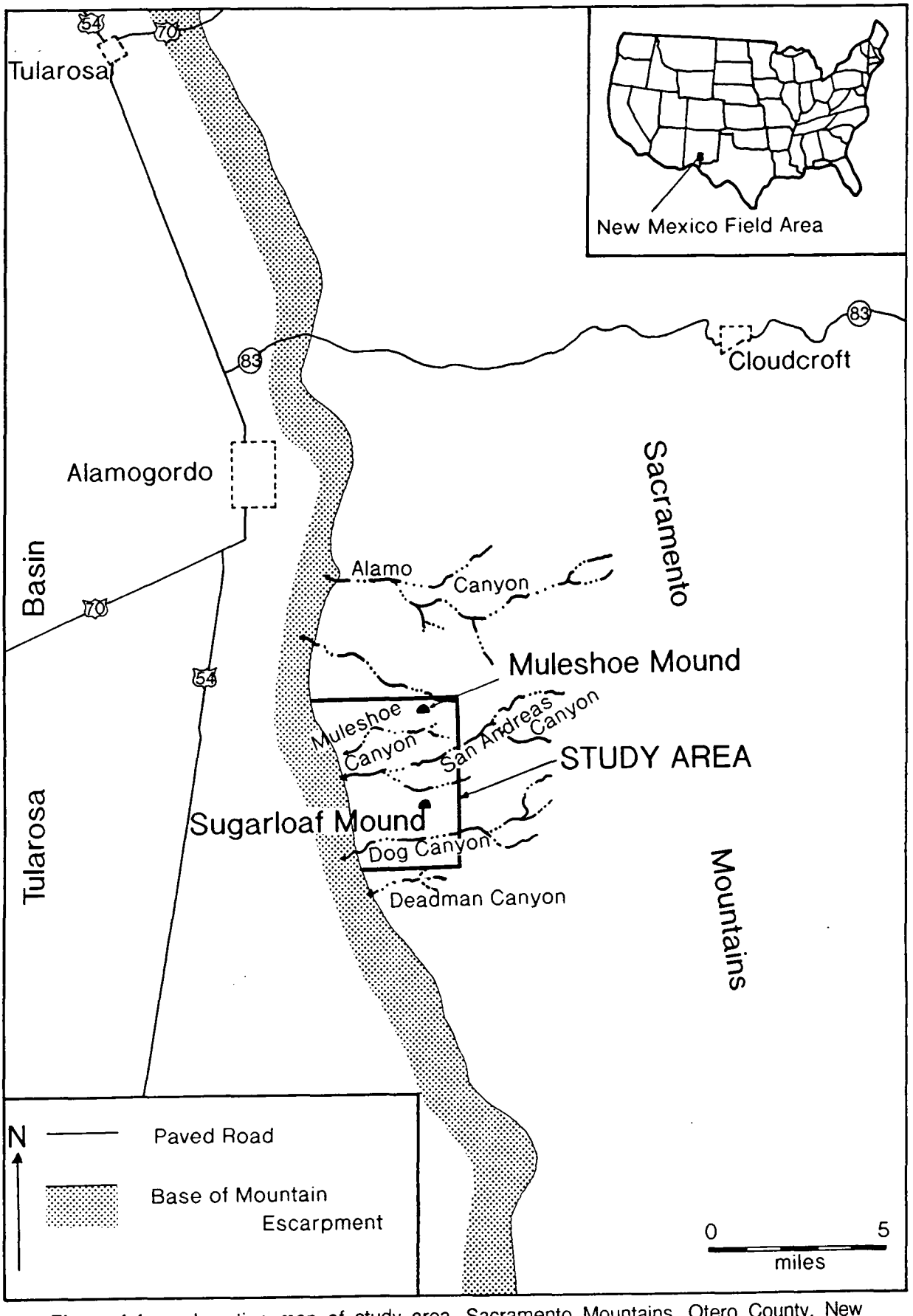

Figure 4.1 Location map of study area, Sacramento Mountains, Otero County, New Mexico.

slope angles (commonly 1 - 2°) developed by differential compaction over such wide areas. Observations at outcrop of submarine fan deposits are limited to the scale of outcrop exposure of specific areas, and this is generally small compared to the scale of the channel system. Therefore studies of discontinuous exposures are limited in the amount of information that they provide concerning compaction, particularly information about the relative timing of compaction and deposition, and the precise mechanisms of differential compaction.

However, that is not to say that such outcrops are totally devoid of useful information for modelling compaction, it is more a question of the scale of the information that they provide. Field observations showed many small scale compactional effects, such as the importance of basal loading and the occurrence and influence of sediment slumping and soft-sediment deformation. These data will all help to improve the modelling of submarine fan deposits at a fine scale in Chapter 5. On the larger scale, however, for the reasons given above and those discussed below, a better insight into compaction processes and their relative timing, is gained from carbonate settings.

The study of differential compaction in a carbonate platform system, particularly those punctuated by offshore pinnacle build-ups, offers several advantages over a clastic submarine fan environment, that allows compactional phenomena to be viewed at the outcrop scale. These advantages reflect:

(1) the development of relatively rigid, uncompactible buildups, against and over which compaction of flank and blanketing strata can be quantitatively evaluated,

(2) the role of early cementation which tends to inhibit compaction in the buildups, and is often quite selective in location,

(3) the high original porosities of carbonate mudstones (up to 75%),

(4) the high depositional angles of flank strata to carbonate platforms and build-ups (up to 40°) compared to surrounding and overlying strata,

(5) the close and quantified relationship between depositional fabric and slope angle (i.e. Kenter, 1990), and,

(6) the highly variable nature of carbonate sedimentation rates, and the potential for platform sedimentation to be abruptly shut-down by environmental change, and/or a rapid relative sea-level rise to develop 'drowning' unconformities (i.e. Schlager, 1989), or subaerial exposure.

Some of these advantages are shared by the submarine fan environment over other siliciclastic environments such as alluvial deposits (e.g. 3 above). However, combination of these advantages makes the flanks of carbonate platforms and buildups a near ideal setting to examine the **timing** and processes of differential compaction, and to observe its possible influence on sedimentation. This chapter therefore aims to draw conclusions derived from field observations, specifically concerning the exact **timing** and **processes** of **near-surface compaction**, and to quantitatively show the effects of differential compaction.

4.2 Porosity and Compaction of Carbonate Strata.

Compaction of carbonate strata reflects several important variables, namely depositional fabric (mud versus grain support), amount of lime mud and clays present, grain size and nature of grain contacts, original porosity and fluid content and early marine diagenesis, particularly the degree of cementation. Providing there is no near-surface cementation/dolomitisation, near-surface compactional processes are dominantly mechanical, and reflect the packing of grains to a more organised structure. This is very important in uncemented grainy and clay-rich sediments and is intimately involved in the dewatering of sediments, particularly important in carbonate mudstones where original porosities can be high (e.g. up to 75%). Experimental studies on cores of modern lime muds (e.g. Shinn & Robbin, 1983) have demonstrated compaction of up to 50% under burial pressures that are equivalent to burial depths of less than 100m (328ft), with an accompanying porosity decrease from 65-75% to 35-40%.

Porosity-depth curves for carbonate strata have been proposed by many authors, including Hardenbol et al. (1981), Schmoker & Halley (1982) and Baldwin & Butler (1985). Data from modern sediments were used by Hamilton (1976), and have been followed by many studies carried out by the Ocean Drilling Program (ODP), particularly around the Bahamas (e.g. Lavoie, 1988).

Mechanical compaction of limestones is only hindered where there has been significant early marine cementation, particularly apparent in

packstones, grainstones and reefal build-ups. Shinn et al. (1983) examined the Mississippian Muleshoe Mound of the Sacramento Mountains (which forms a part of this study) and concluded that the abundance of early marine cements severely inhibited its early mechanical compaction as compared to the Permian Scorpion Mound, a few kilometres north, where, at some intervals, early marine cements were nearly absent.

4.3 Location and Geological Setting.

The Sacramento Mountains are located within south-central New Mexico, USA, running approximately north-south along the eastern edge of the Tularosa Basin (Fig. 4.1). Fieldwork was carried out in an area 5 to 10 miles south of Alamogordo, along the western facing scarp of the Sacramento Mountains within Otero County. The western escarpment, is the uplifted footwall block of a major westerly-dipping Tertiary extensional fault, and exposes a thick sedimentary sequence from Precambrian to Cretaceous in age. The exposures of generally easterly dipping Palaeozoic sediments are spectacular, yet relatively undeformed . These strata are composed of a stacked succession of carbonate platforms, separated by major unconformities (Pray, 1961). Exposures of the Mississippian platform are generally excellent, often particularly so adjacent to Waulsortian buildups, many of which built depositional relief in excess of 100m (328ft) (Plate 4.1) (Laudon & Bowsher, 1941, 1949; Pray, 1961). It is these buildups and their related strata which have been the focus of considerable interest since their discovery and subsequent description by Laudon & Bowsher (1941, 1949) (e.g. Pray, 1958, 1961, 1965, 1969; Schaefer, 1976; Bolton et al., 1982; Shinn et al., 1983; Jackson & DeKeyser, 1984a, b; Bowsher, 1986; Ahr, 1989; Kirkby et al., 1993)

From the point of view of the present study, work was focused on the Mississippian strata between Muleshoe Mound in the north, and a point about half a mile south of Dog Canyon (Fig. 4.1). The area of study encompasses two well exposed Mississippian bioherms (namely Muleshoe and Sugarloaf Mounds), along with at least three other poorly exposed bioherms. Excellent exposure occurs throughout this area along both dip (north-south) and strike (east-west) sections, providing valuable bed thickness, palaeocurrent, and facies data.

Plate 4.1 General view looking east towards the western escarpment of the Sacramento Mountains, Otero County, New Mexico.

4.4 Stratigraphy.

This study deals exclusively with Mississippian strata, which have an overall stratigraphic thickness averaging around 100 to 150 metres (300 to 400 feet) within the area of interest. These strata basically consist of marine limestones and minor shales, which vary greatly across the region due to both facies changes around bioherms, and later erosional events.

In particular, attention is focused on the stratigraphic relationships developed between the Mississippian Lake Valley Formation and the overlying Rancheria Formation. These formations form two mutually compensating wedges (Laudon & Bowsher, 1941, 1949; Pray, 1961; Lane, 1974) (Fig. 4.2). The lower Lake Valley wedge has the external geometry of a basinwards thinning 'bank' (sensu Mitchum et al., 1977), reflecting internal depositional thinning but also, and more importantly, its erosional truncation towards the south (Fig. 4.2). The palaeobathymetry of this lower wedge was subsequently filled by the succeeding and opposing Rancheria wedge, which has the external form of a slope front fill (sensu Mitchum et al., 1977). This second wedge correspondingly thins northwards across its precursor (Lane, 1974). Of particular relevance to the present study, north of the Dona Ana 'slopebreak' (Fig. 4.2) the Lake Valley and Rancheria Formations are separated by a major hiatus. This hiatus is demonstrated by the absence of the conodont zone fossil *Apatognathus scalenus-Cavusgnathus* (Lane, 1974, 1982). Section 4.7 will expand on the presence of this hiatus, and how it effected both the processes of compaction and deposition.

A brief description of the stratigraphy of this region follows, but the reader is recommended to read Pray (1961) for a fuller description of the Sacramento Mountains geology.

4.4.1 Mississippian Formations.

Laudon & Bowsher (1941, 1949) first described and measured the Mississippian rocks of southern New Mexico, setting up much of the present stratigraphic framework. Slight modifications of the earlier work by a variety of workers has since divided the Mississippian strata into four formations; the Caballero, Lake Valley, Rancheria, and Helms Formation (Fig. 4.3). The Lake Valley Formation has been split further into six members by Laudon & Bowsher (1949), and it is within this formation that the extremely large bioherms occur. Hence, this study is restricted to the upper part of the Lake Valley and the overlying Rancheria Formation, both of which have been

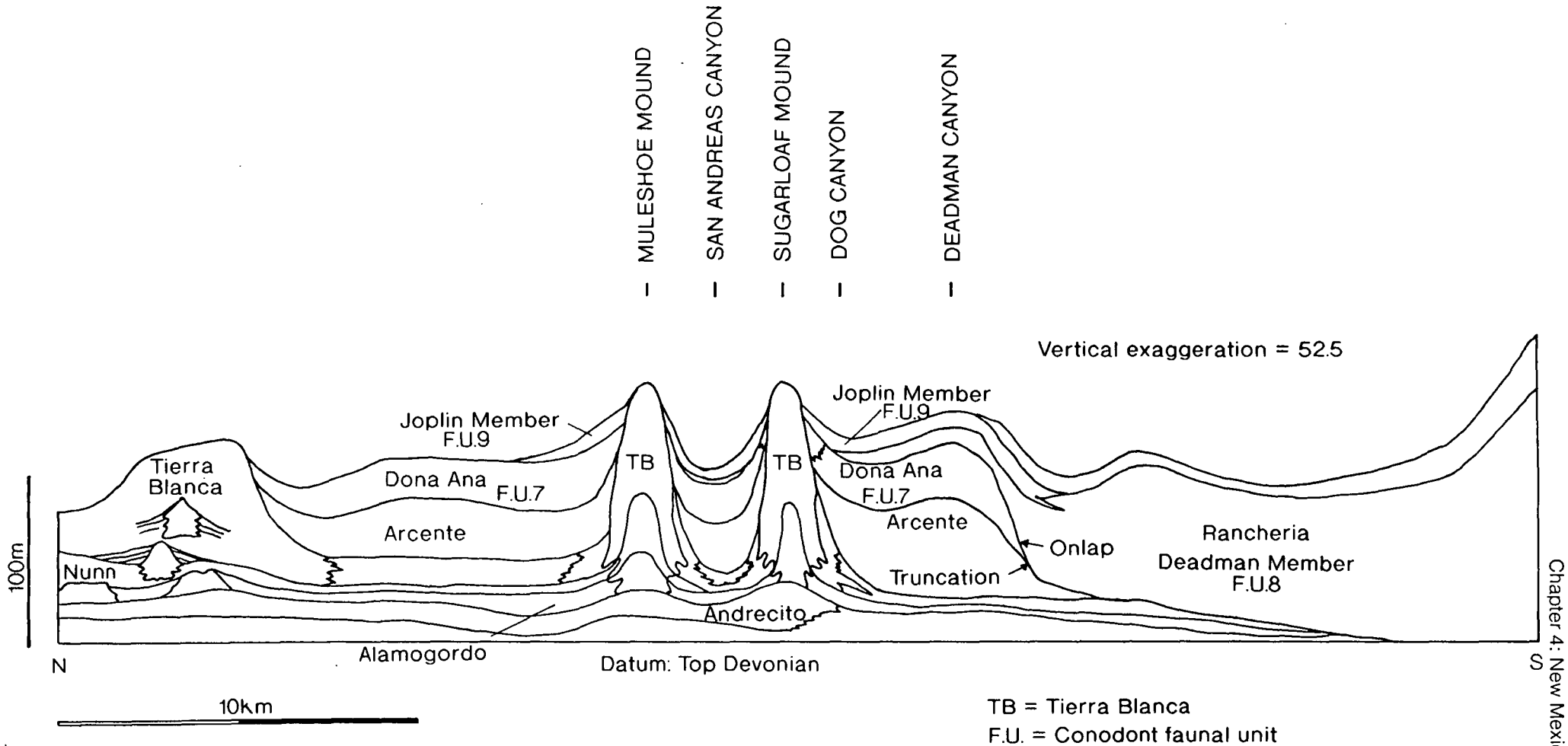

Figure 4.2 Schematic north-south section of Mississippian strata in the Sacramento Mountains (Modified form Lane, 1974). Note the classic wedge-on wedge relationship of the Lake Valley (Alamogordo-Dona Ana Members) and Rancheria Formations (Deadman and Joplin Members). The southwards depositional and erosional thinning of the Lake Valley Formation is onlapped and filled by the succeeding Rancheria.

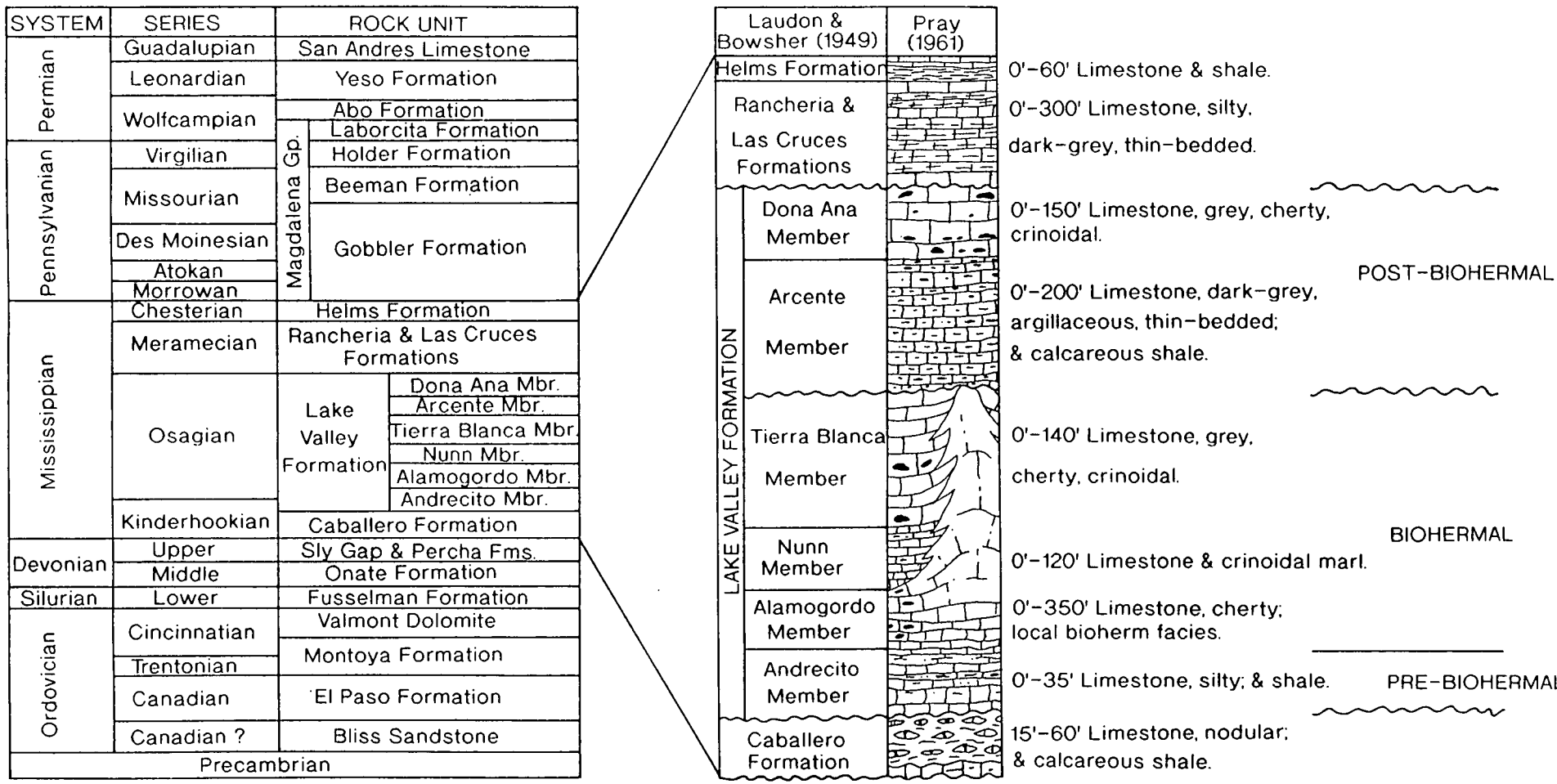

Figure 4.3 Stratigraphy of the Sacramento Mountains, New Mexico.

effected by differential compaction during and after deposition, over and around the 'giant' bioherms.

4.4.1.1 The Lake Valley Formation.

The Lake Valley Formation is well developed throughout the central region of the Sacramento Mountains, reaching a thickness of approximately 120 metres (400 feet) and consisting largely of crinoidal limestones, with minor calcareous siltstones and shales (Pray, 1961). Stratigraphic relationships within the Lake Valley Formation are complex, owing to lateral and vertical variations in lithology and thickness. The thickness changes are caused both by variation of depositional thickness and by subsequent erosion along unconformities either during or subsequent to Mississippian time.

Laudon & Bowsher (1949) subdivided the Lake Valley Formation into the Andrecito, Alamogordo, Nunn, Tierra Blanca, Arcente and Dona Ana Members, listed in ascending order. However, as biohermal growth has so greatly affected the Lake Valley stratigraphy of this area of the Sacramento Mountains, it is easier and more convenient to describe the stratigraphy of the six members as pre-biohermal, biohermal and post-biohermal members (Fig. 4.3). It is also important to note that type sections for the six members are only developed within the inter-mound areas, away from bioherm growth and influence.

Pre-Biohermal Strata.

Only the Andrecito, the basal member of the Lake Valley Formation, is unaffected by major biohermal growth. It consists largely of calcareous shale, marl, thin-bedded argillaceous limestone, well-sorted crinoidal calcarenites, and minor quartz siltstone (e.g. see summary by Ahr, 1989). According to Pray (1961), the unit thins significantly towards the south over a distance of 5Km, from a thickness of 6 to 10 metres (20 to 35 feet) in the northern Sacramento Mountains to approximately 2.5 to 3 metres (8 feet) in the south of the region (e.g. Fig 4.2). The base of the Andrecito Member is a clearly marked disconformity, commonly with observable low angular discordance particularly in the north. Distinguishing characteristics of the member are relatively even bedding, the presence of quartz silt or very fine-grained sand, and the trace fossil *Zoophycos*, which serves as an index fossil for the member in this region.

Biohermal Strata.

Pray (1961) states that nearly all the bioherms occur within the Alamogordo, Nunn, and Tierra Blanca Members of the Lake Valley Formation. The Alamogordo Member usually forms a well exposed ledge of medium-grey cherty calcilutite (lime mudstones), around 1.5 to 3 metres (5 to 10 feet) in thickness. However, in typical inter-mound regions it can reach a thickness of 4.5 to 12 metres (15 to 40 feet). The Nunn Member consists of friable or poorly cemented crinoidal limestone with minor amounts of marl. Its exposure is typically poor throughout the Sacramento Mountains, with the unit's thickness varying greatly throughout the area depending on the proximity to the mound facies (e.g. Fig 4.2).

The Tierra Blanca Member is composed of crinoidal calcarenites and calcirudites forming the upper member of biohermal strata (packstones and grainstones). The limestone is well cemented, and in the northern mountains usually forms a resistant cliff around 30 metres (100 feet) high around the area of the mound facies. However, in the inter-mound areas it can attain thicknesses of nearly 60 metres (200 feet). In the present study area the facies is very thin (<4m) between the mounds.

In area north of Alamo Canyon within the Sacramento Mountains (Fig. 4.1) there is a significant thickening of the Mississippian section after the Andrecito, but before the Arcente (DeKeyser, 1978) (Fig. 4.2). The section here consists of thick Tierra Blanca encrinites, and is interpreted to have been the site for skeletal carbonate accumulation that, along with growth of tabular Waulsortian reef clusters, created a sedimentary prism that had a definite slope break by the end of Tierra Blanca time (Meyers, 1974; Ahr, 1989). This is the Tierra Blanca Shelf of Meyers (1975), and it represents evolution of a ramp into a shelf by depositional processes during relative tectonic stability. The slope break was formed by passive deposition as there was no inherited slope break from Caballero-Andrecito times to shape the Tierra Blanca Shelf (Ahr, 1989).

The bioherms within the study area first appeared in Alamogordo times, and their growth continued episodically during Nunn and Tierra Blanca times. The core facies of light grey massive limestone generally consists of aphanitic calcite (lime mud) and sparry calcite, with a subordinate amount of skeletal fossil constituents, of which fenestrate bryozoans are the most common (Pray, 1961). According to Lees & Miller (1985) this represents type D Waulsortian facies, characteristic of their fourth phase of mound growth. Flank facies to the bioherms have a simpler lithology, consisting of relatively

pure crinoidal packstones and grainstones. These beds dip at very steep angles (>30°) close to the mounds where the transition from mound facies to flank facies is abrupt. However, flank facies become thinner, and more distinctly bedded away from the core facies, and grade into the inter-mound strata as described above.

The formation of the bioherms and their subsequent growth, associated with the production and trapping of large amounts of carbonate mud remain somewhat enigmatic. Their core facies are dominated by bryozoans, crinoids and large brachiopods. Fenestrate bryozoans have certainly aided local buildup of core facies, however, some bioherms only contain accessory amounts of bryozoan debris, and therefore another buildup mechanism is necessary (Pray, 1961). It has been interpreted (Pray, 1961) that the bioherms grew below the zone of wave abrasion, but some managed to grow into more turbulent, shallow waters. This interpretation is also supported by the large amount of crinoid debris found in the flanking facies. Equally the distribution of the flank facies, especially surrounding Muleshoe Mound, illustrates the influence of currents during mound growth. Flanking facies of Muleshoe Mound is notably asymmetric, with thick flank debris exposed to the south of the mound, but relatively thin to absent flank debris to the north, suggesting currents were directed from the north towards the south of the basin at this stage (i.e. basinwards) (compare Figures 4.4 & 4.5).

The ecology of crinoids and crinoidal growth, especially the stalked variety, as found within the study area, suggest that the bioherms grew at a water depth of around 100 metres (330 feet) or deeper, as crinoids are rarely found in shallow waters due to the damaging effects of wave energy on their growth (Clarkson, 1986).

Post-Biohermal Strata.

The Arcente Member and the Dona Ana Member were deposited after the major period of biohermal growth, and they largely fill the depositional topography between the 'giant' mounds. The Arcente is composed of fine-grained, near-black lime-mudstones and interbedded shales. Away from the bioherms it has a maximum thickness of 60 metres (200 feet), whereas near to the bioherms its thickness commonly averages around 20 metres (66 feet). Locally the Arcente abruptly thins and pinches out against the bioherms (e.g. Muleshoe Mound, Fig. 4.6 and Plate 4.2), having the overall effect of subduing topography created by biohermal growth. The change from grain to mud-supported fabrics from the Tierra Blanca to the Arcente is interpreted to

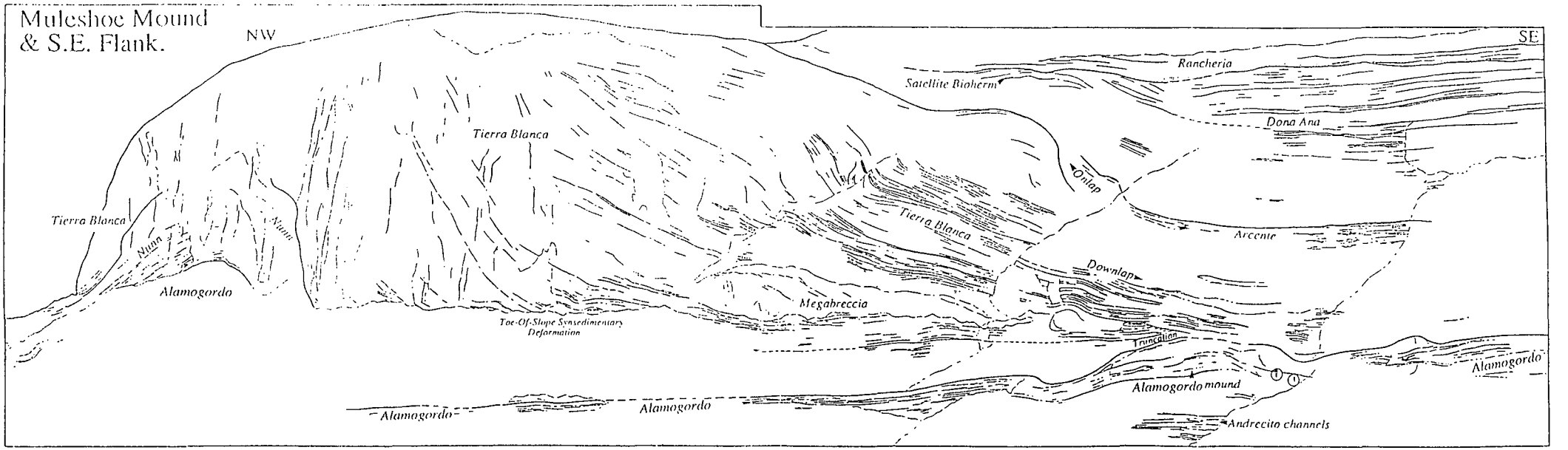

Figure 4.4 Field drawing of the southeastern flank of Muleshoe Mound. Two figures for scale are circled towards the bottom right-hand side (From Hunt & Allsop, 1993).

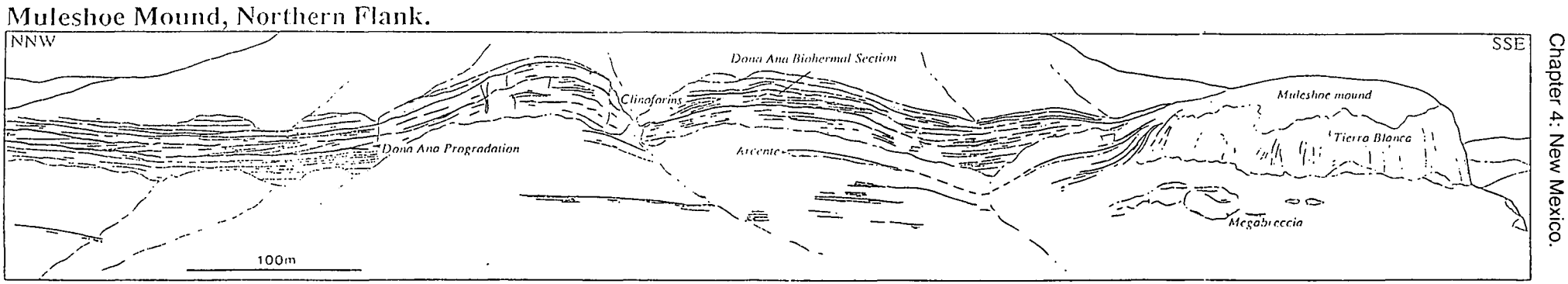

Figure 4.5 Field drawing of the northern flank of Muleshoe Mound, illustrating clinoformed package of the Dona Ana (From Hunt & Allsop, 1993).

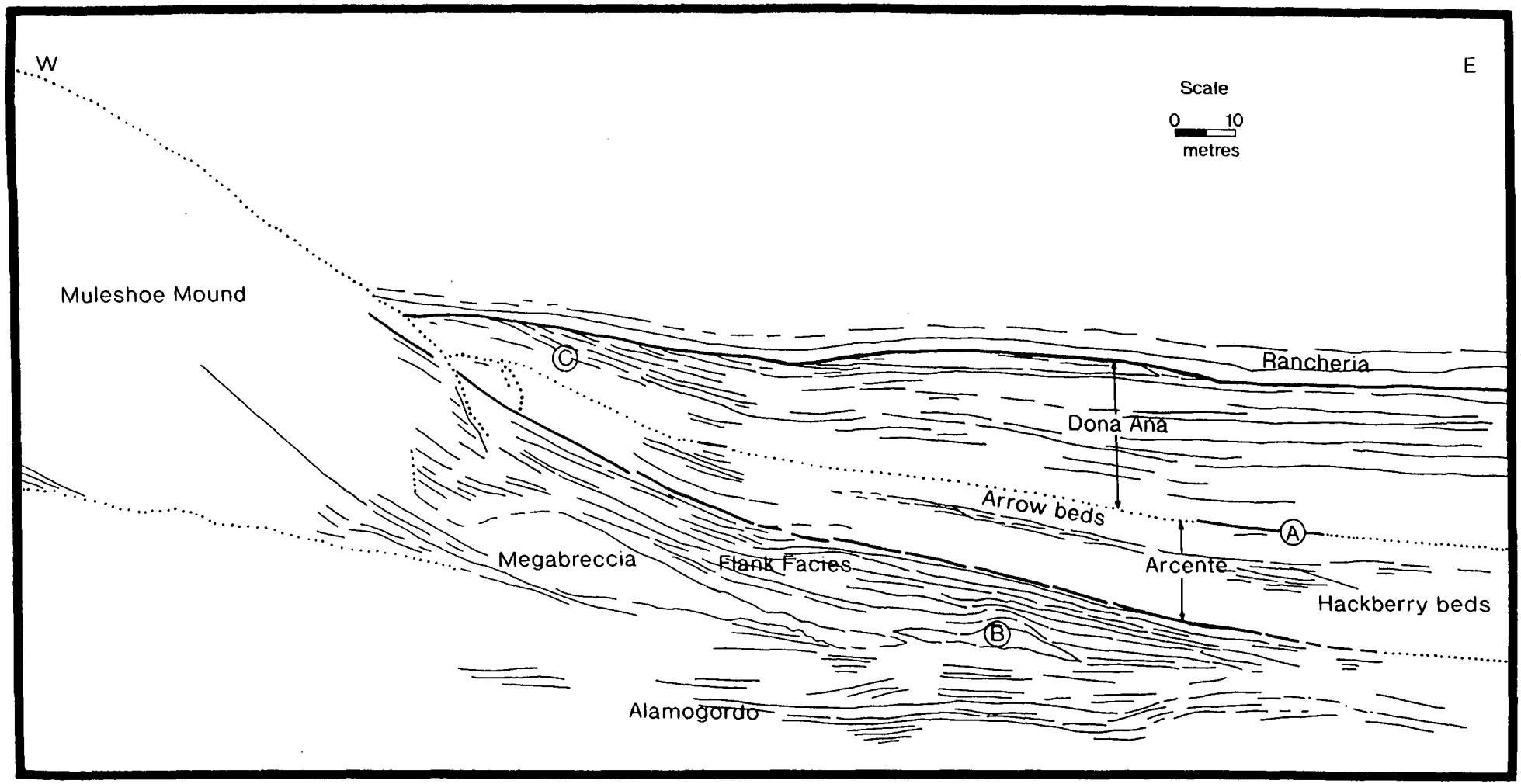

A. Dona Ana – Arcente Contact

B. Compactional Anticline over Megabreccia

C. Exaggerated Dip of Dona Ana, & Angular Uncontormity with Rancheria

Figure 4.6 Field drawing of the south-eastern flank of Muleshoe Mound, illustrating the increase in bed dip toward the mound, and pinch-out of strata.

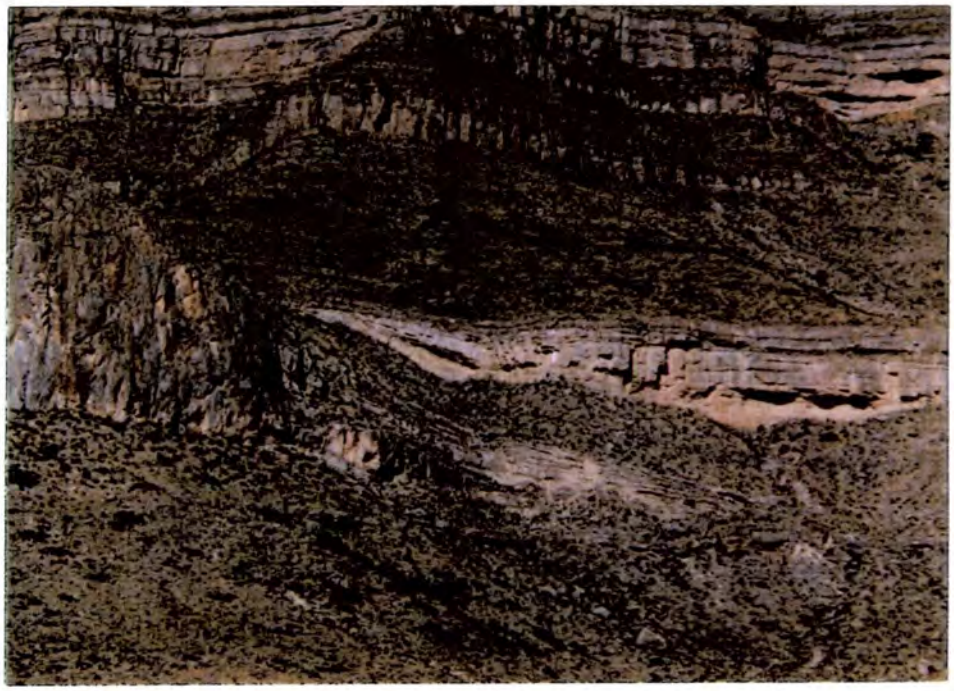

Plate 4.2 View of the southeastern flank of Muleshoe Mound, from which the field drawings and stratal restorations of Figure 4.22 were interpreted.

reflect a decrease of water energy, associated with the development of a stratified water column, normally anoxic towards its base (Meyers, 1975). Within the Arcente, there is a prominently weathering limestone package which can be traced throughout the region, and therefore forms a useful marker horizon. This package is informally referred to as the Hackberry beds, with the Arrow beds of the Arcente above (Fig. 4.6 and Plate 4.2). North of Sugarloaf Mound (Fig. 4.1) the Hackberry beds are typically located 10-12 metres (33-39 feet) above the base of the Arcente, and up to 18 metres (59 feet) below the base of the Dona Ana (see Fig. 4.6 and Plate 4.2). In contrast, south of Sugarloaf Mound the Dona Ana Member rests either directly on top of the Hackberry beds, or only a few metres above them.

Above the Arcente, the Dona Ana Member reflects a return to clear seas and profuse growth of crinoids. In certain areas of the platform the base of the Dona Ana is abrupt, and marked by several gravity flow deposits which may be up to 2m (6.5ft) thick. In these areas, there is often evidence for deformation (e.g. folding) of the Arcente prior to Dona Ana deposition. In contrast, elsewhere the transition from the Arcente to the Dona Ana is gradual (i.e. 375m (1230ft) north of Muleshoe Mound).

The Dona Ana tends to be thickest and coarsest in the proximity (<2km away) of the 'giant' mounds, although it thins immediately adjacent to them (<100m thick) due to differential compaction (see section 4.7). At its thickest part, the Dona Ana forms a cliff of 46m (150ft), however, it more usually forms a 20-30m (66-100ft) high cliff in the vicinity of the bioherms. Lithologically, the Dona Ana is dominated by crinoidal packstones and grainstones, with abundant bryozoans. Short lived bioherms also formed during this time, however, these are considerably smaller than their predecessors, and form within two widespread levels of the Dona Ana. The most important of these are the bioherms which grew from the uppermost flanks of the 'giant' mounds during early Dona Ana times (Muleshoe and Sugarloaf Mounds, see Figures 4.4 & 4.7, and Plates 4.2 & 4.3). More widespread and distinctive low-energy mounds developed in the palaeobathymetric lows. The second 5-10m (16-33ft) thick Dona Ana biohermal level is frequently clinoformed, and dominated by mudstones and wackestones interbedded with graded crinoidal grainstones (i.e. northern side of Muleshoe Mound, Fig. 4.5 and Plate 4.4). Adjacent to the 'giant' mounds this biohermal package is erosionally truncated by the uppermost package of the Dona Ana, informally referred to here as the Apache beds.

Plate 4.3 View of the southeastern flank of Sugarloaf Mound, showing the abundant clinoforms.

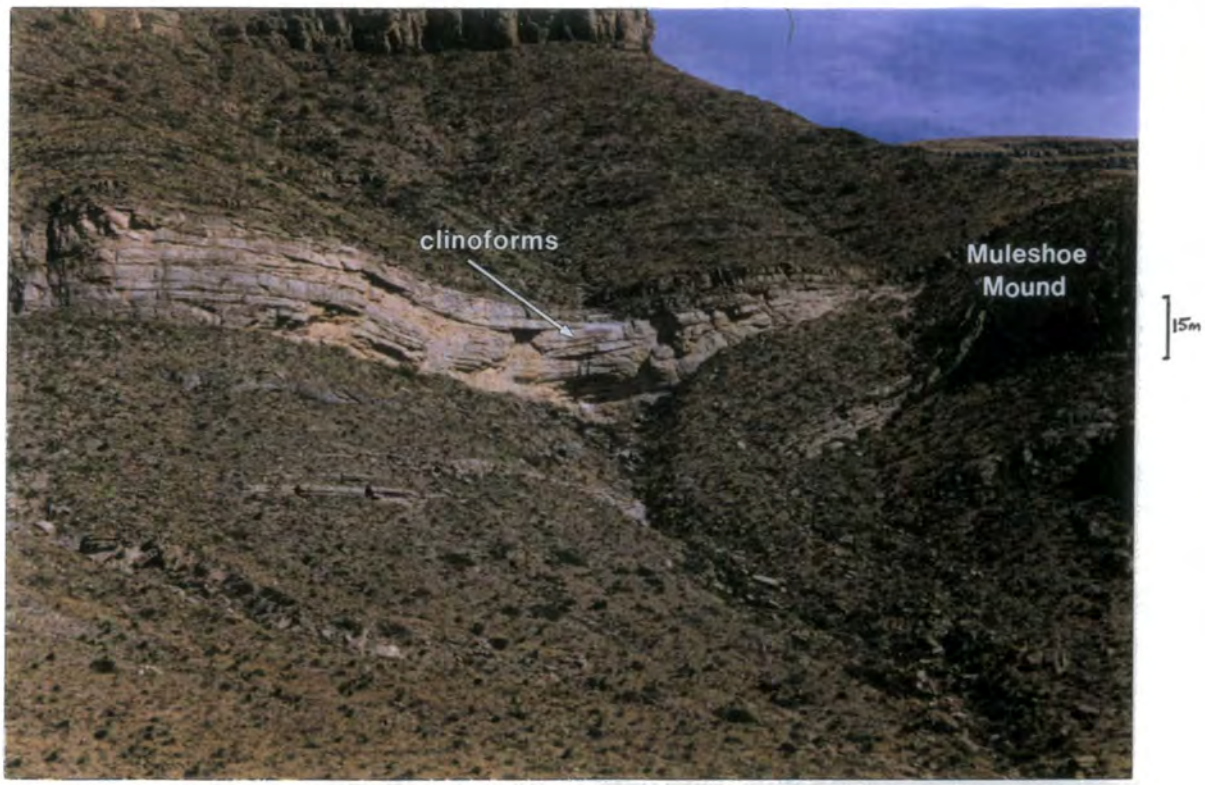

Plate 4.4 Clinoforms in the Dona Ana, exposed on the northern side of Muleshoe Mound.

The Apache beds are found in the topmost section of the Dona Ana, forming a distinctive and prominent pale yellow to white weathering cliff. These beds are composed of coarse-grained and often normally graded, thick-bedded crinoidal sands, with occasional lithoclasts. In the central part of the platform, between Muleshoe and Sugarloaf Mounds, these bioclastic sands form discrete "haloes" around the 'giant' bioherms (e.g. Plate 4.2). However, within Dog Canyon (Fig. 4.1), bioclastic sands of the Apache beds are contained within several spectacularly exposed NW-SE trending, erosionally based channels (Fig. 4.8 and Plate 4.5).

The upper surface of the Dona Ana has long been recognised as a major subaerial exposure surface in the northern part of the platform (Meyers, 1973, 1975, 1989), and also locally across Muleshoe and possibly Sugarloaf Mounds. This surface is a major sequence boundary, and its formation was immediately preceded on the platform by the deposition of the Apache beds. These are interpreted to have been deposited during the 'falling stage' of sea-level, immediately prior to the formation of the sequence boundary at the top of the Lake Valley Formation.

4.4.1.2 The Rancheria Formation.

In the area of interest the basinal Rancheria wedge is composed of two quite different lithofacies; dark, almost black (but light-grey weathering) lime mudstones with interbedded (<<5%) rippled lime-silt packstones and grainstones of the Deadman Member, and brown, well-sorted skeletal and peloidal packstones-grainstones of the Joplin Member. Both members are characterised by exceptional preservation of sedimentary structures which indicate deposition by turbidity and/or density flows below storm wavebase on an anoxic, and mostly abiotic sea-floor (Yurewicz, 1975, 1977).

The Deadman Member represents approximately 90-95% of the Rancheria Formation. It largely filled the palaeoslope basinwards of the Lake Valley wedge, and thins rapidly towards the Lake Valley 'slopebreak' in Deadman Canyon (Yurewicz, 1975, 1977; see Fig. 4.2), and also in Dog Canyon (Hunt & Allsop, 1993). The lime mudstones and intercalated peloidal sands of this lower package are considered by Yurewicz (1975, 1977) to onlap the Lake Valley wedge in Deadman Canyon. However, relationships in Dog Canyon, 3Km to the north, cast some doubt upon this interpretation. In the east of Dog Canyon, the Deadman Member has a parallel bedding relationship with the Apache bioclastic sands which descend relatively steeply (5-10°) basinwards, over the erosionally truncated Lake Valley strata.

Sugarloaf Mound, Southeast Flank.

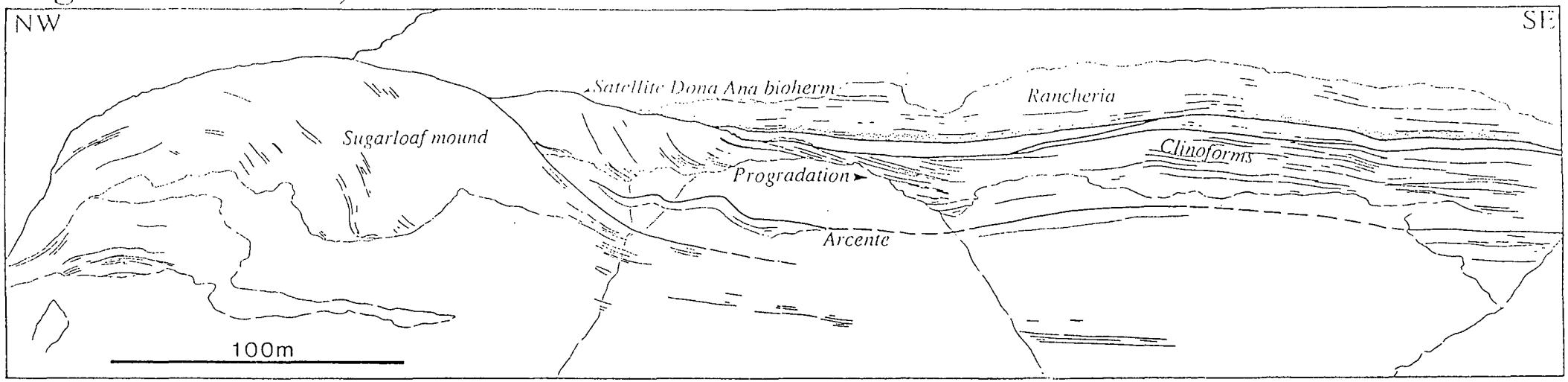

Figure 4.7 Field drawing of the southeastern flank of Sugarloaf Mound. Note the satellite Dona Ana bioherm and the prograding clinoforms (From Hunt & Allsop, 1993).

Dog Canyon, Northern Side.

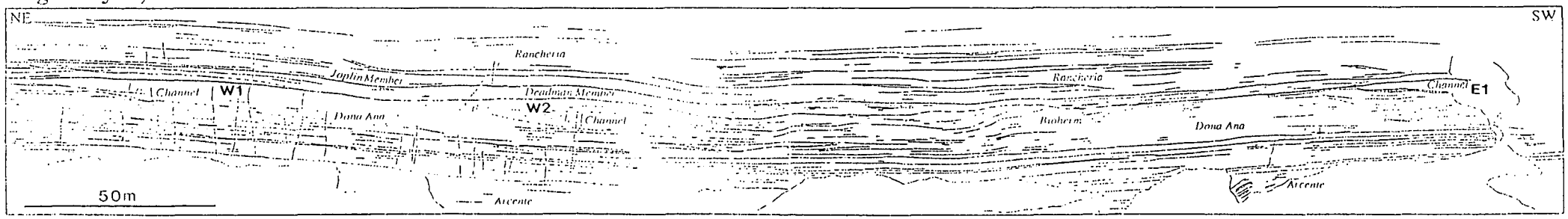

Figure 4.8 Field drawing of the northern flank of Dog Canyon, showing three of the Dona Ana channels (From Hunt & Allsop, 1993).

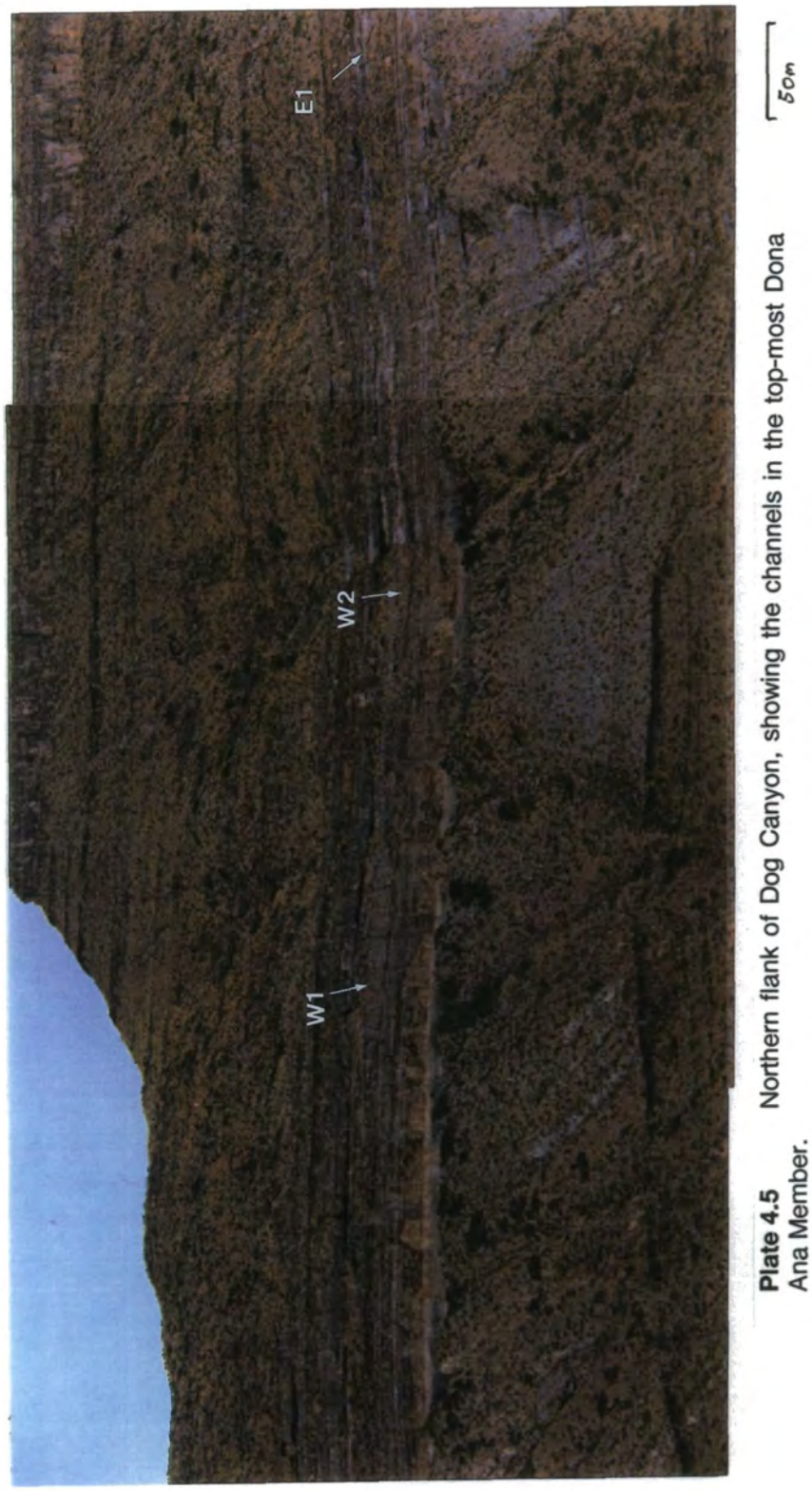

Plate 4.5 Northern flank of Dog Canyon, showing the channels in the top-most Dona Ana Member.

Here, the Deadman Member thickens basinwards across the erosional Lake Valley 'slopebreak' through internal bed thickening and divergence (Hunt & Allsop, 1993).

The upper Joplin Member of the Rancheria Formation gradually thins and fines northwards over the Lake Valley wedge, from 14-16m (46-52ft) in the east of Dog Canyon, to a feather edge between Alamo and Marble Canyons (Figs. 4.1 & 4.2) (Pray, 1961; Meyers, 1973). This may reflect the sedimentary bypass of much of the Lake Valley wedge or, alternatively, a quite different source area for the Rancheria wedge, possibly further to the southwest. The base of the Joplin Member is normally abrupt and is locally erosional. Crinoidal and peloidal grainstones are the dominant microfacies of the Joplin Member. These bioclastic sands also contain occasional ooids and beds with abundant micritized molluscan fragments, the first unequivocally shallow-water grains within the Mississippian succession. The lime sands form beds up to 1.5m (5ft) thick, and are frequently trough cross-bedded, with normally graded tops. They are interpreted to have been deposited by high-density turbidity and/or density currents which bypassed much of the Lake Valley wedge.

4.5 Depositional Model.

This section provides a brief account of the deposition of the Lake Valley and Rancheria Formations, including the 'giant' mounds found within the study area shown on Figure 4.1. This section only aims to give background information to the reader unfamiliar with carbonate systems. A more comprehensive depositional history is provided by Pray (1961), Yurewicz (1975) and Ahr (1989). Further detailed description relevant to the present study is provided in section 4.6, concerning stratal patterns. Figure 4.2 shows a diagrammatic section of the Lake Valley and Rancheria Formation deposits, running north - south along the Sacramento Mountains. This section is based upon conodont faunal units (numbered F.U.1 to F.U.10), and shows where certain units are missing, and, hence the location of the major omission surfaces. This is also illustrated by the schematic chronostratigraphic diagram for Muleshoe Mound, shown in Figure 4.9. Of particular note is the unconformity that exists between the Dona Ana Member and the Rancheria Formation. Here a complete conodont faunal unit is missing (*Apatognathus scalenus-Cavusgnathus*), and this has major implications for compaction modelling around this area, an important point that is considered in the following sections.

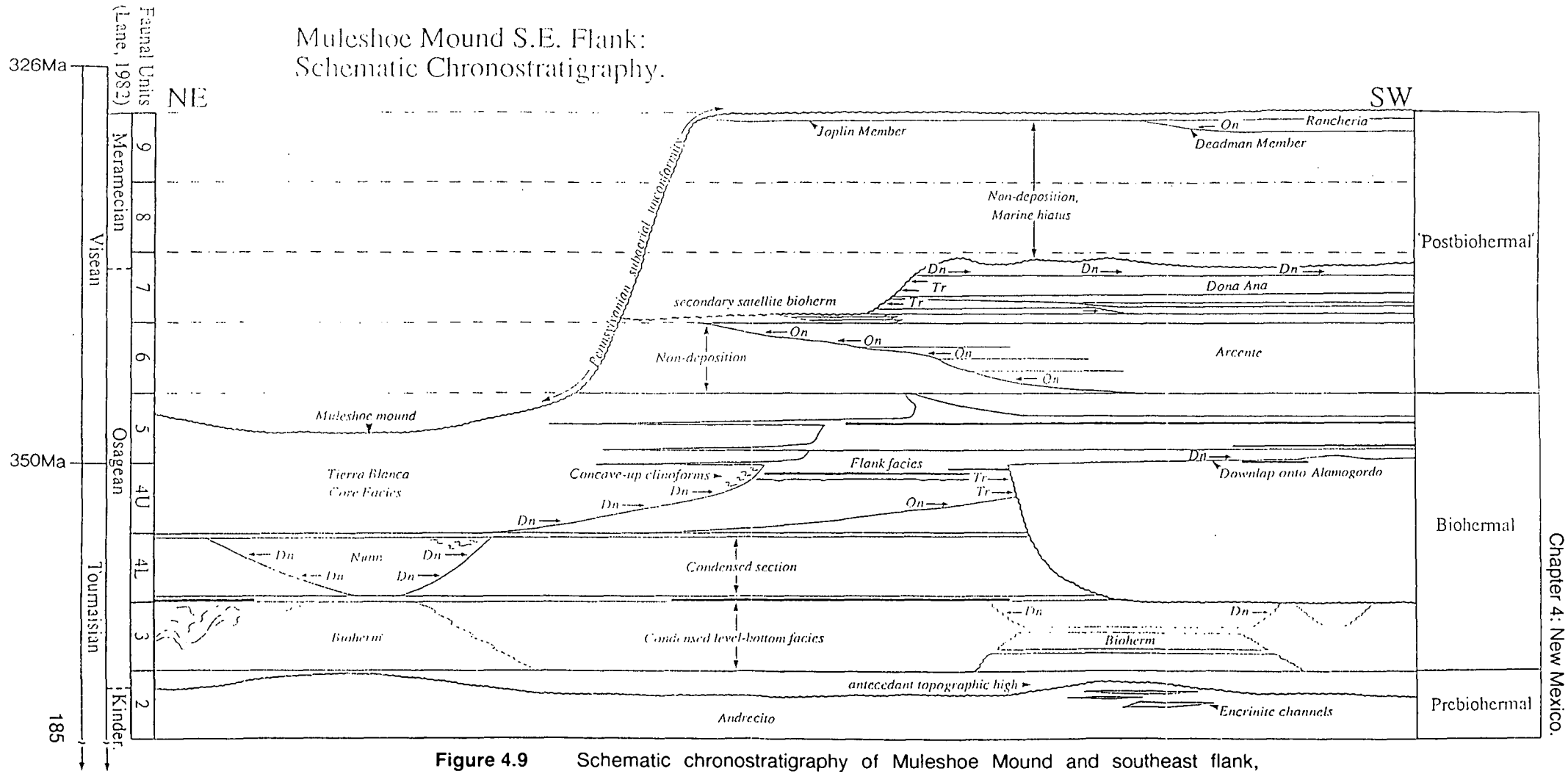

Figure 4.9 Schematic chronostratigraphy of Muleshoe Mound and southeast flank, based upon Figure 4.4 and the faunal units of Lane (1974). The figure emphasises the amplitude of the Mississippian non-depositional and erosional unconformities developed on the flanks of the mound (From Hunt & Allsop, 1993).

Biohermal Formation.

Bowsher (1986) proposed that the Alamogordo bioherms were located upon topographic undulations on the surface of the Andrecito Member, at the base of the Lake Valley Formation. These undulations, he suggested, were created by submarine erosion, producing relief of 3 to 12 metres (10 to 40 feet). The Andrecito can be seen to dip away from the core facies in a radial pattern, suggesting that topography on the Andrecito surface was a possible control upon bioherm positioning and growth, as proposed by Bowsher (1986). Alternatively, it is possible that the Alamogordo mounds founded on calcarenite pods in the underlying Andrecito (e.g. see Ahr, 1989). The control on mound initiation in the Alamogordo is most likely to be a combination of both these processes.

As the bioherms grew, flank debris was shed radially from the buildups as excess material was shed into the surrounding low energy environments. Occasional slope failure along the edges of the mounds also occurred. Within the inter-mound areas, relatively condensed sedimentation of the Alamogordo, Nunn and Tierra Blanca Members occurred to produce the regionally recognised facies associated with these members.

The development/growth of the bioherms themselves is problematical. Mounds in the Sacramento Mountains do not show the classical four growth stages as observed in their European counterparts (Lees & Miller, 1985). Muleshoe Mound, being exceptionally well exposed, provides a conceptual framework for the study of less well-exposed, or subsurface Waulsortian mounds (Kirkby et al., 1993). This is particularly true when considering the other 'giant' bioherms within the Sacramento Mountains, such as Sugarloaf Mound, where the same growth stages as those identified at Muleshoe Mound, outlined below, can also be recognised (Kirkby et al., 1993).

Muleshoe Mound is divisible into four distinct growth stages, each being bounded by unconformities (Kirkby et al., 1993; & in prep.). These are believed to be significant, although the stages that they delineate do not show a systematic change of microfauna as noted from other Waulsortian mounds (e.g. Lees et al., 1985; Lees & Miller, 1985). The stages consist of a start-up phase, a build-up phase, followed by two build-out phases, the first being symmetrical and the second being asymmetrical.

Kirkby et al. (1993) have suggested that regional factors controlled mound geometry and facies, due to the fact that other mounds within the surrounding region (e.g. Sugarloaf Mound) exhibit similar patterns of mound growth and hiatus. They interpret that lower mound developing during open

marine circulation with no terrigenous influx, in relatively deep or quiet water, with episodic higher energy events. The upper mound formed in low to moderate energy, current-influenced water, with at least episodic influx of fine terrigenous clay and silt. The internal phases of the upper mound are interpreted to reflect growth to some accommodation level, progradation, with increasingly asymmetric progradation towards the deeper basin towards the south, as sea-level fell, or water quality declined (Kirkby et al., 1993).

Post-Biohermal Sediment Deposition.

The main phase of mound growth was terminated in Arcente times, possibly due to a change in the water chemistry (possibly becoming dysaerobic) (Meyers, 1975; Kirkby et al., 1993). As discussed (section 4.4.1.1), the Arcente is a thick mud wedge representing a marked reduction in the hydrodynamism. Topography was generally smoothed by the deposition of mudstones, when conditions for bioherm growth were unfavourable. The Arcente facies is characterised by the trace fossil *chondrites.* There is a slight facies variation in the vicinity of the mounds, interpreted to reflect better oxygenated conditions in their immediate vicinity.

With renewed increase in hydrodynamism, skeletal sediments were shed from the mounds, forming the Dona Ana Member. Calcareous siltstones are still present, especially near the base of the unit, but there is an increase in the amount of pack- and grainstones towards the top of the member. Obvious clinoforms can also be seen on the north and south sides of Muleshoe Mound and Sugarloaf Mound within the Dona Ana (Fig. 4.5 and Plate 4.4) where it forms an apron deposit to the mounds themselves. On a regional scale the Dona Ana Member can be seen to thin both to the south and the east, where large bioherms become uncommon. All the evidence suggests that the positive topography of the mounds still remained during this time, and that they acted as point sources of crinoidal debris, with crinoid 'gardens' growing on the relief of the giant antecedent mounds and their flanks.

As stated earlier, the uppermost part of the Dona Ana shows a change in facies forming the Apache beds, which are lithoclastic and generally have an abrupt base. The facies forms an apron deposit to the mounds which still have positive topography at this time. Towards the south in Dog Canyon, the Apache beds form a series of channel and lobe deposits of crinoidal pack- to grainstone (Plate 4.5). In this area there is a major slopebreak, and a marked change in the palaeocurrent directions (Fig. 4.10). The channels are interpreted as representing an area where the sediment is taken into deeper water to the south. After the deposition of the Dona Ana Member, platform

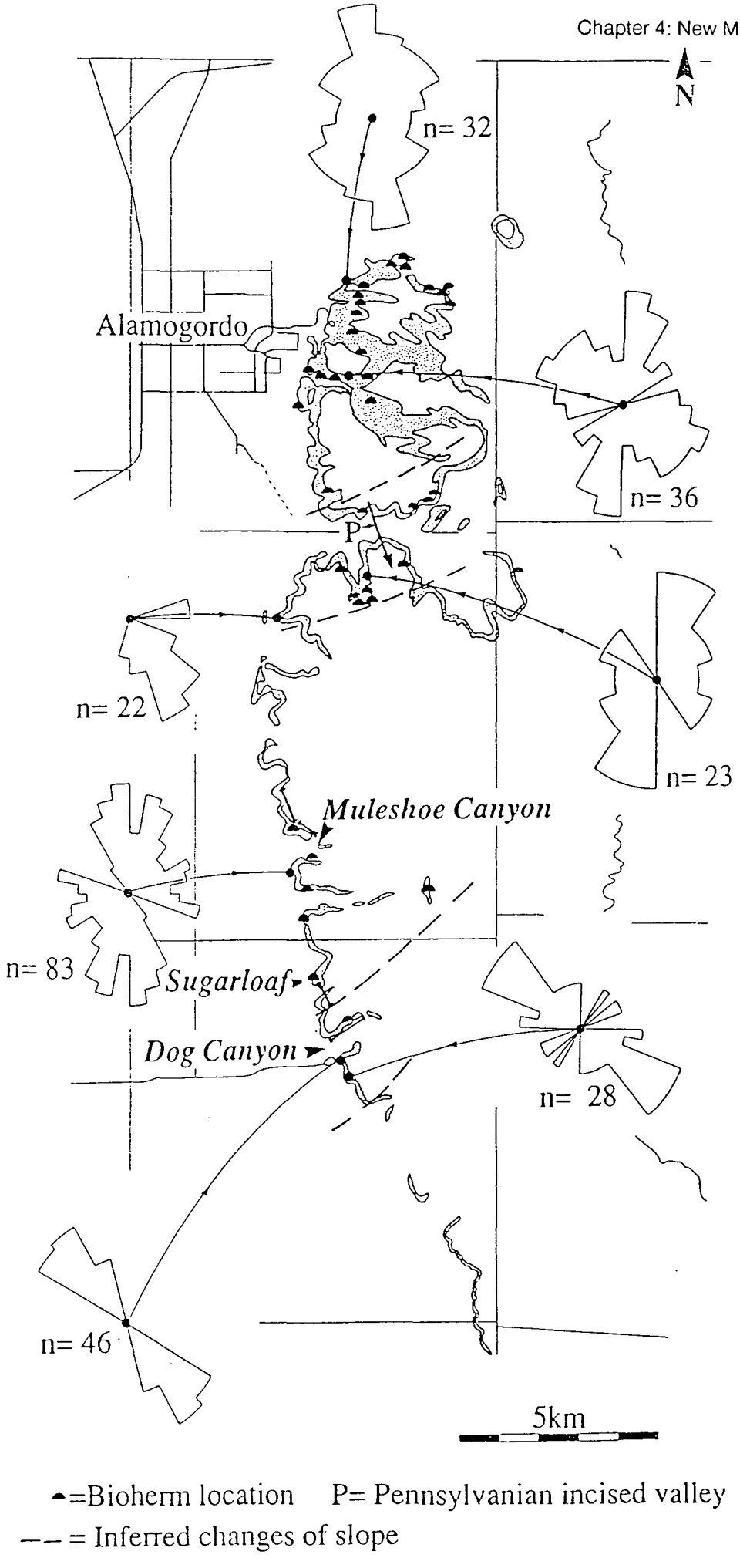

Figure 4.10 Palaeocurrent trends and inferred changes in slope orientation (dotted lines) (From Hunt & Allsop, 1993).

sedimentation is temporarily shut down as the platform was subaerially exposed.

Due to exposure and sedimentary bypass the Deadman Member of the lower Rancheria Formation is deposited as a northward thinning wedge of sediment which onlaps against, and tends to fill, the depositional topography developed by the earlier progradational packages and associated bioherms. Therefore, there is a large time gap in sedimentation which increases towards the north of the area, where the Deadman Member is absent. Evidence for this hiatus is provided by conodont faunal assemblages (Fig. 4.2). The platform is then interpreted to have been rapidly transgressed and drowned, following which relatively deep water sediments of the Rancheria were deposited. Therefore, the Joplin Member forms a second northward thinning wedge across the top of the Deadman Member, and locally forms an angular unconformity with the Dona Ana Member beneath (e.g. the south side of Muleshoe Mound, Fig. 4.6 and Plate 4.6). In particular, three local unconformities are the focus of the present study.

With the depositional setting introduced, section 4.6 discusses the stratal relationships of the study area in greater detail. It is from these relationships that the timing of compaction can be deduced, and because of their importance they are discussed in some depth. Subsequently, section 4.7 discusses the implications of the stratal relationships in terms of compaction.

4.6 Stratal Patterns.

The following sections deal with the stratal relationships between the Waulsortian mounds, the 'postbiohermal' members of the Lake Valley Formation and the Rancheria Formation at Muleshoe and Sugarloaf Mounds. Similar relationships can be viewed on either side of the mounds, however, the southern flanks generally show much better exposure, and therefore particular attention is paid to these areas. Interest is focused on:-

1) sea-floor bathymetry inherited from the main biohermal phase,
2) geometry and stratal patterns of the Arcente and Dona Ana with respect to each other and the mounds,
3) their internal stratal patterns and sedimentology, and
4) the relationships of all these strata to the overlying Rancheria Formation.

Plate 4.6 Unconformity between the Dona Ana and Joplin Members, southeastern side of Muleshoe Mound. Note the pinch-out of these beds across the top of the mound.

A further section deals with the compacted geometry of the channelised Apache bioclastic sands exposed on the northern side of Dog Canyon (Fig. 4.8 and Plate 4.5).

4.6.1 Muleshoe Mound: Southeastern Flank.

Muleshoe Mound initiated within the Alamogordo Member, and built a broad, relatively massive, mud-rich mound which had a depositional relief of 35m (115ft). This start-up phase thinned laterally, and possessed no distinct flank facies (Kirkby et al., 1993). Unconformably overlying the lower mound is a 70m (230ft) thick upper, heterogeneous mound which consists of a further three growth phases: an aggradational phase, a symmetrical progradational phase, and an asymmetric progradational phase (Kirkby et al., 1993) developing an overall depositional relief for the mound of 100-130m (330-430ft). The aggradational phase (stage 2, labelled Nunn in Figs. 4.4 & 4.9) is characterised by the building of a narrow, steep-sided, bell-shaped mound, and is associated with the areal restriction of growth towards the crest of the antecedent Alamogordo mound.

In stages three and four (both progradational), relatively massive facies of the mound core are separated into 5-20m (16-66ft) thick clinothems by thin shale partings, and pass downslope into well-bedded crinoidal packstones of the mound flank (Fig. 4.6 and Plate 4.2). The passage between core and flanking facies is abrupt, and occurs over a few metres, a feature common to other Waulsortian mounds (see Miller, 1986). In the third growth stage, core facies extend down to within a few metres of the adjacent sea-floor. Consequently, flank facies are restricted to the 'toe' of the buildup and volumetrically represent only a minor component of mound growth (<10%). Above the major megabreccia, which marks the boundary between stages three and four, there was a fundamental change in the pattern of mound accretion (Kirkby et al., 1993). In stage four, clinoforms flatten out and shallow upwards as the boundary between core and flank facies climbs in a basinwards direction (i.e. to the south) from the adjacent sea-floor (Fig. 4.6 and Plate 4.2). In this stage, crinoidal flank facies represent up to 40% of mound growth, and form a distinctive 'tail' on the southern side of Muleshoe Mound.

Relationships between the core and flank facies of the mound have been rotated by differential compaction. Differential compaction of flank strata was contemporaneous with bioherm development (Kirkby et al., 1993) and also post-dated it. Geopetal fabrics on the southern side of the mound indicate

that stage four flanking strata have typically been steepened by some 8-10° (localities 5 & 9, Fig. 4.11). Unconformities localised above earlier bioherms, and the thinning of strata above megabreccia clasts within flanking strata to stages three and four, marked as A and B respectively on Figure 4.11, indicate that most of this differential compaction and rotation of flank strata was early and syn-depositional.

Stratigraphic and textural studies of both Muleshoe and Sugarloaf Mounds led Pray (1965) to conclude that they were subject to intense syn-depositional marine cementation. His view, controversial at the time, has been supported by the subsequent diagenetic studies of Meyers (1973, 1975), Meyers et al. (1982) and Shinn et al. (1983). They confirmed that the abundant (up to 90%) cloudy radiaxial cements, specific to the mound cores, were syn-sedimentary and precipitated from normal marine waters. Importantly, these and other cements impaired compaction of the mounds, as compared to the adjacent strata (Shinn et al., 1983).

Arcente.

In Muleshoe Canyon (Fig. 4.1), the thickness of the Arcente is antithetic to that of Muleshoe Mound, being thickest furthest from the mound and pinching-out against it. Although dominated by mudstones, the Arcente is far from a homogenous package, and is separated in two by the Hackberry beds (Figs. 4.6 & 4.12, and Plate 4.2). For example, 400m (1300ft) southeast of Muleshoe Mound (Fig. 4.12), the Hackberry beds, 9.2m (30ft) thick, are positioned 13.9m (46ft) above the top of the Tierra Blanca, and 17.7m (58ft) below the base of the Dona Ana. Here, the Arcente becomes increasingly calcareous from a limestone-shale ratio of 1:8 at its base, to a ratio of 10-20:1 within the Hackberry beds. The limestone-shale ratio then gradually decreases over the next 12m (39ft) above the Hackberry beds (i.e. the Arrow beds) where a value of 1:0.7-1.2 is typical, compared to an average ratio of 1:4 in its upper 5.7m (19ft) (Fig. 4.12). Such lithological changes will have exerted a strong control upon fluid migration pathways within the Arcente.

Northwards towards Muleshoe Mound, the Hackberry beds steepen progressively from a sub-horizontal attitude to dip up to 30° off-mound (Fig. 4.11 and Plate 4.2). These beds diverge and fan away from Muleshoe Mound (Fig. 4.11) as the lower package thins by onlap against the palaeobathymetry of the mound. There is also a change of bedding style and facies in the uppermost exposures of the Hackberry beds (locations 41 to 47, Fig. 4.11 and Plate 4.2). Here beds are lensoid and nodular, with scoop-shaped bases

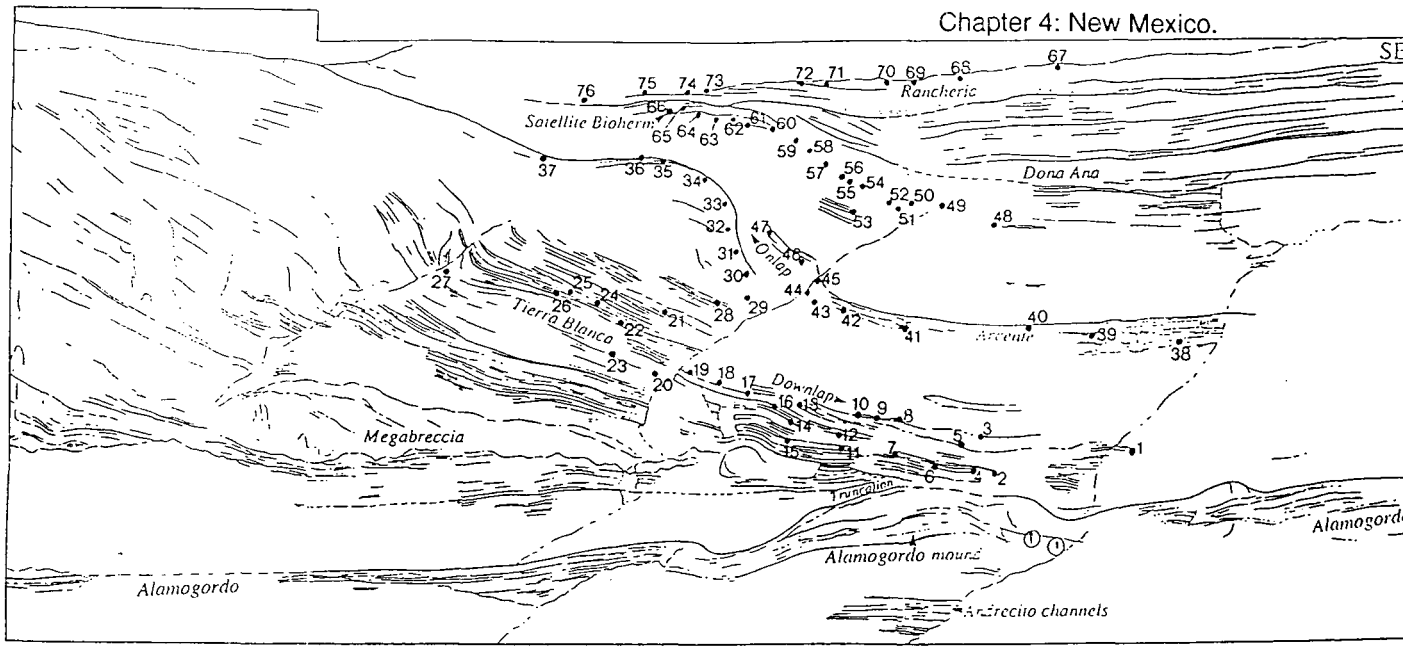

MULESHOE MOUND, Southeast Flank

Locality Number.	1	2	3	4	5	6	7	8	9	10	11	12	13	14	15	16	17
Stratigraphic Level.	T. Blanca	T. Blanca	T. Blanca	T. Blanca	T. Blanca	T. Blanca	T. Blanca	T. Blanca	T. Blanca	T. Blanca	T. Blanca	T. Blanca	T. Blanca	T. Blanca	T. Blanca	T. Blanca	T. Blanca
Bedding Orientation.		336/18NE	016/08E	001/17E	176/14E	360/21E	308/07NE 315/11NE	042/11SE	041/14SE 010/19E	033/15SE	019/15E	353/12E	027/22E	018/23E	357/13E	027/20E	359/11E
Geopetals	4 > 134				6 > 200 11 > 140 86 > 135 54 > 307 8 > 095 9 > 330 12 > 325 6 > 128 7 > 110 1 > 300 4 > 135				6 > 120 15 > 285 24 > 121 14 > 157								

Locality Number.	18	19	20	21	22	23	24	25	26	27	28	29	30	31	32	33	34
Stratigraphic Level.	T. Blanca	T. Blanca	T. Blanca	T. Blanca	T. Blanca	T. Blanca	T. Blanca	T. Blanca	T. Blanca	T. Blanca	T. Blanca	T. Blanca	Arcente	Arcente	Arcente	Arcente	Arcente
Bedding Orientation.	001/12E	358/24E	025/18E	352/19E	348/20NE	016/20E	359/28E	021/21E		350/38E	337/22NE	018/20E	020/35E	011/35E	007/47	357/43E	333/26NE
Geopetals								20 > 088	19 > 059		22 > 053						

Crinoid Orient's
342
10
19
353
15
21
23
26
21
20
23

Locality Number.	35	36	37	38	39	40	41	42	43	44	45	46	47	48	49	50	51
Stratigraphic Level.	Arcente	Arcente	Arcente	Arcente	Arcente	Arcente	Arcente	Arcente	Arcente	Arcente	Arcente	Arcente	Arcente	Dona A.	Dona A.	Dona A.	Dona A.
Bedding Orientation.	305/15NE	175/02W	018/25E		046/07SE	019/07E	028/10E	001/03E	316/18NE	005/25E	025/27E	010/28E	354/30E	141/09E		186/13E	
Geopetals				5 > 006 0 > 079 0 > 049				14 > 119 19 > 082 07 > 112	15 > 088	25 > 135		33 > 092 14 > 130	13 > 125	05 > 110 05 > 106 06 > 100	08 > 144 04 > 085 00 > 102	06 > 140	07 > 148 16 > 116

Locality Number.	52	53	54	55	56	57	58	59	60	61	62	63	64	65	66	67	68
Stratigraphic Level.	Dona A.	Dona A.	Dona A.	Dona A.	Dona A.	Dona A.	Dona A.	Dona A.	D. A. Bio.	D. A. Bio.	D. A. Bio.	D. A. Bio.	D. A. Bio.	D. A. Bio.	D. A. Bio.	Joplin	Joplin
Bedding Orientation.	014/08E 008/19E	344/28NE	200/19E	322/30NE	322/34NE		323/26NE	179/28E	168/31E	179/32E	154/39NE		123/11N			126/10SW	253/02S
Geopetals	15 > 144		13 > 127 09 > 118 11 > 134	29 > 102 15 > 119 27 > 102 14 > 141 16 > 106 16 > 109 12 > 109 19 > 108 14 > 106	21 > 094 34 > 090 40 > 096	27 > 094 05 > 116 06 > 112 13 > 129	21 > 103 22 > 355	21 > 110	18 > 082 28 > 052 28 > 069	11 > 096 07 > 086	04 > 098 01 > 064 04 > 271	05 > 272 00 > 091 01 > 289 09 > 230 08 > 059 02 > 294	11 > 250 16 > 258	10 > 273	09 > 247 18 > 220		

Locality Number.	69	70	71	72	73	74	75	76
Stratigraphic Level.	Joplin	Joplin	Joplin	Joplin	Joplin	Joplin	Joplin	Joplin
Bedding Orientation.	280/05S	027/07SE	332/13NE	296/12NE	188/05E	080/04S	106/06NE	140/05NE

Figure 4.11 Summary diagram of bedding orientation and geopetal data collected from the southeastern flank of Muleshoe Mound.

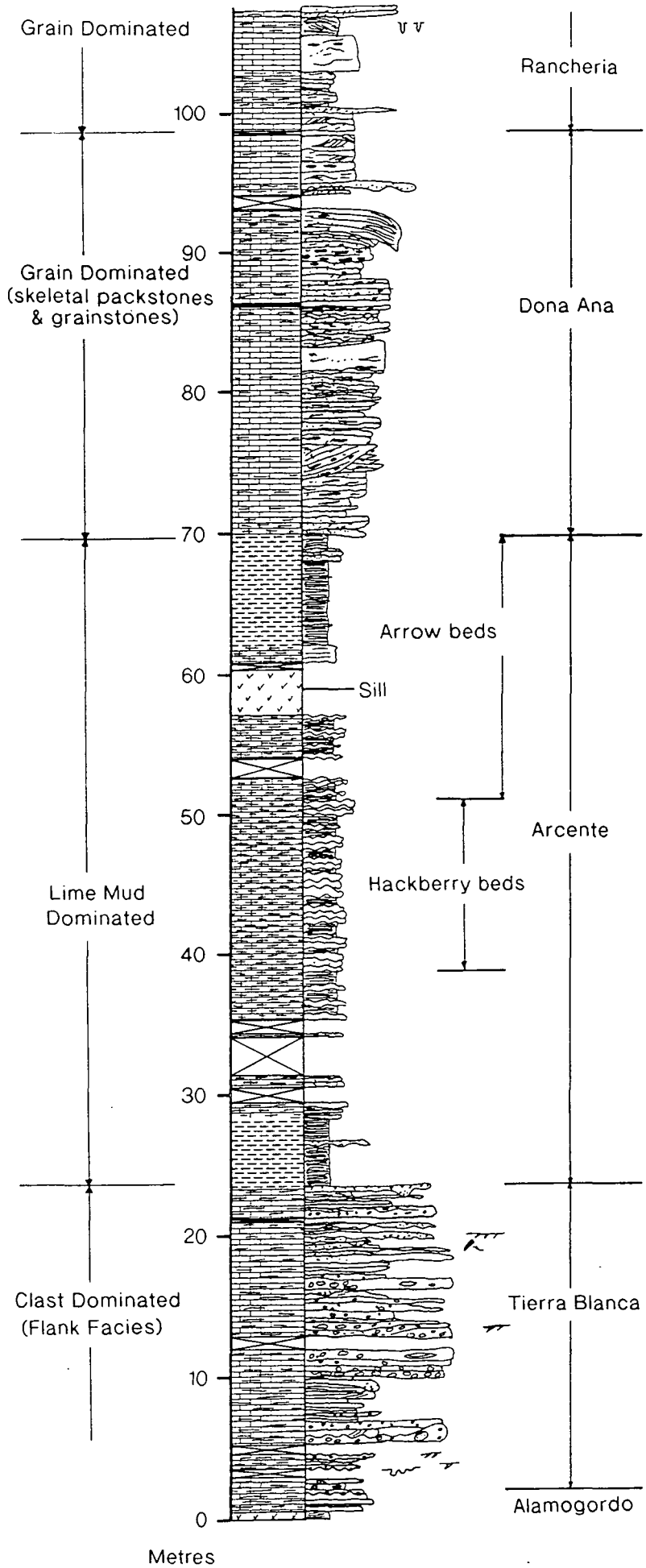

Figure 4.12 Graphic log of the Mississippian strata exposed on the southeastern flank of Muleshoe Mound.

0.3-0.4m (1ft) deep developed over horizontal distances of 1-2m (3.3-6.6ft). Lime mudstones still predominate, but are interbedded with 20-50mm thick encrinite calciturbidites (<10% volumetrically), derived from the bioherm. The top surfaces of these beds are also frequently marked by a 2-3mm thick hash of fenestellid bryozoans, indicating that more oxygenated conditions prevailed in the immediate proximity of the mound.

The external geometry of the uppermost package of the Arcente (the Arrow beds, Fig. 4.6 and Plate 4.2) can be ascertained by comparing the top of the Hackberry beds with the base of the Dona Ana (e.g. Fig. 4.13). These boundaries are near-parallel where the Hackberry beds are sub-horizontal, but become closer as beds steepen towards Muleshoe Mound, defining a northwards tapering wedge on its southeast flank. Unfortunately, the internal stratigraphic relationships of this wedge are difficult to ascertain due to the paucity of its exposure. The base of the Dona Ana does not appear to be erosional on the southern side of the mound, implying that the wedge-shaped geometry of the Arrow beds is depositional, and results from its internal thinning. Two possibilities exist to explain this geometry; either 1) the Arrow beds lap-out against the Hackberry beds and the mound, or 2) they diverge and fan-out from the upper slope. The latter scenario appears to be the most likely as there is no facies change or evidence for a break in sedimentation above the Hackberry beds, factors which would favour onlap of the Arrow beds onto the Hackberry beds.

Dona Ana.

The Dona Ana has a wedge shape on the southern flank of Muleshoe Mound which is synthetic to that of the underlying Arcente; it thins towards the main bioherm (Figs. 4.6 & 4.13, and Plate 4.2). This wedge shape is a reflection of depositional thinning, but more importantly, post-depositional erosional truncation of the Dona Ana, intimately related to differential compaction of the underlying Arcente wedge.

On the southern flank of Muleshoe Mound, the Dona Ana can be separated into four stratal packages (Hunt & Allsop, 1994). The first of these is characterised by the re-establishment of bioherm development on the uppermost flanks of the main mound (Fig. 4.11 and Plate 4.2). This demonstrates that the depositional relief developed during Tierra Blanca times was not entirely filled by the Arcente. The first lens-shaped package of the Dona Ana is generally recessively weathered, and thins both towards, and away from the main mound (Fig. 4.11 and Plate 4.2).

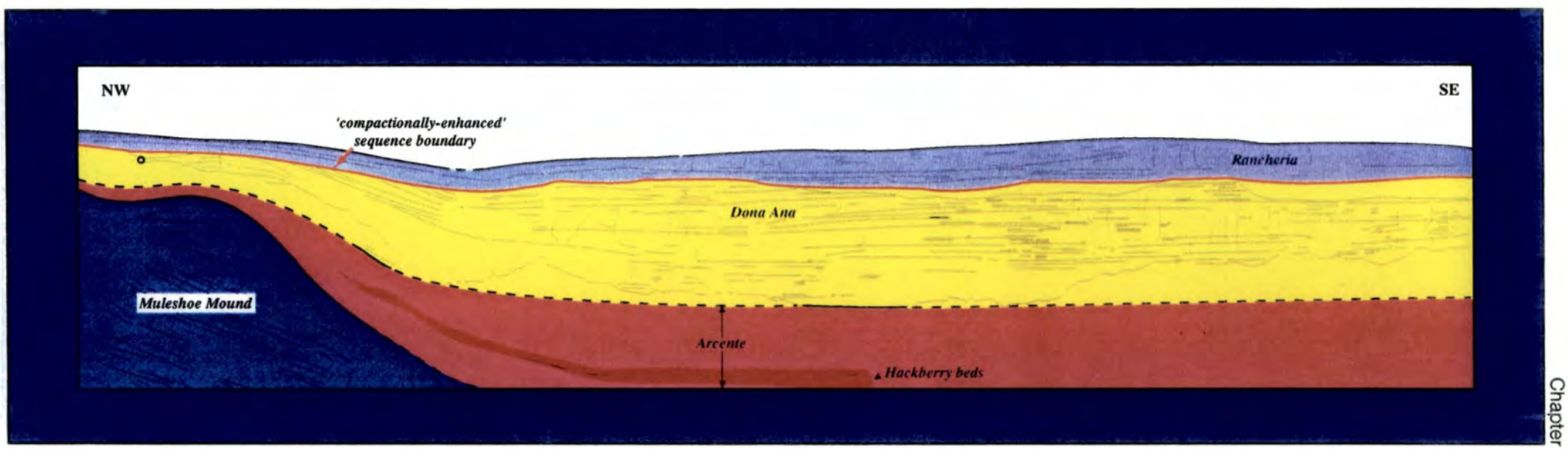

Figure 4.13 Detailed field drawing of the southeastern flank of Muleshoe Mound, illustrating the relationships between the Arcente, Dona Ana and Rancheria (person circled for scale). Note the parallel stratal relationship between the Dona Ana and the Arcente, and the deformation of both into an anticlinal structure, prior to erosion and deposition of the Rancheria.

Foreslope and overlying strata to the bioherm of this package are dominated by lensoid bedded crinoidal wackestones and packstones, which contain abundant geopetal structures. Geopetal fills within this level are progressively rotated, and generally steepen towards Muleshoe Mound (Fig. 4.11), thus allowing the separation of depositional and post-depositional dips. The geopetals are crucial to the reconstruction of the sea-floor bathymetry at the beginning of Dona Ana times. The relationships of the geopetals to bedding have allowed a restoration of strata, indicating that these strata had depositional dips of 3-6° (subsequently steepened up to 30°, Fig. 4.11). This depositional dip explains their thinning to 2m (6.6ft) some 400m (1300ft) further to the southeast (Fig. 4.12).

The second stratal package which forms the main cliff section is much lighter and comprises up to 70% of the Dona Ana on the southeastern flank of Muleshoe Mound (Figs. 4.11 & 4.13, and Plate 4.2). It is dominated by crinoidal packstones and grainstones, and sharply overlies the first package of the Dona Ana, into which it is often erosive and channelised. Strata within the base of this package thin and lap out towards the mound (Fig. 4.13), which reflects the filling of depositional topography inherited from the first package of the Dona Ana. Erosional scours at the base of the bedded sands within this package define broad channel-like bodies. In contrast, the third package of the Dona Ana is characterised by clinoforms of mudstones and wackestones (Fig. 4.5 and Plate 4.4), often silicified and interbedded with crinoidal packstones and grainstones (Fig. 4.12). These strata are sharply overlain by the Apache beds, the uppermost package of the Dona Ana.

All four stratal packages of the Dona Ana steepen considerably as Muleshoe Mound is approached, paralleling relationships seen in the underlying Arcente (Figs, 4.11 & 4.13, and Plate 4.2). Furthermore, these four packages are all truncated and overlain with angular unconformity by the Rancheria Formation adjacent to Muleshoe Mound.

Rancheria.

In Muleshoe Canyon the Joplin Member of the Rancheria Formation rests on progressively older strata as Muleshoe Mound is approached, and eventually laps-out onto the Tierra Blanca of the mound. In contrast to the underlying Lake Valley strata, the Rancheria remains relatively flat-lying adjacent to the mound (Figs. 4.6 & 4.13, and Plate 4.2), implying that the erosion, and most of the rotation of the Arcente and Dona Ana preceded its deposition.

In the southeastern end of Muleshoe Canyon the Joplin Member normally rests abruptly onto the Deadman Member of the Rancheria (up to 3m (10ft) thick, Fig. 4.12). However, within 200m (660ft) of the mound it rests either on the Deadman Member or one of the upper two packages of the Dona Ana. This reflects the erosional, scoop-shaped base of this member near to the mound. Within the Joplin Member, bioclastic sands are often channelised, with well developed lateral accretion surfaces (Fig. 4.13). The Joplin Member is mostly thickly bedded, with some internal trough cross-stratification, although channel-like scours with high width to depth ratios are also developed (Hunt & Allsop, 1993) (Fig. 4.13).

4.6.2 Sugarloaf Mound: Southeastern Flank.

Sugarloaf Mound, 3.2Km south of Muleshoe Mound (Fig. 4.1) is the most basinward 'giant' bioherm on the platform. Its unique palaeogeographic position, facing the open ocean, makes for several important differences with the southern flank of Muleshoe Mound. These allow for contrasts to be drawn concerning the compaction of the Arcente wedge.

Alamogordo - Tierra Blanca.

The growth history of Sugarloaf Mound appears to be similar to that of Muleshoe Mound, and can also be subdivided into four growth packages (Hunt & Allsop, 1994). The differences in the growth patterns of the two mounds and the overlying strata reflect the different palaeogeographic position of the two mounds on the platform, plus the difference in the 'cut' of the present day exposure.

The mound 'starts-up' in the Alamogordo and subsequently builds up and out in three distinct stages of the Tierra Blanca. The most obvious contrast between the southern flanks of Sugarloaf and Muleshoe Mounds is the more symmetrical nature of the fourth growth stage (contrast Fig. 4.11 & 4.14). Sugarloaf Mound lacks the spectacular development and basinward progradation of bioclastic flank facies, with the associated climbing progradation of core facies. The transition from core to flank facies is reflected in the upper surface of Sugarloaf Mound which changes downslope from being convex to concave-up at this boundary.

Arcente.

The Arcente section has an overall wedge shape which thins by onlap against the antecedent palaeobathymetry of Sugarloaf Mound. The Arcente is

Sugarloaf Mound, Southeast Flank.

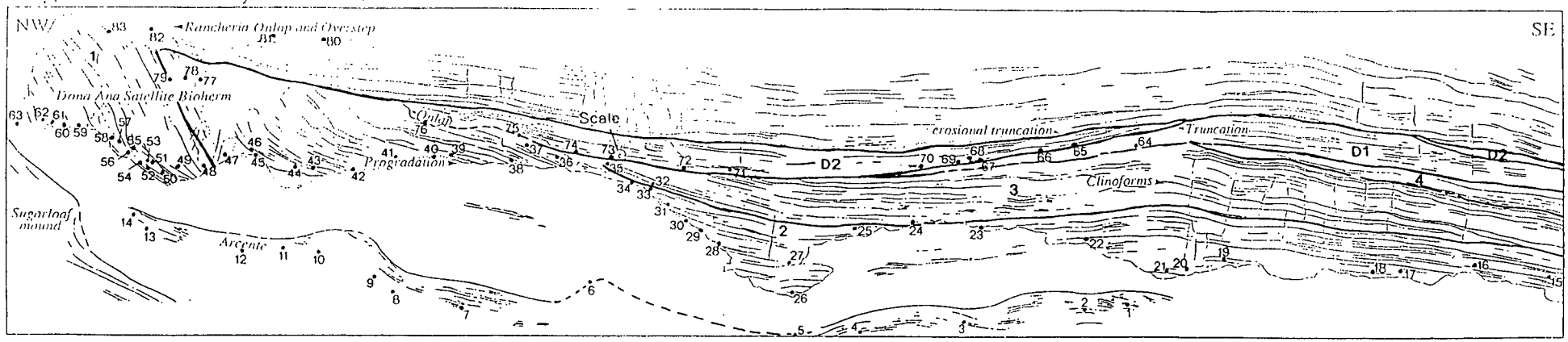

SUGARLOAF MOUND, Southeast Flank

Locality Number.	1	2	3	4	5	6	7	8	9	10	11	12	13	14	15	16	17	18	19	20	21	22	23	24	25	26	27	28
Stratigraphic Level.	Arcente	Arcente	Arcente	Arcente	Arcente	Arcente	Arcente	Arcente	Arcente	Arcente	Arcente	Arcente	Arcente	Arcente	Dona A.	Dona A.	Dona A.	Dona A.	Dona A.	Dona A.	Dona A.	Dona A.	Dona A.	Dona A.	Dona A.	Dona A.	Dona A.	Dona A.
Bedding Orientation.	178/28E	217/14SE	180/35E	271/27N	286/12N	171/30W	200/04E	191/16E	240/40SE	183/52E	183/16E	251/26SE	208/22SE	196/60E	311/09	305/01	290/14	290/06	329/10	335/06	007/07 310/08	335/06	255/05	327/11	333/12	239/05NW	272/01S	295/11

Geopetals

29	30	31	32	33	34	35	36	37	38	39	40	41	42	43	44	45	46	47	48	49	50	51	52	53	54	55	56	57	58
Dona A.	Dona A.	Dona A.	Dona A.	Dona A.	Dona A.	Dona A.	Dona A.	Dona A.	Dona A.	Dona A.	Dona A.	Dona A.	Dona A.	Dona A.	Dona A.	Dona A.	Dona A.	D. A. Bio.	D. A. Bio.	D. A. Bio.	D. A. Bio.	D. A. Bio.	D. A. Bio.	D. A. Bio.	D. A. Bio.	D. A. Bio.	D. A. Bio.	D. A. Bio.	D. A. Bio.
323/13 005/23	341/23	345/20	021/24	011/15	025/20	005/26	021/23	024/16	010/11	009/19	011/21	001/10	350/40	014/26	005/36	069/36	069/36	055/56	034/30SE	032/28SE	019/42SE	005/42E	019/43SE	003/50SE	033/40SE	071/52SE	022/64SE	033/65SE	

63 > 180

59	60	61	62	63	64	65	66	67	68	69	70	71	72	73	74	75	76	77	78	79	80	81	82	83
D. A. Bio.	D. A. Bio.	D. A. Bio.	D. A. Bio.	D. A. Bio.	Dead 1	D1 - D2	D1 - D2	D1 - D2	Dead 2	D1 - D2	Dead 2	Dead 2	Dead 2	Dead 2	Dead 2	Dead 2	Dead 2	D. A. Bio.	D. A. Bio.	D. A. Bio.	Joplin	Joplin	Joplin	Joplin
	023/68SE	031/68SE	033/66SE	020/58E	319/05	281/12	247/10	292/14	267/07	285/10	237/05	314/04	335/05	341/08	342/08	032/11	069/10				030/08SE	020/19SE	025/28E	

68 > 180 | 41 > 180 | 47 > 180 | 38 > 180 | 38 > 040

Figure 4.14 Summary diagram of bedding orientation and geopetal data collected from the southeastern flank of Sugarloaf Mound.

considerably thinner on the southern side of Sugarloaf Mound due to the much reduced thickness of its uppermost package, the Arrow beds (<2m (6.6ft), see Fig. 4.14, and Plates 4.3 & 4.7). The thickness of the Arrow beds appears to reflect the palaeo-oceanographic setting of the southern side of Sugarloaf Mound. It seems that Sugarloaf Mound acted either as a sediment 'dam' behind which the Arrow beds accumulated, or as a 'breakwater' which dampened northwards directed currents generated in the open ocean to the south (i.e. storm currents). In this latter scenario the Arrow beds accumulated in the calmer lee of the mound.

Although deformed, the upper surface of the Arcente, which in this region approximates to the top of the Hackberry beds, gradually steepens towards Sugarloaf Mound (Fig. 4.14 and Plate 4.3). The Hackberry beds define a series of asymmetric, southerly verging folds which decrease in amplitude off-mound, towards the south. Internal deformation and flow within the underlying Arcente mudstones and shales is interpreted to have accommodated this deformation. The important point to note is that this deformation is **not** reflected in the overlying Dona Ana foreslope strata (Fig. 4.14 and Plate 4.3), thus suggesting that the deformation of the Arcente **preceded** the deposition of the Dona Ana sediments.

Dona Ana.

The Dona Ana exposed on the southern flank of Sugarloaf Mound is divisible into four stratal packages, and rests with local angular unconformity on the deformed Hackberry beds of the Arcente, marked on Figure 4.14. Each stratal package is bounded by surfaces of non-deposition and/or erosion, and is positioned further basinward of the antecedent Sugarloaf Mound than its precursor (Figs. 4.14 & 4.15, and Plates 4.3 & 4.7).

The Dona Ana is marked by the spectacular basinwards progradation of a 'secondary' bioherm from the mid-upper flanks of Sugarloaf Mound (Figs. 4.14 & 4.15, and Plate 4.3) (Hunt & Allsop, 1993). This bioherm forms the first stratal package of the Dona Ana, and also part of the second stratal package, with the division of the 'secondary' bioherm possible on the basis of progradational geometry (Fig. 4.14, and Plate 4.3). These stratal packages are interpreted to be separated by a non-depositional hiatus. The first stratal package is characterised by the apparent sub-horizontal to descending clinoform progradation of core facies over their flanking strata. Within the core facies, clinoforms dip at up to 80°, and are slightly convex-up, but become concave-up as they flatten out and rapidly pass into flank strata (Fig.

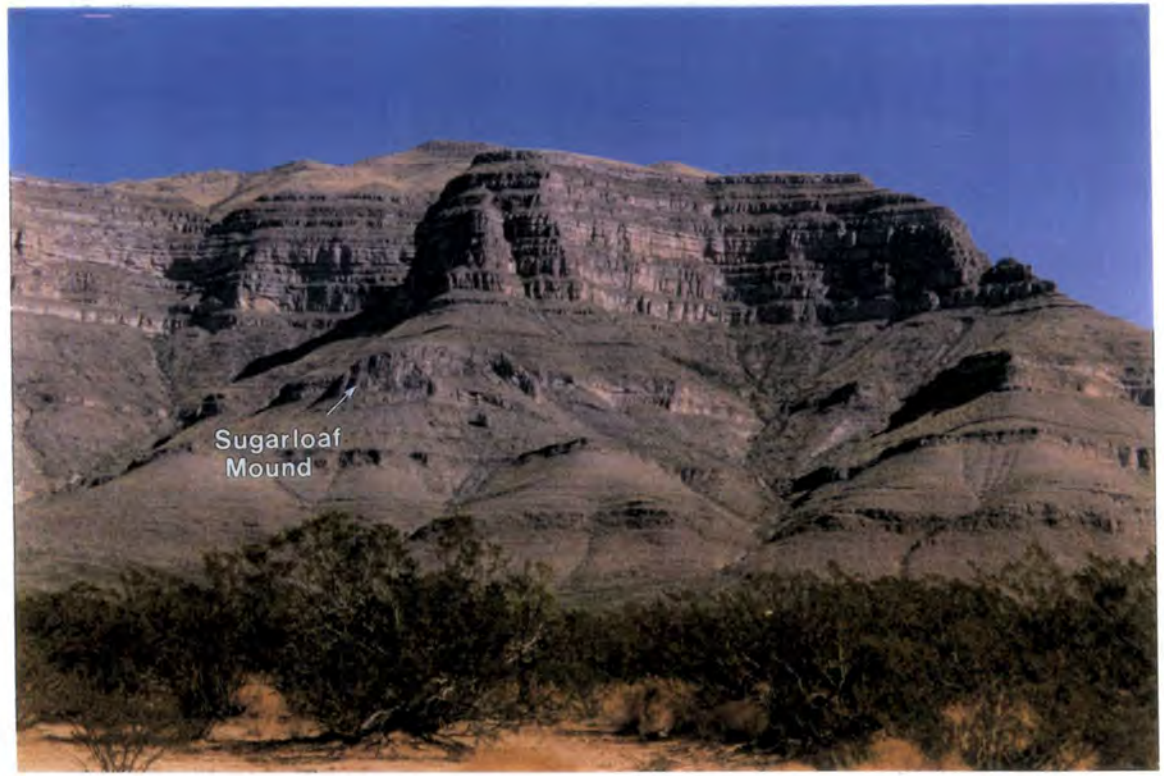

Plate 4.7 General view of Sugarloaf Mound.

Sugarloaf Mound, Southeast Flank.

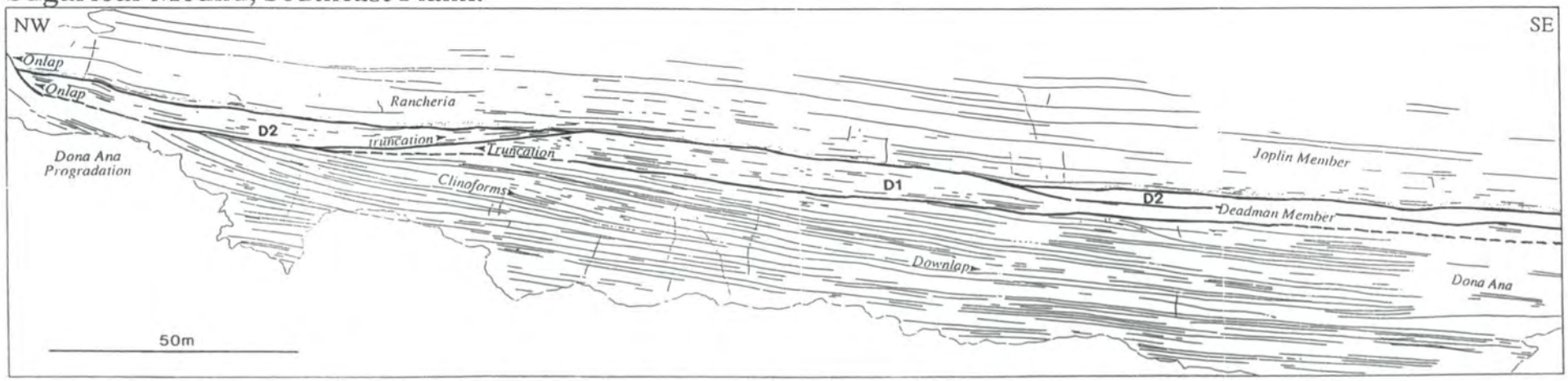

Figure 4.15 Detailed field drawing of the southeastern flank of Sugarloaf Mound (From Hunt & Allsop, 1993).

4.14 and Plate 4.3). Flanking strata are only a minor component of this first stage of the bioherms growth (<10%), and these thicken and fan-out downslope from the toe of the core facies, suggesting upper slope bypass. Across this first stage of the bioherm's growth, geopetal structures shallow from 65-76° in the oldest core facies to 38-40° in the youngest (Fig. 4.14). These geopetal fabrics show that the bioherm rotated clockwise as it grew.

The second stratal package of the Dona Ana records the continued growth of the 'secondary' bioherm, and is characterised by the basinwards progradation of core facies over their flanking strata. In this package clinoforms are concave-up and progressively flatten-out individually from core into flanking facies, and they also collectively thin towards the south (Fig. 4.14 and Plate 4.3). The change of the bioherm's progradational geometry reflects the more significant development of flanking facies in this second biohermal stratal package, and is similar to the geometric change seen between stages three and four of the Tierra Blanca at Muleshoe Mound (e.g. compare Figs. 4.11 & 4.14, and Plates 4.2 & 4.3). Foreslope strata of this second biohermal package fill the sea-floor topography of the deformed Hackberry beds. At the toe-of-slope, foreslope strata are strongly lithoclastic and grain-supported. This is believed to reflect continued upper slope bypass, and the 'plucking' of core-type mudstone nodules from the core - flank transition by crinoidal gravity-flows derived off Sugarloaf Mound.

Downlapping of the third Dona Ana stratal package onto its precursor represents the demise of the 'secondary' bioherm, and followed the deposition of a major toe-of-slope unit that marks the boundary between the second and third packages (e.g. Fig. 4.14 and Plate 4.3). In this third package, clinoforms downlap asymptotically onto the adjacent sea-floor, where their base climbs slightly in a basinwards direction (Fig. 4.14 and Plate 4.3). Here, the boundary between the second and third stratal packages (and termination of the 'secondary' bioherm) is recorded by the change from lithoclastic packstones and grainstones to mud-supported depositional fabrics. This change reflects the change from a bypass to an accretionary foreslope, and is probably due to shallowing of the slope and a change in the pattern and/or the type of grain production after the death of the bioherm (Hunt & Allsop, 1994).

The fourth stratal package of the Dona Ana is formed by the Apache beds. These strata are exposed as a southwards thickening wedge around the antecedent Sugarloaf Mound, and are dominated by lithoclastic crinoidal grainstones. These bioclastic sands are interpreted to have bypassed across

and eroded clinoform topsets and the front of the 'secondary' bioherm, along with the topsets to clinoforms of the third Dona Ana stratal package. The distribution of the Apache beds reflects erosion and sedimentary bypass adjacent to Sugarloaf Mound, not post-depositional erosional truncation (as at Muleshoe, see section 4.6.1).

Rancheria.

The Rancheria Formation comprises both the Deadman and Joplin Members, and these onlap and overstep the antecedent topography of the 'secondary' Dona Ana bioherm and Sugarloaf Mound. The base of the Deadman Member rests on a thin (0.1-0.3m (0.3-1ft)) sub-horizontal bed of the Apache bioclastic sands, and does not rest with angular unconformity on to the eroded clinoforms of the Dona Ana as it first appears (e.g. Figs. 4.14 & 4.15, and Plates 4.3 & 4.7). Deadman Member sediments attain a maximum thickness of 5.5m (18ft), and are divisible into two stratal packages separated by an erosional unconformity (D1 and D2, Fig. 4.15 and Plate 4.8) (Hunt & Allsop, 1993). The lower D1 package has a parallel relationship with the underlying Apache beds, and is cut-out by a scoop-shaped erosional unconformity towards the north. This erosion surface locally exhumed the Dona Ana, and is marked by a thin black chert horizon (10-25mm thick) developed in the top of the D1 Deadman package and the Dona Ana. By analogy to other surfaces, this silicification suggests that a significant non-depositional hiatus separates the D1 and D2 stratal packages.

The upper D2 stratal package of the Deadman Member fills the saucer-shaped depression eroded into D1 (Figs. 4.14 & 4.15, and Plate 4.8). Its lens-shape reflects both depositional thinning, where it laps-out northwards against the exhumed and eroded foreslope of the 'secondary' Dona Ana bioherm (Fig. 4.14 and Plate 4.3), and post-depositional erosional truncation. For example, towards the south, the D2 stratal package drapes the erosional palaeobathymetry of D1 (Fig. 4.14 and Plates 4.3 & 4.8). These draping strata are subsequently planed-off to a sub-horizontal surface on which the overlying Joplin Member lies, developing a local angular unconformity. Towards Sugarloaf Mound, the 'secondary' Dona Ana bioherm and the Joplin Member are separated by an erosive angular unconformity. This angular unconformity reflects the steep original depositional dips of core facies in the second Dona Ana stratal package, which were exposed through erosion of their topsets. In contrast, the dips of core facies in the first Dona Ana

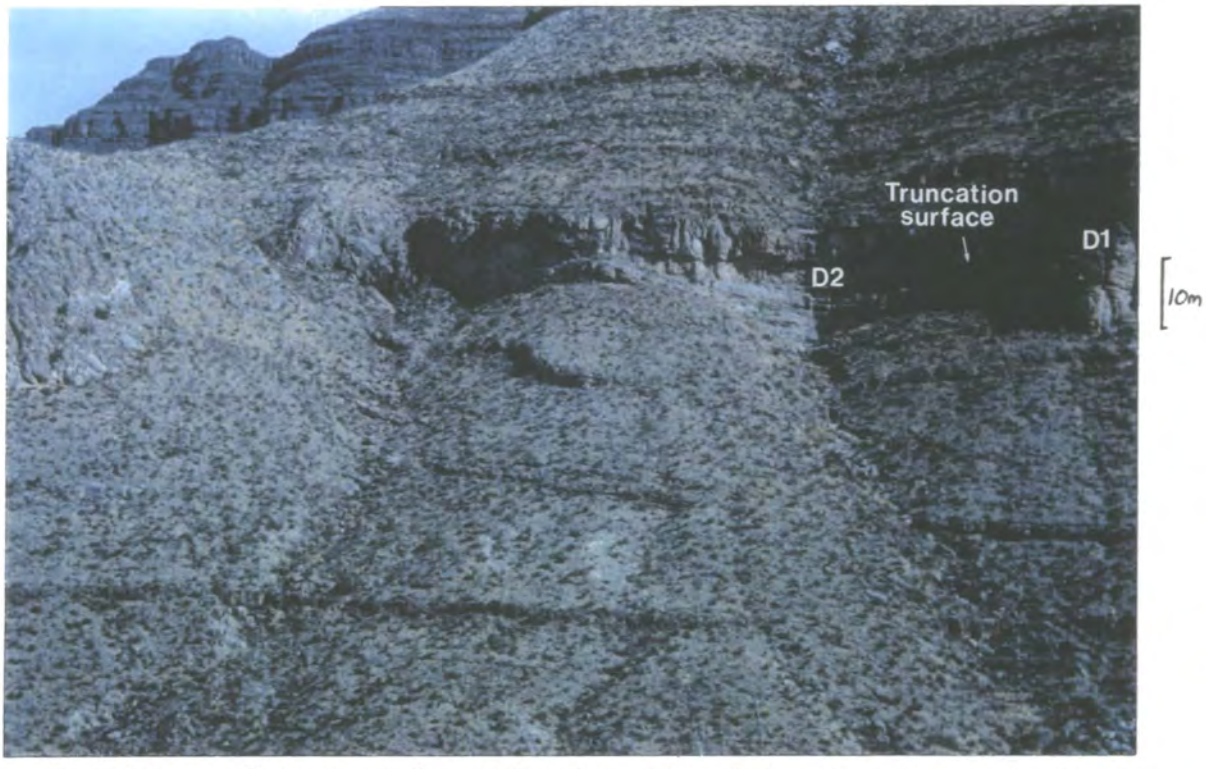

Plate 4.8 Close-up of the southeastern flank of Sugarloaf Mound, showing the truncation surface between the D1 and D2 sequences of the Deadman Member.

Plate 4.9 Close-up of the stratal relationships around the Dona Ana channel, W1, exposed on the northern flank of Dog Canyon.

biohermal stratal package are not depositional, and were rotated during deposition (see earlier Dona Ana section).

4.6.3 Dog Canyon.

The Lake Valley and Rancheria Formations crop-out in imposing cliff exposures within Dog Canyon (Fig. 4.1). In its final few kilometres this canyon cuts a south-westerly course through the Sacramento Mountains and affords two spectacular north-easterly trending strike sections (0.5km apart) through the Lake Valley platform (Fig. 4.8 and Plate 4.5). To the south, cliffs along the western escarpment of the Sacramento Mountains between Dog and Deadman Canyons expose a comparable dip section (Fig. 4.1).

Arcente - Dona Ana.

The rocks of the Arcente and Dona Ana Formations both form easterly thinning wedges in Dog Canyon, and are separated by a depositional hiatus. The base of the Dona Ana is abrupt, and mostly has a parallel relationship with the Arrow beds (<3m (10ft) thick). Several thick gravity flow deposits typically form the basal 3-5m (10-16.5ft) of the Dona Ana, both debrites and lithoclastic high-density turbidites. These redeposited beds locally erosionally truncate and also onlap anticlinal structures developed within the Arrow and Hackberry beds (Fig. 4.8 and Plate 4.5). The anticlines clearly formed positive features on the sea-floor. As on the southern flank of Sugarloaf Mound, the Arcente was deformed either prior to, or during the deposition of the Dona Ana.

On the northern side of Dog Canyon (e.g. Fig. 4.8) packages at the base and top of the Dona Ana frequently have only a limited lateral continuity, resulting in a complex stratigraphy. In contrast, its middle portion is characterised by several light-weathering redeposited beds which can be traced continuously over 1.5km (e.g. Fig. 4.8 and Plate 4.5). These are overlain by a mudstone-dominated level of similar, or greater continuity, which contains in situ Tabulate corals with a well-preserved delicate branching morphology. These corals suggest calm and clear-water conditions, whilst glauconitic grains and abundant silicification points towards low rates of deposition. This coralline level is overlain by the Apache beds, which here comprise up to 50% of the Dona Ana, and are significantly thicker than at Sugarloaf Mound, 1.1km to the north-west (e.g. compare Figs. 4.8 & 4.14, and Plates 4.5 & 4.3).

In strike section along the northern side of Dog Canyon, the Apache beds have the external geometry of a lens, with a tail extending towards the east. To the west they pinch-out against the mid-upper slope of the Dona Ana wedge, across which they are interpreted to have bypassed. The central part of the lens of the Apache beds is shown in Figure 4.8 (Plate 4.5). Here, two levels of bioclastic sands are distinguished, the lower of which has a sheet-form and is overlain by orange-weathering mudstones and wackestones. In the upper level, bioclastic sands are contained within several conspicuous light-weathering channels (Fig. 4.16). These are up to 15m (49ft) thick, 75m (246ft) wide (Figs. 4.8 & 4.16, and Plate 4.9), and contain elongate crinoidal stems with a strong preferred NW-SE trend, which helps constrain the orientation of the channels (Fig. 4.17).

At least one of these Dona Ana channels (E1, Fig. 4.8 and Plate 4.5) has well-developed lateral accretion surfaces, where channelised crinoidal grainstones pass laterally over a constraining raised-lip into levee facies. These levees are dominated by bryozoan-rich wackestones, and downlap onto older strata (Fig. 4.8). A particularly salient feature of the channels is their external geometry, which is lens-shaped in cross-section (e.g. Figs 4.8 & 4.16, and Plates 4.5 & 4.9). These channels have a concave-up base and convex-up top. The geometry of their lower surface is largely depositional, and reflects their scoop-shaped erosive base, and the aggradation and lateral accretion of their fill. In contrast, their convex-up top is thought to be a post-depositional geometry, developed through differential compaction between channel axis and interchannel facies (see section 4.7.3).

On the southern cliff section of Dog Canyon the channels of the Apache beds appear to have coalesced, with a less well-defined interchannel area between two thicker channel sections. It appears possible that the channels fed a lobate fan/apron deposit to the south, and the exposures of the southern cliffs are an intermediate stage, as the channels began to loose their individual identity.

Rancheria.

Exposures of the Rancheria Formation are of great importance within Dog Canyon, with respect to differential compaction. However, there is a pronounced variation in the style of compaction-related deformation of the Rancheria on the northern and southern sides of the canyon, and they will therefore be described in separate sub-sections.

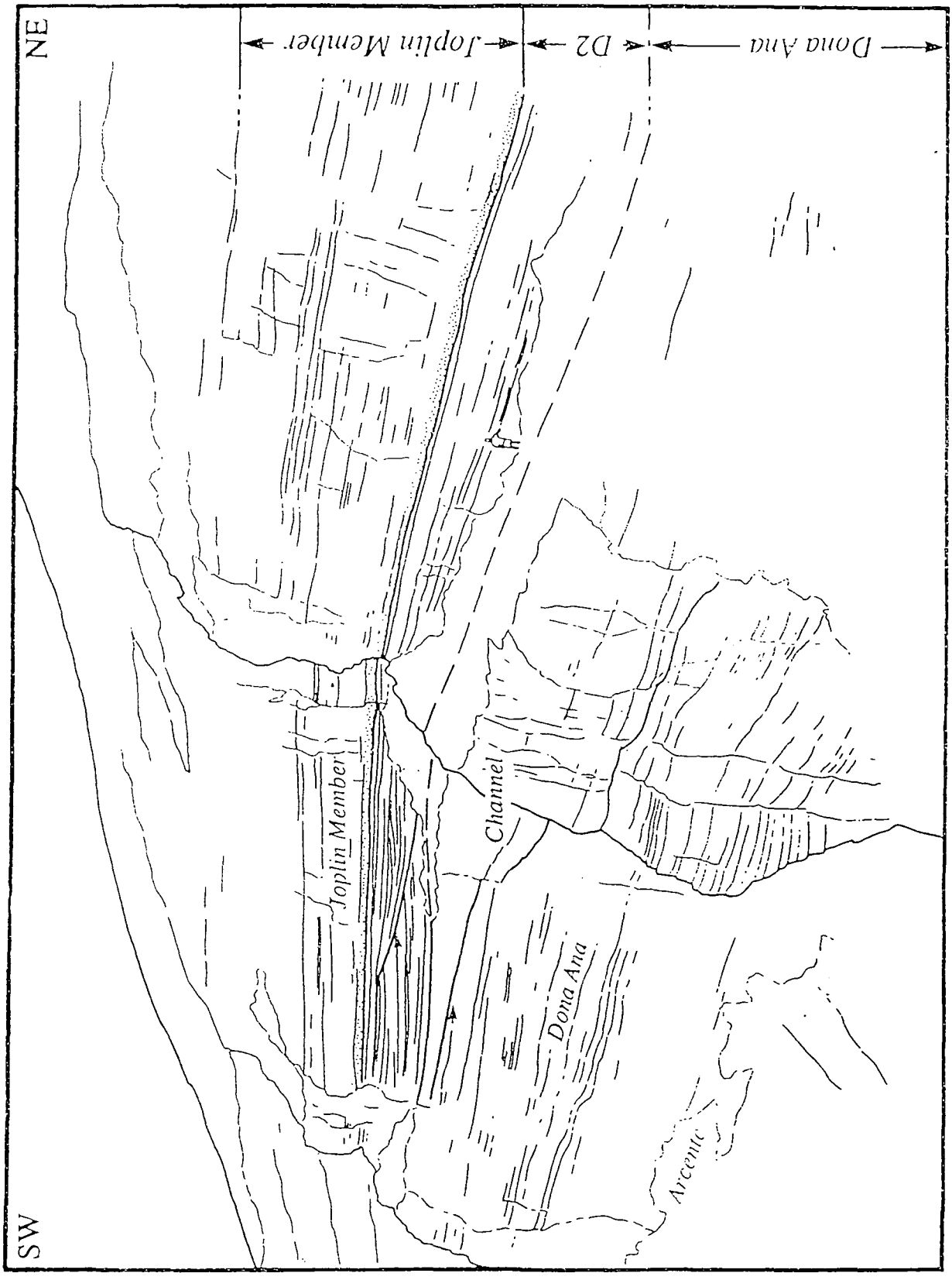

Figure 4.16 Oblique view of the main Dona Ana channel (W1). Note unconformities on the western flank, featured in Figure 4.18 (From Hunt & Allson, 1993).

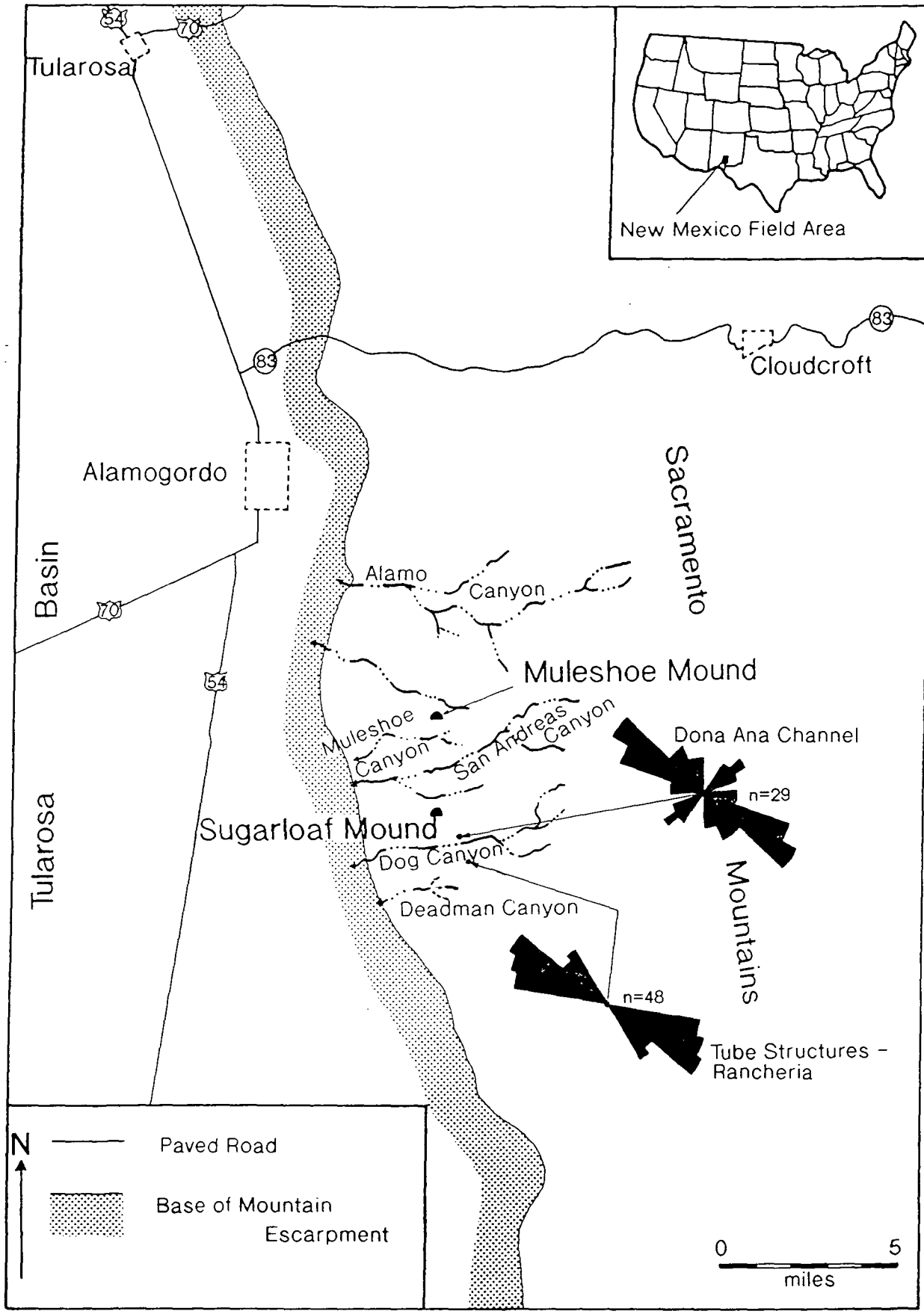

Figure 4.17 Palaeocurrent data collected from the Dona Ana channels, exposed on the northern side of Dog Canyon, and the 'tube' structures, exposed on the southern side of the canyon. Note the close relationship between both sets of data.

Northern Cliffs of Dog Canyon.

The Rancheria is composed of the Deadman and Joplin Members, and these both thicken towards the east in Dog Canyon. The Deadman Member generally has a parallel relationship with the top of the Dona Ana, except above pre-existing channels (and their erosionally truncated levees) at the top of the Apache beds (e.g. Fig. 4.8 and Plate 4.5). Gentle anticlinal structures developed in the Rancheria section are centred over the antecedent Dona Ana channels. These anticlines decrease in amplitude through the Deadman Member into the Joplin Member (Figs. 4.8 & 4.16, and Plate 4.5). On close inspection, the Deadman Member consists of three stratal packages that are locally separated by erosional unconformities. These stratal packages are called D1, D2 and D3 from oldest to youngest. There appears to be an association between the development of the unconformities within the Deadman Member, the anticlinal structures within the Rancheria and the antecedent channels of the Dona Ana (e.g. Fig. 4.8 and Plate 4.5). This possibly reflects the differential compaction of the Apache beds during both deposition and subsequent burial of the Rancheria, and are discussed and modelled in more detail in section 4.7.3.

Strata in the lower package of the Deadman Member (D1) have a concordant relationship with the convex-up top surface of the Dona Ana channels (Figs. 4.8 & 4.16, and Plate 4.9). Concentrating on the W1 channel (Fig. 4.16 and Plate 4.9), and specifically its western flank, the D1 stratal package dips west and is divided in two by a prominent level of dark-weathering peloidal grainstones. Their base is erosive and cuts-out several mudstone beds towards the axis of the underlying W1 channel (Fig. 4.18 and Plate 4.10). In turn, these peloidal sands are onlapped eastwards by basinal mudstones, which form the upper unit of the D1 stratal package (Figs. 4.16 & 4.18, and Plates 4.9 & 4.10). The D1 package is here locally separated from D2 strata by a scoop-shaped erosional unconformity, similar to the feature seen at the same stratigraphic level on the southeast flank of Sugarloaf Mound (compare Figs. 4.15 & 4.16, and Plates 4.8 & 4.10). An erosion surface truncates the D1 stratal package 20m (66ft) east of the W1 channel axis, and extends to the eastern margin of the W2 channel (Fig. 4.8, and Plate 4.5). The D1 strata were completely eroded from above the W1 and W2 channels, whose upper surface was exhumed and silicified. This silicification also extends up the D1 erosional unconformity, and marks the top surface of the D1 stratal package in the adjacent parallel bedded strata (Fig. 4.8). It also suggests that there was a depositional hiatus after the erosion of the D1

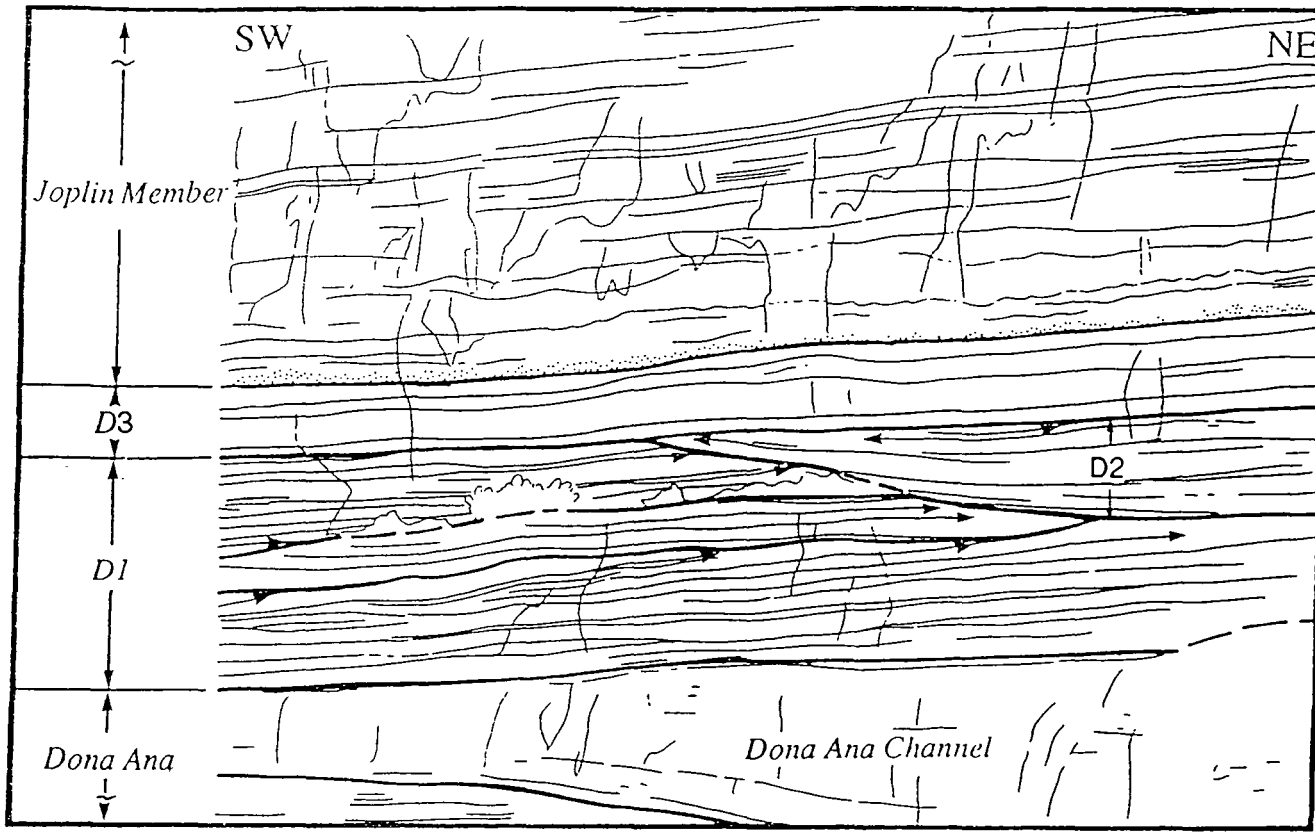

Figure 4.18 Detail of unconformities developed within the Deadman Member, over the Dona Ana channel flank. Note the book (~300mm long) for scale in the bottom diagram (From Hunt & Allsop, 1993).

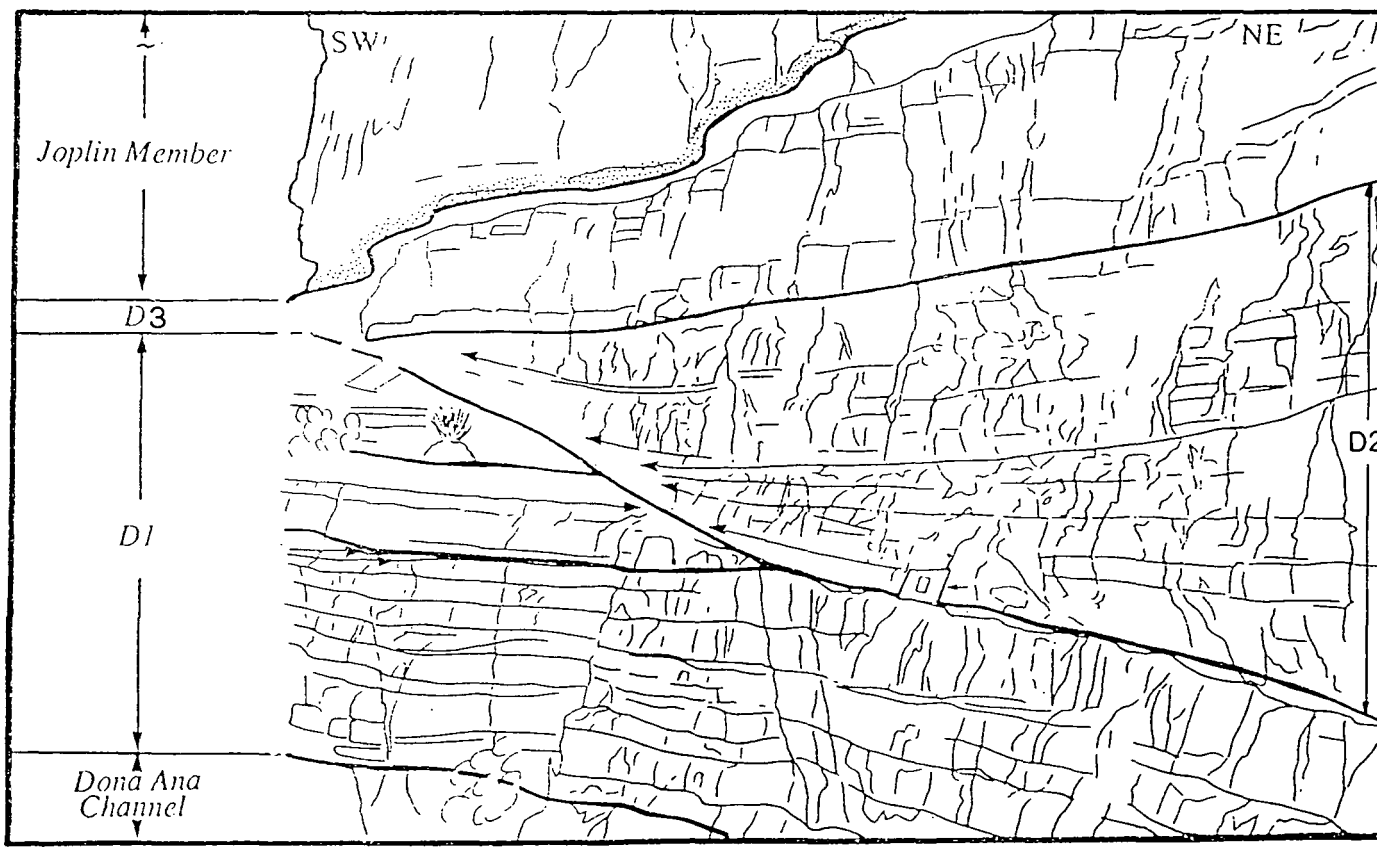

Plate 4.10 Close-up of the stratal relationships of the Deadman Member above the Dona Ana channel, W1, exposed on the northern flank of Dog Canyon.

stratal package. The selective erosion of this D1 package, combined with the internal stratal relationships seen above the pre-existing W1 and W2 channels is believed to indicate that the Dona Ana had begun to compact differentially (See section 4.7.3).

Strata of the D2 package onlap and drape the erosional topography of the D1 stratal package over the western end of the W1 channel and the eastern wing of the W2 Dona Ana channel (Figs. 4.8 & 4.18, and Plate 4.10). The D2 stratal package is dominated by dark lime-mudstones, but is locally coarser within the depressions cut into the D1 stratal unit above the W1 and W2 channels. Here, lime mudstones are interbedded with 30-40mm thick, normally-graded, current-rippled, dark bioclastic and peloidal sands, up to very coarse sand grade, and whose bases are frequently loaded. These sands were funnelled into the 'channel-like' structures cut into the D1 package.

Like D1, D2 strata are also deformed into anticlinal structures centred over the axis of the pre-existing Dona Ana channels. Further to this, individual beds within the D2 stratal package thin as they are traced over the earlier W1 channel, suggesting early, syn-depositional differential compaction and subsidence over the W1 and W2 channels. The presence of syn-sedimentary boudinage (Plate 4.11) within units of the D2 package also support the view that the underlying Dona Ana channels were compacting differentially during their deposition.

An angular unconformity locally separates the D2 and D3 stratal packages over the western and eastern margins of the antecedent W1 and W2 Dona Ana channels. This lies directly above the D1-D2 erosional unconformity (Figs. 4.8, 4.16 & 4.18, and Plates 4.9 & 4.10). Elsewhere, the D2 stratal package has a parallel relationship with the third, and strongly lithoclastic stratal package of the Deadman Member (D3), which is typically 0.5-1m (1.6-3.3ft) thick (Fig. 4.8).

The Joplin Member has a sharp, parallel basal contact with the D3 stratal package of the underlying Deadman Member (Fig. 4.8 and Plate 4.5).

Southern Cliffs of Dog Canyon.

In contrast to the near-parallel contact between the Joplin Member and the Deadman Member on the northern side of Dog Canyon (Fig. 4.8), the contact above the channels on the southern side of the canyon has an unusual erosional relief. The western escarpment to the Sacramento Mountains exposes the continuation of relationships exposed on the south

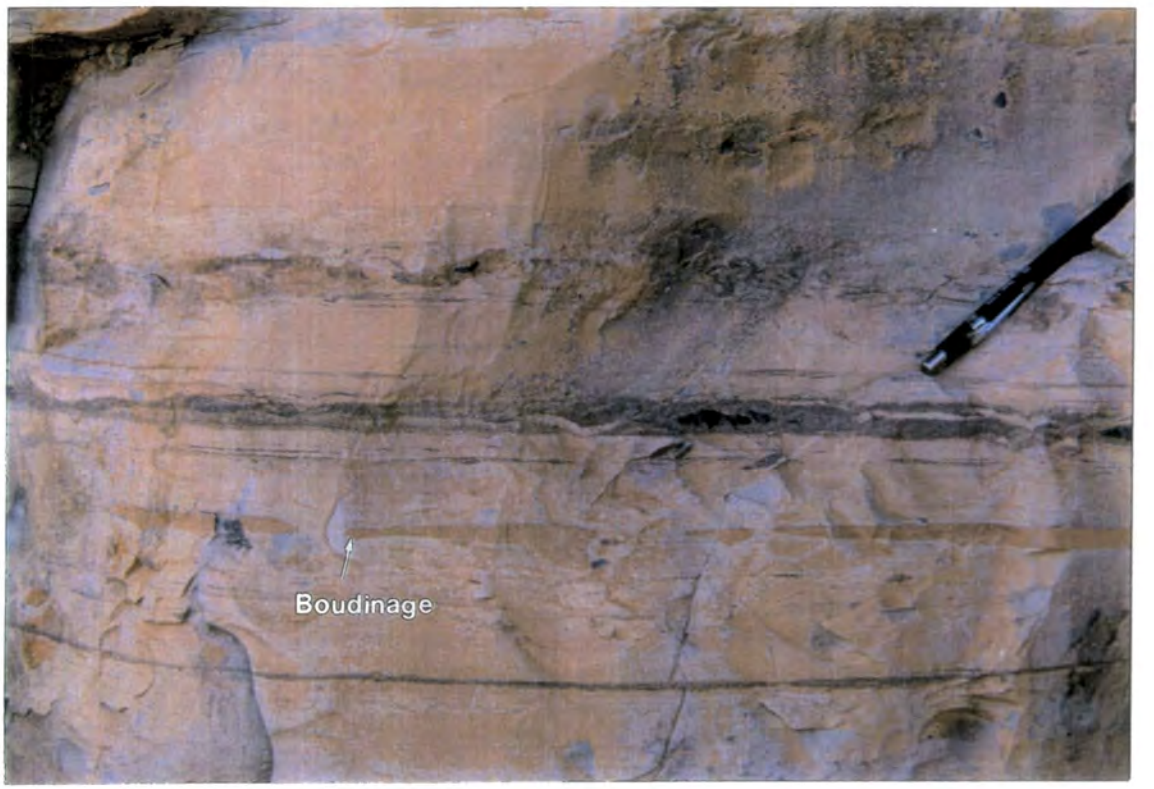

Plate 4.11 Syn-sedimentary boudinage within the Deadman Member, exposed immediately above, and across the top of the Dona Ana channel, W!, northern flank of Dog Canyon.

Plate 4.12 Irregular contact between the Deadman and Joplin Members, southern flank of Dog Canyon. Photograph is looking up to the base of the Joplin Member.

side of Dog Canyon. Here, the contact between the Deadman and Joplin Members is irregular and unusual, with 'tube-like' structures cut into the Deadman Member, and filled by bioclastic and peloidal sands of the Joplin Member.

In areas between the 'tube' structures the Deadman - Joplin Member contact is also complex. On the scale of 10m (33ft) or more it is sub-horizontal, although at a smaller scale the contact is characterised by irregular troughs (<2m (6.6ft) across, and <0.8m (2.6ft) deep) and pedestals (<0.3m (1ft) high by 0.2m (0.7ft) wide) cut into the Deadman Member (Plate 4.12). The irregular relief (e.g. overhangs) and bioturbation of this surface suggests that the Deadman Member was at least partially lithified. However, there are several locations where flame-like projections of the Deadman Member penetrate up to 0.5m (1.6ft) into the Joplin Member (Plate 4.13). Alternatively, the latter structures suggest that the Deadman Member was in part unlithified, and could therefore become liquefied when loaded.

The 'tube' structures locally represent up to 20% of the Deadman - Joplin Member contact, and are filled by erosively based, cross-bedded and normally-graded bioclastic sands of the Joplin Member (Fig. 4.19 and Plate 4.14). There is a strong preferred orientation to the 'tubes' both individually, and as a set, and this is near-identical to that of the antecedent Dona Ana channels (Fig. 4.17) (Hunt & Allsop, 1993). The 'tubes' have a cylindrical external form, with high length to width ratios of 40:1 or greater. Their top surface is typically located just below the 'normal' Deadman - Joplin Member contact. In cross-section they have a circular, ellipsoidal (with the long axis horizontal), or more rarely a U-shaped profile. Widths of 0.1-0.5m (0.3-1.6ft), and depths of 0.1-1m (0.3-3.3ft) are typical. However, larger ones also exist (such as shown in Figure 4.19 & Plate 4.14), and these provide the best clues as to the origin of the structures. Frequently the 'tubes' narrow upwards towards the 'normal' Deadman - Joplin Member contact, and their side walls are often corrugated (Fig. 4.19 and Plate 4.14). These corrugations appear to have resulted from preferential erosion of less-well cemented beds of the Deadman Member. The corrugations often correspond to individual graded beds in their fill. A similar origin is envisaged for ellipsoid 'tubes' which appear to have "tunnelled" laterally into softer beds of the Deadman Member.

The morphology of most 'tube' structures is quite similar (as discussed above), however, there are some notable exceptions within the larger 'tubes'. The largest of these are up to 2.4m (8ft) wide and extend to 3m (10ft) below

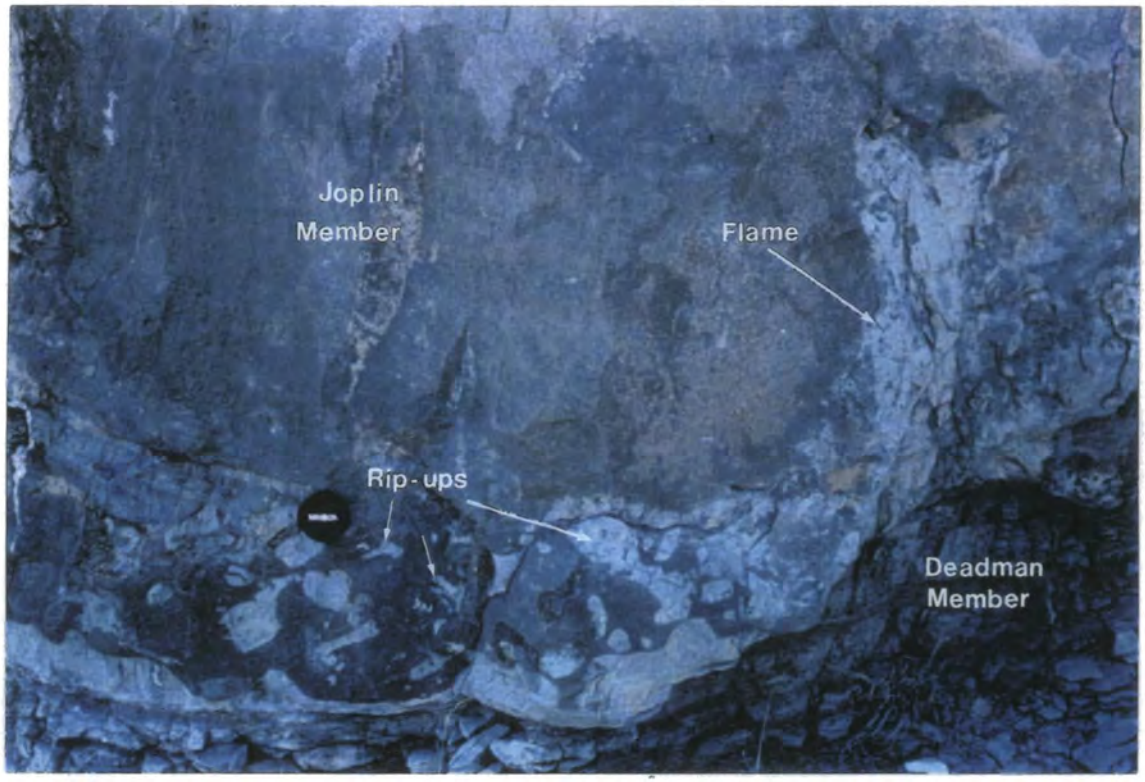

Plate 4.13 Flame structure of Deadman Member into overlying Joplin Member. However, also note rip-ups of Deadman Member contained in the Joplin Member, suggesting patchy cementation of the Deadman package.

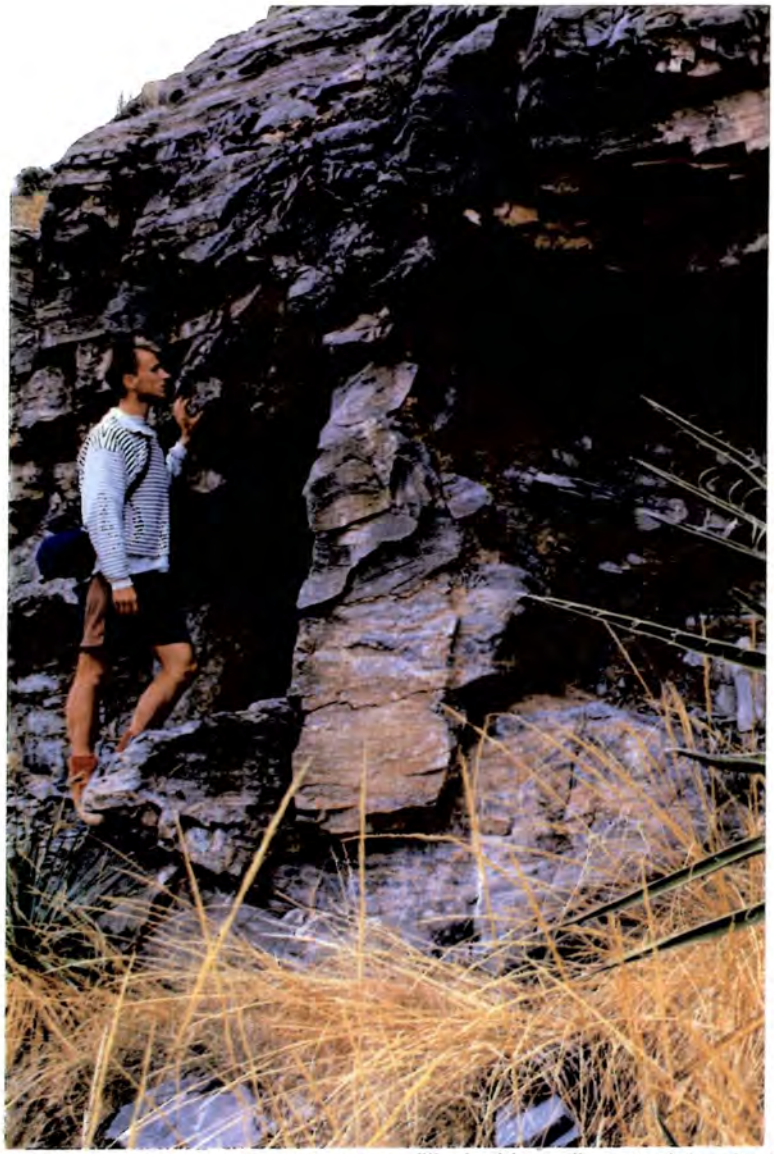

Plate 4.14 Large 'tube' structure, filled with sediment of the Joplin Member, and cut into the Deadman Member, southern flank of Dog Canyon.

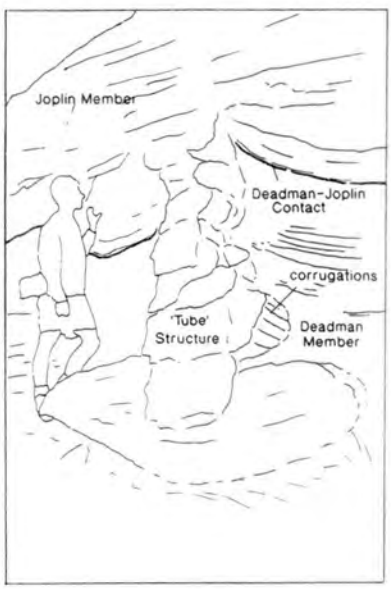

Figure 4.19 'Tube' structure exposed at the Deadman-Joplin contact, southern flank of Dog Canyon.

the sub-horizontal Deadman - Joplin Member contact. Two different types of 'tube' are recognised:-

1) 'tubes' with discrete "feeder" pipes, and
2) composite 'tubes'.

The ellipsoid 'tube' illustrated in Figure 4.19 (Plate 4.14) is an example of type 1. It shows corrugated side walls, with a maximum width of 2.4m (8ft), with its top and base 1.7m (5.6ft) and 2.85m (9.4ft) respectively below the Deadman - Joplin Member contact (Fig. 4.19 and Plate 4.14). This 'tube' was "fed" via a vertical corrugated pipe which widens downwards. The pipe has a parallel orientation to the 'tube', and is interpreted as being the modified remnant of a neptunean dyke. It is thought that there was a suite of V-shaped neptunean dykes which developed parallel to the axis of the underlying Dona Ana channels (NW-SE). These dykes are believed to have originated as extension fractures, formed through stretching of the Deadman Member over the differentially compacting Dona Ana channel. This mechanism is described in further detail in section 4.7.3.

Composite 'tubes' tend to have a more complex external geometry due to the "tunnelling" and lateral extension of their component 'tubes' into less-well cemented beds of the Deadman Member (Fig. 4.20 and Plate 4.15). These comprise of vertically stacked, and partially amalgamated 'tubes' (e.g. Fig. 4.20 and Plate 4.15). Their varying cross-sectional profiles are thought to reflect the differential cementation of the Deadman Member. Like the pipe fed 'tubes' described above, the composite 'tubes' are also interpreted to have initiated as neptunean dykes, but formed in areas where there were significant contrasts between the cementation of beds within the Deadman Member.

Many of the mid-sized and larger 'tubes' (widths >0.3m (1ft)) are bioturbated on their side and overhanging upper walls, and so is the irregular Deadman - Joplin Member contact in the inter-tube areas. Importantly this bioturbation indicates that:-

1) the 'tubes' are not cut and fill structures, but were open features on the sea-floor,
2) the relief of the contact in inter-tube areas formed an irregular sea-floor bathymetry, and therefore,
3) the Deadman Member must have been at least partially lithified to support such an irregular erosional relief (Figs. 4.19 & 4.20, and Plates 4.14 & 4.15).

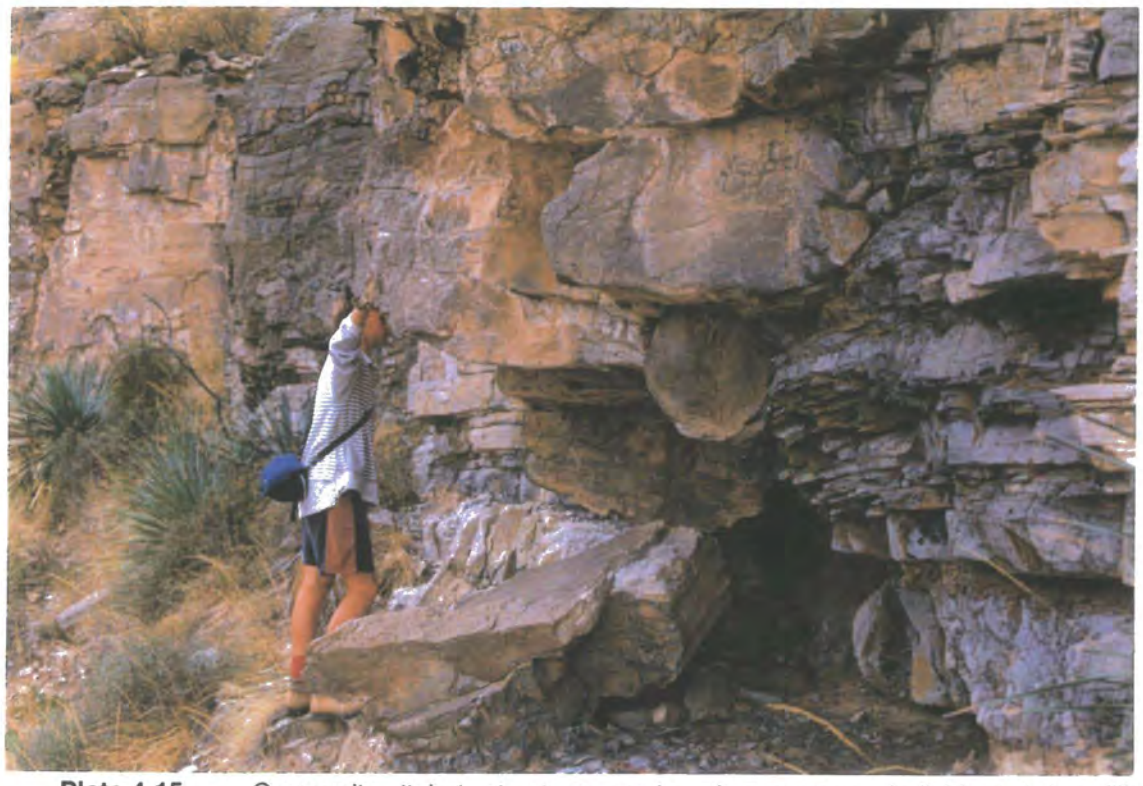

Plate 4.15 Composite 'tube' structure made of numerous, individual 'tube' filled deposits, consisting of Joplin Member sediment, cut into the Deadman Member, southern flank of Dog Canyon.

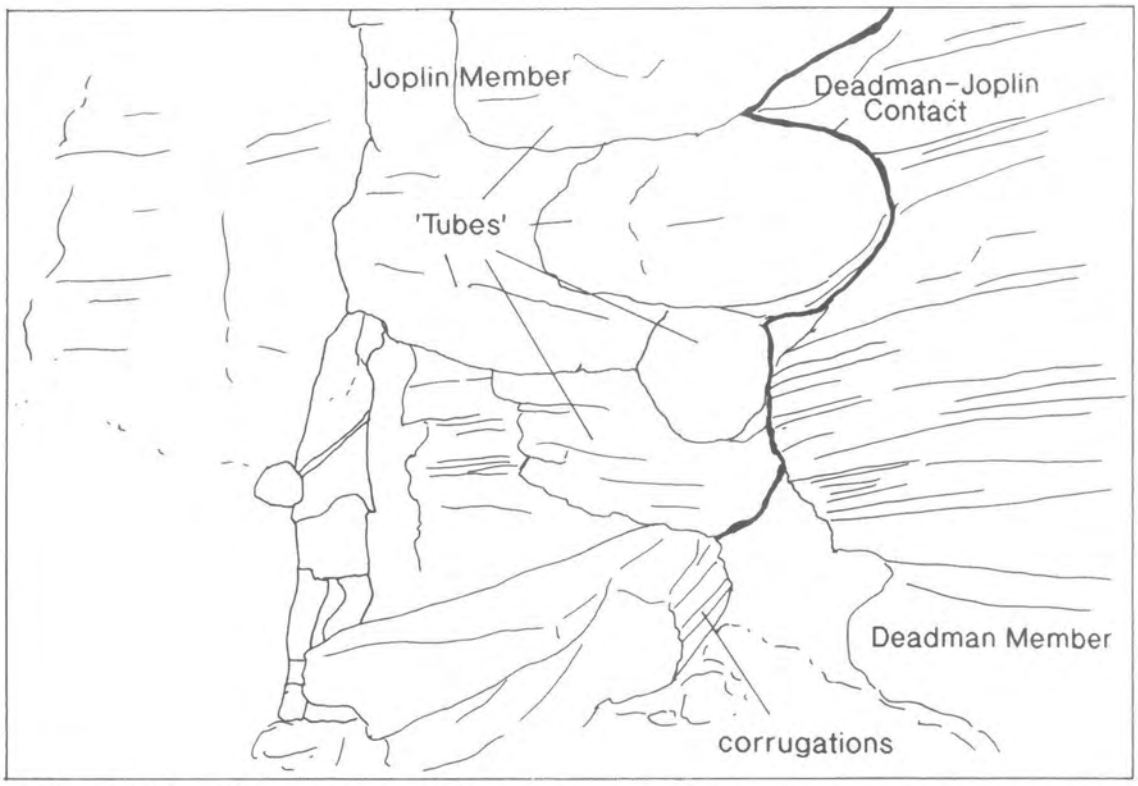

Figure 4.20 Composite 'tube' structure exposed at the Deadman-Joplin contact, southern flank of Dog Canyon. Note the separate 'tubes' compared to Figure 4.19.

The bioturbation does not, however, have a uniform density and tends to form in discrete clusters surrounded by areas of unbioturbated sediment. It is associated with the excavation of two types of dwelling structures, *Trypanites* and *Gastrochaenolites*. Both *Trypanites* and *Gastrochaenolites* have a single and simple un-lined chamber which was open to the sediment surface (Plate 4.16). These types of domiciles are common to hard and firmground surfaces respectively (Pemberton et al., 1992).

The *Trypanites* borings and *Gastrochaenolites* burrows in the Deadman Member are contemporaneous with the trace fossil *Palaeohelminthodia* found in flaggy, upper stage plane beds of the Joplin Member. The latter trace fossil is typically included within the deep-water Nerites ichnofacies (Pemberton et al., 1992) which agrees with the sedimentological observations of the Deadman and Joplin Members. These suggest that the sea-floor was far below storm-wavebase and mainly anaerobic, with occasional dysaerobic intervals probably associated with the passage of turbidity currents. These currents are thought to have washed in short-lived, but ultimately doomed, opportunistic organisms which bioturbated the upper surface of the Deadman Member.

The *Trypanites* and *Gastrochaenolites* association of domiciles, considered with the unusual erosional topography of the Deadman - Joplin Member contact, strongly suggests that the Deadman Member was either wholly or partially lithified. In contrast, the preferential excavation of certain beds, development of corrugations, and occasional flame structures indicates other beds remained uncemented/lithified. From the evidence described above it clearly appears that the Deadman Member was differentially cemented.

4.7 Compaction Phenomena.

The following sections deal with the process of differential compaction, specifically the effects it produces, the timing, and the rate at which compaction appears to proceed. In order to achieve this, the effects of differential compaction are described and modelled for both Muleshoe and Sugarloaf Mounds. These two examples show contrasting bedding relationships produced by differential compaction, which mainly reflects differences in the timing of compaction. Also described and modelled is the effect of differential compaction that occurs across the Dona Ana bioclastic channels within Dog Canyon, providing interpretations for both the north and south cliff sections.

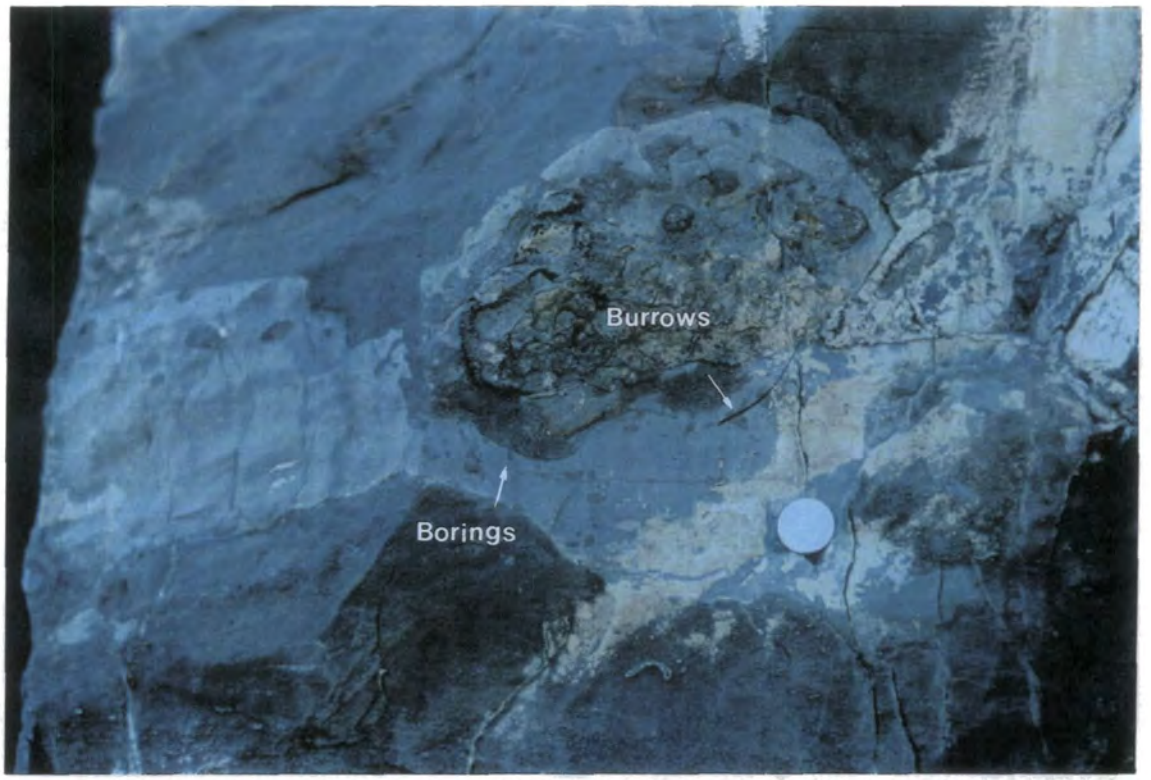

Plate 4.16 Burrows and borings within the mudstone of the Deadman Member along the contact of the 'tube' structures, and filled by Joplin Member sediment.

All the examples viewed in the field illustrate how compaction varied both spatially and temporally, and how this variety contributed in the development of differing bed geometries and arrangements. It is also apparent that the effects of differential compaction are most obvious at hiatal surfaces when sedimentation was relatively condensed, such as occurs at the base of the Joplin Member of the Rancheria. It therefore follows that the process of differential compaction is intimately associated with the local development of angular unconformities. Examples of this fact are described from all three areas mentioned above.

4.7.1 Differential Compaction Around Muleshoe Mound.

A. Introduction.

The southern flank section of Muleshoe Mound offers continuous exposure of the Arcente, Dona Ana and Rancheria deposits, which facilitates compactional modelling and bed restorations. Compactional modelling is primarily concerned with the development of the angular unconformity between the Dona Ana and the overlying Joplin Member of the Rancheria Formation. On the southern side of Muleshoe Mound, Dona Ana beds dip at very steep angles as the bioherm is approached (Fig. 4.11 and Plate 4.2). The Dona Ana is then truncated with angular unconformity by the overlying Joplin Member of the Rancheria Formation, with the angle of unconformity increasing, then decreasing again, towards the mound. The boundary between the Dona Ana and the overlying Joplin Member represents a significant hiatus, as evidenced by conodont biostratigraphy (Fig. 4.2) (e.g. Lane, 1974; 1982) and the abundant phosphate fragments within the basal units of the Joplin Member.

A combination of quantitative data and qualitative observations are used to constrain the compaction of the Arcente muds and limestones surrounding Muleshoe Mound. **Quantitative** data consist of geopetal measurements, and bed thickness information. These data are obtained directly from field measurements, and also from the use of scaled field photographs and line drawings, divided into equally spaced measured sections. **Qualitative** data consist of field observations of stratal relationships (see section 4.6.1) and depositional fabrics. These data help in the constraining of the depositional profile at each time stage (e.g. deposition of the Hackberry beds, end of the Arcente, etc.), and the timing of compaction throughout the burial process.

Most importantly, quantitative data allows the interpretation of:-

- the original thickness of the Arcente;
- the present day compacted thickness of the Arcente;
- the original position of the top Hackberry beds surface;
- the deflection of the Rancheria from an original sub-horizontal attitude.

Combination of these points with qualitative field observations allows:-

- the reconstruction of the original Arcente thickness;
- the assessment of the time evolution of deposition and compaction;
- the removal of the effects of total burial compaction;

by making some relatively simple assumptions.

B. Qualitative Data.

Stratal relationships facilitate division of strata on the southern flank of Muleshoe Mound into separate time increments, from which the influence and timing of compaction can be assessed at various stages of burial. For each increment, the relationships between the mound and flank deposits, the Arcente, Dona Ana and Rancheria Formation can be reconstructed. It is possible, therefore, to remove the effects of burial compaction, and view the early compaction evolution of the Arcente for each time increment from reconstructions of the beds at each stage.

Geopetal data combined with bedding information and depositional fabrics allows the reconstruction of original bed orientations and dips. The geopetal data presented on Figure 4.11 illustrate that, in general, geopetal dips reflect the dip of bedding at the same point within the Arcente and Dona Ana and, therefore, geopetal information can be directly related to bed attitude at the time of deposition, showing that a large amount of bed rotation has occurred within the Arcente and Dona Ana deposits since.

Stratal relationships show that the bedding of the Dona Ana is concordant to the bedding of the underlying Arcente, however, dips measured along the silt layers within the lower part of the Dona Ana approach a maximum of 40° very close to the margin of the mound, and shallow to 13° about 75m (246ft) from the mound edge (Fig. 4.11). The change in dip is mimicked by the underlying Arcente (Fig. 4.11 and Plate 4.2). It is proposed that differential compaction of the underlying fine-grained Arcente muds and limestones has produced the exaggerated dip within this region. Differential compaction occurs because of the abrupt thinning and

pinch out of the Arcente muds against the flank and mound facies (Fig. 4.11 and Plate 4.2). Therefore, the main control on the post-depositional dips of the Dona Ana section is the local thickness of the underlying Arcente section. Some compaction would have occurred within the flank beds of the mound beneath the Arcente, but this would have probably been relatively minor due to the coarser nature of the sediment, and the fact that it was derived from the bioherm itself which is highly cemented at a very early stage (Shinn et al., 1983). Indeed, differential compaction can be seen in a small (6 metre) section of the flank facies units where a small anticlinal structure has formed over a large block of megabreccia shed from Muleshoe (Fig. 4.11 and Plate 4.17). This structure does not affect the top surface of the Tierra Blanca flank facies, suggesting that the pore fluid was expelled during early burial, and the majority of compaction in the flanking beds had taken place before the deposition of the overlying Arcente wedge.

At this point it is instructive to consider two end-member models for the deposition, stratal relationships, and pore fluid pressure development of the southern Muleshoe Mound section. These models are based on the relative timings of deposition and compaction. Each model produces differing stratal relationships, and can therefore be assessed by comparison with the qualitative field data. The implications for porosity-depth evolution and pore fluid pressure evolution are quite different. Figure 4.21a illustrates a situation where the depositional rate of the Dona Ana is matched by the compaction rate of the underlying Arcente. During deposition, equilibrium compaction is maintained by pore fluid loss throughout the Arcente section, and hence, pore fluid pressure remains hydrostatic. This results in the Dona Ana having a wedge shape synthetic to that of the Arcente, with individual beds fanning/diverging and thickening away from the mound. Older Dona Ana beds dip more steeply than younger beds due to the greater progressive compactional rotation. At the end of Dona Ana deposition no further compaction of the Arcente occurs as pore fluid pressure is already hydrostatic. This results in a flat depositional surface on the top of the Dona Ana, with no subsequent angular unconformity being produced between the Dona Ana and the Rancheria.

Figure 4.21c depicts the depositional arrangement and pore fluid pressure history for a situation where the deposition rate of the Dona Ana is greater than the compaction rate of the Arcente. In this scenario the Dona Ana develops a wedge shape due to the post-depositional rotation of the beds and erosional truncation by the subsequent Rancheria Formation.

Plate 4.17 Small anticlinal structure above megabreccia clast, within the flank strata on the southeastern side of Muleshoe Mound.

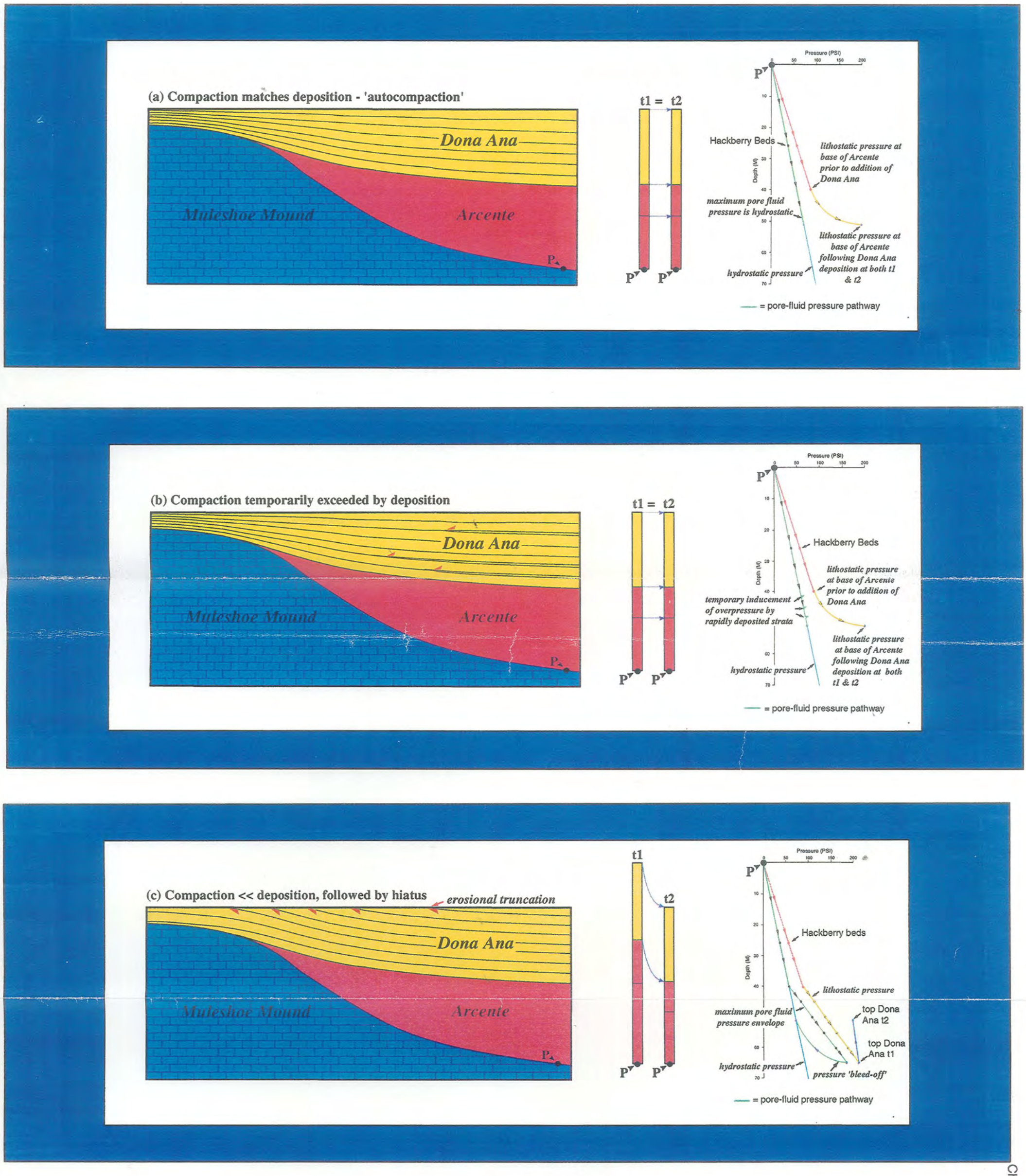

Figure 4.21a-c Models of compaction rate versus deposition rate, and the implications for pore fluid pressure and stratal relationships, for the southeastern flank of Muleshoe Mound.

Internally, beds are parallel and generally steepen towards the mound. However, older beds do not dip more steeply as in the previous model. Compaction only attains an equilibrium condition after Dona Ana deposition, and it is during this stage of 'compactional catch-up' when bed rotation occurs, with the development of a compaction-induced post-depositional high developed over the mound itself. Subsequent erosion will create an angular unconformity at its base between the rotated beds of the Dona Ana and the Rancheria Formation (as shown in Fig. 4.21c). One implication of this model is that deposition of the Dona Ana will induce near-surface overpressure in the Arcente, with no compaction occurring during Dona Ana times. Once deposition is halted, compaction of the Arcente will occur as overpressured pore fluids 'bleed off', until a state of hydrostatic pressure and equilibrium compaction has been achieved.

The final model shown in Figure 4.21b represents a mid-point example between the two previous models. Here, the deposition rate of the Dona Ana is only temporarily greater than the compaction rate of the Arcente. This means that during deposition of some rapidly deposited strata no accompanying compaction of the Arcente occurs, with the development of near-surface overpressure. With a slight hiatus in, or slowing of deposition, compaction 'catch-up' begins and pore fluid pressures equilibrate to hydrostatic, with the associated bed rotation. The reequilibration of pore fluid pressure will have an exponential decay curve, meaning that immediately when sedimentation stops the compaction rate of the Arcente will be greatest, but this will diminish progressively as pore fluid pressure nears hydrostatic. Internally therefore, beds show a divergence and thickening away from the mound, but they also have younger strata onlapping against rotated older strata. Again, older strata dip more steeply than younger strata, and compaction is complete and in a state of equilibrium at the end of Dona Ana deposition. The implication here is that overpressure is only temporarily induced in the Arcente muds, hence affecting compaction rates during Dona Ana deposition.

Observations of the stratal relationships on the southern flank of Muleshoe Mound are most similar to model 4.21c, in fact strikingly so, although elements of model 4.21b may also be seen. Therefore, it is interpreted that deposition of the Dona Ana was greater than the rate of Arcente compaction for most of its deposition. However, there were times when compaction proceeded at a greater rate than Dona Ana deposition,

producing internal onlap. During the hiatus following Dona Ana deposition it is therefore interpreted that bleed off occurred.

The present day dip and deflection of the top Rancheria surface from an inferred horizontal position reflects the total burial compaction of the Arcente after deposition of the Rancheria Formation. It is important to firstly correct Arcente bed thicknesses for this burial compaction before modelling the compaction due to the Dona Ana deposition.

C. Methodology.

Field observations were made on photomosaics of the exposed sections, plotting stratal relationships, dip and strike of beds, depositional fabric information, bedding style, presence of fauna, and geopetal information (e.g. Fig. 4.11). The exposed section of the southern cliffs of Muleshoe Mound was divided into twelve equally spaced sections, approximately 12m (39ft) apart (Fig. 4.22). For each section the present day thicknesses for the depositional units were recorded, after being corrected for perspective variations of the topography (see Table 4.1). No assumptions are made when measuring the present day thicknesses of the Arcente, the Rancheria, and the height of the Hackberry beds above the Tierra Blanca flank strata.

However, three basic assumptions are required for the compactional modelling of the outcrop. Firstly, the inference of a 4° slope on the top surface of the Arcente allows the reconstruction of the original depositional surface immediately after the end of the Arcente deposition, and prior to loading by the Dona Ana. Secondly, the reconstruction of the top Rancheria surface to horizontal is required to enable the removal of the effects of burial compaction during and after Rancheria times. Finally it is assumed that the point at which the Arcente and Rancheria impinges northwards onto the edge of the mound itself, represents a fixed point about which differential compaction rotates the bedding surface. The combination of these three assumptions allows the measurement of:-

- The deflection of the Rancheria from an original horizontal attitude.
- The original Arcente thickness.
- The original height of the Hackberry beds, assuming that the Arcente compacts evenly throughout its thickness.
- The amount of differential compaction of the Arcente, if a uniform thickness of 25m of Dona Ana is deposited on top.

Table 4.1 shows all sets of data concerning Muleshoe Mound.

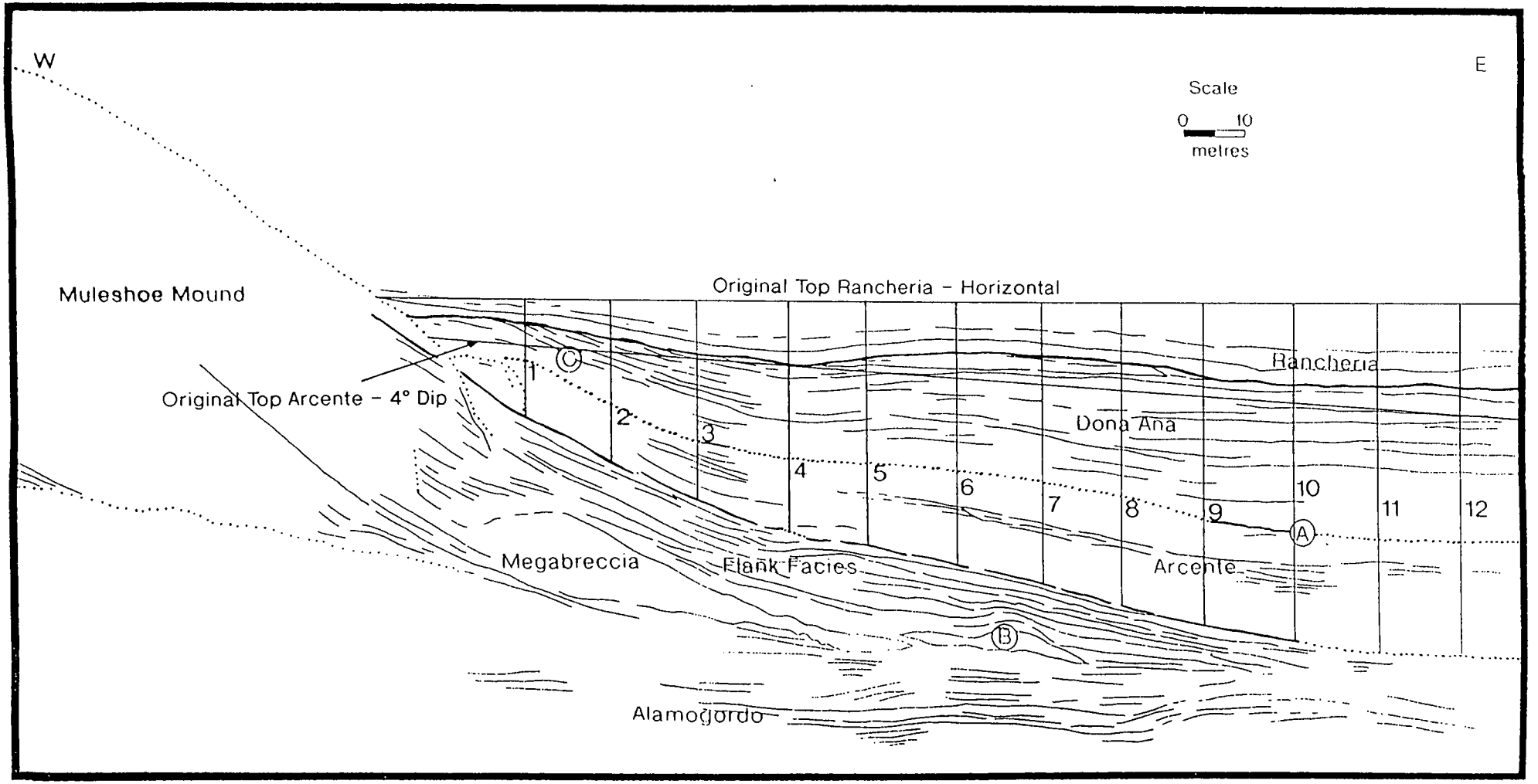

Figure 4.22 Southeastern flank of Muleshoe Mound, divided into 12 stations for the restoration of stratal relationships, and the assessment of differential compaction.

As stated above, no assumptions are made when the present day thicknesses of units are measured, although, some justification must be made for the assumptions which allow the restoration of stratal relationships during early burial. It is presumed that the top Rancheria surface was horizontal immediately after deposition. This appears to be a reasonable assumption with the interpretation of the Joplin Member being deposited by high-density turbidity and/or density currents, which would tend to fill the lowest topographic areas first, and generally smooth all topographic variations. Unfortunately there are no geopetals within the Joplin Member to back up this assumption, but sedimentary structures such as cross-bedding can be seen to be rotated from their original position. Therefore, to calculate the compacted thickness of the Arcente post-Dona Ana deposition, the measurements must be corrected for the additional compaction that has occurred during and after the deposition of the Rancheria Formation.

Likewise, it is assumed that the top Arcente surface had a dip of approximately 4° immediately after its deposition. This assumption is supported by two sources of data. Firstly, the geopetals measured within the Arcente and Hackberry beds (Fig. 4.11) show that a dip of 6°, decreasing to 3°, was present on this surface, and therefore 4° is a good average. Secondly, taking the work of Kenter (1990), it can be assumed that the maximum angle of dip for a freshly deposited lime mudstone is approximately 4° (Fig. 4.23). Using this angle of deposition as a first approximation the top surface of the Arcente wedge can be drawn by simply rotating it around the point at which it impinges upon Muleshoe Mound, akin to the top Rancheria surface (Fig. 4.22).

Finally further calculations, explained below, are based on the loading of the Arcente by an even 'blanket' of Dona Ana measuring 25m (82ft) thick. This assumption is based on the relationships seen at other mounds, especially the small mound exposed on the southern cliff section of Muleshoe Canyon (Plate 4.18). At this location it can be seen that the Dona Ana approximately remains the same thickness right the way across the top of the mound. However, this does not follow for other mounds (e.g. Sugarloaf Mound), and it is apparent that in general all mounds are different in their stratal relationships. Indeed, at Muleshoe Mound the Dona Ana can be seen to coarsen as the mound is approached suggesting that Muleshoe Mound acted as the sediment source area. Therefore, it is difficult to constrain the original thickness of the Dona Ana section any better. Bed relationships tend to form the only argument for this assumption, and these in turn are

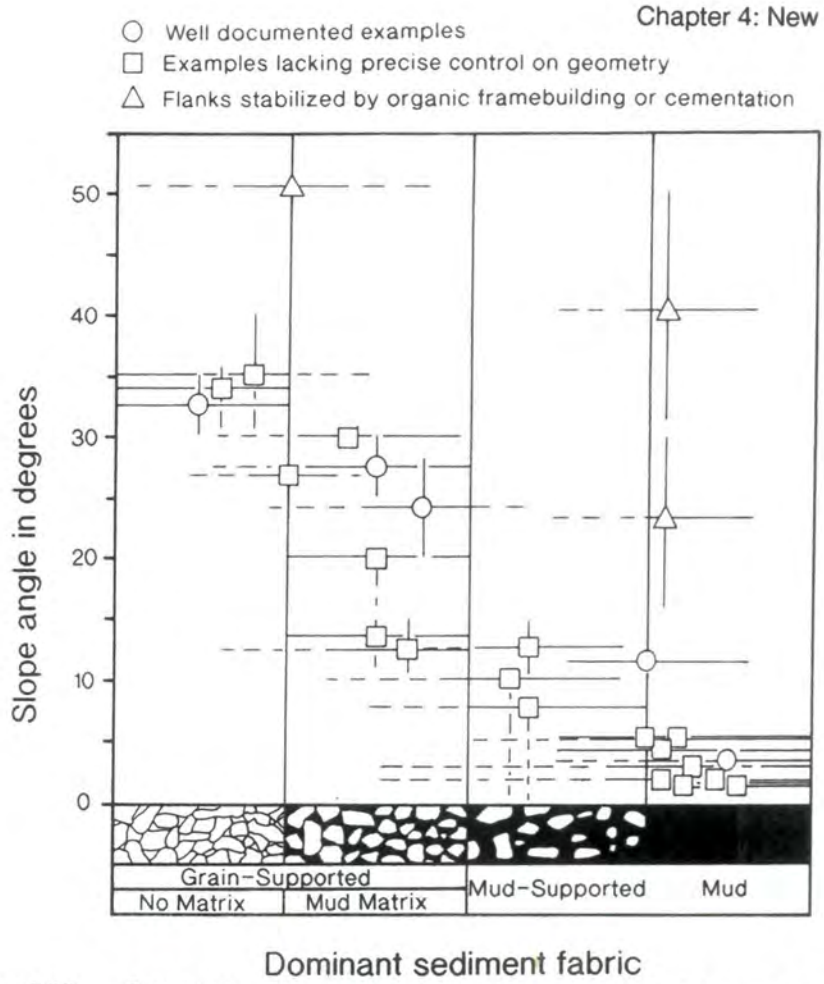

Figure 4.23 Plot of slope angle versus dominant sediment fabric. For each data point the range in fabric and slope angle is indicated by bars (From Kenter, 1990).

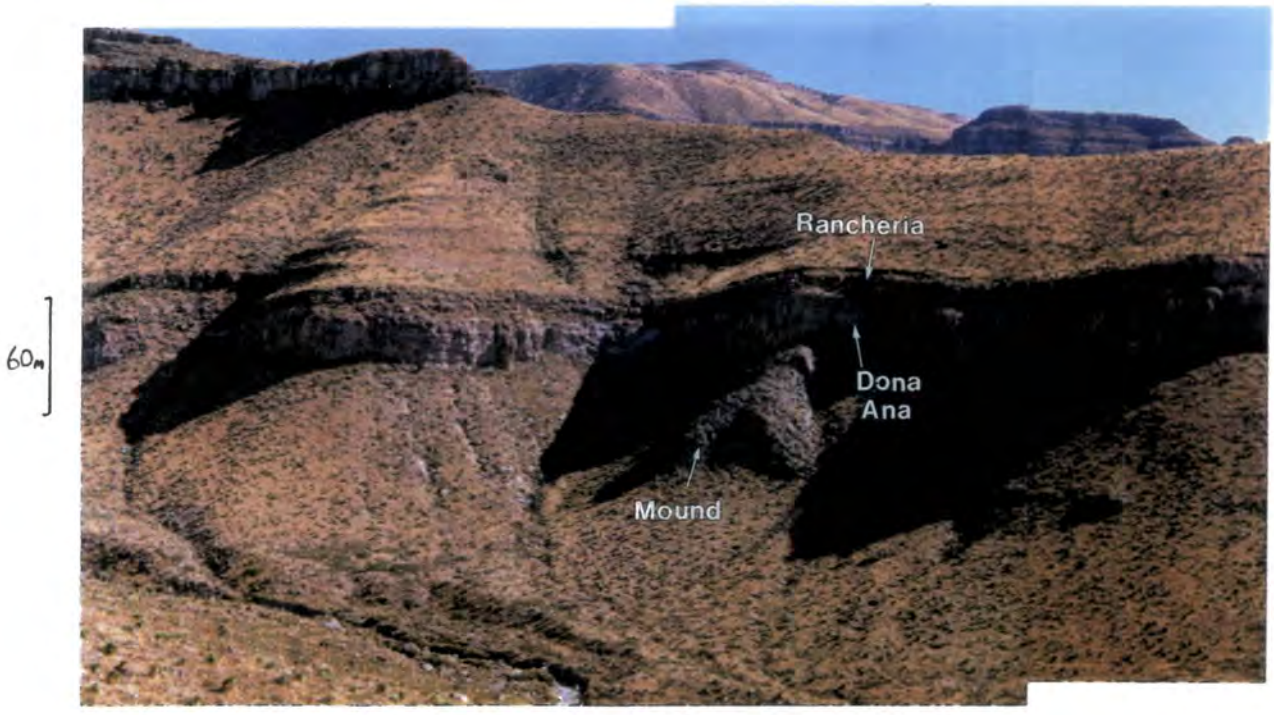

Plate 4.18 Minor mound located in the cliffs to the south of Muleshoe Mound. Note how the Dona Ana package thins over the mound, and is also deformed into an anticlinal structure due to differential compaction.

supported by geopetal data, demonstrating the large scale rotation of the Dona Ana beds. Finally, the absence of clinoforms on a cliff scale (as seen at Sugarloaf Mound) illustrate a different style of loading the Arcente by the Dona Ana. Small clinoforms are only seen within the mounded unit of the Dona Ana at Muleshoe Mound (Fig. 4.5 & Plate 4.4).

D. Calculations.

Table 4.1 shows the primary data measured from field photographs, and bed thicknesses corrected for total burial compaction. The second part of Table 4.1 illustrates how this data have been used to calculate porosities and pore fluid pressures through a series of simple mathematical calculations. All calculations use the original or compacted Arcente thickness, and therefore, these are the first in the second half of the table.

The Rancheria deflection represents the distance from the assumed horizontal depositional surface to the present day top surface of the Rancheria. This distance is added to the present day compacted thickness of the Arcente, providing the corrected compacted Arcente thickness, allowing the thickness of the Arcente immediately before the deposition of the Rancheria Formation and effects of burial compaction to be calculated. In turn, it also allows the calculation of the percentage of Arcente compaction by Dona Ana deposition to be calculated. Percentage compaction is calculated by the following formula:-

$$\frac{\text{Initial thickness - compacted thickness}}{\text{Initial thickness}} \times 100$$

(equation 4.1, Weller, 1959)

Further assumptions are required concerning the depositional porosities and the porosity-depth profile of lime muds, so that the original porosity and the compacted porosities of the Arcente can be calculated during progressive burial. Firstly, it was assumed that the original depositional porosity of a lime mud was 70% at the depositional surface, and that the porosity-depth profile approximated a straight line for the first 50m (164ft) of burial. These values reflect the curve presented by Hardenbol et al. (1981) (Fig. 4.24). Secondly, because of autocompaction, the porosity at half-height depths for any thickness of Arcente are taken to represent the average porosity of the unit. For a linear porosity-depth profile this assumption is true. Therefore, average depositional porosities for the Arcente can be estimated, varying due to the change on thickness across the 12 measured stations (Table 4.1).

TABLE 1 - Primary Data.

Section no.	1	2	3	4	5	6	7	8	9	10	11	12
Rancheria Deflection (m)	1.30	2.48	4.97	5.53	5.78	5.90	5.90	5.90	6.09	6.21	6.46	6.21
Rancheria Thickness (m)	2.86	3.79	3.79	4.97	4.60	4.22	4.60	4.78	5.34	5.90	5.84	5.90
Present Dona Ana Thickness (m)	5.77	10.98	14.72	15.21	15.95	16.63	18.04	19.94	23.56	24.42	24.88	24.95
Dona Ana thickness (m)	25.00	25.00	25.00	25.00	25.00	25.00	25.00	25.00	25.00	25.00	25.00	25.00
Compacted Arcente Thickness (m)	9.32	9.38	9.69	12.73	13.11	14.78	16.58	18.26	18.07	18.63	19.38	19.50
Original Arcente Thickness (m)	10.80	17.20	22.48	26.96	28.20	30.12	32.61	35.40	37.64	39.01	40.06	39.44
Present Height of Hackberry beds (m)			6.46	7.64	6.99	9.10	10.07	8.19	11.85	13.04	13.32	15.10
Original Height of Hackberry Beds (m)			11.35	16.19	13.07	17.88	20.47	16.92	22.79	24.98	25.81	29.84

TABLE 2 - Calculated Data.

Section no.		1	2	3	4	5	6	7	8	9	10	11	12
Original Arcente Thickness (m)		10.80	17.20	22.48	26.96	28.20	30.12	32.61	35.40	37.64	39.01	40.06	39.44
Compacted Arcente Thickness (m)		9.32	9.38	9.69	12.73	13.11	14.78	16.58	18.26	18.07	18.63	19.38	19.50
Rancheria Deflection (m)		1.30	2.48	4.97	5.53	5.78	5.90	5.90	5.90	6.09	6.21	6.46	6.21
Corrected Compacted Arcente Thickness (m)		10.62	11.86	14.66	18.26	18.89	20.68	22.48	24.16	24.16	24.84	25.84	25.71
% Compaction by Dona Ana Deposition		1.70	31.00	34.80	32.30	33.00	31.30	31.10	31.80	35.80	36.30	35.50	34.80
Arcente Depositional Porosity (%)		69.58	69.34	69.11	68.92	68.88	68.80	68.70	68.60	68.50	68.45	68.40	68.42
Calculated Arcente Compacted Porosity		69.06	55.54	52.63	54.11	53.54	54.56	54.60	53.99	50.92	50.45	51.01	51.56
Compaction Ratio		1.02	1.45	1.53	1.48	1.49	1.46	1.45	1.47	1.56	1.57	1.55	1.53
Basal Arcente Fluid Pressure	Hydro	15.95	25.39	33.19	39.81	41.64	44.47	48.15	52.27	55.57	57.60	59.15	58.23
Prior to loading (psi)	Litho	23.26	37.14	48.66	58.47	61.18	65.40	70.88	77.03	81.98	85.01	87.34	85.97
Matrix Stress (psi)		7.32	11.75	15.47	18.67	19.55	20.93	22.74	24.76	26.41	27.42	28.20	27.74
Dona Ana Porosity (%)		42.00	42.00	42.00	42.00	42.00	42.00	42.00	42.00	42.00	42.00	42.00	42.00
Basal Arcente Fluid Pressure After	Hydro	52.59	54.42	58.56	63.87	64.80	67.44	70.10	72.58	72.58	73.59	75.06	74.87
Loading and Pore Fluid Bleed-off (psi)	Litho	146.29	160.04	169.50	177.19	179.32	182.78	187.22	192.05	195.40	197.67	199.62	198.67

Table 4.1 Primary data (Table 1) measured from Figure 4.22, for the southeastern flank of Muleshoe Mound. Table 2 illustrates the calculated data concerning the differential compaction and pore fluid pressure of the Arcente, prior and post loading by the Dona Ana sediments. Table 3 shows the calculations concerning compaction and pore fluid pressure of the Arcente for 5m increments of Dona Ana sedimentation, followed by total burial compaction of the present day.

Compaction After 5m of Dona Ana Deposition		1	2	3	4	5	6	7	8	9	10	11	12
Burial Depth (m)		15.80	22.20	27.48	31.96	33.20	35.12	37.61	40.40	42.64	44.01	45.06	44.44
Basal Arcente Fluid Pressure	Hydro	23.33	32.78	40.57	47.19	49.02	51.85	55.53	59.65	62.96	64.98	66.53	65.61
After 5m Dona Ana (psi)	Litho	47.87	61.77	73.31	83.15	85.86	90.09	95.58	101.74	106.71	109.74	112.08	110.70
Matrix Stress (psi)		7.32	11.75	15.47	18.67	19.55	20.93	22.74	24.76	26.41	27.42	28.20	27.74
Pore Pressure (assuming no fluid loss) (psi)		40.55	50.02	57.84	64.48	66.31	69.16	72.85	76.98	80.29	82.32	83.88	82.96

Compaction After 10m of Dona Ana Deposition													
Burial Depth (m)		20.80	27.20	32.48	36.96	38.20	40.12	42.61	45.40	47.64	49.01	50.06	49.44
Basal Arcente Fluid Pressure	Hydro	30.71	40.16	47.96	54.57	56.40	59.24	62.91	67.03	70.34	72.36	73.91	73.00
After 10m Dona Ana (psi)	Litho	72.47	86.40	97.97	107.82	110.54	114.78	120.28	126.45	131.43	134.46	136.81	135.43
Matrix Stress (psi)		7.32	11.75	15.47	18.67	19.55	20.93	22.74	24.76	26.41	27.42	28.20	27.74
Pore Pressure (assuming no fluid loss) (psi)		65.15	74.65	82.50	89.15	90.99	93.85	97.54	101.69	105.02	107.05	108.61	107.69

Compaction After 15m of Dona Ana Deposition													
Burial Depth (m)		25.80	32.20	37.48	41.96	43.20	45.12	47.61	50.40	52.64	54.01	55.06	54.44
Basal Arcente Fluid Pressure	Hydro	38.09	47.54	55.34	61.95	63.78	66.62	70.29	74.41	77.72	79.74	81.29	80.38
After 15m Dona Ana (psi)	Litho	97.07	111.03	122.62	132.49	135.22	139.47	144.98	151.16	156.15	159.19	161.54	160.16
Matrix Stress (psi)		7.32	11.75	15.47	18.67	19.55	20.93	22.74	24.76	26.41	27.42	28.20	27.74
Pore Pressure (assuming no fluid loss) (psi)		89.75	99.28	107.15	113.83	115.67	118.53	122.24	126.40	129.74	131.78	133.34	132.42

Compaction After 20m of Dona Ana Deposition													
Burial Depth (m)		30.80	37.20	42.48	46.96	48.20	50.12	52.61	55.40	57.64	59.01	60.06	59.44
Basal Arcente Fluid Pressure	Hydro	45.47	54.92	62.72	69.33	71.16	74.00	77.68	81.80	85.10	87.13	88.68	87.76
After 20m Dona Ana (psi)	Litho	121.67	135.65	147.27	157.17	159.90	164.16	169.68	175.87	180.87	183.92	186.27	184.89
Matrix Stress (psi)		7.32	11.75	15.47	18.67	19.55	20.93	22.74	24.76	26.41	27.42	28.20	27.74
Pore Pressure (assuming no fluid loss) (psi)		114.35	123.91	131.80	138.50	140.35	143.22	146.94	151.11	154.46	156.50	158.07	157.15

Compaction After 25m of Dona Ana Deposition													
Burial Depth (m)		35.80	42.20	47.48	51.96	53.20	55.12	57.61	60.40	62.64	64.01	65.06	64.44
Basal Arcente Fluid Pressure	Hydro	52.86	62.31	70.10	76.72	78.55	81.38	85.06	89.18	92.48	94.51	96.06	95.14
After 25m Dona Ana (psi)	Litho	146.27	160.28	171.93	181.84	184.58	188.84	194.38	200.58	205.59	208.64	211.00	209.62
Matrix Stress (psi)		7.32	11.75	15.47	18.67	19.55	20.93	22.74	24.76	26.41	27.42	28.20	27.74
Pore Pressure (assuming no fluid loss) (psi)		138.95	148.53	156.46	163.18	165.03	167.91	171.64	175.82	179.18	181.23	182.81	181.88

Total Burial Compaction													
Original Arcente Thickness (m)		10.80	17.20	22.48	26.96	28.20	30.12	32.61	35.40	37.64	39.01	40.06	39.44
Compacted Arcente Thickness (m)		9.32	9.38	9.69	12.73	13.11	14.78	16.58	18.26	18.07	18.63	19.38	19.50
Total % Compaction (Total Burial)		13.70	45.50	56.90	52.80	53.50	50.90	49.20	48.40	52.00	52.20	51.60	50.60
Arcente Depositional Porosity (%)		69.58	69.34	69.11	68.92	68.88	68.80	68.70	68.60	68.50	68.45	68.40	68.42
Calculated Arcente Compacted Porosity		64.75	43.78	28.34	34.18	33.06	36.42	38.44	39.13	34.39	33.94	34.68	36.13
Compaction Ratio		1.16	1.83	2.32	2.12	2.15	2.04	1.97	1.94	2.08	2.09	2.07	2.02

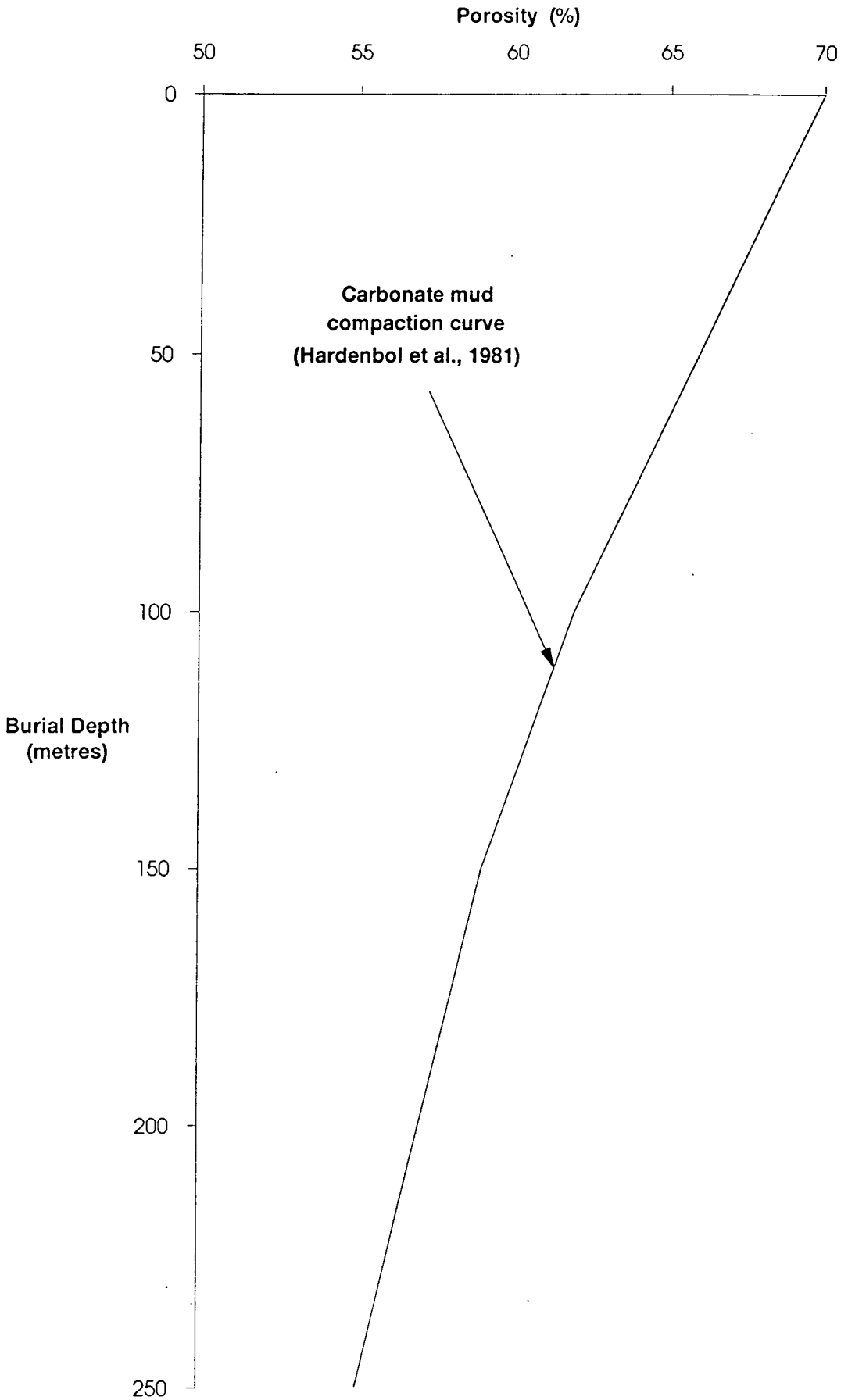

Figure 4.24 Porosity-Depth profile for carbonate mud, proposed by Hardenbol et al. (1981).

Using the original Arcente thickness (X_O), the compacted Arcente thickness (Y_C), and the original depositional porosity ($ø_O$) it is possible to calculate the compacted porosity ($ø_C$) of the Arcente using the formula of Van Hinte (1978) (see also Chapter 2):-

$$X_o = \frac{(1-\phi_c)Y_c}{(1-\phi_o)} \qquad \text{(equation 4.2)}$$

A second useful calculation to assess the amount of compaction occurring is the compaction ratio as described by Truyol (1989), using the compacted porosity and the original porosity ($ø_C$ and $ø_O$, respectively):-

$$\text{Compaction Ratio} = \frac{(1-\phi_c)}{(1-\phi_o)} \qquad \text{(equation 4.3)}$$

Work by Truyol (1989) show that compaction ratios of 1.5 to 2.0 are typical of fine-grained muds within 25 to 30m (80 - 100ft) of burial.

Calculations concerning pore fluid pressures are all presented in Table 4.1 for the base of the Arcente section at each measured station. Hydrostatic pore fluid pressures are simply calculated using the burial depth and a standard pressure gradient, dependant upon the salinity of the pore fluid (based on ODP data for the Bahamas, e.g. Lavoie, 1988). Lithostatic pore pressures however, require a more complicated calculation:-

$$\text{Lithostatic pressure} = \left[\left[(\phi.\rho_f) + \left((1-\phi)\rho_m\right)\right] \times \frac{\text{depth}}{10}\right] \times 14.223$$

(equation 4.4)

where, ø is the average porosity, ρ_f is the fluid density, ρ_m is the matrix density, and the answer is converted into pounds per square inch per metre (psi/m). Assumptions have to be made concerning the fluid density, dependant upon the salinity, and the matrix density of freshly deposited lime mudstones. The estimates are based on ODP (Ocean Drilling Program) data from the Bahamas (e.g. Lavoie, 1988).

Utilising Terzaghi's (1925) equation:-

$$S = \sigma + P \qquad \text{(equation 4.5)}$$

where, S is the total stress (or overburden stress), σ is the matrix stress (or effective stress) and P is the pore fluid pressure, it is possible to evaluate the matrix stress (σ) from the variables already calculated. At the initial stage of the Arcente deposition, with no Dona Ana yet deposited, pore fluid pressure (P) is hydrostatic and can be calculated. The total stress (S) can only achieve

a maximum value equal to the lithostatic pressure before geologically instantaneous dewatering occurs, and hence subtracting the hydrostatic pressure from the lithostatic pressure it is possible to calculate the maximum matrix stress for the Arcente.

Further calculations can be made showing the change in maximum pore fluid pressure during the addition of the Dona Ana, utilising the matrix stress previously evaluated. Table 4.1 shows the calculations for the addition of an extra 5m of Dona Ana sediment at each stage. Firstly a new burial depth is calculated, always presuming no pore fluid is expelled from the Arcente, and therefore no compaction or bed thickness reduction has occurred. The new hydrostatic pressure is then evaluated as before. Lithostatic pressure is recalculated as before, but the effect of the addition of the Dona Ana sediment is built into equation 4.4, hence requiring an estimation of the Dona Ana depositional porosity. Estimates are based on the work of Meyers & Hill (1983). Matrix stress stays exactly the same as no compaction of the Arcente has occurred. A simple subtraction of the matrix stress from the recalculated lithostatic pressure (i.e. rewriting equation 4.5) provides an estimation of the maximum pore fluid pressure (P, in equation 4.5).

Similar calculations are made for every addition of 5m of Dona Ana sediment, recalculating lithostatic pore pressure at each stage, and therefore, estimating the maximum pore fluid pressure evolution at the base of the Arcente during Dona Ana deposition. These results can be plotted on a pressure depth graph to outline the pressure 'window' in which pore fluid pressures existed for the Arcente during Dona Ana times, with the maximum pore fluid pressure representing the scenario of no compaction or pore fluid loss from the Arcente during Dona Ana deposition. As stated earlier (section 4.6.1), stratal relationships suggest that this is a fair approximation.

E. Results and Implications.

The following section attempts to outline the compaction history of the Arcente, along with the prediction for the limits of the pore pressure development within the basal section of the unit.

The calculations show that the Arcente underwent approximately 31 to 36% (an average of 33.4%) bed thickness reduction after the deposition of 25m (82ft) of Dona Ana. Column 1, the closest section to the mound, is ignored in these calculations as it appears to provide anomalous results. Three reasons are postulated for this anomaly:

1. There is poor exposure here and the exact position of the Arcente - Dona Ana contact is difficult to place.
2. Satellite bioherm growth has occurred within the Dona Ana and may complicate the compaction history in the area.
3. Results may reflect early cementation of the Arcente in this region, as pore fluids would have been expelled in this direction through the porous and permeable Hackberry beds.

However, 33% compaction at such a shallow depth of burial appears to be extremely large, especially as Fruth et al. (1966) report that experimentally, 30% compaction of carbonate mud occurs after 30bars confining pressure, equivalent to a burial depth of approximately 300m (984ft) at hydrostatic pressure (1bar equals 14.5psi). The more recent work of Shinn & Robbin (1983) appears closer to the calculated values, as they report 50% compaction of lime sediments for 100m (328ft) of burial.

Bed thickness values allowed the calculation of compacted porosities for the Arcente, and these are plotted on a porosity-depth diagram (Fig. 4.25), showing a very rapid decrease in carbonate mud porosity. Indeed, a decrease much greater than that proposed by published porosity-depth curves for carbonate rocks (e.g. Hardenbol et al., 1981; Schmoker & Halley, 1982). However, compaction ratios calculated average 1.51 for the southern flank of Muleshoe Mound, a similar figure to that found by Truyol (1989) for the shallow burial of fine-grained sediments.

To model the pore fluid pressure history for the Arcente calculations were made for 5 stages during the deposition of the Dona Ana, allowing no pore fluid release from the Arcente. Hence the values represent a maximum value for the pore fluid pressure. Calculations are based on a formation fluid density of 1.04g/cm^{-3}, equivalent to a fluid salinity of 36,000mg/l Cl^- at 20°C, and a mud density of 2.60g/cm^{-3}, which have been estimated on the basis of ODP data from the Bahamas (Schlumberger, 1972; Lavoie, 1988). The modelling also assumes that the Arcente formed a sealed unit during Dona Ana times. Figure 4.26 illustrates the fluid pore pressure 'window' within which the fluid pressure at the base of the Arcente must have been during the deposition of the Dona Ana. Bedding patterns, particularly in the lowermost stratal package of the Dona Ana, suggest some compaction of the Arcente occurred syn-depositionally, although this appears to be only a very small percentage of the total compaction, the majority of which can be demonstrated to have occurred post-depositionally. Any syn-depositional compaction of the Arcente means that the pore fluid pressure lies to the left of

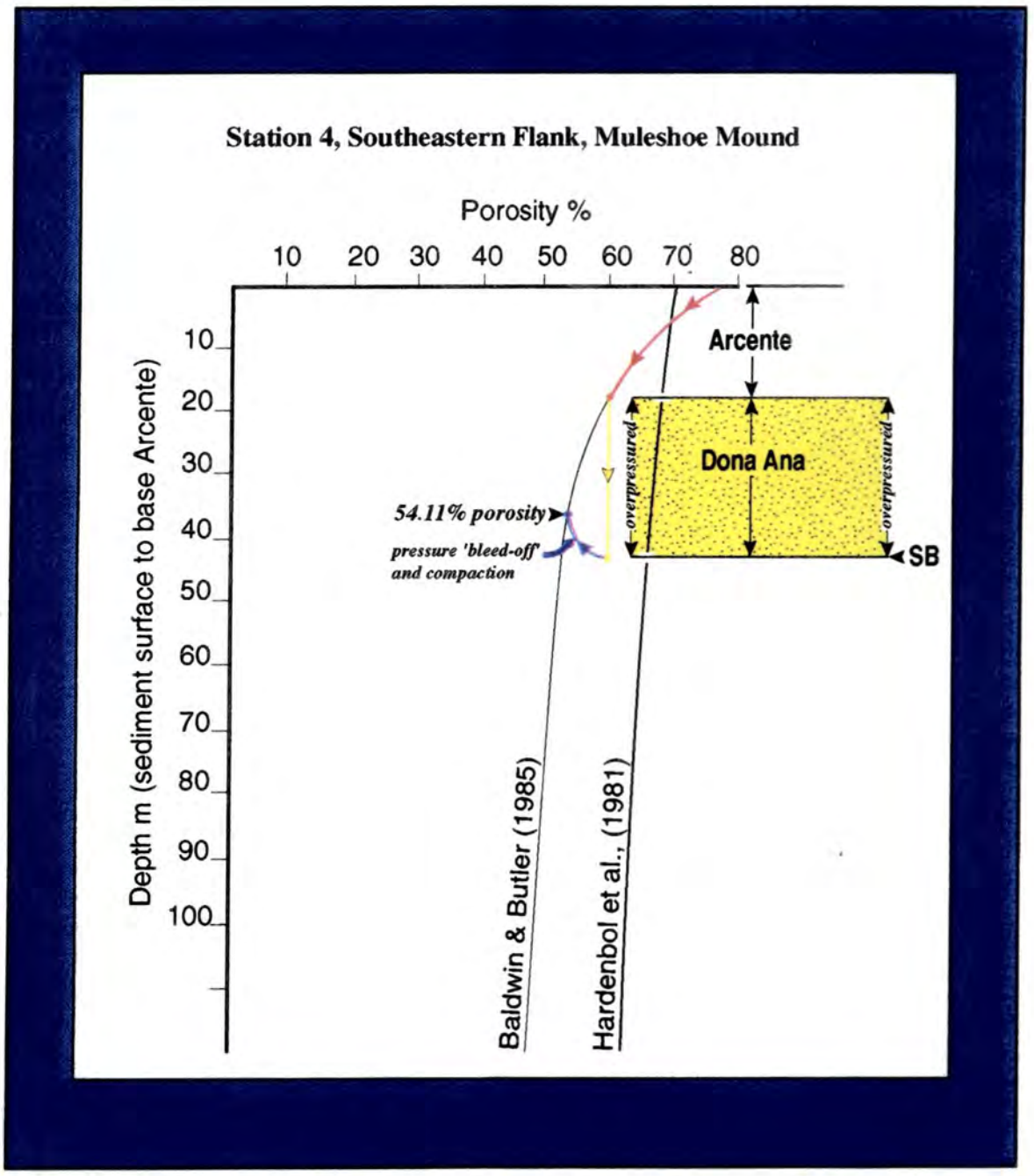

Figure 4.25a-c Porosity-Depth profile for the Arcente at: (A) station 4, (B) station 7, and (C) station 11, of the southeastern flank of Muleshoe Mound (see Figure 4.22). Porosity evolution is believed to follow a path similar to the Baldwin & Butler (1985) curve until the Dona Ana is deposited. At this point, a situation of no porosity-loss is shown (i.e. zero compaction), until the end of Dona Ana deposition, when pore fluid pressure bleeds-off during the hiatus, and Arcente porosity is reduced by compaction to a point on/close to the Baldwin & Butler (1985) curve.

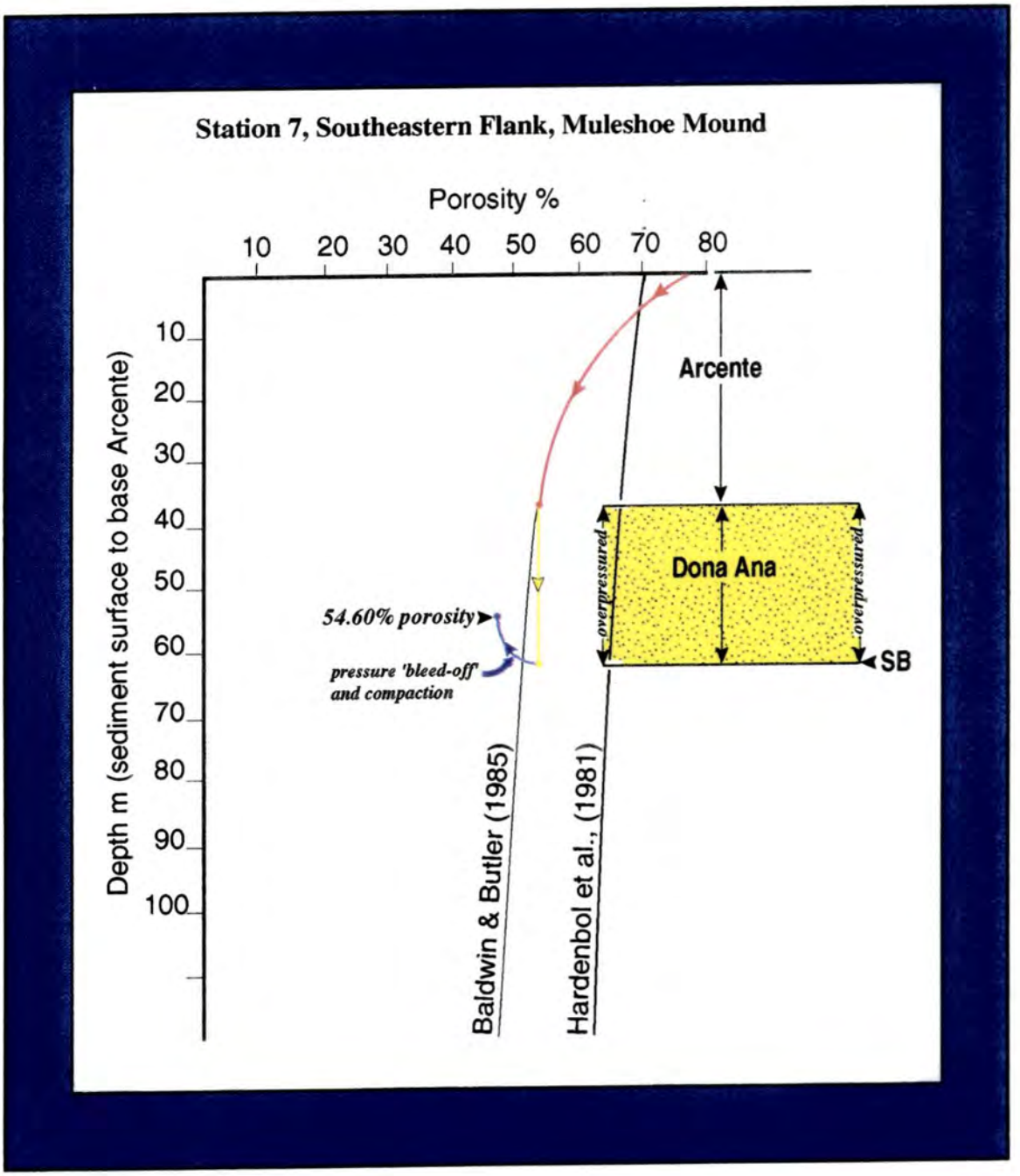
Station 7, Southeastern Flank, Muleshoe Mound
Porosity %
10
20
30
40
50
60
70
80
Depth m (sediment surface to base Arcente)
10
20
30
40
50
60
70
80
90
100
Arcente
Dona Ana
overpressured
overpressured
SB
54.60% porosity
pressure 'bleed-off' and compaction
Baldwin & Butler (1985)
Hardenbol et al., (1981)

Figure 4.25b

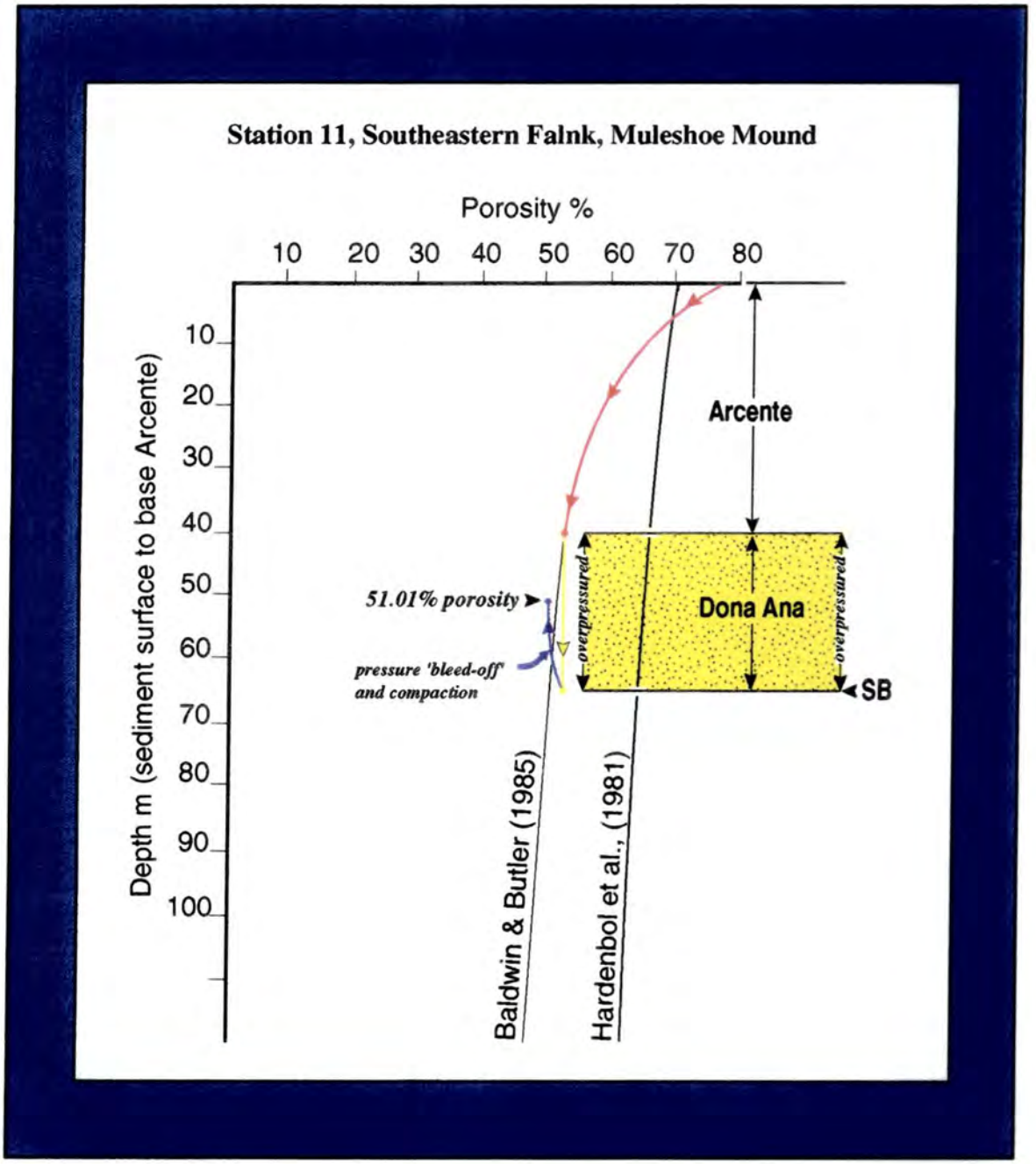
Station 11, Southeastern Falnk, Muleshoe Mound
Porosity %
10
20
30
40
50
60
70
80
Depth m (sediment surface to base Arcente)
10
20
30
40
50
60
70
80
90
100
Arcente
Dona Ana
overpressured
overpressured
SB
51.01% porosity
pressure 'bleed-off' and compaction
Baldwin & Butler (1985)
Hardenbol et al., (1981)

Figure 4.25c

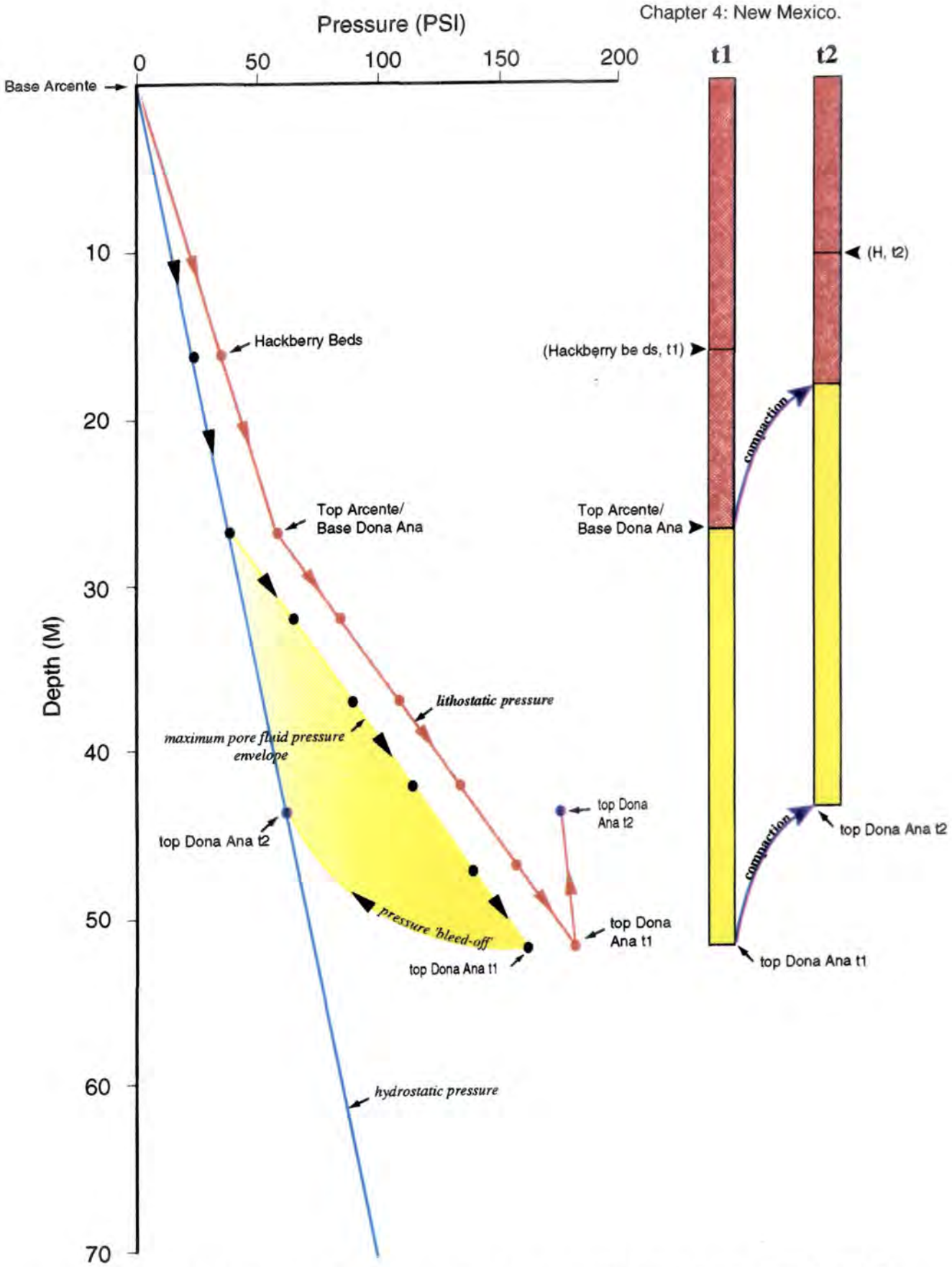

Figure 4.26a-c Pressure-Depth plot for the Arcente at: (A) station 4, (B) station 7, and (C) station 11, of the southeastern flank of Muleshoe Mound (see Figure 4.22). Dark arrows show the pore fluid pressure evolution, which is hydrostatically pressured until the Dona Ana is deposited. The yellow envelope of the graph illustrates the maximum possible pore fluid pressure (i.e. no compaction during Dona Ana deposition). Pore fluid pressures are interpreted to lie somewhere within this envelope, and can never attain lithostatic pressure. The thicknesses t1 and t2 represent the Arcente (red) and Dona Ana (yellow) before and after compaction, respectively.

Hydrostatic, Lithostatic and Maximum Pore Fluid Pressure Paths
Station 7, Southeastern Flank, Muleshoe Mound,
Sacramento Mountains, New Mexico

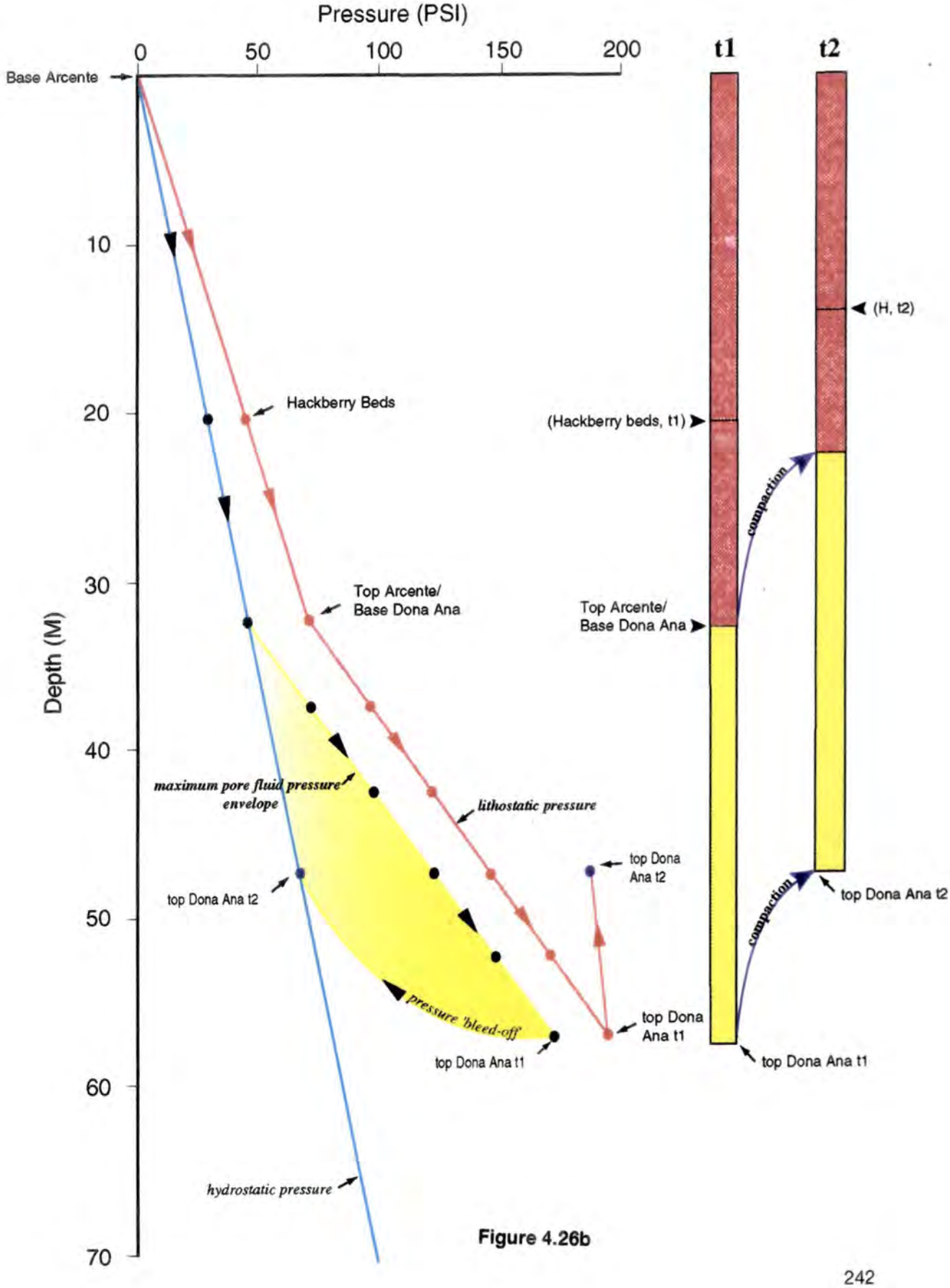

Figure 4.26b

Hydrostatic, Lithostatic and Maximum Pore Fluid Pressure Paths
Station 11, Southeastern Flank, Muleshoe Mound,
Sacramento Mountains, New Mexico

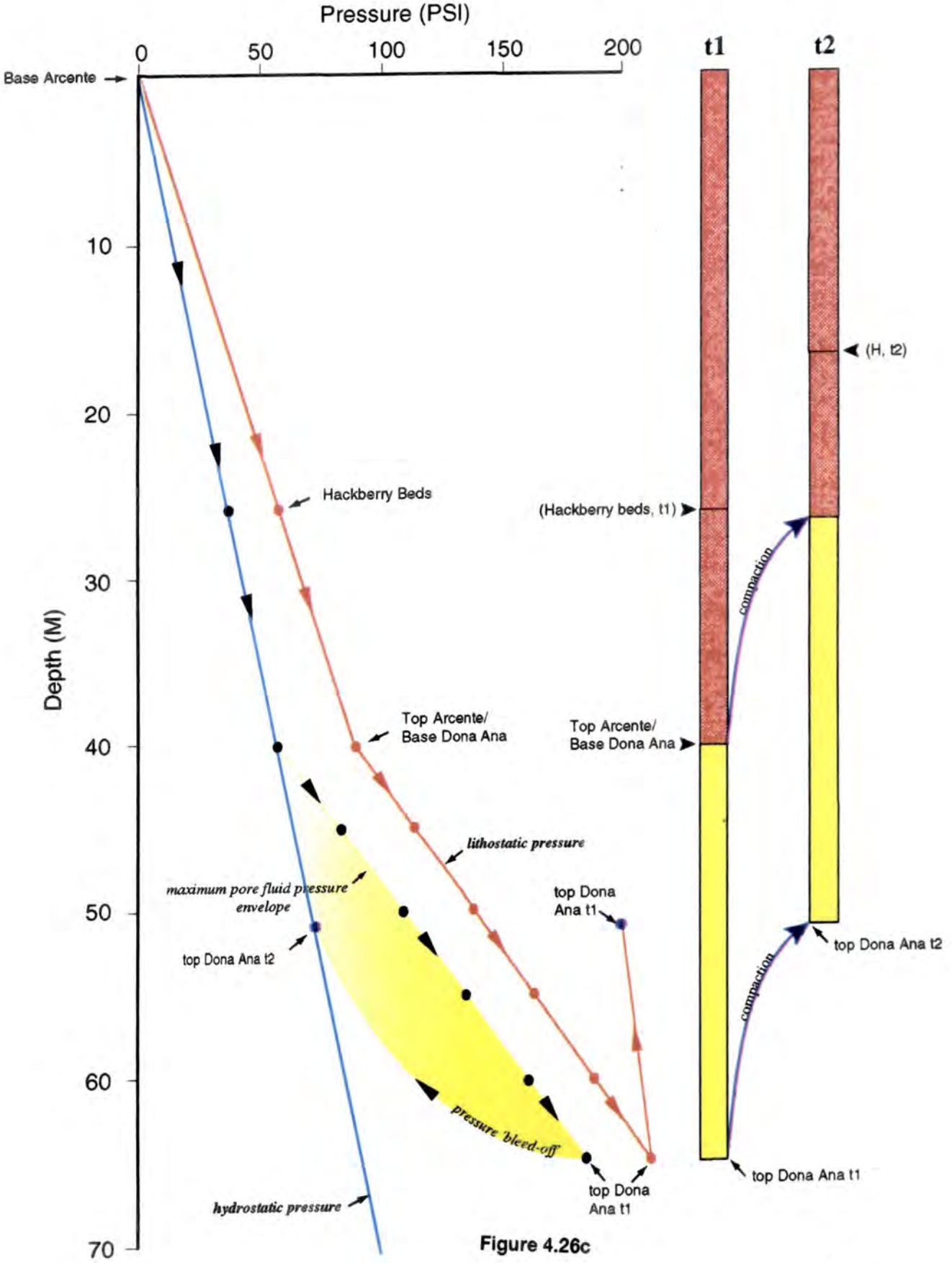

Figure 4.26c

the maximum pore fluid pressure line on Figure 4.26 (i.e. somewhere in the pressure 'window'). Figure 4.26 also illustrates that the maximum pore fluid pressure within the Arcente never reached lithostatic pressure, the point at which the sediment will 'fail' and catastrophically dewater. This point is also supported by the fact that no sedimentary structures are apparent within the exposures of the Arcente to suggest that rapid dewatering had occurred in the sediments surrounding Muleshoe Mound.

The production of overpressure allows a qualitative assessment of the relative rates of deposition and compaction (Fig. 4.27). During the deposition of the Dona Ana the rate of compaction must have been considerably less than the rate of deposition, reflecting the low permeability of the Arcente muds. Possibly only slow dewatering and compaction of the Arcente occurred at this early stage of burial, until a more effective seal was formed. As more Dona Ana was deposited the compaction rate of the Arcente became appreciably less than the rate of deposition. This is interpreted to represent either an improvement in the sealing of the Arcente, or a more rapid deposition of the Dona Ana, resulting in progressively larger amounts of overpressure building up within the Arcente (Fig. 4.28a-b), as described earlier. Once deposition ceased at the end of the Dona Ana, compaction rates exceeded the deposition rates and pore fluid began to bleed off in an attempt to attain equilibrium compaction and hydrostatic pore fluid pressure (Fig. 4.28c). It was during this period, when the compaction rate had risen relative to the deposition rate, which was effectively zero, that the majority of the 33% compaction of the Arcente occurred as overpressure was reduced by dewatering, and the Dona Ana beds were rotated due to thickness variations approaching the mound. Rates of dewatering were greatest immediately after deposition ceased due to the greater pore fluid pressure gradients after Dona Ana deposition, and compaction rates gradually decreased along with the decrease in pressure gradients (Fig. 4.27). This story is slightly complicated as compaction proceeded at a lower rate than the rate of pore fluid pressure build-up during a 'forced regression' (Fig. 4.27) when pore fluid pressure built once more. Compaction 'catch-up' occurred immediately after this episode as the overpressured pore fluids bled off (Fig. 4.27). The effects of sea-level on compaction rates and pore fluid pressures will be discussed in more detail later.

Pore fluid would have flowed at a slow rate, with the overpressure acting as the driving force to dewatering. Flow pathways can probably be separated into three groups depending upon the position of pore fluid within the

Compaction Rate vs Time

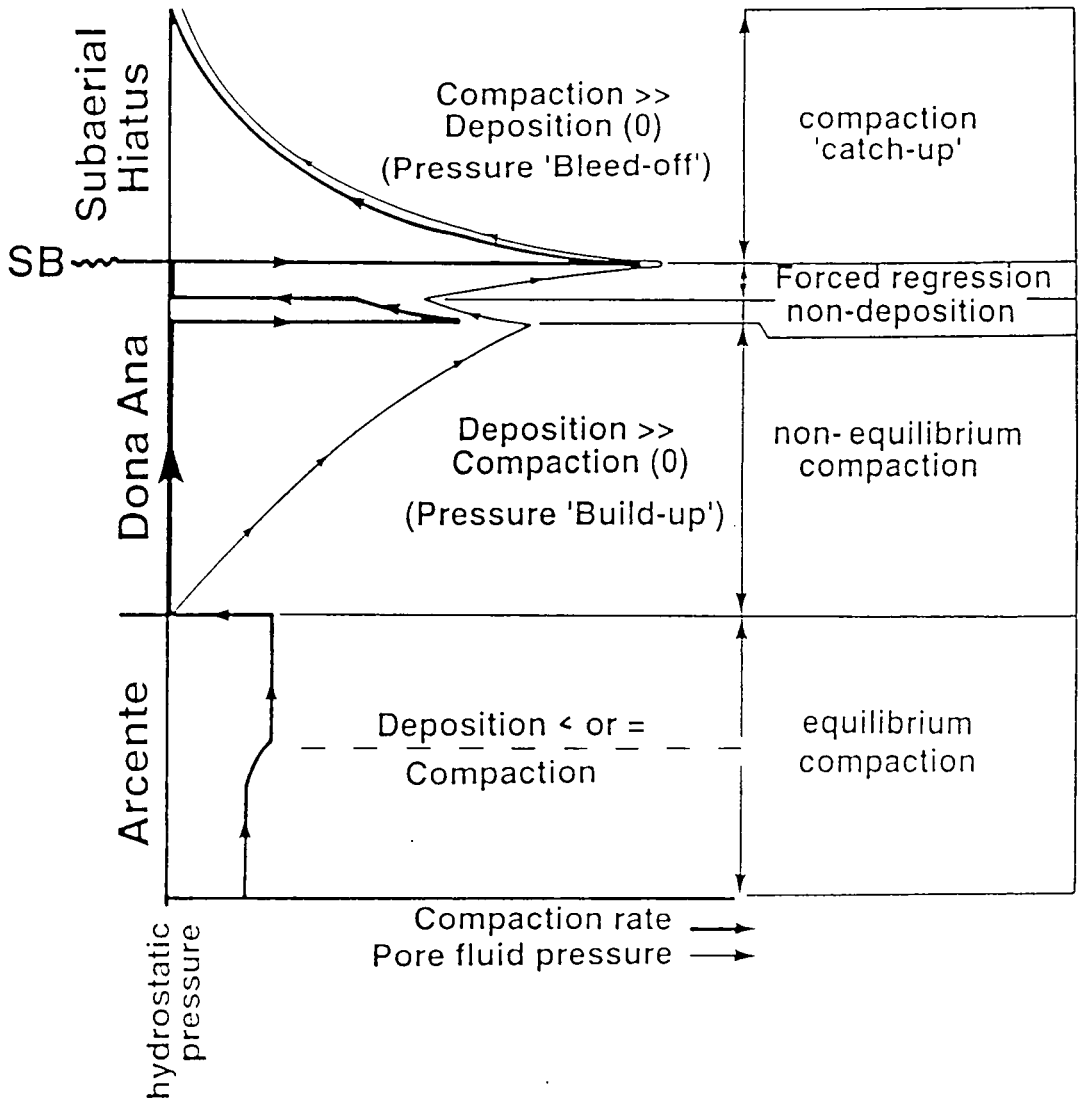

Figure 4.27 Schematic diagram of compaction rate versus time. Note the majority of compaction occurring during the hiatus post Dona Ana deposition, after pore fluid pressures have built up during the Dona Ana, a period of very little/no compaction.

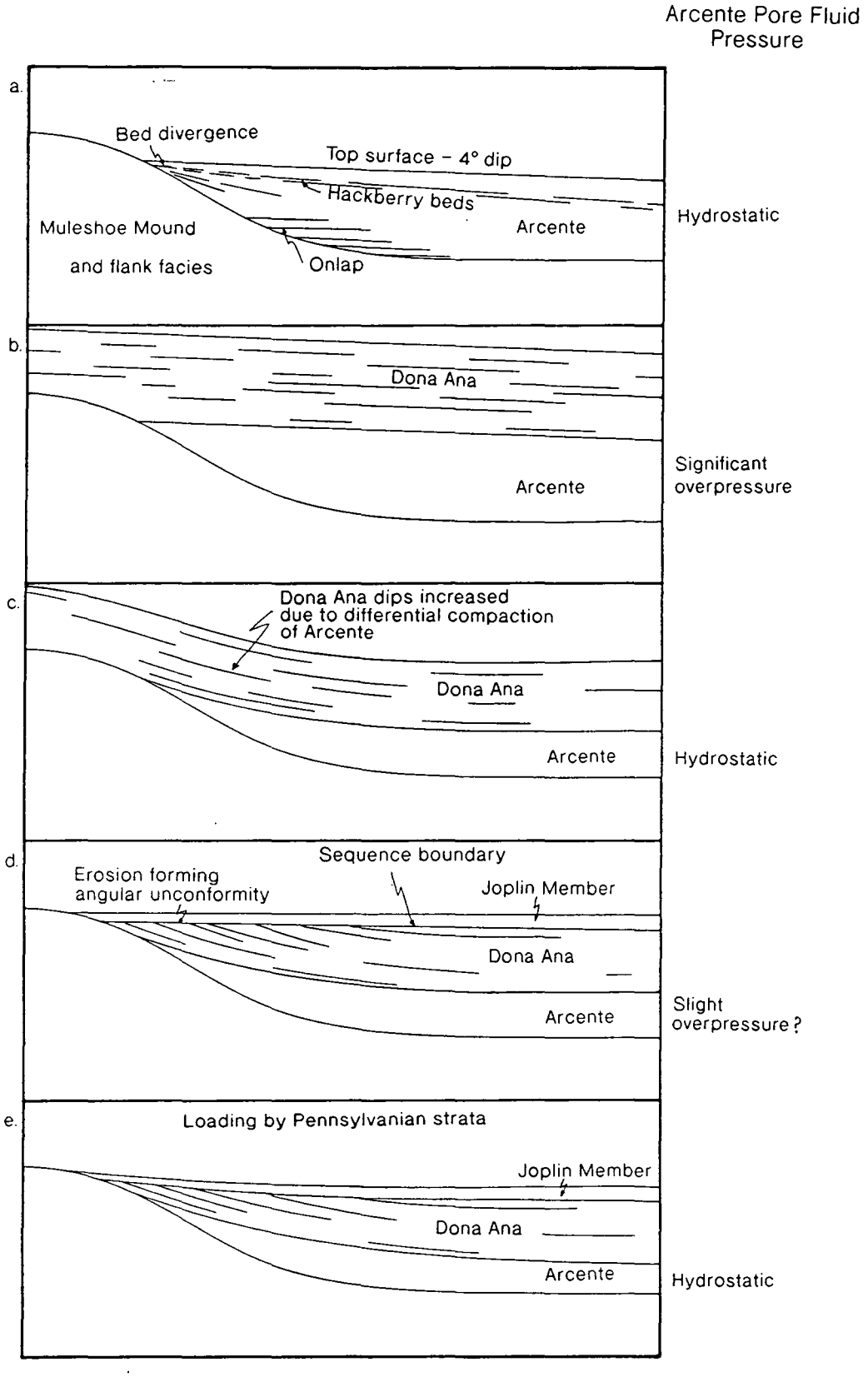

Figure 4.28a-e Interpreted depositional history and pore fluid pressure development, for the southeastern flank of Muleshoe Mound.

Arcente. Firstly, pore fluid within the Arrow beds, the uppermost section of the Arcente, would probably have been forced upwards into the more permeable grainstones of the Dona Ana. This pathway will have provided the fastest route for fluid expulsion, and therefore represents the fastest region of compaction. Secondly, pore fluid near the base of the Arcente section may have been forced down into the flank sediments of Muleshoe Mound, where permeabilities would have probably been greater than the lime muds within certain coarser horizons. At this point fluid flow would most likely have been oblique, climbing up bedding towards the mound itself, to be expelled at the upper mound contact with the Arcente. Finally, the slightly more grainy units within the Hackberry beds may also have provided more permeable flow pathways that would have expelled pore fluid in a horizontal direction towards Muleshoe Mound. Pore fluid within these central parts of the Arcente section probably required the longest periods of time to be expelled, and hence, were the main contributing factors to the slow compaction rates of the Arcente.

After a 25 to 30° bed rotation of the Dona Ana had occurred during the period of non-deposition, erosion of the topographically high areas took place during subaerial exposure, resulting in the formation of the sequence boundary. Loading of the Arcente was re-established by the Rancheria Formation (Fig. 4.28c-d), mainly consisting of the later Joplin Member in the proximity of Muleshoe Mound, and containing no lithoclasts of the underlying Dona Ana. The reintroduction of sedimentation created the local angular unconformity between the Dona Ana and the Rancheria Formation (Fig. 4.28d). Unlike the Dona Ana, it is impossible to separate the amount of Arcente compaction that occurred during this stage from the total amount of compaction seen today. It is also impossible to compare the compaction rate of the Arcente to the deposition rate of the Joplin Member, and propose overpressure or its absence within the Arcente section at this time. Therefore, from this point only total burial compaction can be assessed (Fig. 4.28e). The final part of Table 4.1 shows the calculations where between 45 and 57% compaction (an average of 51% compaction) of the Arcente has occurred. Compacted porosities are calculated as before, but burial depth is uncertain (Estimates of the thickness of sediments above indicate a minimum depth of 2Km). Compaction ratios for total burial average 2.06. Bed rotation occurred further during subsequent burial as the top surface of the Joplin Member is rotated from its presumed original horizontal attitude (Fig. 4.28e). However, the amount of rotation at this stage is an order of magnitude less than that which occurred due to loading by the Dona Ana.

4.7.2 Differential Compaction Around Sugarloaf Mound.

Superficially, Sugarloaf Mound provides a similar example of differential compactional control upon stratal relationships as seen at Muleshoe Mound. A similar angular relationship between the base of the Rancheria Formation and the underlying Dona Ana can be seen, with the beds of the Dona Ana becoming increasingly older as the mound is approached (e.g. Fig. 4.15). However, the angular relationship is a result of the depositional dips of clinoformed Dona Ana strata, being truncated by the Apache beds and Rancheria deposits. Therefore, the two 'giant' mounds show a very different bedding relationship between the Lake Valley Formation and the overlying Rancheria Formation. The relationship between the Arcente and the Dona Ana is also significantly different compared to Muleshoe Mound, which probably provides the reason as to why stratal patterns differ. The main difference concerns the exact timing of compaction within the Arcente Member surrounding Sugarloaf Mound.

Exposures of the flanking strata to Sugarloaf Mound are complicated by the 'secondary' Dona Ana bioherm, and the large clinoforms of the Dona Ana (Fig. 4.14 and Plate 4.3). The underlying Arcente Member is thinner here, and only fills a small part of the depositional topography created by the bioherm, unlike Muleshoe Mound. Also, the topmost section of the Arcente, the Arrow beds, is considerably thinner (<2m (6.6ft)) with the Dona Ana deposited very close to the top of the Hackberry beds. The major contrast between the Arcente - Dona Ana contact is that at Sugarloaf Mound the Arcente muds are deformed and folded (Fig. 4.14 and Plate 4.3). Importantly, there is discordance between the bedding of the Arcente and the overlying Dona Ana units, with the Dona Ana beds downlapping onto the top surface of the deformed Arcente muds (Fig. 4.11 and Plate 4.2). This contrasts with the exposures of Muleshoe Mound where the bedding between the Arcente and Dona Ana units is concordant.

The angle of unconformity between the Dona Ana and the overlying Deadman Member of the Rancheria Formation does not appear to be increased by differential compaction of the Arcente mud. Dips within the Dona Ana beds are depositional, reflecting their deposition as clinoforms that have been eroded (Fig. 4.29c-d). Their offlapping relationship means that the individual units of the Dona Ana young away from the mound. There is no indication of post-Dona Ana bed rotation due to differential compaction of the Arcente Member. This contrasts with Muleshoe Mound where bed rotation occurred during the hiatus in sedimentation at this level, leading to the

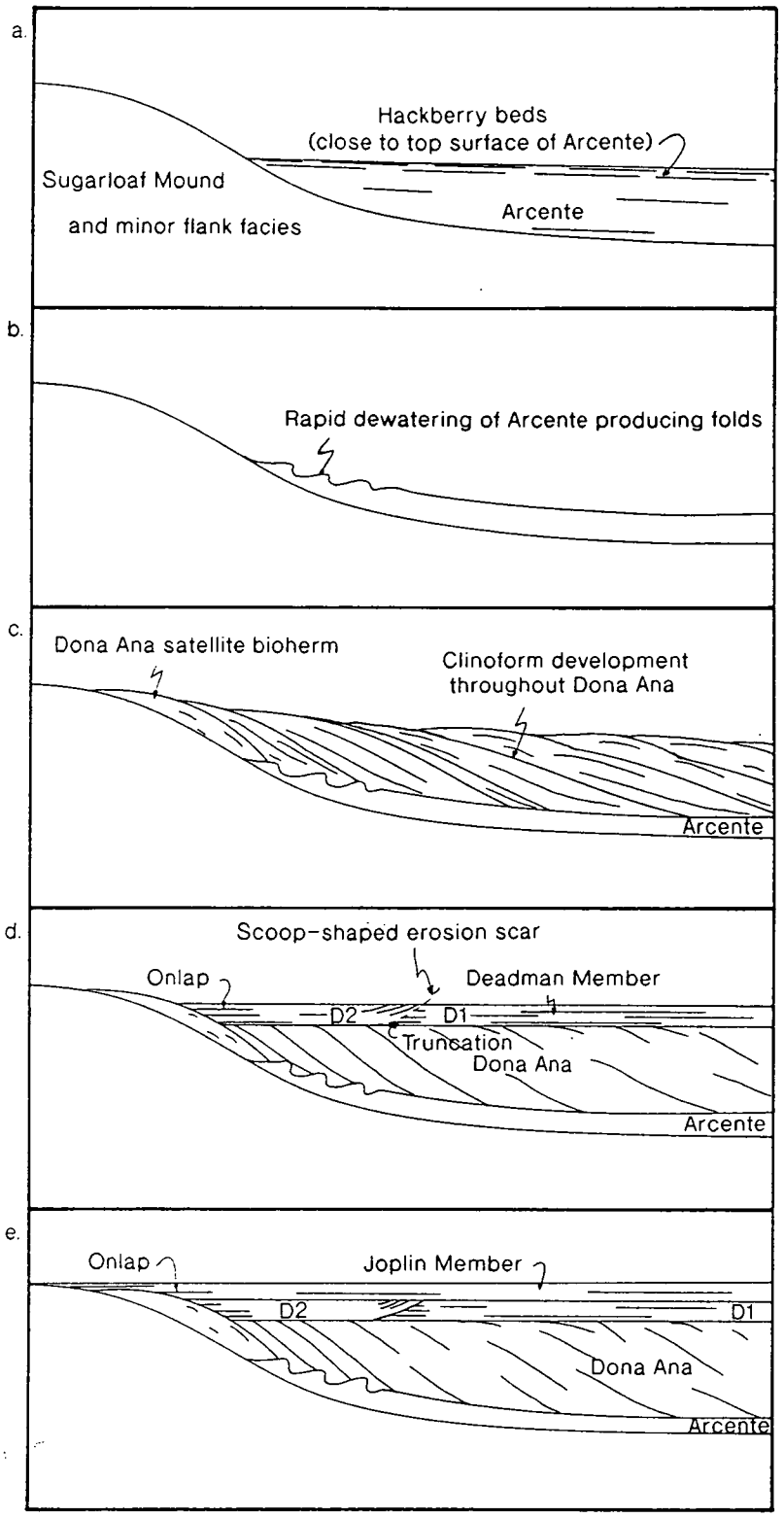

No significant bed rotation due to differential compaction of the Arcente as large amounts of pore fluids are expelled early.

Figure 4.29a-e Interpreted depositional history and pore fluid pressure development, for the southeastern flank of Sugarloaf Mound.

conclusion that the compaction of the Arcente muds at Sugarloaf Mound occurs in a different fashion and time to that at Muleshoe Mound.

The stratal relationships suggest that at Sugarloaf Mound the Arcente muds had fully autocompacted to an equilibrium condition prior to Dona Ana deposition (Fig. 4.29a). During the initial stage of bioherm growth loading of the Arcente occurred to the south of Sugarloaf Mound by the satellite bioherm. Its growth is interpreted to have created higher pore fluid pressures in the underlying region of the Arcente, as the bioherm growth and loading of the Arcente exceeded the rate of pore fluid bleed off during this early stage. However, as loading increased the process is interpreted to have continued until pore fluid pressures reached the point at which catastrophic dewatering occurred (Fig 4.29b). This sudden dewatering of the Arcente probably occurred as pore fluid flowed horizontally away from the mound in a 'wave-like' action, deforming the bedding within the Arcente into a series of asymmetric folds (Fig 4.29b). Further satellite bioherm growth and progradation in the Dona Ana developed clinoforms which prograded and downlapped onto the deformed Arcente, which had now reached equilibrium compaction and hydrostatic pore fluid pressure (Fig. 4.29c-d). The Apache beds are only developed to the south of the flank strata, and probably represent the remnant depositional topography and sedimentary bypass after progradation (Fig. 4.29e). They eroded the topsets of the Dona Ana clinoforms, producing the angular relationship (Fig. 4.7). Finally, the Rancheria Formation was deposited, and eroded the uppermost section of the satellite bioherm, producing the angular relationship in this area (Fig. 4.7)

Differences in the stratal patterns between Muleshoe and Sugarloaf Mounds can be attributed to the different compactional behavior of the Arcente section at both locations. It appears that at Sugarloaf Mound the Arcente had mainly dewatered **prior** to loading and there was no production of large amounts of near-surface overpressure during the deposition of the later stratal packages of the Dona Ana (Fig. 4.29a-c). In contrast, at Muleshoe Mound the Arcente section had failed to dewater at a rate equal to that of deposition of the Dona Ana sediments and had, therefore, built up near-surface overpressure. Indeed, the Arcente section may not have autocompacted at a rate necessary to achieve equilibrium pore fluid pressures during its own deposition at Muleshoe Mound. There is also a major difference in the style of the loading of the Arcente between the two mounds. At Sugarloaf Mound, the Arcente is 'point-loaded' by the satellite bioherm, creating a pressure wave of pore fluid away from the mound. In

contrast, the Arcente surrounding Muleshoe Mound has a broad load of Dona Ana effectively blanketing the entire surface, therefore not producing a pressure wave of pore fluid away from the mound.

It is proposed that the local thickness of the Arrow beds may play an important role in the compactional behavior of the Arcente section. The Arrow beds may have formed a temporary 'seal' to the section, hindering the expulsion of pore fluid and thus producing under-compaction and near-surface overpressure in the Muleshoe Mound region. This in turn may reflect the difference in the palaeogeographic location of the two mounds, with Sugarloaf Mound being closer to the open ocean in the south, and having only a very thin section of Arrow beds. Pore fluid flow within the Arcente muds may have been easier due to the lack of "confinement" of the Arcente section at Sugarloaf Mound, contrasting with the same section on the platform that was "baffled" by numerous large and small buildups.

4.7.3 Differential Compaction Above Dona Ana Channels - Dog Canyon.

A. Introduction.

Unlike the previous two examples, where the emphasis has been on the differential compaction of the Arcente muds and its specific timing, the following section deals with the compaction of the Apache beds within the topmost section of the Dona Ana. As described in section 4.6.3 the Apache beds on the northern cliff section of Dog Canyon form lens-shaped channel cross-sections (Fig. 4.8 and Plate 4.5). The underlying Arcente beds are also folded and deformed as at Sugarloaf Mound, and therefore, using that location as an analogy, it is assumed that the compaction of the Arcente section had very little effect on the deposition of the Dona Ana and the overlying Rancheria Formation in the area. Hence, the present study concentrates on the deposition and compaction of the Dona Ana, the overlying Deadman Member (D1 to D3), and the Joplin Member. It investigates the production of topography above the channels, the development of unconformities within the Deadman Member, and the formation of the 'tube' structures on the southern side of Dog Canyon.

B. Qualitative Data.

Compactional modelling of the Dog Canyon channels is slightly more difficult and subjective than the earlier examples. The reason is that unlike at Muleshoe Mound, where the bioherm is early cemented and therefore incompactible, making it simple to reconstruct the original surface of the

Arcente section with very few assumptions, no such reconstruction can be made for the exposures in Dog Canyon. Here, there is no "reference point" of zero compaction about which beds can be rotated to their original thicknesses. Therefore, with all horizons having been compacted during their subsequent burial, estimation of their original depositional thickness is extremely difficult. The same problem was encountered for the modelling of Ridge Basin sediments in Chapter 3, where vitrinite reflectance data aided estimation of the maximum depth of burial. In the present case, Meyers & Hill (1983) show that similar coarse-grained skeletal grainstones were deposited at 42% original porosity, and have compacted to 27% porosity. These data provides the best estimates for compacted porosities of the Dona Ana channels, and will be used throughout the subsequent modelling.

C. Methodology.

Modelling of the channel sections is generally similar to the modelling of Muleshoe Mound (see section 4.7.1). Figure 4.30 shows channel W1, which was divided into ten equally spaced sections. To allow calculations to be carried out several assumptions have to be made:-

- The Arcente - Dona Ana contact approximates a horizontal surface.
- The Dona Ana channels were original deposited with flat tops.
- The Dona Ana deposits consist of a lower sandy horizon, a middle mud dominated section, and topped by sand dominated channels.
- The average compacted porosity of the channel sands is 27%, and can be estimated by comparison with the study of Meyers & Hill (1983).
- The average depositional porosity of the channel sands is 42% (Meyers & Hill, 1983).
- Sands compact according to the equation of Sclater & Christie (1980); lime muds compact according to the curve of Hardenbol et al. (1981)
- Section 7 formed the thickest original section of the Dona Ana.

The first assumption permits the present thickness of the Dona Ana sand, the Dona Ana mud, the Apache beds, and the Deadman Member to be measured (i.e. the primary data). Assuming that the Apache beds were deposited as flat-topped channels with interchannel areas enables the construction of a horizontal line to represent the compacted position of the

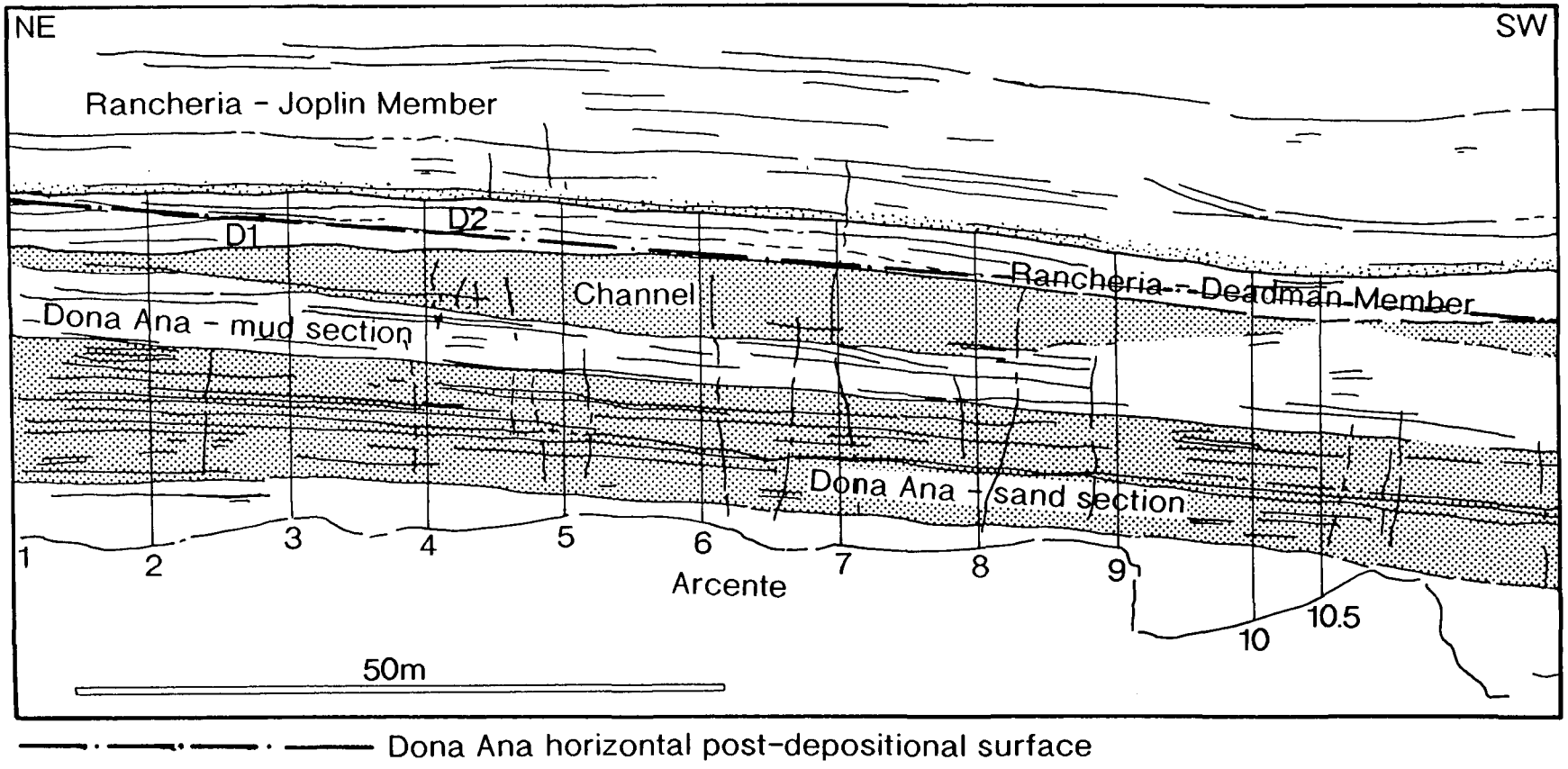

Figure 4.30 Channel W1, northern flank of Dog Canyon, divided into 11 stations for stratal restoration and compaction modelling

original depositional surface. The line forms a tangent to the present day channel top because of the differential compaction that has occurred due to the change in thickness of the muddy Dona Ana section immediately underlying the channels, and due to the change in facies from coarse-grained channel deposits to fine-grained interchannel muds (Fig. 4.30).

The porosity estimates from the work of Meyers & Hill (1983) allow the calculation of the original depositional thicknesses of both the basal sand section, and the Apache beds. Further, their porosity estimates enable an estimation of the compacted mud porosity at the same depth of burial, assuming the sands compact according to Sclater & Christie (1980), and the lime muds compact according to the curve of Hardenbol et al. (1981). Taking section 7 as the thickest, it is now possible to calculate the original thickness of the mud unit for all the other measured sections. Hence, the percentage compaction of the mud unit can now be assessed.

D. Calculations.

Table 4.2 shows the primary data taken from field photographs and line drawings of channel W1. Calculation of original thicknesses are made possible using equation 4.2, and compaction ratios from equation 4.3 (see section 4.7.1). The original mud unit thickness is calculated by subtracting the original basal sand thickness and the original channel sand thickness from the decompacted thickness of section 7. Percentage compaction of the mud is then assessed using equation 4.1.

E. Results and Implications.

The original thickness of section 7 is 28.55m (94ft), and therefore represents the thickness of the Dona Ana blanket at this location. Correcting all the mud thicknesses to produce a flat topped and based Dona Ana section, provides the estimates for the mud unit thickness, from which the percentage compaction can be assessed. Percentage compaction of mud ranges from 46-61% with an average of 54.53%. The compaction ratio for the mud deposited at 70% porosity and compacted to 29% porosity is approximately 2.3.

Estimates for the percentage compaction of the muddy section of the Dona Ana, and the interchannel areas are very close to those calculated for the Arcente section compaction at Muleshoe Mound (i.e. 54% compaction compared to 51%). However, care is needed as the modelling of the Dog Canyon channels is only one end-member to several possibilities, with a

number of assumptions having to be made. Most of the assumptions explained above can be justified using published research, and changes in the values assumed make little difference to the final calculation. However, taking section 7 as the total thickness of the Dona Ana means that all mud thicknesses are corrected to produce an even 'blanket' of Dona Ana. Changes are made in the mud thickness because it is this unit where most errors in thickness estimation and compactional modelling will occur. Further to this is the fact that the Dona Ana mud unit is not purely fine-grained mud like the Arcente, but contains some coarser-grained beds within it, thus affecting its compactibility.

Compactional modelling provides useful information on the amount sediments compact when buried. Often it is somewhat harder to understand at what time, and at what rate, this compaction has occurred. However, the Apache bed channels exposed in Dog Canyon provide unique evidence that begin to answer the questions concerning the timing of compaction. The evidence comes in the form of small scale angular unconformities (exposures up to 10m (33ft) across), where angular differences of <10° are developed within the overlying Deadman Member. These unconformities usually, but not always, separate the three stratal packages of the Deadman Member (D1 to D3), described in section 4.6.3.

As stated earlier in section 4.6.3 the lowermost D1 stratal package is parallel with the convex top of the buried channel. The following dark-weathering peloidal grainstone eroded the top of the D1 strata forming a subtle angular unconformity (Fig. 4.18 and Plate 4.10). It is therefore postulated that the D1 stratal package was deposited at a rate slightly greater than the rate of underlying compaction, hence producing near-surface overpressure. As deposition stopped compaction of the buried section occurred in an attempt to achieve equilibrium compaction. A product of this differential compaction was bed rotation within the D1 stratal package, and the slight doming of the top surface of the Apache bed channels. Deposition of the dark-weathering peloidal grainstone eroded the topography of the depositional surface, producing the angular unconformity (Figs. 4.16 & 4.18, and Plates 4.9 & 4.10). Sedimentation temporarily stopped again, with compaction occurring post-depositionally creating topography over the channel deposits. When sedimentation began again, the deposited beds onlapped the peloidal grainstone from the east, and eventually covered the entire section, forming the upper section of the D1 stratal package (Figs. 4.16 & 4.18, and Plates 4.9 & 4.10).

Sedimentation rates during D1 deposition overall appear to have been greater than compaction rates, and therefore once deposition of D1 had ceased compaction 'catch-up' occurred in the underlying section. This created significant topography on the depositional surface, with the palaeotopographic highs situated above the Apache bed channels (Fig 4.31). In the region of channels W1 and W2 it appears that the topography produced by differential compaction created instability within the sediment which subsequently slumped, leaving behind a scoop-shaped slump scar. Silicification along the scoop-shaped slump scar shows that there was a significant break in sedimentation between the deposition of the D1 and D2 stratal packages. Deposits of the D2 stratal package filled the erosional topography (Figs. 4.16, 4.18 & 4.31, and Plate 4.9). Field evidence of syn-sedimentary boudinage (Plate 4.11) developed within the D2 stratal package suggests that some differential compaction was occurring during deposition of D2, creating a stretching effect of the beds as they rotated due to underlying differential compaction across the channel axes. However, differential compaction also occurred post-D2 deposition, once again creating topography over the channels. This was finally eroded by, or prior to the deposition of the D3 stratal package creating another angular unconformity (Figs. 4.16 & 4.18, and Plates 4.9 & 4.10).

Concordant with the exposures around the Muleshoe Mound area, the observations made in Dog Canyon support a model of near-surface compaction occurring syn-depositionally to a small degree, but with depositional loading occurring at a greater rate than underlying compaction. This created a substantial amount of near-surface overpressure. Excess pore pressure dissipated during a hiatus in sedimentation, as the pore fluids attempted to reach a value equivalent to hydrostatic pressure. During periods of pore pressure dissipation bed rotation occurred, and a small angular unconformity could be created due to erosion of the topography produced on the depositional surface, or by the onlapping of this topography.

Stratal patterns on the southern side of Dog Canyon differ significantly, but still show evidence of differential compaction. Section 4.6.3 describes the unique 'tube' structures found within the Rancheria Formation of the southern cliffs of Dog Canyon, and the western escarpment of the Sacramento Mountains, running south to Deadman Canyon (Fig. 4.1). Within this region there appears to have been differential near-surface cementation of the Deadman beds which cover the Dona Ana section. Once deposition of the Deadman beds ceased, differential compaction occurred across the

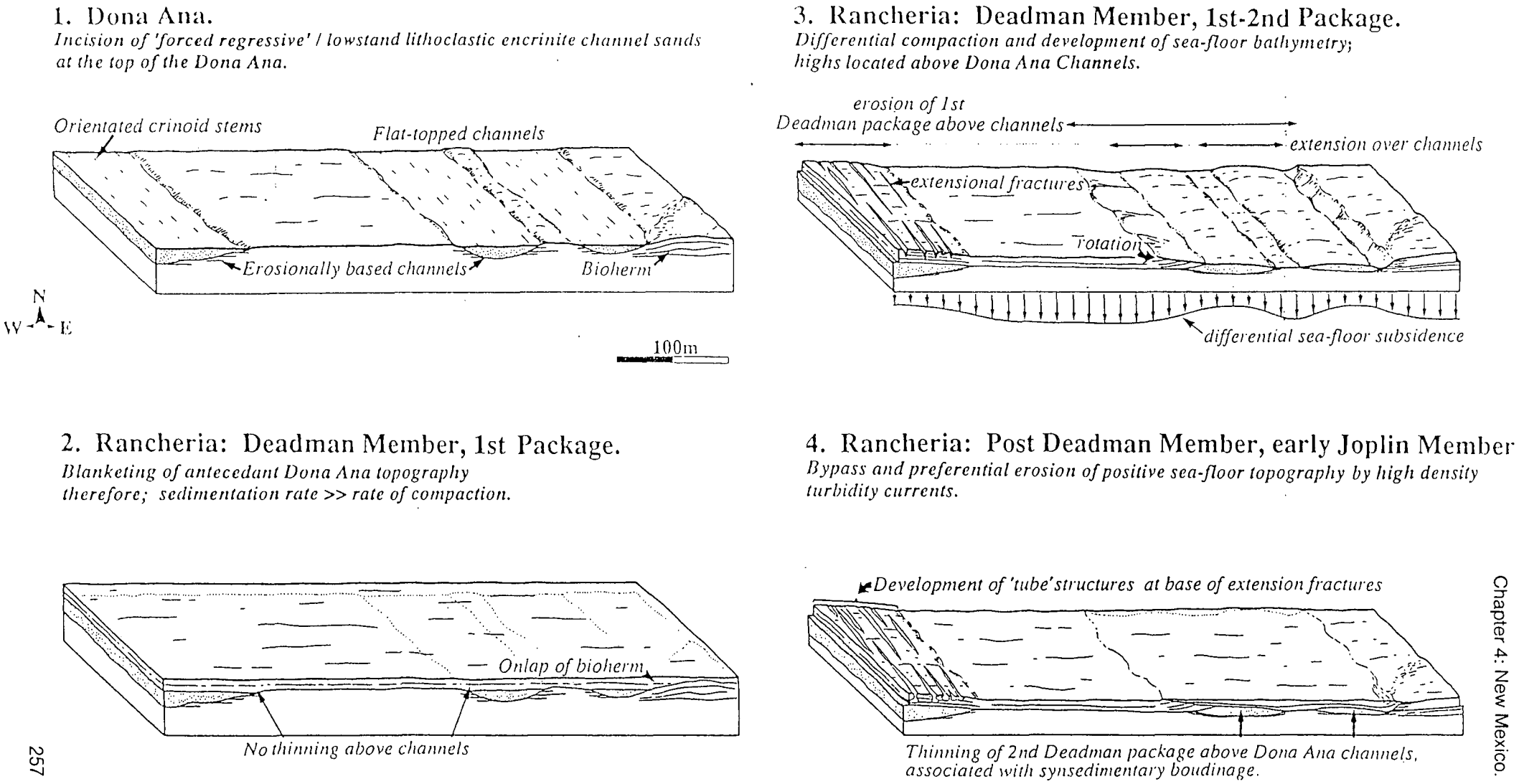

Figure 4.31 Block diagrams showing the influence of differential compaction over the Dona Ana channels upon Rancheria sedimentation (From Hunt & Allsop, 1993).

underlying Apache bed channels with the associated production of topography across the channel sections (Fig. 4.31). Due to the cementation of the Deadman beds in this region, the extension over the channels resulting from differential compaction was accommodated by a series of neptunean dykes aligned parallel to the underlying channels (Fig. 4.31d). The dykes formed open fractures on the sea-floor, and defined the course of the earlier channels. Turbidite deposits of the Joplin Member scoured the dykes, enlarging them by eroding the less cemented beds within the Deadman section. The introduction of turbidites also temporarily improved the oxygenation level of the sea water (from anaerobic to dysaerobic) allowing opportunistic organisms (*Trypanites* and *Gastrochaenolites*) to bioturbate the Deadman beds, including the neptunean dykes (Plate 4.16).

4.8 Conclusions.

The field outcrops viewed in the Sacramento Mountains of New Mexico provide a considerable amount of information concerning differential compaction and the overall process of sediment compaction. Importantly, the outcrops provide unique data concerning the exact timing of compaction, and some clues as to the speed at which this compaction may have occurred. Therefore, the understanding of the compactional process is greatly enhanced, enabling the refinement of forward modelling techniques of compactional effects within other depositional systems (e.g. submarine fan deposition, see Chapters 5 & 6).

With regards to differential compaction, evidence appears to show that large amounts of bed rotation, and sea-floor topography can be produced provided that compaction occurs post-depositionally. If compaction occurs syn-depositionally any sea-floor topography is subdued more or less instantaneously, resulting in an essentially flat sea-floor (in most clastic and bioclastic settings). However, outcrop data from Muleshoe Mound suggest that this may not generally be the case. Stratal patterns surrounding Muleshoe Mound illustrate that the depositional rate of the Dona Ana section is greater than the compaction rate of the underlying Arcente mud. Bed relationships within the lower stratal packages of the Dona Ana show evidence for a small amount of syn-depositional compaction. However, this only forms a very small proportion of the total amount of compaction appropriate to the applied load.

A necessary requirement of post-depositional compaction is that near-surface overpressure must have been developed within the Arcente section.

Overpressure will be reduced when the rate of compaction is greater than the rate of sedimentation, leading to the fact that the effects of compaction are expressed greatest at hiatal surfaces or condensed sections. This in turn produces angular discordances and unconformities through erosion, and/or once sedimentation begins again. The outcrops at Muleshoe Mound and exposures across the channel deposits in Dog Canyon illustrate this process. Mathematical calculations allow the limits of the amount of overpressure to be quantified and assessed, hence outlining a pore pressure envelope within which pore fluid pressure existed during the loading of the Arcente by the Dona Ana.

What is the cause of the delay in compaction of the underlying sedimentary section? At this shallow depth of burial (0-100m (328ft)), sediment compaction essentially consists of mechanical grain rearrangement and a large amount of dewatering concurrent with porosity destruction. The permeability of the sediment is therefore the main control upon the speed at which a sediment may dewater, and thus the speed of compaction. Permeability is also reduced along with porosity during compactional grain rearrangement, thus as burial and compaction proceed the ability for the sediment to compact, and the rate at which compaction occurs will slowly be reduced. It therefore follows that the deeper within the sedimentary column, the less favourable the sediment characteristics become with respect to dewatering and the inherent compaction involved. Thus the length of time needed for these sediments to compact to an equilibrium state increases.

When a hiatus in sedimentation occurs, as is interpreted between the Deadman Beds of the lower Rancheria Formation and the Joplin Beds of the upper Rancheria Formation in Dog Canyon, compaction still occurs within the sedimentary section, providing it has been loaded at a rate greater than the rate at which it can compact during deposition. This happens especially within the deeper buried sedimentary sequences, and if the resulting compaction is differential, topography will be created upon the depositional surface by bed rotation. The local thickness of the Arrow beds may also play an important role in the compaction of the Arcente, forming a seal to dewatering. Where these beds are thicker, such as surrounding Muleshoe Mound, the seal is more effective than in areas where the Arrow beds are thin, around Sugarloaf Mound for example.

Sea-Level Effects on Near-Surface Compaction.

Variations in relative sea-level may also have an effect on pore fluid pressure, and hence compaction rate. The magnitude of this effect depends upon the rate, amplitude and direction of the fluctuation in sea-level, combined with the prior condition of the strata in terms of equilibrium compaction. This is an extremely important observation as it adds a sequence stratigraphic context to compaction, a link not previously made.

Near-surface overpressure may be produced/accentuated by a rapid fall in relative sea-level, as the component of the overburden represented by the sea water column is removed. Such a mechanism has been proposed to account for the widespread, contemporaneous redeposition of pelagic sediments across western Europe in the upper Cretaceous (Hilbrecht, 1989). The amount of overpressure induced is a function of the rate and amplitude of the sea-level fall (Hilbrecht, 1989). During the sea-level fall, overpressure will be induced in the sediment as the water column is gradually reduced, and compaction will be restricted. Compaction will recommence in strata that were previously in a state of disequilibrium compaction, once sea-level has reached its lowest point, or when the rate of fall is equal to or less than the rate of compaction. Sediments which were previously in a state of equilibrium compaction before the fall in sea-level will dewater, however, this will not be related to compaction as overburden has been removed from the section. Immediately after the fall in sea-level dewatering, and hence, compaction rates will be increased due to the greater pore fluid pressure gradients.

Rises in sea-level may also have a similar effect, causing an increase in the rate of compaction. In strata that were previously in a state of equilibrium compaction, the compaction rate can increase to match that of the rising sea-level. However, compaction rates can only keep up with the rate of sea-level rise until the rate of rise exceeds the rate of sediment dewatering. If the latter scenario occurs then pore fluids become overpressured, delaying compaction. Subsequently, compaction rates will be temporarily accelerated once the rate of sea-level rise has fallen below that of dewatering.

Both falling and rising sea-level can therefore induce compaction, and in any scenario where the resultant compaction occurs differentially bed rotation may occur. Across shallow-water carbonate shelves, compaction-induced subsidence will therefore be most apparent if sea-level fall exposes the platform, after rapid progradation over wedge-shaped basinal sediments. During the lowstand the shelf is deformed by the differential compaction of the basinal sediments, and the topography induced may be onlapped when

the shelf is subsequently transgressed. The upper surface of the Cassian dolomites of the Triassic Sella platform, Northern Italy (e.g. Doglioni & Goldhammer, 1988) is an example of where unconformities develop in such a way (Fig. 4.32). Here, the highstand systems tract (HST) progradation of the Cassian Dolomite was greater than the compaction rate of the underlying San Cassiano Formation, a wedge-shaped mudstone package. During the falling stage and lowstand systems tract (LST) the platform top was rotated by differential compaction as the San Cassiano Formation dewatered in an attempt to achieve equilibrium compaction. At the same time, the Durrenstein Formation lowstand wedge was deposited, and the platform was arched into a gentle anticline (Fig. 4.32). The succeeding Raibl Formation (transgressive systems tract) thins by onlap across the toplap strata of the deformed platform (Fig. 4.32).

Likewise, the VP2 sequence boundary in Apache Canyon, Sierra Diablo platform (Fig. 4.33) is also developed along basinwards rotated toplap strata (Fitchen & Starcher, 1992). In this example the VP1 HST strata, whose toplap strata were originally deposited sub-horizontally, prograded over and filled the erosional relief of the Hueco Group. Subsequent differential compaction rotated the toplap strata in a basinwards direction (Fitchen & Starcher, 1992). Compaction-induced subsidence created two important features. Firstly, it provided the accommodation space in which the VP2 LST and TST are developed (Hunt et al., 1994). Only poor development of both these sequences in a more basinward location would have occurred without the differential compaction. Secondly, it induced fractures within the top of the VP1 platform as beds attempted to rotate, and hence controlled Karst development at this location. The VP2 TST strata finally onlap the rotated HST toplap strata. As on the southern flank of Muleshoe Mound, the sequence boundaries were "enhanced" through differential compaction.

Similar deformation of the shelf-top can also be developed when platforms are drowned. A possible example seen on seismic of this type of unconformity occurs across the margins of an isolated Miocene platform, offshore Sarawak (Epting, 1989). Topsets of the platform's final progradational phase are domed upwards above the margins of its initial build-up phase, over which they prograded. These are onlapped by basinal sediments of the following drowning succession, and downlapped by the terminal buildup phase (Fig. 4.34) (interpreted from Epting, 1989). This example illustrates how compaction catch-up occurred during times when carbonate sedimentation was temporarily shut-down, both during the LST,

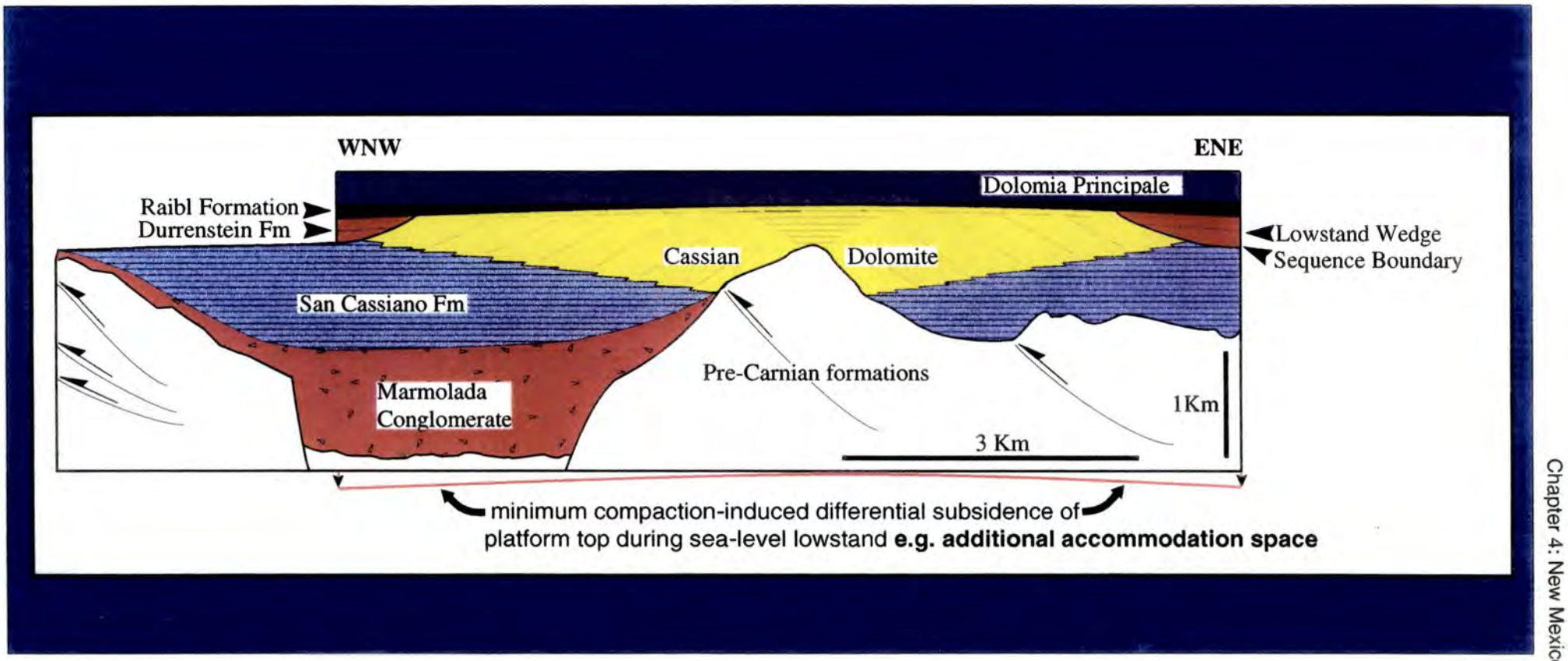

Figure 4.32 The Triassic Sella Platform in the Dolomites of northern Italy (From Doglioni & Goldhammer, 1988), deformed into a broad anticline due to the differential compaction of the San Cassiano Formation, during deposition of the Durrenstein lowstand wedge. Deformation creates the 'compactionally-enhanced' unconformity between the Cassian Dolomite and the overlying, wedge-shaped Raibl Formation.

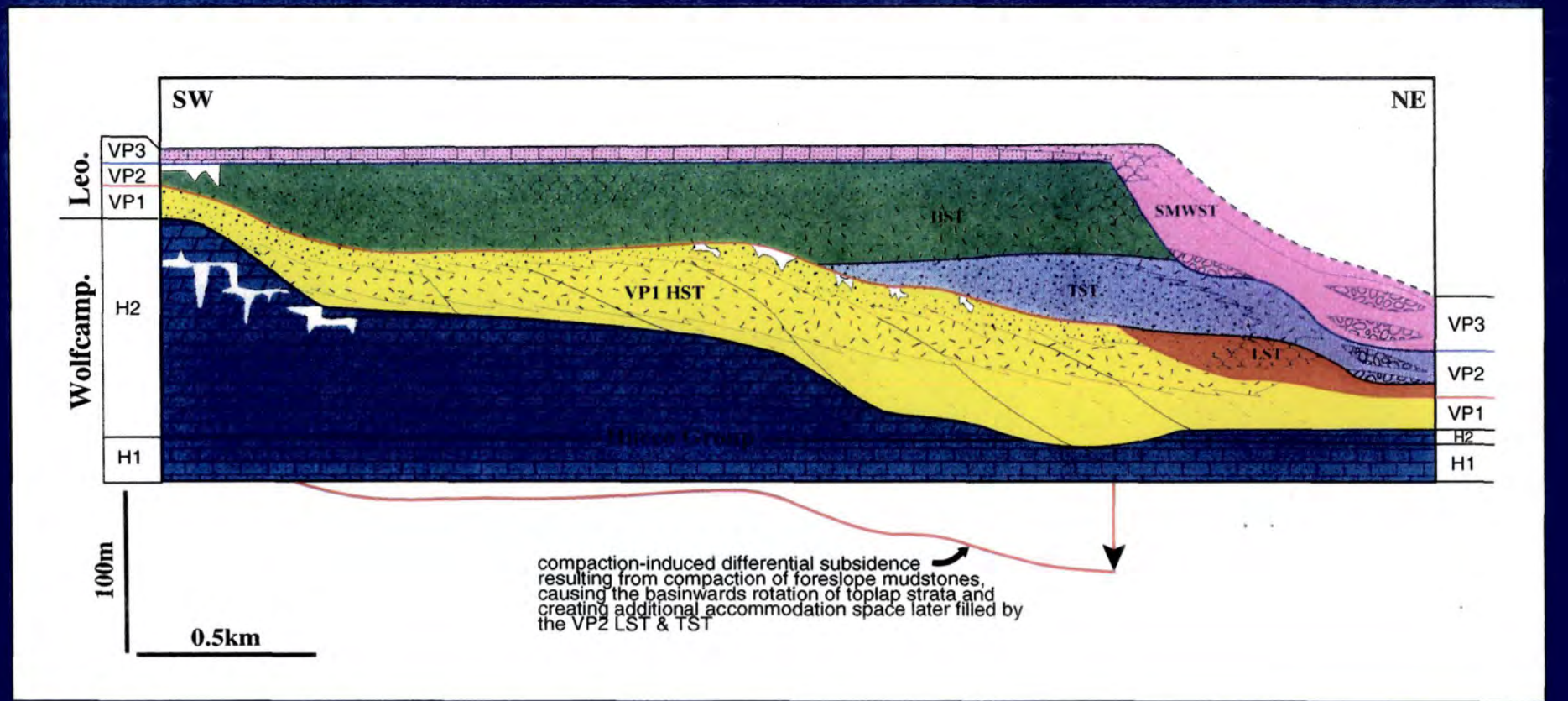

Figure 4.33 The Permian platform as seen in Apache Canyon, Sierra Diablo, West Texas (From Fitchen & Starcher, 1992), where toplap strata of sequence VP1 are rotated basinwards due to differential compaction. The resulting topography controls the location and size of the VP2 lowstand and transgressive systems tracts. The unconformity between VP1 and VP2 is 'compactionally-enhanced', and karst also appears to be controlled by the differential compaction of the underlying strata.

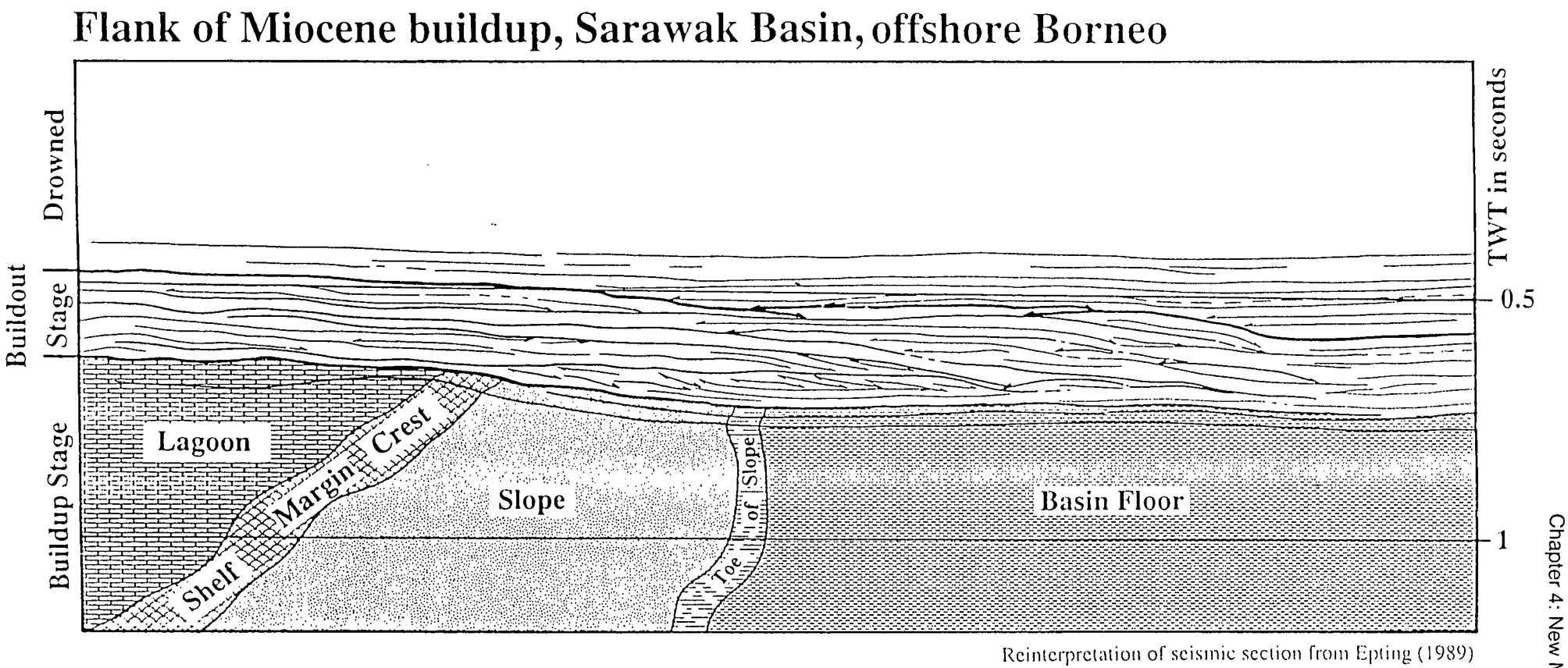

Figure 4.34 Isolated Miocene Platform, offshore Sarawak (From Epting, 1989), showing doming of final progradation phase due to differential compaction, onlapped by subsequent basinal sediments.

and when the platform was temporarily drowned in the TST. On the deep water flanks of carbonate platforms, reduced sedimentation rates may coincide with lowstands of relative sea-level, when the platform is exposed. The drowning of the shelf by rapid relative sea-level rises and environmental changes can also shut-down or severely impair carbonate sedimentation. These times can also be associated with the development of compaction-induced topography, as is seen above the Apache bed channels in Dog Canyon.

To summarise, during the HST, rapid progradation leads to dis-equilibrium compaction of low permeability basinal mudrocks. During the falling stage of sea-level, the LST and the TST, compaction catch-up occurs in the overpressured muds, providing that rates of compaction are greater than the rate of sea-level fluctuation. During this time, the combined effects of both increased rates of underlying compaction, and reduced sedimentation rates can cause the development of 'enhanced' unconformities, particularly if the underlying mud is wedge-shaped, and therefore differential compaction and bed rotation occurs.

4.9 Summary.

Incremental restoration of stratal relationships on the flanks of two carbonate buildups and across a bioclastic submarine channel complex in the Sacramento Mountains, New Mexico, demonstrate:-

- Temporal and spatial variations in the attainment of 'equilibrium' compaction (i.e. when overburden is entirely supported by matrix grains in the underlying strata, and pore fluid pressure is hydrostatic).
- The development of sea-floor topography during a non-depositional hiatus as a result of differential compaction.
- The influence of compaction-induced topography on subsequent patterns of sedimentation.

These and other observations are significant as they imply that compaction of lime mudstones up to 50-60% occurred with only shallow burial (<50m (164ft)), a figure markedly different from that obtained from published compaction curves for carbonate rocks (see Hardenbol et al., 1981; Schmoker & Halley, 1982; Baldwin & Butler, 1985). This discrepancy is attributed to a disparity between the rates of overburden accumulation and formation dewatering.

The results of this part of the present work suggest that porosity variations within the shallow subsurface (here <130m (427ft)) reflect a complex interplay between rates of dewatering and sedimentation, relative sea-level changes and also load distribution. They suggest that a simple, predictable relationship between the depth of burial and porosity (as apparently implied by idealised porosity-depth curves) may be unlikely at shallow depths of burial (i.e. <100m (328ft)).

The conclusion follows that the delay in compaction interpreted from the fieldwork in the Sacramento Mountains of New Mexico, is probably due to the permeability characteristics of the buried sediments and the sealing capability of mud horizons, especially the Arcente muds in the case of Muleshoe Mound. This conclusion is likely to hold true for other sedimentary settings such as submarine fans, where the pelagic muds are loaded at a very high rate by turbidite deposits that are laid down in a matter of hours/days (i.e. geologically instantaneous) (Reading, 1986). Near-surface pore pressure will therefore be increased due to this rapid loading, with the muds compacting at a slower rate relative to turbidite sand deposition. Subsequently topography will be created on the depositional surface during times of non-deposition due to muds compacting post-depositionally to a greater amount than the coarse-grained channel deposits, and the fact that turbidite deposition upon submarine fans is intermittent. Differing mud types will probably compact at different rates, some compacting quickly, while others may compact relatively slowly. The slower the rate of compaction of the mud the greater the topography produced post-depositionally during a hiatus in sedimentation, allowing dewatering, grain packing and equilibrium compaction to be attained.

Field data, observations, stratal reconstructions and modelling of the Mississippian deposits of the Sacramento Mountains of New Mexico have allowed important insights into the process of compaction. For the modelling of siliciclasic deposition in the submarine fan environment these insights will provide a greater control upon the production of topography at the depositional surface by gravitational differential compaction. A qualitative assessment of compaction rates with respect to depositional rates can also be attempted, and built into the modelling process.

Chapter 5: North Sea - Montrose and Arbroath Oilfields.

5.1 Introduction.

This chapter aims to apply the principles of compaction, and differential compaction, to the Arbroath and Montrose oilfields (Blocks 22/17 and 22/18 of the U.K. North Sea). This chapter includes a stratigraphy of the fields and the general area, the facies and their geometries, a depositional model for the reservoir section, along with a basic history of field development. Data consist of a detailed seismic survey, mainly covering the Arbroath oilfield to the south, but also overlapping the southeastern section of the Montrose oilfield. Well data are available from both oilfields, comprising of 20 deviated wells drilled from the platform at Arbroath, and a similar 26 deviated wells from the platform at Montrose. A further 4 vertical wells are present within this area. A few wells contain cored sections of the reservoir interval, and these have been included in the present study.

Combination and analysis of all the available datasets have allowed a detailed model of sediment deposition, distribution, geometry and sedimentology to be formulated. This has further allowed a model upon which the influence of compaction, especially differential compaction, can be assessed and modelled. Additional data, interpreted from fieldwork in both California and New Mexico (see Chapters 3 & 4) have enabled a detailed model of compactional control and influence upon deposition, facies geometry and distribution to be formulated for the Montrose - Arbroath area.

5.2 Field Stratigraphy.

The Montrose and Arbroath fields are located approximately 130 miles (208Km) east of Aberdeen, and are situated toward the south-central part of the Forties-Montrose High (Fig. 5.1). The Forties-Montrose High is an important structural feature, 50 miles (80Km) long within the Central Graben, that extends from Block 21/10 and the Forties Field in the north, to Block 22/24 and the Marnock discovery in the south. Development of this hörst feature, which has an approximate NNW to SSE trend, and plunges towards the south, can be related back to the Carboniferous, where the hörst area formed part of a larger positive Carboniferous block of Variscan tectonic origin (Crawford et al., 1991). During the early stages of the opening of the Atlantic, in late Permian times, the development of the North Sea graben system began, along with the formation of the Forties-Montrose High. The high itself is bounded on the east and west by normal faults (Fig. 5.1).

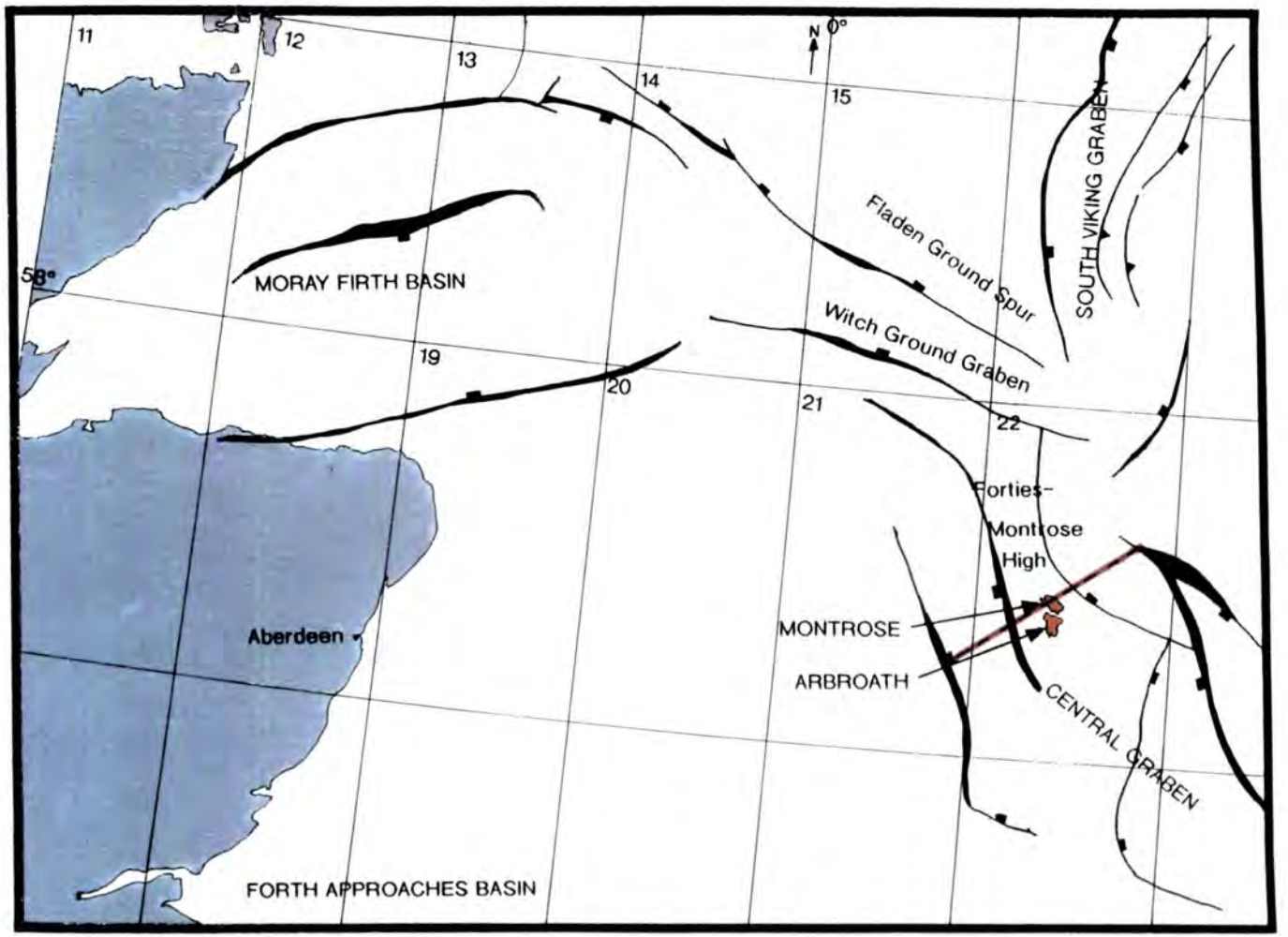

Figure 5.1 Location map of the Montrose and Arbroath oilfields, and major tectonic structures of the area. Red line represents Zieglers (1982) cross-section of the region (see Fig. 5.49).

Likewise, its north and south ends are also bounded by normal faults with an approximate east-west trend, however these faults are believed to be defined by probable Carboniferous (Variscan) features which were rejuvenated in the late Permian period (Crawford et al., 1991). Movement on all the bounding faults reached a maximum during the Triassic, but still continued into the Jurassic. Due to the complete absence of any Carboniferous and Jurassic section in the Montrose - Arbroath area, combined with a regional thinning seen in the Zechstein, Triassic, Cretaceous and Palaeocene sections, it is suggested that the area was a dominant, positive feature from the Palaeozoic through to the Tertiary (Fig. 5.2) (Crawford et al., 1991).

Both wells 22/18-1 and 22/18-4 penetrate Devonian age sediments in the Montrose - Arbroath area, these being the oldest rocks penetrated (Fig. 5.2 & 5.3). They consist of a siltstone/shale sequence with infrequent intercalations of thin, fine sandstone beds. As stated before, no Carboniferous strata are present in the area. Combined with the fact that no derived clasts of Carboniferous origin have been identified in the Permian siliciclastic section it has been suggested that the Montrose-Forties hörst was a positive feature during Carboniferous times, resulting in non-deposition (Fig. 5.3) (Crawford et al., 1991). The Permian is represented by rocks attributed to both the Rotliegendes Formation and the Zechstein Group. The Rotliegendes Formation comprises shales interbedded with tight and porous sandstones deposited in an, as yet, undetermined environment (Fig. 5.3). The overlying Zechstein is represented by a carbonate section composed entirely of amorphous micritic dolomites, sometimes vuggy with vugs open or fully dolomite cemented. The depositional environment of the Zechstein has proved difficult to interpret, but the absence of any evaporites in this region, coupled with the presence of the sometimes thick, massive dolomite beds with thin shale beds suggest that the Montrose - Arbroath area was positive in Zechstein times (Crawford et al., 1991).

Throughout the Triassic the area remained positive, resulting in the subaerial exposure of the Zechstein section, and the creation of karstic porosity and microporosity in some areas, with coeval cementation elsewhere (Crawford et al., 1991). The Triassic is thin, approximately 122m (400ft) thick, and is represented by continental red beds of mudstone and siltstone (Fig. 5.3). Tectonic activity at periods throughout the Triassic is evidenced by the presence of conglomerates, composed of boulders and pebbles of the same red beds, deposited along the Forties-Montrose High fault scarp (Crawford et al., 1991). Drilling has so far shown that sediments belonging to the Jurassic

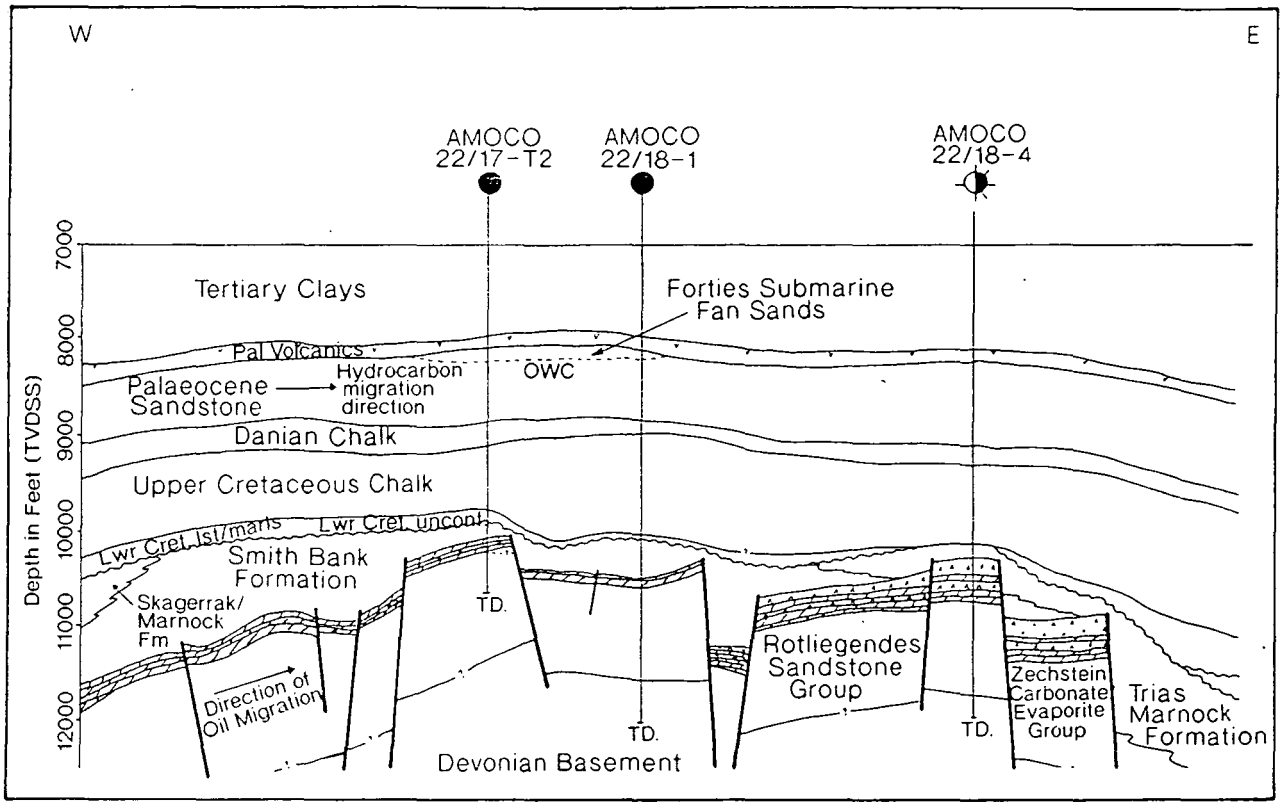

Figure 5.2 Forties-Montrose High and Arbroath Field structural cross-section (From Crawford et al., 1991).

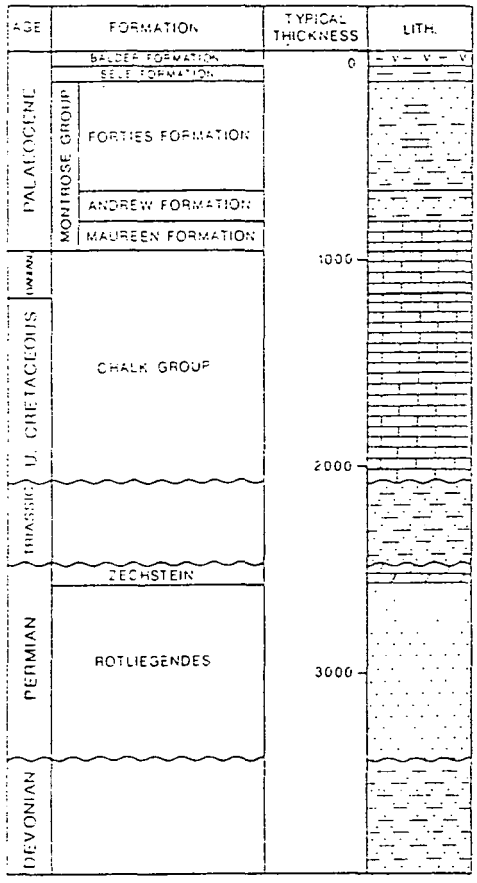

Figure 5.3 Stratigraphic succession for the Montrose - Arbroath area (Modified from Crawford et al., 1991).

System are absent in the Montrose - Arbroath area, and Lower Cretaceous sedimentation is represented only by a thin sequence of Aptian to Albian chalk-marls. Chalk of the Upper Cretaceous is of the order of 300m (1000ft) thick (Fig. 5.3) (Crawford et al., 1991).

Chalk sedimentation is represented throughout the area by the Ekofisk Formation, continuing into the Early Palaeocene (Fig. 5.3). The majority of the Palaeocene interval however, is represented by mass flow deposits of the Montrose and Moray Group (Fig. 5.3 & 5.4) (Mudge & Copestake, 1992). These begin with resedimented chalk conglomerates/breccias and sandstones of the Maureen Formation, which are of variable thickness (up to 60m (200ft)). The overlying Andrew Member of the Lista Formation (Fig. 5.4), is approximately 30 to 107m (100 to 350ft) thick, and represented by shales and turbidite sandstones (Fig. 5.3). Overall the Andrew Member sequence exhibits a general coarsening, and sometimes thickening, upwards trend. Sandstone units reach a maximum thickness of approximately 30m (100ft). Likewise, the overlying Forties Member of the Sele Formation, the beginning of the Moray Group, preserves a similar tendency to coarsen and thicken upwards. The Forties Member is 90 to 180m (300 to 600ft) thick, consisting of a turbidite sand sequence, where the beds reach a maximum thickness of 18 to 21m (60 to 70 ft). This section was termed the Forties Sandstone Member by Carman & Young (1981), and formed the upper part of the Forties Formation of Deegan & Scull (1977). Underlying this sandstone dominated section there is a mudstone dominated interval, with thin turbidite interbeds which was previously considered as the Forties Shale Member by Carman & Young (1981), which in turn formed the lower part to the Forties Formation (Deegan & Scull, 1977). However, recent revision of the Lower Palaeogene lithostratigraphy by Mudge & Copestake (1992), relegates the Forties Formation of Deegan & Scull (1977) to member status, and separates the sand from the underlying mud dominated section. The sand dominated section becomes the Forties Member, and the lateral equivalent muds are of the Sele Formation (Fig. 5.4). The underlying shale dominated section is, in fact, the Lista Formation, which forms the lateral equivalent to the Andrew Member (Fig. 5.4).

Towards the close of the Palaeocene, subsidence, which was previously centred on the Central Graben, became widespread. A marine transgression over the Moray Firth delta system cut off the sediment supply to the Forties submarine fan complex, resulting in the deposition of grey to black, sometimes laminated mudstones of the Sele Formation. Tuffaceous

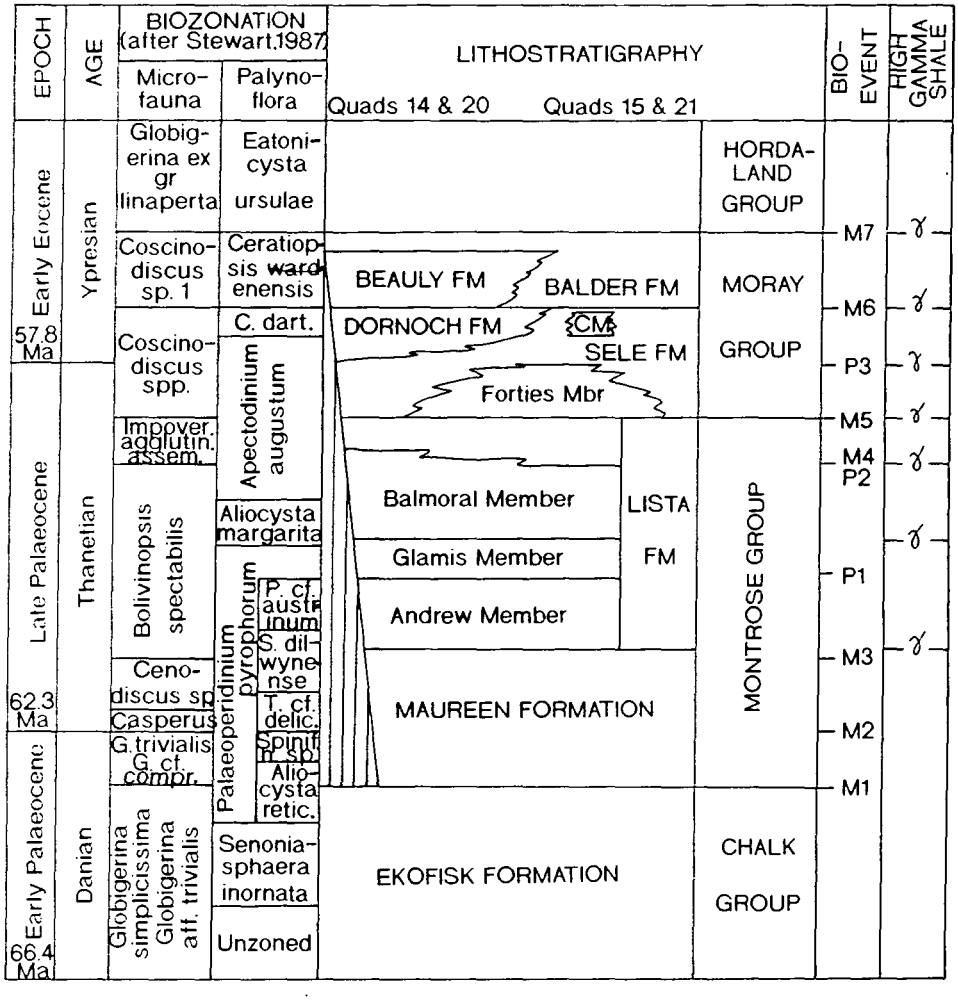

Figure 5.4 Revised lithostratigraphy for the Outer Moray Firth area, North Sea. CM=Cromarty Member (From Mudge & Copestake, 1992).

siltstones and mudstones of the Balder Formation record the close of Palaeocene deposition. The overlying Eocene to Recent deposits consist of undifferentiated mudstones and siltstones up to 2450m (8000ft) thick.

5.3 Geophysics.

A comprehensive seismic survey was undertaken in 1985, mainly concentrating on the Arbroath Field which the survey completely covered, but also covering the majority of the Montrose Field, especially its southern area (Fig. 5.5). The 1985 survey consists of 850Km of seismic data with a dominant northeast to southwest line orientation, and 250m (820ft) line separation (Fig. 5.5). Previous seismic data did not allow the picking of the top Forties Member which could only be mapped by isopaching downwards from the top Balder Ash Formation which forms a distinct continuous reflector across the entire region. However, the 1985 seismic survey allowed the more accurate picking of the top Forties Member facilitated by reprocessing of the data by Amoco, and including horizontal velocity analysis (Crawford et al., 1991).

Due to the variable nature of the quality of the Forties sandstone seen in the early wells, some work was carried out to see if the seismic data could define the lateral distribution of the cleanest sands. This work concluded that the definition of the lateral distribution of the uppermost shaley sands was beyond the resolution of the seismic data (Crawford et al., 1991).

Figure 5.6 shows a section of seismic line, illustrating that the strongest and most continuous reflectors on the section are identified as the Palaeocene Balder Ash/Sele Shale composite, and the Top Maureen/ Ekofisk event. Upper zero crossings were correlated for both events.

The Balder Ash reflector is a composite response produced by both the Balder Ash and the Sele Formation, due to the close proximity of these two reflectors to each other (19-26m (62-84ft)). Individual seismic responses from these horizons mutually interfere leaving the top Sele Formation reflector indiscernible (Crawford et al., 1991). The top of the Forties Member has been picked on the next upper zero crossing after that of the Balder Ash. Within the field boundary this pick is unequivocal across varying lengths of the line between sharply defined zones of discontinuity. These interruptions are interpreted as small slump faults in some cases and facies boundaries in the Forties Sandstone in others (Crawford et al., 1991).

Within the Forties Member and the underlying Lista Formation no field-wide continuous events are seen on the seismic sections. Small scale faults

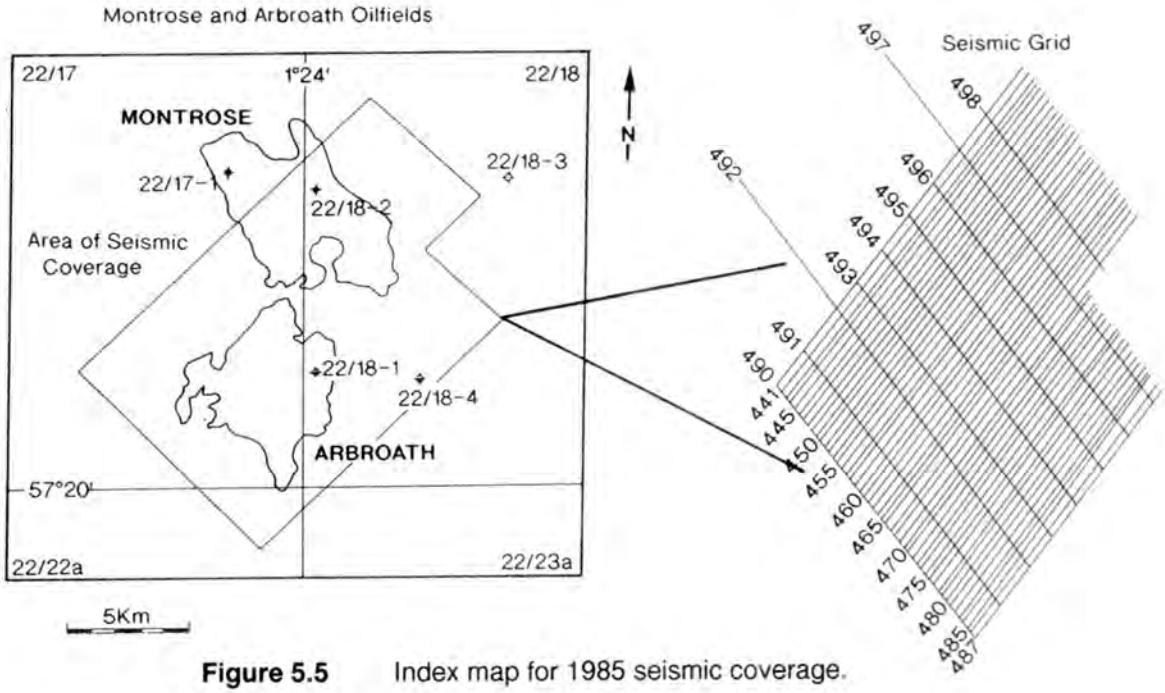

Figure 5.5 Index map for 1985 seismic coverage.

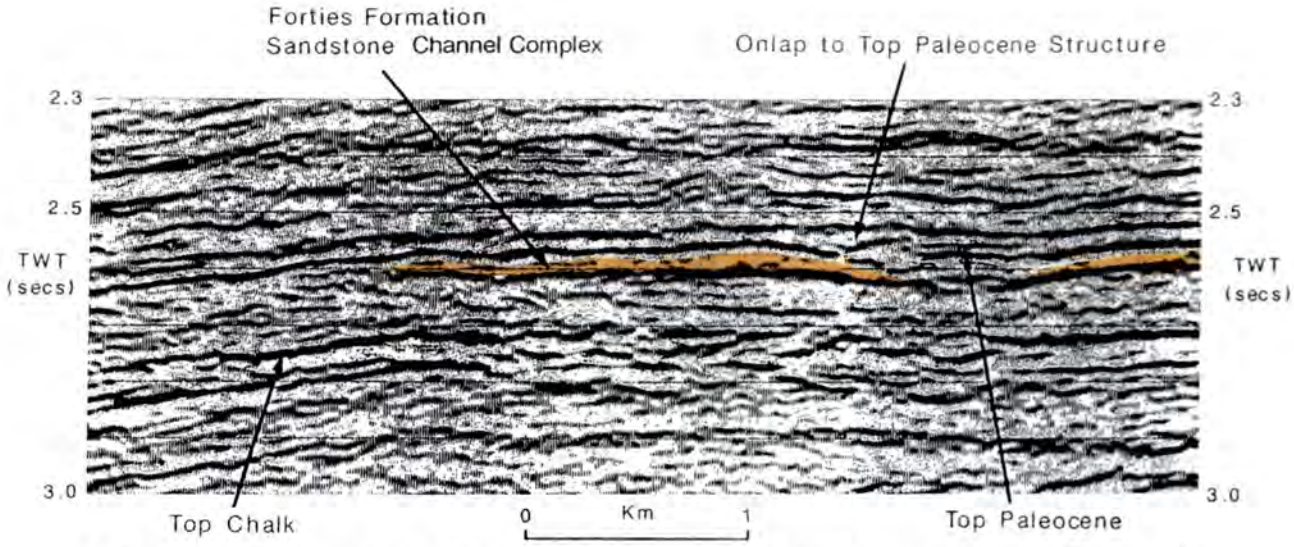

Figure 5.6 Interpreted seismic line showing Balder Ash/Sele composite (Top Paleocene), and Top Maureen/Ekofisk (Top Chalk). Sandstone channel complex is also identified.

do appear as mentioned above, but there is no suggestion of regional or local faulting causing localised displacements of the reservoir (Crawford et al., 1991).

5.4 Oilfields.

The following sections describes the petroleum geological setting of the Montrose and Arbroath oilfields, namely the trap, reservoir and source of the two fields.

5.4.1 Trap.

Oil in both the Montrose and Arbroath oilfields is trapped by dip closure of the Forties Member, which in turn is sealed by the overlying Sele Formation muds. Crawford et al. (1991) states that structures formed at top Palaeocene level in early Eocene times, and as similar structures can be mapped at the top Danian horizon, they are probably of tectonic origin. Second-order relief has then been added to them by differential compaction occurring between the sand and shale rich sections of the Forties Member, which forms the reservoir to the oilfields. The structures themselves are broadly defined as domal anticlines with gently dipping (1-2°) non-faulted limbs. Later sections of this chapter will illustrate how the top Palaeocene structural highs are related to the lithofacies of the Forties Member, and the implications this may have regarding individual field geometry, and additionally, the separation between the Montrose and Arbroath oilfields.

The structural features have a maximum relief of approximately 70m (230ft) and an areal extent of 6 by 8km, and are filled to their spill points. The oil-water contacts are variable, being deepest (8265ft subsea at Arbroath, 8318ft subsea at Montrose) where the sandstone package is thick and clean towards the centre of the fields. They are shallowest where the sandstones are argillaceous and of lower permeability, generally towards the field perimeters (Crawford et al., 1991). The original reservoir pressures in both the fields are of the order of 3700psi, indicating a **normal** (i.e. hydrostatic) pressure gradient.

5.4.2 Reservoir.

The productive interval of both the oilfields lies entirely within the topmost section of the Forties member (Fig. 5.4 & 5.7). Here, the section is sand dominated, consisting of massive, stacked sands. Oil-bearing sandstones do not extend down into the mudstone dominated section of the

WELL 22/17-T3

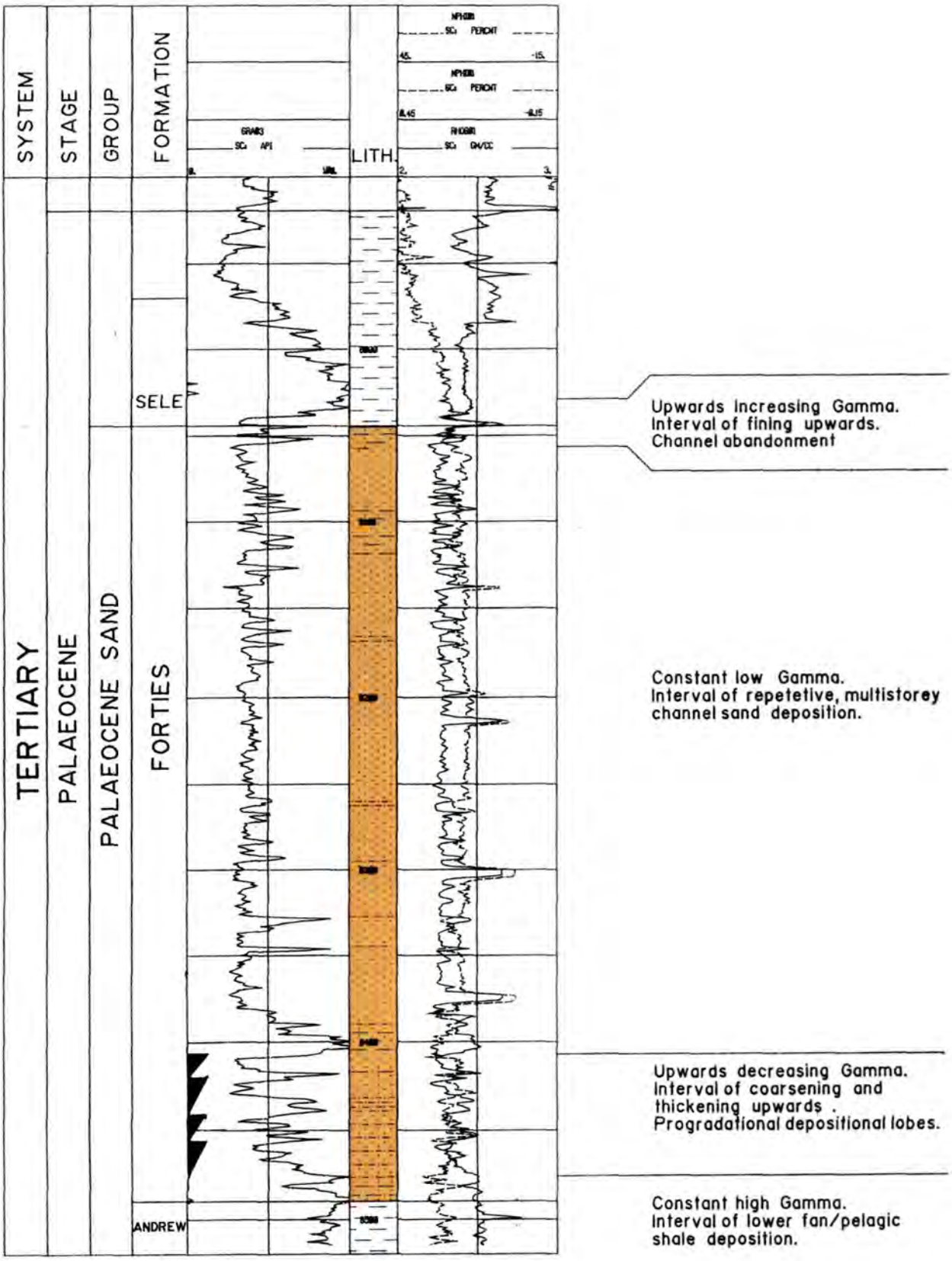

Figure 5.7 Interpreted well log for the Arbroath well 22/17-T3, showing massive, stacked, amalgamated sands of the Forties Member. Interpretations are based on those of Hill & Wood (1980) (see Fig. 5.38). Depths in feet.

underlying Lista Formation, and they are not known in the Andrew Member sandstones below.

The Forties Member of the Sele Formation (Fig 5.4) is composed of a sequence of sandstones and mudstones which overall show a general trend of coarsening and thickening upwards (Fig. 5.7). It is similar to the underlying Andrew Member of the Lista Formation, although the latter is significantly thinner with more interbedded shale present compared to the Forties Member. Often dividing these two sand dominated sections in this region, is a unit of grey-green Lista Formation shale, which has been termed the Balmoral Member by Mudge & Copestake (1992) (Fig. 5.5).

Throughout the Montrose and Arbroath oilfields the Forties Member varies in thickness from 60m (200ft) to 120m (400ft), and generally shows increasing sand content upwards. Bed thickness also shows a wide variety, but often the thickest beds, defined by shale breaks, attain a thickness of 18 - 24m (60 - 80ft) (Fig. 5.8). However, as the core log shows (Fig. 5.8), these sections are represented by several amalgamated events. In both oilfields, seismic data appear to show that the sands have a sheet-like geometry, though the individual thickness and lithofacies, interpreted form wireline logs and core data, varies throughout the area. Structural highs occur where the events are represented by thick amalgamated sand sequences, often with granule/pebble lag deposits at the base of the events. This is usually the thickest section of the deposit which becomes thinner and mud-rich towards the perimeter of the field area.

Sorting of the reservoir sands is typically poor, with the grain size varying from very fine to medium or even coarse grained. The sands are friable with angular to sub-angular grains (Plate 5.1). The average sandstone is composed of grains of monocrystalline quartz (42 to 60%) and feldspar (4 to 16%), rock fragments (trace to 30%), the majority of which are mudstone intraclasts, mica (<2%), chert and occasionally glauconite (Plate 5.1). Zircon and tourmaline occur as heavy mineral traces with the absence of epidote (Lowrey, 1985; Crawford et al., 1991). The latter feature is important as it suggests that the sands have their provenance in the Orkney-Shetland Platform area (Knox et al., 1981). Plagioclase dominates the feldspar component with only minor amounts of orthoclase and microcline present. Orthoclase shows high degrees of alteration, whereas plagioclase and microcline are fresh (Plate 5.2). Diagenesis occurs late in the paragenetic sequence, and has resulted in the precipitation of quartz, calcite, kaolinite and chlorite cements (Plate 5.3). Throughout the Montrose - Arbroath area,

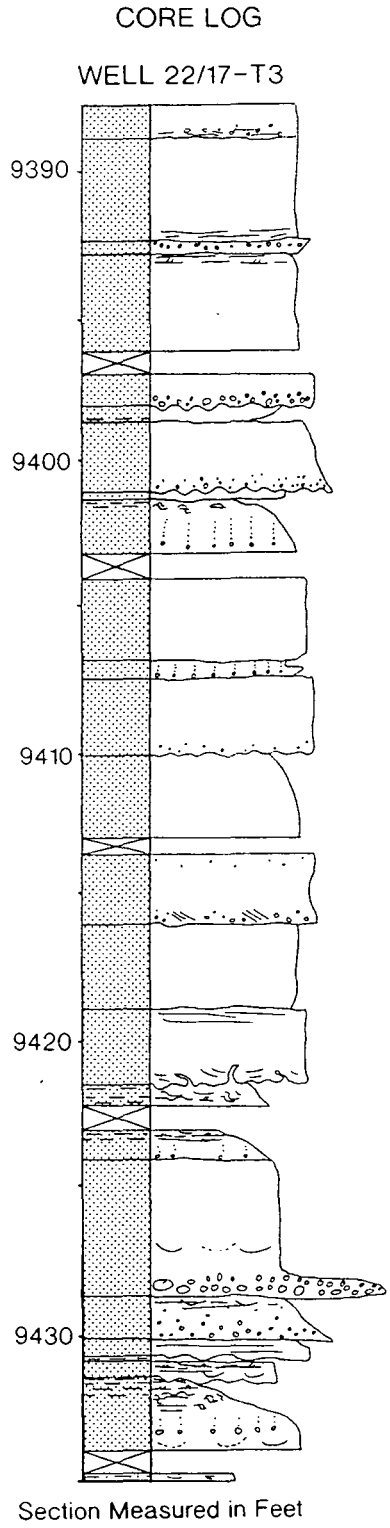

Figure 5.8 Core log for the Arbroath well 22/17-T3, illustrating amalgamation of sandstone beds.

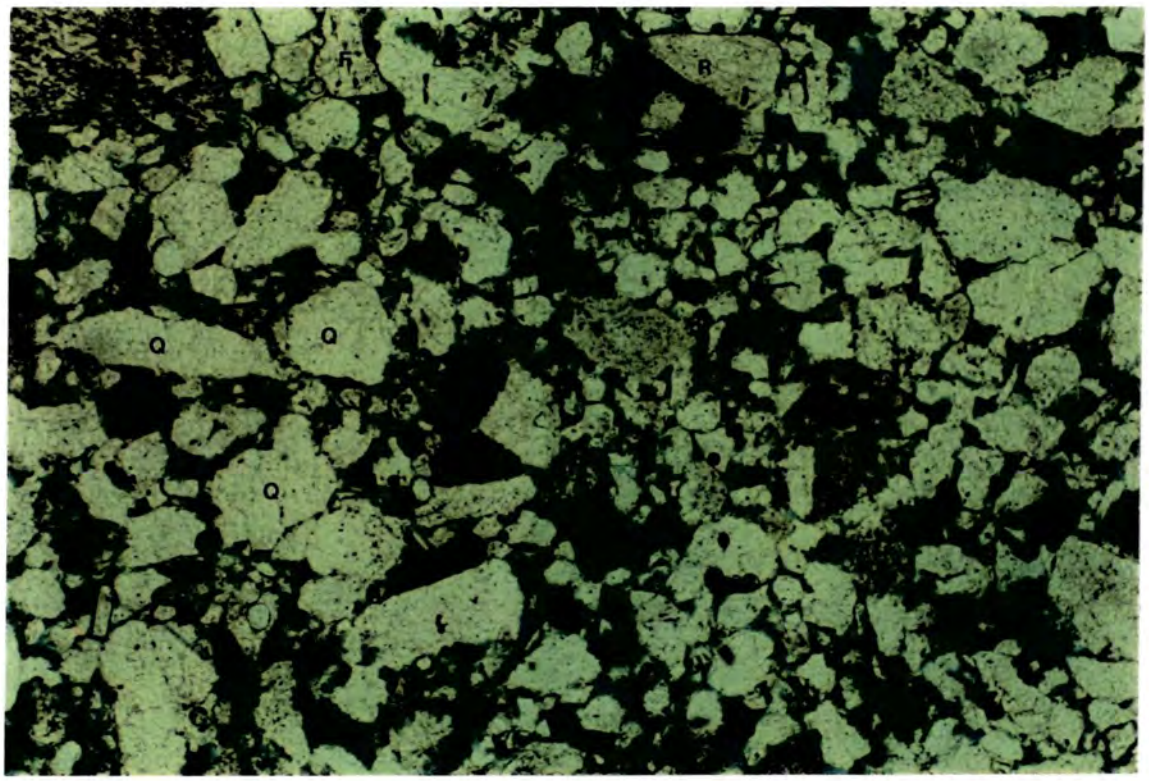

Plate 5.1 Photomicrograph of Forties sand, showing fine to medium grain size, and angular to sub-angular grain shape. Quartz predominates (Q), with minor amounts of feldspar (F) and rock fragments (R). Sample is taken from well 22/17-T4 at a measured depth of 10102.90' (Field of view is 3.3mm).

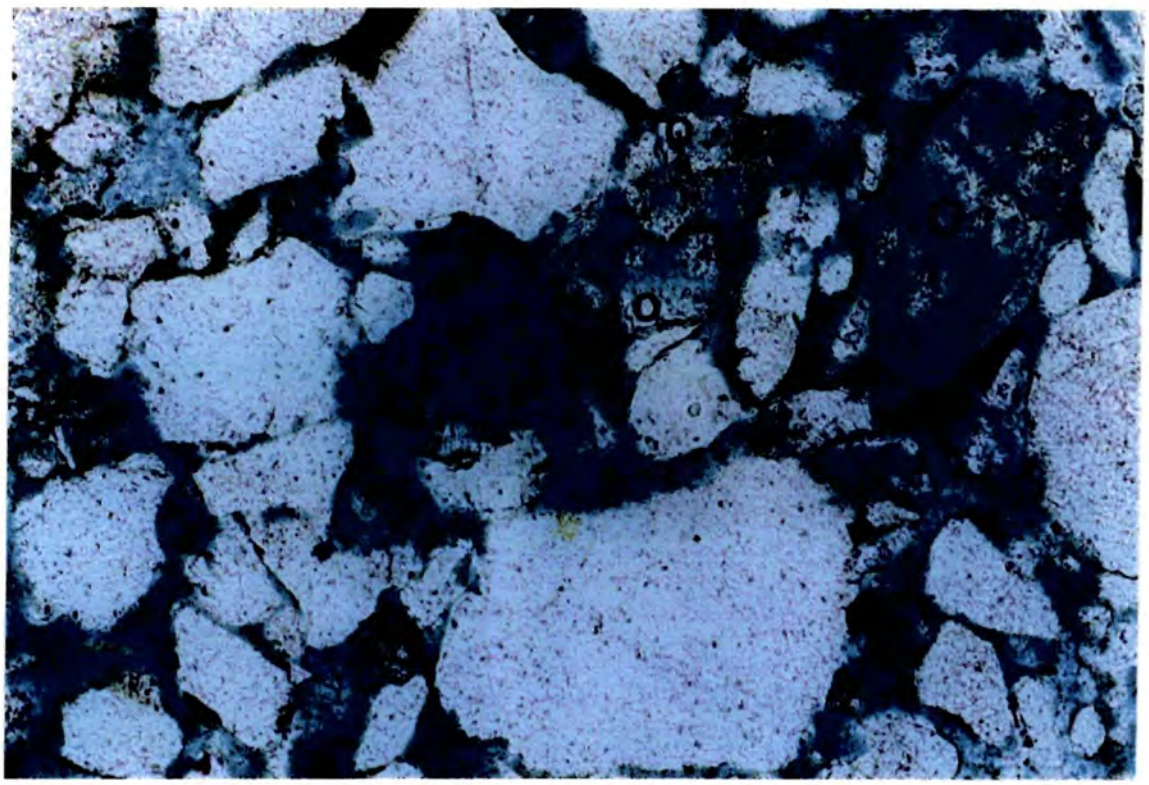

Plate 5.2 Photomicrograph illustrating the alteration of orthoclase feldspar grains (O), and the oversized pore spaces (P) left behind. Sample is taken from well 22/17-T1 at a measured depth of 10227' (Field of view is 1.5mm).

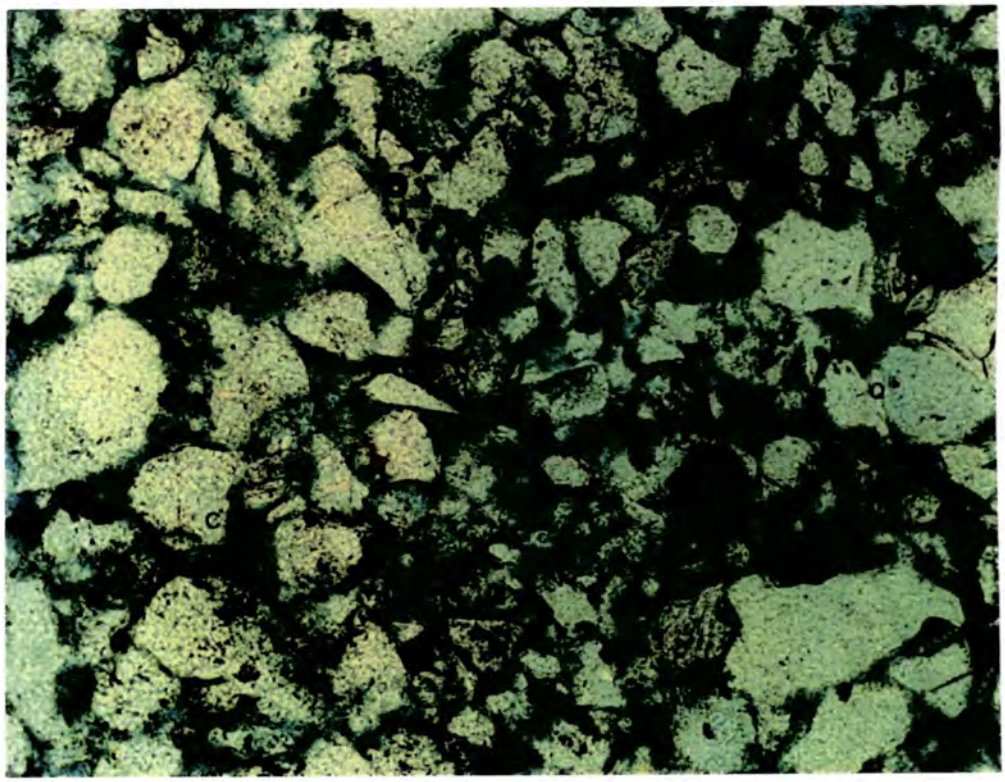

Plate 5.3 Photomicrograph illustrating cementation within the Forties sand. Quartz overgrowths (Q), kaolinite (K) and chlorite (C) are present. Sample is taken from well 22/17-T6 at a measured depth of 11735' (Field of view is 1.5mm).

none of these cements are interpreted to be a significant porosity occluder. However, their effect is mainly to reduce the permeability of the reservoir sands by blocking pore throats (Crawford et al., 1991).

The sediments of the Forties Member are interpreted to have been deposited by turbidity currents, and to have accumulated in a prograding submarine fan setting (Fowler, 1975; Crawford et al., 1991). Section 5.5.4 of this chapter will elaborate further on the depositional model for the area, and the implications of differential compaction upon such a model. However, it is possible to see from the well logs and the cored sections that the base of the section is dominated by pelagic mudstones (Lista Formation). Thin turbidite sands are gradually introduced, which show an overall trend which thickens and coarsens upwards (Forties Member of the Sele Formation). The culmination of the Forties Member shows a thick sequence of stacked turbidite sandstones with a typical 'box-car' log motif (Fig. 5.7). Crawford et al. (1991) suggest that the sands were deposited in stacked mid-fan channels, with the deposition of the sands concentrated in these channel areas (now the zones of structural highs) where the turbidity currents were strongest (see section 5.6 for further information).

Core data show that porosities throughout the reservoir are commonly in the range of 23-25%, and permeabilities are commonly 70 to 90md. However, permeabilities range from less than 1md to 2000md, and show a tendency to increase upwards through the section (Fig. 5.9).

5.4.3 Source.

Oil at Montrose and Arbroath has been "typed" to an Upper Jurassic Kimmeridge Clay source which is mature (present day vitrinite reflectances are greater than 1.3%) within the Central Graben area to the west of the fields in Blocks 22/16, 22/21 and 22/22 (Crawford et al., 1991). In these blocks the Kimmeridge Clay is 30 to 305m (100 to 1000ft) thick, and has an average total organic carbon (TOC) content of 8%, composed predominantly of amorphous, marine, type 1 kerogen. It is believed to have reached peak oil generation (vitrinite reflectance = 1.0%) 10 to 20 million years before present (Crawford et al., 1991). Migration through the Jurassic and Cretaceous sections is thought to have followed normal fault systems and over steepened beds which mark the edge of the Forties-Montrose High. Once within the Tertiary section the oil followed a more gently inclined route through the Maureen and Andrew Members of the Lista Formation, to be trapped in the thick sands of the Forties Member, and sealed beneath the

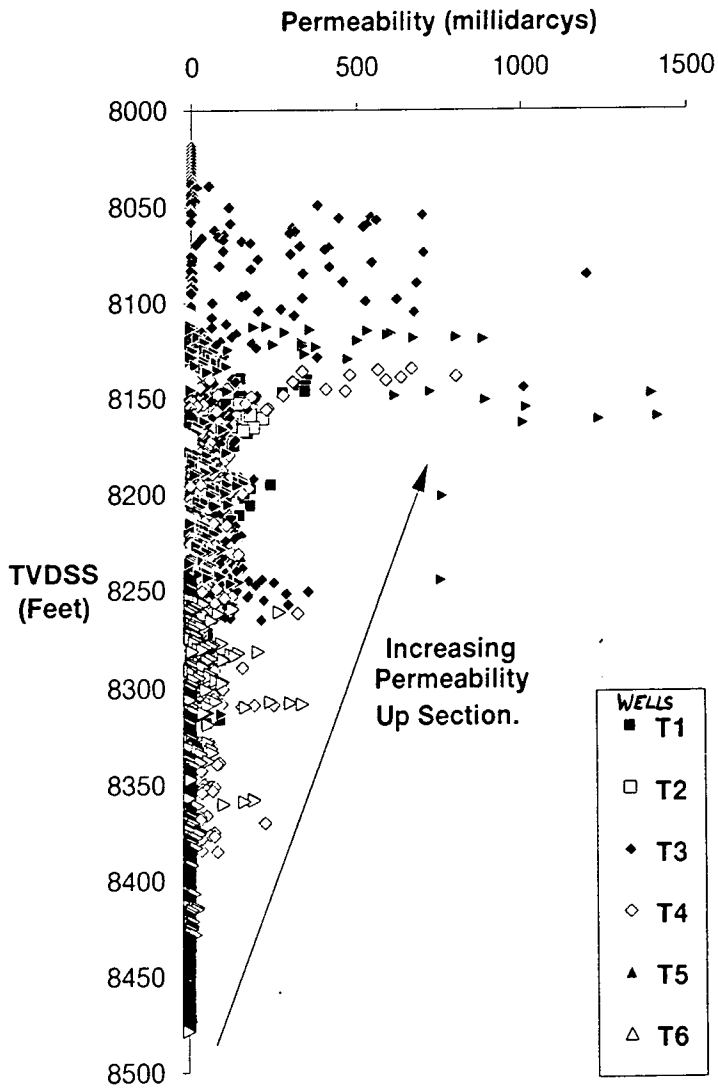

Figure 5.9 Graph illustrating permeability increasing up-section.

mudstone section of the Sele Formation. Hydrocarbon migration is interpreted to have been driven by buoyancy pressure, to concentrate hydrocarbon deposits in any structural culmination/high. Lateral migration need only to have been 10-16Km (6-10 miles) from mature source rock to trap (Crawford et al., 1991).

5.5 Depositional Model.

Discoveries of oil, gas and gas condensate in sandstones of Tertiary age have been made in an area stretching from 56° 10'N in the Central North Sea (Quadrants 29 and 30) northwards to 60° 50'N in the Viking Graben (Quadrants 2 and 3), and extending westwards into the Outer Moray Firth (Quadrants 15 and 21) as well as onto the East Shetland and Western platforms, and eastwards into Norwegian waters (Fig. 5.10) (Bain, 1993). Since oil was first discovered in the UK North Sea in 1969 by the Montrose Well 22/18-1, some 106 Tertiary discoveries have been made in the area up to the end of 1990 (Bain, 1993).

These discoveries fall into many different groups, defined by their stratigraphic age, their depositional environment, and their structural setting and development. The present study, concentrating on the Montrose and Arbroath oilfields, is therefore mainly interested in the Palaeocene and Eocene sandstone reservoirs that were primarily deposited within a submarine fan environment. Numerous papers concerning the oil and gas fields of the Tertiary section of the North Sea are given in the volumes edited by Woodland (1975), Illing and Hobson (1981), Brooks and Glennie (1987), Spencer et al. (1987), Abbots (1991), and Parker (1993). These references are a valuable source of information concerning the depositional models, geometries and styles of the various Tertiary fields, which often form analogue models to the two oilfields of the present study.

Detailed study of the literature (e.g. Fowler, 1975; Hill & Wood, 1980; Crawford et al., 1991), combined with interpretation of the well logs and cored sections of the Montrose and Arbroath wells, along with seismic interpretation and sequence stratigraphic studies (e.g. Harding et al., 1991; Milton et al., 1991; Vining et al., 1993; Galloway et al., 1993; Armentrout et al., 1993; Hartog Jager et al., 1993) show that the oilfields of the present study were deposited within a large submarine fan system. It is also apparent that all the submarine fans in the Palaeogene of the North Sea are channelised, with channels continuing near to the fan fringe (Hartog Jager et al., 1993).

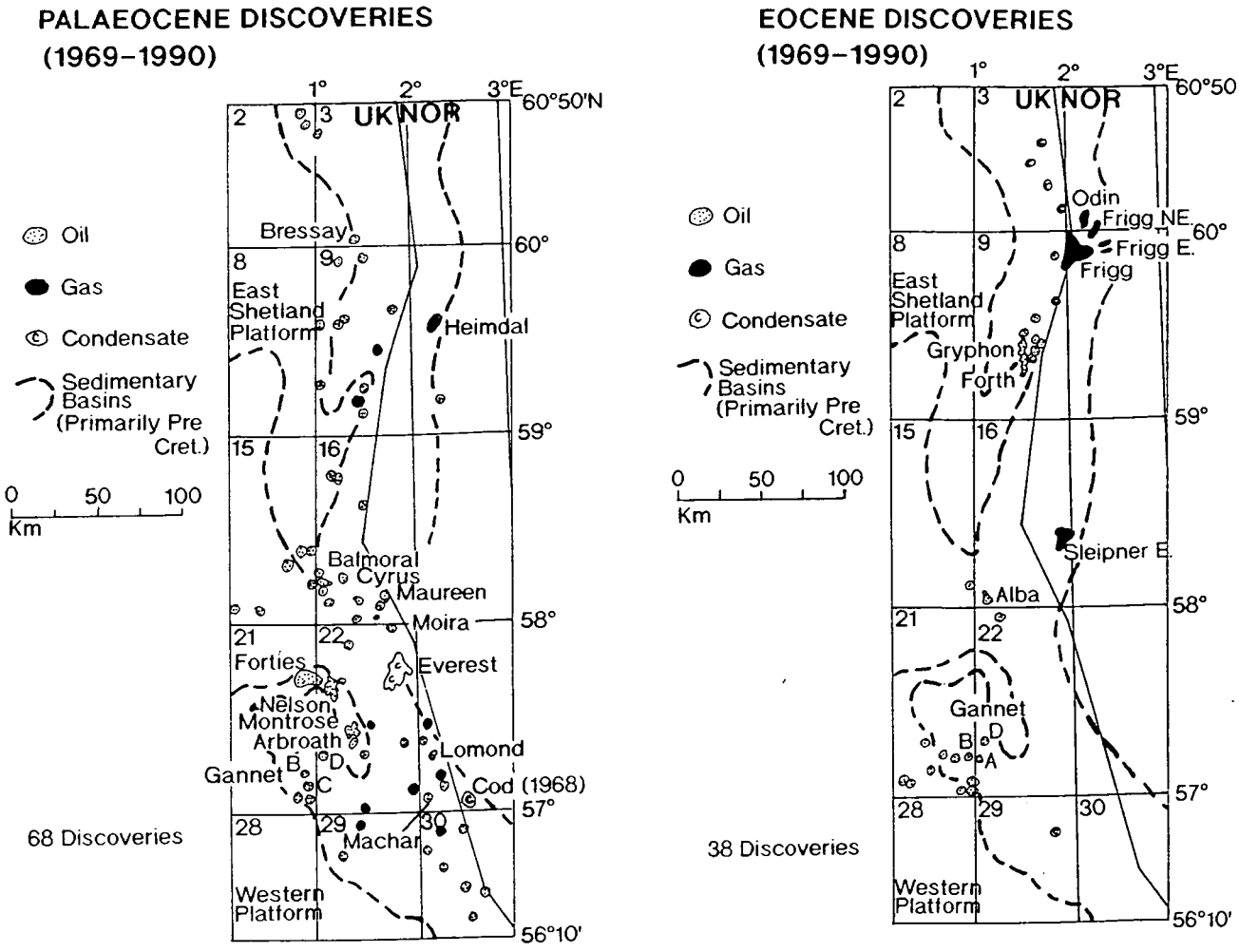

Figure 5.10 Area of Tertiary discoveries (From Bain, 1993).

It is important, therefore, that this chapter reviews the broad aspects of submarine fan depositional systems and models, and also those models proposed for other Palaeocene and Eocene oil and gas fields of the North Sea. Finally, a depositional model can then be proposed for the Montrose - Arbroath oilfields upon which compactional modelling can be based.

5.5.1 General Submarine Fan Models.

Submarine fans have been of great interest throughout the world because of their potential to form hydrocarbon reservoirs (Walker, 1978; Stow, 1985). With the advent of sophisticated deep-tow geophysical instruments such as side-scan sonar and Gloria, combined with high resolution seismic data, there have been many detailed studies of modern fans, world-wide (e.g. Shepard & Buffington, 1968; Shepard ,et al., 1969; Normark, 1970, 1978; Piper, 1970; Normark et al., 1979; Damuth et al., 1983a, 1983b; Graham & Bachman, 1983; Barnes & Normark, 1984; Alonso et al., 1991).

Problems begin to arise, however, when these studies and models concerning modern fans are compared to the models proposed for ancient submarine fan deposits (e.g. Mutti & Ricci Lucchi, 1972). Even at the level of classifying certain areas of the fan problems occur. For example, the lower fan of Normark (1970) (Fig. 5.11) would be classified as part of the basin plain in the scheme of Mutti & Ricci Lucchi (1972) (Fig. 5.12). Figure 5.12 also shows how the deposits of ancient fans are recognised by their facies associations and vertical sequences of facies, as first proposed by Mutti & Ghibaudo (1972) and Mutti & Ricci Lucchi (1972).

The model illustrates that the **inner fan** is characterised by conglomerate and coarse sandstone facies (facies classes A and B (Fig. 5.13, Pickering et al., 1989)) in large channels, cut into fine-grained deposits (facies class E). The **middle fan** consists of packets of sandstone with minor amounts of conglomerate (facies classes A and B) arranged into thinning- and fining-upwards sequences, alternating with packets dominated by facies classes C, D, and E. Finally the **outer fan**, which has few or no channels, possesses parallel-sided turbidites arranged in thickening- and coarsening-upward sequences.

Recently, submarine fan models from both the modern and ancient record have been undergoing considerable redefinition and interpretation. Due to the high degree of variability in the morphology and scale of modern fans (Pickering, 1982; Barnes & Normark, 1984; Stow et al., 1984) there

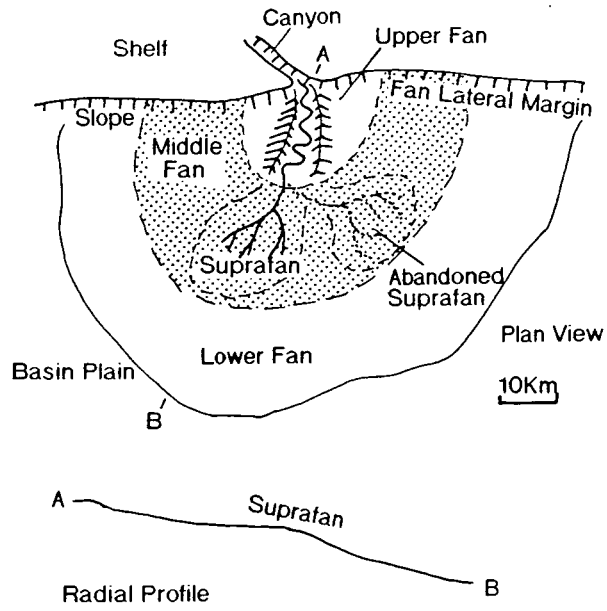

Figure 5.11 Submarine fan model of Normark (1970, 1978) emphasizing growth by successive addition of suprafan lobes on the middle fan. The middle fan region is stippled.

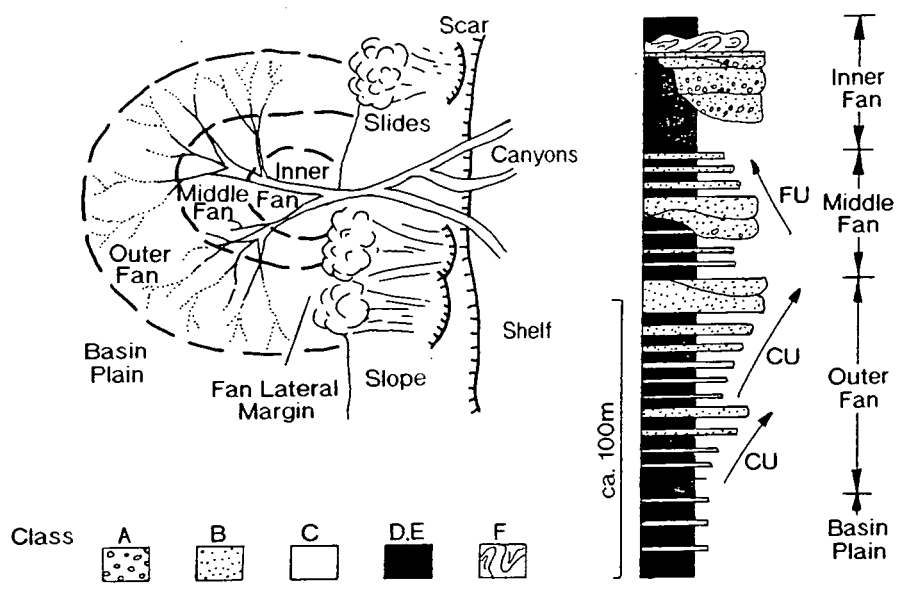

Figure 5.12 Submarine fan moel of Mutti & Ricci Lucchi (1972) based on relationships observed in ancient deposits. Facies classes are those of Pickering et al. (1989) (see Fig. 5.13).

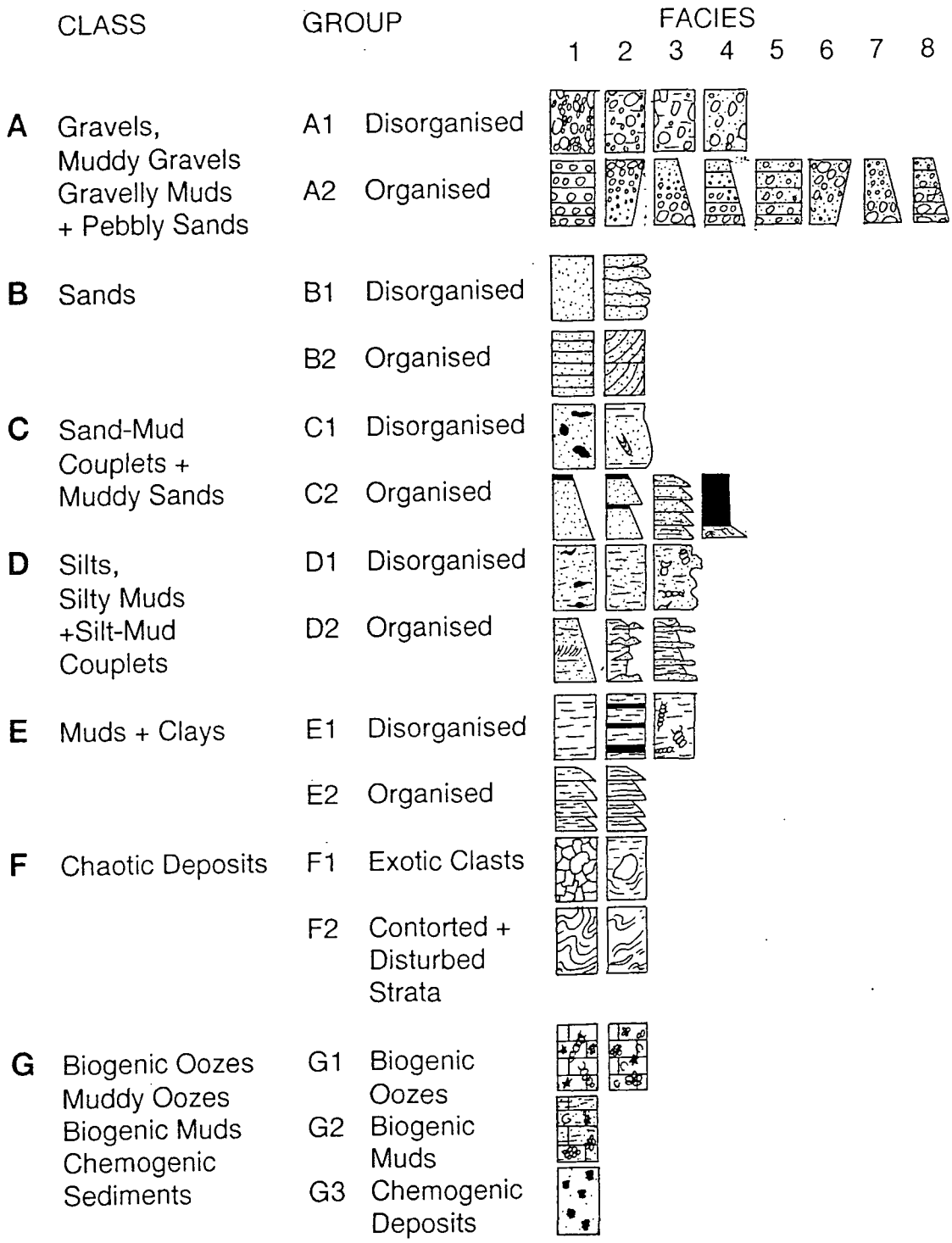

Figure 5.13 Facies classification scheme for deep-water sediments, according to Pickering et al. (1982). Facies classes are defined on the basis of grain size (Facies Classes A-E), internal organisation (Facies Class F) and composition (Facies Class G). Facies groups are distinguished mainly on the basis of internal organisation of structures and textures. Individual facies are based on internal structures, bed thicknesses and composition.

seems little reason to erect a single universal model to encompass all fan types (Pickering et al., 1989). Side-scan sonar is also helping in the understanding of the depositional processes occurring on modern fans, particularly imagery of meandering and braided channels (Garrison et al., 1982; Damuth et al., 1983a; Belderson et al., 1984; Kastens & Shor, 1985). Deep-sea drilling, mainly concentrated on the Mississippi Fan, is further modifying and aiding these ideas (Bouma et al., 1986).

Likewise, in the study of ancient fans, many of the early models suggested by Mutti & Ricci Lucchi (1972), Ricci Lucchi (1975) and Walker (1978) are found to be oversimplified, and do not reflect the complex nature of many ancient submarine fan deposits. The facies sequences of such deposits reflect a complex interaction between sediment texture, rate of sediment supply, tectonic regime, sea-level rises and falls, and fan processes such as channel switching and mass wasting (Stow et al., 1984; Bouma et al., 1985; Mutti, 1985; Mutti & Normark, 1987; Pickering et al., 1989). It has also been shown by various authors that many ancient fan deposits do not show the abundance of simple thinning- and thickening-upward sequences implicit in the published models (Hiscott, 1981; Chan & Dott, 1983; McLean & Howell, 1984). Hiscott (1981) not only questions the presence of such asymmetric 'cycles', but also illustrates how such 'cycles' are difficult to explain in terms of known fan processes.

Thickening-upward cycles have usually been attributed to basinward progradation of suprafan depositional lobes (Mutti & Ghibaudo, 1972; Mutti & Ricci Lucchi, 1972; Walker & Mutti, 1973; Mutti, 1974; Ricci Lucchi, 1975; Walker, 1978; Ghibaudo, 1980), although minor thickening-upward trends may result from deposition of thicker sand units in primary depressions on the fan surface (Mutti et al., 1978). However, deep-sea fan processes favour vertical aggradation rather than progradation (Hiscott, 1981), a fact that is echoed by the work of Normark et al. (1979). Their detailed study of the Navy Fan indicates that channels do not gradually prograde across their depositional lobes, but shift abruptly along the marginal depression at the edge of the lobe. Subtle lateral shifts in the site of turbidity-current deposition have now been accepted as the likely method for producing thickening-upward cycles, and have been termed compensation cycles (Fig. 5.14) (Mutti & Sonnino, 1981; Mutti, 1984; Ricci Lucchi, 1984). The process of differential compaction may also form a control to compensation cycles, a fact previously ignored, and will be addressed in later sections of the present chapter.

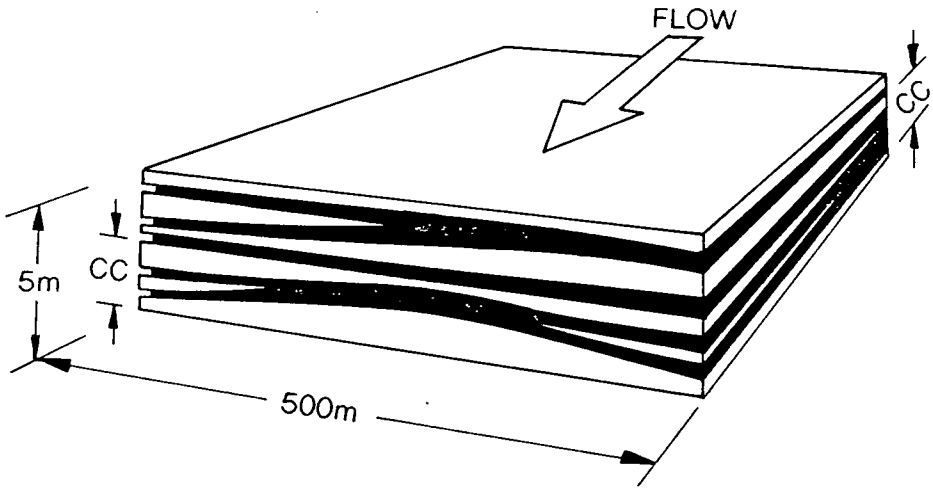

Figure 5.14 Block diagram illustrating the origin of compensation cycles (CC) by lateral shifts in the thickest parts of successive turbidites, resulting in a smoothing of bottom topography, and in formation of thickening-upward cycles (From Pickering et al., 1989).

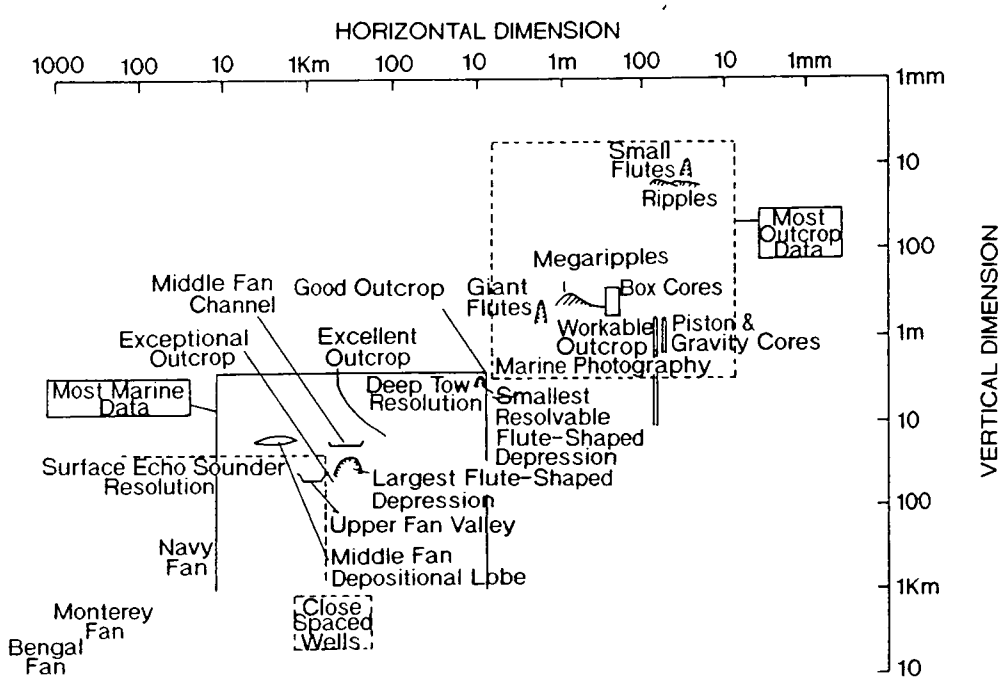

Figure 5.15 Size of submarine fans and component morphological and sedimentological features compared with the limits of resolution of various marine survey techniques (From Pickering et al., 1989).

Nilsen (1980) points out that meandering or braided thalweg channels on the floors of inner-fan channels do not appear to produce thinning-upward cycles. Instead, such cycles have been attributed to changes in the longitudinal gradient and shallowing and widening of channel cross-sections during progressive abandonment (Ricci Lucchi, 1975). Alternatively, they may be produced by the bypassing of currents over or around topographically high sand deposits (Martini & Sagri, 1977; Ricci Lucchi & Valmori, 1980), or by the plugging of a channel by a large flow, followed by a progressive thinning as subsequent flows are diverted to a new channel system (Walker, 1978; Hiscott, 1980). Work on the modern Indus Fan (Kolla & Coumes, 1987), however, suggests common fining-upward sequences are present throughout the channel fills of the upper and middle fan segments.

Many of the problems in relating ancient submarine fan and modern submarine fan depositional models and the depositional processes involved, originate in the scale of observations available from either setting (Normark et al., 1979; Shanmugam et al., 1985; Mutti & Normark, 1987; Pickering et al., 1989). A further complication is the fact that most modern fans have been largely inactive since the last rise in sea level, and are presently blanketed by hemipelagic mud (facies class E). With regards to scale, even exceptionally good outcrop shows features that are still beyond the resolution that can be attained with available ship-board deep-sea imagery (Fig. 5.15). Even deep-tow instrument packages only have a maximum resolution of 2-3m (6.5-10ft) vertically and 10-20m (33-66ft) horizontally (Normark et al., 1979).

Classification of deep-water depositional systems has therefore proved extremely difficult, with numerous models proposed for submarine fan deposition, interpreted for both the ancient and modern systems (e.g. Normark, 1970, 1978, 1980; Nelson & Nilsen, 1974; Mutti & Ricci Lucchi, 1972, 1975; Walker, 1978, 1980; Nilsen, 1980; Stow, 1981, 1986; Howell & Normark, 1982; Barnes & Normark, 1984; Bouma et al., 1985; Stow et al., 1985; Mutti, 1985; Heller & Dickinson, 1985; Surlyk, 1987; Shanmugam & Moiola, 1991). With so many different models proposed, Reading & Richards (1994) have attempted to classify all deep-water, basin margin turbidite systems by way of their grain size and feeder system. They propose 12 classes: mud-rich, mud/sand-rich, sand-rich, and gravel-rich "point-source submarine fans"; mud-rich, mud/sand-rich, sand-rich, and gravel-rich "multiple-source submarine ramps"; mud-rich, mud/sand-rich, sand-rich, and gravel-rich "linear-source slope aprons". Ancient and modern turbidite

systems can be subsequently classified (Fig 5.16 & 5.17), although their precise, individual position in the scheme may be altered by changes in tectonics, climate, supply, and sea level (Mutti, 1985).

Reading & Richards (1994) classify the Forties-Montrose Fan system as a multiple source ramp, lying between mud/sand-rich to sand-rich. Recent studies by Anderton (1993) have shown that the Palaeocene ramp systems, equivalent to the Maureen Formation, Andrew and Forties Members (Fig. 5.4), represent the composite stratigraphic record of a complex association of these two systems. Table 5.1 lists the characteristics of both deep-water basin-margin systems.

Mud/sand-rich multiple-source systems (Fig. 5.16) are generally fed by a mixed sand-mud delta that may prograde directly across a gently sloping shelf, or may feed the basin via multiple slope valleys. Sedimentation may be active during periods of either rising or falling sea level. These systems are distinguished from fan systems by the presence of several feeders that are active more or less simultaneously, and from slope aprons by the presence of portions of slope apron between the discrete channel lobe systems. The Forties Fan (Knox et al., 1981; Stewart, 1987; Whyatt et al., 1991) forms the sandier end of the spectrum in the class, building 130Km into the Central Graben with a width of 80Km. Amalgamated sandstones, 50-100m thick, formed in 2.5-3Km wide channels, and were separated by 500m wide interchannel areas where shales were deposited (Reading & Richards, 1994).

Sand-rich ramps (Fig 5.17) are difficult to distinguish from the sandier mud/sand-rich ramps, but the lack of silt and mud inhibits the development of levees and discrete channels, resulting in the deposition of sheet-like sand bodies (Reading & Richards, 1994). They are fed along a broad front by sandy deltas or coastal plains with a relatively narrow shelf. Multiple channels linked to river and distributary channels cut the slope and divide the sediment inflows so that penetration into the basin is limited. The distal ramp and basin plain receive little sediment. The Palaeocene Montrose Group (Fig. 5.4) forms a belt that extends for more than 350Km but penetrates less than 30Km into the basin.

5.5.2 Submarine Fan Processes.

Two processes of extreme importance to the present study are **flow stripping** and **lobe switching**, both of which predominantly occur in the middle fan environment. Both processes are well known on certain modern

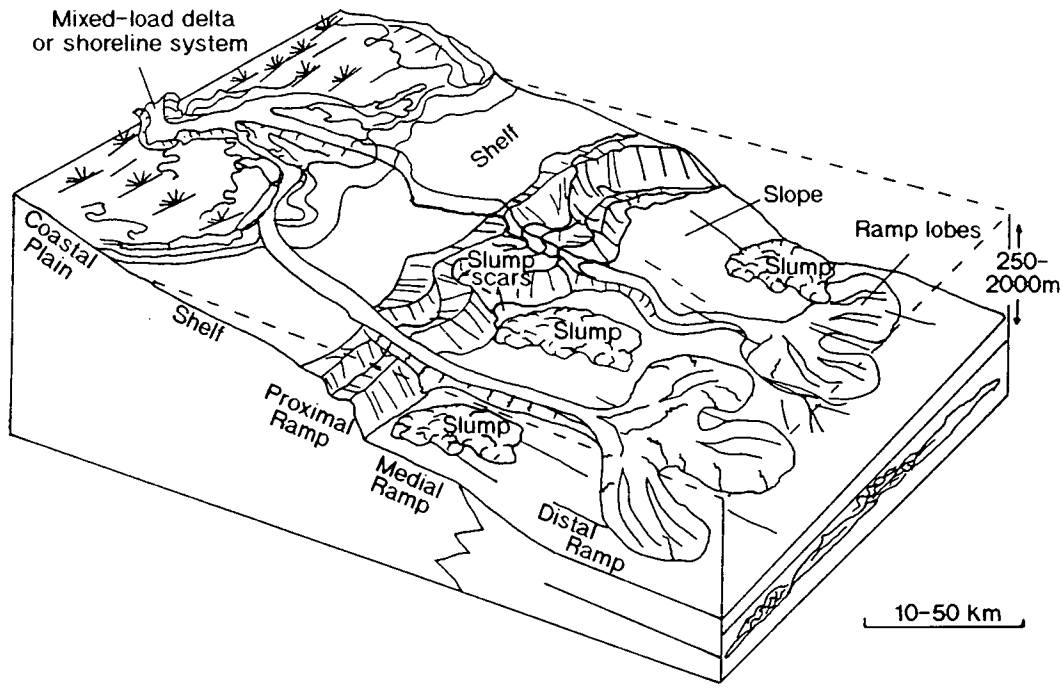

Figure 5.16 Depositional model for a mud/sand-rich, multiple-source ramp system (From Reading & Richards, 1994).

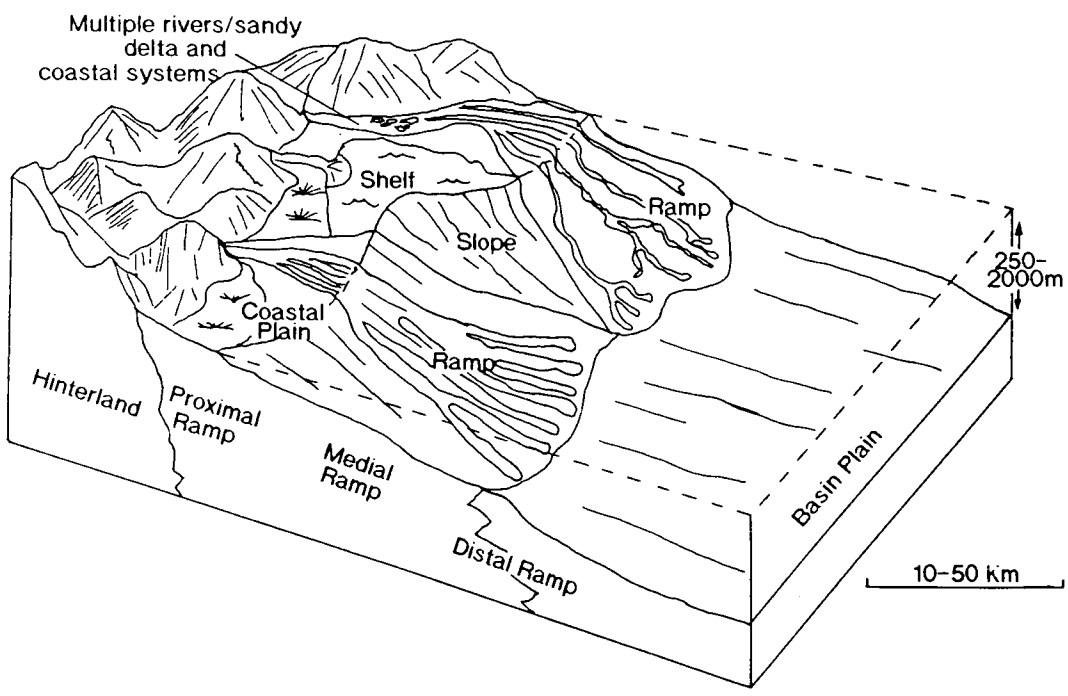

Figure 5.17 Depositional model for a sand-rich, multiple-source ramp system (From Reading & Richards, 1994).

Multiple-source Submarine Ramps

	Mud/Sand	Sand
Size	Moderate	Moderate
Slope Gradient	Moderate 7-35m/km	Moderate >35m/km
Shape Radius/length	Lobate 5-75km	Linear-belt 1-50km
Source Area Size Gradient Distance	 Moderate-small Moderate Moderate	 Small Moderate Close
Feeding Systems	Mixed-load delta, linear shoreline	Sand-rich clastic shoreline/shelf
Supply Mechanism	Mainly high- and low-density turbidity currents	Reworking or direct access to shelf clastics; low-efficiency turbidity currents
Size of Flows	Moderate	Moderate-small
Channel System	Multiple, leveed channels with meandering to straight platform	Multiple, laterally migrating braided to low-sinuosity channels
Distal Slope/Lower Fan Sediments	Mixed-load turbidity current flows forming lobes of interbedded sands and mud	Sand-rich turbidity current flows forming low-relief lobes and sand sheets
Principal Basin Plain Deposits	Hemipelagics	Hemipelagics
Principal Architectural Elements Proximal Area Distal Area	 Channel levees Lobes	 Channels Channelised lobes
Seismic Architecture	Channel levees and mounds	Constructional, low-relief mounds
Sand Percentage	≥30-≤70% Sand	≥70% Sand
Sand-Body Geometry	Offset, stacked lenticular channel sand bodies bounded by fines; levee passing downdip into offset stacked lobate sand bodies formed of sandstones and mudstones	Broad, sheet-like to low-relief lobate sand-body geometries dominated internally by channelised sandstone units
Turbidite Facies	C, D	B, C
Reservoir Heterogeneity	High-moderate	Low
Sand-Body Communication Vertical Lateral	 Moderate Moderate	 Good Good
Common Reservoir Trap Type	Stratigraphic	Structural
Play Concepts	1) Combined structural-stratigraphic trap in proximal ramp channels. 2) Updip pinch-out of channel and/or ramp-lobe sands	Combined structural and stratigraphic traps of ramp sandstone
Key Exploration Risks	Reservoir definition, delineation, and quality; seal integrity	Trap requires structural component; seal integrity
Importance and Position on Relative Sea Level Cycle	Potentially important; highstand and lowstand	Not important; highstand and lowstand; major flooding events

Table 5.1 Depositional characteristics for mud/sand-rich and sand-rich, multiple-source submarine ramps (From Reading & Richards, 1994).

fans, especially Navy Fan (Normark, 1970; Hess & Normark, 1976; Normark et al., 1979; Piper & Normark, 1983; Bowen et al., 1984). These individual processes are important to the present study in terms of sediment deposition and distribution, and to the understanding of differential compaction within submarine fan depositional systems.

On Navy Fan, Normark et al. (1979) noticed sharp channel bends at the apices of abandoned lobes, indicating that aggradation of the depositional lobe eventually forces the channel to switch to a new course along one of the marginal depressions at the edge of the lobe (Fig. 5.18). A new lobe develops at the mouth of the new channel. This is the process of **lobe switching** (Normark et al., 1979). Subsequent turbidity currents that travel down the channel system are therefore forced to negotiate a series of sharp bends. On submarine fans such as the Amazon Fan, these sharp bends may also be produced due to the natural meandering of the channel system (Damuth et al., 1983a). Thin sand-rich flows are able to remain in the channel as they pass down the submarine fan system. However, thicker mud-rich turbidity currents are unable to do so (Bowen et al., 1984). In this scenario the upper part of the turbidity current may flow straight over the crest of the levee on the outside of the bend, resulting in:

1) Formation of a flute-shaped scour at the levee crest,
2) deposition of a mud turbidite on top of the former, but now abandoned lobe, and
3) the deposition of the remainder of the turbidity current just around the bend of the channel, due to the momentum loss caused by the stripping of the upper part of the turbidite flow.

Piper & Normark (1983) call this process **flow stripping**, and it enriches the deposited sand load in the channel, illustrated in Figure 5.19. Timbrell (1993) proposes flow stripping as a major process, possibly controlling the depositional arrangement of the Balder Formation in Quadrant 9 of the U.K. North Sea (Fig 5.20a & b).

Lobe switching develops a depositional history of the submarine fan system, which may be interpreted from seismic data or wireline log correlations. Figure 5.21 schematically illustrates such a correlation of wireline logs, and the depositional history this depicts. Depositional histories for many modern fans have been described, mainly using shallow seismic data, but occasionally aided by Gloria data and other deep-tow geophysical tools. Examples of these include the Navy Fan (Piper & Normark, 1983), the Rhône Fan (Droz & Bellaiche, 1985; Pickering et al., 1989), the Amazon Fan

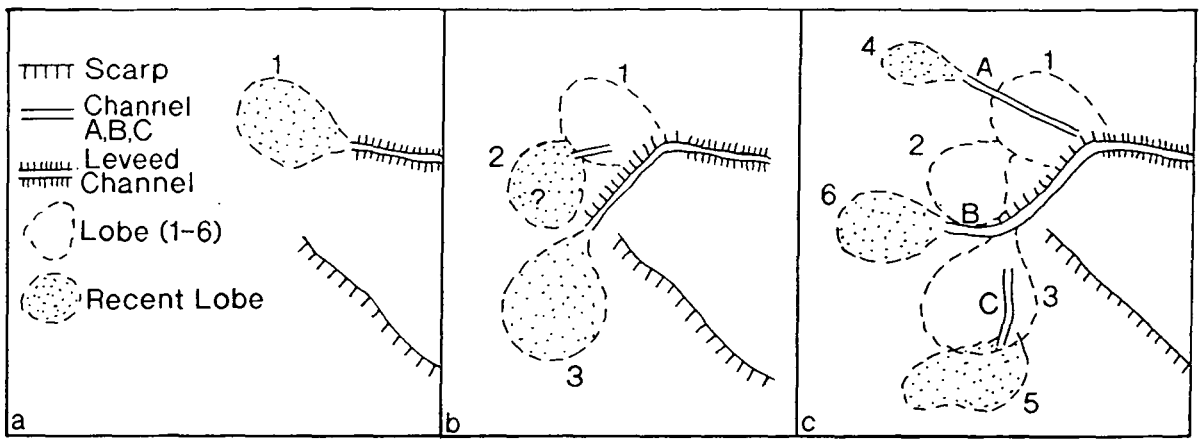

Figure 5.18 Development of depositional lobe pattern on Navy Fan (From Normark, 1979).

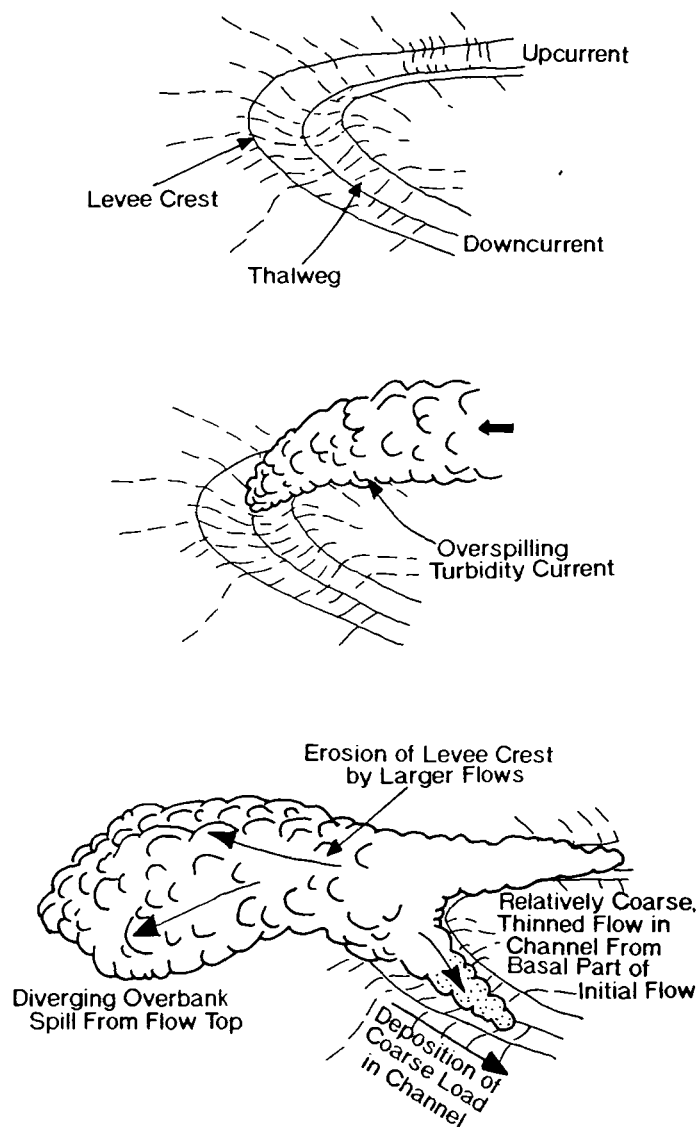

Figure 5.19 Illustration of flow stripping (From Piper & Normark, 1983). Channel curvature causes eventual splitting of the initial flow into two parts. Loss of momentum by overbank spill results in deposition of sand just beyond the channel bend.

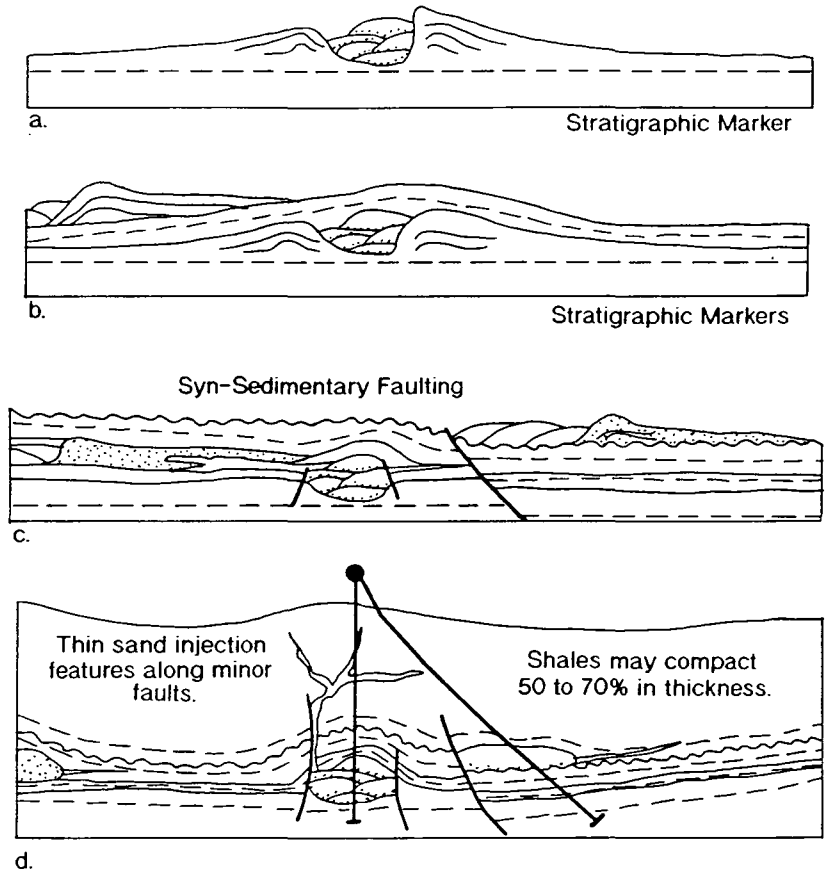

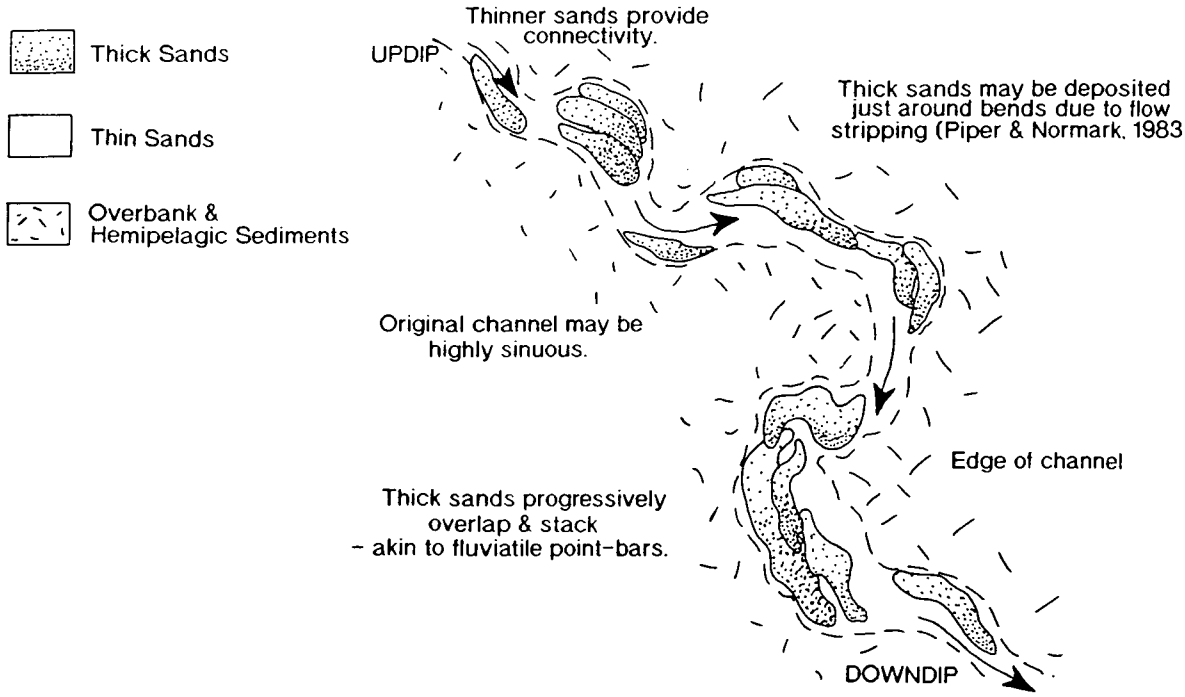

Figure 5.20a Resultant sequences from constructional channel model. a) Lowstand wedge deposition; b) hemipelagic shale deposition; c) continued lowstand wedge deposition - younger sands deposited on flanks, sand injection sills ('wings') may form at <100m burial; d) burial to approximately 5500ft - in an aggradational model, a well and sidetrack will find the same time markers; e) schematic plan view of predicted reservoir depositional geometry 'string of pearls' (From Timbrell, 1993).

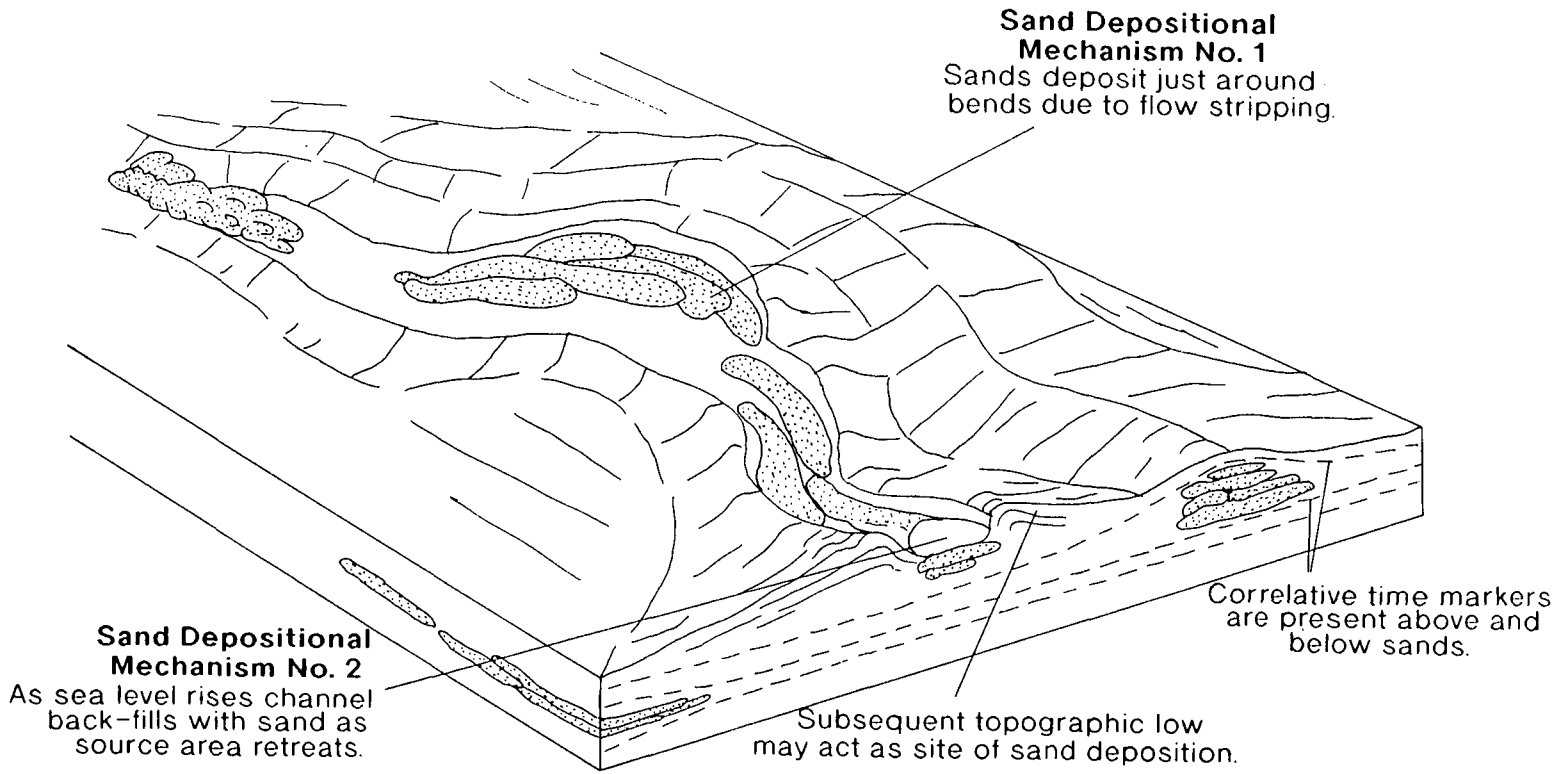

Figure 5.20b Schematic model for depositional submarine channel development (From Timbrell, 1993).

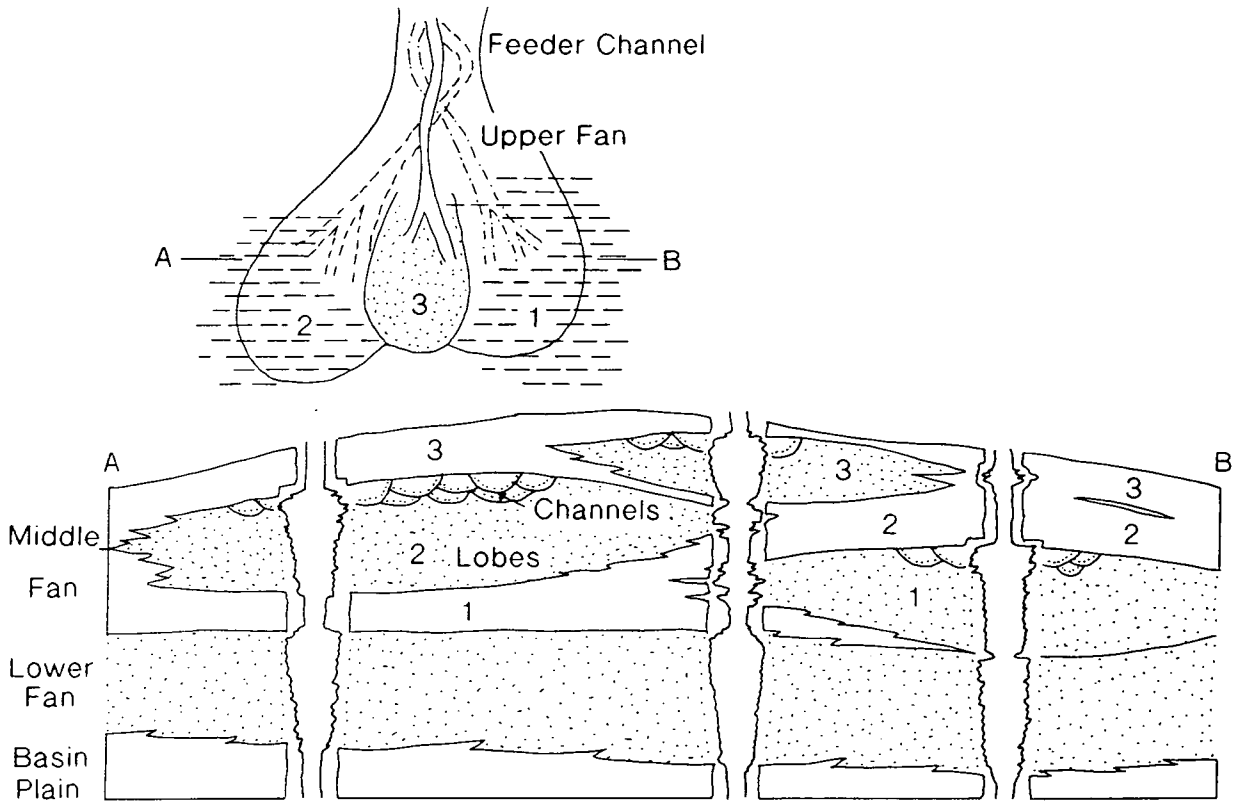

Figure 5.21 Hypothetical model showing lateral switching of suprafan lobes (1-3) in plan view (upper diagram) and facies distribution in cross section (lower diagram). Stippled area denotes sandstone and black area represents mudstone in the cross-section. Logs show expected SP of GR (left) and resistivity (right) responses. The offset stacked suprafan lobes with mudstone blankets would develop excellent stratigraphic traps (From Walker, 1978).

(Fig. 5.22) (Damuth et al., 1983a, 1983b), and the Mississippi Fan (Weimer, 1989). Weimer's (1989) study of the Mississippi Fan identifies and maps 17 different channels and distributary channels, which have deposited sediment within the fan system from the late Pliocene to the Pleistocene (Fig. 5.23). His work also illustrates that, taken separately, each channel acts as a point source of sediment, whereas the combined picture of all the channels and their distributaries shows that the fan actually has a linear source (Reading, 1992).

The depositional histories of submarine fan deposits are extremely important to the present study, as it is in this area of submarine fan deposition where the process of differential compaction may influence subsequent depositional locations and geometries (Allsop & Swarbrick, 1992; Allsop et al., 1992). There are essentially two possibilities for differential compaction to control deposition depending on the rate at which compaction occurs with respect to deposition, outlined in section 2.3, Chapter 2.

Either scenario illustrates how differential compaction can influence the locations and geometries of turbidite sand deposits, as described in modern fan settings (e.g. Damuth et al., 1983a; Weimer, 1989). In simple terms the process favours deposition of sand above the previous mud, and encourages the off-setting of subsequent sand bodies, a phenomena often described in both modern and ancient systems (Heritier et al., 1979; Damuth et al., 1983a; Weimer, 1989; Berg & Royo, 1990; Kulpecz & Van Geuns, 1990; Hall & Link, 1990; Imperato & Nilsen, 1990; Whyatt et al., 1991; Timbrell, 1993; Newman et al., 1993; Jenssen et al., 1993; O'Connor & Walker, 1993). Sections 5.5.4 and 5.6 will attempt to show how the present study envisages this process working within the submarine fan depositional system of the Montrose and Arbroath area of the North Sea.

5.5.3 Similar Field Models.

As mentioned before submarine fan deposits commonly form hydrocarbon reservoirs throughout the world (Walker, 1978; Stow, 1985), mainly due to their relationship to basinal, organic rich mud rocks, the common occurrence of thick, high porosity sandstones within the channel and lobe deposits, and mud rocks often blanketing such deposits, producing the perfect source, reservoir, and seal arrangement. For this reason there are many papers in the literature concerning depositional models for submarine fans, although there is a wide variety of models due to the differences mentioned in the previous sections (i.e. basin size, tectonic

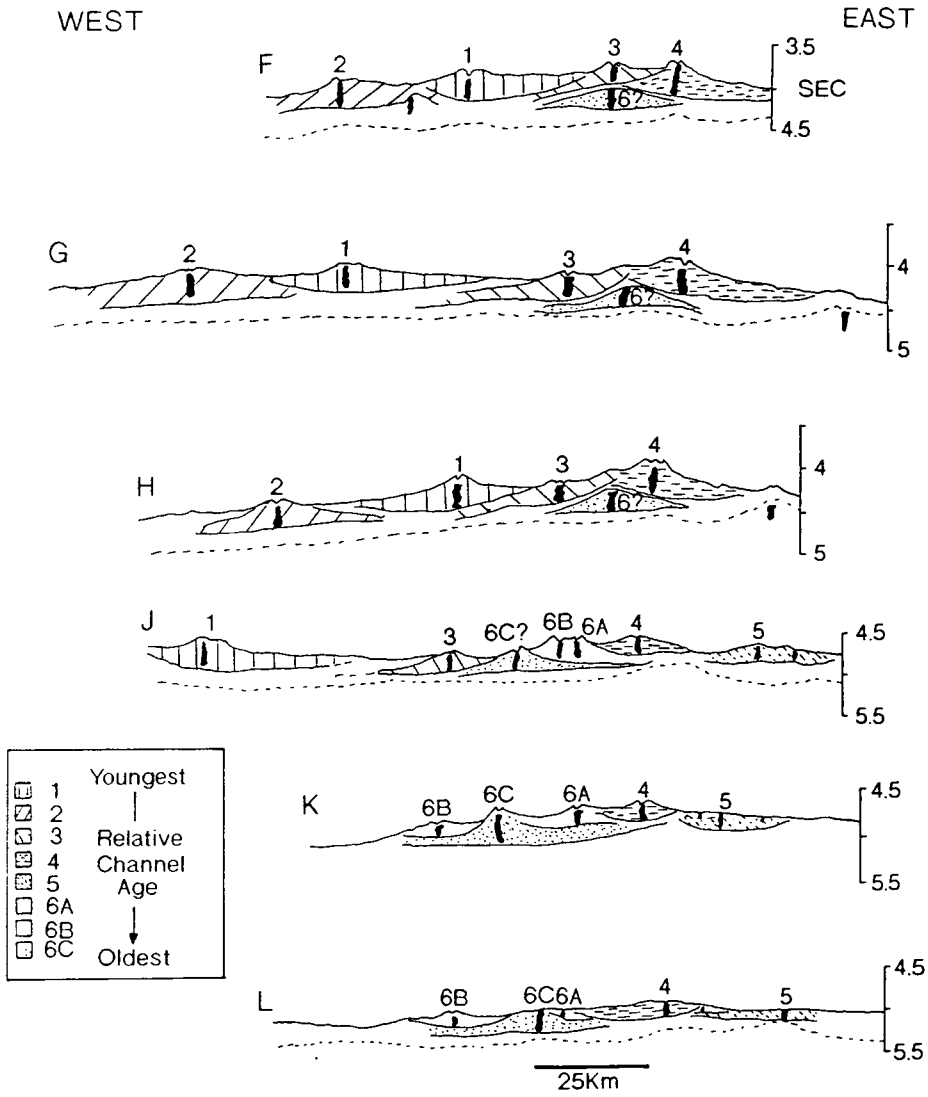

Figure 5.22 Line drawings traced from original seismic profiles showing stratigraphic relationships between major channel-levee systems on middle Amazon Fan. Numbers 1 through 6C over channel axes indicate relative age of each major channel-levee system (in order of increasing age). Heavy lines and shading patterns show lateral extent of levee sequence associated with each channel. Black area beneath each channel axis represents high-amplitude reflectors (possibly from coarse sediment). Dashed line is prominent acoustic reflector (From Damuth et al., 1983).

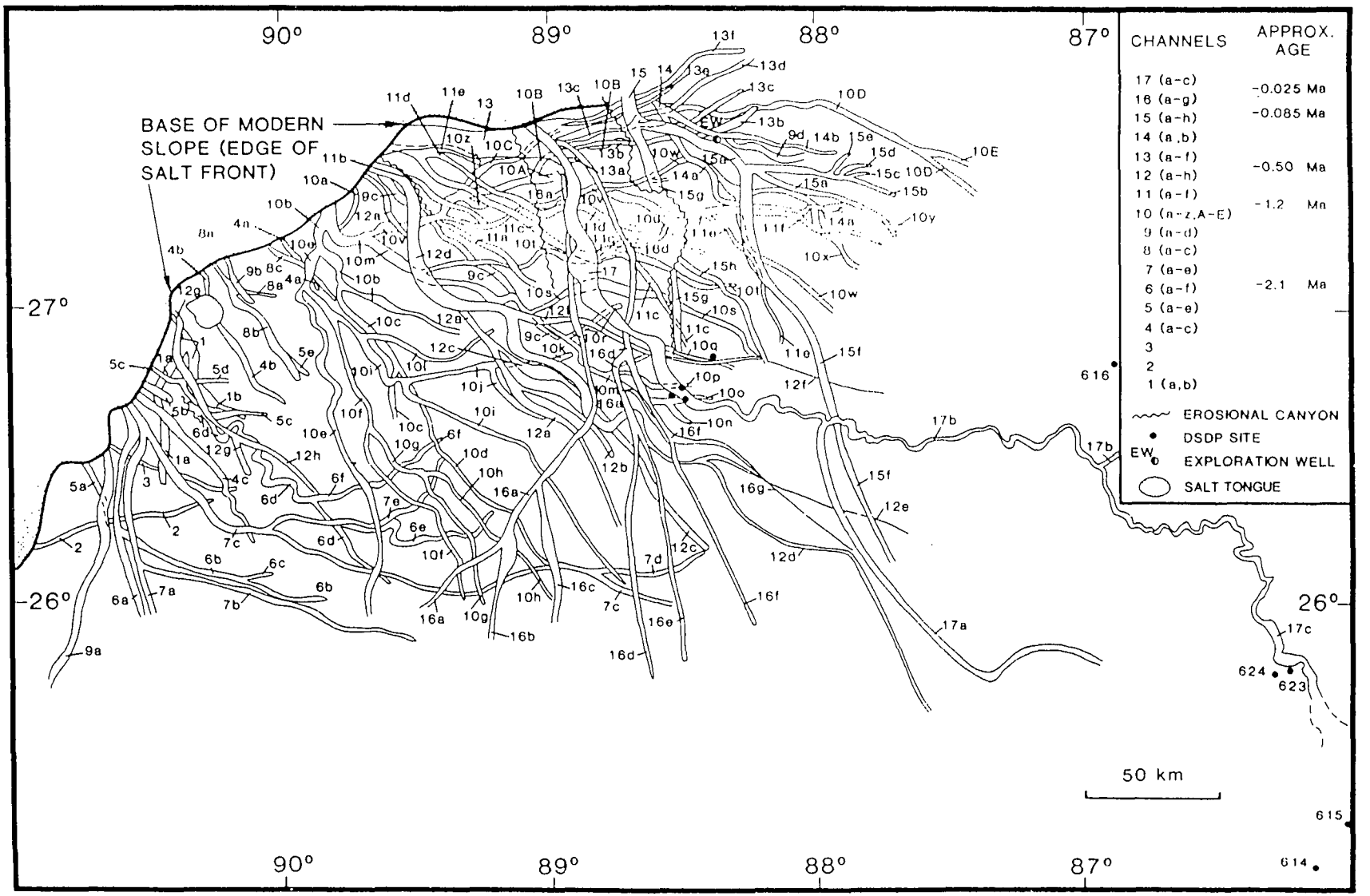

Figure 5.23 Composite map of the 17 channel-levee systems identified in the Mississippi Fan (From Weimer, 1989).

setting, and sediment supply). The following section summarises the important papers relating to the Montrose - Arbroath area of the North Sea, resulting in the proposal for a depositional model for the area.

Many of the fields of similar stratigraphy and depositional style from the North Sea are Tertiary in age, e.g. the Frigg Field (Heritier et al., 1979), the Forties Field (Walmsley, 1975; Hill & Wood, 1980; Carman & Young, 1981; Kulpecz & Van Geuns, 1990), the Nelson Field (Whyatt et al., 1991) the Balder Formation, Block 9 (Timbrell, 1993), the Gryphon Oil Field (Newman et al., 1993), and the Balder Field, Norway (Jenssen et al., 1993). However, studies of other oilfields with submarine fan reservoirs, particularly in California, also bear some similarities to the oilfields of the present study, e.g. the Yowlumne Field (Berg & Royo, 1990), Midway-Sunset Field (Hall & Link, 1990), and the Arbuckle Field (Imperato & Nilsen, 1990). Depositional models and processes within the papers describing these fields can also provide excellent insights for the present study.

5.5.3.1 North Sea Sequence Stratigraphy.

Many regional studies of the sand development and sequence stratigraphy of the Palaeogene and Cenozoic fill of the Central and Northern North sea have been published (e.g. Parker, 1975; Sutter, 1980; Rochow, 1981; Knox et al., 1981; Morton, 1982; Stewart, 1987; Vining et al., 1993; Anderton, 1993; Galloway, et al., 1993; Armentrout et al., 1993; Hartog Jager et al., 1993; Morton et al., 1993). This section will deal with the recent understanding of the sequence stratigraphy and sand distribution for these areas, concentrating particularly with the Palaeocene, but also providing a broad overview of the Palaeogene Period.

Regionally, Stewart (1987) developed a seismic stratigraphic framework for the Palaeogene sediments of the Central North Sea, using unconformities to separate the stratigraphy into ten mappable depositional sequences (Fig. 5.24). Biostratigraphic correlation of the ten sequences enabled Stewart (1987) to produce a chronostratigraphy for the area (Fig. 5.25), in addition to a coastal onlap curve (Fig. 5.26), the latter having major significance concerning the regional sea-level and subsidence pattern of the North Sea.

Galloway et al. (1993) provides a detailed study of the sequence stratigraphy of the Cenozoic fill of both the Central and Northern North Sea Basin. They divided the region into four tectonosequences, the Palaeocene, the Eocene, the Oligocene and the Miocene, which when combined record the regional structural evolution of the basin and adjacent source areas.

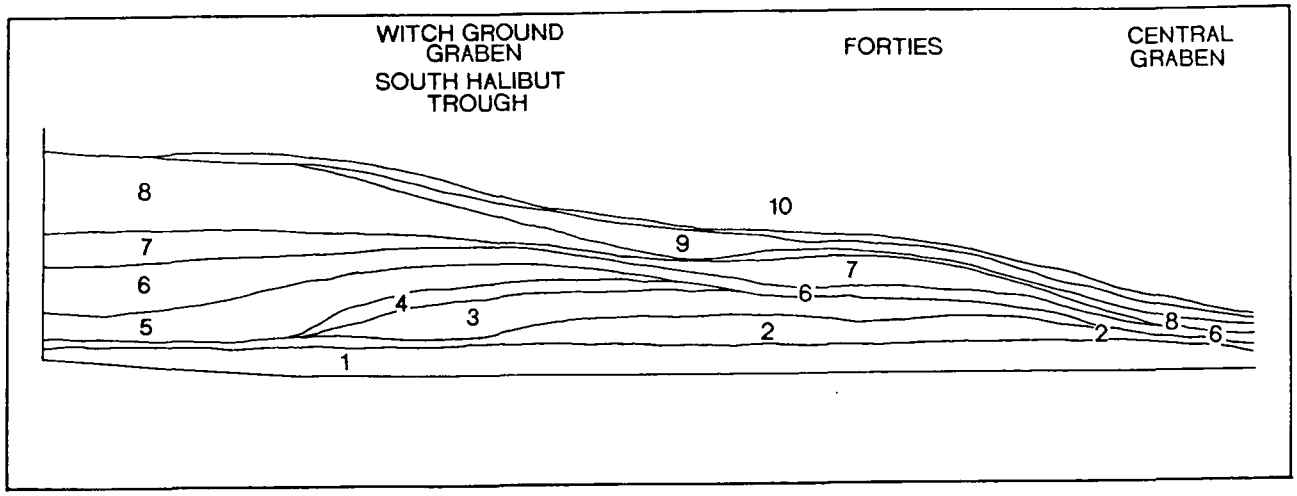

Figure 5.24 Early Palaeogene depositional sequences, central North Sea (From Stewart, 1987).

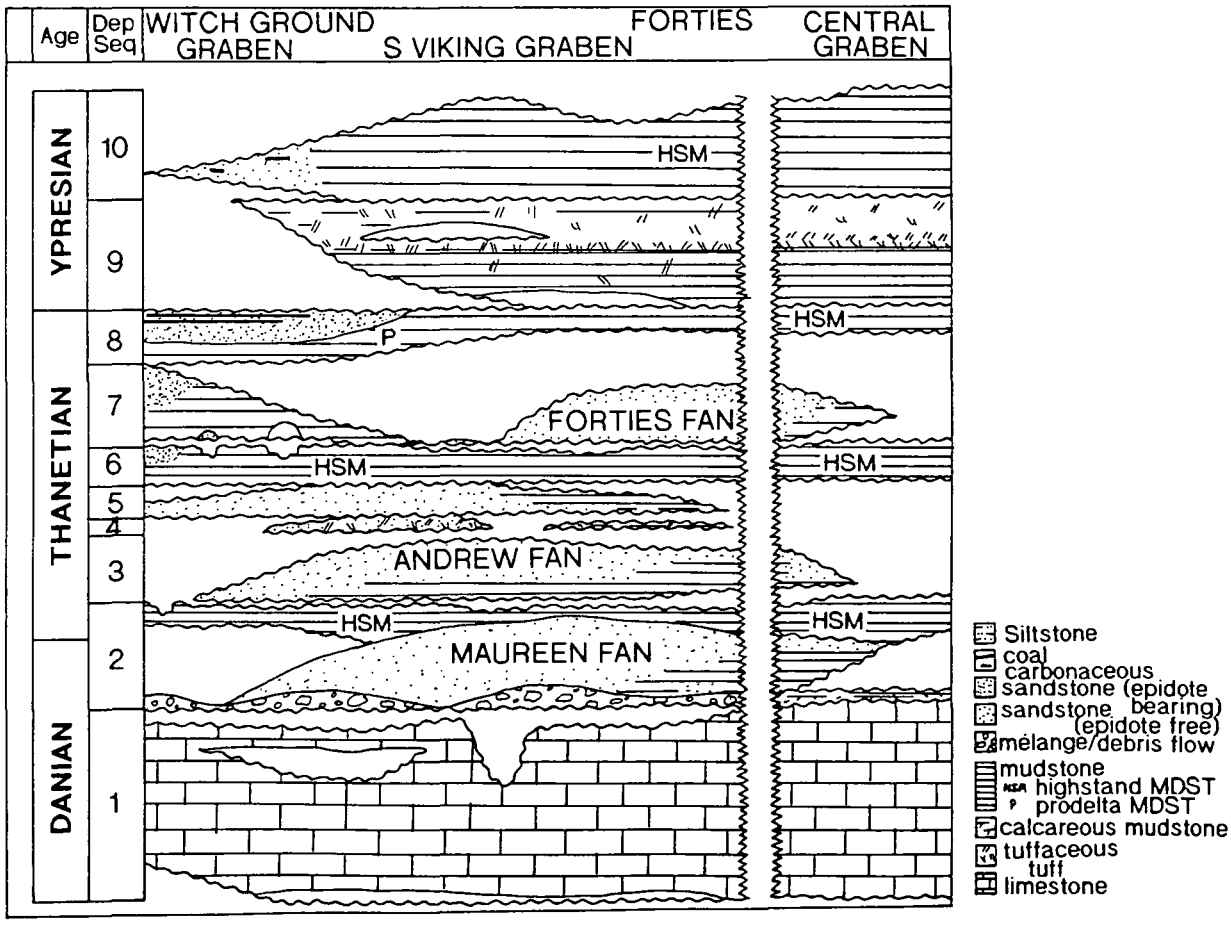

Figure 5.25 Composite chronostratigraphical diagram for the early Palaeogene of the central North Sea (From Stewart, 1987).

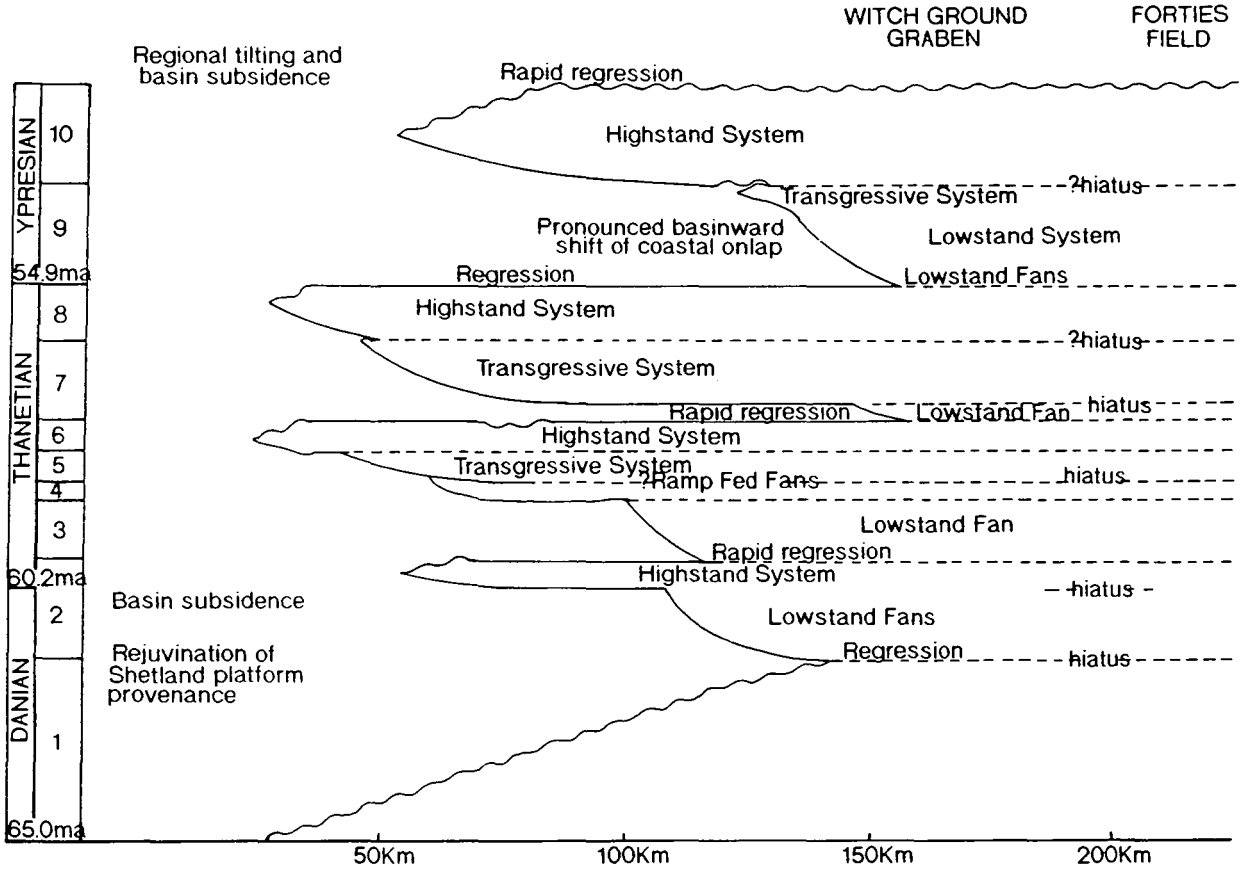

Figure 5.26 Coastal-onlap curve for the early Palaeogene of central North Sea, showing the relative onlap position of each of 10 depositional systems. The terms highstand and lowstand refer only to the relative position of sea level (From Stewart, 1987).

Each tectonosequence contains a number of depositional episodes, which are stratigraphic sequences, which accumulated during distinct episodes of sediment influx and accumulation (Galloway et al., 1993). As a general rule, each tectonosequence begins with deposition concentrated within the basin centre, in or near the axial troughs. Sediments of subsequent sequences extend up onto one or both basin margins, onlapping older stratigraphic units (Galloway et al., 1993).

The Palaeocene tectonosequence was initiated by large-scale uplift of the British Isles, related both to the opening of the Atlantic and Thulean volcanism. The uplift was also accompanied by tilting to the southeast (Hartog Jager et al., 1993). Uplifting was a result of rejuvenation of faulting, inversion, with greater regional uplifting of the sandstone-rich Shetland and Scottish source areas (Galloway et al., 1993). Depositional responses in the basal Maureen episode include the reworking of chalk and the introduction of coarse siliciclastic material into the basin (Johnson, 1987; Stewart, 1987). By early Thanetian time (approximately 60Ma), the combination of the drainage patterns from the Shetland and Scottish uplands (a source area of about 45,000Km^2) focused the bulk of sediment supply into the NW Moray Firth Basin. Sand deposition during the lower Andrew, upper Andrew and Forties depositional sequences, was concentrated in a prograding sand-rich braid delta system, which built south and eastward along the axis of the Moray Firth, and also in a succession of extensive delta-fed submarine aprons that spilled out of the Moray Firth and into the Viking and Central troughs. Galloway et al. (1993) uses the term apron for shelf or delta-fed submarine systems, restricting the use of the term fan to point-sourced, toe-of-slope, and basin-floor depositional systems, that commonly show a radial sediment distribution and facies organisation. Sutter (1980) illustrates the Late Palaeocene palaeogeography, showing the extent of the Moray Firth delta, and the basinal deposits (Fig. 5.27).

Further seismic mapping and decompaction of the Moray Firth braid-delta front show that its approximate original depositional thickness indicates a platform relief in the order of 300m (980ft), and prodelta slope angles of 3-5° (Galloway et al., 1993). Combination of the substantial bathymetry, and the steep depositional slope to the delta front would efficiently trigger, and accelerate, high-density turbidity currents which would deposit sediment further southeast in the basin (Fig. 5.27). Additionally, at this time, subsidiary drainage axes prograded smaller braid delta and associated sandy slope apron systems into the East Shetland (Ninian apron) and Forth Approaches

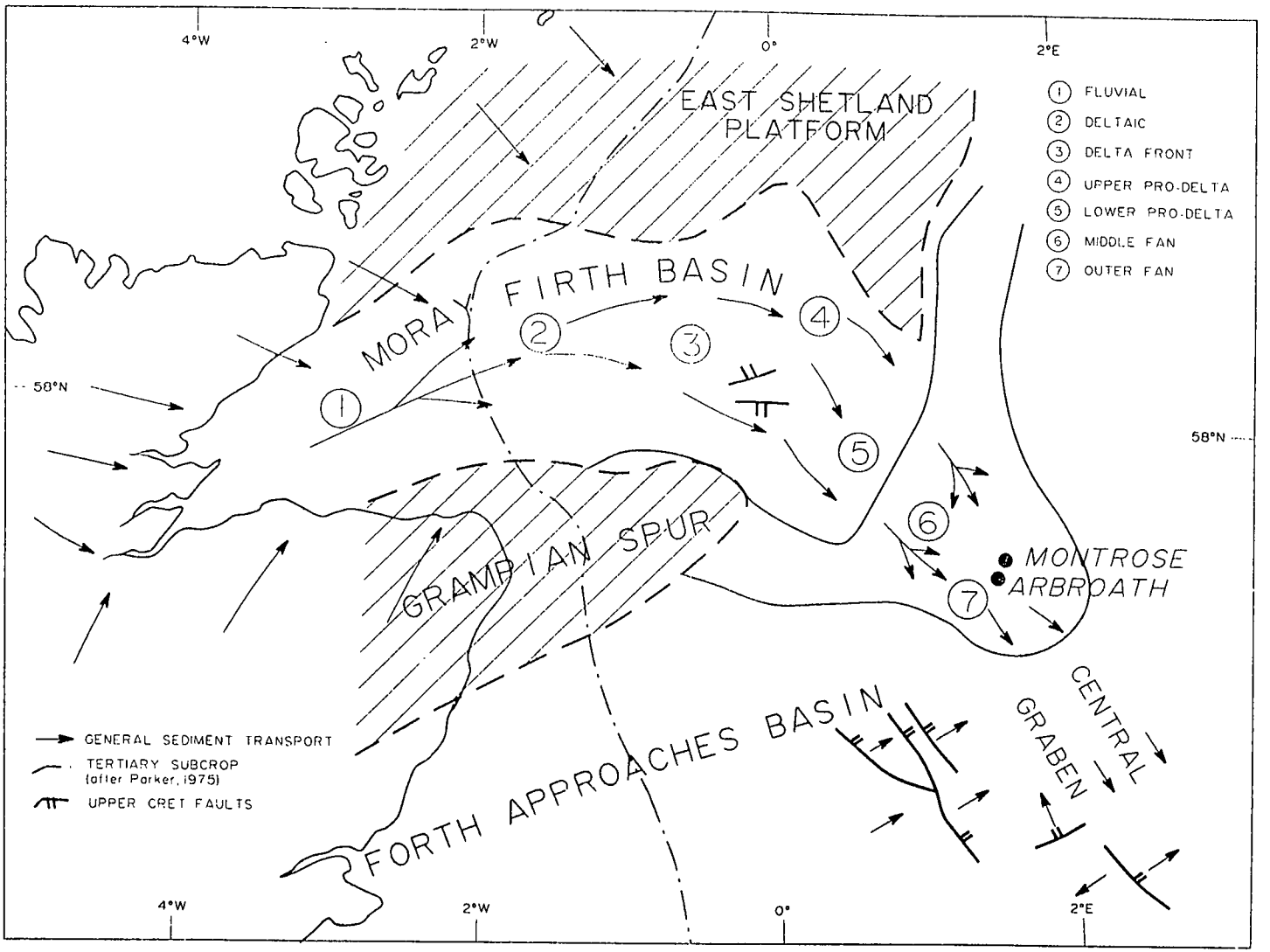

Figure 5.27 Late Palaeocene palaeogeography(Modified from Sutter, 1980).

(Gannet apron) basins. The Shetland Platform appears to have been largely a high-energy bypass shelf locally traversed by seismically imaged small erosional channels (Galloway et al., 1993).

During late Thanetian time (56.5-57Ma), braid-delta progradation was forced eastwards due to the effects of ongoing inversion and eastward tilting of the inner Moray Firth basin, reworking older braid-delta deposits (Milton et al., 1991). Also, the slope apron system became inactive as sand remobilisation from the delta front diminished (Galloway et al., 1993). The result was the deposition of the Dornoch and Beauly/Balder sequences, which consist chiefly of sandy braid-delta deposits fronted by muddy, basinal muds in the axial trough. Several possible reasons exist for the decrease of sand remobilisation including:

- reduced bathymetric relief of the delta front as the basin-floor apron aggraded.
- a decrease in seismic activity as a trigger for large-scale slope failure.
- decreasing rate of supply of sediment from the source area to the braid-delta system (Galloway et al., 1993).

Extensive progradation of the Beauly sequence braid-delta into the East Shetland Basin, and contemporary retrogradation of the youngest delta lobes in the Moray Firth depocentre suggests that sediment supply was diverted northward. A strike-fed shore zone system prograded across the Shetland Platform, between the two deltaic depocentres, to the bounding faults of the Viking Graben (Galloway et al., 1993).

The Beauly/Balder episode was, in part, a response to the terminal Palaeocene collapse of the Scotland/Shetland uplift and the North Sea Basin. The episode ended with transgression and submergence of the basin margin with widespread deposition of a transgressive sediment blanket culminating in the Balder tuff marker, forming a condensed section (Galloway et al., 1993). Foundering of the depositional shelf margins and tectonic adjustments associated with the plate boundary reorganisation that initiated opening of the Norwegian Sea resulted in considerable mass wasting of the depositional slope that fronted the deltaic headlands and inter-deltaic shore zone. Mounded, chaotic slump and debris flow lobes form a basinal apron deposit that extends into the Viking trough. As transgression proceeded, discrete turbidite mounded forms (e.g. the Balder fan and the Gryphon fan) and protofans (lower Frigg sands of Brewster (1991)) were fed by localised submarine channel systems (Galloway et al., 1993). These channel systems

later became conduits for submarine sediment bypass during the subsequent early Eocene depositional episode. A seismically defined channel complex in the inner Moray Firth, suggests the evolution of a transgressive estuarine system in the coastal embayment. Tidal and wave reworking of late Palaeocene sediments here supports the assumption of high marine energy flux throughout this time (Galloway et al., 1993).

Looking in more detail at the submarine fan sedimentation throughout the Palaeogene Period of the North Sea it is possible to recognise four 'second-order sequences' (Vail et al., 1977) on regional seismic data. These are the Andrew, Forties, Frigg/Tay and Alba sequences (Hartog Jager et al., 1993). In sequence stratigraphic terms a sufficiently large relative fall in sea-level, eustatically or tectonically induced, can initiate deposition of a submarine fan system (Fig. 5.28). The relative fall in sea-level results in erosion of the hinterland and shelf, incision of rivers, and possibly the excavation of canyons across the shelf and slope (Hartog Jager et al., 1993). Over the hinterland, shelf and slope areas, an unconformity will be created, corresponding to a Type I sequence boundary (Van Wagoner et al., 1987). The eroded sediment bypasses the shelf and is deposited in the deep marine realm as a submarine fan. Subsequent sea-level rise causes the trapping of sediment on the shelf (which gradually back-fills incised valleys) and causes flooding of the pre-existing shelf area. The ideal pattern of facies development can generally be found where a clear slope break occurs, with a relatively abrupt transition from shallow to deep water. Where the transition is more gentle, a relative sea-level fall can cause rapid progradation of the shelf, as seen in the Palaeocene 'Ninian' shelf sequence in the East Shetland Basin (Hartog Jager et al., 1993). Throughout the Tertiary, in both the Central and Northern North Sea, phases of repeated shelf progradation and erosion with associated submarine fan deposition can be recognised on regional seismic data.

Hartog Jager et al. (1993) have compiled the Palaeogene sequences for the Central and Northern North Sea based on log interpretation of shelf/slope progradational cycles, seismic stratigraphic studies, and extensive biostratigraphy (both palynology and micro-palaeontology) (Fig. 5.29). The four second-order sequences each contains a submarine fan system in its basal part, named after its sequence, with the upper sections formed by a clay-rich interval which can generally be correlated across the entire deep basin. These are the Lista, Sele, Horda and Hutton Clay formations (Hartog Jager et al., 1993).

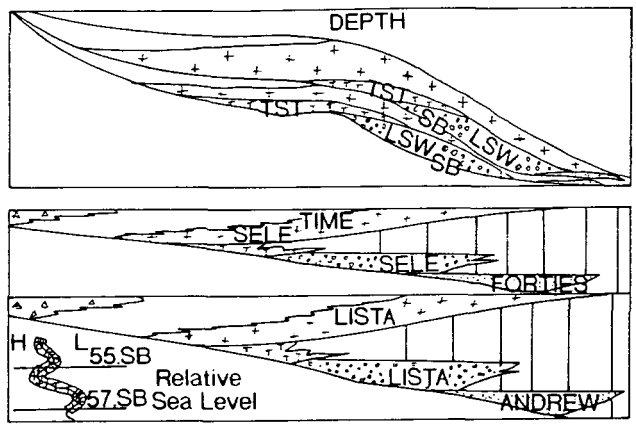

Figure 5.28 Sequence stratigraphy: two conceptual sequences are shown in both depth and geological time. The depth section shows the relationship of different systems tracts, whereas the temporal relationships of the systems tracts are shown in the lower section. The vertical striped areas are condensed intervals or depositional hiatuses. The relationship of the systems tracts to relative sea-level is shown (SB=sequence boundary) (Modified from Vining et al., 1993).

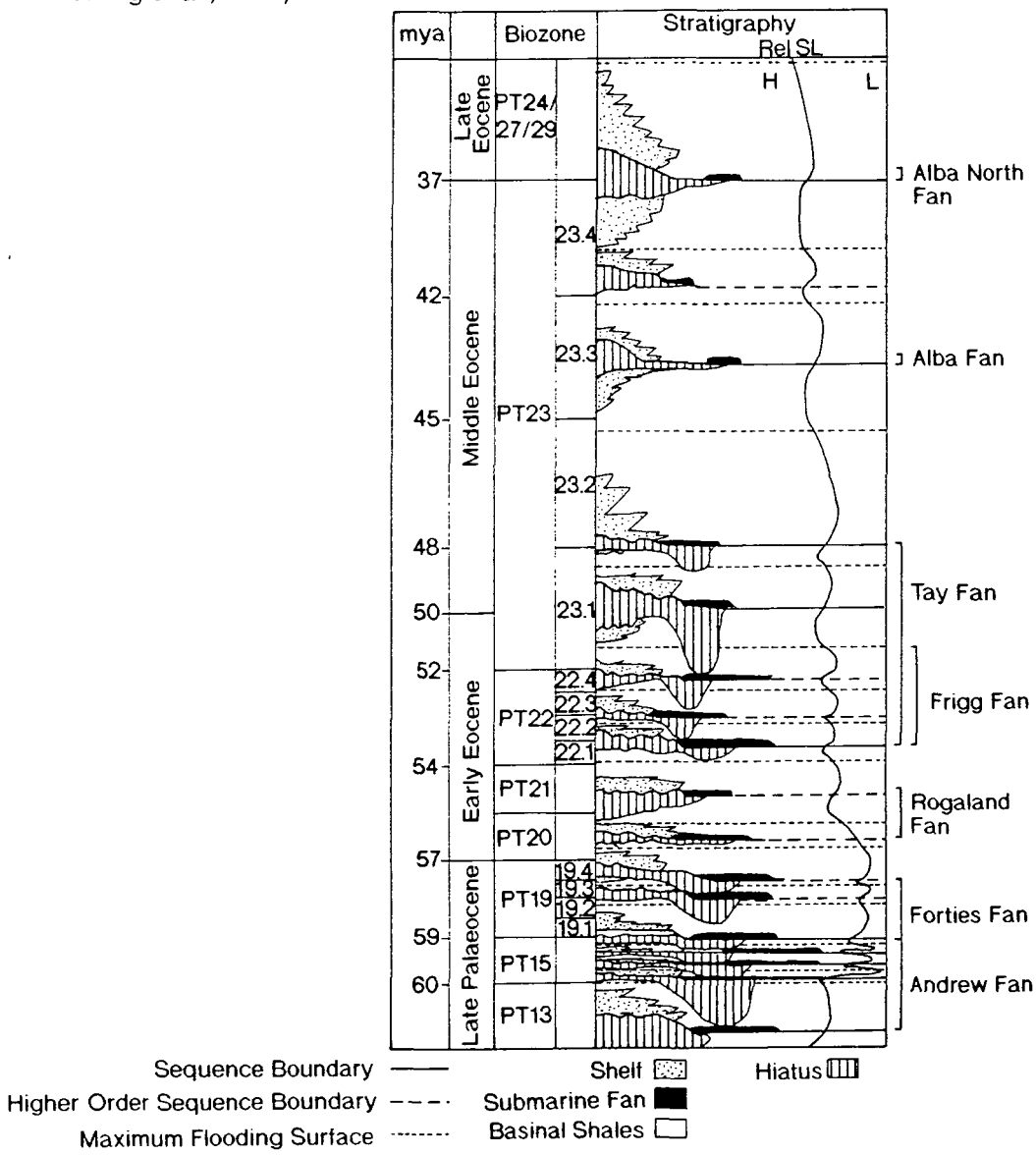

Figure 5.29 Palaeocene/Eocene sequences (From Hartog Jager et al., 1993).

Seismic facies analysis by Hartog Jager et al. (1993) has enabled the mapping of the facies distributions, showing the shelf, slope and basin environments, with the sand and mud-prone areas indicated (Figs. 5.30a, b & c). Further regional seismic and sedimentological data, including 3D seismic data, allowed Hartog Jager et al. (1993) to build up a picture of the geometries of the Tertiary submarine fans. Their observations, summarised in Table 5.2, show a range in fan types from widespread sand-rich 'sheet-like' fans, to narrow isolated channel complexes encased in shale.

	General Fan Type	Individual Channel Dimensions (width/depth)	Degree of Channel Connectivity
Alba Fan	Slope Fans and Clay-Rich Systems	Large (1-2Km wide, up to 100m deep	Low (isolated channels)
Rogaland Fan			
Frigg Fan, Tay Fan		Intermediate (0.5-2Km wide, tens of metres deep)	
Forties Fan			Medium
Andrew Fan			
	Basin Floor Fans	Unchannelised	High (amalgamated channels)

Table 5.2 Internal geometries within various submarine fans in the North Sea Palaeogene (from Hartog Jager et al., 1993).

The Andrew and Forties Fans ('Sheet-like').

The Andrew Fan is more extensive than the younger Forties Fan, although both are centred over the Outer Moray Firth and Central Graben (Hartog Jager et al., 1993). The time-equivalent fan systems active in the Viking Graben were somewhat smaller. Overall, the Andrew Fan displays a giant wedge-shaped geometry, which exceeds 700m (2000ft) at its thickest point. The seismic facies of both the Andrew and Forties fan systems consists of discontinuous, sub-parallel reflectors (Hartog Jager et al., 1993).

Figure 5.29 shows that the Andrew Fan may be divided into three units, which ideally fine upwards. The base of each of these units is a third-order sequence boundary, and is marked by the sudden appearance of massive channelised sands in the basin (Hartog Jager et al., 1993). Subsequently, the fan becomes less channelised, with a greater amount of fine overbank

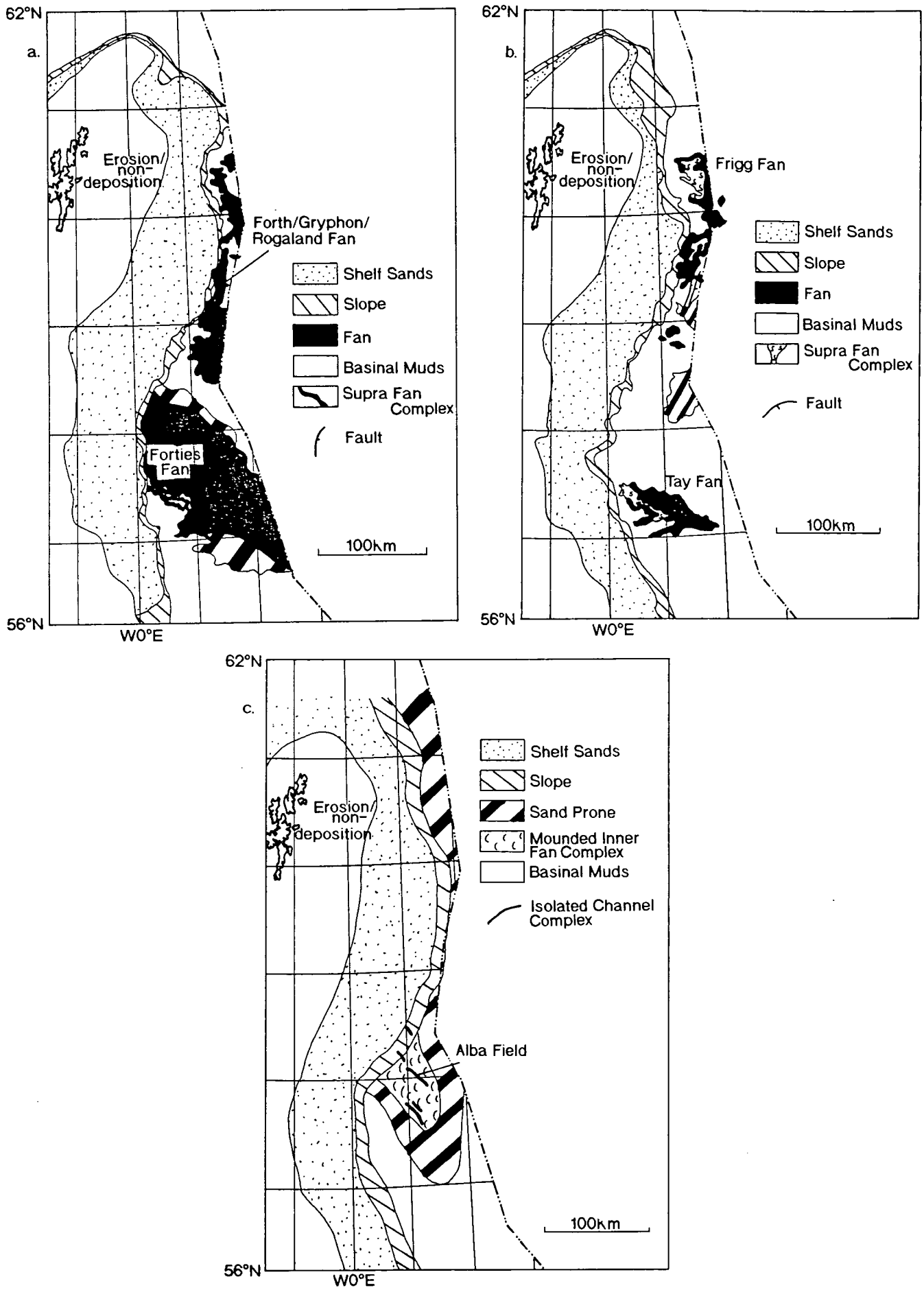

Figure 5.30a,b,c Facies maps of a) Upper Palaeocene, Forties sequence; b) Lower Eocene Frigg/Tay sequence; c) Middle-Upper Eocene, Alba sequence (Modified from Hartog Jager et al., 1993).

deposits forming, presumably due to sea-level rise and a decrease in sand supply to the fan.

The Forties Fan shows a similar overall wedge shape in cross-section, however, it is smaller in volume and thinner, reaching a maximum thickness of 411m (1350ft), than its predecessor. Variations in thickness are generally related to the distance from the source area, the presence of local palaeo-highs and salt activity. Log correlations and biostratigraphic studies have shown that the Forties Fan system can be divided into two third-order sequences, each marked by the widespread deposition of massive channel sands (Hartog Jager et al., 1993). Well logs indicate that massive stacked channel complexes can be found in both the basal and upper parts of the fan system, although these are not usually visible on 2D seismic data. The stacked channel complexes do, however, occur right up to the fan fringe, as seen in the Cod Field (Kessler et al., 1980) and the Everest Field (Thompson & Butcher, 1990).

Forties Fan channels appear to be 2.5-3km wide, 50-100m thick and separated by interchannel areas of approximately 500m width, within the Montrose - Arbroath area (Whyatt et al., 1991). The gentle bi-directional downlap seen on cross-sections of the channels in the area also suggests that the sand dies out gradually.

The controls on the thalweg of the central channel complex in these systems are poorly understood (Hartog Jager et al., 1993). Three main possibilities exist; pre-existing relief, an erosional feature, or confinement by stable muddy levees. In the upper reaches of the fan systems incision of the channels can be seen, however, this generally dies out in a basinward direction with little or no erosion occurring at the base of channel complexes. Hartog Jager et al. (1993) point out that to produce the middle fan aspect of these systems on logs and in core, the sand-rich nature of the fan as a whole and its overall 'sheet-like' geometry, requires both a large number of channels and a high degree of channel switching. Flow stripping, as described in section 5.5.2, will produce such a phenomenon with rapid abandonment of the distal portions of the original channel complex, and new channel formation, probably aided by differential compaction of the former fine, muddy, overbank deposits.

Thickness variations seen within the Andrew and Forties fans indicate that the directions of channels have sometimes been influenced by underlying faults (Hartog Jager et al., 1993). These may have affected the topography of the Palaeocene sea-floor in two ways: either as a result of

higher subsidence rates on the hanging wall (due to differential compaction) or as a result of syn-sedimentary reactivation. The fans can be seen to thin over major basement highs, such as the Forties-Montrose High in the Central Graben. Also, in the Gannet area, syn-sedimentary salt movement has produced the thickening of the fans in the rim synclines, and its thinning or disappearance over the apex of the salt structures (Armstrong et al., 1987).

The Frigg and Tay Fans (Mounded).

Both the Frigg and Tay fans, whose distributions are shown in Figure 5.30b, show an upward increase in mounding on regional seismic data, reflecting the evolution from basin-floor, sheet-like fans, to slope fans (Hartog Jager et al., 1993).

The Alba and Rogaland 'Fans' (Isolated Channel Complexes).

These type of fans form by the persistent vertical stacking of turbidite channel complexes, resulting in linear, massive sand fairways which pass rapidly into fine overbank muds in a lateral direction. Differential compaction across such channel complexes can form characteristic mounded geometries on seismic sections, approximately 1-2Km in width (e.g. the Forth Field).

The best examples of this type of fan are the Alba Fan (Middle to Upper Eocene) and parts of the Rogaland Fan (lowermost Eocene) (Hartog Jager et al., 1993). Both fans were deposited after minor relative sea-level falls, during an overall transgressive regime. In both cases deposition of the sands took place towards the end of a major uplift phase, with hinterland relief lower during the Eocene (Hartog Jager et al., 1993).

Evolution of Submarine Fans Through Space and Time.

The work of Hartog Jager et al. (1993) has shown that the Tertiary fans of the North Sea show a wide variation in geometries, ranging from wedge-shaped fans (Andrew Fan) to linear fans (Alba Fan). However, throughout all the fans a large amount of channelling is extremely common. Fan geometry will be determined by several factors, some of which having already been discussed in earlier sections of the present work, include:

- Elevation of the source area.
- Depth of the basin.
- Composition of the shelf sediments.
- Quantity of sediment supplied to the deep basin.
- Sand/mud ratio within the turbidites.

- Basin floor topography.

Many of these factors are inter-related.

Hartog Jager et al. (1993) recognise the evolution of individual fans from an initial 'sheet-like' geometry to a more mounded and channelised geometry, as shown by log correlations and seismic data. They also propose that the evolution can be directly explained in terms of sequence stratigraphy. During the Lowstand Systems Tract, a relative sea-level fall initiates deposition of a larger scale of sediment which also has a high sand/mud ratio. This promotes the formation of sheet-like basin-floor fans, whose channels switch frequently, and whose levees are easily breached, resulting in large areas with a middle fan aspect, as seen in the Andrew and lower part of the Forties Fan (Hartog Jager et al., 1993). At the start of the Transgressive Systems Tract, accommodation space increases, and increasing amounts of sediment become trapped on the shelf. The proportion of bed load in this shelf sediment will be relatively large, and the last stage of deep-sea fan deposition will involve relatively mud-rich sediment. This will cause the stability of levees to increase, and the position of channel complexes to become fixed, resulting in a situation of the most massive submarine fan sands being deposited (e.g. Alba Field) during a period when the actual overall sand supply is decreasing (Hartog Jager et al., 1993).

The evolutionary sequence of individual fans described above can also be ascribed to the complete Palaeogene sequence of submarine fans in the North Sea (Fig. 5.31). The scale on which this occurs can be interpreted as a first-order mega-sequence, punctuated by second-order sequences which represent the individual fans (Hartog Jager et al., 1993). This Palaeogene mega-sequence can also be interpreted in terms of eustasy (Hartog Jager et al., 1993), and it is at this point where the similarities between the models of Mutti (1985) and the submarine fans of the North Sea becomes clear (compare Fig. 5.31 taken from the North Sea with Figs. 5.32 & 5.33 (Mutti, 1985)).

Unfortunately Hartog Jager et al. (1993) neglect Mutti's (1985) submarine fan models based on sea-level, sand supply, and the position in the basin where deposition accordingly occurs (Figs. 5.32, 5.33, & 5.34). According to Mutti (1985), the Andrew and Forties fans partly represent a Type I, but mainly a Type II depositional system, with the Rogaland Fan probably representing the Type II to Type III depositional system above. The Frigg/Tay fan system represents the reintroduction of a Type II depositional sequence, which is subsequently overlain by the Alba Fan representing the

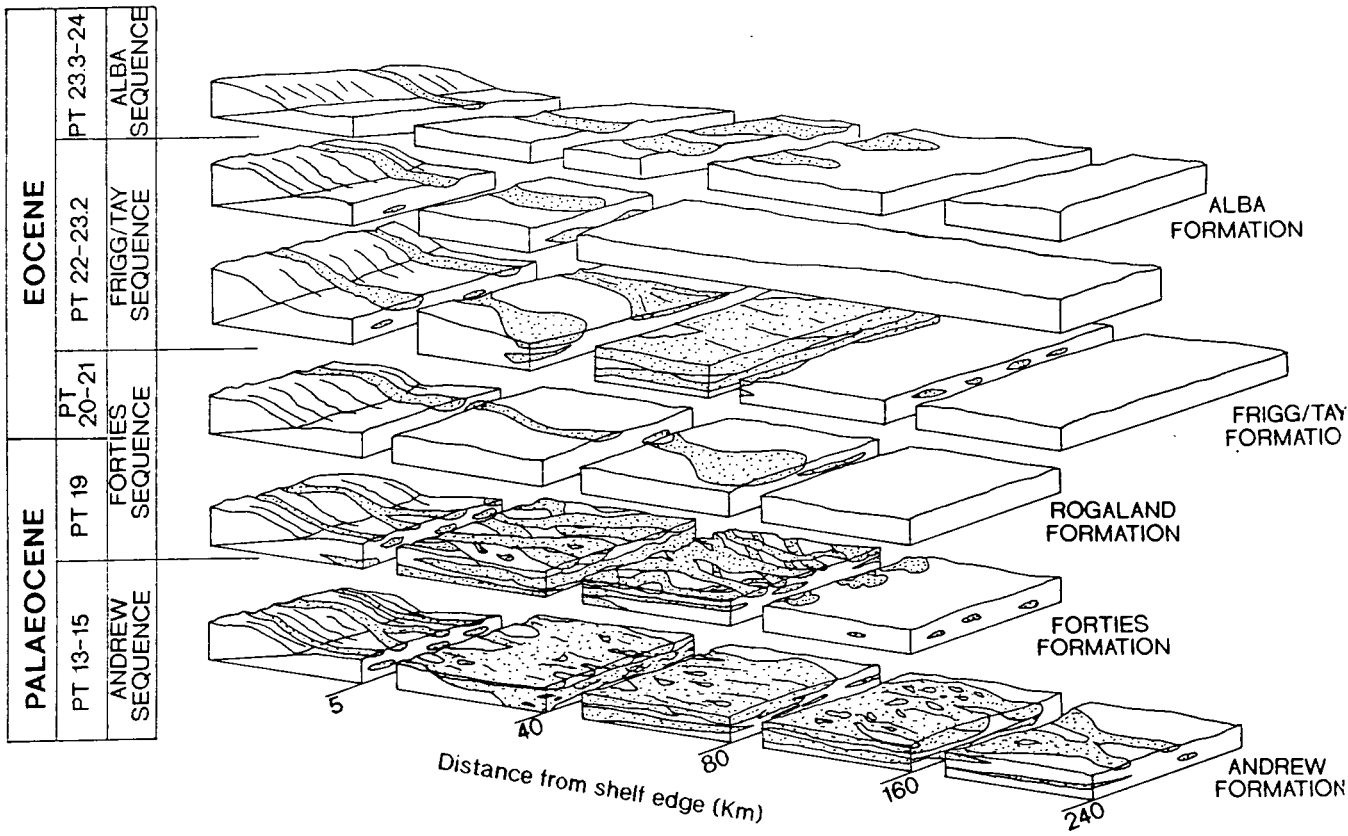

Figure 5.31 Schematic change in fan geometry through the Palaeocene and Eocene (From Hartog Jager et al., 1993).

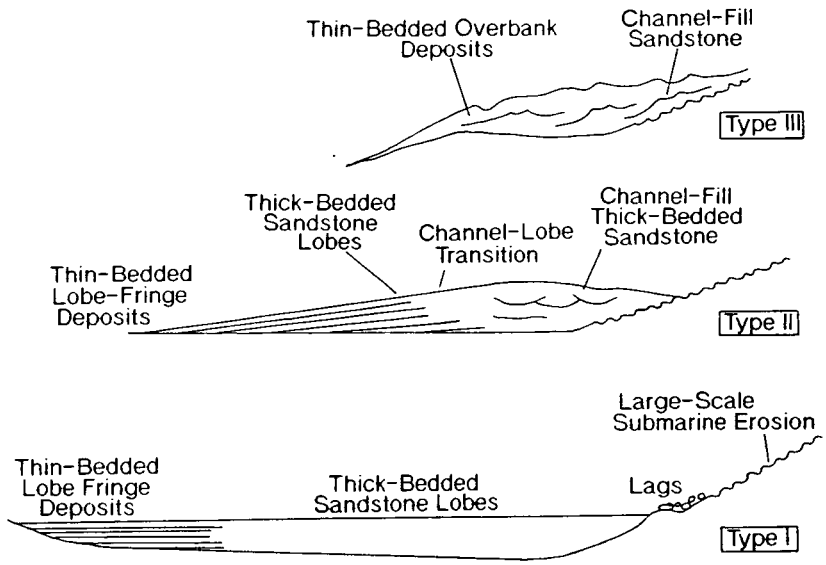

Figure 5.32 Three main types of turbidite systems recognised by Mutti (1985). The systems differ from one another mainly in terms of where sand is concentrated.

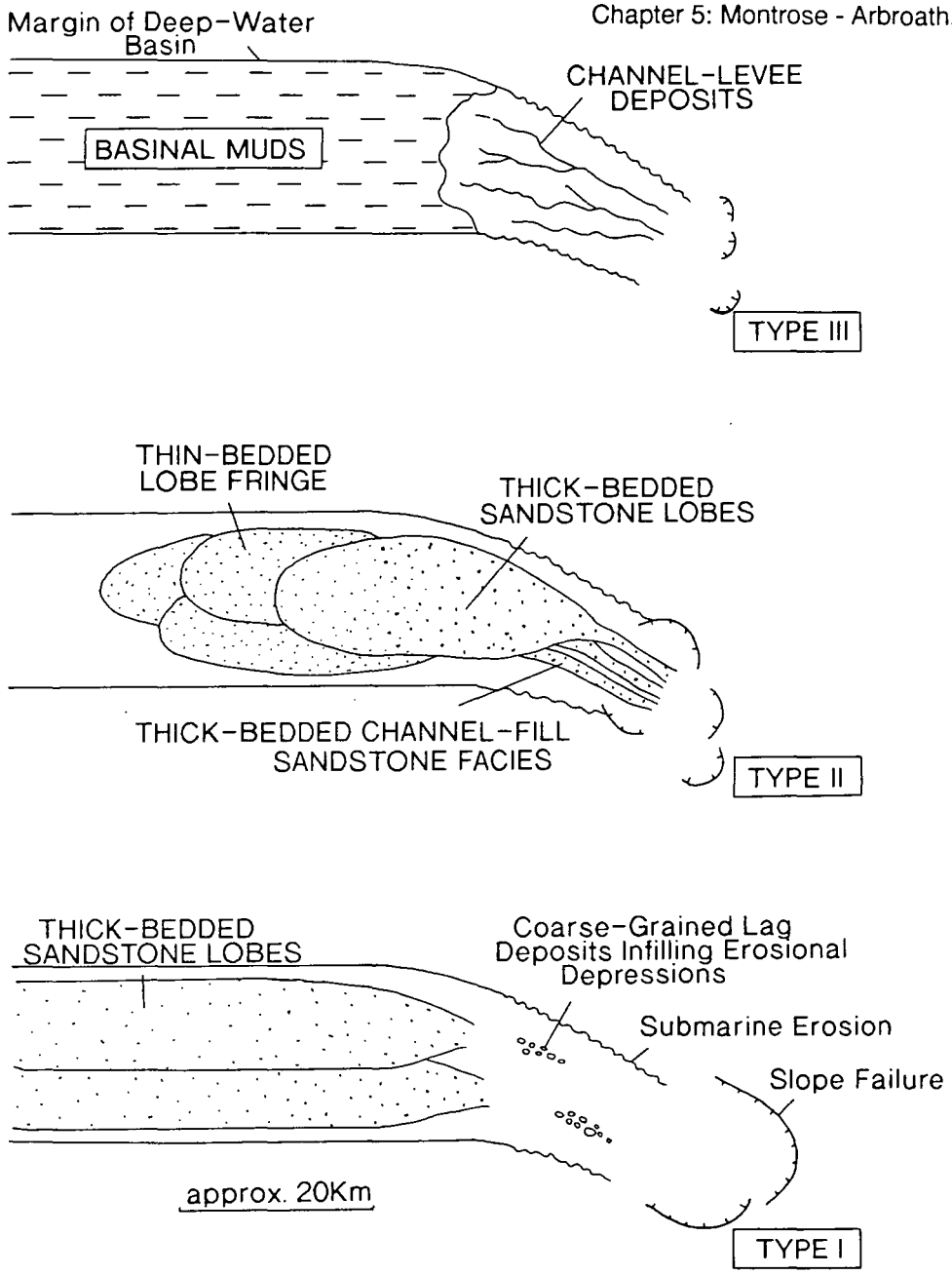

Figure 5.33 Main types of turbidite depositional systems. Deposition of sands within channels is progressively enhanced by the decrease in the volume of gravity flows (From Mutti, 1985).

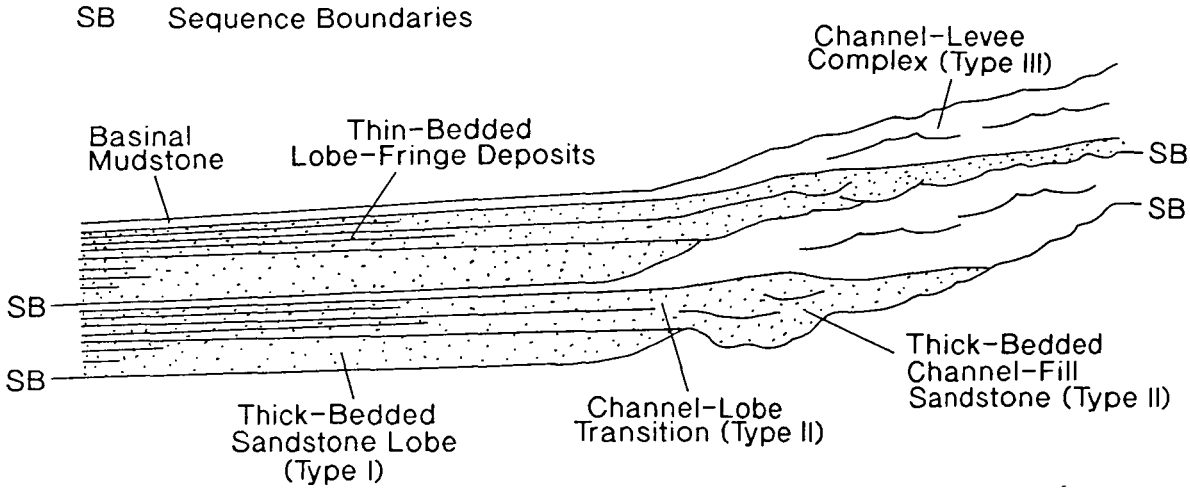

Figure 5.34 Changing character of sequence boundaries from the basin margin into the deeper parts of the basin. In this hypothetical example, the sequences are complete and show an evolution from Type I to Type II to Type III systems (From Mutti, 1985).

Type III depositional system. The relative sea-level curve shown in Figure 5.29 illustrates that both the Rogaland and Alba fans (Type III) are deposited during periods of relatively high sea-level compared with the underlying fans that form the Type II depositional sequences. Mutti's (1985) three types of depositional sequences can also be recognised on a smaller scale for the individual fans, although here the full sequence (Fig. 5.34) is not always developed.

5.5.3.2 North Sea Oil and Gas Fields.

The Frigg Field.

The Frigg Field (Fig. 5.10), one of the world's largest offshore gas fields, represents one of the early discoveries within the Palaeocene/Eocene submarine fan deposits of the Viking Graben. However, even at this early stage in development of such plays, it was noted that the structure of the reservoir was mainly submarine fan depositional topography enhanced by draping and differential compaction of the sands and muds (Heritier et al., 1979).

The overall lobate shape of the structure on seismic sections and maps (Fig. 5.35), combined with various sedimentological evidence suggested submarine deposition, and Heritier et al. (1979) noted that differential compaction in such an environment favours the vertical off-setting of clastic deposits, with new sediment being deposited above the shaley section on the flank of former thick sandy deposits (Figs. 5.36 & 5.37). They propose that the main structure represents the upper part of the fan and the apex its feeder channel. Lobes represent outer channels and levees in the middle part of the fan, whereas the low areas between lobes are formed due to the compaction of the more shaley beds between the channels (Heritier at al., 1979).

A complex history of deposition within the area resulted in the present field geometry, structure and extent of reservoir facies. The control on deposition began as a structural control, with sands being deposited on the southeastern flanks of the Frigg and East Frigg late Cretaceous anticlines (Heritier et al., 1979). However, subsequent depositional control resulted from a combination of the initial topography of the developing submarine fan, and the differential compaction between channel sands and their muddy levees/interchannel areas.

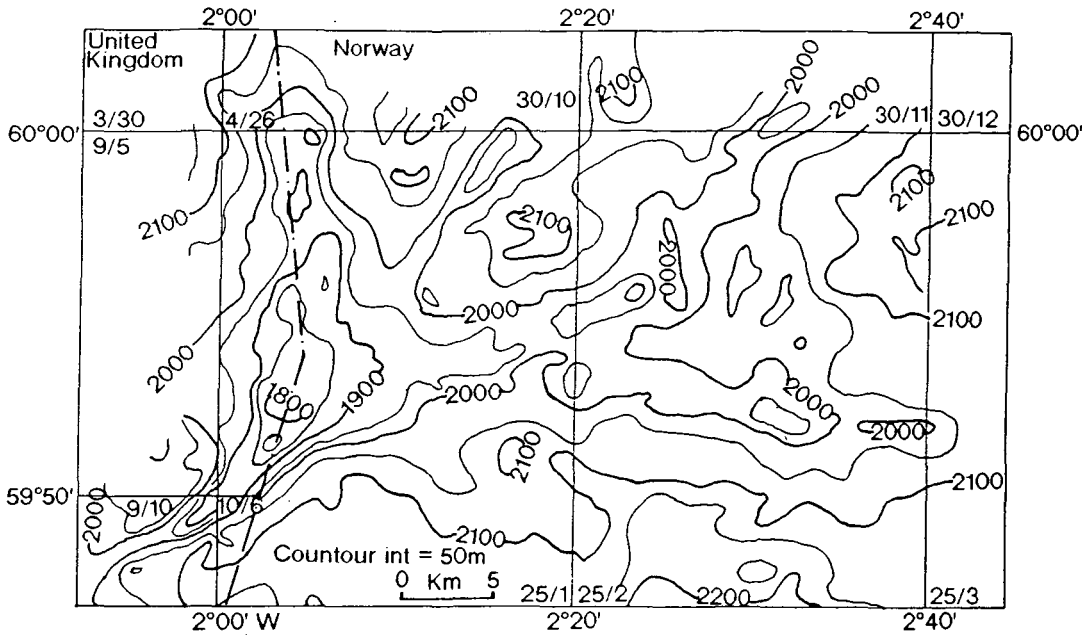

Figure 5.35 Seismic structure of Frigg Field at top of Frigg sand (From Heritier et al., 1979).

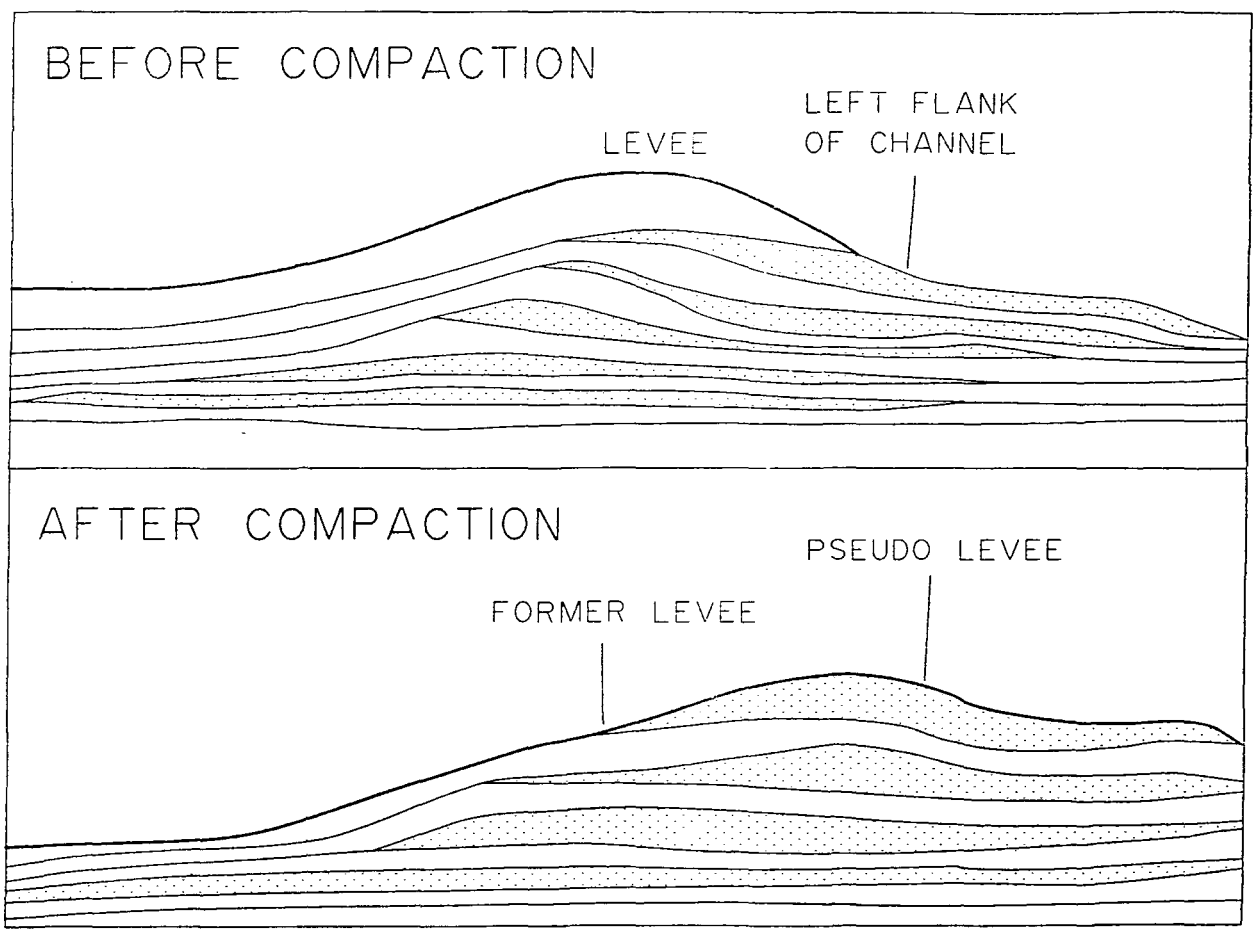

Figure 5.36 Differential compaction across a submarine fan channel-levee complex results in the production of a pseudo-levee (Modified from Heritier et al., 1979).

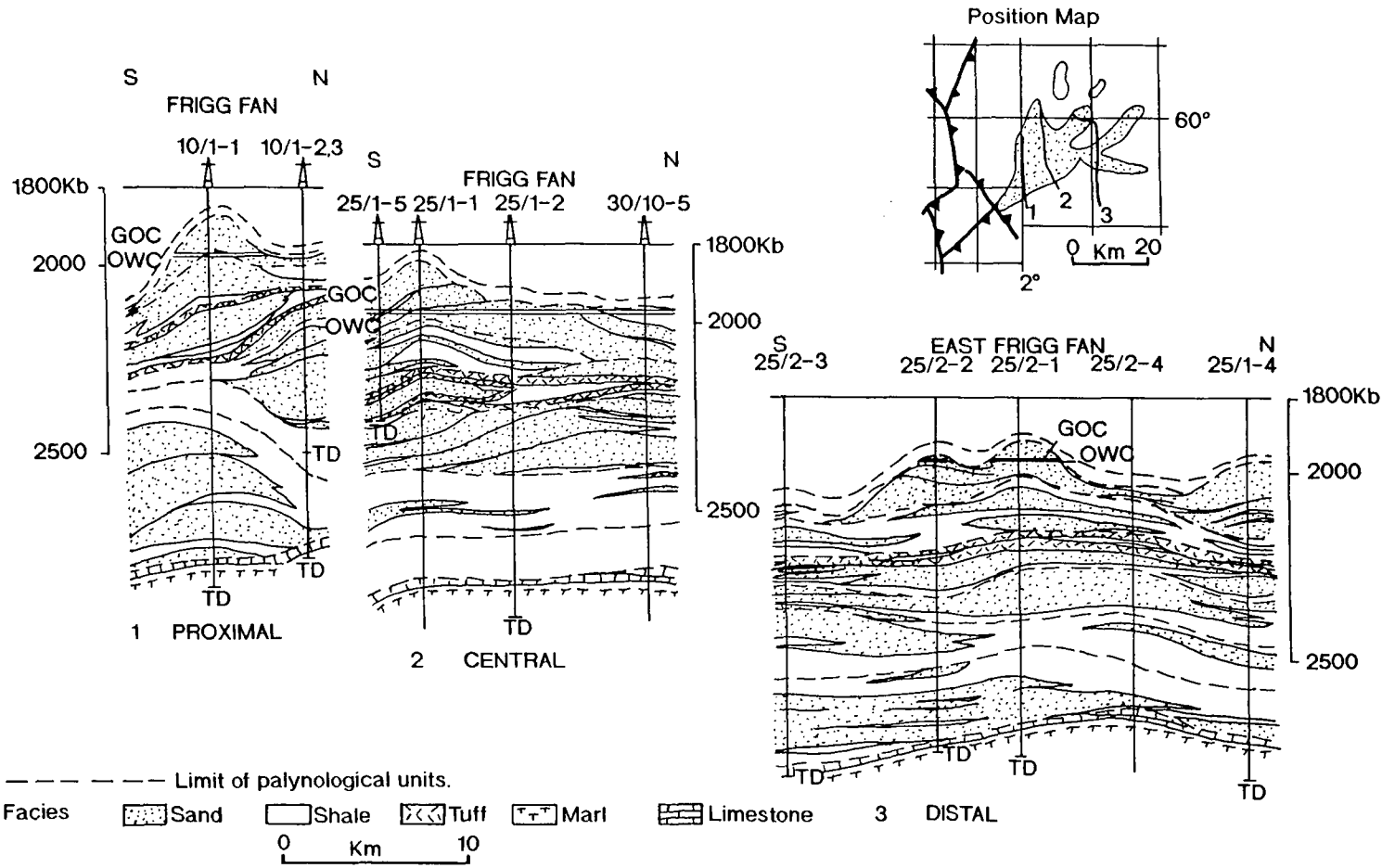

Figure 5.37 Cross-sections of Frigg Field show deposition of thick sands (channels) on flanks of earlier structural features (Modified from Heritier et al., 1979).

The Forties Field.

The Forties Field (Fig. 5.10) was discovered in 1970, within Palaeocene sandstones of the Forties Formation (Walmsley, 1975) (now redefined by Mudge & Copestake, 1992, and reduced to member status). Early work, particularly by Hill & Wood (1980), proposed that the facies relationships and associations, and the sedimentological structures present, characterised deposition in the middle to lower fan area of a submarine fan environment, as described by Walker (1978). They also described the log patterns seen in various wells throughout the field, and an interpretation of these patterns based on the submarine fan model (Fig. 5.38). Hill & Wood (1980) also proposed a correlation of sequential, and specific, depositional events based on the log patterns described in Figure 5.38, of the 50 development wells that had been drilled at that time, and which were closely spaced across the reservoir. However, subsequent studies, including the present one, have found log pattern correlation extremely difficult (see section 5.5.4), and often incorrect and misleading. Kulpecz & Van Geuns (1990) point out that the abrupt vertical and lateral changes in the facies make log correlation too difficult if based on log pattern alone, and additional information, such as biostratigraphy and pressure data, may help with correlation.

The depositional model interpreted for the Forties Field by Kulpecz & Van Geuns (1990), incorporates the switching of feeder channels to control sandstone distribution and geometry of the reservoir, with channel separation aided by differential compaction. Stacking arrangements are therefore controlled by palaeotopography, upon which differential compaction has some influence. They also note that clay drapes separating channel bodies are sometimes pressure barriers, and therefore control sand body connectivity throughout the reservoir, along with fluid flow. Hence, pressure data can also be used to aid well correlation. This means that to understand the precise nature of the reservoir, and the recoverability of hydrocarbons from the play, an accurate model for submarine fan deposition is required, along with a knowledge of the processes such as differential compaction, that combine to control sand body geometries and stacking patterns.

The Nelson Field.

The Nelson Field, of Blocks 22/11 and 22/6a, represents the same Palaeocene sand reservoir as the Forties Field, but is located 5Km to the northwest, and 25Km north-northwest of the Montrose and Arbroath Fields (Whyatt et al., 1991) (Fig. 5.10). For this reason Nelson Field provides an excellent analogue for the present study of the Montrose - Arbroath area.

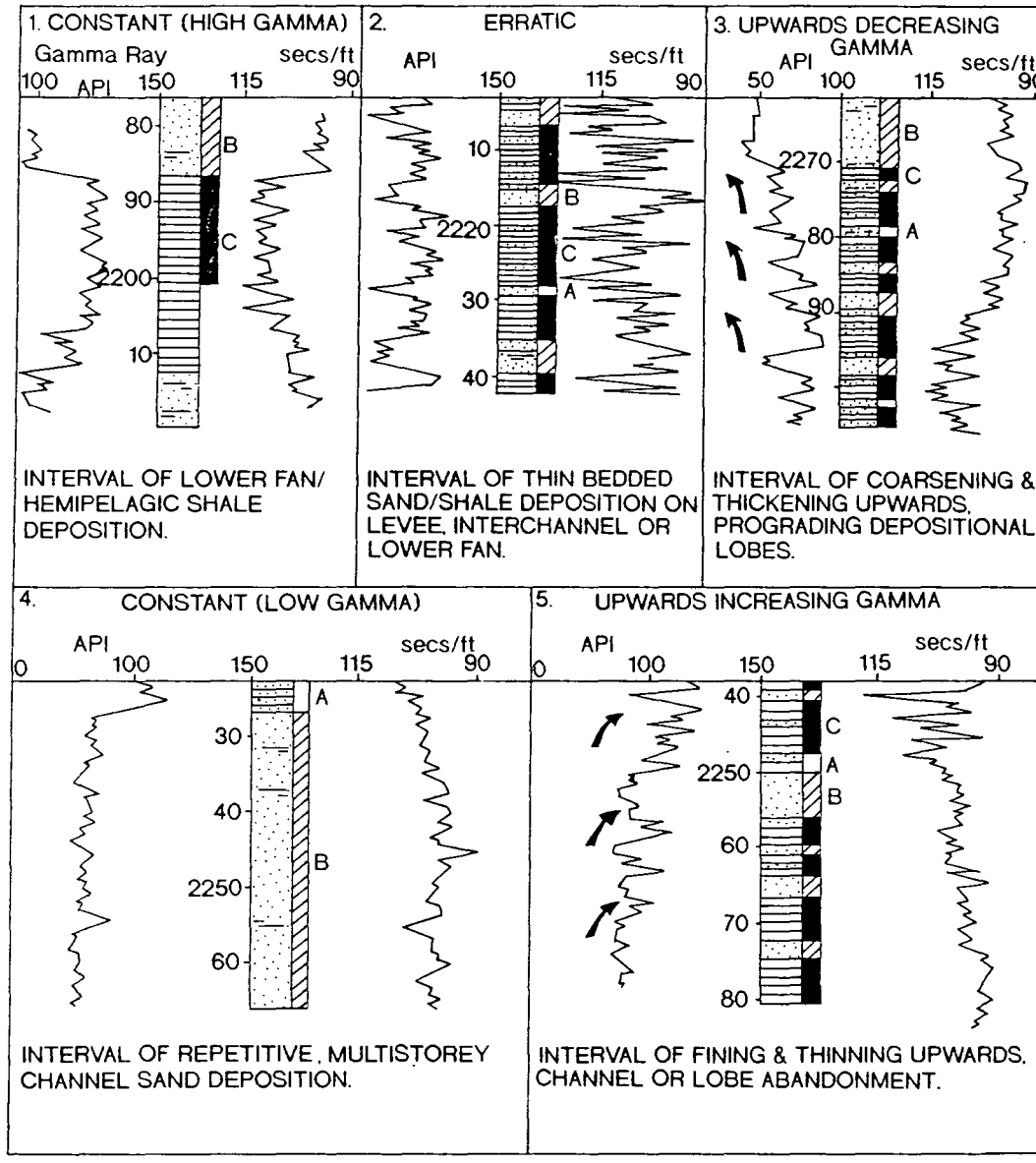

Figure 5.38 Characteristic log patterns seen in the Forties Member, Forties Field. An interpretation of the preferred depositional location within a submarine fan complex is shown below each pattern. Facies types seen in the cores are shown to the right of the lithology. Depths are in metres (true vertical depth below rotary table) (Modified from Hill & Wood, 1980).

However, due to the fact that Montrose - Arbroath were discovered before Nelson, the depositional model for the latter is based on data concerning the Montrose - Arbroath area, discussed in the following section.

It is important to note, however, that Whyatt et al. (1991) believed that the structure at top Forties level within the Nelson area had two origins. Firstly, the presence of flat-lying seismic events above the level of the Eocene, whilst significant structure exists below, indicates basin inversion at the end of Eocene times. Secondly, isopach maps of the Upper Forties member (now Forties Member (Mudge & Copestake, 1992)) indicated that sea-floor topography at the end of fan sedimentation may have shown variations of at least 50m (164ft) (Whyatt et al., 1991). Comparisons to the Indus Fan (Kolla & Coumes, 1987) and Amazon Fan (Damuth et al., 1988) are made, where channel-levee complexes may have 100-200m (330-660ft) of topographic relief above the fan surface. Whyatt et al. (1991) conclude that burial compaction will suppress the relief, but differential compaction will work to enhance the overall structural expression of the channel bodies (Figs. 5.39a & b).

Finally, Whyatt et al. (1991) propose that the reservoir of the Nelson Field was deposited in a submarine channel system, with no evidence of lobe deposits throughout the region. This interpretation differs from the earlier models concerning the Forties Field (e.g. Hill & Wood, 1980) which lies in an up-fan direction to the Nelson Field. Later models for the Forties Field (e.g. Kulpecz & Van Geuns, 1990) acknowledge the fact that the majority of the thick sands forming the reservoir are almost exclusively submarine channel deposits.

The Balder Formation, Quadrant 9.

Due to the many recent discoveries of hydrocarbon accumulations within the Palaeocene/Eocene sections of the Central and Northern North Sea (e.g. Nelson, Gryphon and Forth (see Fig. 5.10)), many recent publications have proposed depositional models for the reservoirs of these fields, and for the specific area of the North Sea (e.g. the Viking Graben, Beryl Embayment, etc.). The majority of these fields have combination traps with elements of both structure and stratigraphy playing a role. As seen earlier with the Nelson Field, these models often provide analogues for the present study. This is particularly true for the Balder Formation of Quadrant 9, interpreted by Timbrell (1993).

The sedimentology within the Balder Formation of Quadrant 9 is identical to that of the Palaeocene section of the Montrose - Arbroath area, with

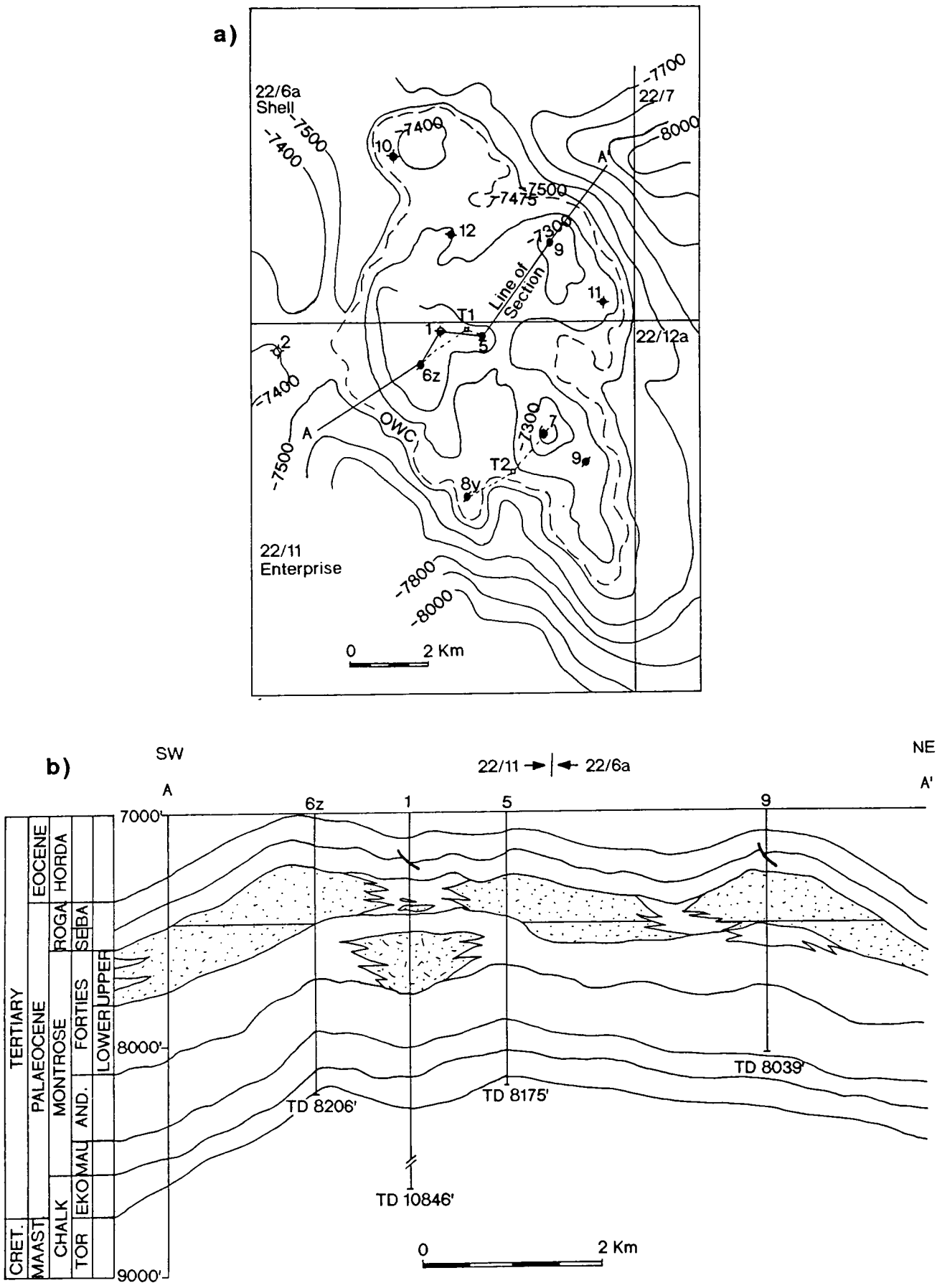

Figure 5.39a,b Nelson Field, a) top Forties Member depth structure map, and b) structural cross-section of the Palaeocene sequence (Modified from Whyatt et al., 1991).

stacked, amalgamated sands which are structureless apart from water-escape dish structures. Of extreme importance is the presence of differing oil - water contacts (OWC) in the wells of the area, showing that the reservoir sands are poorly interconnected and that the reservoir is partitioned (Figs. 5.40 & 5.41). Figure 5.42 also illustrates the off-set stacking pattern of the channel sands in this area slightly further downslope, and the problematic correlation of the wells this creates. Timbrell (1993) points out that the wells can only be accurately correlated by "desanding" them (i.e. removing the sand sections from the well logs) and using biostratigraphic information.

A great advantage of Timbrell's (1993) study over the study of the Montrose - Arbroath area, is the existence of not only a large number of wells in the area, but also the availability of new 3D seismic survey data. These data has shown that the thickness of sand within 'sand fairways' varies greatly, with the sand forming pods, strung down the fairway. The data has also shown that the fairways meander sharply, presumably due to a low angle of the depositional slope, with similar dimensions to those of modern submarine fan channels. The key points concerning the sand fairway geometry are:-

- The sands have a remarkably consistent character. They may be classified as generally massive and structureless high-density turbidites.
- The sandbodies are proven to be diachronous by quantitative biostratigraphy and detailed correlations of tuff marker beds.
- There is considerable evidence for 'lateral stacking' of sandbodies within a depositional fairway, implying that the topographic expression of 'older' sandbodies strongly influenced the location of subsequent turbidite flows.
- Very sharp lateral sandbody limits have been observed from well and sidetrack data and they appear to be distributed within channels.
- Possible levee facies has been noted on seismic and in Sedgwick Field wells.
- Location of the very thick B1 facies class (Fig. 5.13) stacked sandbodies can be correlated with large bathymetric lows at Top Sele level.
- In contrast to the above, the location of moderately thick B1 sandstone bodies does not appear to be strongly controlled by palaeobathymetry at Top Sele level. However, the position of pre-existing sandbodies has had considerable influence.

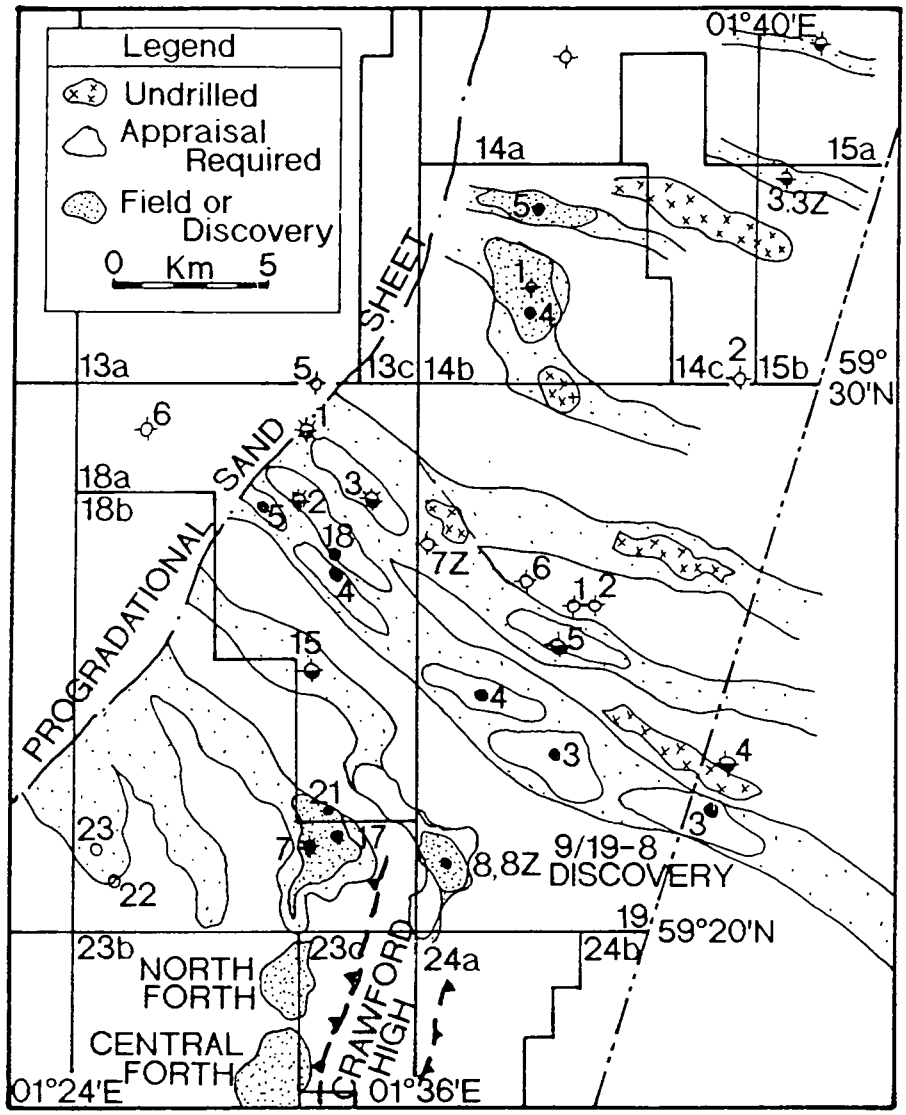

Figure 5.40 Block 9/18a, 9/19 Tertiary discoveries and prospects (From Timbrell, 1993).

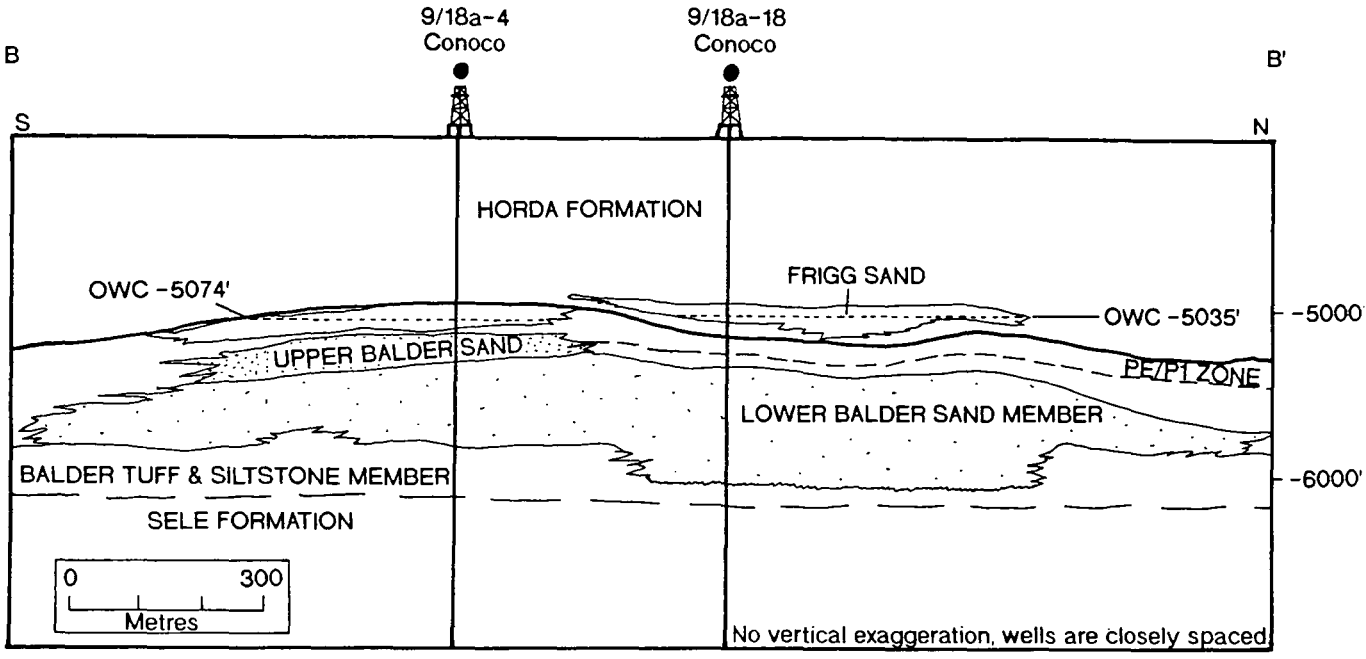

Figure 5.41 Geoseismic section illustrating stacked nature of channels (From Timbrell, 1993).

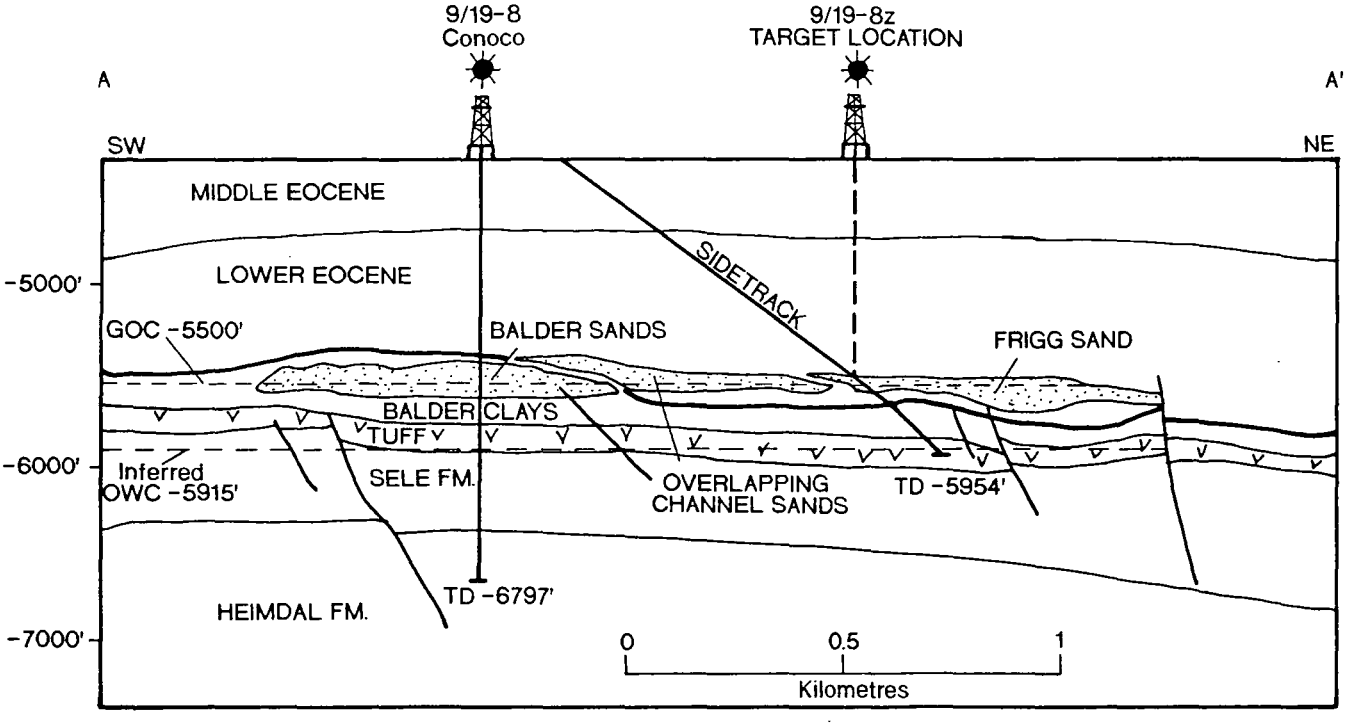

Figure 5.42 Cross-section through Conoco 9/19-8 straight hole and 8Z sidetrack (From Timbrell, 1993).

- Reservoir thickness may vary markedly along a sandstone fairway giving target sands a 'string of pearl' or pod-like nature.
- Seismic data show that several channel fairways appear to meander with a high degree of sinuosity indicative of a relatively low depositional slope.

(Timbrell, 1993).

On a regional scale, the geological model for the Quadrant 9 area shows that the high-density turbidity currents have no single point-source, comparable to the modern fans such as the Rhône, Magdalena, Amazon and Navy Fans (Timbrell, 1993). However, these modern fans do not appear to provide exact analogues to the Balder Formation, and Timbrell (1993) proposes two end-member models for the deposition of the Balder sands. The two models consist of an erosive model and a constructive model, and both are described below.

The Erosive Model.

Figure 5.43 illustrates an erosive gully depositional model, akin to the model of Surlyk (1987). Gully erosion by turbidity currents occurs during a lowstand in sea-level, and are subsequently filled by stacked turbidites. The bases of such deposits are highly erosive, with many mudstone clasts ripped-up into the sandbody. Also apparent is that the sands must be younger than the containing mudstones, with biozones being cut out by the gully erosion. This fact is untrue for the Balder Formation, as no biozones are missing between the sands and shales surrounding the fairways and detailed biostratigraphic correlation is possible between the two facies. Therefore it appears that the erosive model does not fit the well and seismic data for the Balder Formation (Timbrell, 1993).

The Constructional Model.

This model consists of a line-source of sediment, and can essentially be classified as a 'prograding slope' type model (Fig. 5.44) such as the submarine ramp model of Heller & Dickinson (1985). Timbrell (1993) proposes the Valencia margin of northeast Spain, documented by Field & Gardner (1990) and Alonso et al. (1991),as a better example of this model. In this area, submarine canyons incise the shelf break where axial gradients are 2.4° to 7.5°, but constructional channel-levee complexes are present where the gradients shallow to 0.4° to 1.9° (Timbrell, 1993). Field & Gardner (1990) see the channel-levee complexes as forming the main facies of the margin, the slope section being characterised by a series of 'shoe-string' sands encased in fine-grained levee deposits. Alonso et al. (1991) illustrate how the

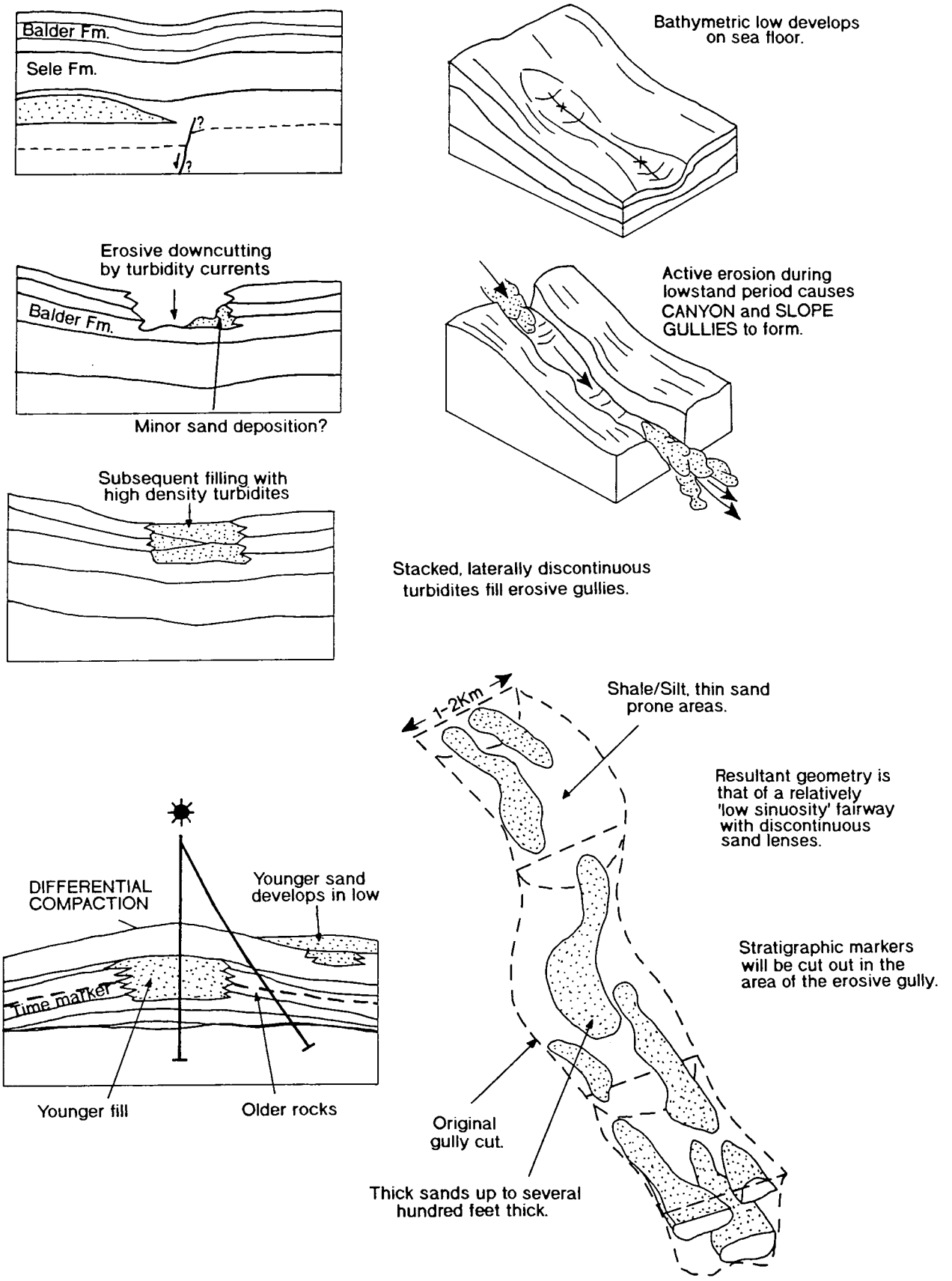

Figure 5.43 Erosive trubidite model, sandstone gully/canyon development (From Timbrell, 1993).

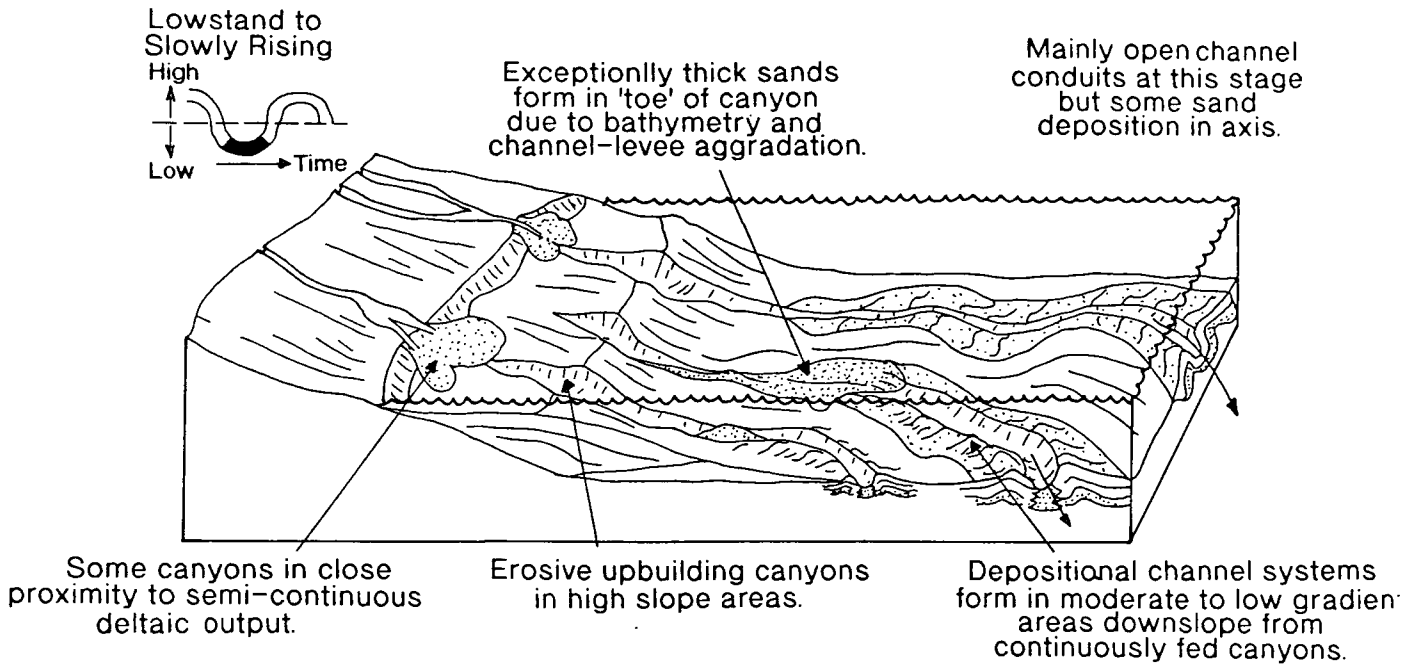

Figure 5.44 Prograding slope model (From Timbrell, 1993).

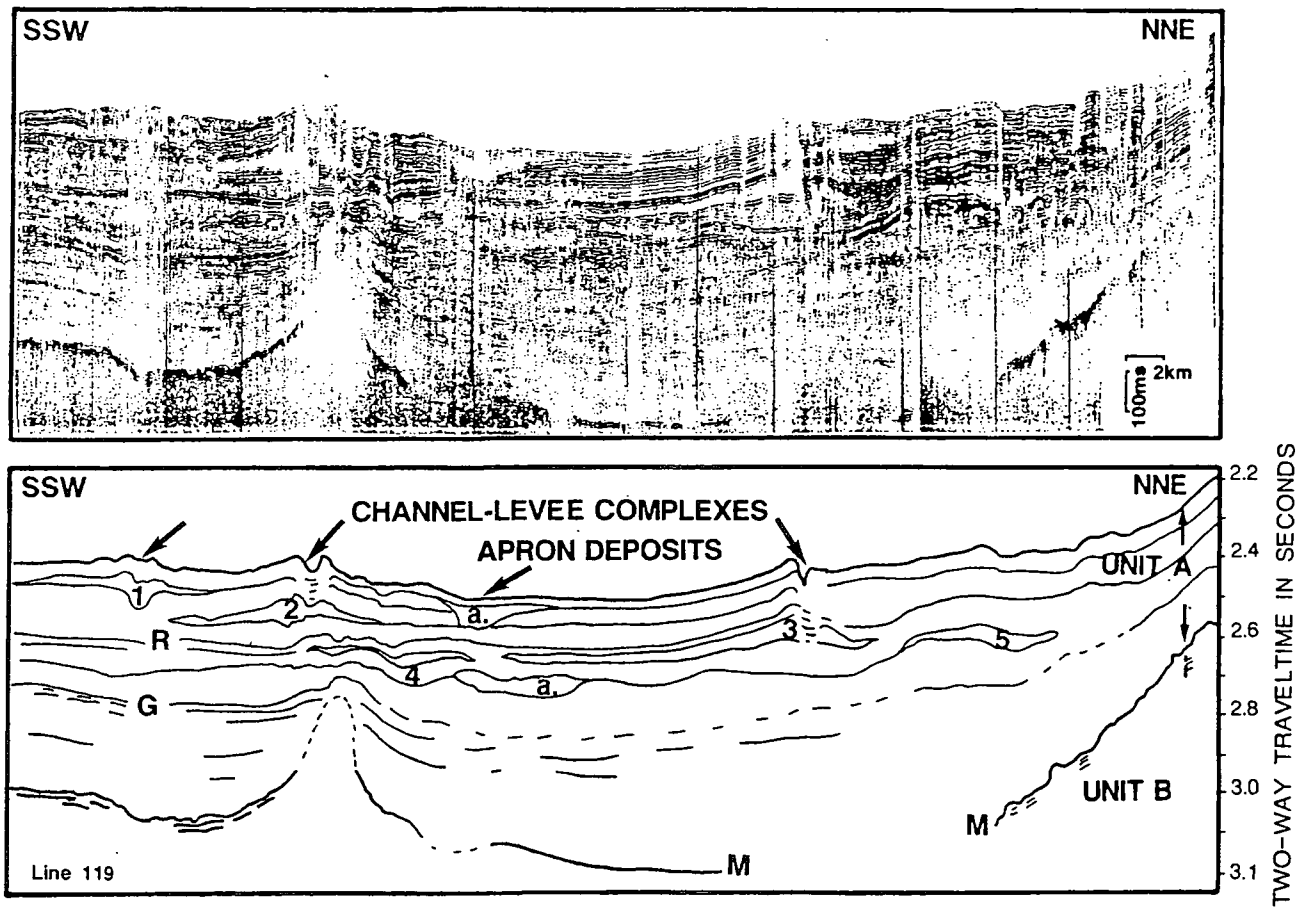

Figure 5.45 Representative sparker profile of unit A showing the stratigraphic distribution of channel-levee complexes 1-5 and apron deposits (a) in the Ebro base-of-slope. The top of the Miocene (reflector M), the middle Quaternary (reflector R), and the Pliocene-Quaternary boundary (reflector G) are also indicated (From Alonso et al., 1991).

channel-levee complexes overlie each other, having stratigraphically different ages, and as before, showing a typical vertical off-set pattern (Fig. 5.45).

For the Balder Formation of Quadrant 9 the constructional model appears to fit the data better, with erosive submarine canyons and gullies occurring in areas of higher gradient (e.g. in the Forth Field area (Timbrell, 1993)), with constructional complexes occurring downslope to this. Problems with the model do exist, such as no convincing levee deposits have been found in the area. Another problem is the pod-like nature of the sandstone reservoir bodies. Timbrell (1993) proposes that flow-stripping (Fig. 5.19), as defined by Piper & Normark (1983), is a possible depositional control to the sandbodies. The resultant depositional model is shown in Figures 5.20a & 5.53b. An alternative mechanism to flow stripping is lateral accretion, however, there are no convincing outcrop examples of this from the submarine environment (Timbrell, 1993).

Numerous other North Sea oil and gas fields exhibit similar depositional patterns that have been affected by differential compaction at some stage during their deposition. The effects of differential compaction are noted in the descriptions of the reservoirs depositional development, but often only play a minor role. Examples include:-

- The Cod Field (Kessler et al., 1980).
- The Miller Field (McClure & Brown, 1992; Garland, 1993).
- The Everest Field (O'Connor & Walker, 1993).
- The Gryphon Field (Newman et al., 1993).
- The Balder Field, Norway (Jenssen et al., 1993).
- The Alba Field (Newton & Flanagan, 1993).

Also noteworthy in this section are various examples of submarine fan sandstone reservoirs from the Californian oilfields. Similar techniques of log correlation based upon biostratigraphic data and pressure data have been used to attempt to accurately define the depositional models for these fields. Observations show that very little erosion occurs at the base of the submarine channels, and pods of sand are located within the meanders (Yowlumne Field (Berg & Royo, 1990)), as seen in the Balder Formation of Quadrant 9 (Timbrell, 1993). The study of the Midway-Sunset Field by Hall & Link (1990) relies entirely on well log data, as no seismic data exist for the area. They show that through detailed well log correlation, it is possible to define a lower section of depositional lobes, followed by an upper section of submarine channel deposits, akin to Mutti's (1985) Type II or Type III

deposits (Figs. 5.32 & 5.33). The channels are vertically off-set, with no levee deposits.

Almost identical relationships are seen in the Arbuckle Field (Imperato & Nilsen, 1990), however, levee deposits are more common here as the fan system is dominantly muddy. Importantly, Imperato & Nilsen (1990) note that the Arbuckle Field consists of six intervals separated by shale marker horizons, each of which contain numerous channel-levee complexes. Fluid communication within a single interval can be proven, but fluid communication between intervals does not occur, producing a partitioned reservoir.

5.5.4 Montrose - Arbroath Model.

5.5.4.1 Geological Model.

The combination of seismic data, well data, and sedimentology, derived from core data, makes it possible to show that the sediments of the Montrose - Arbroath area were deposited within submarine fan channel complexes, by high-density turbidity currents. Well log motifs clearly show the depositional pattern (Fig. 5.7). Detailed seismic mapping, combined with the calibration of seismic facies analysis to core sedimentology, reveals that there are approximately three sandstone fairways running NNW-SSE (Fig. 5.46). Isochores of the Forties Member are thickest within these fairways. In the Montrose - Arbroath area the channels are 2.5-3Km wide, 50-100m thick and are separated by interchannel areas around 500m wide, and 15-30m thick (Whyatt et al., 1991).

The basic depositional model for the North Sea during early Palaeocene time shows that a prograding sand-rich braid delta system built along the axis of the Moray Firth area (Sutter, 1980; Galloway et al., 1993) (Fig. 5.27). Local variations in sea-level, combined with seismic activity due to Thulean volcanism, initiated deposition of submarine fan deposits within the Central and Viking Graben regions (Hartog Jager et al., 1993). Sediment was shed from the delta front, forming a mud/sand-rich, multiple-sourced submarine ramp (Figs. 5.16 & 5.17) (Reading & Richards, 1994). As shown by Hartog Jager et al. (1993), the precise nature and geometry of the submarine fan deposits depended upon many factors including the precise scale of sea-level fluctuation. Sheet-like fans, such as the Andrew Fan, occurred during the Lowstand Systems Tract, and the subsequent Forties Fan was deposited during the Transgressive Systems Tract, as accommodation space began to increase (Hartog Jager et al., 1993) (see section 5.5.3.1).

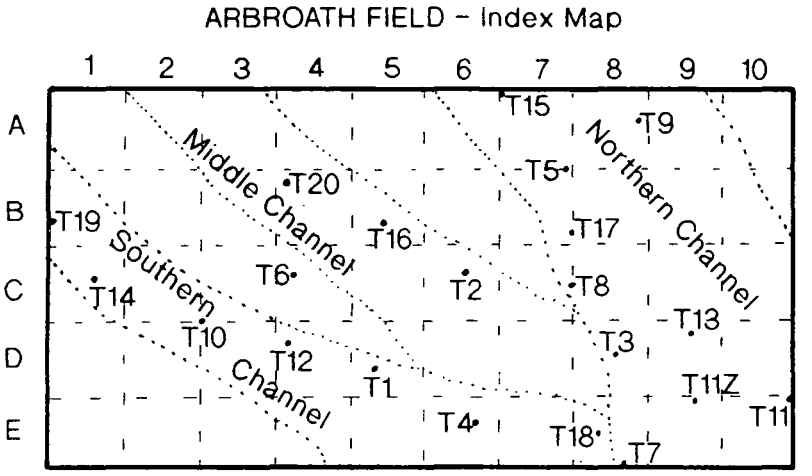

Figure 5.46 Index map for the Arbroath Field illustrating well location, division of region for use with maps of Appendix 1, and the general locations of the 3 submarine channels.

Channel complexes within the Montrose - Arbroath area are interpreted to be analogous to those described by Timbrell (1993) for the Balder Formation of Quadrant 9. Core log evidence appears to show little erosion at the base of individual flows, with only minor rip-up clasts being present near the base of these deposits (Fig. 5.8). It is therefore interpreted that the channel complexes were not initiated by erosion, and are generally of the constructional type, as described by Timbrell (1993). Further evidence to support this interpretation comes from the work of Weimer (1989); Berg & Royo (1990); Hartog Jager (1993); Newmann et al. (1993), where little erosion is reported at the base of submarine fan channels. For the Montrose - Arbroath area some underlying topographic variation in the top Lista Formation controlled the initial channel deposition. This control could quite possibly have been some small-scale structural control (Birch, pers. comm., 1993). Subsequent flows were focused within the channel complex, possibly due to minor growth of levees. Flow stripping is also believed to have played an important role in the depositional location of the thick sand deposits, and may also explain the separation between the Montrose and Arbroath oilfields. Figure 5.47a-f illustrate the proposed depositional model for the Montrose - Arbroath area which was used for the modelling, and the assessment of compactional control upon deposition.

5.5.4.2 Seismic Data.

As shown earlier, Figure 5.6 illustrates part of a typical seismic section across the Arbroath Field, indicating the important horizons to be picked. Using well information and vertical seismic profiles (VSP) the present study picked all the horizons and correlated them across the entire area of seismic coverage (Fig. 5.5). This allowed the mapping of the entire Arbroath Field, plus part of the Montrose Field, in time (TWTT), along with the position of faults, especially within the lower half of the stratigraphic section. Depth conversion is then possible using interval velocities from well log information.

However, the present study recognised at an early stage that the resolution of the seismic data was well below that required to model differential compaction on a useful scale. The only purpose for the seismic data therefore, was to produce a field map, and this was deemed not to be required.

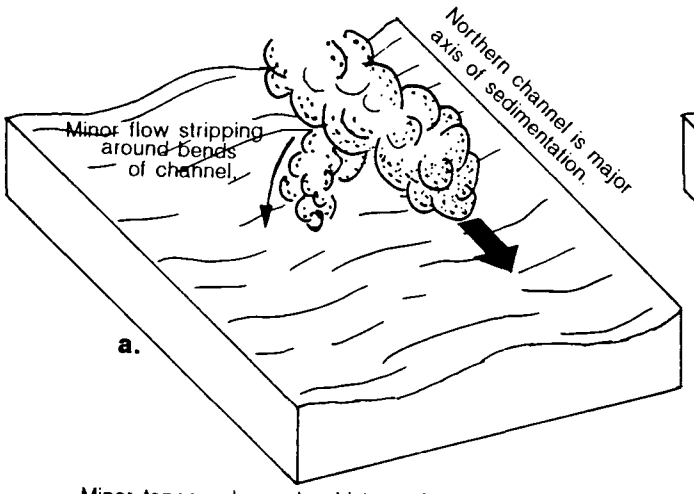

Minor topography on top Lista surface confines turbidite flows.

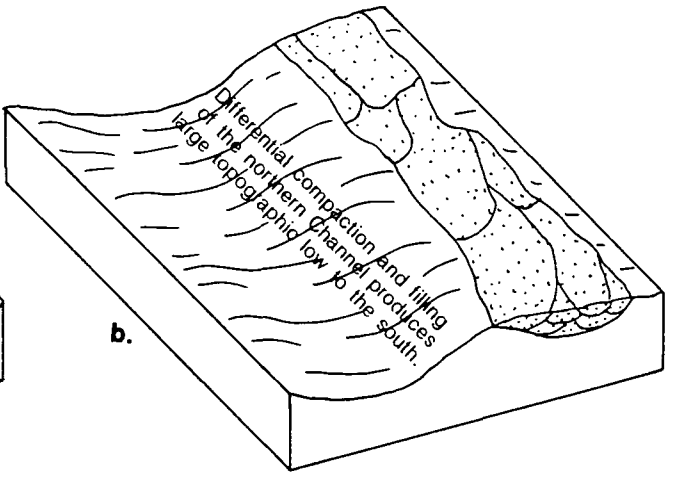

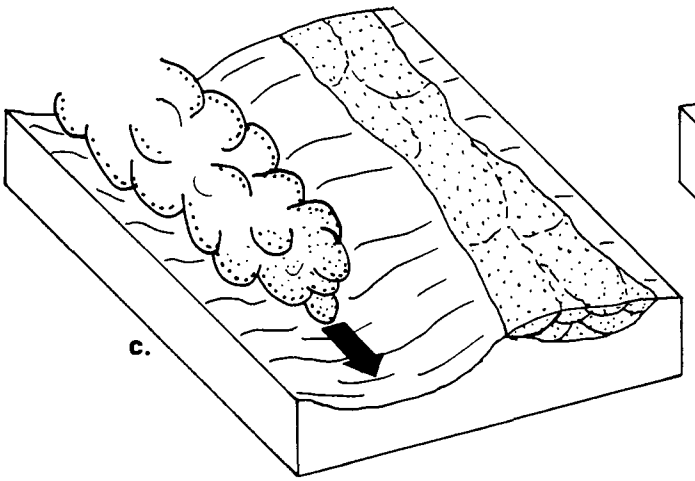

Deposition of turbidites controlled by the Southern Channel.

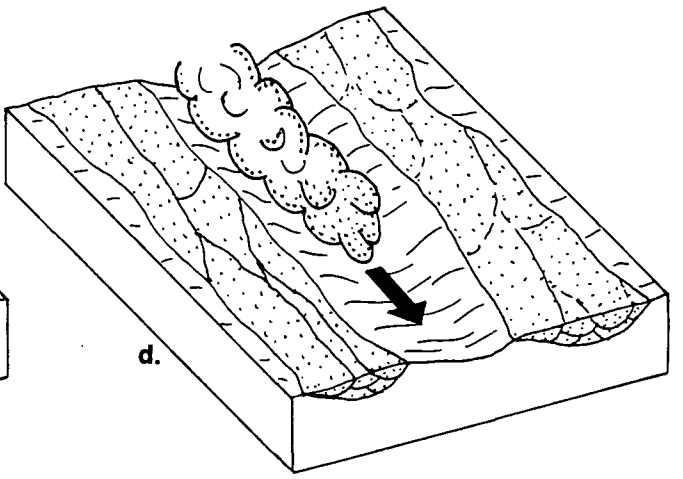

Differential compaction across the channels produces a topographi low between them, hence deposition in the Middle Channel.

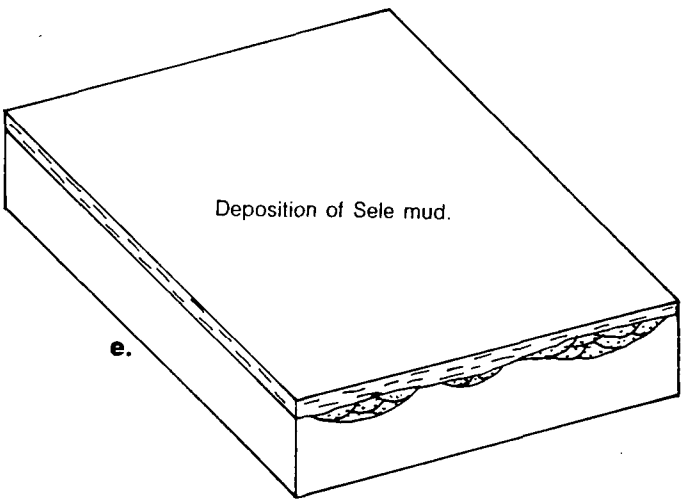

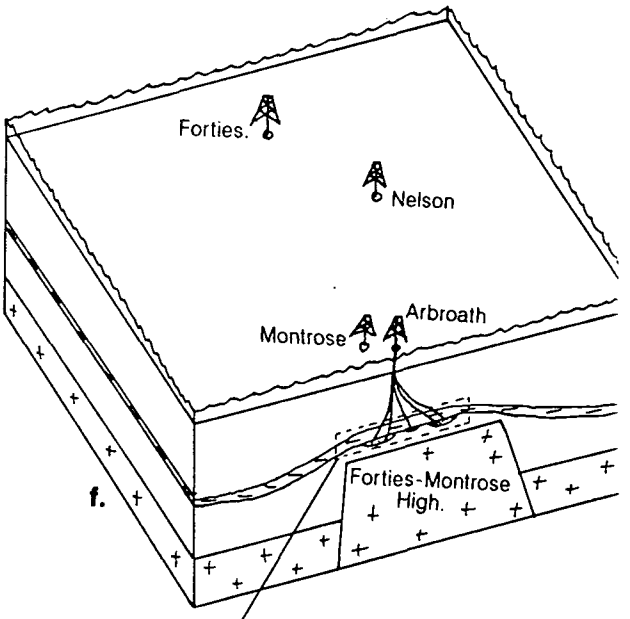

Area of figs. a-e

Differential compaction across the Forties-Montrose High produces the present field geometry.

Figure 5.47a-f Interpreted depositional model for the Montrose and Arbroath oilfields.

5.5.4.3 Well Correlation.

The Arbroath oilfield was selected for modelling primarily due to the more recent and better quality well data available, plus the greater seismic coverage. For the twenty deviated wells (22/17-T1 to T20) and the one vertical well (22/18-1) (Fig. 5.46) a detailed correlation was carried out. Correlation lines were primarily based on biostratigraphic data, available for a selection of the wells (T1 to T8) (Table 5.3) and core data for wells T1-T6. In addition to this certain wells had Repeat Formation Test (RFT) pressure data which was built into the biostratigraphic data for well correlation. This allowed a further number of wells to be correlated. Finally, all the wells were correlated using log character, primarily the gamma ray log, allowing the greater division of certain units, plus the enlargement of the correlation to encompass all the Arbroath wells. Core data also aided the assessment of the correlation for certain wells.

Facies correlations within a turbidite environment are extremely difficult when using log character alone, and are therefore often incorrect (Whyatt et al., 1991; Armentrout et al., 1993). However, with a fully integrated approach, using all available data sources, errors in correlation can be minimised and greater confidence in the depositional facies geometries can be obtained. The present study has attempted this integrated approach as it is of prime importance that a detailed picture of facies development and geometry is developed, so that the effects of differential compaction can be assessed. Table 5.4 shows the correlation depths as true vertical depth below sea level (TVDSS) for the Arbroath wells, and Figure 5.48 graphically illustrates a correlated cross-section. Depths are with respect to the present day. The object of this study is to remove the effects of burial compaction, enabling the estimation of original depositional thicknesses of chronostratigraphic units. Depositional patterns, differential compaction, and sea-floor topography can then be assessed at each chronostratigraphic stage, with relatively few assumptions, outlined below. The effects of differential compaction and sea-floor topography on the stacking patterns of subsequent horizons and facies can be interpreted, enabling a qualitative assessment of the control on deposition provided by compaction.

For each well an estimation of the percentage sand and mud was recorded at every correlated horizon (Table 5.5), at each time noting whether the sand was at the top or bottom of the horizon in question. Estimations are based on the gamma ray/composite log for each chronostratigraphic unit. Finally, the present day unit thickness was also calculated (Table 5.5). These

Events	22/17-T1	22/17-T2	22/17-T3	22/17-T4	22/17-T5	22/17-T6	22/17-T7	22/17-T8
1	8129.6	8106.2	8047.6	8125	8101.2	8254	8226.8	N.I.
4	8160.3	8147.6	8078.4	8130	8120.1	8289	8267	8132.7
3	8137.2	8120.5	8052	8134.9	8126	8293	N.I.	N.I.
5	8178	8159.11	8090	8154	8135.5	8314	8284	8151.4
9	8204.5	8200.9	8142.5	8200	8162.4	8347	8302.7	8188.7
12	N.I.	N.I.	8107.5	8213.8	8178	8408	N.I.	N.I.
13	8233.5	N.I.	8168.5	8226	8186	8433	8302.7	8207.4
14	8277.5	8264.4	8186	8257.5	8265	8445	8354.7	8263.4
15	8314	N.I.	8213	8297.7	8309	8468	8389.6	8375.3
16	8330	8334	8246	8344	8360	8468	8424.5	8413
17	8480	N.I.	8330	8362	8395	8484	N.I.	8468
18	8556	8453	8460	8402	8412	8490	8546	8468
19	N.I.	8478	8506	8462	8494	8510	8546	8523
21	8656	8660	8560	8500	8598	8574	8670	8600

Table 5.3 Biostratigraphic events for the Arbroath Field. Depths are TVDSS, and the events key is given below.

Key to Biostratigraphic Events.

1. Prasinophycean Association.
4. *Apectodinium augustum* Association.
3. *Inaperturopollenites* spp. - *Caryapollenites veripites* Association.
5. *Apectodinium homomorphum* Association.
9. Decrease in *Caryapollenites* spp.
12. *Lejeunecysta* spp. Association.
13. *Pediastrum* spp. - *Glaphyrocysta* spp. Association.
14. *Pteris* spp. Association.
15. *Caryapollenites veripites* - *Caryapollenites simplex* Association.
16. *Ulmipollenites* spp. - *Nyssapollenites krutschii* Association.
17. *Apectodinium augustum* - *Apectodinium summissum* Association.
18. Pre-*Apectodinium* Association.
19. *Alnipollenites verus* - *Platycaryapollenites platycaryoides* Association.
21. *Areoligera* cf. *senonensis sensu* RRI Association.

WELL NUMBER	T1	T2	T3	T4	T5	T6	T7	T8	T9	T10	T11	T11Z	T12	T13	T14	T15	T16	T17	T18	T19	T20
HORIZON	TVDSS	TVDSS	TVDSS	TVDSS	TVDSS	TVDSS	TVDSS	TVDSS	TVDSS	TVDSS	TVDSS	TVDSS	TVDSS	TVDSS	TVDSS	TVDSS	TVDSS	TVDSS	TVDSS	TVDSS	TVDSS
PALAEOCENE/BALDER	8015	7990	7921	7989	7986	8119	8104	7961	8030	8068	8078	8005	8058	7971	8037	8025	8034	7965	8039	8064	8047
SELE Fm.	8052	8046	7972	8047	8035	8173	8140	8018	8071	8114	8140	8057	8102	8032	8087	8077	8085	8009	8087	8105	8100
FORTIES Mem.	8128	8117	8040	8117	8108	8250	8224	8089	8135	8192	8213	8128	8168	8105	8176	8161	8156	8075	8163	8183	8182
1	8129	8124	8048	8125	8114	8254	8226	8101	8142	8203	8219	8134	8177	8110	8182	8166	8160	8093	8166	8198	8185
4	8160	8148	8078	8130	8120	8289	8267	8133	8145	8215	8228	8150	8184	8118	8265	8173	8166	8111	8218	8248	8194
3	8170	8154		8135	8126	8293	8270	8142	8150	8217	8236	8166	8188	8134	8295	8179	8175	8119	8226	8274	8201
5	8178	8159	8090	8154	8136	8314	8284	8151	8158	8229	8256	8205	8198	8170	8332	8184	8182	8144	8246	8312	8212
9	8205	8201	8143	8200	8162	8347	8303	8189	8181	8286	8309	8243	8239	8194	8392	8192	8224	8172	8283	8426	8266
12	8223	8212	8156	8214	8178	8408		8202	8217	8332	8322	8250	8256	8203	8423	8208	8276		8291	8461	8324
13	8234		8169	8226	8186	8433	8303	8207	8254	8340	8331	8261	8280	8209	8451	8232	8341	8185	8298	8500	8382
14	8278	8264	8186	8258	8265	8445	8355	8263	8270	8347	8424	8336		8293	8455	8294	8344	8292	8348	8504	8388
15	8314	8285	8213	8298	8309	8468	8390	8375	8313	8352	8438	8367	8349	8302	8466	8340	8356	8362	8378	8510	8394
A		8315		8319	8317		8412	8384	8316	8396	8448		8412	8322	8475	8344	8372	8380		8521	8426
16	8330	8334	8246	8344	8360	8468	8425	8413	8410	8425	8463	8375	8440	8338	8481	8398	8388	8461	8392	8528	8451
17	8480	8352	8330	8362	8395	8484	8455	8413		8455	8479	8390	8464	8340	8496	8417	8399	8493	8423	8545	8463
B	8515	8402	8403	8373	8403		8524	8452		8474	8553	8482	8478	8463		8450	8434	8520	8492		8498
18	8556	8453	8460	8402	8412	8490	8546	8468		8491	8573	8500	8502	8507		8517	8453	8553	8516	8550	8528
LISTA Fm.	8579	8468	8485	8450	8481	8490	8546	8517	8410	8504	8573	8565	8521	8524	8502	8542	8483	8610	8541	8552	8556
19	8585	8478	8506	8462	8494	8510	8546	8523	8417	8516	8584	8574	8532	8529	8510	8548	8514	8617	8558	8556	8570
ANDREW Mem.	8647	8594	8547	8495	8524	8572	8648	8573	8473		8640	8659	8592	8595	8666	8568	8551	8646	8739		
21	8656	8660	8560	8500	8598	8574	8670	8600	8483		8646	8668	8604	8600		8586	8584	8660	8742		
C	8675	8665	8578	8535		8598	8734	8672			8718	8735	8620	8671			8600				
D		8694		8580		8721	8752						8649				8639				
E	8695			8602			8756						8677								
F	8718	8700		8685		8802	8769						8692				8655				
G	8747	8742		8728		8818	8780						8707				8691				
H	8779	8794		8756		8907	8792						8726				8732				
MAUREEN Fm.	8798	8807	8695	8864	8834	9040	8813		8788		8888	8821					8751		8820		
EKOFISK FM.		8895	8765	8987	9000	9245	9028		9008		8976	9013									

Table 5.4 Correlation depth (True vertical depth sub-sea, TVDSS) for the Arbroath Field wells. Correlation horizons are those shown in Table 5.3, plus extras based on wireline logs and pressure data.

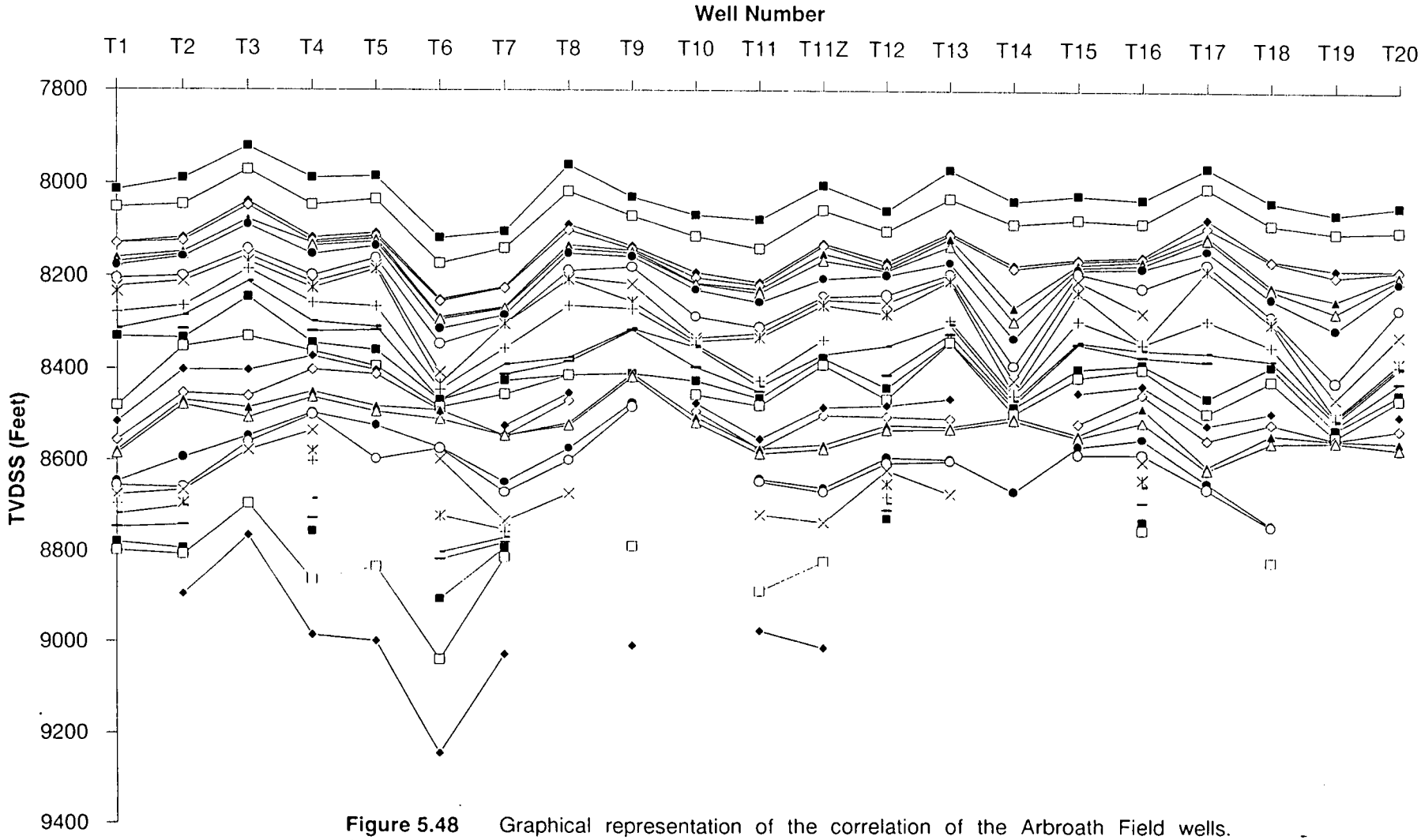

Figure 5.48 Graphical representation of the correlation of the Arbroath Field wells. Symbols represent the correlation horizons shown in Table 5.4.

Well No.	22/17-T1

Horizon	Depth (TVDSS)	Depth (TVDSS)	% Sand	% Mud	% Sand at Top (T) or Base (B)	Unit Thickness
Palaeocene/Balder	8015	2443.00	0	100		11.28
Sele Fm.	8052	2454.28	0	100		23.17
Forties Mem.	8128	2477.44	100	0		0.30
1	8129	2477.75	88	12	T	9.45
4	8160	2487.20	100	0		3.05
3	8170	2490.25	100	0		2.44
5	8178	2492.68	100	0		8.23
9	8205	2500.91	58	42	T	5.49
12	8223	2506.40	100	0		3.35
13	8234	2509.75	88	12	T	13.41
14	8278	2523.17	83	17	T	10.97
15	8314	2534.14	100	0		4.88
A		0.00				0.00
16	8330	2539.01	56	44	T	45.72
17	8480	2584.74	38	62	T	10.67
B	8515	2595.40	28	72	B	12.50
18	8556	2607.90	36	64	B	7.01
Lista Fm.	8579	2614.91	0	100		1.83
19	8585	2616.74	18	82	B	18.90
Andrew Mem.	8647	2635.64	0	100		2.74
21	8656	2638.38	45	55	T	5.79
C	8675	2644.17	0	100		6.10
D		0.00				0.00
E	8695	2650.27	51	49	T	7.01
F	8718	2657.28	26	74	T	8.84
G	8747	2666.12	36	64	T	9.75
H	8779	2675.87	0	100		5.79
Maureen Fm.	8798	2681.66				?
Ekofisk Fm.		0.00				?

Table 5.5 Example correlation table for Arbroath well 22/17-T1. First depth column shows TVDSS in feet, second column is in metres. Percentages of sand and mud are estimated from the gamma ray log, along with the position of the sand relative to the mud within a chronostratigraphic horizon. Finally each chronostratigraphic units thickness is shown. This table forms the basis for the decompaction of the Arbroath oilfield.

parameters are all important during the decompaction stage of modelling as explained in section 5.6.

5.6 Modelling.

It is possible to broadly subdivide the compaction effects that occur within the Montrose - Arbroath area on the basis of the scale at which they occur. Three scales of compactional effects are seen, namely:-

- Mega-Scale - Observable on regional seismic data, and occurring over distances ranging from 500m and above.
- Meso-Scale - Observable through well correlation, and occurring at the scale of submarine channel systems.
- Small-Scale - Observable only at outcrop, and occurring at the scale of individual turbidites.

The following sections will deal with each scale in turn, with special interest directed at meso-scale compaction effects as a control upon deposition. Small-scale compaction effects are unobservable at the Montrose - Arbroath area, and are therefore dealt with in a qualitative way.

5.6.1 Mega-Scale Compaction Effects.

The Forties-Montrose High has certainly influenced sedimentation within the Central Graben from Permian times onwards. The deepest stratigraphy penetrated by drilling (e.g. 22/11-1, 22/17-1 on the high; 22/23b-1 in the adjacent basin) demonstrates the contrasting stratigraphy both on and off the high. Over the hörst, Tertiary and Upper Cretaceous section rest unconformably on Triassic and Permian strata. Lower Cretaceous and Jurassic rocks are absent, as well as the Zechstein evaporite, although Zechstein carbonates are present. In the adjacent basinal areas, in addition to the Lower Cretaceous and Jurassic sections present, the Triassic and Upper Cretaceous sections are considerably expanded in thickness relative to the high. Using the regional cross-section across the Montrose - Arbroath area from Ziegler (1982) (Fig 5.49), and bed thicknesses measured from regional seismic data (CNST86-29), the amount of compactional drape expected over the basement high at top Palaeocene level has been evaluated.

Assumptions concerning lithologies, present day thicknesses and porosities for each stratigraphic level are detailed in Table 5.6. Compaction

AGE	DOMINANT LITHOLOGY	PRESENT POROSITY		PRESENT THICKNESS		ORIGINAL POROSITY		ORIGINAL THICKNESS	
		BASIN	HIGH	BASIN	HIGH	BASIN	HIGH	BASIN	HIGH
Post Palaeocene	MUDSTONE	22%	22.50%	2500	2350				
Palaeocene	SANDSTONE	21%	23%	500	400	42%	43%	681	540
Upper Cretaceous	CHALK	10%	10%	1000	500	31%	39%	1304	738
Jurassic	MUDSTONE/SHALE	5.50%	Absent	400	Absent	15%	Absent	445	Absent
Triassic	MUDSTONE/SHALE	3%	8%	1000	500	11%	19%	1090	568

Original Porosity = Porosity immediately post Palaeocene deposition.

Thicknesses measured in metres.

	Basin Compaction	High Compaction
Palaeocene	181m	140m
Upper Cretaceous	304m	238m
Jurassic	45m	0
Triassic	90m	68m
TOTAL	**620m**	**446m**

Difference = 174m

Table 5.6 Decompaction table for the mega-scale modelling of the Palaeocene section across the Forties-Montrose High.

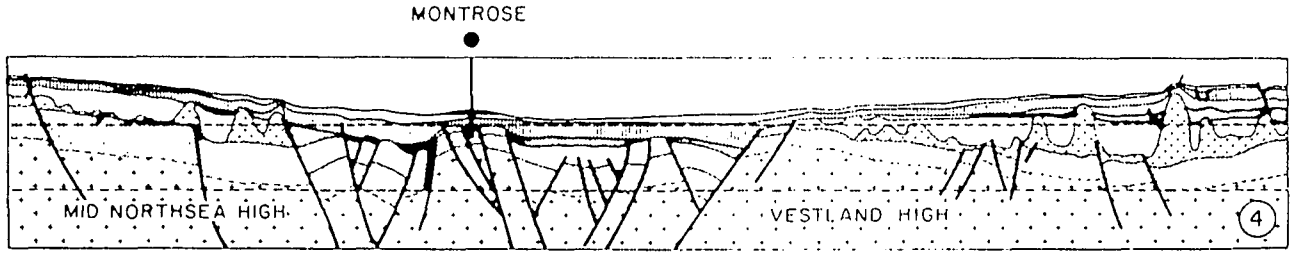

Figure 5.49 Cross-section of the Montrose area (From Zeigler, 1982).

of muds is modelled using the curve of Baldwin & Butler (1985), and compaction of sands by Sclater & Christie (1980). Chalk compaction was modelled using a porosity-depth relationship derived from velocity data (Fig. 5.50). Finally, it was assumed that there has been no differential subsidence between the basin and high below the base Triassic.

Modelling of the post-Palaeocene compaction across the hörst reduces the gross thickness of the top Palaeocene to base Triassic section due to compaction by 620m in the basin. In comparison, a corresponding reduction in section over the Montrose - Arbroath area basement high of 446m is calculated. The contrast between these figures of 174m compares with actual relief, measured from an ENE-WSW regional seismic line (CNST86-29) across the same area, of approximately 120 to 170m.

Since the Forties-Montrose High trends approximately NNW-SSE, the above observations from adjacent basins across the high only explain structural relief across the bounding normal faults, and not along the strike of the structural high. There, NW-SE trending seismic data show segmentation of the high apparently controlled by ENE-WSW trending extensional and/or oblique slip faults. However, there is significantly less throw on this set of faults in comparison with those which bound the hörst. Consequently a further explanation for structure along the crest of the hörst is required to explain the field traps, including an explanation for the separation of the two oil accumulations. Compaction effects occurring on a smaller (meso-) scale are the most likely explanations (see following section).

5.6.2 Meso-Scale Compaction Effects.

The initial stage of modelling consisted of taking a single well correlation (Table 5.5) and estimating the present day porosity for each horizon. Each chronostratigraphic unit had to be separated into its individual sand and mud components, and the average porosities of each component was assumed to be the porosity at the mid point (see section 2.4, Chapter 2).

The next stage involves the removal of the post-Palaeocene section from above the oilfield, and the consequent decompaction of each horizon. Firstly, the average porosities must be estimated. As before, Baldwin & Butler's (1985) power law is used for muds and Sclater & Christie's (1980) exponential equation is used for sands. At these shallower depths of burial porosity estimation is extremely difficult, and usually highly variable. However, fieldwork in both California (Chapter 3) and New Mexico (Chapter 4) has shown that these equations appear to work well for the modelling

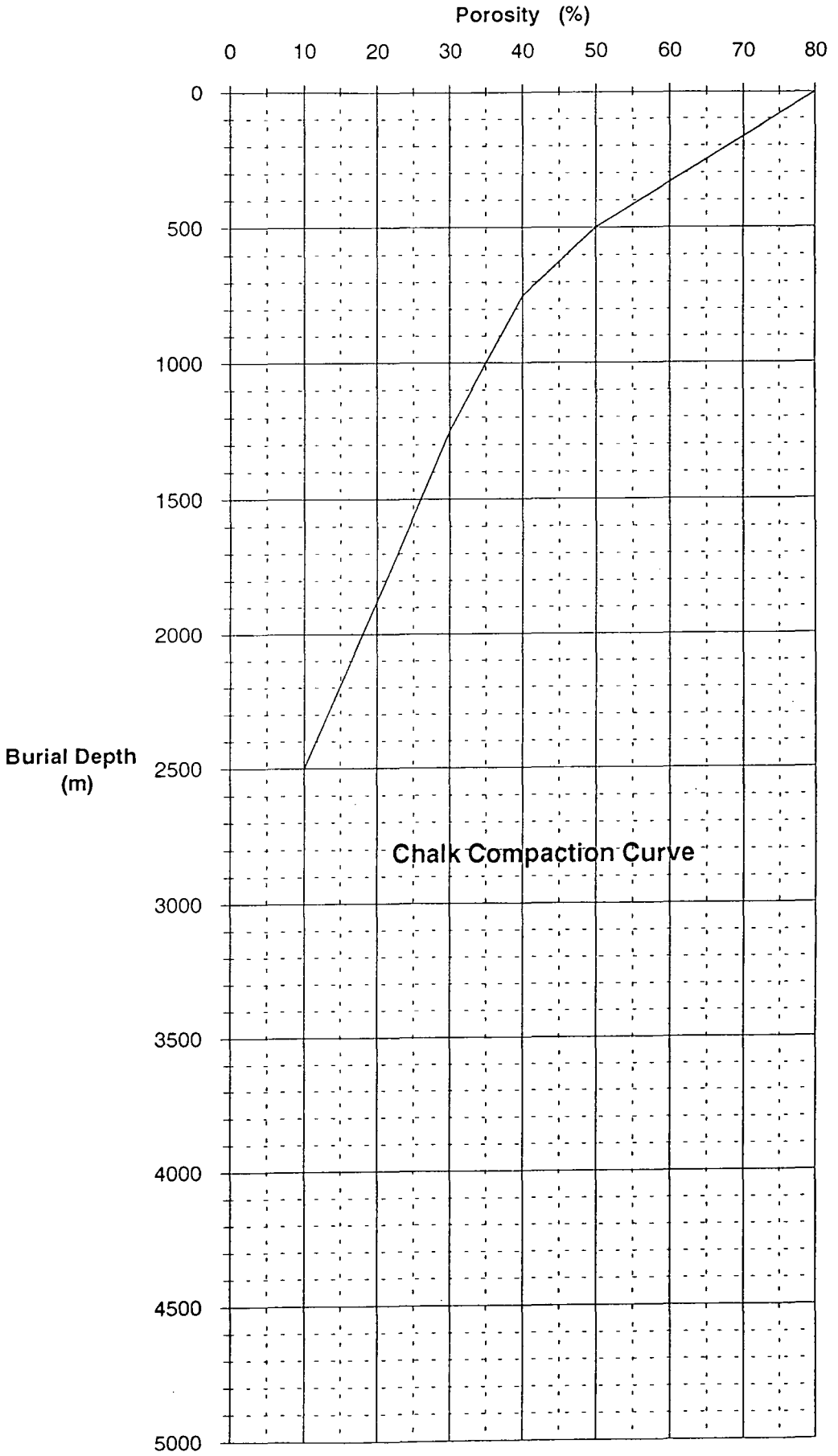

Figure 5.50 Porosity-depth curve derived from well log evidence for chalk.

process at shallow burial depths (i.e. 0-100m). Figures obtained using these mathematical methods often equate quite closely with those produced by mechanical tests of real sediment. For example, compaction ratios measured from shallow boreholes (Truyol, 1989) closely match those calculated using the equations above (see modelling of Muleshoe Mound, Chapter 4).

Once porosities have been evaluated, the unit's new thickness can be calculated using the equation of Van Hinte (1978), and summing the component sand and mud parts together. Similar calculations can then be carried out for the progressive removal of each horizon (Tables 5.7 & 5.8 show an example of the method for well T15). Once the uncompacted thicknesses for all the chronostratigraphic horizons are known it is a simple task of rebuilding the stratigraphy unit by unit on the base map over the Arbroath Field, plotting the thicknesses at the well locations and contouring the area. This allows a qualitative assessment of the role of compaction during deposition of the reservoir section. Taking results of fieldwork into account, the timing of compaction can also be qualitatively assessed, and the resulting depositional topography can be interpreted.

The results form a series of contour maps (Appendix 1), which not only show the topographic development of the Arbroath area, but also illustrate the isopachs of each separate time horizon along with the distribution of sand within each unit. The contour maps allow the assessment of topographic control upon subsequent deposition, as well as any control provided by the proximity of buried sand bodies. Contour maps of the depositional surface topography are based on the thickness of sediment in each well above the top chalk horizon (Top Maureen). Some wells (i.e. T1-T7, T9, T11-T11Z, T16, T18) have been drilled deep enough to locate this horizon accurately. For the remaining wells, the depth to the top chalk horizon was obtained from the seismic data. A suitable interval velocity for the overlying sections was determined from the wells that did intercept the top chalk horizon, which was used to calculate the depth to the same horizon for the shallower penetrating wells.

To carry out the assessment of topographical and compactional control upon sedimentation the contour maps were divided into an even grid (10cm x 5cm) (Fig. 5.46). It was then possible to take the initial depositional surface (Unit 19) and define the most likely depositional sites (MLDS) upon that surface (i.e. the topographically lowest areas). This was firstly done for the uncompacted surface, followed by the compacted surface (Appendix 2). The depositional sites (DS) were interpreted from the chronostratigraphic units

Well No.	22/17-115															
									SAND	MUD	SAND	MUD				
Horizon	Depth (TVDSS)	Depth (TVDSS)	% Sand	% Mud	% Sand at Top (T) or Base (B)	Unit Thickness	SAND Present Av. Porosity	MUD Present Av. Porosity	Av. Porosity after Post-Pal Removal	Av. Porosity after Post-Pal Removal	Unit Thickness after Palaeocene	Unit Thickness after Palaeocene	UNIT THICKNESS	Cumulative Section Thickness	Cumulative Sand Thickness	% SAND
Palaeocene/Balder	8025	2446.05	0	100		15.85	0.00	13.18	0.00	64.81	0.00	39.11	39.11	374.60	233.03	62.21
Sele Fm.	8077	2461.90	0	100		25.60	0.00	13.06	0.00	52.69	0.00	47.05	86.16	335.49	233.03	69.46
Forties Mem.	8161	2487.50	100	0		1.52	22.97	0.00	43.96	0.00	2.09	0.00	88.26	288.44	233.03	80.79
1	8166	2489.03	100	0		2.13	22.96	0.00	43.93	0.00	2.93	0.00	91.19	286.34	230.93	80.65
4	8173	2491.16	85	15	T	1.83	22.95	12.96	43.90	48.16	2.13	0.46	93.79	283.41	228.00	80.45
3	8179	2492.99	0	100		1.52	0.00	12.96	0.00	48.01	0.00	2.55	96.34	280.82	225.86	80.43
5	8184	2494.51	80	20	B	2.44	22.92	12.95	43.83	47.84	2.68	0.81	99.83	278.26	225.86	81.17
9	8192	2496.95	45	55	B	4.88	22.89	12.93	43.76	47.45	3.01	4.44	107.28	274.77	223.19	81.23
12	8208	2501.83	95	5	T	7.32	22.86	12.88	43.67	46.43	9.52	0.59	117.39	267.32	220.18	82.37
13	8232	2509.14	90	10	B	18.90	22.78	12.87	43.47	46.14	23.24	3.06	143.68	257.21	210.66	81.90
14	8294	2528.04	85	15	T	14.02	22.69	12.70	43.22	43.71	16.23	3.26	163.17	230.92	187.43	81.17
15	8340	2542.06	90	10	T	1.22	22.63	12.69	43.05	43.28	1.49	0.19	164.85	211.43	171.20	80.97
A	8344	2543.28	95	5	T	16.46	22.58	12.60	42.95	42.42	21.22	1.25	187.32	209.75	169.71	80.91
16	8398	2559.74	80	20	B	5.79	22.51	12.60	42.74	42.07	6.27	1.75	195.34	187.28	146.49	79.29
17	8417	2565.53	95	5	T	10.06	22.47	12.52	42.63	41.27	12.91	0.75	209.00	179.27	142.22	79.34
B	8450	2575.59	90	10	T	20.42	22.38	12.41	42.42	40.26	24.78	2.99	236.77	165.60	129.31	78.08
18	8517	2596.01	85	15	T	7.62	22.29	12.37	42.17	39.65	8.70	1.66	247.14	137.83	104.53	75.84
Lista Fm.	8542	2603.63	0	100		1.83	0.00	12.36	0.00	39.48	0.00	2.65	249.78	127.47	95.82	75.18
19	8548	2605.46	30	70	T	6.10	22.25	12.33	42.05	39.27	2.45	6.16	258.40	124.82	95.82	76.77
Andrew Mem.	8568	2611.56	95	5	T	5.49	22.20	12.30	41.94	38.89	6.98	0.39	265.77	116.20	93.37	80.35
21	8586	2617.04	80	20	T	80.96	21.99	11.91	41.52	36.44	86.39	22.44	374.60	108.83	86.39	79.38
C		0.00	0	0										0.00	0.00	0.00
D		0.00	0	0										0.00	0.00	0.00
E		0.00	0	0										0.00	0.00	0.00
F		0.00	0	0										0.00	0.00	0.00
G		0.00	0	0										0.00	0.00	0.00
H		0.00	0	0										0.00	0.00	0.00
Maureen Fm.		0.00	0	0										0.00	0.00	0.00
Ekofisk Fm.		0.00	0	0										0.00	0.00	0.00

Table 5.7 Decompaction table for Arbroath well 22/17-T15, for the removal of sediment to the Top Palaeocene level. The second unit thickness column shows the decompacted thickness of the chronostratigraphic units at this stage. Cumulative thickness and sand percentage is also calculated.

| | | |

isopach maps, and the number of matches between the presumed MLDS and the actual DS was calculated. Depositional sites that did not match with the MLDS on the uncompacted surface were scrutinised in terms of their compactional geometry, and their capacity for compaction by looking at the amounts of underlying sand. It was possible to look at not only the total amount of sand underlying these areas but also the immediately underlying sand concentration from the preceding unit (Appendix 1). Finally, an assessment of the depositional characteristics of each chronostratigraphic unit was outlined, both in terms of topography and compaction (Appendix 2), with the results outlined below.

RESULTS.

A general view of the resulting contour patterns for the Arbroath area shows that subsequent depositional units fill the topographic lows of the preceding topography, as would be expected. Also, the overall sand distribution increases as the younger units are deposited (e.g. compare the sand percentage map of unit 18 to that of unit 1). Most isopachs pick out the channelled nature of the depositional units, particularly from unit 17 and younger. However, it is more important to look at the sand concentration maps, as these pick out the channelised nature of the deposits much clearer, and illustrate how the sand fairways have formed through time. Particularly clear channels are picked out from unit 18 onwards (Fig. 5.51). Three channels appear to be delineated running generally northwest-southeast, and have been described as the northern, middle and southern channels in the descriptions of the topographic surfaces and the following isopachs in Appendix 2 (Fig. 5.46). Two general statements concerning the sand distribution can be made:-

1. Sand concentrations are high where a chronostratigraphic units isopach is thin.
2. Sand concentrations are high where the underlying topography is low angle or sloping, especially on the lower, northern sides of slopes, where turbidity flow velocities will be initially slowed.

It is also worth noting that the topography of the depositional surface remains essentially the same from the time immediately after the deposition of unit 17 up to the deposition of the top of the Forties Member. The deep topographic low in the south-western corner of the area is probably due to the lack of data and well control in this area.

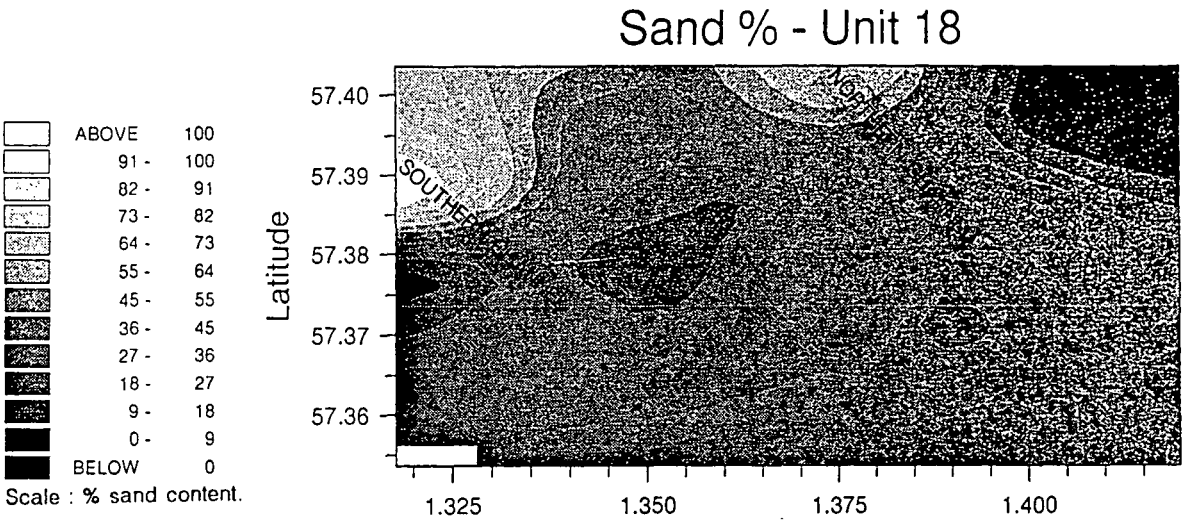

Figure 5.51 Submarine channels of the Arbroath Field evident from the sand percentage map of chronostratigraphic unit 18.

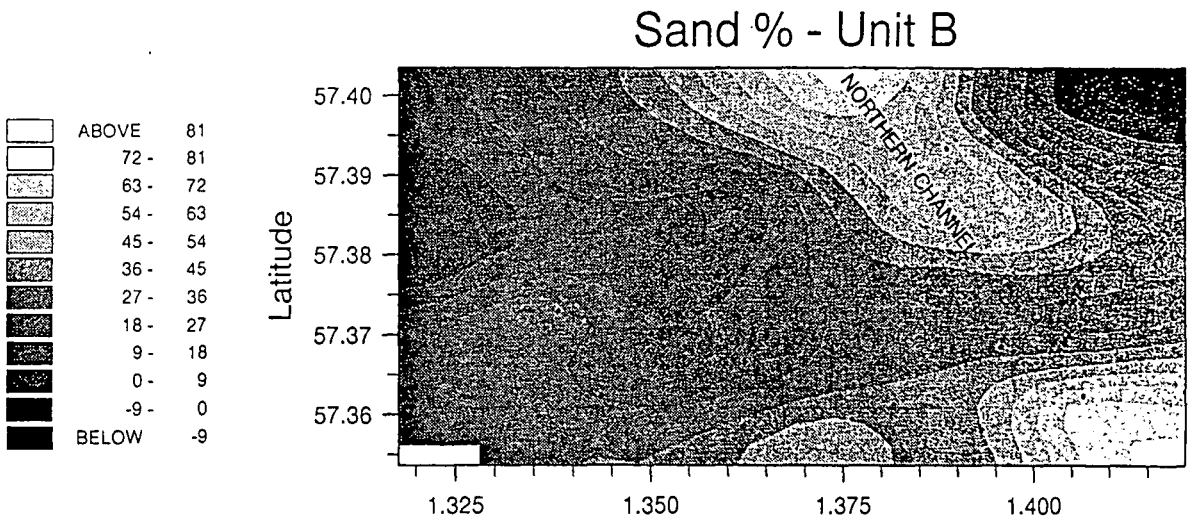

Figure 5.52 Northern submarine channel of the Arbroath Field illustrated by the chronostratigraphic sand percentage map of unit B.

There is also a strong correlation, especially in the older units, between the previous unit's sand component and the succeeding unit's isopach. Often where high percentages of sand are found in a deposited unit the succeeding unit is generally thinner in this region, illustrating how the compaction qualities of the underlying sediments may influence sedimentation.

Results, outlined in Appendix 2, show that compaction greatly enhances the possible depositional area for each unit. There is a strong correlation between the MLDS of the compacted depositional surface and the following depositional sites (on average 67% of MLDS match with the DS). Whereas, the correlation between the depositional sites and the MLDS of the uncompacted depositional surface is not as good, being only 44% of MLDS matching the actual DS. The channelised sands are generally fixed in their position, but on close inspection a horizontal off-set in sand distribution can be seen occurring at certain stages in the depositional buildup of the Arbroath region. For example, the northern channel, running along T15-T9-T5-T17-T8-T13-T3, is the main channel used by the turbidites, especially during the early phases of growth. Unit B is probably the first horizon to clearly define the channel (Fig 5.52), and deposits moderately thick sands in the T15, T5 and T17 area. Further sands of units 17 and 16 are also deposited in the same location, however, these are becoming successively thinner. Unit A, which marks a return of thick sedimentation in this area shows a clear horizontal off-set of its sand deposition to the northeast (T9 area) from the underlying sand deposits (Figs. 5.53a & b). Further off-setting of sand deposits occurs between the deposition of unit 15, unit 14 and unit 13. The depositional build-up of the Arbroath region is discussed in more detail below.

Arbroath Depositional Development.

The top surface of unit 19 is taken as the starting point to modelling as this correlation crosses all the wells of the area. This correlation comes only just above the top of the Andrew Member, and therefore documents all the Forties Member depositional history (Fig. 5.4).

19 Depositional Surface - Lista Isopach Deposition.

The Lista unit is relatively thin and mud-rich, but deposits sands in both the northern and southern channels, with a probable levee separating the two channels where the isopach is thickest around the T20-T16-T2-T3 region. Sands are found in small lobate deposits in both channels, in the north, around the T5-T9-T17 area on the southern slope and following low

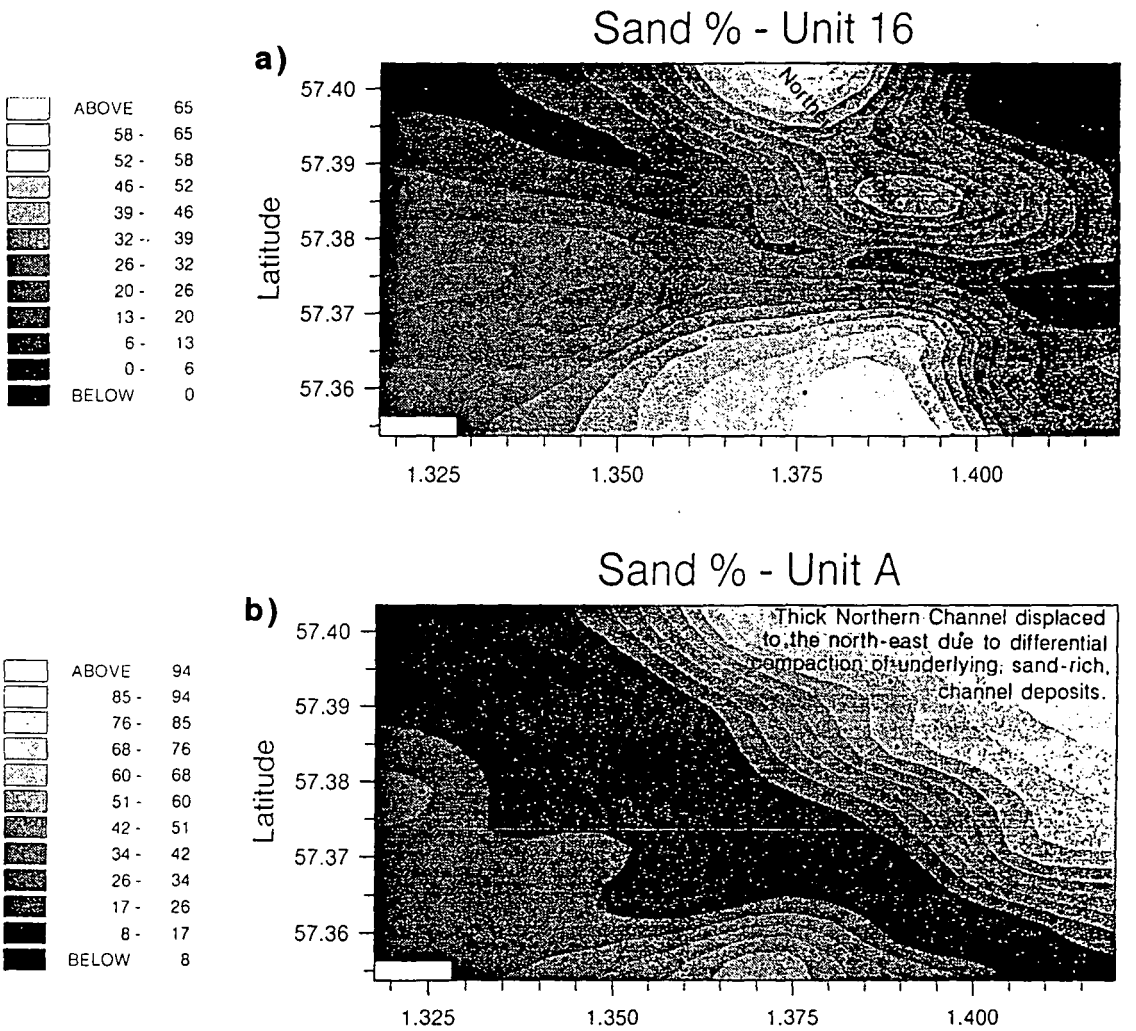

Figure 5.53a,b Off-setting of successive submarine channel deposits from unit 16 to unit A.

area of a major topographic high in the depositional surface, and in the south channel around the T10-T6 area, again on the southern slopes of a minor topographic high. In general, sand deposition is enhanced by compaction of the unit 19 depositional surface, especially in the southern channel.

Lista Depositional Surface - 18 Isopach Deposition.

Sands are found pushing into the very northern ends of both the northern (T15 area) and southern channels (T19-T14 area). They are probably confined due to the compactional topography of the top Lista surface, which creates a low-lying ridge running east-northeast from T14 to T9 that forms a barrier across which the majority of sand does not cross. Further mud deposition tends to fill topographically low areas upon the depositional surface.

18 Depositional Surface - B Isopach Deposition.

The northern channel becomes well defined at this stage, showing high sand concentrations around T15-T5-T17-T8 area, and is confined by the topographic highs at T9 in the north and T20-T16-T2 in the south. As before, a large proportion of the sand content is deposited on the initial ridge area of T5, however, more sand crosses the compactionally lowered ridge and spills into the southeastern corner of the area, where it appears to pond in the T11Z-T11-T7 area. Mud deposition fills and generally smooths the topography of the depositional surface.

B Depositional Surface - 17 Isopach Deposition.

Once again the northern channel is dominant, with a possible levee built up along the middle channel of T20-T16-T2, with additional sands deposited into a developing southern channel around the T19-T14 area where the isopach is thin. Northern channel sands are initially concentrated in the T15 area behind an ever decreasing ridge. However, as unit 17 is relatively thick most of the sediment, including large amounts of sand breached the lowered saddle between T16 and T5 to be deposited in the topographic low area of T3-T13-T18-T11Z-T11, which is lowered further by compaction, providing greater accommodation space for thicker sediment accumulation. Hence, the unit 17 isopach is thickest in this region, and both the sand concentration and isopach is off-set to the north from the thick sands deposited in a similar position in the preceding unit B.

17 Depositional Surface - 16 Isopach Deposition.

The southern channel appears to become dominant during this phase, with thicker and sandier sediment deposited within it than the northern channel which still shows some use, although the isopach is extremely thin

(<18m). Southern channel sediment can be interpreted as running along T19-T14-T10-T12-T1, with larger concentrations of sand found around the T4-T18 area in a lobe-shaped deposit. It appears that sand was fed down the southern channel, which was an initial low-lying area, but was compactionally enhanced due to very low amounts of underlying sand. Turbidites were fed towards the T4 area where they became temporarily dammed by a significant ridge running northeast from T4, through T3 to T13. Sands were banked against this high region as the isopach map shows, with only small amounts spilling over into the southeast corner.

16 Depositional Surface - A Isopach Deposition.

The northern channel becomes the focus of sedimentation during the deposition of unit A, with very thick and sandy deposits found in the northern channel around T15-T9-T5-T17-T8-T13. Sediment was partly controlled by topography, filling low areas, and being trapped behind a major ridge between T4-T3-T13, but deposition was also controlled by compaction of underlying sand bodies. The northern channel, outlined by unit A, is off-set to the northeast to flow nearer the T9 region than the previous channel outlines of units 16, 17 and B. Differential compaction across the northern channel prior to unit A deposition results in topography being created around T5, which forces turbidite flow towards this area. Only minor, thin sands are found in the southern channel.

A Depositional Surface - 15 Isopach Deposition.

As topography upon the depositional surface has generally been smoothed due to unit A deposition the southern channel becomes the major carrier of sediment as it forms one of the lowest areas in the region. Thick sands are found along T14-T12-T1, and are banked against a southern high area around T4. Some sand does manage to spill over into the southeastern corner, which also forms a low topographic area. A minor sandy levee deposit also forms on the northern side of the channel along the line of T20-T16, and can be clearly seen on the isopach map. Minor sands are found in the northern channel, and are now off-set to the south from the underlying thick sands of unit A. compaction of the depositional surface after unit A deposition shows that the low in topography on the northern edge of the region has migrated to the west resulting in the sands being deposited in the T15 area rather than around T9 as before.

15 Depositional Surface - 14 Isopach Deposition.

Deposition of unit 14 is mainly controlled by topography and the fact that the northern channel is the main axis of sediment supply. An east-west ridge

has developed in the north of the region running from T16 and through T5, mainly due to differential compaction across the thick underlying sands. Therefore, sands of unit 14 are trapped behind this ridge and off-set to the north, back around the T9 area. Minor sands make it over the ridge, and are generally deposited on the north facing up-slopes of the topography. Mud deposition fills previous topographic low areas, particularly the area around T17 and T8. However, due to the muddy nature of the sediment the small circular hollow still remains and grows as compaction continues.

14 Depositional Surface - 13 Isopach Deposition.

Following on from unit 14, thick sands are deposited in the northern channel, again slightly off-set to the south by the immediately underlying sands. Unit 13 also shows that sand is partially banked against the small ridge in the north (T15 region), but as this is a thick unit the majority of the sediment makes it over the ridge to be deposited in the topographically low area of T17-T3-T13-T11Z-T11. Minor sediment is present in the southern channel, and this is very sandy around T10-T12-T1-T4, but is also very thin (<22m, compared with 50m in the northern channel). No definable levee deposits are forming at this stage, possibly due to the fact that the channels are separated by a north to south trending area of high topography running up from T4 through T2 to the northern ridge at T16 to T5. The two channels are quite firmly entrenched either side, but topography is generally subdued after the deposition of unit 13, with a low embayment area beginning to form along the line of T20-T16-T2, which widens after compaction.

13 Depositional Surface - 12 Isopach Deposition.

Unit 12 is extremely sandy, especially where the isopach is thin. Both the northern and southern channels are defined by the sand deposition, and thick overbank muds are present in the topographically low area of T20-T16-T2. However, due to these sediments being mud it is not long before compaction makes this area a prime site for deposition once more. Once again the northern channel has high concentrations of sand banked behind the significant northern ridge running from the T5-T17 area southeatwards. As before, this ridge is created by differential compaction across the underlying channel sands of unit 13, displacing unit 12 sands to the northeast. Also major sands are found along the length of the southern channel, ponded against the northern slopes of the high region just south of T1 and T4. Sediment has also spilled over the minor saddle in the north-south ridge into the low area of the southeast corner of the region.

12 Depositional Surface - 9 Isopach Deposition.

For the first time the middle channel begins to accumulate sandy turbidite deposits, as unit 9 deposits sand along T20-T16, an area underlain by very low amounts of sand, and therefore, compactionally enhanced. This sand is banked against the main north-south ridge through the region, although thin amounts of sandy sediment make it over the high into the low southeast corner of the region. Some thin sediment may also have come down the northern channel to add to this deposit.

9 Depositional Surface - 5 Isopach Deposition.

Both the southern and middle channels are operative during this period of sedimentation, which is becoming increasingly sandier. The region is the topographically lowest, especially with the combined effects of differential compaction of a relatively underlying sand starved section, compared to that underlying the northern channel. High concentrations of sand are found banked against the high ridges in both the southern (T12-T1 area) and middle channels (T2 area). Further sand is found in the deep topographic low at the head of the southern channel around T19 and T14. Southern channel sands lie off-set to the northeast from the previous underlying sand bodies of units 12 and 13.

5 Depositional Surface - 3 Isopach Deposition.

Unit 3 deposition continues the trends begun by the previous unit. Once again the southern and middle channels are the main conduits of sandy turbidites, banking sediment against the topographic high ridges of the depositional surface. The middle channel deposits all its sand against the western slopes of the ridge in the T16-T2-T8 area, while the southern channel deposits sand in the deep topographic low, on the western slopes of the high region south of T1 and T4, and over the saddle in the low southeast corner of the Arbroath region. All these sands tend to be thin, with mud deposition generally filling the remaining topographically low areas of the depositional surface.

3 Depositional Surface - 4 Isopach Deposition.

Unit 4 is a very thin sand rich section, and therefore has little effect on the overall topographic shape of the Arbroath area. As before, it appears to show that the middle and southern channels are the active sites of sedimentation, with the northern channel has remained dormant for some period of time. This is presumably due to the large amounts of sand deposited earlier in the northern channel, now effectively damming the channel from further sediment, especially after the effects of differential

compaction. Once more unit 4 deposits high concentrations of sand on the slopes of the topographic high regions, now slightly displaced upstream (northwestwards) after the deposition of unit 3. Therefore, the sands of the middle channel are found around T20-T16, and the sands of the southern channel around T10-T12-T1. Sands also spill into the low southeast corner of the region in the T18-T7-T11Z-T11 area.

4 Depositional Surface - 1 Isopach Deposition.

Topography is the main contributing factor to the deposition of unit 1, although compaction undoubtedly enhances the topographic variations in certain areas. The reason topography may form the main control to depositional patterns at this stage may be due to the fact that most areas have high sand percentages close to the depositional surface making early compaction more difficult and less significant than before. Unit 1 again shows widespread sand distribution, especially where the isopach is generally thinner. Sands appear to be found in the southern channel, especially deposited on the upslope to the high region around T1 and T4. Further thin sands (<6m) are found in the northern end of the northern channel around T15 and T5, where they have probably been trapped by the topography. The northern channel has therefore become favourable for deposition once again as other areas have been filled. This is probably why the middle channel mainly receives a thin overbank mud section. Mud-rich areas appear to fill topographically low areas, and generally smooth topographic variations.

1 Depositional Surface - Forties Isopach Deposition.

The final submarine fan deposition of the area appears to flow exclusively down the middle channel although slightly displaced to the southwest relative to previous units such as 3 and 4. Therefore, sand is generally found along T20-T16-T2, but it also overlaps with the northeastern edge of the southern channel at T1 and T4. Deposition continued along the length of the middle channel, funnelling sediment into the low southeast corner, to deposit thin sands around T3-T13-T18-T7-T11Z-T11. Thicker mud deposition generally filled topographically low areas in the top unit 1 surface, especially around T17-T8 and T10-T12.

5.6.3 Small-Scale Compaction Effects.

As small-scale compaction effects can only be viewed on the scale of single turbidite beds and less, only submarine fan deposits examined in field outcrops can help in the understanding of compactional processes. However,

petrology of core samples can also be carried out to see compaction effects on the grain to grain scale.

Petrography has shown many compaction effects between grains, notably concavo-convex contacts between quartz grains (Plate 5.4), bending of mica flakes (Plate 5.5) and sutured contacts (Plate 5.6). Further to this, studies of the core from the Montrose and Arbroath wells illustrated many examples of sandstone injection features, along with widespread dish structures, both created by extremely rapid dewatering under the influence of compaction.

5.7 Conclusions.

Differential compaction can be modelled at various scales throughout the Montrose - Arbroath area, and is responsible for many features, including the field's geometry, location, and depositional development. Depositional models for the Montrose - Arbroath area and other related fields have been described by many authors (e.g. Walmsley, 1975; Heritier et al., 1979; Hill & Wood, 1980; Carman & Young, 1981, Kulpecz & Van Geuns, 1990; Crawford et al., 1991; Whyatt et al., 1991; Timbrell, 1993; Newman et al., 1993; Jenssen et al., 1993) allowing the development of a concise and thorough depositional model for the region to be established (section 5.5.4). The model basically consists of a series of channels (Fig. 5.46) fed from a prograding delta source, through which turbidite flows are funnelled, depositing their sand load, mainly by flow-stripping, in discontinuous pods. It is also apparent that sand is often deposited when turbidite flow encounters variations in slope upon the depositional surface, particularly depositing sand on the upstream side of regions where the local gradient increases. Fieldwork has illustrated that basal loading of sandy turbidites is extremely common, and often helps in the amalgamation of beds. Evidence suggests little erosion occurs during turbidite flow in this particular regime of the submarine fan, and therefore basal loading becomes an important process in minimising the amount of shale beds within a sand sequence, and greatly effecting the overall compactability of that sequence.

Starting with the largest scale at which compaction has been modelled for the Montrose - Arbroath area it is possible to recognise the significance of differential compaction around the Forties-Montrose High on the development of the fields' structure. Indeed, the structure of the Montrose and Arbroath oilfields owe their origin primarily to differential compaction across the hörst, generating structure upon the top Palaeocene surface

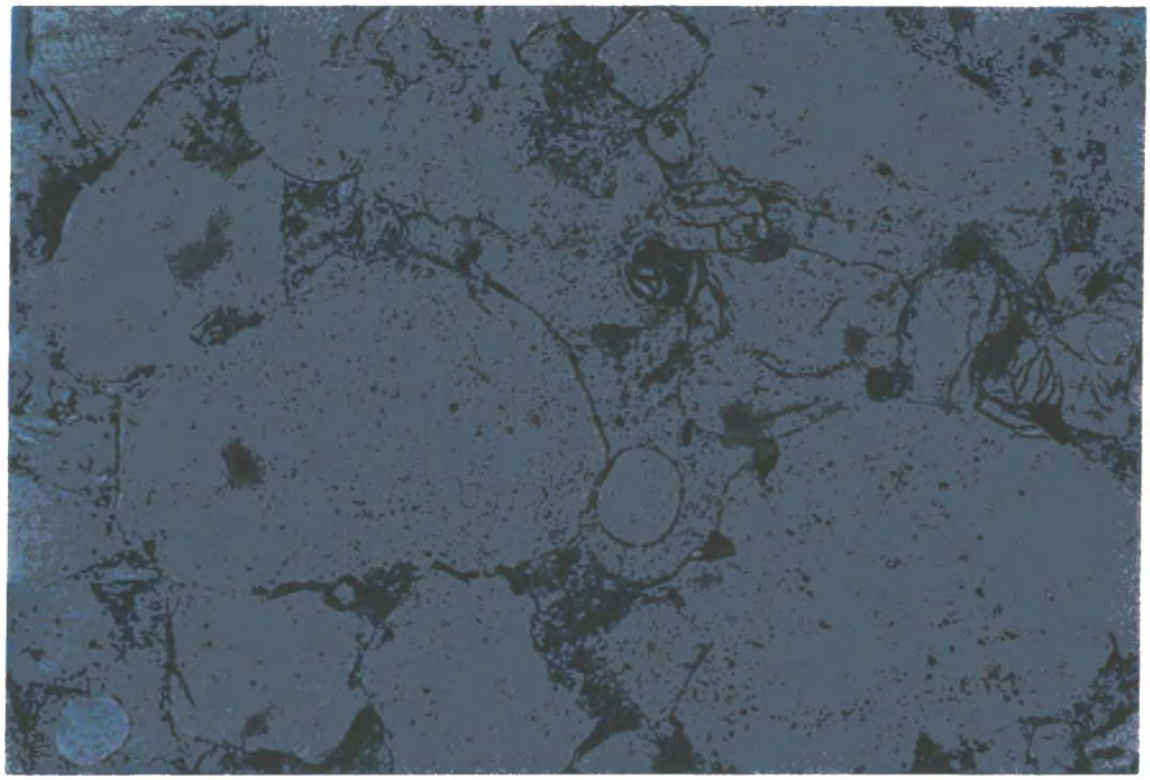

Plate 5.4 Concavo-convex quartz grains (Q) produced by compaction on a grain to grain scale. Sample comes from Arbroath well 22/17-T4 at a measured depth of 10374' (Field of view is 1.5mm).

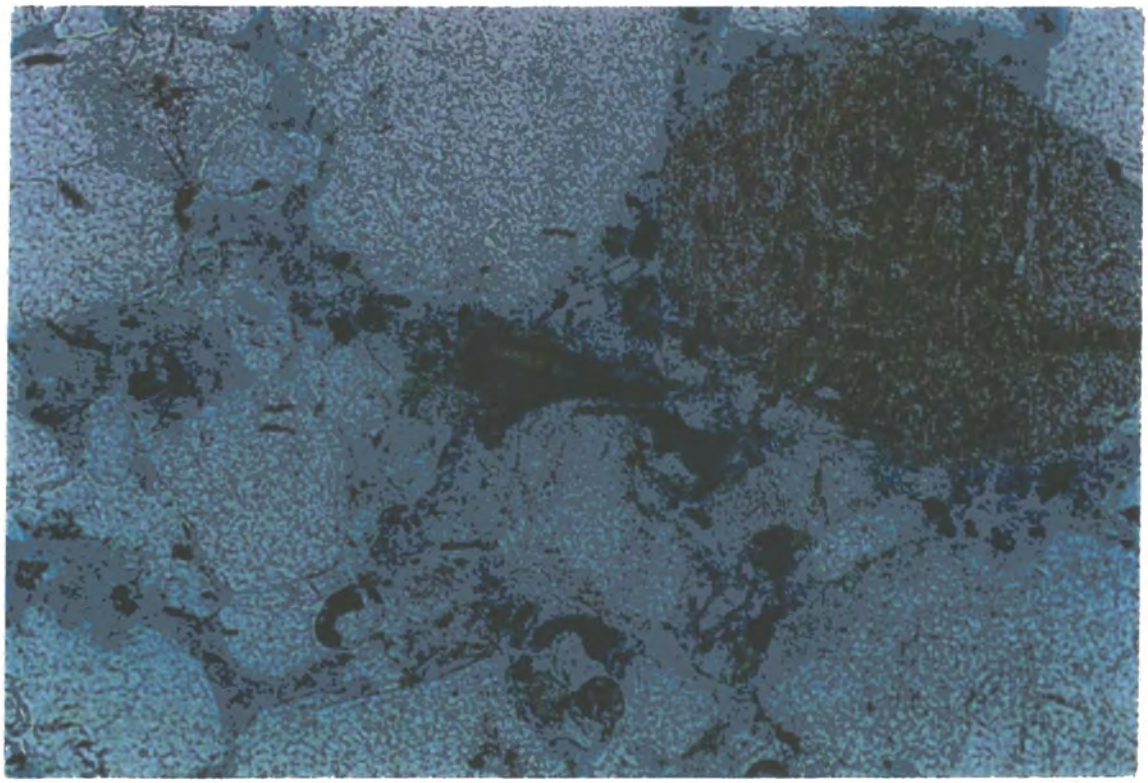

Plate 5.5 Bending of mica flake (M) due to compaction around a more rigid quartz grain (Q). Sample comes from Arbroath well 22/17-T4 at a measured depth of 10319.10' (Field of view is 1.5mm).

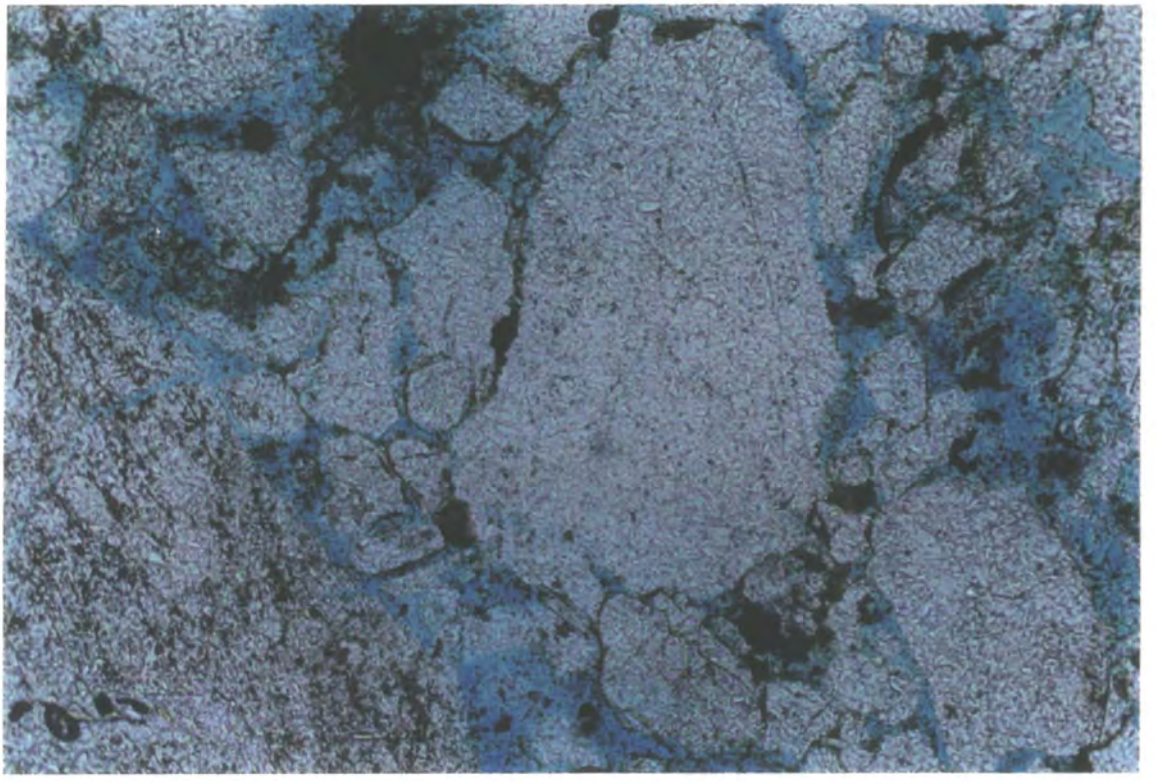

Plate 5.6 Sutured contacts between compacted quartz grains (Q). Sample comes from Arbroath well 22/17-T3 at a measured depth of 9355' (Field of view is 1.5mm).

orthogonal to the axis of the hörst. Further to this, contrasts in lithologies within the reservoir section of the submarine fan system have resulted in enhanced relief at the top reservoir level due to the differential compaction of the underlying muds and sands. This process has ultimately led to the separation of the two hydrocarbon accumulations, as the intervening region between the Montrose and Arbroath oilfields consists of a relatively mud-rich Palaeocene section, as compared to the sand-rich, channelised Palaeocene sections of the fields themselves. During progressive Tertiary burial, structure has therefore developed by differential compaction.

Moving down a scale of compactional modelling, and looking at the development of the submarine fan channels themselves, the present study has assessed the relationship between facies organisation and the differential compaction of the underlying section. This has been achieved through detailed fieldwork and the development and correlation of the Arbroath depositional model.

Detailed modelling of the Arbroath Oilfield has allowed the development of the depositional surface through time to be evaluated. In addition to this it has also been possible to show individual isopachs of chronostratigraphic units, plus the concentration of sand within each body. A simple assessment has then been performed, matching the following chronostratigraphic isopach to the preceding compacted topography of the depositional surface. In general three sand fairways (Fig. 5.46) are operative during the deposition of the Forties Member, and the timing of sedimentation within these channels varies not only due to sediment supply, but also due to the topographic expression of the channels at each successive time stage. Topography is greatly effected by differential compaction between sand-rich channel bodies and mud-rich overbank/levee areas. The abandonment of the northern channel from unit 12 until unit 1 deposition is a good example of this, as early deposited, thick sands produce a topographic ridge once differential compaction has occurred to effectively block the channel.

A second example is the fact that a middle channel does not exist until the youngest sediments are encountered. The area formed levee deposits early in the depositional history of the area, and it is not until differential compaction between the northern sand-rich channel, and to some degree the southern sand-rich channel has occurred, that the middle channel becomes a favourable site for turbidite flow and deposition. This type of model is reminiscent of Walker's (1985) channel - levee - interchannel model for the Wheeler Gorge sediments (Chapter 3).

Fieldwork can refine the compaction-driven model for deposition in the Montrose - Arbroath area. Data derived from New Mexico (Chapter 4) illustrates the importance of the precise relationship between the compaction rate and the deposition rate of sediment. From the evidence of the depositional surface maps and the isopachs for the various chronostratigraphic units of the Arbroath region, it appears that the majority of compaction occurs post-depositionally, enhancing topography upon the depositional surface and increasing the area of most likely depositional sites (MLDS).

It is therefore proposed that upon sedimentation little compaction of the underlying section occurs, especially as turbidite flows are deposited geologically instantaneously and far outstrip the compaction rate. During the following break in rapid sedimentation, when deposition rates are extremely low, compaction rates are now faster than deposition, and compaction catch-up occurs in the underlying sequences producing enhanced topography on the depositional surface due to differential compaction. This process is demonstrated by the rotated beds of the Dona Ana exposed on the southern side of Muleshoe Mound, where differential compaction between the mound and the underlying Arcente muds has the greatest effects at periods where sedimentation is low to absent (see Chapter 4). Rotation of beds is interpreted to have occurred in the Arbroath area, although the scale of the rotation will be significantly less than that seen around Muleshoe Mound because of the lower angle of slopes over which differential compaction, created by lateral facies changes, can occur. In summary, a period of topographic smoothing by deposition is followed by a period of compaction, which, because of the differing lithologies involved, produces enhanced topography to influence subsequent deposition.

The general view of the Arbroath depositional development during the Forties Member period consists of an interplay between three submarine channels. Initial deposition occurred within the northern channel, especially around the T15-T5-T9-T17-T8 region. Larger amounts of sediment were fed along this channel, and more importantly, they became sandier as time passed. In turn, this was related to the sediment supply from the Moray Firth delta.

A southern channel also began to develop as less sediment was funnelled down the northern channel. Differential compaction of the northern channel began to create a ridge in the T5-T9 region because of the high proportion of sand contained within it relative to the thick, mud-rich overbank

deposits that occurred within the area of T20-T16-T2 and westwards. At some stages both the northern and southern channels were operating as sediment conduits, and the isopach maps suggest that a muddy levee section developed between the two channels along the line of T20-T16-T2. Eventually, due to the low topography of the region, the southern channel took over as the main sediment transport system, depositing thick sands along the line of T19-T14-T10-T12-T1-T4. High topography on the depositional surface south of T1 and T4 was the main control upon sand deposition. However, large turbidite flows often made it across the topography enabling the development of thick sands in the topographic low area of T3-T13-T18-T11Z-T11-T7.

Near the end of Forties Member deposition, as submarine fan development began to dwindle, differential compaction within the Arbroath region created a middle channel region along the line of T20-T16-T2-T8-T3-T11Z-T11. Both the northern and southern channels created topographically higher areas due to the sand-rich nature of the deposits within them, whereas the middle channel line was nearly exclusively underlain by mud-rich overbank and levee deposits. Therefore, the final channel deposits of turbidite sand are found within the middle channel. Figure 5.54 illustrates the interpreted development of the Arbroath Oilfield, showing the influence of differential compaction on channel location and deposition. A cross-section constructed across the oilfield (Fig. 5.55) also clearly indicates the interplay of deposition within the three channels and differential compaction.

The assessment of the Arbroath area therefore illustrates the strong control of compaction upon facies organisation, development, stacking patterns and geometry. The majority of compaction occurs post-depositionally, resulting in the production of topography on the depositional surface. As the effects of the topography become greater through time channels are required to switch their position, locating themselves in the topographically lowest area.

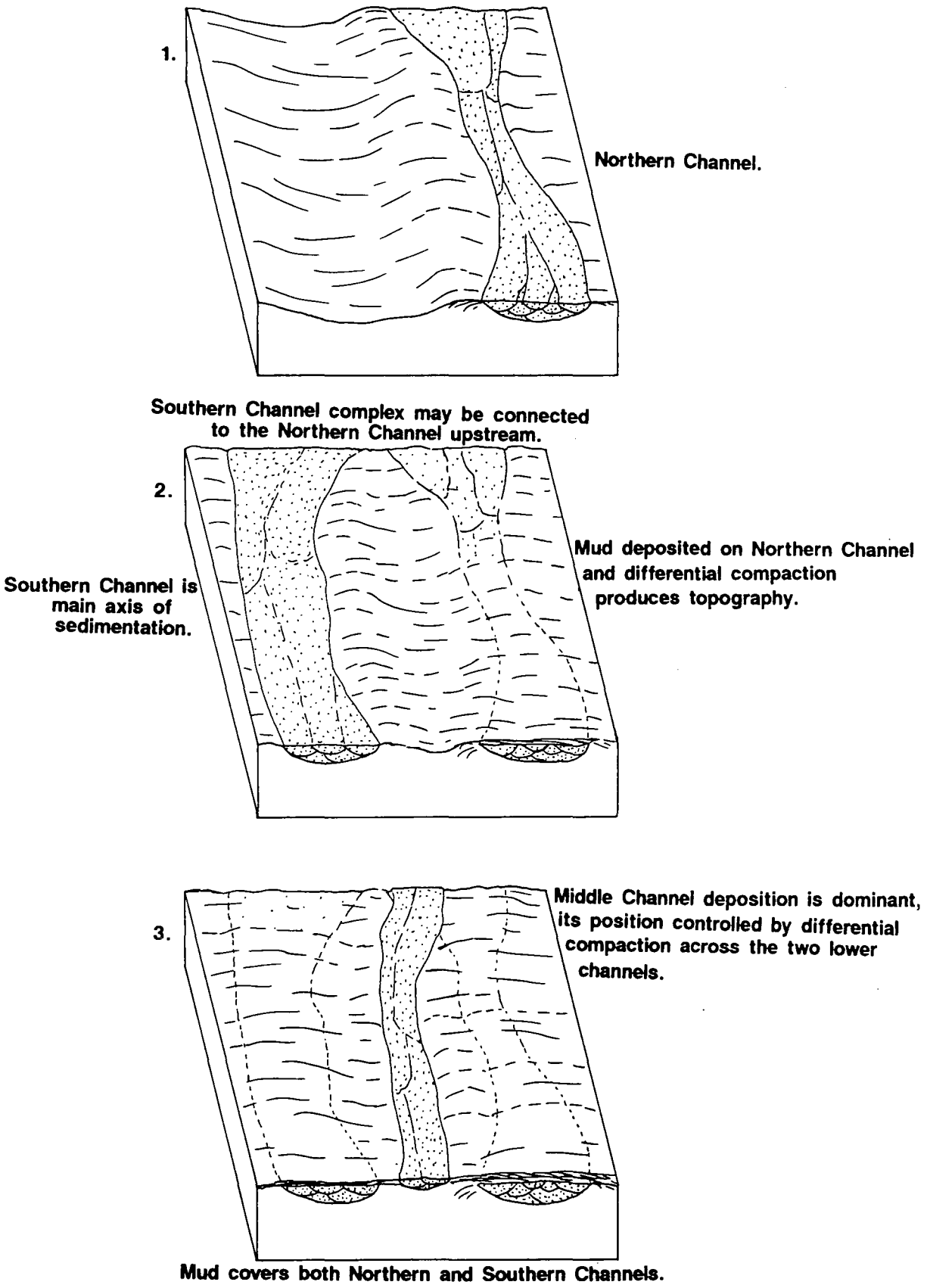

Figure 5.54 Interpreted stratigraphic development of the Arbroath Field.

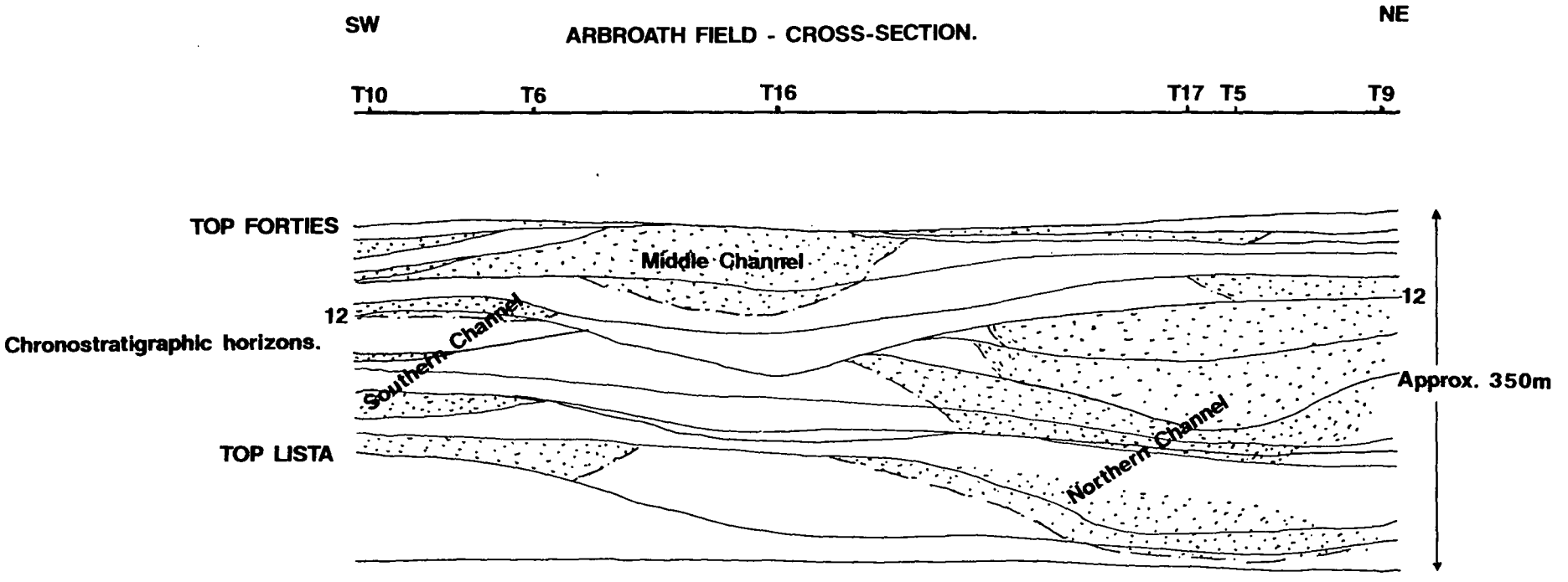

Figure 5.55 Cross-section of the Arbroath Field based on decompaction data. The section illustrates all 3 submarine channels.

Chapter 6: Conclusions.

The conclusions arising from the present study have been outlined at the end of the relevant chapters. This final section will summarise the conclusions, showing the inter-relationship of the various aspects of the present work.

Firstly, Chapter 2 illustrates the principle that because of the high initial mud porosities encountered in a submarine fan environment, the effects of differential compaction based on lateral and vertical facies changes will be greatest as compared to similar effects in the alluvial or deltaic environment, for example. It has also been shown that the rate of compaction of a sedimentary unit is extremely important with respect to the production of topography on the depositional surface. If compaction occurs syn-depositionally, at a rate equal to deposition, then once deposition ceases or is halted no further compaction occurs, and the depositional surface remains flat. However, if compaction proceeds at a rate slower than that of deposition, then once deposition ceases or is halted, compaction of the underlying sequences may occur with no further addition of load (sediment). Post-depositional compaction, such as described, can therefore create topography on the depositional surface which may influence subsequent deposition. Hence, depositional control may be emphasized due to intermittent deposition, especially true for deposition in the submarine fan environment, where turbidite deposition is not only episodic, but is extremely fast, and is believed to outstrip the rate of underlying compaction.

In order to test compaction, and differential compaction theories for the submarine fan environment, Ridge Basin in southern California was studied (Chapter 3). Exposure in the area provided evidence suggesting that a certain degree of differential compaction occurs syn-depositionally. This is most likely due to the very high initial depositional porosities of the muds (Approximately 80%). Exposures also showed that slumping and loading of beds is another important aspect to be noted when modelling differential compaction of submarine fan deposits. Overall, however, it was concluded that exposures of submarine fan deposits provide only limited data concerning compactional control on deposition due to the low angle of facies changes and the large lateral dimensions of submarine channel complexes over which these facies changes occur. The scale of observation was therefore a major hindrance, with the outcrop scale being below what was required for such modelling.

Carbonate environments, however, may provide outcrop scale evidence of differential compaction due to the steep angles over which facies changes may occur. This is especially true in areas where early-cemented carbonate buildups have developed. The Sacramento Mountains of New Mexico (Chapter 4) provides excellent exposure of such buildups and their flanking strata.

Data collected from Muleshoe Mound conclusively shows that differential compaction occurred post-depositionally, with a large amount of associated bed rotation. Using the incompactible mound as a reference frame, the reconstruction of the flanking beds, and hence the calculation of the amount of early compaction was possible. Calculations showed that early compaction is extremely rapid, accounting for approximately 50% bed thickness reduction in mudstone beds. This figure is considerably greater than what may be expected when using proposed porosity-depth curves or functions (e.g. Baldwin & Butler, 1985; Audet & McConnell, 1992). The main conclusion arising therefore, is the fact that although proposed curves such as Baldwin & Butler's (1985) work well for porosity-depth data taken from burial depths of greater than approximately 300m, it appears that they completely under-estimate the amount of near-surface compaction that occurs in muds. The discordance most likely arises from the fact of the general lack of near-surface porosity data, and therefore calculated curves are falsely distorted due to the bias produced by the large volume of deeper porosity data.

A further implication of post-depositional compaction is the production of overpressure at very shallow depths. Essentially, if a mudstone unit is loaded and not allowed to compact, the pore fluid will support some of the weight of the overburden, and hence become overpressured. Modelling of Muleshoe Mound also enabled the calculation of the limits for the near-surface overpressure of the pore fluids within the Arcente mud section. Results show a large amount of overpressure may be generated due to under-compaction depending on the balance between the two rates of deposition and dewatering of the sedimentary pile. Numerous factors are involved in the rate of dewatering such as the permeability of the mud, the presence/absence of fluid pathways which enable pore fluid to escape, which is also probably related to the frequency of the interbedding between sandstone and mudstone beds. Finally, it is also shown in Chapter 4 how the variation in relative sea-level may also effect compaction rates of mudstone units, in turn effecting the amount and relative position of accommodation

space available for subsequent deposits. This aspect alone appears to form an excellent subject for further research.

Finally, Chapter 5 attempts to combine the conclusions concerning near-surface compaction gained from fieldwork with the interpreted depositional model for the Montrose and Arbroath oilfields of the North Sea. The depositional model for the area is relatively well documented, generally consisting of a series of sandstone-rich submarine fan channel complexes and mud-rich overbank and interchannel deposits. Such deposits also account for the Forties and Nelson fields in the area, and similar types of deposits also account for other oilfields, both in the North Sea and other hydrocarbon provinces. Seismic data across the Montrose - Arbroath region defines the location of the submarine channels. However, the internal organisation and overall relative ages of the channels is beyond the resolution of the seismic data, and therefore the present study relies on detailed well correlations, especially throughout the Arbroath field. Well correlation is extremely difficult in turbidite environments, however, as much data as possible was used to achieve the correlation for the present study (e.g. biostratigraphy, RFT pressure data, core logs, etc.). Backstripping of the correlated wells was performed, which further allowed the sequential reconstruction of each chronostratigraphic unit. Contour maps and cross-sections provided a picture of how the stratigraphy of the area evolved, hence allowing a qualitative view of the control of deposition provided by differential compaction.

Utilising the conclusions derived from fieldwork it is possible to conclude that sand-rich turbidite deposits developed in the channels with relatively small amounts of compaction of the underlying sediments occurring during their deposition. During the subsequent hiatus in deposition, differential compaction modified the topography of the depositional surface, resulting in the off-setting of individual sand-rich turbidite flows within the channels (e.g. deposits in the northern Arbroath channel). Further, to this differential compaction also controlled which channel was active at every stage of turbidite deposition within the Montrose - Arbroath region. This is especially illustrated by the presence of the middle channel in the Arbroath field. Topography dictated the location of the northern and southern channels in the region through most of the Forties Member time. However, the eventual differential compaction between these sand-rich areas and the mud-rich central region, finally led to the evolution of the central channel which

became active and sand-rich during the very final stage of the Forties Member deposition.

Differential compaction on a larger scale can also be seen to effect the Palaeocene section of the region. The underlying topography of the Forties-Montrose High provides the framework across which differential compaction occurs due to the lateral changes in thickness of sedimentary units across the high. Structure created by the differential compaction enhances the structural relief of the submarine fan channels, emphasizing their topography on the top Palaeocene surface, and making such deposits prime reservoirs for hydrocarbons, and therefore ideal targets for large hydrocarbon accumulations.

Although the present study can only qualitatively assess the role of differential compaction in the Montrose - Arbroath region, it highlights the importance of near-surface compaction effects, and the relative timing of sediment compaction with regards to deposition. Near-surface compaction also appears to account for a much greater destruction in porosity than suggested by published porosity-depth curves. It is suggested that differential compaction in the submarine fan environment provides a major control on the areal development, distribution and geometry of submarine fan channel systems. The collection of reliable near-surface porosity data from such environments would provide a much clearer picture than is possible to define at this stage The present study also suggests that near-surface overpressure would be detected in submarine fan deposits immediately after the deposition of a turbidite flow. The overpressure is likely to account for sedimentary features such as sandstone injection dykes, formed when the bleed-off of overpressure is extremely rapid and localised along certain areas of weakness (e.g. fault planes). Greater study of modern submarine fans, utilising both geological and geophysical techniques will hopefully provide a greater database for such a model of deposition, and the controls exerted on that deposition, especially differential compaction.

REFERENCES.

ABBOTS, I. L. (Ed) 1991. *United Kingdom Oil and Gas Fields, 25 Years Commemorative Volume.* Geological Society Memoir No. **14.**

AHR, W. M. 1989. Sedimentary and Tectonic Controls on the Development of an Early Mississippian Carbonate Ramp, Sacramento Mountains Area, New Mexico. In: CREVELLO, P. D., WILSON, J. L., SARG, J. F. & READ, J. F. (Eds) *Controls on Carbonate Platform and Basin Development.* Special Publication of the Society of Economic Paleontologists and Mineralogists, Tulsa, **44**, 203-212.

ALLEN, J. R. L. 1978. Studies in Fluviatile Sedimentation: An Exploratory Quantitative Model for the Architecture of Avulsion-Controlled Alluvial Suites. *Sedimentary Geology,* **21**, 129-147.

ALLSOP, T. & SWARBRICK, R. E. 1992. Differential Compaction and its Control upon Siliciclastic Deposition Within the Submarine Fan Environment. *Abstract Volume.* 31st Annual Meeting of the British Sedimentological Research Group, 16-19th December, Southampton.

ALLSOP, T., SWARBRICK, R. E. & FARFAN, P. 1992. Influence of Compaction in Controlling Siliciclastic Facies Distribution in the Paleocene Sediments of the North Sea. Abstract. *Deep Water Clastics: Dynamics of Modern and Ancient Systems.* B.S.R.G. Workshop, 20-21st March, Oxford.

ALONSO, B., CANALS, M., GOT, H. & MALDONADA, A. 1991. Sea Valleys and Related Depositional Systems in the Gulf of Lion and Ebro Continental Margins. *Bulletin of the American Association of Petroleum Geologists,* **75**, 1195-1214.

ANDERSON, S. 1991. Differential Compaction in Alluvial Sediments. *Unpublished Ph.D. Thesis, University of Cardiff.* 199pp.

ANDERTON, R. 1993. Sedimentation and Basin Evolution in the Paleogene of the Northern North Sea and Faeroe-Shetland Basins. Abstract. In: PARKER, J. R. (Ed) *Petroleum Geology of Northwest Europe: Proceedings of the 4th Conference.* The Geological Society, London, 31.

ANGEVINE, C. L., HELLER, P. L. & PAOLA, C. (Eds) 1990. *Quantitative Sedimentary Basin Modeling. Continuing Education Course Note Series #32,* The American Association of Petroleum Geologists, Tulsa, Oklahoma, 133pp.

ARMENTROUT, J. M., MALECEK, S. J., FEARN, L. B., SHEPPARD, C. E., NAYLOR, P. H., MILES, A. W., DESMARAIS, R. J. & DUNAY, R. E. 1993. Log-Motif Analysis of Paleogene Depositional Systems Tracts, Central and Northern North Sea: Defined by Sequence Stratigraphic Analysis. In: PARKER, J. R. (Ed) *Petroleum Geology of Northwest Europe: Proceedings of the 4th Conference.* The Geological Society, London, 45-57.

ARMSTRONG, L., TEN HAVE, T. & JOHNSON, H. D. 1987. The Geology of the Gannet Fields, Central North Sea, U.K. Sector. In: BROOKS, J. & GLENNIE, K. W. (Eds) *Petroleum Geology of North West Europe.* Graham & Trotman, London, 533-548.

ATHY, L. F. 1930. Density, Porosity and Compaction of Sedimentary Rocks. *Bulletin of the American Association of Petroleum Geologists,* **14**, 1-24.

ATKINSON, J. H. & BRANSBY, P. L. (Eds) 1978. *The Mechanics of Soils: an Introduction to Critical State Soil Mechanics.* McGraw-Hill, London. 375pp.

AUDET, D. M. & FOWLER, A. C. 1992. A Mathematical Model for Compaction in Sedimentary Basins. *International Journal of Geophysics,* **110**, 577-590.

AUDET, D. M. & McCONNELL, J. D. C. 1992. Forward Modelling of Porosity and Pore Pressure Evolution in Sedimentary Basins. *Basin Research,* **4**, 147-162.

BAIN, J. S. 1993. Historical overview of Exploration of Tertiary Plays in the UK North Sea. In: PARKER, J. R. (Ed) *Petroleum Geology of Northwest Europe: Proceedings of the 4th Conference.* The Geological Society, London, 5-13.

BALDWIN, B. 1971. Ways of Deciphering Compacted Sediments. *Journal of Sedimentary Petrology,* **41**, 293-301.

BALDWIN, B. & BUTLER, C. O. 1985. Compaction Curves. *Bulletin of the American Association of Petroleum Geologists,* **69**, 622-626.

BARNES, N. E. & NORMARK, W. R. 1984. Diagnostic Parameters for Comparing Modern Submarine Fans and Ancient Turbidite Systems. *Geo-Marine Letters,* **3**, 224.

BAYER, U. & WETZEL, A. 1989. Compactional Behaviour of Fine Grained Sediments - Examples from Deep Sea Drilling Project Cores. *Geologische Rundsschau,* **78**, 807-819.

BEARD, D. C. & WEYL, P. K. 1973. Influence of Texture on Porosity and Permeability of Unconsolidated Sand. *Bulletin of the American Association of Petroleum Geologists,* **57**, 349-369.

BELDERSON, R. H., KENYON, N. H., STRIDE, A. H. & PELTON, C. H. 1984. A 'Braided' Distributary System on the Orinoco Deep-Sea Fan. *Marine Geology,* **56**, 195-206.

BERG, R. R. & ROYO, G. R. 1990. Channel-Fill Turbidite Reservoir, Yowlumne Field, California. In: BARWIS, J. H., McPHERSON, J. G. & STUDLICK, J. R. J. (Eds) *Sandstone Petroleum Reservoirs.* Springer-Verlag, New York, 467-487.

BERNAL, J. D. & FINNEY, J. L. 1967. Random Packing of Spheres in Non-Rigid Containers. *Nature,* **214**, 265-266.

BERNAL, J. D. & MASON, J. 1960. Co-ordination of Randomly Packed Spheres. *Nature,* **188**, 910-911.

BHATTACHARYYA, A. & FREIDMANN, G. M. 1984. Experimental Compaction of Ooids Under Deep-Burial Diagenetic Temperatures and Pressures. *Journal of Sedimentary Petrology,* **50**, 362-372.

BISHOP, R. S. 1979. Calculated Compaction States of Thick Abnormally Pressured Shales. *Bulletin of the American Association of Petroleum Geologists,* **63**, 918-933.

BJØRLYKKE, K. 1988. Sandstone Diagenesis in Relation to Preservation, Destruction and Creation of Porosity. In: CHILINGARIAN, G. V. & WOLF, K. H. (Eds) *Developments in Sedimentology 41: Diagenesis, I.* Elsevier, Amsterdam, 555-588.

BLACKWELDER, E. 1920. The Origin of the Central Kansas Oil Domes. *Bulletin of the American Association of Petroleum Geologists,* **4**, 39-94.

BLOCH, S. 1991. Empirical Prediction of Porosity and Permeability in Sandstones. *Bulletin of the American Association of Petroleum Geologists,* **75**, 1145-1160.

BLOCH, S., McGOWAN, J. H., DUNCAN, J. R. & BRIZZOLARA, D. W. 1990. Porosity Prediction, Prior to Drilling, in Sandstones of the Kekiktuk Formation (Mississippian), North Slope, Alaska. *Bulletin of the American Association of Petroleum Geologists,* **74**, 1371-1385.

BOLTON, K., LANE, H. R. & LeMONE, D. V. (Eds) 1982. Symposium on the Paleoenvironmental Setting and Distribution of Waulsortian Facies. *El Paso Geological Society and the University of Texas, El Paso, TX.*

BOUMA, A. H., STELTING, C. E. & COLEMAN, J. M. 1985. Mississippi Fan, Gulf of Mexico. In: BOUMA, A. H., NORMARK, W. R. & BARNES, N. E. (Eds) *Submarine Fans and Related Turbidite Systems.* Springer-Verlag, New York. 143-150.

BOUMA, A. H., COLEMAN, J. M., MEYER, A. W., et al. 1986. *Initial Reports of the Deep Sea Drilling Project, **96**.* Washington (U.S. Government Printing Office), 824pp.

BOWEN, A. J., NORMARK, W. R. & PIPER, D. J. W. 1984. Modelling of Turbidity Currents on Navy Submarine Fan, California Continental Borderland. *Sedimentology,* **31**, 169-185.

BOWSHER, A. L. 1986. Late Paleozoic Reef Complexes of the Northern Sacramento Mountains, New Mexico. In: AHLEN, J. L. & HANSON, M. E. (Eds) *Southwestern Section of AAPG Transactions and Guidebook of 1986 convention, Ruidoso, New Mexico.* New Mexico Bureau of Mines & Mineral Resources, Socorro, NM, 49-72.

BREDEHOEFT, J. D. & HANSHAW, B. B. 1968. On the Maintenance of Anomalous Fluid Pressures: I. Thick Sedimentary Sequences. *Bulletin of the Geological Society of America,* **79**, 1097-1106.

BREWSTER, J. 1991. The Frigg Field, Block 10/1 UK North Sea and 25/1, Norwegian North Sea. In: ABBOTS I. L. (Ed) *United Kingdom Oil and Gas Fields, 25 Years Commemorative Volume.* Geological Society Memoir No. **14**, 117-126.

BRIDGE, J. S. & LEEDER, M. R. 1979. A Simulation Model of Alluvial Stratigraphy. *Sedimentology,* **26**, 617-644.

BRIDGE, J. S. & MACKEY, S. D. 1993. A Revised Alluvial Stratigraphy Model. In: MARZO, M. & PUIGDEFÁBREGAS, C. (Eds) *Alluvial Sedimentation.* Special Publication of the International Association of Sedimentologists, **17**, 319-336.

BRIGAUD, F., CHAPMAN, D. S. & DOUARAN, S. L. 1990. Estimating Thermal Conductivity in Sedimentary Basins using Lithologic Data and Geophysical Well Logs. *Bulletin of the American Association of Petroleum Geologists,* **74**, 1459-1477.

BROOKS, J. & GLENNIE, K. W. (Eds) 1987. *Petroleum Geology of North West Europe.* Graham & Trotman, London.

BROWN, L. F. Jr. 1975. Role of Sediment Compaction in Determining Geometry and Distribution of Fluvial and Deltaic Sandstones. (Case Study: Pennsylvanian and Permian Rocks of North-Central Texas). In: CHILINGARIAN, G. V. & WOLF, K. H. (Eds) *Compaction of Coarse-Grained Sediments, I.* Elsevier, Amsterdam, 247-292.

BURLAND, J. B. 1990. On the Compressibility and Shear Strength of Natural Clays. *Géotechnique,* **40**, 329-378.

BURLEY, S. D., MULLIS, J. & MATTER, A. 1989. Timing Diagenesis in the Tartan Reservoir (UK North Sea): Constraints from Combined Cathodoluminescence and Fluid Inclusion Studies. *Marine and Petroleum Geology,* **6**, 98-120.

BURST, J. F. 1969. Diagenesis of Gulf Coast Clayey Sediments and its Possible Relationship to Petroleum Migration. *Bulletin of the American Association of Petroleum Geologists,* **53**, 73-93.

BURYAKOVSKIY, L. A., DJEVANSHIR, R. D. & CHILINGARIAN, G. V. 1991. Mathematical Simulation of Sediment Compaction. *Journal of Petroleum Science and Engineering,* **5**, 151-161.

CAMPBELL, A. E. & STAFLEU, J. 1992. Seismic Modeling of an Early Jurassic, Drowned Carbonate Platform: Djebel Bou Dahar, High Atlas, Morocco. *Bulletin of the American Association of Petroleum Geologists,* **76**, 1760-1777.

CARMAN, G. J. & YOUNG, R. 1981. Reservoir Geology of the Forties Oil Field. In: ILLING, L. V. & HOBSON, G. D. (Eds) *Petroleum Geology of the Continental Shelf of North-West Europe.* Institute of Petroleum, Heyden, London, 371-379.

CHAN, M. A. & DOTT, R. H. 1983. Shelf and Deep-Sea Sedimentation in Eocene Forearc Basin, Western Oregon - Fan or Non-Fan? *Bulletin of the American Association of Petroleum Geologists,* **67**, 2100-2116.

CHEN, H. L. & LUO, X. R. 1988. The Quantitative Calculation of Abnormal Fluid Pressure in Argillaceous and Arenaceous Rocks and its Geological Application. *Geology Review,* **34**, 54-63. (in Chinese).

CLARKSON, E. N. K. (Ed) 1986. *Invertebrate Palaeontology and Evolution. Second Edition.* Allen & Unwin, London, 382pp

COLLIER, R. E. Ll. 1989. Modelling the Role of Differential Compaction and Tectonics upon Westphalian Facies Architecture in the Northumberland Basin. In: ARTHURTON, R. S., GUTTERIDGE, P. & NOLAN, S. C. (Eds) *The Role of Tectonics in Devonian and Carboniferous Sedimentation in the British Isles.* Publication of the Yorkshire Geological Society, 189-199.

COSKUN, S. B., WARDLAW, N. C. & HAVERSLEW, B. 1993. Effects of Composition, Texture and Diagenesis on Porosity, Permeability and Oil Recovery in a Sandstone Reservoir. *Journal of Petroleum Science and Engineering,* **8**, 279-292.

CRAWFORD, R., LITTLEFAIR, R. W. & AFFLECK, L. G. 1991. The Arbroath and Montrose Fields, Blocks 22/17, 18, UK North Sea. In: ABBOTS I. L. (Ed) *United Kingdom Oil and Gas Fields, 25 Years Commemorative Volume.* Geological Society Memoir No. **14**, 211-217.

CROWELL, J. C. 1954. Geologic Map of the Ridge Basin Area, California. *California Division of Mines Bulletin,* **170**, Map Sheet 7.

CROWELL, J. C. 1982a. The Tectonics of Ridge Basin, Southern California. In: CROWELL, J. C. & LINK, M. H. (Eds) *Geologic History of Ridge Basin, Southern California,* Pacific Section, Society of Economic Paleontologists and Mineralogists, 25-42.

CROWELL, J. C. 1982b. The Violin Breccia, Ridge Basin, Southern California. In: CROWELL, J. C. & LINK, M. H. (Eds) *Geologic History of Ridge Basin, Southern California,* Pacific Section, Society of Economic Paleontologists and Mineralogists, 89-98.

CROWELL, J. C. & LINK, M. H. (Eds) 1982. *Geologic History of Ridge Basin, Southern California,* Pacific Section, Society of Economic Paleontologists and Mineralogists, 304pp.

DAMUTH, J. E., KOLLA, V., FLOOD, R. D., KOWSMANN, R. O., MONTEIRO, M. C., GORINI, M. A., PALMA, J. J. C. & BELDERSON, R. H. 1983a. Distributary Channel Meandering and Bifurcation Patterns on the Amazon Deep-Sea Fan as Revealed by Long-Range Side-Scan Sonar (GLORIA). *Geology,* **11**, 94-98.

DAMUTH, J. E., KOWSMANN, R. O., FLOOD, R. D., BELDERSON, R. H. & GORINI, M. A. 1983b. Age Relationships of Distributary Channels on Amazon Deep-Sea Fan: Implications for Fan Growth Pattern. *Geology,* **11**, 470-473.

DAMUTH, J. E., FLOOD, R. D., KOWSMANN, R. O., BELDERSON, R. H. & GORINI, M. A. 1988. Anatomy and Growth Pattern of Amazon Deep-Sea Fan as Revealed by Long-Range Side-Scan Sonar (GLORIA) and High-Resolution Seismic Studies. *Bulletin of the American Association of Petroleum Geologists,* **72**, 855-911.

DANA, S. W. 1967. Investigation of Lateral and Vertical Variation of Density within Sedimentary Rock. *Compass,* **44**, 172-178.

DEEGAN, C. E. & SCULL, B. J. 1977. A Proposed standard Lithostratigraphical Nomenclature for the Central and Northern North Sea. *Report 77/25, Institute of Geological Sciences.*

DEKYSER, T. 1978. The Early Mississippian of the Sacramento Mountains, New Mexico - an Ecofacies Model for Carbonate Shelf Margin Deposition. *Unpublished Ph.D. Thesis, Oregon State University, Corvallis.* 304pp.

DEMKO, T. M. & GASTALDO, R. A. 1992. Paludal Environments of the Mary Lee Coal Zone, Pottsville Formation, Alabama: Stacked Clastic Swamps and Peat Mires. *International Journal of Coal Geology,* **20**, 23-47.

DESMAISON, Y. & BEAUDOIN, B. 1989. Role of Compaction in Basin Filling Analysis: Sedimentation Rate Evaluation During Mesozoic, SE France. *(Abstract)* IAS Meeting *"Compaction - Decompaction of Sediments",* Paris, 30-31st March 1989.

DICKINSON, G. 1953. Reservoir Pressures in Gulf Coast Louisiana. *Bulletin of the American Association of Petroleum Geologists,* **37**, 410-432.

DOBRYNIN, V. M. 1970. Deformation and Changes of Physical Properties of Oil and Gas Reservoir Rocks. *Nedra, Moscow.* 239p.

DOGLIONI, C. & GOLDHAMMER, R. K. 1988. Compaction-Induced Subsidence in the Margins of a Carbonate Platform. *Basin Research,* **1**, 237-246.

DROZ, L. & BELLAICHE, G. 1985. Rhône Deep-Sea Fan: Morphostructure and Growth Pattern. *Bulletin of the American Association of Petroleum Geologists,* **69**, 460-479.

DYKSTRA, J. 1987. Compaction Correction for Burial History Curves: Application to Lopatin's Method for Source Rock Maturation Determination. *Geobyte,* **2**, 16-23.

DZEVANSHIR, R. D., BURYAKOVSKIY, L. A. & CHILINGARIAN, G. V. 1986. Simple Quantitative Evaluation of Porosity of Argillaceous Sediments at Various Depths of Burial. *Sedimentary Geology,* **46**, 169-175.

EBHARDT, G. 1968. Experimental Compaction of Carbonate Sediments. In: MÜLLER, G. & FRIEDMAN, G. M. (Eds) *Recent Developments in Carbonate Sedimentology in Central Europe.* Springer-Verlag, New York, 255pp.

EHRENBERG, S. N. 1989. Sandstone Porosity as a Function of Thermal Maturity: Comment. *Geology,* **17**, 866-867.

EINSELE, G. 1977. Range, Velocity, and Material Flux of Compaction Flow in Growing Sedimentary Sequences. *Sedimentology,* **24**, 639-655.

ENOS, P. & SAWATSKY, L. H. 1981. Pore Networks in Holocene Carbonate Sediments. *Journal of Sedimentary Petrology,* **51**, 961-985.

EPTING, M. 1989. The Miocene Carbonate Buildups of Central Luconia, Offshore Sarawak. In: BALLY, A. W. (Ed) *Atlas of Seismic Stratigraphy.* Volume 3, American Association of Petroleum Geologists Studies in Geology, **27**, 168-173.

FALVEY, D. A. & MIDDLETON, M. F. 1981. Passive Continental Margins: Evidence for a Pre-Breakup Deep Crustal Metamorphic Subsidence Mechanism. In: BLANCHET, R. & MONTADERT, L. (Eds) *Geology of Continental Margins.* Oceanologica Acta, Proceedings of the 26th International Geological Congress C3, 103-114.

FATT, I. 1958. Compressibility of Sandstones at Low to Moderate Pressures. *Bulletin of the American Association of Petroleum Geologists,* **42**, 1924-1957.

FERM, J. C. & STAUB, J. R. 1984. Depositional Controls of Mineable Coal Bodies. In: RAHMAIN, R. A. & FLORES, R. M. (Eds) *Sedimentology of Coal and Coal-Bearing Sequences.* Special Publication of the International Association of Sedimentologists, 275-289.

FERTL, W. H. 1976. *Abnormal Formation Pressures - Implications to Exploration, Drilling, and Production of Oil and Gas Resources.* Elsevier, Amsterdam, 382pp.

FIELD, M. E. & GARDNER, J. V. 1990. Plio-Pleistocene Growth of the Rio Ebro Margin, Northeast Spain: A Prograding Slope Model. *Bulletin of the Geological Society of America,* **102**, 721-733.

FIELDING, C. R. 1982. Sedimentology and Stratigraphy of the Durham Coal Measures, and Comparisons with other British Coalfields. *Unpublished Ph.D. Thesis, University of Durham.*

FIELDING, C. R. 1984. A Coal Depositional Model for the Durham Coal Measures of NE England. *Journal of the Geological Society of London,* **141**, 919-931.

FIELDING, C. R. 1986. Fluvial Channel and Overbank Deposits from the Westphalian of the Durham Coalfield, NE England. *Sedimentology,* **33**, 119-140.

FITCHEN, B. & STARCHER, M. A. 1992. Early Permian Sequence Boundaries and Carbonate Platform Development, Western Delaware Basin, West Texas. Abstract. *Carbonate Stratigraphic Sequences: Sequence Boundaries and Associated Facies Conference.* La Leu, Spain, August 30th-September 3rd, 40-41.

FOWLER, C. 1975. The Geology of the Montrose Field. In: WOODLAND, A. W. (Ed) *Petroleum and the Continental Shelf of North-West Europe, Vol 1 Geology.* Applied Science Publishers, Barking, 467-476.

FRASER, H. J. 1935. Experimental Study of the Porosity and Permeability of Clastic Sediments. *Journal of Geology,* **43**, 910-1010.

FRUTH, L. S. Jr., ORME, G. R. & DONATH, F. A. 1966. Experimental Compaction Effects in Carbonate Sediments. *Journal of Sedimentary Petrology,* **36**, 747-754.

GAITHER, A. 1953. A Study of Porosity and Grain Size Relationships in Experimental Sands. *Journal of Sedimentary Petrology,* **23**, 180-195.

GALLAGHER, K. 1989. An Examination of Some Uncertainties Associated with Estimates of Sedimentation Rates and Tectonic Subsidence. *Basin Research,* **2**, 97-114.

GALLOWAY, W. E., GARBER, J. L., XIJIN LIU, & SLOAN, B. J. 1993. Sequence Stratigraphic and Depositional Framework of the Cenozoic Fill, Central and Northern North Sea Basin. In: PARKER, J. R. (Ed) *Petroleum Geology of Northwest Europe: Proceedings of the 4th Conference.* The Geological Society, London, 33-43.

GARLAND, C. R. 1993. Miller Field: Reservoir Stratigraphy and its Impact on Development. In: PARKER, J. R. (Ed) *Petroleum Geology of Northwest Europe: Proceedings of the 4th Conference.* The Geological Society, London, 401-414.

GARRISON, L. E., KENYON, N. H. & BOUMA, A. H. 1982. Channel Systems and Lobe Construction in the Mississippi Fan. *Geo-Marine Letters,* **2**, 31-39.

GHIBAUDO, G. 1980. Deep-Sea Fan Deposits in the Macigno Formation (middle - upper Oligocene) of the Gordana Valley, Northern Apennines. *Journal of Sedimentary Geology,* **50**, 723-742.

GILES, M. R. 1987. Mass Transfer and Problems of Secondary Porosity Creation in Deeply Buried Hydrocarbon Reservoirs. *Marine and Petroleum Geology,* **4**, 188-204.

GLUYAS, J. & COLEMAN, M. 1992. Material Flux and Porosity Changes During Sediment Diagenesis. *Nature,* **356**, 52-54.

GRAHAM, S. A. & BACHMAN, S. B. 1983. Structural Controls on Submarine-Fan Geometry and Internal Architecture : Upper La Jolla Fan System, Offshore Southern California. *Bulletin of the American Association of Petroleum Geologists,* **67**, 83-96.

GRATON, L. C. & FRASER, H. J. 1935. Schematic Packing of Spheres with Particular Attention to Porosity and Permeability. *Journal of Geology,* **43**, 785-909.

GRETENER, P. E. & LABUTE, G. J. 1969. Compaction - A Discussion. *Bulletin of Canadian Petroleum Geology,* **17**, 296-303.

HALL, B. R. & LINK, M. H. 1990. Reservoir Description of a Miocene Turbidite Sandstone, Midway-Sunset Field, California. In: BARWIS, J. H., McPHERSON, J. G. & STUDLICK, J. R. J. (Eds) *Sandstone Petroleum Reservoirs.* Springer-Verlag, New York, 509-533.

HALLEY, R. B. & SCHMOKER, J. W. 1983. High-Porosity Cenozoic Carbonate Rocks of South Florida: Progressive Loss of Porosity with Depth. *Bulletin of the American Association of Petroleum Geologists,* **67**, 191-200.

HAM, H. H. 1966. New Charts Help Estimate Formation Pressures. *Oil and Gas Journal,* **64**, 58-63.

HAMILTON, E. L. 1976. Variations of Porosity and Density with Depth in Deep-Sea Sediments. *Journal of Sedimentary Petrology,* **46**, 280-300.

HARDENBOL, J., VAIL, P. R. & FERRER, J. 1981. Interpreting Paleoenvironments, subsidence History and Sea-level changes of Passive Margins from Seismic and Biostratigraphy. *Oceanologica Acta,* No. SP, 3-44.

HARDING, A. W., HUMPHREY, T. J., LATHAM. A., LUNSFORD, M. K. & STRIDER, M. H. 1991. Controls on Eocene Submarine Fan Deposition in the Witch Ground Graben. In: HARDMAN, R. F. P. & BROOKS, J. (Eds) *Tectonic Events Responsible for Britain's Oil and Gas Reserves.* Geological Society, London, Special Publication, **55**, 353-367.

HARPER, D. & OLYPHANT, G. A. 1991. Superposed Deposits of Thick Coal on the Eastern Edge of the Illinois Basin and their Association with Underlying Geologic Features. *International Journal of Coal Geology,* **17**, 273-296.

HARTOG JAGER, D. Den., GILES, M. R. & GRIFFITHS, G. R. 1993. Evolution of Paleogene Submarine Fans of the North Sea in Space and Time. In: PARKER, J. R. (Ed) *Petroleum Geology of Northwest Europe: Proceedings of the 4th Conference.* The Geological Society, London, 59-71.

HASZELDINE, 1989. Coal Reviewed: depositional controls, modern analogues and ancient climates. In: WHATELEY, M. K. G. & PICKERING, K. T. (Eds) *Deltas: Sites and Traps for Fossil Fuels.* Geological Society Special Publication, **41**, 289-308.

HEDBERG, H. D. 1926. The Effect of Gravitational Compaction on the Structure of Sedimentary Rocks. *Bulletin of the American Association of Petroleum Geologists,* **10**, 1035-1072.

HEDBERG, H. D. 1936. Gravitational Compaction of Clays and Shales. *American Journal of Science,* **31**, 241-287.

HELLER, P. L. & DICKINSON, W. R. 1985. Submarine Ramp Facies Model for Delta-Fed, Sand-Rich Turbidite Systems. *Bulletin of the American Association of Petroleum Geologists,* **69**, 960-976.

HERITIER, F. E., LOSSEL, P. & WATHNE, E. 1979. Frigg Field - Large Submarine-Fan in Lower Eocene Rocks of North Sea Viking Graben. *Bulletin of the American Association of Petroleum Geologists,* **63**, 1999-2020.

HERMANRUD, C. 1993. Basin Modelling Techniques - An Overview. In: DORÉ, A. G. et al. (Eds) *Basin Modelling: Advances and Applications.* Special Publication No. **3**, Norwegian Petroleum Society, Elsevier, Amsterdam, 1-34.

HESS, G. R. & NORMARK, W. R. 1976. Holocene Sedimentation History of the Major Fan Valleys of Monterey Fan. *Marine Geology,* **22**, 233-251.

HILBRECHT, H. 1989. Redeposition of Late Cretaceous Pelagic Sediments Controlled by Sea-Level Fluctuations. *Geology,* **17**, 1072-1075.

HILL, P. J. & WOOD, G. V. 1980. Geology of the Forties Field, U.K. Continental Shelf, North Sea. In: HALBOUTY, M. T. (Ed) Giant Oil and Gas Fields of the Decade 1968-1978. *Memoir of the American Association of Petroleum Geologists,* **30**, 81-93.

HINCH, H. H. (Ed) 1978. *The Nature of Shales and the Dynamics of Hydrocarbon Expulsion in the Gulf Coast Tertiary Section.* American Association of Petroleum Geologists, Course Note Series No. **8**, 1-31.

HISCOTT, R. N. 1980. Depositional Framework of Sandy Mid-Fan Complexes of Tourelle Formation, Ordovician, Quebec. *Bulletin of the American Association of Petroleum Geologists,* **64**, 1052-1077.

HISCOTT, R. N. 1981. Deep-Sea Fan Deposits in the Macigno Formation (middle - upper Oligocene) of the Gordana Valley, Northern Apennines, Italy - Discussion. *Journal of Sedimentary Geology,* **51**, 1015-1021.

HOTTMAN, C. E. & JOHNSON, R. K. 1965. Estimation of Formation Pressures from Log-Derived Shale Properties. *Journal of Petroleum Technology,* **16**, 717-722.

HOUSEKNECHT, D. W. 1987. Assessing the Relative Importance of Compaction Processes and Cementation to Reduction of Porosity in Sandstones. *Bulletin of the American Association of Petroleum Geologists,* **71**, 633-642.

HOUSEKNECHT, D. W. 1989. Assessing the Relative Importance of Compaction Processes and Cementation to Reduction of Porosity in Sandstones: Reply. *Bulletin of the American Association of Petroleum Geologists,* **73**, 1277-1279.

HOWELL, D. G. & NORMARK, W. R. 1982. Sedimentology of Submarine Fans. *Memoir of the American Association of Petroleum Geologists,* **31**, 365-404.

HSÜ, K. J. 1977. Studies of Ventura Field, California, II: Lithology, Compaction and Permeability of Sands. *Bulletin of the American Association of Petroleum Geologists,* **61**, 169-191.

HUNT, D. & ALLSOP, T. 1993. Mississippian Strata of the Sacramento Mountains, New Mexico: Sketches of Stratal Patterns, Palaeogeography, and Some Preliminary Interpretations. *Unpublished Fieldguide, May 19-21st, Alamogordo, New Mexico,* 35pp.

HUNT, D. & ALLSOP, T. 1994. (In Prep.) Differential Compaction, Differential Cementation and the Development of Corrugated 'Tube' Structures on the Deep-Sea Floor: Examples from the Mississippian of Southern New Mexico.

HUNT, D., ALLSOP, T. & SWARBRICK, R. E. 1994. (In Press) Differential Compaction and Sequence Stratigraphy over the Margins of Carbonate Platforms and Buildups. *Submitted to Geology.*

ILLING, L. V. & HOBSON, G. D. (Eds) 1981. *Petroleum Geology of the Continental Shelf of North-West Europe.* Institute of Petroleum, Heyden, London, 521pp.

IMPERATO, D. P. & NILSEN, T. H. 1990. Deep-Sea-Fan Channel-Levee Complexes, Arbuckle Field, Sacramento Basin, California. In: BARWIS, J. H., McPHERSON, J. G. & STUDLICK, J. R. J. (Eds) *Sandstone Petroleum Reservoirs.* Springer-Verlag, New York, 535-555.

JACKSON, W. D. & DeKYSER, T. 1984a. Microfacies analysis of Muleshoe Mound (early Mississippian), Sacramento Mountains, New Mexico: a Point-Source depositional model, Part I. *West Texas Geological Society,* **23**, No. 5, 6-10.

JACKSON, W. D. & DeKYSER, T. 1984b. Microfacies analysis of Muleshoe Mound (early Mississippian), Sacramento Mountains, New Mexico: a Point-Source depositional model, Part II. *West Texas Geological Society,* **23**, No. 5, 6-10.

JENSSEN, A. I., BERGSLIEN, D., RYE-LARSEN, M. & LINDHOLM, R. M. 1993. Origin of Complex Mound Geometry of Paleocene Submarine-Fan Sandstone Reservoirs, Balder Field, Norway. In: PARKER, J. R. (Ed) *Petroleum Geology of Northwest Europe: Proceedings of the 4th Conference.* The Geological Society, London, 135-143.

JOHNSON, H. 1987. Seismic Expression of Major Chalk Reworking Events in the Palaeocene of the Central North Sea. In: BROOKS, J. & GLENNIE, K. W. (Eds) *Petroleum Geology of North West Europe.* Graham & Trotman, London, 591-598.

JONES, M. E. & ADDIS, M. A. 1985. Burial of Argillaceous Sediments. *Marine and Petroleum Geology,* **2**, 247-253.

KASTENS, K. A. & SHOR, A. N. 1985. Depositional Processes of a Meandering Channel on Mississippi Fan. *Bulletin of the American Association of Petroleum Geologists,* **69**, 190-202.

KENTER, J. A. M. 1990. Carbonate Platform Flanks: Slope Angle and Sediment Fabric. *Sedimentology*, **37**, 777-794.

KESSLER, L. G., ZANG, R. D., ENGLEHORN, J. A. & EGER, J. D. 1980. Stratigraphy and Sedimentology of a Paleocene Submarine Fan Complex, Cod Field, Norwegian North Sea. In: *The Sedimentation of North Sea Reservoir Rocks.* Proceedings, Geilo Conference, Norwegian Petroleum Society (NPF).

KIRKBY, K. C., HUNT, D. & VAN DEN BERGH, T. C. V. 1993. Ontogeny of a "Waulsortian Buildup": Muleshoe Mound, Lower Carboniferous, Sacramento Mountains, New Mexico. (Abstract) *Geological Society of America 1993 Annual Meeting, Boston, Massachusetts, October 25-28th*, 63.

KIRKBY, K. C., HUNT, D. & VAN DEN BERGH, T. C. V. (in prep.).

KNOX, R. W. O'B., MORTON, A. C. & HARLAND, R. 1981. Stratigraphical Relationships of Palaeocene Sands in the UK Sector of the Central North Sea. In: ILLING, L. V. & HOBSON, G. D. (Eds) *Petroleum Geology of the Continental Shelf of North-West Europe.* Institute of Petroleum, Heyden, London, 267-281.

KOLLA, V. & COUMES, F. 1987. Morphology, Internal Structure, Seismic Stratigraphy, and Sedimentation of Indus Fan. *Bulletin of the American Association of Petroleum Geologists,* **71**, 650-677.

KOMORNIK, A., ROHRLICH, V. & WISEMAN, G. 1970. Overconsolidation by Desiccation of Coastal Late-Quaternary Clays in Israel. *Sedimentology*, **14**, 125-140.

KORVIN, G. 1984. Shale Compaction and Statistical Physics. *Geophysical Journal of the Royal Astronomical Society,* **78**, 35-50.

KULPECZ, A. A. & VAN GEUNS, L. C. 1990. Geological Modelling of a Turbidite Reservoir, Forties Field, North Sea. In: BARWIS, J. H., McPHERSON, J. G. & STUDLICK, J. R. J. (Eds) *Sandstone Petroleum Reservoirs.* Springer-Verlag, New York, 489-507.

LABUTE, G. J. & GRETENER, P. E. 1969. Differential Compaction Around a Leduc Reef - Wizard Lake Area, Alberta. *Bulletin of Canadian Petroleum Geology,* **17**, 304-325.

LAMBE, T. W. & WHITMAN, R. V. (Eds) 1979. *Soil Mechanics: SI Version.* John Wiley & Sons, New York. 553pp.

LANE, H. R. 1974. The Mississippian of Southeastern New Mexico and West Texas - a Wedge-on-Wedge Relation. *Bulletin of the American Association of Petroleum Geologists,* **58**, 269-282.

LANE, H. R. 1982. The Distribution of Waulsortian Facies In North America as Exemplified in the Sacramento Mountains of New Mexico. In: BOLTON, K., LANE, H. R. & LeMONE, D. V. (Eds) *Symposium on the Paleoenvironmental Setting and Distribution of the Waulsortian Facies.* El Paso Geological Survey and the University of Texas, El Paso, 96-114.

LAUDON, L. R. & BOWSHER, A. L. 1941. Mississippian Formations of the Sacramento Mts., New Mexico. *Bulletin of the American Association of Petroleum Geologists,* **25**, 2107-2160.

LAUDON, L. R. & BOWSHER, A. L. 1949. Mississippian Formations of Southwestern New Mexico. *Bulletin of the American Association of Petroleum Geologists,* **60**, 1-88.

LAVOIE, D. 1988. Geotechnical Properties of Sediments in a Carbonate-Slope Environment: Ocean Drilling Program Site 630, Northern Little Bahama Bank. In: AUSTIN, J. A., Jr., SCHLAGER, W., ET AL. (Eds) *Proceedings of the Ocean Drilling Program, Scientific Results,* **101**, 315-326.

LEDER, F. & PARK, W. C. 1986. Porosity Reduction in Sandstone by Quartz Overgrowth. *Bulletin of the American Association of Petroleum Geologists,* **70**, 1713-1728.

LEEDER, M. R. 1978. A Quantitative Stratigraphic Model for Alluvium, with Special Reference to Channel Deposit Density and Interconnectedness. In: MIALL, A. D. (Ed) *Fluvial Sedimentology.* Memoir of the Canadian Society of Petroleum Geologists, **5**, 587-596.

LEES, A., HALLET, V. & HIBO, D. 1985. Facies Variations in Waulsortian Buildups, Part 1: a Model From Belgium. *Journal of Geology,* **20**, 133-158.

LEES, A. & MILLER, J. 1985. Facies Variations in Waulsortian Buildups, Part 2: Mid-Dinantian Buildups from Europe and North America. *Journal of Geology,* **20**, 159-180.

LINK, M. H. 1982a. Stratigraphic Nomenclature and Age of Miocene Strata, Ridge Basin, Southern California. In: CROWELL, J. C. & LINK, M. H. (Eds) *Geologic History of Ridge Basin, Southern California.* Pacific Section, Society of Economic Paleontologists and Mineralogists, 5-12.

LINK, M. H. 1982b. Slope and Turbidite Facies of the Miocene Castaic Formation and the Lower Part of the Marple Canyon Sandstone Member, Ridge Route Formation, Ridge Basin, Southern California. In: CROWELL, J. C. & LINK, M. H. (Eds) *Geologic History of Ridge Basin, Southern California.* Pacific Section, Society of Economic Paleontologists and Mineralogists, 79-87.

LINK, M. H. 1983. Miocene Castaic Formation Slope and Deep-Sea Fan Facies, Ridge Basin, Southern California. In: LARUE, D. K. & STEEL, R. J. (Eds) *Cenozoic Marine Sedimentation, Pacific Margin, U.S.A.* Pacific Section, Society of Economic Paleontologists and Mineralogists, 169-185.

LINK, M. H. & SMITH, P. R. 1982. Organic Geochemistry of Ridge Basin, Southern California. In: CROWELL, J. C. & LINK, M. H. (Eds) *Geologic History of Ridge Basin, Southern California.* Pacific Section, Society of Economic Paleontologists and Mineralogists, 191-197.

LOHMAR, J. M., MAY, J. A., BOYER, J. E. & WARME, J. E. 1979. Shelf Edge Deposits of the San Diego Embayment. In: ABBOTT, P. L. (Ed) *Eocene Depositional Systems San Diego, California.* Pacific Section, Society of Economic Paleontologists and Mineralogists, 15-34.

LOPATIN, N. V. 1971. Temperature and Geologic Time as Factors in Coalification (in Russian). *Akad. Nauk SSSR Izv. Ser. Geol.* ***3,*** 95-106.

LOWREY, C. J. 1985. Amoco 22/17-T3: A Petrographic Study of Seven Sidewall Core Samples. *Report No. 5549P/C, Robertson Research International Limited,* 9pp.

LUDWICK, J. C. 1956. A Volumeter for Measuring Porosity of Incoherent Sands. *Journal of Sedimentary Petrology,* **26**, 276-283.

LUO, X., BRIGAUD, F. & VASSEUR, G. 1993. Compaction Coefficients of Argillaceous Sediments: Their Implications, Significance and Determination. In: DORÉ, A. G. et al. (Eds) *Basin Modelling: Advances and Applications.* Special Publication No. **3**, Norwegian Petroleum Society, Elsevier, Amsterdam, 321-332.

MAGARA, K. 1968. Compaction and Fluid Migration of Fluids in Miocene Mudstone, Nagoka Plain, Japan. *Bulletin of the American Association of Petroleum Geologists,* **52**, 2466-2501.

MAGARA, K. 1976. Water Expulsion from Clastic Sediments During Compaction - Directions and Volumes. *Bulletin of the American Association of Petroleum Geologists,* **60**, 543-553.

MAGARA, K. (Ed) 1978. *Compaction and Fluid Migration - Practical Petroleum Geology.* Elsevier, Amsterdam, 319pp.

MAILLART, J. 1991. Differenciation Entre Tectonique Synsedimentaire et Compaction Differentielle. *Memoires Des Sciences de la Terre, No. **12**, Ecole des Mines de Paris.* 196pp.

MANUS, R. W. & COOGAN, A. H. 1974. Bulk Volume Reduction and Pressure-Solution Derived Cement. *Journal of Sedimentary Petrology,* **44**, 466-471.

MATRINI, I. P. & SAGRI, M. 1977. Sedimentary Fillings of Ancient Deep-Sea Channels: Two Examples from Northern Apennines (Italy). *Journal of Sedimentary Petrology,* **47**, 1542-1553.

MAXWELL, J. C. 1964. Influence of Depth, Temperature and Geologic Age on Porosity of a Quartzose Sandstone. *Bulletin of the American Association of Petroleum Geologists,* **48**, 697-709.

MAY, J. A. & WARME, J. E. 1987. Synchronous Depositional Phases in West Coast Basins: Eustacy or Regional Tectonics? In: INGERSOLL, R. V. & ERNST, W. G. (Eds) *Cenozoic Basin Development of Coastal California.* Rubey Volume VI, Prentice-Hall, New Jersey. 25-46.

McBRIDE, E. F., DIGGS, T. N. & WILSON, J. C. 1991. Compaction of Wilcox and Carrizo Sandstones (Paleocene - Eocene) to 4420m, Texas Gulf Coast. *Journal of Sedimentary Petrology,* **61**, 73-85.

McCLURE, N. M. & BROWN, A. A. 1992. Miller Field: A Subtle Upper Jurassic Submarine Fan Trap in the South Viking Graben, United Kingdom Sector, North Sea. In: HALBOUTY, M. T. (Ed) Giant Oil and Gas Fields of the Decade 1978-1988. *Memoir of the American Association of Petroleum Geologists,* **54**, 307-322.

McCOY, A. W. 1934. An Interpretation of Local Structural Development in Midcontinent Areas Associated with Deposits of Petroleum. In: WRATHER, E. L. & LAHEE, F. H. (Eds) *Problems of Petroleum Geology.* Publication of the American Association of Petroleum Geologists, Tulsa, Oklahoma, 581-627.

McCULLOCH, T. H. 1965. A Confirmation by Gravity Measurements of an Underground Density Profile Based on Core Densities. *Geophysics,* **30**, 1108-1132.

McLEAN, H. & HOWELL, D. G. 1984. Miocene Blanca Fan, Northern Channel Islands, California: Small Fans Reflecting Tectonism and Volcanism. *Geo-Marine Letters,* **3**, 161-166.

MEADE, R. H. 1966. Factors Influencing the Early Stages of Compaction of Clays and Sands - Review. *Journal of Sedimentary Petrology,* **36**, 1085-1101.

MEHL, M. J. 1919. The Influence of the Differential Compression of Sediments on the Attitude of Bedded Rocks. Paper presented at meeting of *The American Association of Advanced Science, St. Louis, Dec. 1919.* Abstract. Published in *Science, New Series,* **51** (May, 1920), 520.

MEYERS, W. J. 1973. Chertification and Carbonate Cementation in the Mississippian Lake Valley Fm, Sacramento Mts., New Mexico. *Unpublished Ph.D. Thesis, Rice University, Houston, TX,* 353pp.

MEYERS, W. J. 1975. Stratigraphy and Diagenesis of the Lake Valley Formation, Sacramento Mountains. In: PRAY, L. C. (Ed) *A Guidebook to the Mississippian Shelf-Edge and Basin Facies Carbonates, Sacramento Mountains and Southern New Mexico.* Dallas Geological Society, Dallas, TX, 45-66.

MEYERS, W. J. 1980. Compaction in Mississippian Skeletal Limestones, Southwestern New Mexico. *Journal of Sedimentary Petrology,* **50**, 457-474.

MEYERS, W. J. 1989. Paleokarstic Features in Mississippian Limestones, New Mexico. In: JAMES, N. P. & CHOQUETTE, P. W. (Eds) *Paleokarsts.* Springer-Verlag, New York, 306-328.

MEYERS, W. J., COWAN, P. & LOHMANN, K. C. 1982. Diagenesis of Mississippian Skeletal Limestones and Bioherm Muds, New Mexico. In: BOLTON, K., LANE, H. R. & LeMONE, D. V. (Eds) *Symposium on the Paleoenvironmental Setting and Distribution of Waulsortian Facies.* El Paso Geological Society and the University of Texas, El Paso, TX, 80-95.

MEYERS, W. J. & HILL, B. E. 1983. Quantitative Studies of Compaction in Mississippian Skeletal Limestones, New Mexico. *Journal of Sedimentary Petrology,* **53**, 231-242.

MILLER, J. 1986. Facies Relationships and Diagenesis in Waulsortian Mudmounds from the Lower Carboniferous of Ireland and N. England. In: SCHROEDER, J. H. & PURSER, B. H. (Eds) *Reef Diagenesis.* Springer-Verlag, Berlin, 309-335.

MILTON, N. J., BERTRAM, G. T. & VANN, I. R. 1991. Early Palaeogene Tectonics and Sedimentation in the Central North Sea. In: HARDMAN, R. F. P. & BROOKS, J. (Eds) *Tectonic Events Responsible for Britain's Oil and Gas Reserves.* Geological Society, London, Special Publication, **55**, 339-351.

MITCHUM, R. M., VAIL, P. R. & SANGREE, J. B. 1977. Seismic Stratigraphy and Global Changes of Sea-Level, Part 6: Stratigraphic Interpretation of Seismic Patterns in Depositional Sequences. In: PAYTON, P. M. (Ed) *Seismic Stratigraphy - Applications to Hydrocarbon Exploration.* Memoir of the American Association of Petroleum Geologists, **26**, 117-134.

MONNETT, V. E. 1922. Possible Origin of Some of the Structures of the Midcontinent Oil Field. *Economic Geology,* **17**, 194-200.

MORGAN, N. A. 1969. Physical Properties of Marine Sediments as Related to Seismic Velocities. *Geophysics,* **34**, 529-545.

MORGAN, S. R. & CAMPION, K. M. 1987. Eustatic Controls on Stratification and Facies Associations in Deep-Water Deposits, Great Valley Sequence, Sacramento Valley, California. Abstract. *Bulletin of the American Association of Petroleum Geologists,* **71**, 595.

MORROW, N. R., HUPPLER, J. D. & SIMMONS, A. B. 1969. Porosity and Permeability of Unconsolidated Upper Miocene Sands from Grain Size Analysis. *Journal of Sedimentary Petrology,* **39**, 312-321.

MORTON, A. C. 1982. Lower Tertiary Sand Development in Viking Graben, North Sea. *Bulletin of the American Association of Petroleum Geologists,* **66**, 1542-1559.

MORTON, A. C., HALLSWORTH, C. R. & WILKINSON, G. C. 1993. Stratigraphic Evolution of Sand Provenance During Paleocene Deposition in the Northern North Sea Area. In: PARKER, J. R. (Ed) *Petroleum Geology of Northwest Europe: Proceedings of the 4th Conference.* The Geological Society, London, 73-84.

MUDGE, D. C. & COPESTAKE, P. 1992. Revised Lower Palaeogene Lithostratigraphy for the Outer Moray Firth, North Sea. *Marine and Petroleum Geology,* **9**, 53-69.

MUTTI, E. 1974. Examples of Ancient Deep-Sea Fan Deposits from Circum-Mediterranean Geosynclines. In: DOTT, R. H. & SHAVER, R. H. (Eds) *Modern and Ancient Geosynclinal Sedimentation.* Special Publication of the Society of Economic Paleontologists and Mineralogists, **19**, 92-105.

MUTTI, E. 1984. The Hecho Eocene Submarine-Fan System, South-Central Pyrenees, Spain. *Geo-Marine Letters,* **3**, 199-202.

MUTTI, E. 1985. Turbidite Systems and their Relations to Depositional Sequences. In: ZUFFA, G. G. (Ed) *Provenance of Arenites.* D. Reidel Publishing Company, Dordrecht, 65-93.

MUTTI, E. & GHIBAUDO, G. 1972. Un esempio di torbiditi di conoide sottomarina esterna - Le Arenarie di San Salvatore (Formazione di Bobbio, Miocene) nell' Appennino di Piacenza. *Memorie dell'Accademia della Scienze di Torino,* Classe di Scienze Fisiche, Matematiche e Naturali, Serie 4, no. **16**, 40pp.

MUTTI, E. & RICCI LUCCHI, F. 1972. Turbidites of the Northern Apennines: Introduction to Facies Analysis (English Translation by NILSEN, T. H. 1978). *International Geology Review,* **20**, 125-166.

MUTTI, E. & RICCI LUCCHI, F. 1975. Turbidite Facies and Facies Associations. In: *Examples of Turbidite Facies and Facies Associations from Selected Formations of the Northern Apennines, Field Trip Guidebook A-11.* IX International Congress of Sedimentologists, Nice, France. International Association of Sedimentologists, 21-36.

MUTTI, E. & NORMARK, W. R. 1987. Comparing Examples of Modern and Ancient Turbidite Systems: Problems and Concepts. In: LEGGETT, J. K. & ZUFFA, G. G. (Eds) *Marine Clastic Sedimentology.* Graham & Trotman, London, 1-38.

MUTTI, E. & SONNINO. 1981. Compensation Cycles: a Diagnostic Feature of Turbidite Sandstone Lobes. In: *Abstracts Volume.* 2nd European Regional Meeting, Bologna, Italy. International Association of Sedimentologists. 120-123.

MUTTI, E., NILSEN, T. H. & RICCI LUCCHI, F. 1978. Outer Fan Depositional Lobes of the Laga Formation (Upper Miocene and Lower Pliocene), East-Central Italy. In: STANLEY, D. J. & KELLING, G. (Eds) *Sedimentation in Submarine Canyons, Fans, and Trenches.* Stroudsberg, PA: Dowden, Hutchinson & Ross, 210-223.

NAESER, N. D. & McCULLOH, T. H. (Eds) 1989. *Thermal History of Sedimentary Basins. Methods and Case Histories.* Springer-Verlag, New York.

NAFE, J. E. & DRAKE, C. L. 1957. Variation with Depth in Shallow and Deep Water Marine Sediments of Porosity, Density and the Velocities of Compressional and Shear Waves. *Geophysics,* **22**, 523-552.

NAGTEGAAL, P. J. C. 1978. Sandstone - Framework Instability as a Function of Burial Diagenesis. *Journal of the Geological Society of London,* **135**, 101-105.

NELSON, C. H., MUTTI, E. & RICCI LUCCHI, F. 1977. Upper Cretaceous Resedimented Conglomerates at Wheeler Gorge, California: Description and Field Guide - Discussion. *Journal of Sedimentary Petrology,* **47**, 926-928.

NELSON, C. H. & NILSEN, T. 1974. Depositional Trends of Modern and Ancient Deep-Sea Fans. In: DOTT, R. H. & SHAVER, R. H. (Eds) *Modern and Ancient Geosynclinal Sedimentation.* Special Publication of the Society of Economic Paleontologists and Mineralogists, **19**, 69-91.

NEWMAN, M. St. J., REEDER, M. L., WOODRUFF, A. H. W. & HATTON, I. R. 1993. The Geology of the Gryphon Oil Field. In: PARKER, J. R. (Ed) *Petroleum Geology of Northwest Europe: Proceedings of the 4th Conference.* The Geological Society, London, 123-133.

NEWTON, S. K. & FLANAGAN, K. P. 1993. The Alba Field: Evolution of the Depositional Model. In: PARKER, J. R. (Ed) *Petroleum Geology of Northwest Europe: Proceedings of the 4th Conference.* The Geological Society, London, 161-171.

NILSEN, T. H. 1980. Modern and Ancient Submarine Fans: Discussion of Papers by R. G. Walker and W. R. Normark. *Bulletin of the American Association of Petroleum Geologists,* **64**, 1094-1101.

NORMARK, W. R. 1970. Growth Patterns of Deep-Sea Fans. *Bulletin of the American Association of Petroleum Geologists,* **54**, 2170-2195.

NORMARK, W. R. 1978. Fan Valleys, Channels, and Depositional Lobes on Modern Submarine Fans: Characters for Recognition of Sandy Turbidite Environments. *Bulletin of the American Association of Petroleum Geologists,* **62**, 912-931.

NORMARK, W. R. 1980. Modern and Ancient Submarine Fans: Reply. *Bulletin of the American Association of Petroleum Geologists,* **64**, 1108-1112.

NORMARK, W. R., PIPER, D. J. W. & HESS, G. R. 1979. Distributary Channels, Sand Lobes, and Mesotopography of Navy Submarine Fan, California Borderland, with Applications to Ancient Fan Sediments. *Sedimentology,* **26**, 749-774.

O'CONNOR, S. J. & WALKER, D. 1993. Paleocene Reservoirs of the Everest Trend. In: PARKER, J. R. (Ed) *Petroleum Geology of Northwest Europe: Proceedings of the 4th Conference.* The Geological Society, London, 145-160.

PARASNIS, D. S. 1960. The Compaction of Sediments and its Bearing on some Geophysical Problems. *Geophysical Journal of the Royal Astronomical Society,* **3**, 1-28.

PARKER, J. R. 1975. Lower Tertiary Sand Development in the Central North Sea. In: WOODLAND, A. W. (Ed) *Petroleum and the Continental Shelf of North-West Europe, Vol 1 Geology.* Applied Science Publishers, Barking, 447-453.

PARKER GAY, S. Jr. 1989. Gravitational Compaction, a Neglected Mechanism in Structural and Stratigraphic Studies: New Evidence from Mid-Continent, USA. *Bulletin of the American Association of Petroleum Geologists,* **73**, 641-657.

PATE, C. R. 1989. Assessing the Relative Importance of Compaction Processes and Cementation to Reduction of Porosity in Sandstones: Discussion. *Bulletin of the American Association of Petroleum Geologists,* **73**, 1270-1273.

PEMBERTON, S. G., FREY, R. W., RANGER, M. J. & MACEAHERN, J. 1992. The Conceptual Framework of Ichnology. In: HARRIS, P. M. (Ed) *Applications of Ichnology to Petroleum Exploration. A Core Workshop.* Society of Economic Paleontologists and Mineralogists Core Workshop, **17**, 1-32.

PERRIER, R. & QUIBLIER, J. 1974. Thickness Changes in Sedimentary Layers During Compaction History; Methods for Quantitative Evaluation. *Bulletin of the American Association of Petroleum Geologists,* **58**, 507-520.

PETTIJOHN, F. J., POTTER, P. E. & SIEVER, R. 1972. *Sand And Sandstone.* Springer-Verlag, New York, 618pp.

PICKERING, K. T. 1982. The Shape of Deep-Water Siliciclastic Systems: A Discussion. *Geo-Marine Letters,* **2**, 41-46.

PICKERING, K. T., HISCOTT, R. N. & HEIN, F. J. (Eds) 1989. *Deep-Marine Environments: Clastic Sedimentation and Tectonics.* Unwin Hyman Ltd., London, 416pp.

PIPER, D. J. W. 1970. Transport and Deposition of Holocene Sediment on La Jolla Deep Sea Fan, California. *Marine Geology,* **8**, 211-227.

PIPER, D. J. W. & NORMARK, W. R. 1983. Turbidite-Depositional Patterns and Flow Characteristics, Navy Submarine Fan, California Borderland. *Sedimentology,* **30**, 681-694.

PITTMAN, E. D. & LARESE, R. E. 1991. Compaction of Lithic Sands: Experimental Results and Applications. *Bulletin of the American Association of Petroleum Geologists,* **75**, 1279-1299.

POWERS, M. C. 1967. Fluid Release Mechanisms in Compacting Marine Mudrocks and their Importance in Oil Exploration. *Bulletin of the American Association of Petroleum Geologists,* **17**, 233-259.

PRAY, L. C. 1958. Fenestrate Bryozoan Core Facies, Mississippian Bioherms, Southwestern United States. *Journal of Sedimentary Petrology,* **28**, 261-273.

PRAY, L. C. 1961. *Geology of the Sacramento Mountains Escarpment, Otero County, New Mexico.* Bulletin of the New Mexico Bureau of Mines & Resources, **35**, 144pp.

PRAY, L. C. 1965. Clastic Limestone Dikes and Marine Cementation, Mississippian Bioherms, New Mexico. Abstract. *Permian Basin Section, Society of Economic Paleontologists and Mineralogists Program and Abstracts, Annual Meeting,* 21-22nd.

PRAY, L. C. 1969. Micrite and Carbonate Cement: Genetic Factors in Mississippian Bioherms. *Journal of Paleontology,* **43**, 895.

PRYOR, W. A. 1973. Permeability-Porosity Patterns and Variations in some Holocene Sand Bodies. *Bulletin of the American Association of Petroleum Geologists,* **57**, 162-189.

RAY, M. B. 1985. Empirical Relation Between Carbonate Porosity and Thermal Maturity: An Approach to Regional Porosity Prediction: Discussion. *Bulletin of the American Association of Petroleum Geologists,* **69**, 2021-2022.

READING, H. G. (Ed.) 1986. *Sedimentary Environments and Facies.* Second Edition. Blackwell Scientific Publications, Oxford, 615pp.

READING, H. G. 1992. Grain Size and Feeder Systems: A Framework for the Classification of Deep Water Depositional Systems. Abstract. *Deep Water Clastics: Dynamics of Modern and Ancient Systems.* B.S.R.G. Workshop, 20-21st March, Oxford.

RICCI LUCCHI, F. 1975. Depositional Cycles in Two Turbidite Formations of Northern Apennines. *Journal of Sedimentary Petrology,* **45**, 1-43.

RICCI LUCCHI, F. 1984. The Deep-Sea Fan Deposits of the Miocene Marnoso-arenacea of the Northern Apennines. *Geo-Marine Letters,* **3**, 203-210.

RICCI LUCCHI, F. & VALMORI, E. 1980. Basin-Wide Turbidites in a Miocene, Over-Supplied Deep-Sea Plain: A Geometrical Analysis. *Sedimentology,* **27**, 241-270.

RIEKE, H. H. & CHILINGARIAN, G. V. (Eds) 1974. *Compaction of Argillaceous Sediments.* Developments in Sedimentology, 16. Elsevier, Amsterdam. 424pp.

RITTENHOUSE, G. 1971. Mechanical Compaction of Sands Containing Different Percentages of Ductile Grains: A Theoretical Approach. *Bulletin of the American Association of Petroleum Geologists,* **55**, 92-96.

ROBINSON, A. & GLUYAS, J. 1992a. Model Calculations of Loss of Porosity in Sandstones as a Result of Compaction and Quartz Cementation. *Marine and Petroleum Geology,* **9**, 319-323.

ROBINSON, A. & GLUYAS, J. 1992b. The Duration of Quartz Cementation in Sandstones, North Sea and Haltenbanken Basins. *Marine and Petroleum Geology,* **9**, 324-327.

ROCHOW, K. A. 1981. Seismic Stratigraphy of the North Sea 'Palaeocene' Deposits. In: ILLING, L. V. & HOBSON, G. D. (Eds) *Petroleum Geology of the Continental Shelf of North-West Europe.* Institute of Petroleum, Heyden, London, 225-266.

ROGERS, J. J. & HEAD, W. B. 1961. Relationships Between Porosity, Median Size and Sorting Coefficients of Synthetic Sands. *Journal of Sedimentary Petrology,* **31**, 467-470.

RUBEY, W. W. & HUBBERT, M. K. 1959. Role of Fluid Pressure in Mechanics of Overthrust Faulting. *Bulletin of the Geological Society of America,* **70**, 167-206.

SCHAEFER, P. J. 1976. Microfacies Analysis and Cementation History of a Mississippian Mud Mound. *M.S. Thesis, SUNY at Stonybrook, New York,* 154pp.

SCHERER, M. 1987. Parameters Influencing Porosity in Sandstones: a Model for Sandstone Porosity Prediction. *Bulletin of the American Association of Petroleum Geologists,* **71**, 485-491.

SCHERER, M. 1988. Parameters Influencing Porosity in Sandstones: a Model for Sandstone Porosity Prediction: Reply. *Bulletin of the American Association of Petroleum Geologists,* **72**, 854-855.

SCHLAGER, W. 1989. Drowning Unconformities on Carbonate Platforms. In: CREVELLO, P. D., WILSON, J. L., SARG, J. F. & READ, J. F. (Eds) *Controls on Carbonate Platform and Basin Development.* Society of Economic Palaeontologists and Mineralogists, Special Publication **44**, 15-25.

SCHLANGER, S. O. & DOUGLAS, R. G. 1974. The Pelagic Ooze - Chalk - Limestone Transition and its Implications for Marine Stratigraphy. In: HSÜ, K. J. & JENKYNS, H. C. (Eds) *Pelagic Sediments: On Land and Under the Sea.* Special Publication of the International Association of Sedimentologists, **1**. Blackwell Scientific Publications, Oxford, 117-148.

SCHLUMBERGER, 1972. *Log Interpretation. Volume i - Principles.* Schlumberger Limited, New York. 113pp.

SCHMOKER, J. W. & GAUTIER, D. L. 1988. Sandstone Porosity as a Function of Thermal Maturity. *Geology,* **16**, 1007-1010.

SCHMOKER, J. & GAUTIER, D. L. 1989a. Sandstone Porosity as a Function of Thermal Maturity: Reply. *Geology,* **17**, 867-868.

SCHMOKER, J. & GAUTIER, D. L. 1989b. Compaction of Basin Sediments: Modeling Based on Time-Temperature History. *Journal of Geophysical Research,* **94B**, 7379-7386.

SCHMOKER, J. W. 1985. Empirical Relation Between Carbonate Porosity and Thermal Maturity: An Approach to Regional Porosity Prediction: Reply. *Bulletin of the American Association of Petroleum Geologists,* **69**, 2023.

SCHMOKER, J. W. & HALLEY, R. B. 1982. Carbonate Porosity Versus Depth: A Predictable Relation for South Florida. *Bulletin of the American Association of Petroleum Geologists,* **66**, 2561-2570.

SCLATER, J. G. & CHRISTIE, P. A. F. 1980. Continental Stretching: An Explanation of the Post-Mid Cretaceous Subsidence of the Central North Sea Basin. *Journal of Geophysical Research,* **85**, 3711-3739.

SCOTT, G. D. 1960. Packing of Equal Spheres. *Nature,* **188**, 908-909.

SELLEY, R. C. 1978. Porosity Gradients in North Sea Oil-Bearing Sandstones. *Journal of the Geological Society of London,* **135**, 119-132.

SERRA, O. (Ed) 1984. *Developments in Petroleum Science, 15A: Fundamentals of Well-Log Interpretation: 1. The Acquisition of Logging Data.* Elsevier, Amsterdam, 423pp.

SHANMUGAM, G. & ALHILALI, K. A. 1988. Parameters Influencing Porosity in Sandstones: a Model for Sandstone Porosity Prediction: Discussion. *Bulletin of the American Association of Petroleum Geologists,* **72**, 852-855.

SHANMUGAM, G. & MOIOLA, R. J. 1991. Types of Submarine Fan Lobes: Models and Implications. *Bulletin of the American Association of Petroleum Geologists,* **75**, 156-179.

SHANMUGAM, G., DAMUTH, J. E. & MOIOLA, R. J. 1985. Is the Turbidite Facies Association Scheme Valid for Interpreting Ancient Submarine Fan Environments? *Geology,* **13**, 234-237.

SHAW, E. W. 1918. Anomalous Dips. *Economic Geology,* **13**, 598-610.

SHEPARD, F. P. & BUFFINGTON, E. C. 1968. La Jolla Submarine Fan-Valley. *Marine Geology,* **6**, 107-143.

SHEPARD, F. P., DILL, R. F. & VON RAD, U. 1969. Physiography and Sedimentary Processes of La Jolla Submarine Fan and Fan-Valley, California. *Bulletin of the American Association of Petroleum Geologists,* **53**, 390-420.

SHINN, E. A. & ROBBIN, D. M. 1983. Mechanical and Chemical Compaction in Fine-Grained Shallow-Water Limestones. *Journal of Sedimentary Petrology,* **53**, 595-618.

SHINN, E. A., ROBBIN, D. M., LIDZ, B. H. & HUDSON, J. H. 1983. Influence of Deposition and Early Diagenesis on Porosity and Chemical Compaction in Two Paleozoic Buildups: Mississippian and Permian Age Rocks in the Sacramento Mountains, New Mexico. In: HARRIS P. M. (Ed) *Carbonate Buildups, a Core Workshop.* Society of Economic Paleontologists and Mineralogists, Core Workshop, **4**, 182-222.

SIMONS, N. E. & MENZIES, B. K. (Eds) 1977. *A Short Course in Foundation Engineering.* Newnes-Butterworth, London.

SKEMPTON, A. W. 1970. The Consolidation of Clays by Gravitational Compaction. *Quarterly Journal of the Geological Society of London,* **125**, 373-411.

SKOLNICK, H. & ARNAL, R. E. 1959. Ventura Basin Edge Environment. *Bulletin of the American Association of Petroleum Geologists,* **43**, 477-483.

SMOSNA, R. 1989. Compaction Law for Cretaceous Sandstones of Alaska's North Slope. *Journal of Sedimentary Petrology,* **59**, 572-584.

SORBY, H. C. 1908. On the Application of Quantitative Methods to the Study of the Structure and History of Rocks. *Quarterly Journal of the Geological Society of London,* **64**, 171-232.

SPENCER, A. M. et al. (Eds) 1987. *Geology of the Norwegian Oil & Gas Fields.* Graham & Trotman, London.

STANTON, R. J., Jr. 1960. Paleoecology of the Upper Miocene Castaic Formation, Los Angeles County, California. *Unpublished Ph.D. Dissertation. Californian Institute of Technology,* 355pp.

STANTON, R. J., Jr. 1966. Megafauna of the Upper Miocene Castaic Formation, Los Angeles County, California. *Journal of Paleontology,* **40**, 21-40.

STECKLER, M. S. & WATTS, A. B. 1978. Subsidence of Atlantic-Type Continental Margin off New York. *Earth and Planetary Science Letters,* **41**, 1-13.

STEWART, I. J. 1987. A Revised Stratigraphic Interpretation of the Early Paleogene of the Central North Sea. In: BROOKS, J. & GLENNIE, K. W. (Eds) *Petroleum Geology of North West Europe.* Graham & Trotman, London, 557-576.

STOW, D. A. V. 1981. Laurentian Fan: Morphology, Sediments Processes, and Growth Pattern. *Bulletin of the American Association of Petroleum Geologists,* **65**, 375-393.

STOW, D. A. V. 1985. Deep-Sea Clastics: Where are we and where are we going? In: BRENCHLEY, P. J. & WILLIAMS, B. P. (Eds) *Sedimentology: Recent Developments and Applied Aspects.* Blackwell Scientific Publications, London, 67-93.

STOW, D. A. V. 1986. Deep Clastic Seas. In: READING, H. G. (Ed) *Sedimentary Environments and Facies.* Second Edition. Blackwell Scientific Publications, Oxford, 399-444.

STOW, D. A. V., HOWELL, D. G. & NELSON, C. H. 1984. Sedimentary, Tectonic, and Sea-Level Controls. In: BOUMA A. H., NORMARK, W. R. & BARNES N. E. (Eds) *Submarine Fans and Related Turbidite Systems.* Springer, New York, 15-22.

SURLYK, F. 1987. Slope and Deep Shelf Gully Sandstones, Upper Jurassic, East Greenland. *Bulletin of the American Association of Petroleum Geologists,* **71**, 464-475.

SUTTER, A. A. 1980. Palaeogene Sediments from the United Kingdom Sector of the Central North Sea. *Unpublished Ph.D. Thesis, University of Aberdeen.*

TAYLOR, J. M. 1950. Pore Space Reduction in Sandstones. *Bulletin of the American Association of Petroleum Geologists,* **34**, 701-716.

TEAS, L. P. 1923. Differential Compacting the Cause of Certain Clairborne Dips. *Bulletin of the American Association of Petroleum Geologists,* **9**, 370-373.

TEODOROVICH, G. I. & CHERNOV, A. A. 1968. Character Changes with Depth in Productive Deposits of Aspheron Oil-Gas Bearing Region. *Soviet Geology,* **4**, 83-93.

TERZAGHI, K. 1925. Principles of Soil Mechanics II. Compressive Strength of Clays. *Engineering News Records,* **95**, 796-800.

TERZAGHI, K. & PECK, R. B. (Eds) 1948. *Soil Mechanics in Engineering Practice.* Wiley, New York. 566pp.

THOMPSON, P. J. & BUTCHER, P. D. 1990. The Geology and Geophysics of the Everest Complex, Central North Sea. Abstract. *Bulletin of the American Association of Petroleum Geologists,* **74**, 778.

TIMBRELL, G. 1993. Sandstone Architecture of the Balder Formation Depositional System, UK Quadrant 9 and Adjacent Areas. In: PARKER, J. R. (Ed) *Petroleum Geology of Northwest Europe: Proceedings of the 4th Conference.* The Geological Society, London, 107-121.

TRASK, P. D. 1931. Compaction of Sediments. *Bulletin of the American Association of Petroleum Geologists,* **15**, 271-276.

TRUYOL, V. 1989. The Influence on Deep-Sea Sediments Compaction in the First Tens of Metres of the Lithological and Depositional Parameters. Abstract. *"Compaction-Decompaction of Sediments".* Meeting of the International Association of Sedimentologists, 30-31st March, Paris, 27.

VAIL, P. R., MITCHUM, R. M., Jr. & THOMPSON, S. III. 1977. Seismic Stratigraphy and Global Changes of Sea-Level, Part 4: Global Cycles of Relative Changes of Sea Level. In: PAYTON, C. E. (Ed) *Seismic Stratigraphy - Applications to Hydrocarbon Exploration.* Memoir of the American Association of Petroleum Geologists, **26**, 83-97.

VAN DE KAMP, P. C. 1976. Inorganic and Organic Metamorphism in Siliciclastic Rocks. Abstract. *Bulletin of the American Association of Petroleum Geologists,* **60**, 729.

VAN HINTE, J. E. 1978. Geohistory Analysis - Application of Micropaleontology in Exploration Geology. *Bulletin of the American Association of Petroleum Geologists,* **62**, 201-222.

VAN WAGONER, J. C., MITCHUM, R. M., POSAMENTIER, H. W. & VAIL, P. R. 1987. Seismic Stratigraphy Interpretation Using Sequence Stratigraphy, Part II: Key Definitions of

Sequence Stratigraphy. In: BALLY, A. W. (Ed) *Atlas of Seismic Stratigraphy.* American Association of Petroleum Geologists Studies in Geology, **27**, 1-10.

VINING, B. A., IOANNIDES, N. S. & PICKERING, K. T. 1993. Stratigraphic Relationships of some Tertiary Lowstand Depositional Systems in the Central North Sea. In: PARKER, J. R. (Ed) *Petroleum Geology of Northwest Europe: Proceedings of the 4th Conference.* The Geological Society, London, 17-29.

VON HUENE, R., PIPER, D. J. W. & DUNCAN, J. 1973. Measurements of Porosity in Sediments of the Lower Continental Margin, Deep-Sea Fans, the Aleutian Trench, and Alaskan Abyssal Plain. In: KULM, L. D., VON HUENE, R., et al. (Eds) *Initial Reports of the Deep Sea Drilling Project,* **18**, Washington (U.S. Government Printing Office), 889-895.

WALKER, R. G. 1975. Upper Cretaceous Resedimented Conglomerates at Wheeler Gorge, California: Description and Field Guide. *Journal of Sedimentary Petrology,* **45**, 105-112.

WALKER, R. G. 1978. Deep-Water Sandstone Facies and Ancient Submarine Fans: Models for Exploration for Stratigraphic Traps. *Bulletin of the American Association of Petroleum Geologists,* **62**, 932-966.

WALKER, R. G. 1980. Modern and Ancient Submarine Fans: Reply. *Bulletin of the American Association of Petroleum Geologists,* **64**, 1101-1108.

WALKER, R. G. 1985. Mudstones and Thin-Bedded Turbidites Associated with the Upper Cretaceous Wheeler Gorge Conglomerates, California: A Possible Channel - Levee Complex. *Journal of Sedimentary Petrology,* **55**, 279-290.

WALKER, R. G. & MUTTI, E. 1973. Turbidite Facies and Facies Associations. In: MIDDLETON, G. V. & BOUMA, A. H. (Eds) *Turbidites and Deep-Water Sedimentation.* Society of Economic Paleontologists and Mineralogists, Pacific Section Short Course Notes, Anaheim, 119-157.

WALMSLEY, P. J. 1975. The Forties Field. In: WOODLAND, A. W. (Ed) *Petroleum and the Continental Shelf of North-West Europe, Vol 1 Geology.* Applied Science Publishers, Barking, 477-484.

WAPLES, D. W. 1980. Time and Temperature in Petroleum Formation, Application of Lopatin's Method to Petroleum Exploration. *Bulletin of the American Association of Petroleum Geologists,* **64**, 916-926.

WAPLES, D. W. & KAMATA, H. 1993. Modelling Porosity Reduction as a Series of Chemical and Physical Processes. In: DORÉ, A. G. et al. (Eds) *Basin Modelling: Advances*

and Applications. Special Publication No. **3**, Norwegian Petroleum Society, Elsevier, Amsterdam, 303-320.

WATTS, A. B. 1981. The U.S. Atlantic Continental Margin: Subsidence History, Crustal Structure and Thermal Evolution. In: BALLY, A. W., WATTS, A. B., GROW, J. A., MANSPEIZER, W., BERNOULLI, D., SCHREIBER, C. & HUNT, J. M. (Eds) *Geology of Passive Continental Margins: History, Structure and Sedimentologic Record.* American Association of Petroleum Geologists, Educational Course Note Series, **19**, 175pp.

WATTS, A. B. & RYAN, W. B. F. 1976. Flexure of the Lithosphere and Continental Margin Basins. *Tectonophysics,* **36**, 24-44.

WEAVER, C. E. (Ed) 1989. *Developments in Sedimentology 44: Clays, Muds, and Shales.* Elsevier, Amsterdam, 819pp.

WEIMER, P. 1989. Sequence Stratigraphy of the Mississippi Fan (Plio-Pleistocene), Gulf of Mexico. *Geo-Marine Letters,* **9**, 185-272.

WEISENFLUH, G. A. & FERM, J. C. 1984. Geologic Controls on Deposition of the Pratt Seam, Black Warrior Basin, Alabama, U.S.A. In: RAHMAIN, R. A. & FLORES, R. M. (Eds) *Sedimentology of Coal and Coal-Bearing Sequences.* Special Publication of the International Association of Sedimentologists, 275-289.

WELLER, J. M. 1959. Compaction of Sediments. *Bulletin of the American Association of Petroleum Geologists,* **43**, 273-310.

WHITTEN, D. G. A. & BROOKS, J. R. V. (Eds) 1987. *Dictionary of Geology.* Penguin Books, Middlesex, England. 520pp.

WHYATT, M., BOWEN, J. M. & RHODES, D. N. 1991. Nelson - Successful Application of a Development Geoseismic Model in North Sea Exploration. *First Break,* **9**, 265-280.

WILSON, J. C. & McBRIDE, E. F. 1988. Compaction and Porosity Evolution of Pliocene Sandstones, Ventura Basin, California. *Bulletin of the American Association of Petroleum Geologists,* **72**, 664-681.

WILSON, J. C. & McBRIDE, E. F. 1989. Compaction and Porosity Evolution of Pliocene Sandstones, Ventura Basin, California: Reply. *Bulletin of the American Association of Petroleum Geologists,* **73**, 1280.

WOOD, D. A. 1988. Relationships Between Thermal Maturity Indices Calculated Using Arrhenius Equation and Lopatin Method; Implications for Petroleum Exploration. *Bulletin of the American Association of Petroleum Geologists,* **72**, 115-134.

WOODLAND, A. W. (Ed) 1975. *Petroleum and the Continental Shelf of North-West Europe, Vol 1 Geology.* Applied Science Publishers, Barking.

YAMAMOTO, T., TREVORROW, M. V., BADIEY, M. & TURGUT, A. 1989. Determination of the seabed porosity and shear modulus profiles using a gravity wave inversion. *International Journal of Geophysics,* **98**, 173-182.

YUREWICZ, D. A. 1975. Basin Margin Sedimentation, Rancheria Formation, Sacramento Mountains, New Mexico. In: PRAY, L. C. (Ed) *A Guidebook to the Mississippian Shelf-Edge and Basin Facies Carbonates, Sacramento Mountains and Southern New Mexico.* Dallas Geological Society, Dallas, TX.

YUREWICZ, D. A. 1977. Sedimentology of Mississippian Basin-Facies Carbonates, New Mexico and West Texas - the Rancheria Formation. In: COOK, H. E. & ENOS, P. (Eds) *Deep-Water Carbonate Environments.* Special Publication of the Society of Economic Paleontologists and Mineralogists, Tulsa, **25**, 203-219.

Appendix 1.

Isopach - Unit 19

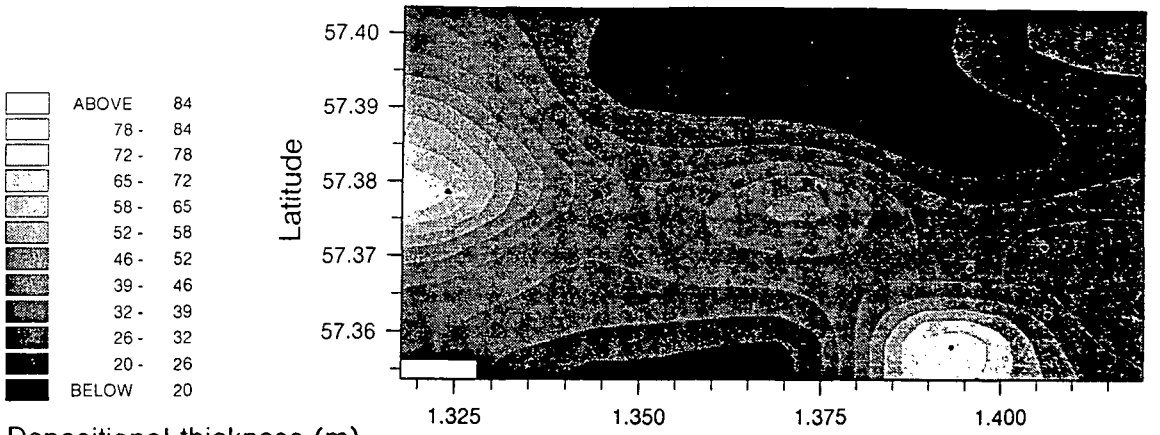

Scale: Depositional thickness (m)

Isopach - Lista

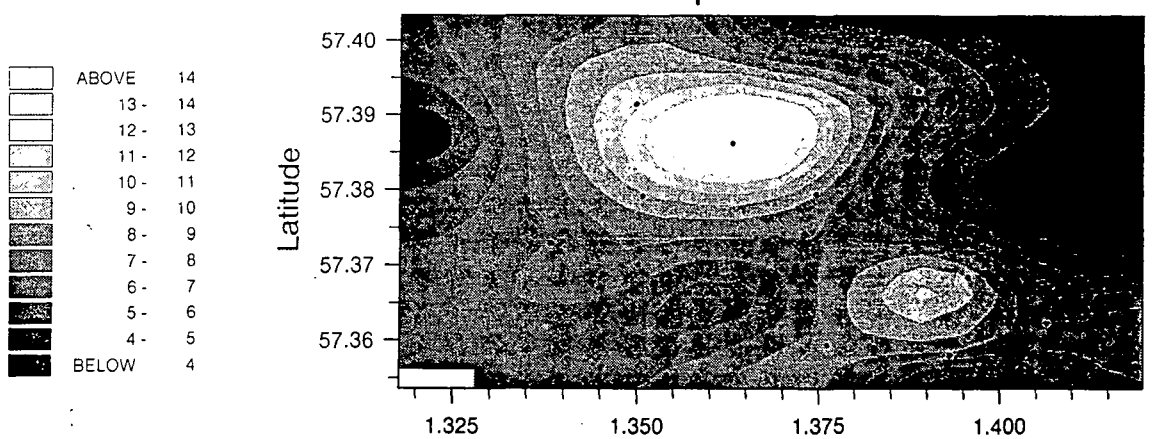

Isopach - Unit 18

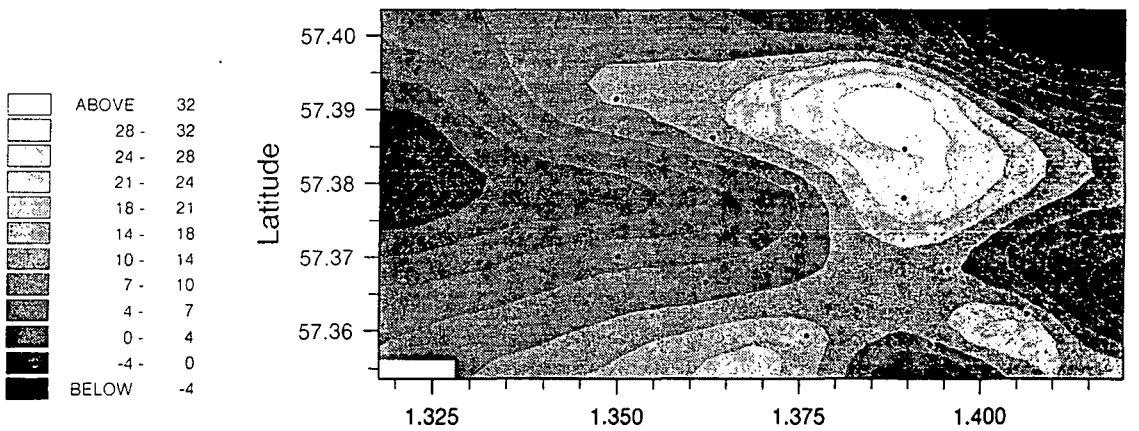

Isopach - Unit B

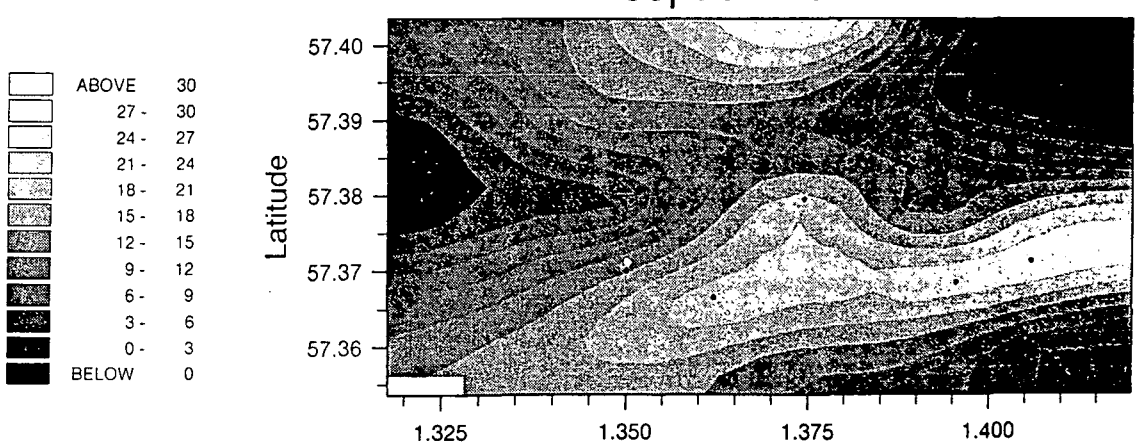

Isopach - Unit 17

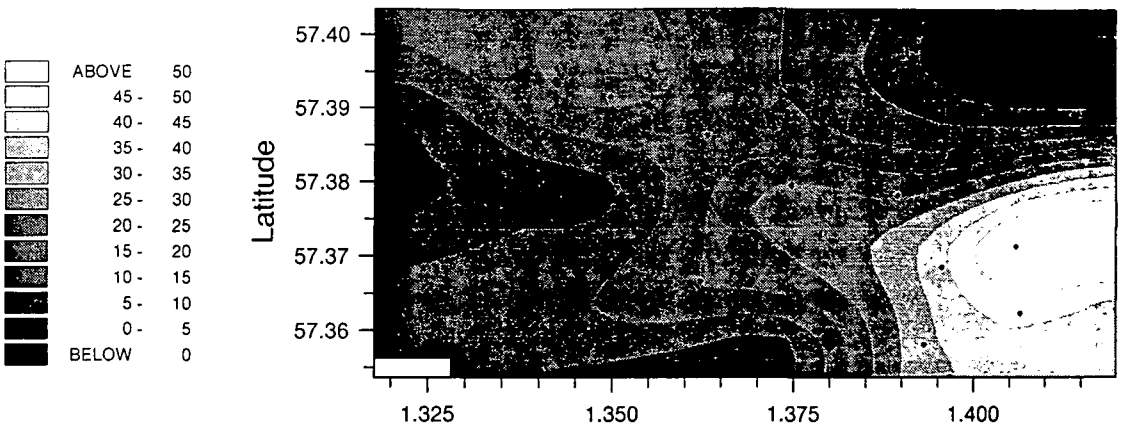

Isopach - Unit 16

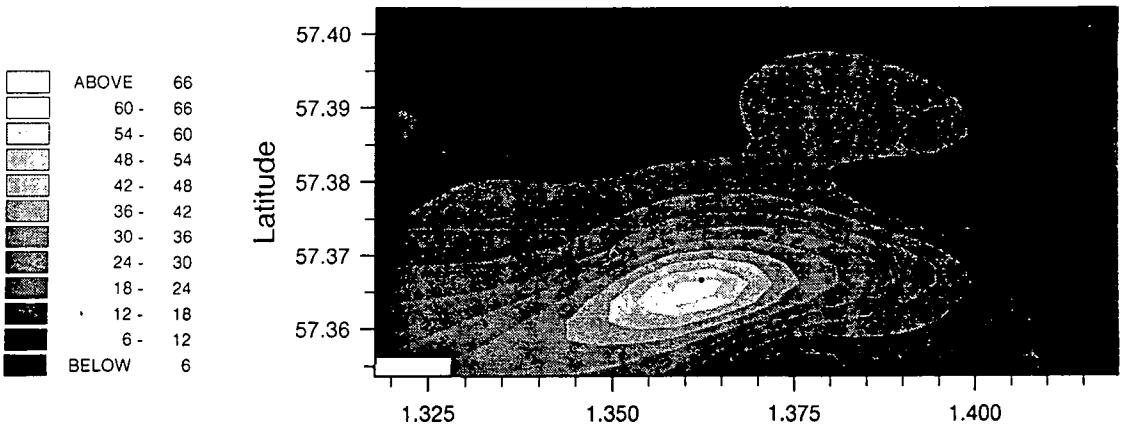

Isopach - Unit A

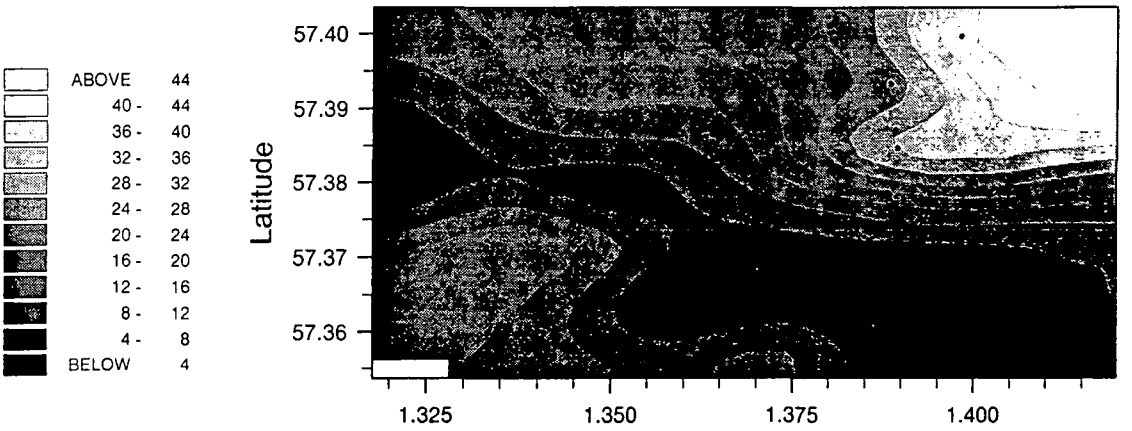

Isopach - Unit 15

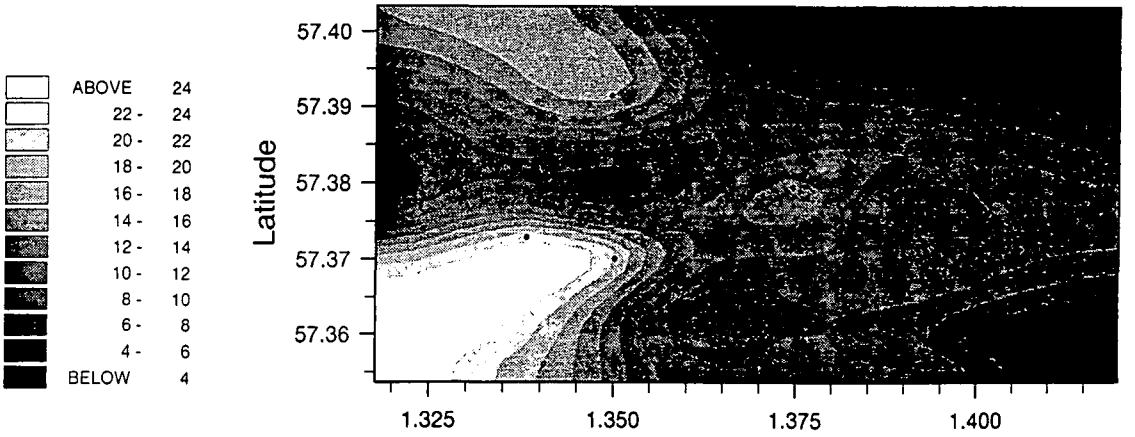

Isopach - Unit 14

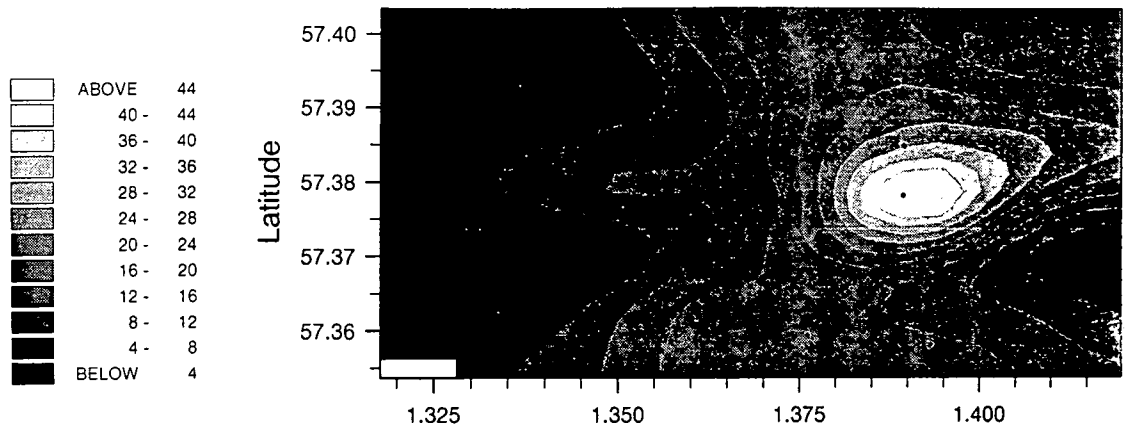

Isopach - Unit 13

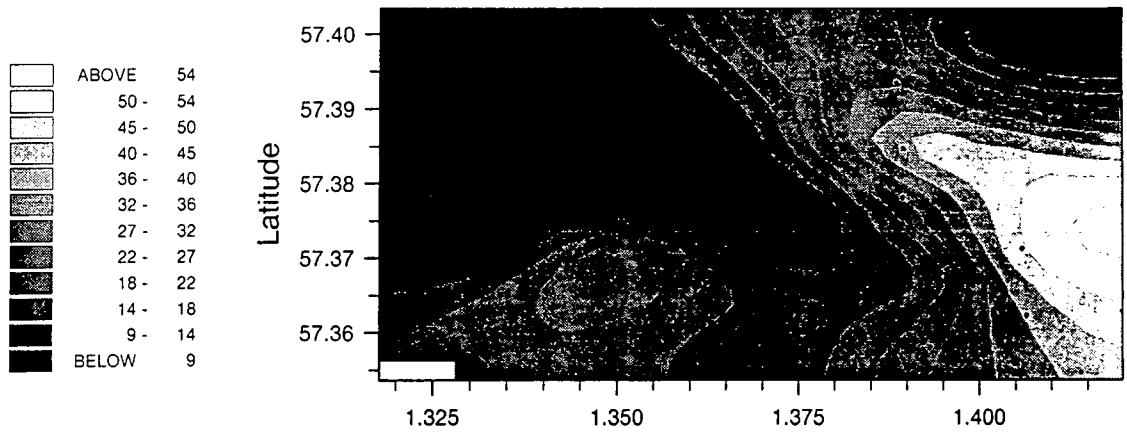

Isopach - Unit 12

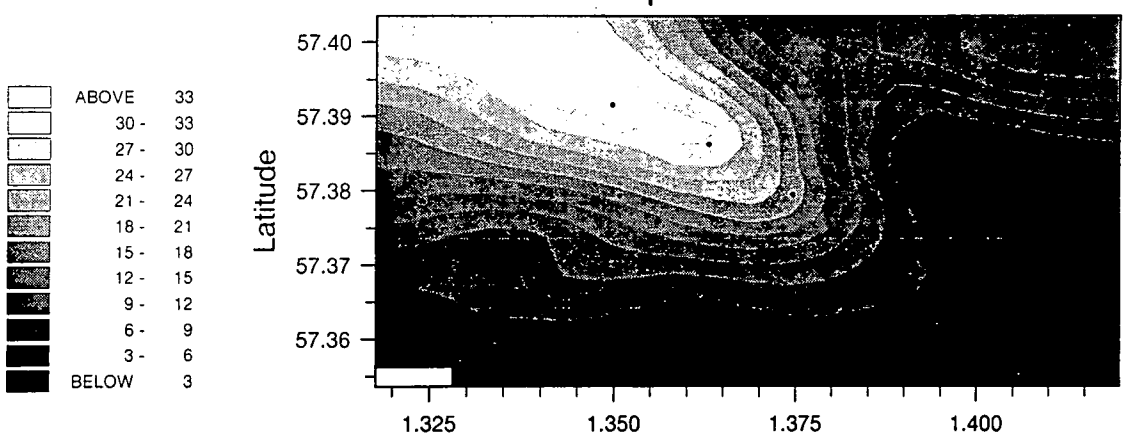

Isopach - Unit 9

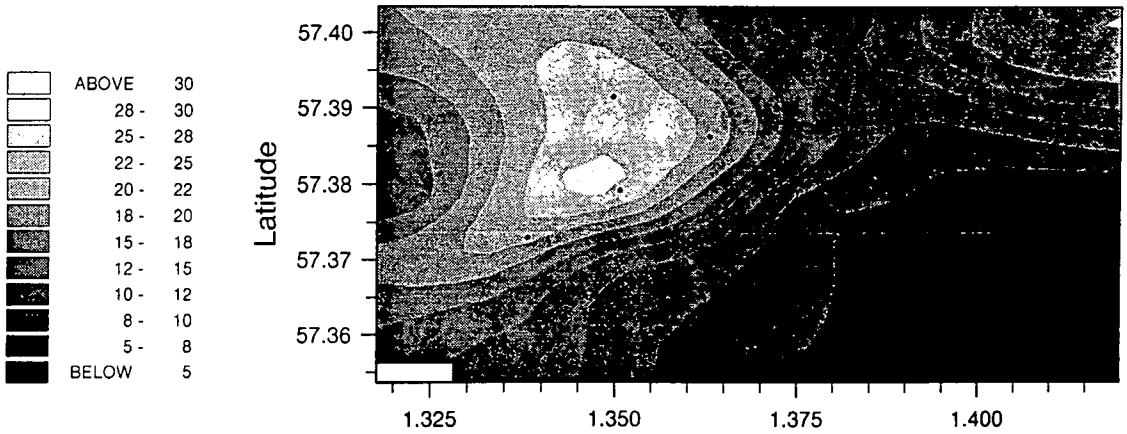

Isopach - Unit 5

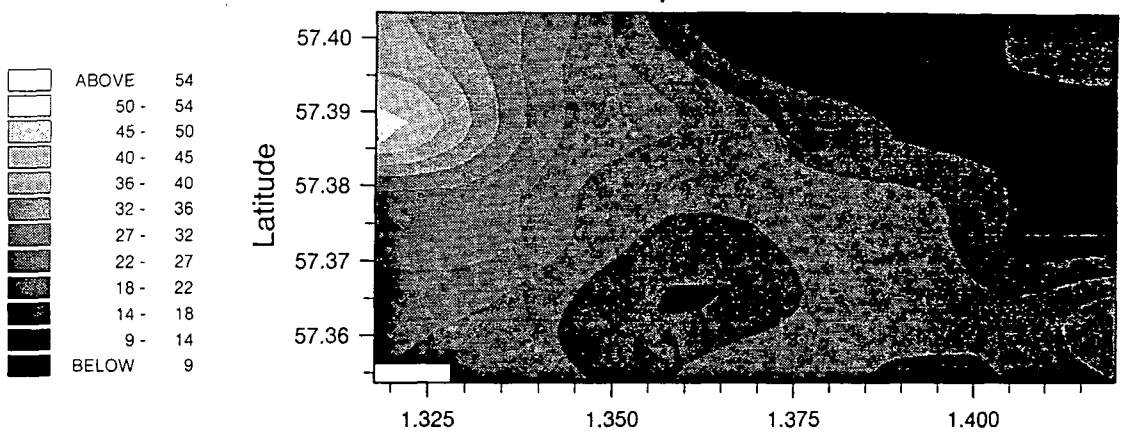

Isopach - Unit 3

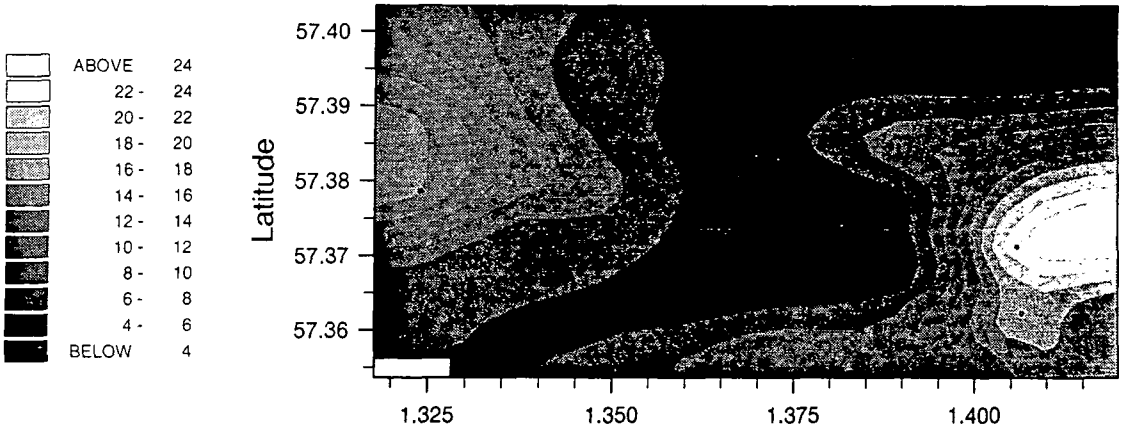

Isopach - Unit 4

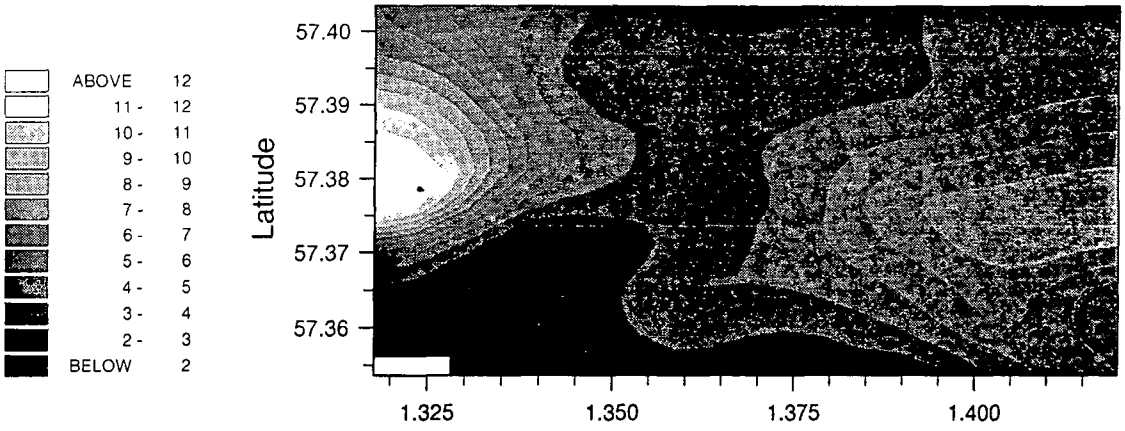

Isopach - Unit 1

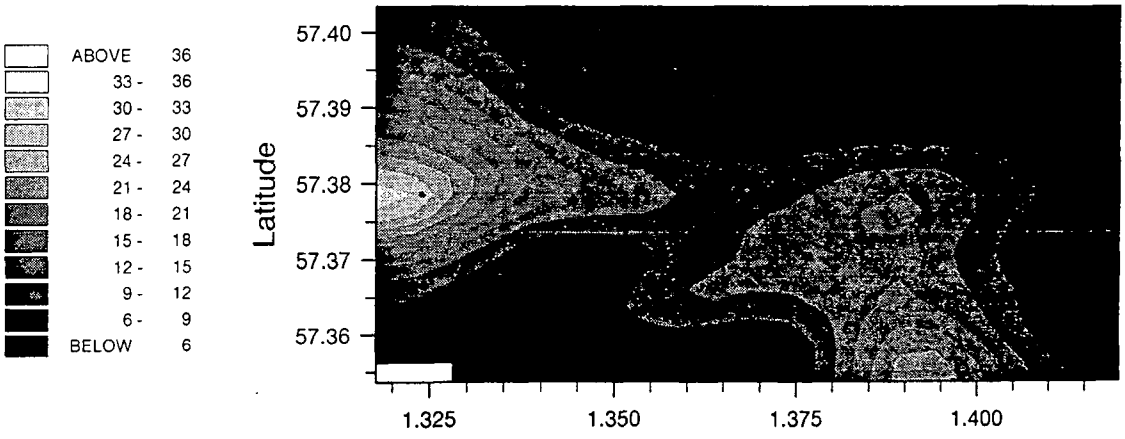

Isopach - Forties

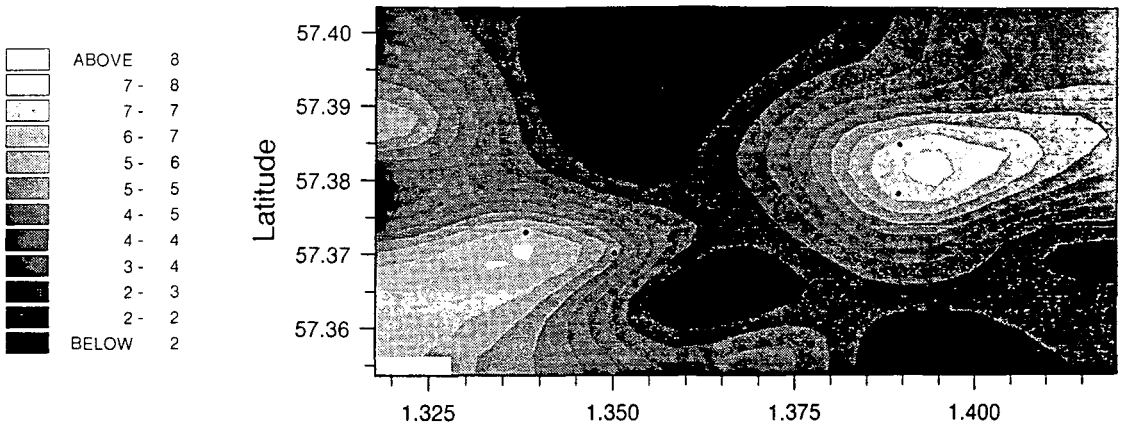

Sand % - Unit 19

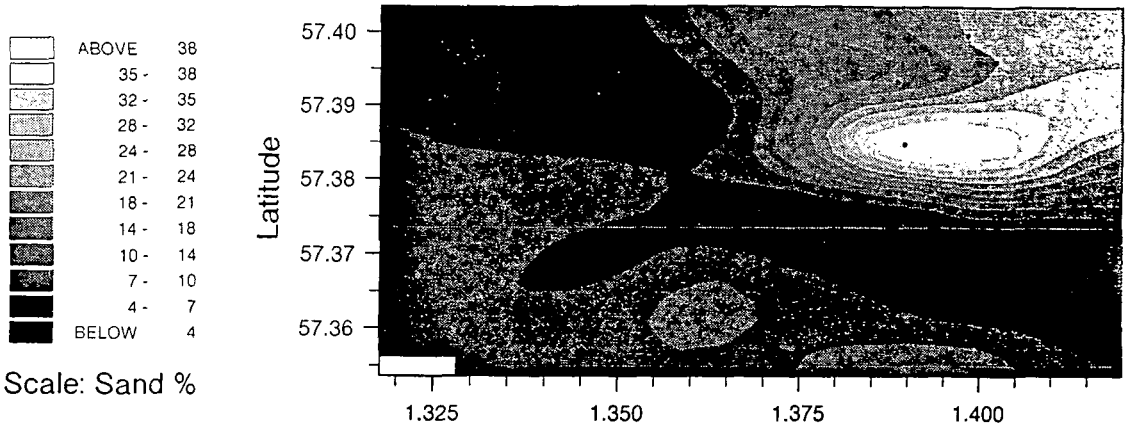

Sand % - Lista

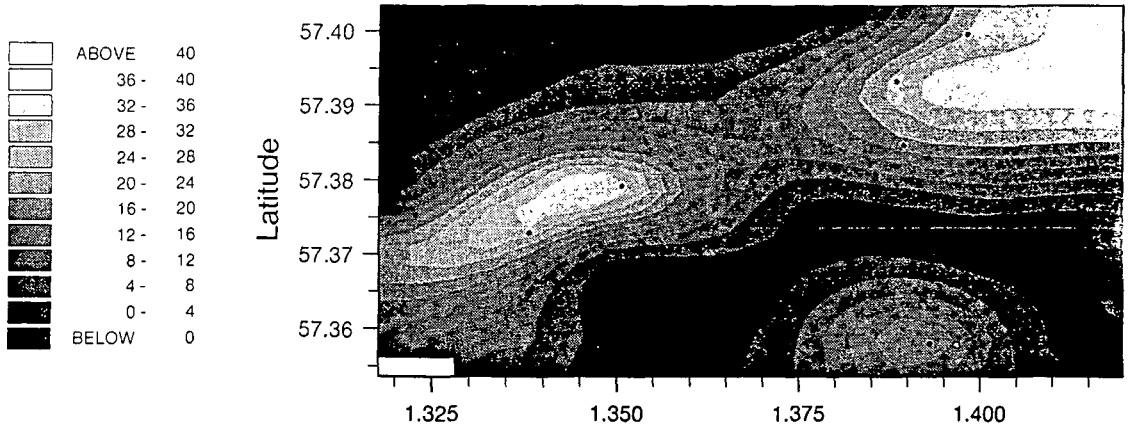

Sand % - Unit 18

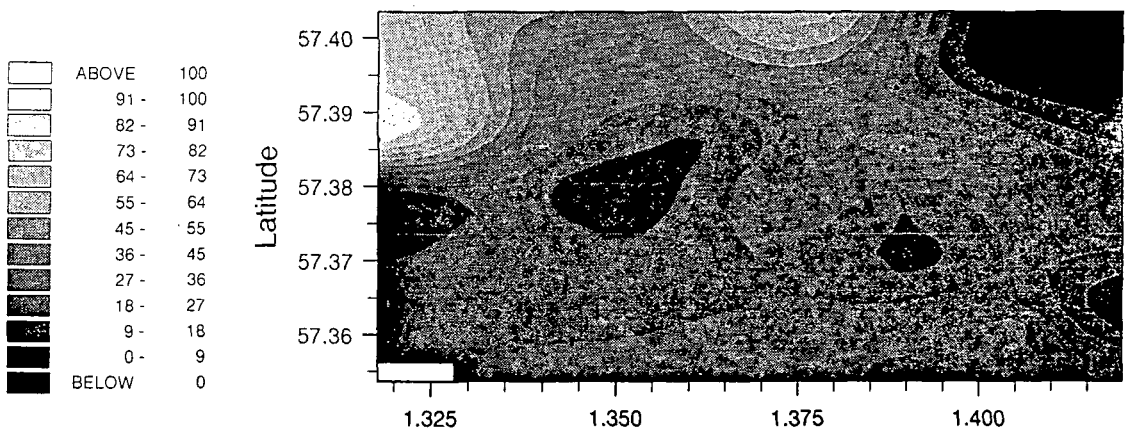

Sand % - Unit B

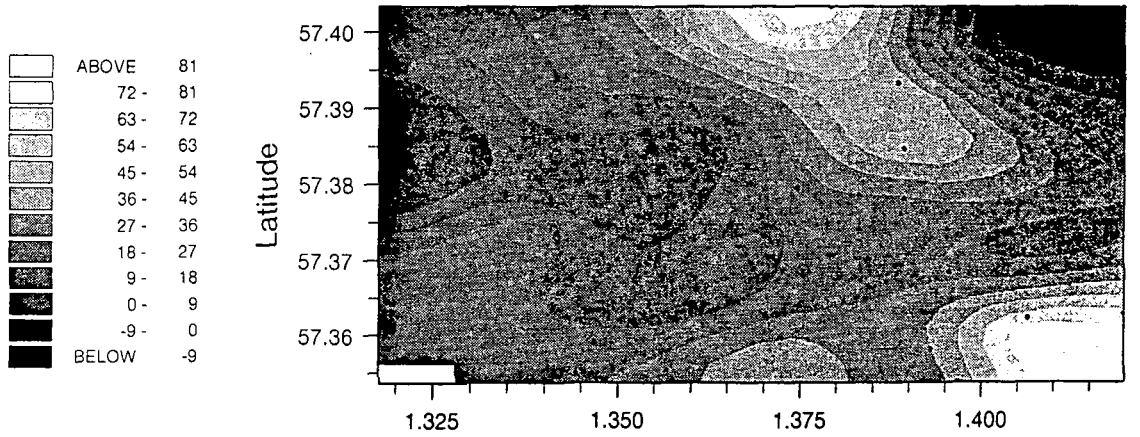

Sand % - Unit 17

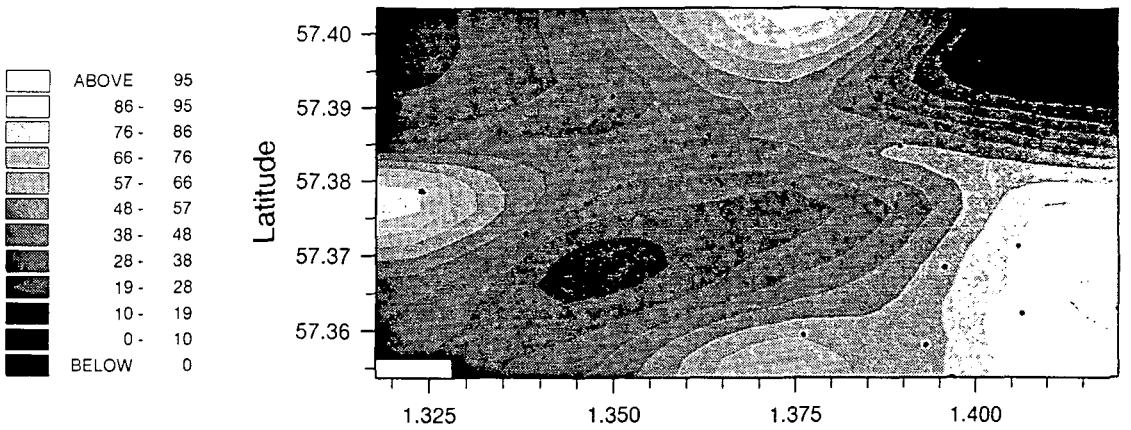

Sand % - Unit 16

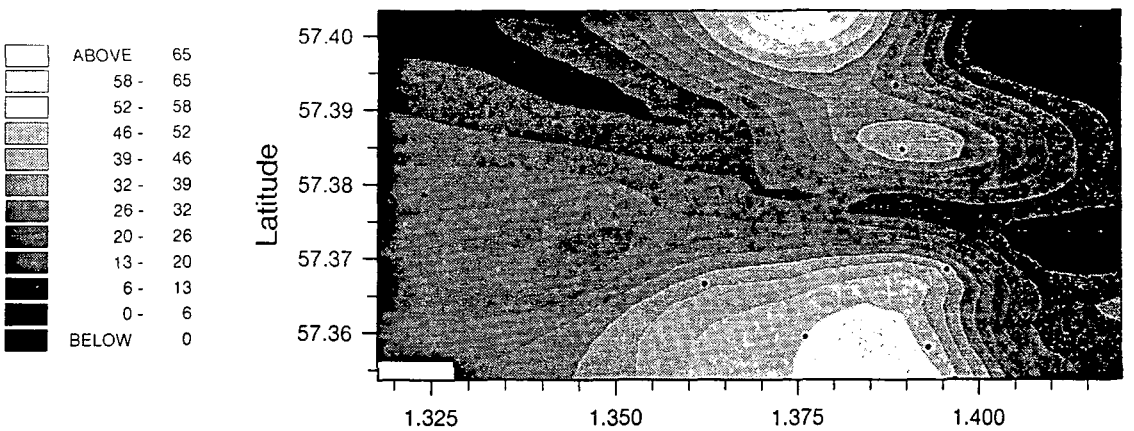

Sand % - Unit A

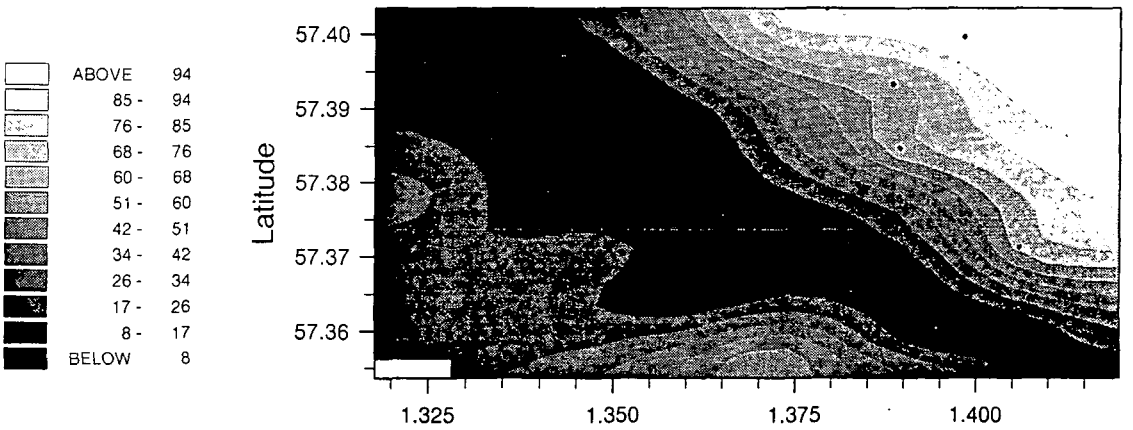

Sand % - Unit 15

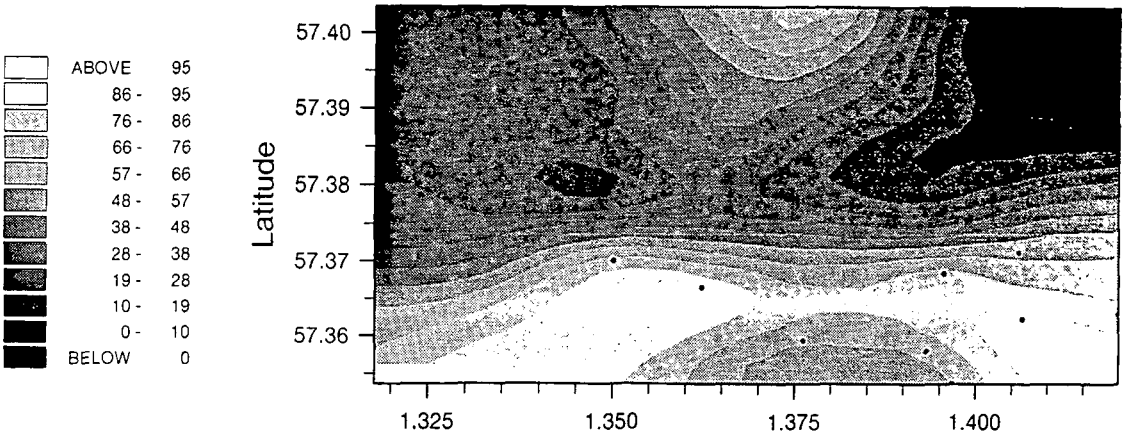

Sand % - Unit 14

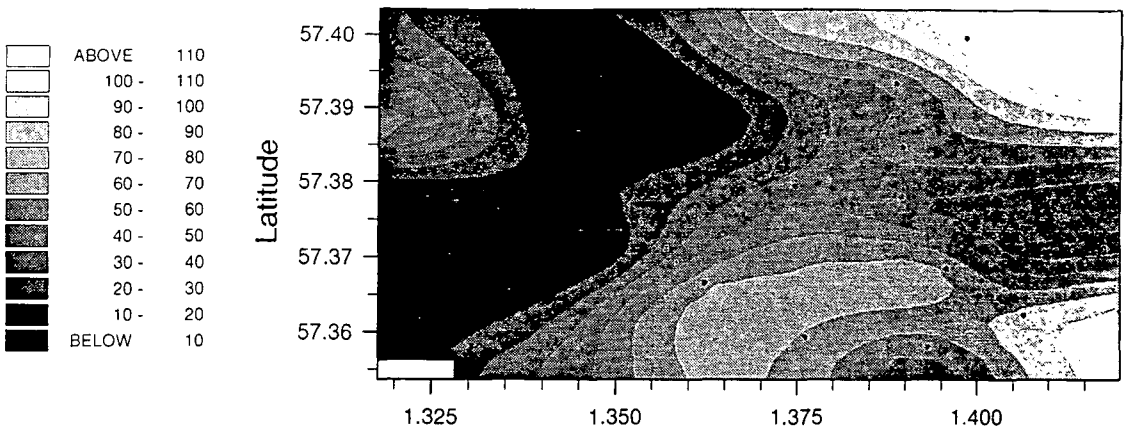

Sand % - Unit 13

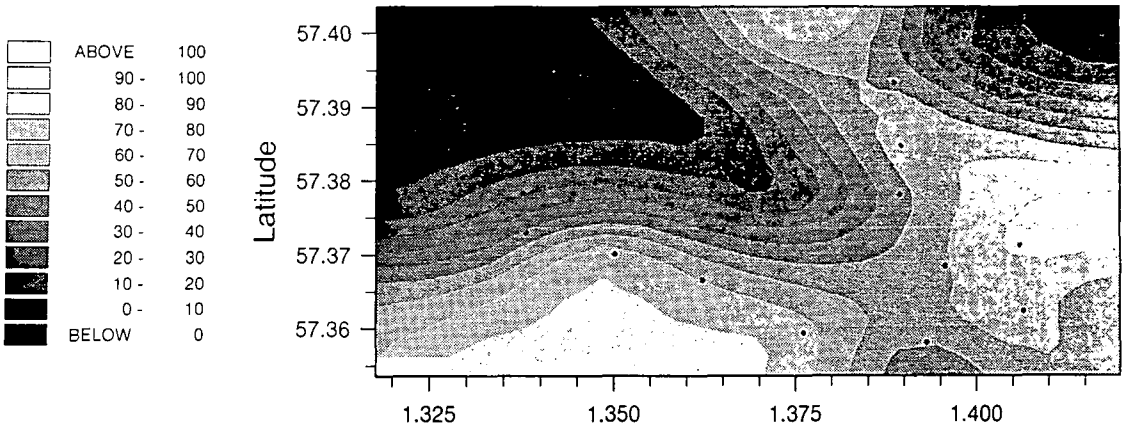

Sand % - Unit 12

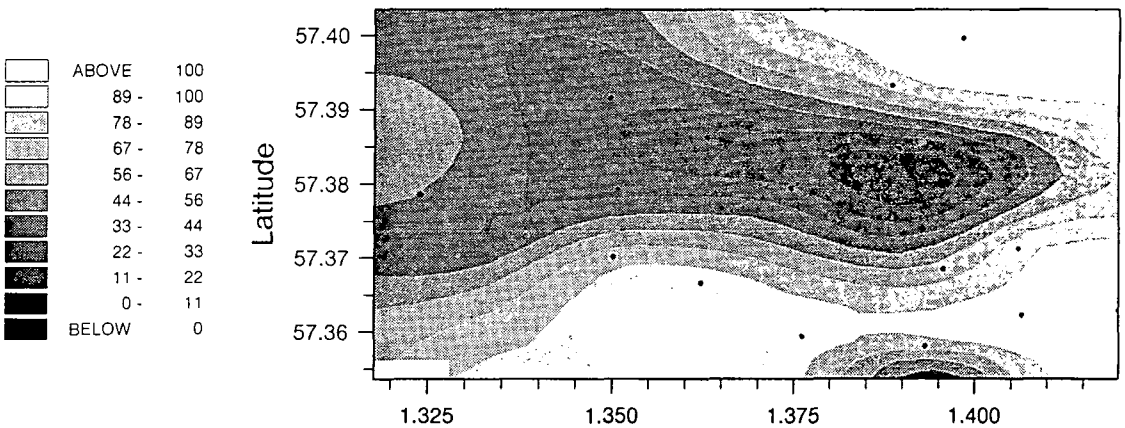

Sand % - Unit 9

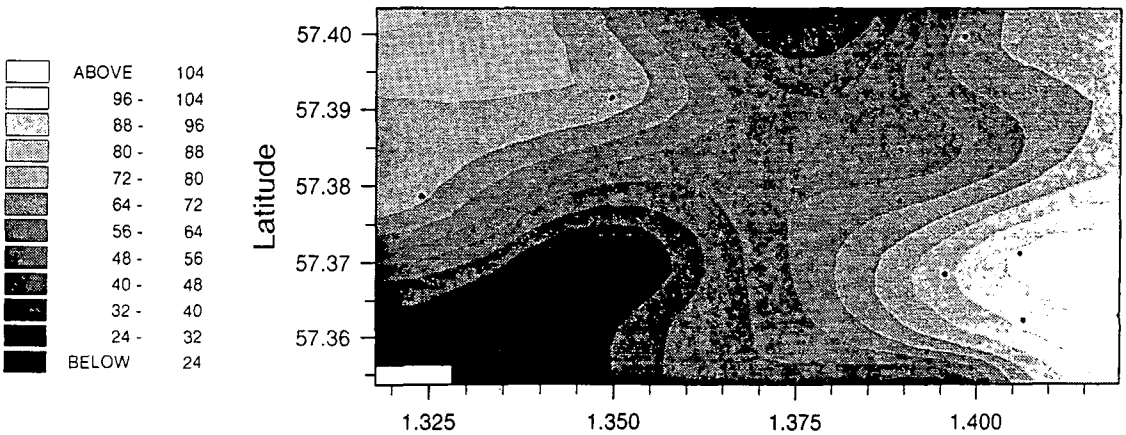

Sand % - Unit 5

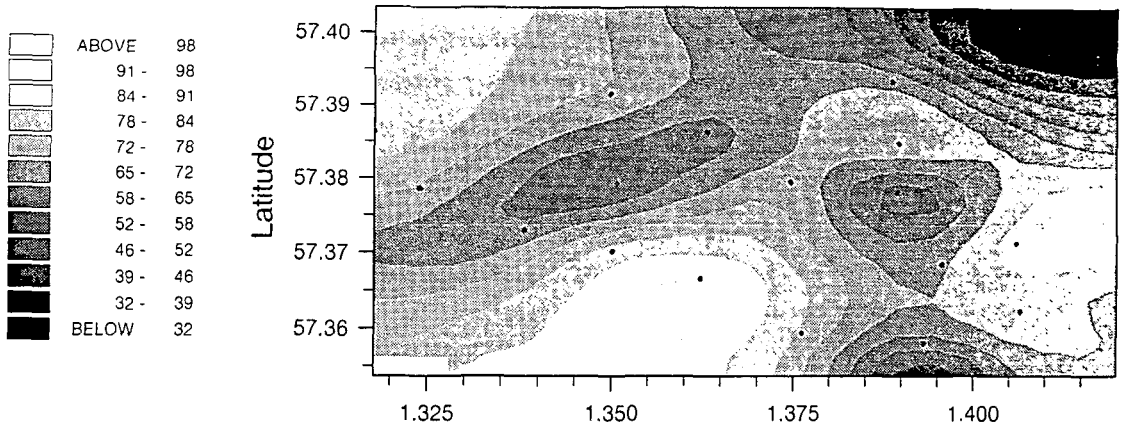

Sand % - Unit 3

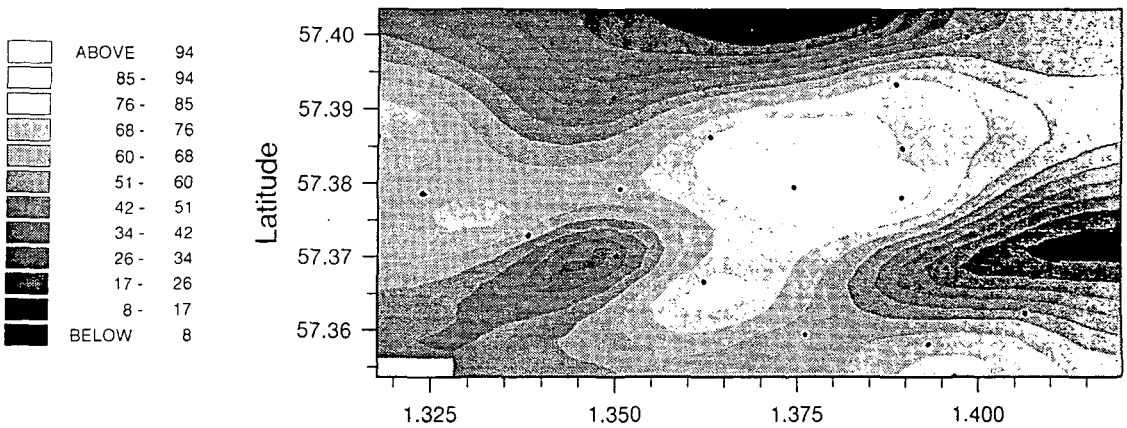

Sand % - Unit 4

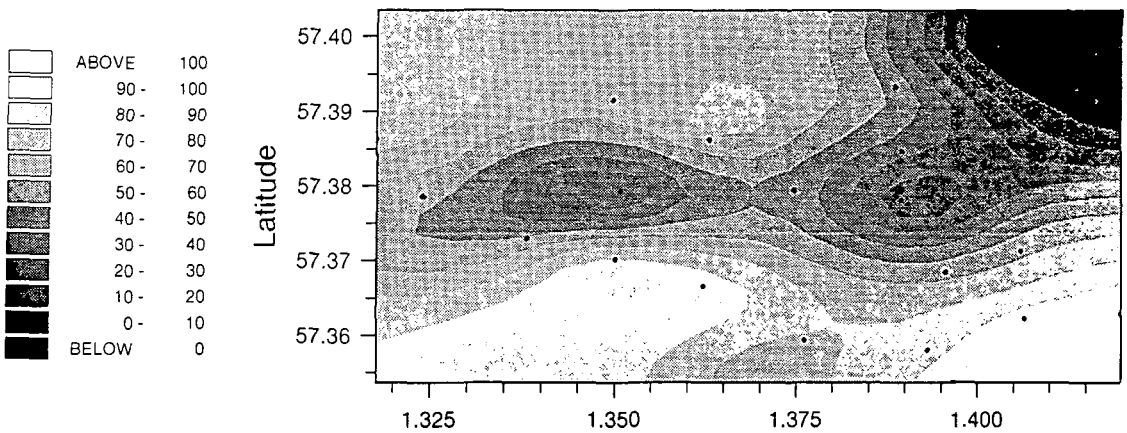

Sand % - Unit 1

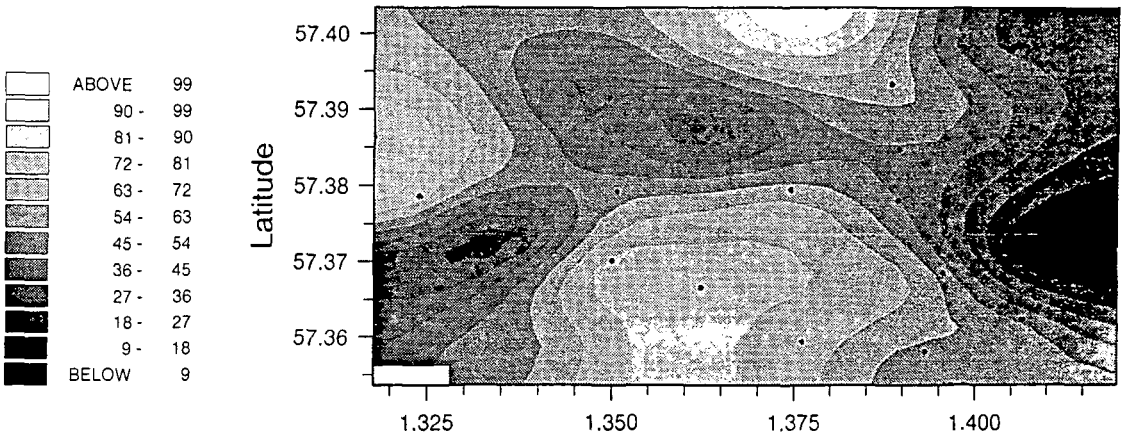

Sand % - Forties

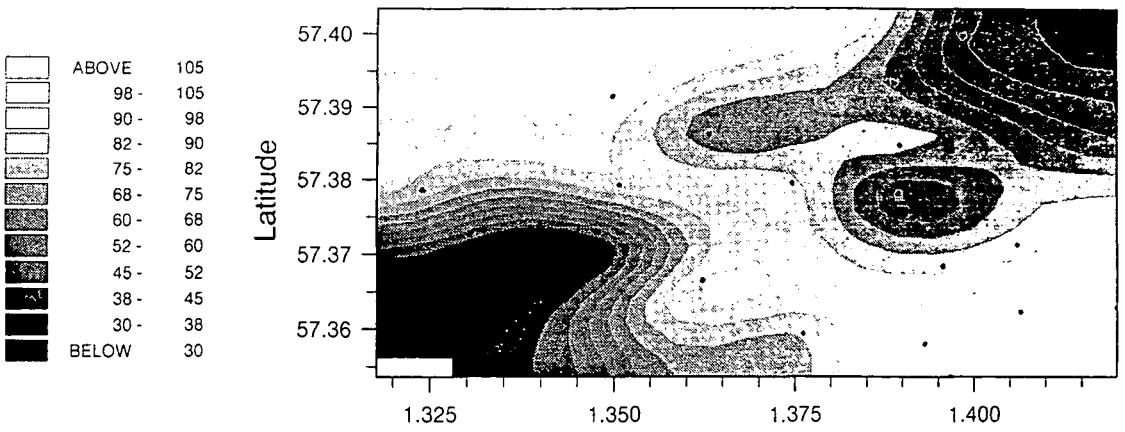

Top 19 (compacted)

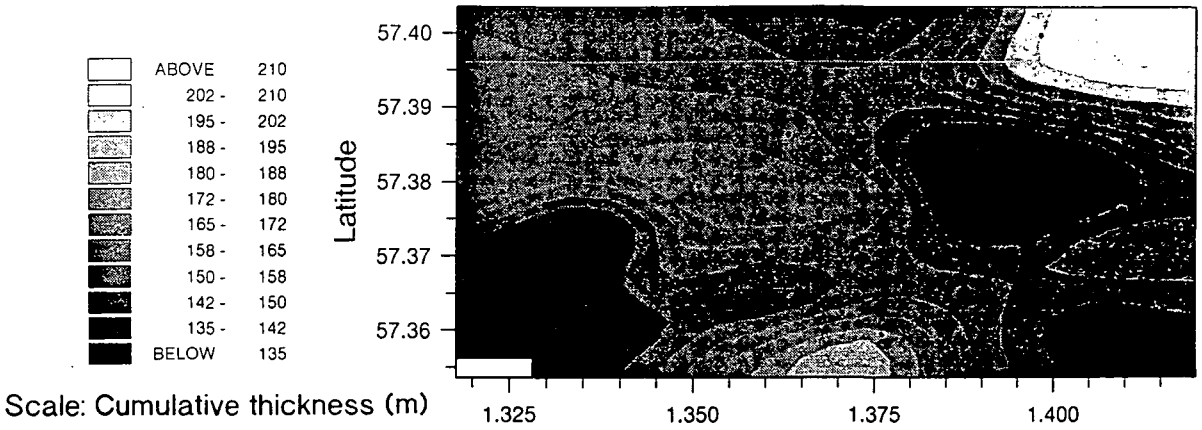

Scale: Cumulative thickness (m)

Top Lista (compacted)

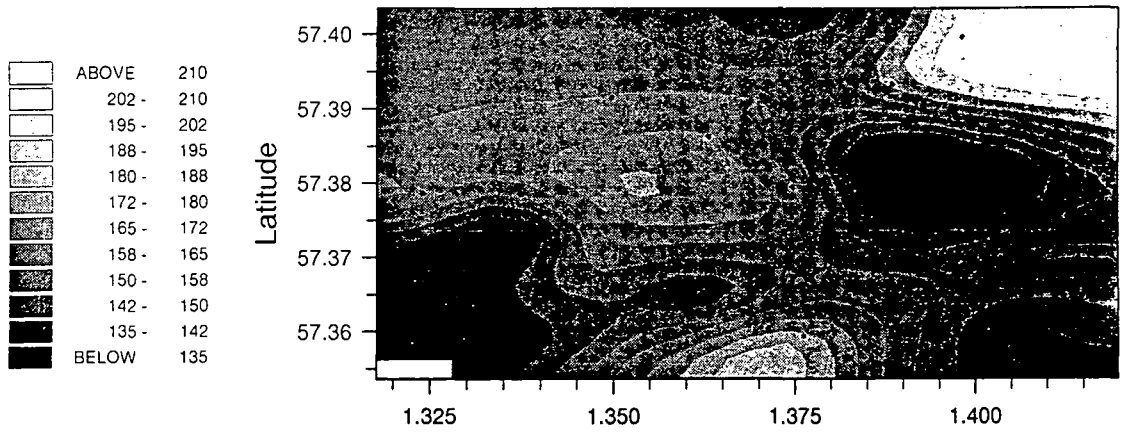

Top 18 (compacted)

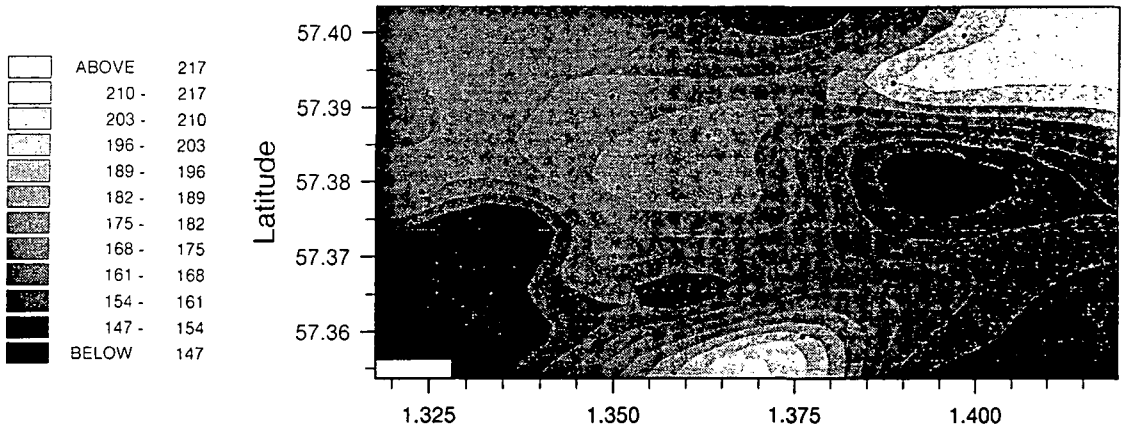

Top B (compacted)

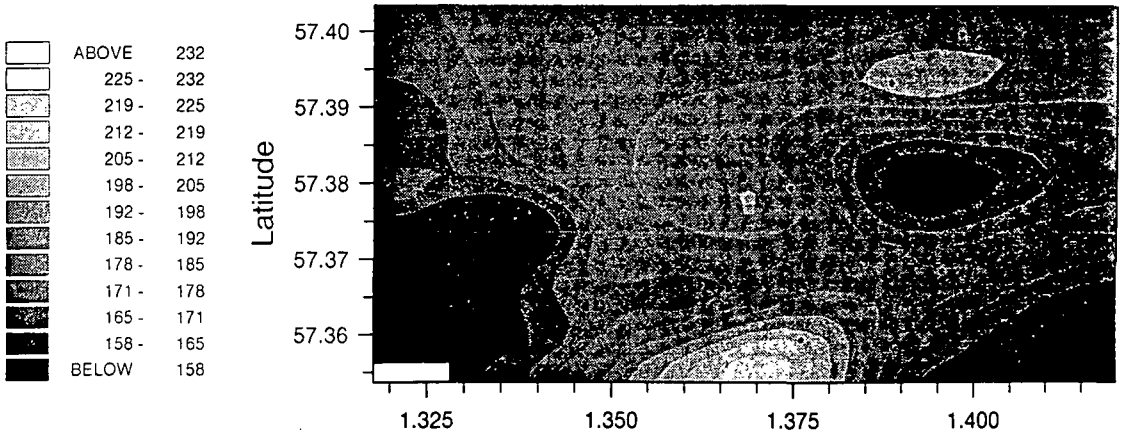

Top 17 (compacted)

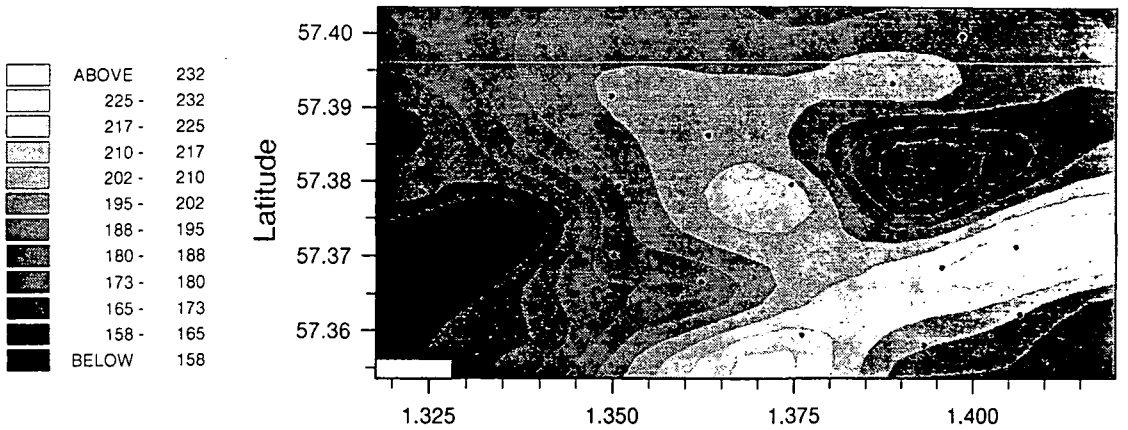

Top 16 (compacted)

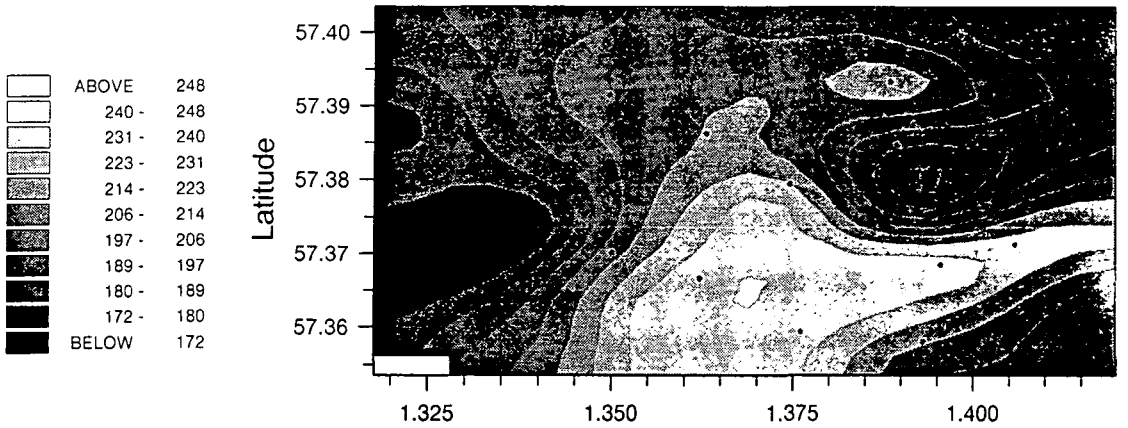

Top A (compacted)

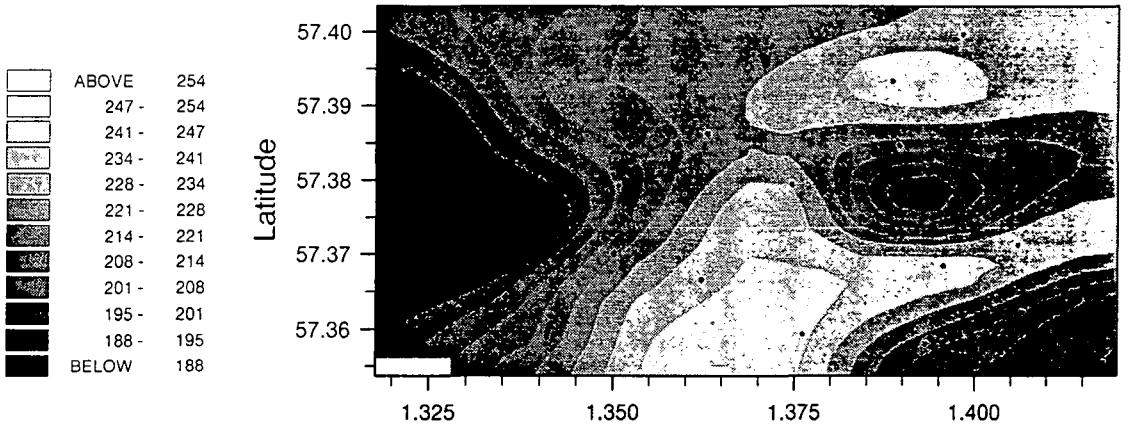

Top 15 (compacted)

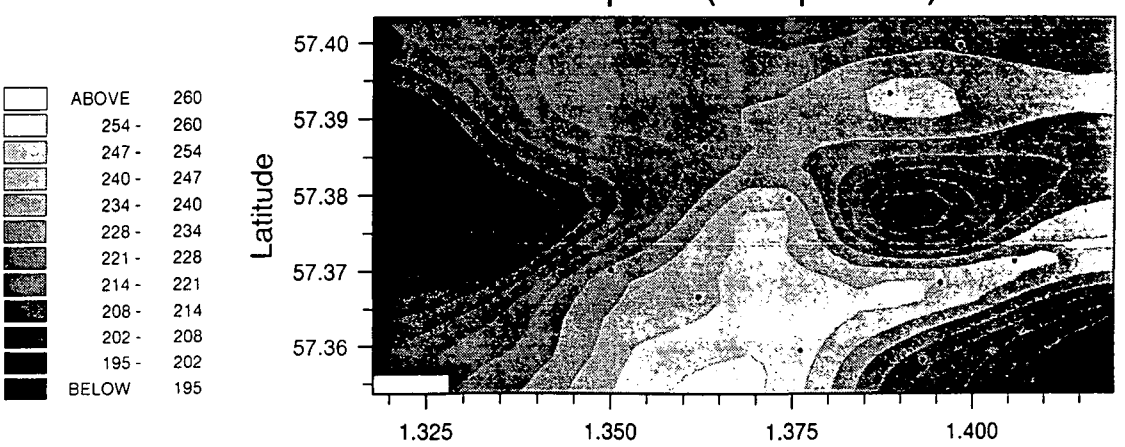

Top 14 (compacted)

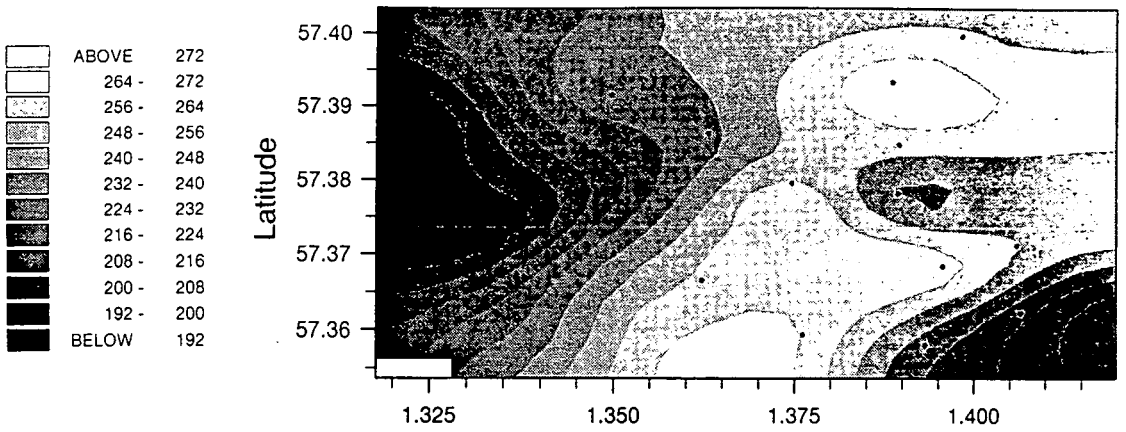

Top 13 (compacted)

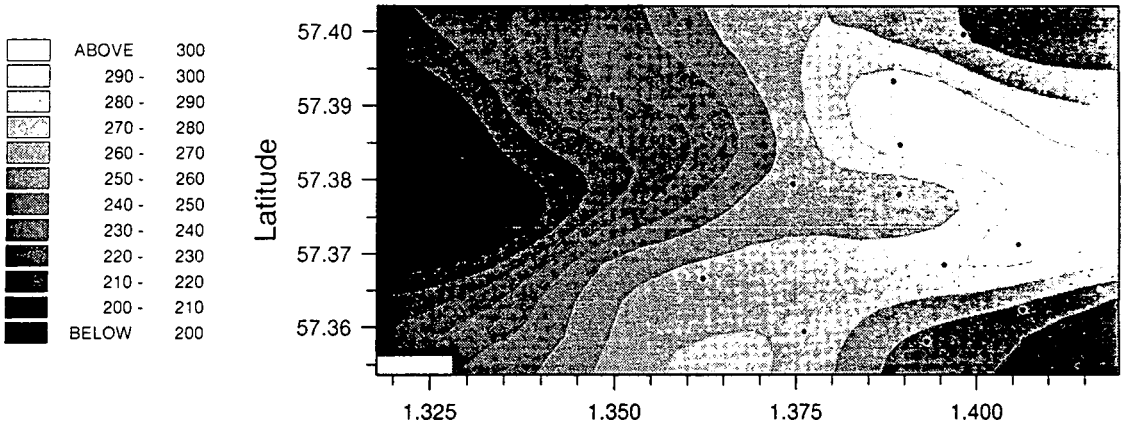

Top 12 (compacted)

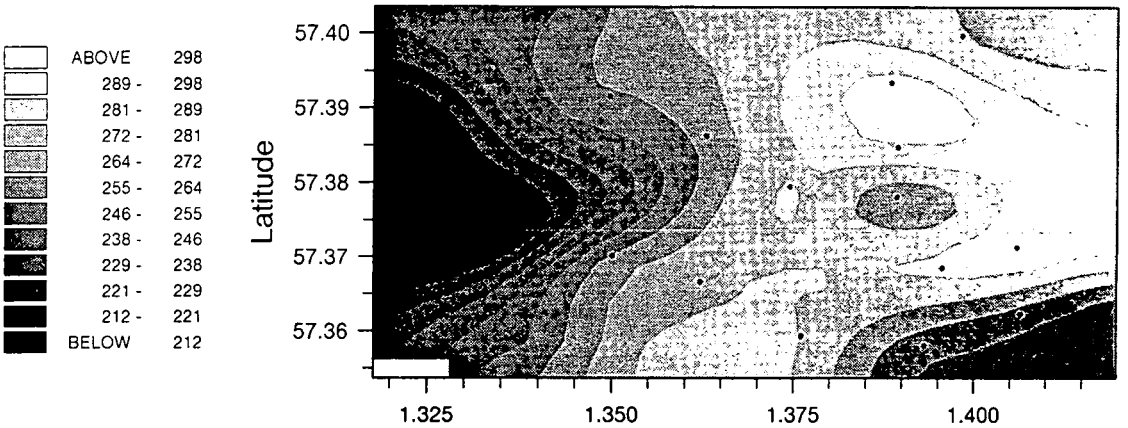

Top 9 (compacted)

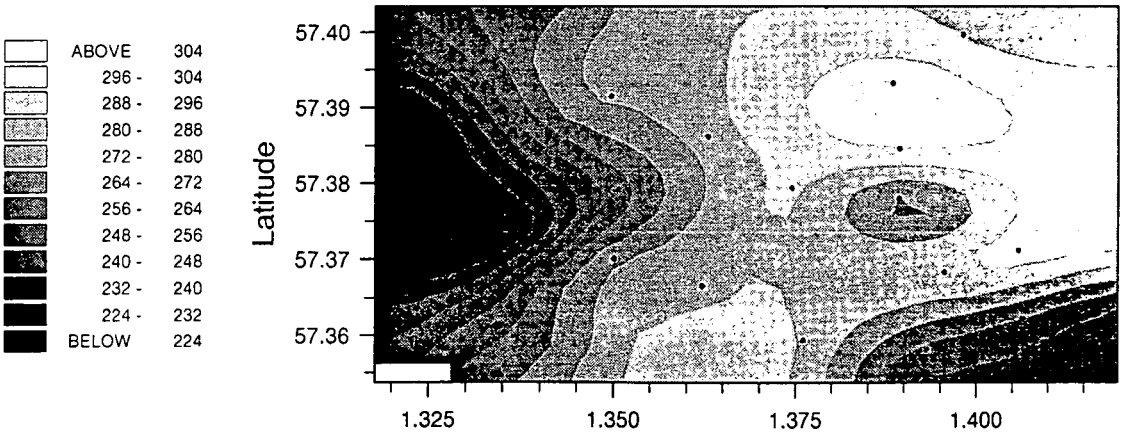

Top 5 (compacted)

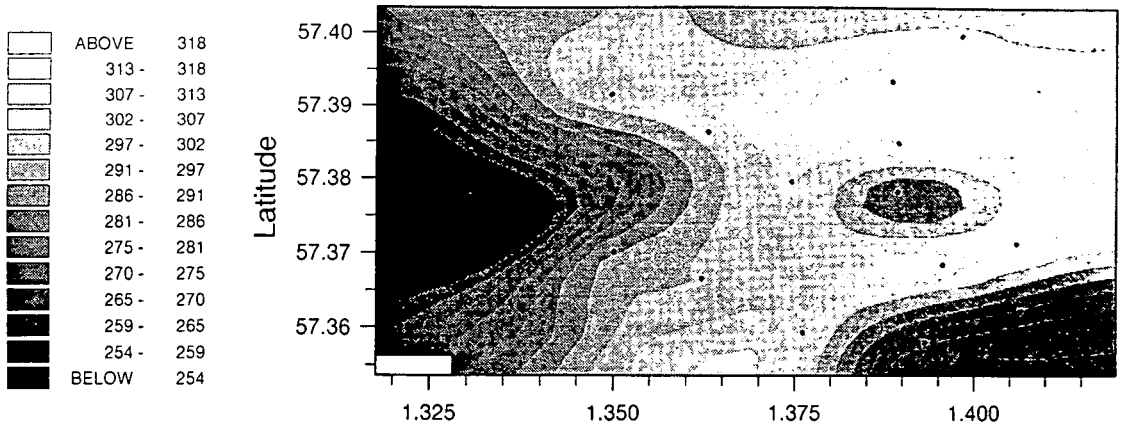

Top 3 (compacted)

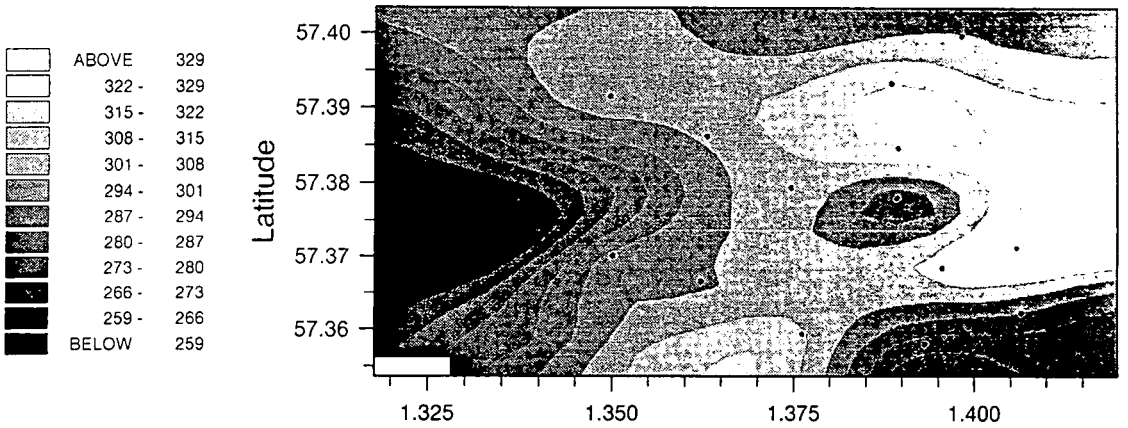

Top 4 (compacted)

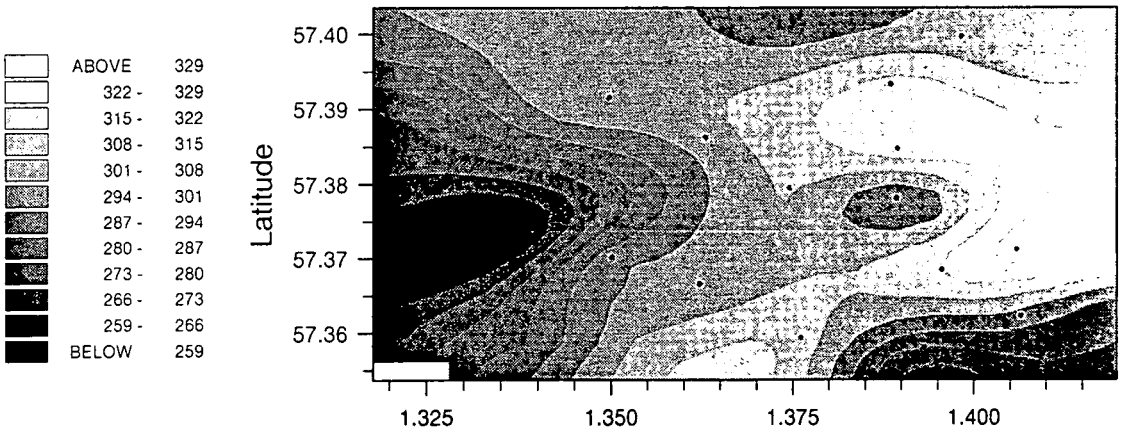

Top 1 (compacted)

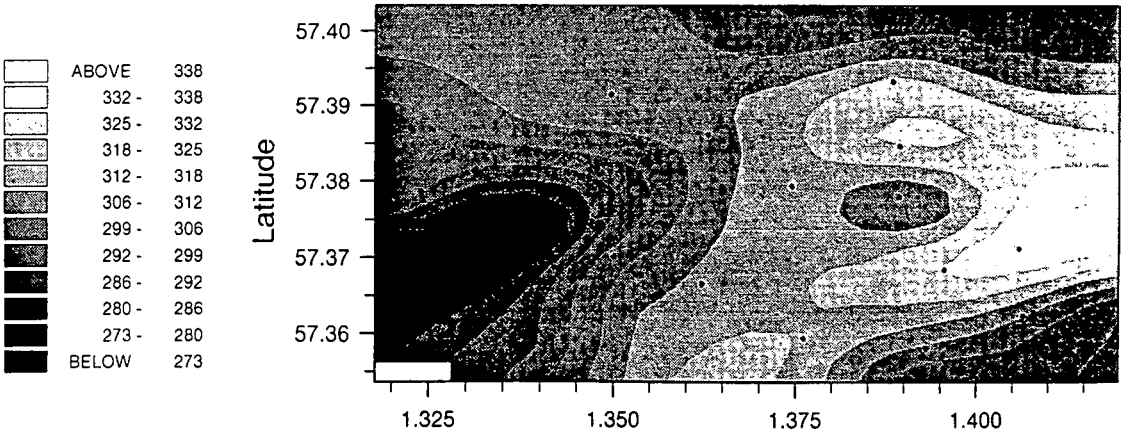

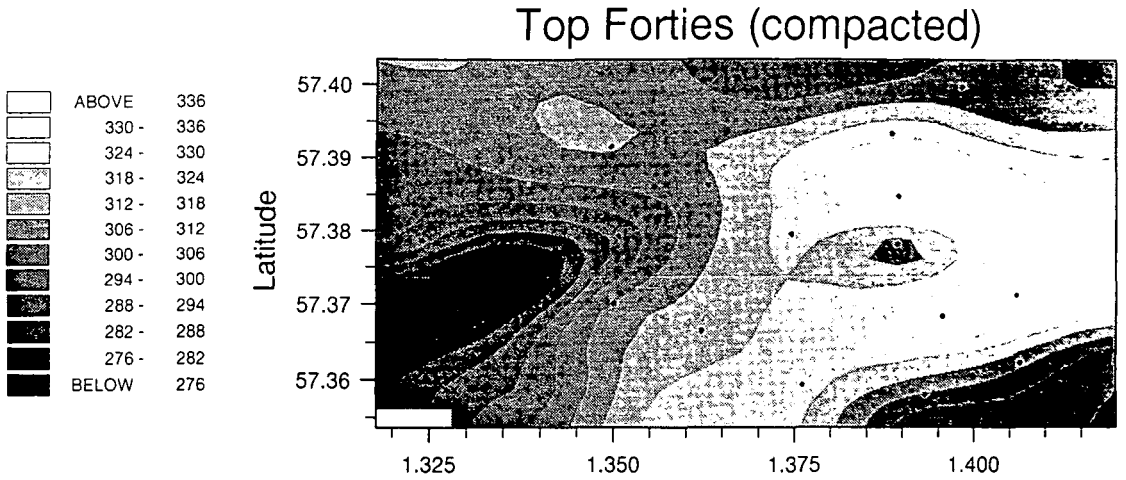
Top Forties (compacted)
ABOVE 336
330 - 336
324 - 330
318 - 324
312 - 318
306 - 312
300 - 306
294 - 300
288 - 294
282 - 288
276 - 282
BELOW 276
Latitude
57.40
57.39
57.38
57.37
57.36
1.325
1.350
1.375
1.400

Top 19 (compacted)

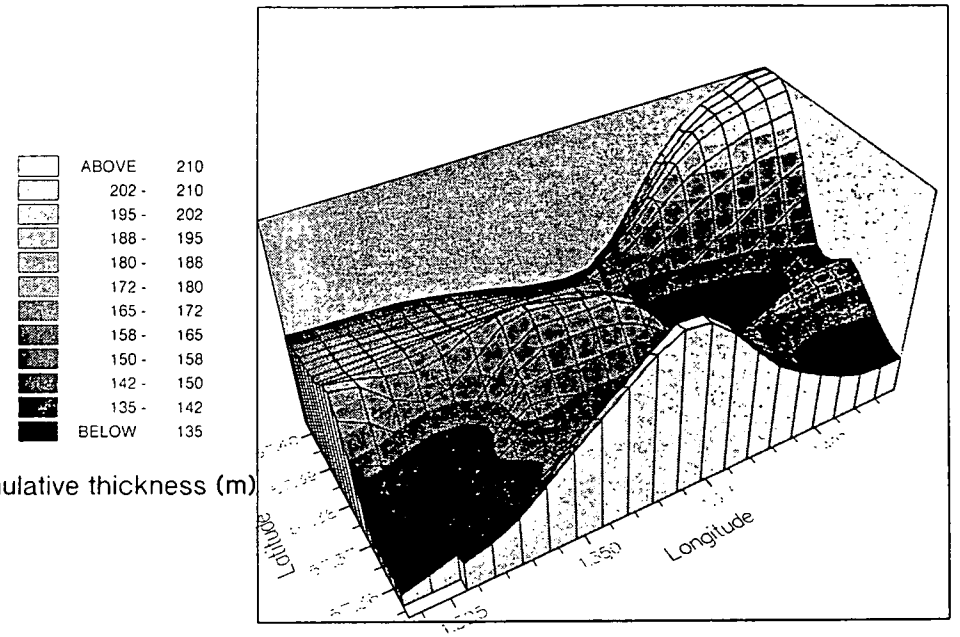

Top Lista (compacted)

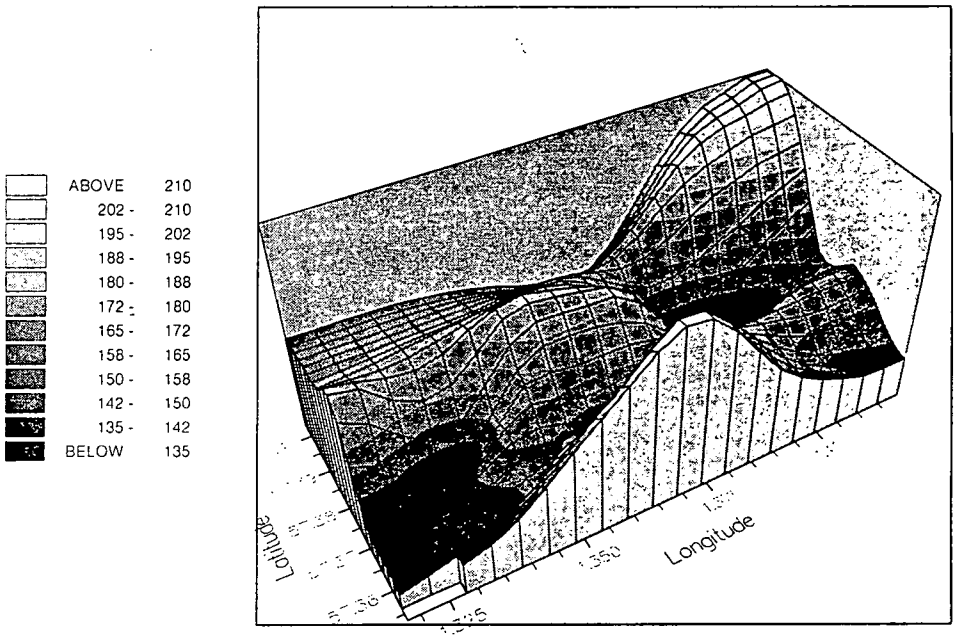

Top 18 (compacted)

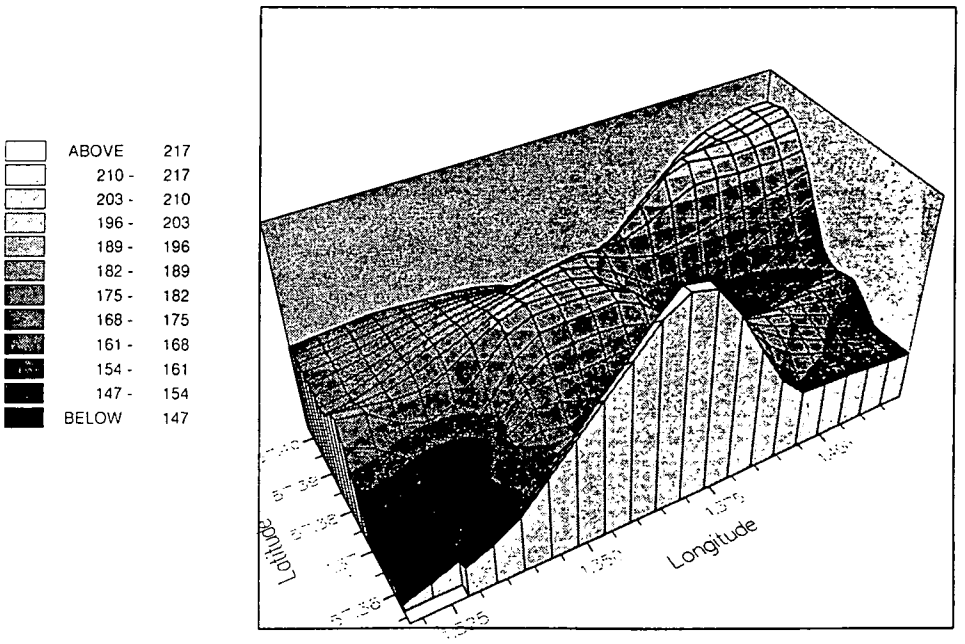

Top B (compacted)

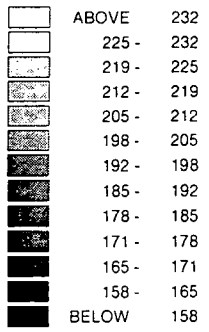

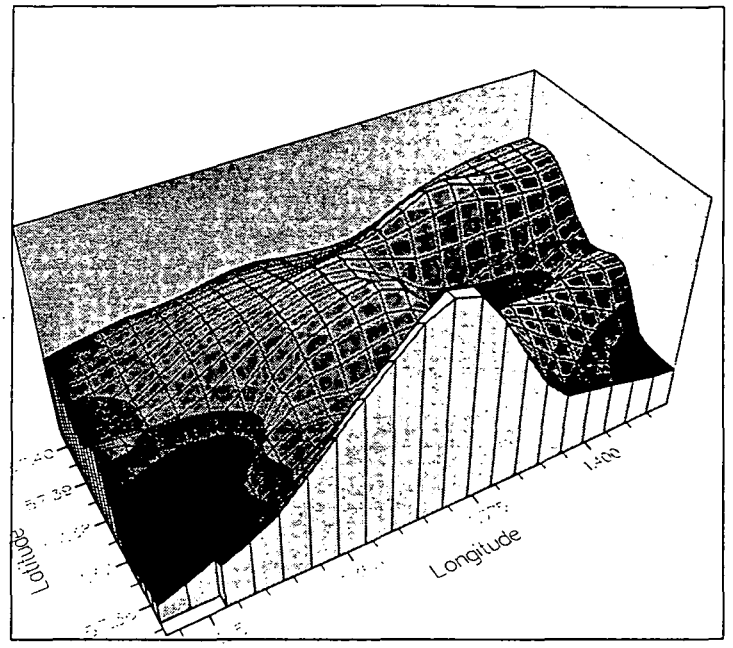

Top 17 (compacted)

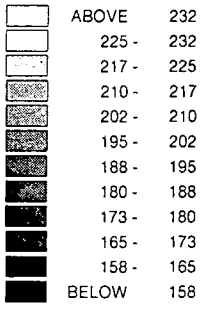

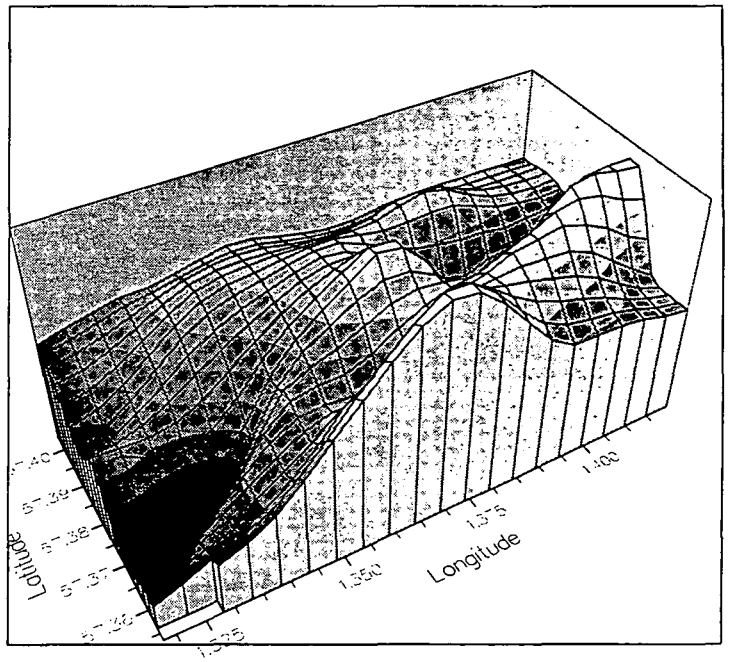

Top 16 (compacted)

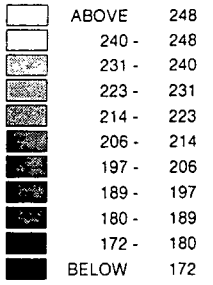

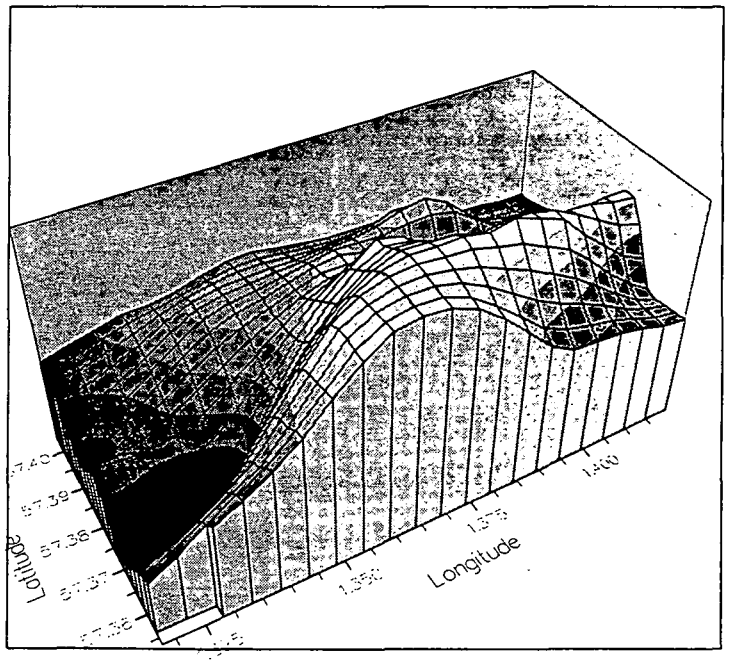

Top A (compacted)

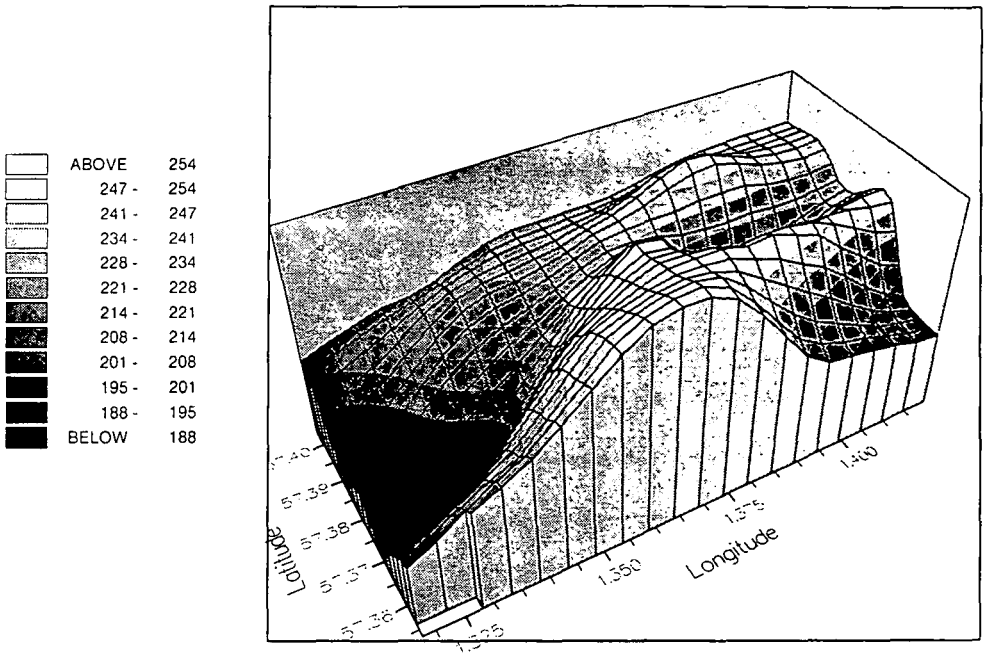

Top 15 (compacted)

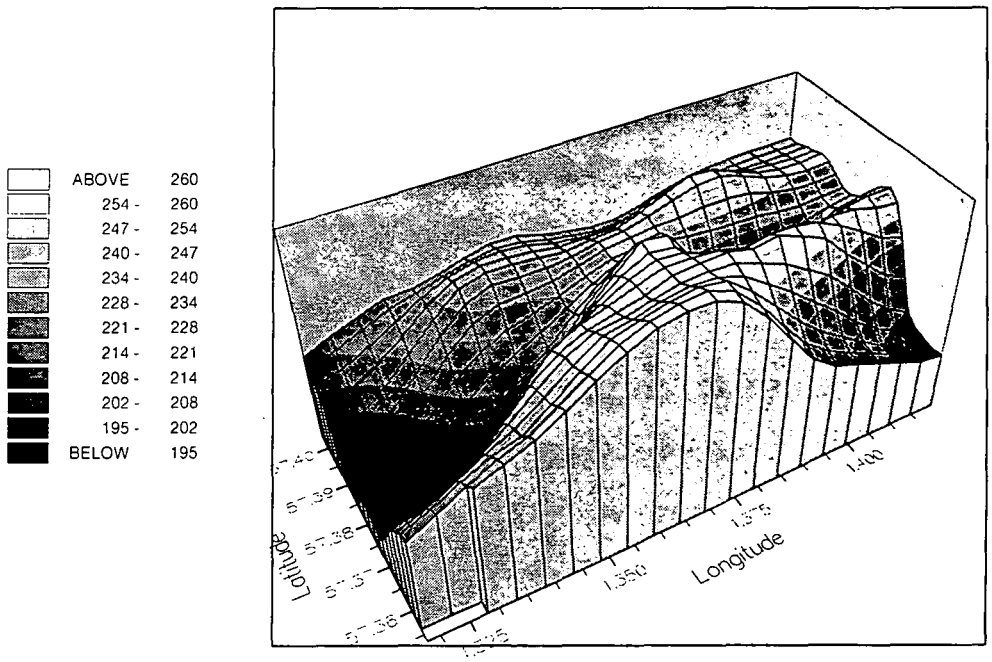

Top 14 (compacted)

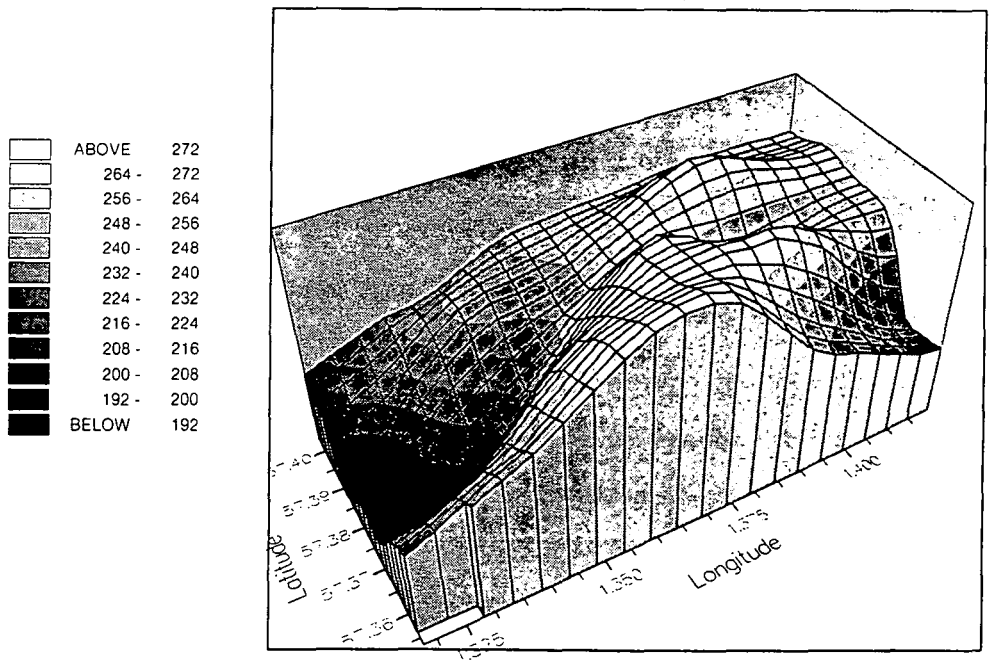

Top 13 (compacted)

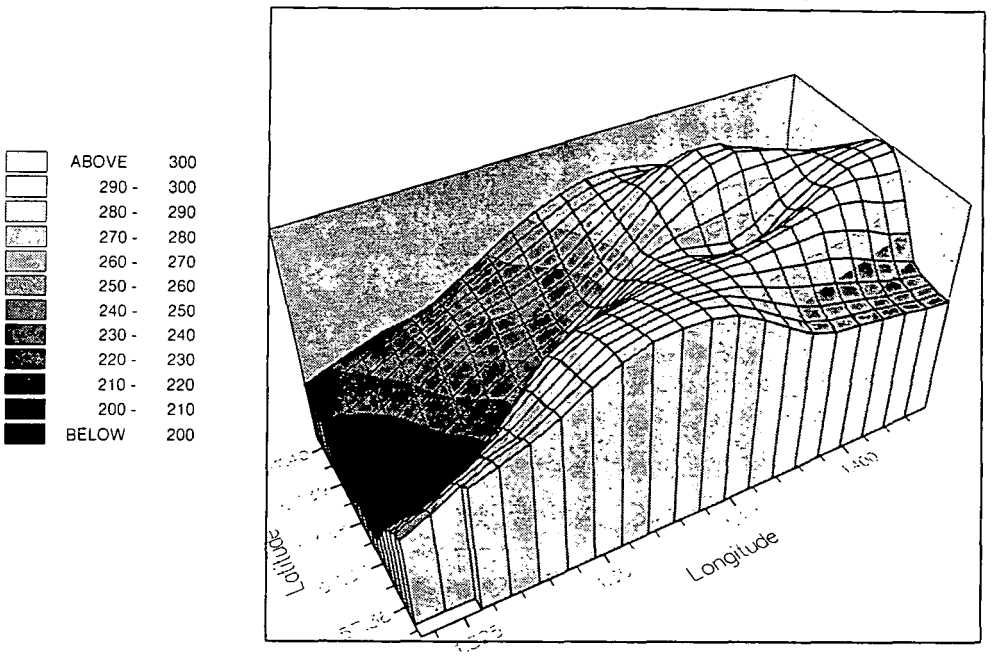

Top 12 (compacted)

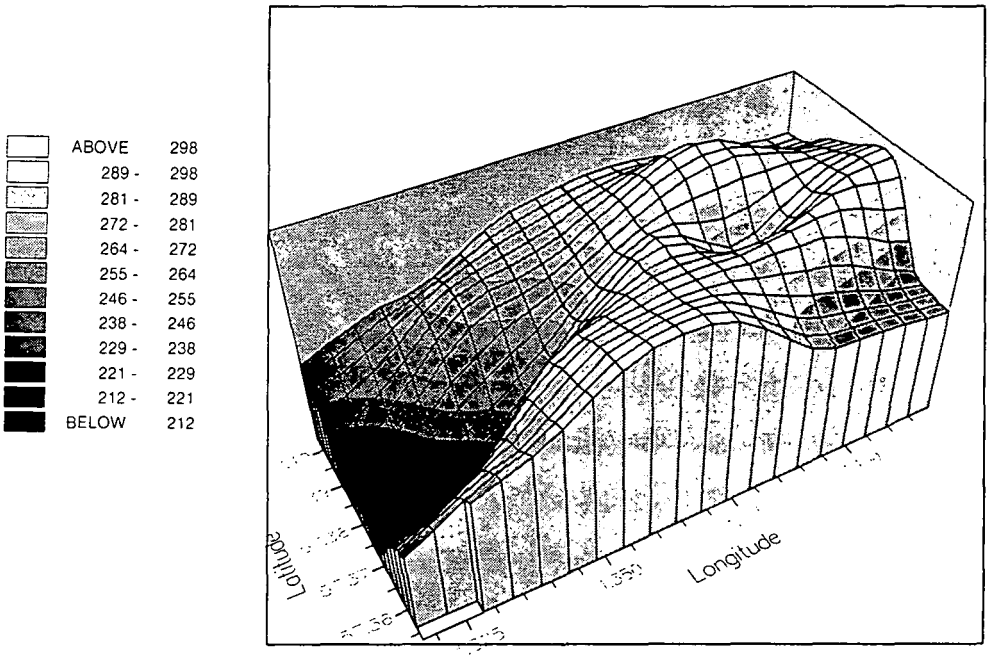

Top 9 (compacted)

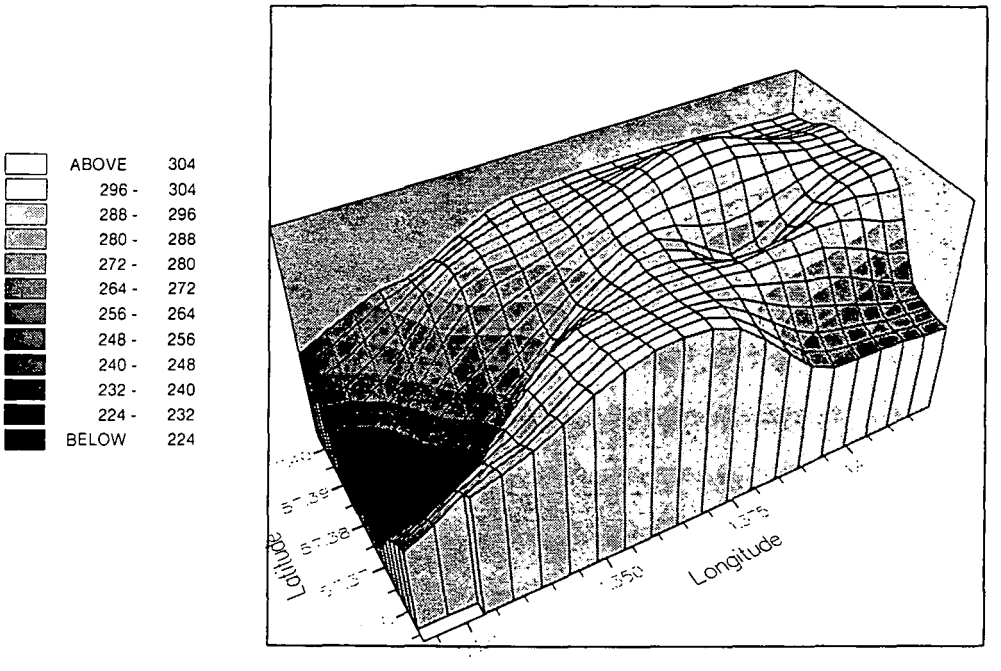

Top 5 (compacted)

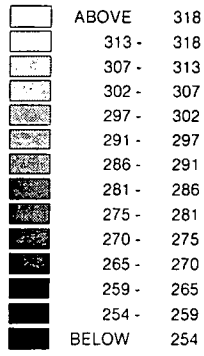

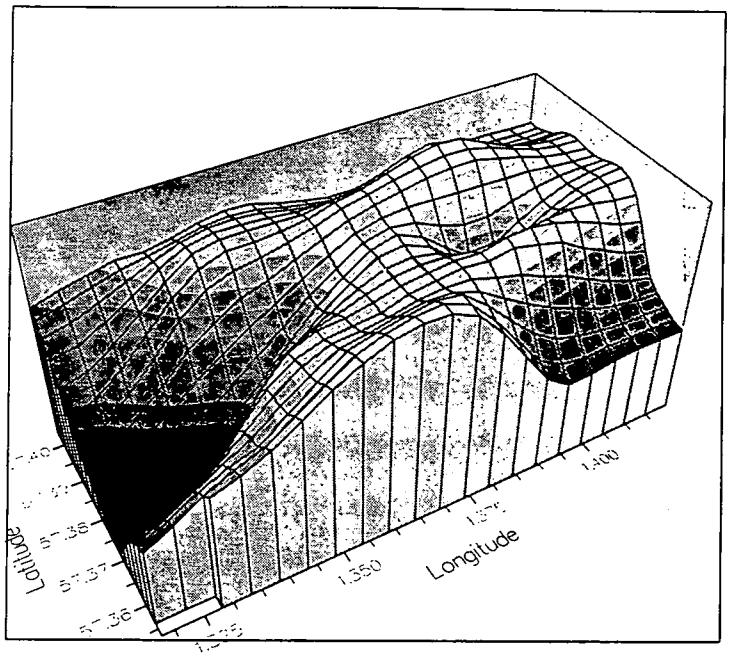

Top 3 (compacted)

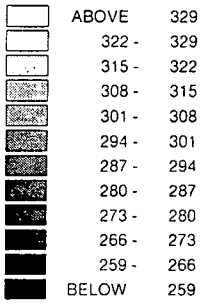

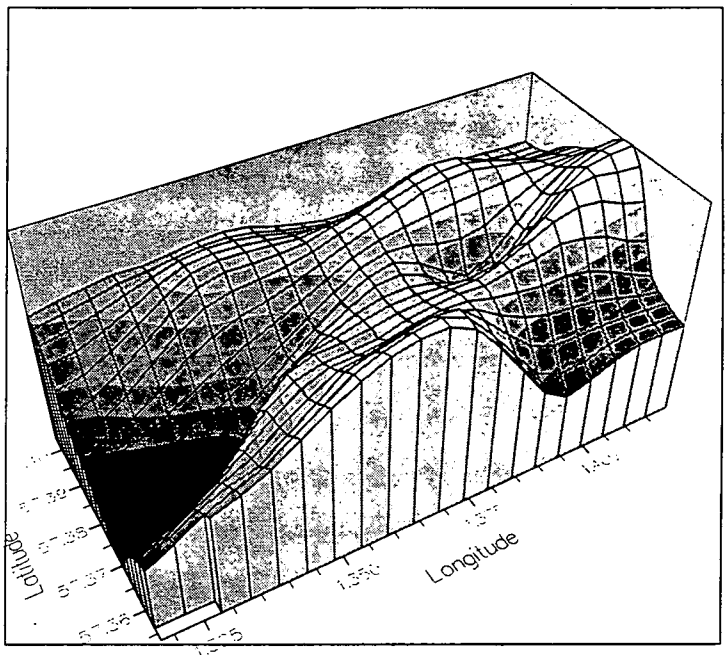

Top 4 (compacted)

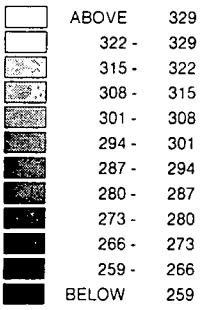

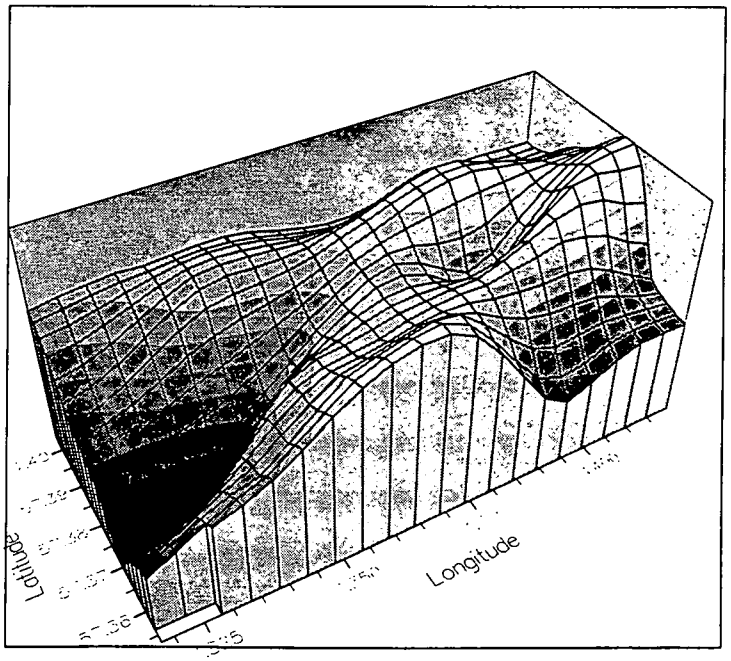

Top 1 (compacted)

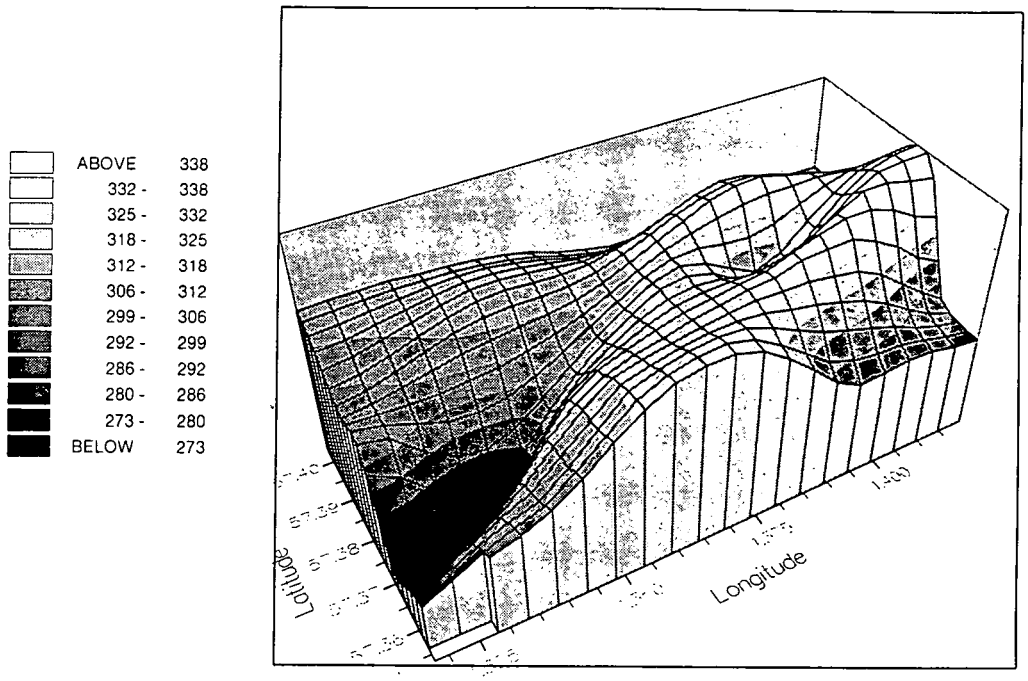

Top Forties (compacted)

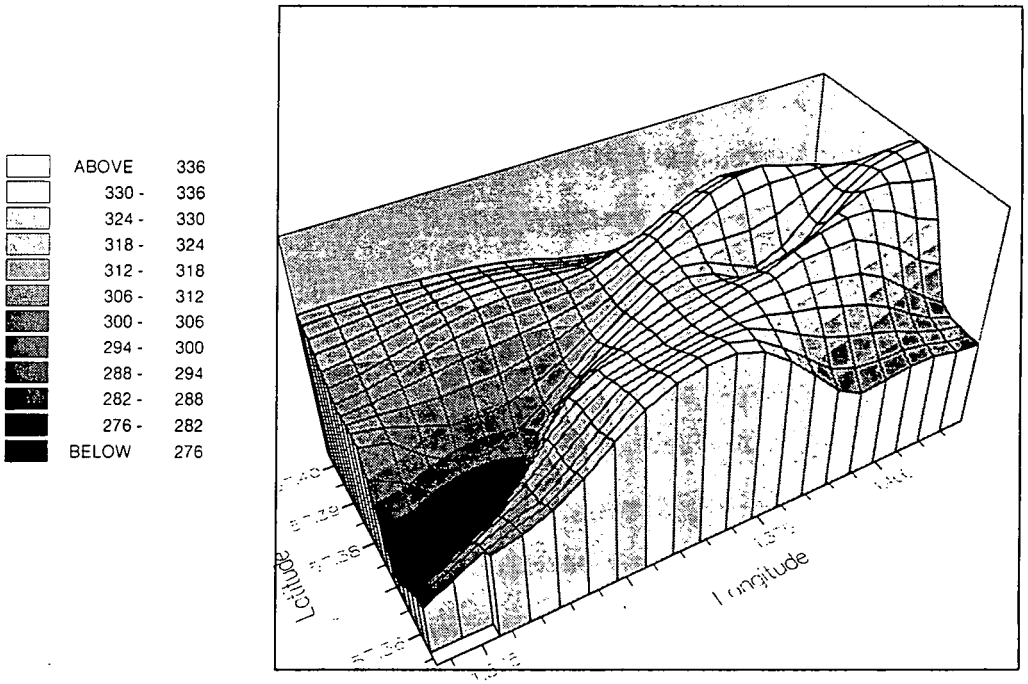

Appendix 2.

TOP UNIT 19 SURFACE - DEPOSITION OF LISTA ISOPACH.

Maximum Lista Thickness	No. of Depositional Sites	Uncompacted MLDS	No. of Uncompacted Matches	Compacted MLDS	No. of Compacted Matches	Topographic Control on Deposition	Deposition in Alternative Areas
14m *(Thin)*	14	14	2 (14%)	30	7 (50%)	A5-A6	B3-B6, C3-C6, D7-D8.

Other Areas of Deposition	**Uncompacted Relief**	**Compacted Relief**	Total % Sand Below	% Sand in Previous Unit.
B3-B6	Fairly low lying saddle area.	Area lowered further by compaction, making B6 a MLDS.	Medium (54%)	V. Low (<7%)
C3-C6	Minor high topographic area.	Area lowered and smoothed making C3 a MLDS.	Low (<45%)	V. Low (<10%)
D7-D8	Low saddle area around T3 on an east-west ridge, between highs at T13 and T4	Saddle area is lowered making the entire area a MLDS	V. Low (<32%)	V. Low (<7%)

General Observations

The Lista unit is a relatively thin, mud-rich isopach (>60% mud), and tends to be sandier where the isopach is thinner (<10m). Sands are deposited within the northern channel around T5, T9 and T17 on the southern slope of the locally high area. Another sand concentration forms in the southern channel around T10 and T6, again on the southern slope of minor high topography, within a small east-west embayment. The thickest part of the Lista isopach may therefore represent a levee deposit along the line of T20-T16-T2-T3 separating the two channels.

TOP LISTA SURFACE - DEPOSITION OF UNIT 18 ISOPACH.

Maximum Unit 18 Thickness	No. of Depositional Sites	Uncompacted MLDS	No. of Uncompacted Matches	Compacted MLDS	No. of Compacted Matches	Topographic Control on Deposition	Deposition in Alternative Areas
32m *(Moderate)*	23	16	13 (57%)	26	15 (65%)	A5-A7, B7-B9, C7-C9, E2, E9-E10.	A4 and A8, B4-B6, D7-D8, E3-E6, E8.

Other Areas of Deposition	**Uncompacted Relief**	**Compacted Relief**	Total % Sand Below	% Sand in Previous Unit.
A4 and A8	Both these areas are relatively low lying at either ends of a MLDS, with A8 lying on an easterly up-slope.	Area lowered further by compaction, and making the slopes less steep. isopach of unit 18 wedges out against this slope.	Moderate (54-63%)	Low (<16%)
B4-B6	Northern edge of a moderate topographic high area.	Area lowered to a gentle slope, making B6 a MLDS.	Low (<50%)	Low (<16%)
D7-D8	Moderate flat region.	Lowered to form a low-lying saddle region making the area a MLDS.	V. Low (<32%)	Low (<16%)
E3-E6	Slope area at E3 up to high area at E6.	Similar geometry after compaction, but E3 is lowered to become a MLDS.	Variable E6-E3 (<54%-<32%)	V. Low (<12%)
E8	Moderate to low slope region.	Lowered to become a MLDS.	V. Low (<32%)	Low (<24%)

General Observations

The unit 18 isopach is thickest around T5, T17 and T8 area and tends to form a ridge flanking the southern channel along T20-T16-T2. Sand percentages for unit 18 show that they tend to flow mainly along the southern channel of T19, but only just reach T14. therefore the isopach ridge is mainly mud-rich and possibly formed as a levee. Sand also just shows in the northern part of the northern channel around T15. Sand in both cases is deposited within fairly low lying regions, generally on the northern up-slope side of minor topographic highs.

TOP UNIT 18 SURFACE - DEPOSITION OF UNIT B ISOPACH.

Maximum Unit B Thickness	No. of Depositional Sites	Uncompacted MLDS	No. of Uncompacted Matches	Compacted MLDS	No. of Compacted Matches	Topographic Control on Deposition	Deposition in Alternative Areas
30m *(Moderate)*	22	13	6 (27%)	25	11 (50%)	A5-A7, C7, C9, D3.	A3-A4, C5-C6, C10, D4-D10, E2-E5.

Other Areas of Deposition	**Uncompacted Relief**	**Compacted Relief**	Total % Sand Below	% Sand in Previous Unit.
A3-A4	Fairly low lying areas, north of minor high.	Compaction lowers and flattens this area, creating a low flat region where most of unit B is deposited behind the T16 high. Damming of high at T16 and T5 probably constrain unit B.	Moderate (50-63%)	Moderate (<64%)
C5-C6	The southern edge of T16 high region that slopes south to south-east.	Creates an easterly slope into the topographic low area at C7-C10.	Low (<45%)	Moderate (<45%)
C10	Low area, close to MLDS.	Lowered to form a MLDS.	Low (32-54%)	Moderate (<45%)
D4-D10	Low area at D4 which rises over a saddle region in the middle, dropping to a similar low area at T10. The saddle forms across a north-south ridge, on the northern side of a high area around T4 in the south of the region.	Saddle height is greatly reduced by compaction, making the extremities of D4-D5 and D10 MLDS. Therefore, the overall width of the saddle is reduced as well as lowered.	V. Low (<36%)	Low (<36%)
E2-E5	Western slope from the topographic high at T4, where E2 is close to a MLDS, but E5 is quite high.	Slope is lowered and its steepness is reduced making E2-E3 a MLDS.	Low (<50%)	Moderate (<45%)

General Observations

Unit B shows the northern channel extremely well with the sand % map, which is only slightly off-set from the thick on the isopach map. It illustrates that the northern channel is confined by the northern highs at T16 and T9, and therefore the sand banks upon the northern edge of this high region. Sediment which breaches across the ridge by the saddle between T16 and T5 banks against the southern high around the T4 area, forcing the sediment to spread east and west. Sediment preferentially spreads east into the topographically low areas where sand is ponded.

TOP UNIT B SURFACE - DEPOSITION OF UNIT 17 ISOPACH.

Maximum Unit 17 Thickness	No. of Depositional Sites	Uncompacted MLDS	No. of Uncompacted Matches	Compacted MLDS	No. of Compacted Matches	Topographic Control on Deposition	Deposition in Alternative Areas
50m *(Thick)*	9	16	3 (33%)	23	8 (89%)	C8-C9, E10.	C10, D8-D10, E8-E9.

Other Areas of Deposition	**Uncompacted Relief**	**Compacted Relief**	Total % Sand Below	% Sand in Previous Unit.
C10	Eastern edge of moderate/low area, close to being a MLDS.	Lowered to form a MLDS.	Low (<54-<40%)	Low (<36%)
D8-D10	Moderate ridge area running ENE from the high area around T4, and separating two low areas at T8 and T11Z.	Greatly reduced ridge height, with lesser gradients and larger MLDS either side	V. Low (<36%)	Variable, N-S (<18-81%)
E8-E9	Low area on south-eastern slope from high area and ridge around T4.	Slope is lowered into a MLDS with E10.	V. Low (<40%)	Variable E8-E9 (<45-81%)

General Observations

The unit 17 isopach shows a ridge area running down the middle channel line of T20-T16-T2. Where the isopach is thinner, especially in the northern side, sand is concentrated in the northern channel around T15. Being a thick unit, more sediment was able to breach the lowered saddle area between T16 and T5, so that not only was sand dumped where gradients increased at T15, but also made it over into the southeast corner of the region around T3, T13, T18, T11Z and T11. Here, the sands lay slightly off-set from the thick sands of unit B below. Also, where the isopach is thin along the southern channel, sands are again found around T19 and T14.

TOP UNIT 17 SURFACE - DEPOSITION OF UNIT 16 ISOPACH.

Maximum Unit 16 Thickness	No. of Depositional Sites	Uncompacted MLDS	No. of Uncompacted Matches	Compacted MLDS	No. of Compacted Matches	Topographic Control on Deposition	Deposition in Alternative Areas
66m *(Thick)*	7	6	0 (0%)	19	3 (43%)	-	D3-D6, E3-E5.

Other Areas of Deposition	**Uncompacted Relief**	**Compacted Relief**	Total % Sand Below	% Sand in Previous Unit.
D3-D6	Low area in the west, sloping up to the east to the top of a fairly high ridge area at D6. An embayment into the ridge occurs along this line.	The area is lowered making D3-D5 a MLDS, along with widening the embayment into a now lowered ridge.	V. Low (40-<32%)	Low (38-<10%)
E3-E5	Northeast slope area from a high at E5 to a low at E3.	Slope is lowered.	V. Low (50-<36%)	High (86-<48%)

General Observations

The isopach of unit 16 is rather curious, and appears to pond as a lobe shape behind the high southern ridge area from T4-T3-T13, spilling slightly into the western low around T1. Again sand concentrations are higher where the isopach is thin, showing both the northern and southern channels very well. The northern channel sand body is slightly dammed by the small ridge between T16 and T5, but some sand is deposited over the other side into the minor low around T17 and T8, where the unit is <18m thick. The southern channel also appears to be outlined as well, running along T19-T14-T10-T12-T1, with larger concentrations of sand found around T4 and T18 in a lobe shaped deposit. Here, the isopach is slightly thicker, and the sand may be dammed by the southern ridge of T4-T3-T13, with small amounts overspilling into the southeast corner. The southern channel sands appear to sit over the low area within the total % sand concentration of the Arbroath area.

TOP UNIT 16 SURFACE - DEPOSITION OF UNIT A ISOPACH.

Maximum Unit A Thickness	No. of Depositional Sites	Uncompacted MLDS	No. of Uncompacted Matches	Compacted MLDS	No. of Compacted Matches	Topographic Control on Deposition	Deposition in Alternative Areas
44m *(Medium)*	11	9	3 (33%)	23	8 (73%)	C7-C9	A7-A10, B7-B10.

Other Areas of Deposition	**Uncompacted Relief**	**Compacted Relief**	Total % Sand Below	% Sand in Previous Unit.
A7-A10	Low area behind the minor northern ridge between T5 and T16.	The area is lowered and flattened, along with the lowering of the ridge area, resulting in the eastern end (A9-A10) becoming a MLDS.	High (>63%)	Variable A7-A9 (58-<6%)
B7-B10	Minor high area at B7 where the ridge is encountered, which lowers towards the east. The area also slopes south into the MLDS at C7-C9.	The area is lowered by compaction, resulting in the flattening and widening of the MLDS.	High (58-<72%)	Variable B7-B10 (46-<6%)

General Observations

Unit A differs from other chronostratigraphic units as it has the greatest percentage sand where the units is thickest. It therefore appears that unit A flowed down the northern channel of T15-T9-T5, before spilling over the compactionally lowered northern ridge between T5 and T16, to fill the small low area around T17 and T8. Sediment was probably trapped in this area by the major east-west ridge between T4-T3-T13, resulting in the filling of the major topographic low areas of the Top unit 16 surface. Minor amounts of sand also flowed down the southern channel, found in the T12 to T4 area. However, the isopach of unit A is, in general, less than half the thickness here than it is in the northern channel.

TOP UNIT A SURFACE - DEPOSITION OF UNIT 15 ISOPACH.

Maximum Unit 15 Thickness	No. of Depositional Sites	Uncompacted MLDS	No. of Uncompacted Matches	Compacted MLDS	No. of Compacted Matches	Topographic Control on Deposition	Deposition in Alternative Areas
24m *(Thin)*	13	14	6 (46%)	19	8 (62%)	C2-C3, D1-D3, E1.	A1-A3, B3-B4, D4, E2-E3.

Other Areas of Deposition	**Uncompacted Relief**	**Compacted Relief**	Total % Sand Below	% Sand in Previous Unit.
A1-A3	Low southwest slope area toward the T19 region.	The area is lowered and the slope is lessened making A1 a MLDS.	Low (<50%)	V. Low (17-<8%)
B3-B4	Moderate area forming an embayment up into the central high area.	Area greatly lowered, with the smoothing of topography around T6 and T20.	Low (<50%)	V. Low (17-<8%)
D4	Moderate/high area on the northwest slope to the high at T1 and T4, but still directly connected to the low regions of C1-C3, D1-D3.	Slope is lowered.	V. Low (<40%)	V. Low (<17%)
E2-E3	Same low/moderate northwest slope area as described for D4.	Slope is greatly lowered making E2 a MLDS, and lowering E3.	v. Low (<45%)	Low (34-<26%)

General Observations

Sand percentages appear to show the northern channel again, with a possible sandy levee along the line of the middle channel of T20-T16 where the isopach is considerably thicker. However, the southern channel appears to be the main depositional area with the isopach being thick along with the sand percentage, especially into the south. It appears that the sand is banked against the southern high area around T4, and spills east and west to fill the topographic low areas in the SE and SW corners.

TOP UNIT 15 SURFACE - DEPOSITION OF UNIT 14 ISOPACH.

Maximum Unit 14 Thickness	No. of Depositional Sites	Uncompacted MLDS	No. of Uncompacted Matches	Compacted MLDS	No. of Compacted Matches	Topographic Control on Deposition	Deposition in Alternative Areas
44m *(Moderate)*	6	13	3 (50%)	22	3 (50%)	C7-C9.	B7-B9.

Other Areas of Deposition	**Uncompacted Relief**	**Compacted Relief**	Total % Sand Below	% Sand in Previous Unit.
B7-B9	Southern facing gentle slope area, into the narrow low area of C7-C9.	This area is steepened as the low area of C7-C9 is lowered and widened.	Moderate (50-68%)	Low (38-<19%)

General Observations

Generally unit 14 is controlled by topography, filling the hollow which is widened by compaction around T8, and banking the sediment against the ridge of T4-T3-T13. The sand percentages of unit 14 mainly show the northern channel, with the sand lost early as the first ridge (T20-T16-T5) is crossed. The topographic low around T8 is mainly mud filled, with sand deposited on the flanks of the further high at T4, and minor sands spilling over the south ridge into the SE corner. Some minor sand is also seen in the southern channel around T19, but the isopach is very thin here (<8m).

TOP UNIT 14 SURFACE - DEPOSITION OF UNIT 13 ISOPACH.

Maximum Unit 13 Thickness	No. of Depositional Sites	Uncompacted MLDS	No. of Uncompacted Matches	Compacted MLDS	No. of Compacted Matches	Topographic Control on Deposition	Deposition in Alternative Areas
54m *(Thick)*	10	10	2 (20%)	19	4 (40%)	E9-E10.	B7-B9, C8-C10, D9-D10.

Other Areas of Deposition	**Uncompacted Relief**	**Compacted Relief**	Total % Sand Below	% Sand in Previous Unit.
B7-B9	High region around T5 and T17, forming the peak of the north area, with the ridge running SSW from here to the T4 area. This region is just on the south slope.	Compaction lowers the area of the southern slope into the minor low that still exists around T8. The isopach wedges out against this slope.	Moderate (68-52%)	Moderate to High (50-80%)
C8-C10	Moderate embayment area on the main SSW ridge.	Compaction lowers the embayment making C8 a minor MLDS.	Low (56-<44%)	Low (30-50%)
D9-D10	Southeast dipping slope area from the embayment described above (T13 region), to low at E10 (T11 region).	Area lowered making D10 a MLDS.	Low (44-52%)	Variable N-S (30-80%)

General Observations

Both the isopach map and the map of sand concentration show more or less identical patterns for unit 13. The northern channel is excellently outlined from T15-T5-T17-T8 and spilling over into the T3-T11 area. It appears that sediment within the northern channel was able to overcome the small ridge in the north, and spill over into the embayment which was compactionally enhanced. Some sand was trapped by the northern high, but large amounts made it across as well, to become deposited around T3, T13, T18, T11Z and T11. A thinner area of deposition is also found in the southwest corner around the line of the southern channel, where the section is also very sandy. It therefore also appears that the southern channel was also operative at this stage with slightly less sediment supplied to it. However, this sandy sediment was fed down T10-T12-T1-T4 and ponded against the southern high region just south of T1 and T4, forming a lobate deposit.

TOP UNIT 13 SURFACE - DEPOSITION OF UNIT 12 ISOPACH.

Maximum Unit 12 Thickness	No. of Depositional Sites	Uncompacted MLDS	No. of Uncompacted Matches	Compacted MLDS	No. of Compacted Matches	Topographic Control on Deposition	Deposition in Alternative Areas
33m *(Moderate)*	15	8	4 (27%)	19	11 (73%)	A1, B1-B2, C3.	A2-A5, B3-B6, C4-C6.

Other Areas of Deposition	**Uncompacted Relief**	**Compacted Relief**	Total % Sand Below	% Sand in Previous Unit.
A2-A5	Low gentle slope region up to the east, to the ridge at T15.	Compaction lowers the slope considerably, making A2 and A3 MLDS.	Variable A2-A5 (<44-76%)	Variable A2-A5 (<20-70%)
B3-B6	Similar gentle slope region as described above, sloping down to the west, to the MLDS at B1-B2. Forms the northern edge of an embayment.	Compaction reduces the slope and widens the MLDS area.	Low (56-<44%)	Variable B3-B6 (<10-60%)
C4-C6	Low gentle slope region along an embayment into the main ridge, up from the MLDS at C3 (T6 region) up to the T2 area.	Compaction lowers and widens the embayment.	V. Low (<44%)	Moderate (<30-60%)

General Observations

The unit 12 isopach shows the middle channel well. But, here the unit is generally mud-rich suggesting a possible levee. However, this area is one of the lowest regions, and the mud-rich nature probably represents the filling of this low area by early or late mud deposition. Sand concentrations again appear to be highest down the length of the northern channel where the isopach is thin. These sands are found slightly off-set further north than those of the underlying unit 13 (i.e. off-set channel sands), banked behind the easterly ridge running from T5, T17 area, SE towards T13. As before, high proportions of sand are also found right across the entire southern region which appears to suggest flow down the southern channel. Sands are then ponded against the southern high area just south of T1 and T4. Some sand spills over the saddle between T4 and T3 into the SE region around T11Z and T11.

TOP UNIT 12 SURFACE - DEPOSITION OF UNIT 9 ISOPACH.

Maximum Unit 9 Thickness	No. of Depositional Sites	Uncompacted MLDS	No. of Uncompacted Matches	Compacted MLDS	No. of Compacted Matches	Topographic Control on Deposition	Deposition in Alternative Areas
30m *(Moderate)*	13	9	4 (31%)	13	8 (62%)	B2, C2-C3, D2.	A1-A4, B3-B5, C4-C5.

Other Areas of Deposition	**Uncompacted Relief**	**Compacted Relief**	Total % Sand Below	% Sand in Previous Unit.
A1-A4	Low slope to the west, with approximately 50m relief.	Compaction lowers the slope but steepens it to approximately 60m relief, with A1-A2 becoming a MLDS.	Variable A1-A4 (<52-64%)	Low for unit 12 (<67%)
B3-B5	Similar slope region as described above, sloping down to the west, therefore low at B3, becoming moderate to high at B5.	Compaction significantly reduces the entire slope making B3 a MLDS, and widening the embayment into the main N-S ridge. The isopach of unit 12 pinches out against this slope.	V. Low (<48%)	V. Low (<33%)
C4-C5	Slope of embayment into the main N-S ridge, with approximately 45m of relief.	Compaction lowers and widens the embayment.	V. Low (<48%)	Variable N-S (22-78%)

General Observations

Sediment distribution for unit 9 appears to show that both the nothern and middle channels were operating at these times. The isopach is thickest within the middle channel where it ponds in the main low embayment area around T6 and the west. Sand percentages show how sand is deposited in the NW corner of the middle channel around T20 and T16. Some sand may also have made it over the high ridge where mud is deposited, and is dumped in the SW corner around T3, T13, T11 and T11Z. However, this may have been added to by sand travelling down the northern channel where the isopach is considerably thinner (<8m).

TOP UNIT 9 SURFACE - DEPOSITION OF UNIT 5 ISOPACH.

Maximum Unit 5 Thickness	No. of Depositional Sites	Uncompacted MLDS	No. of Uncompacted Matches	Compacted MLDS	No. of Compacted Matches	Topographic Control on Deposition	Deposition in Alternative Areas
54m *(Thick)*	4	13	4 (100%)	15	4 (100%)	A1, B1-B2, C1.	-

General Observations

The deposition of unit 5 can be explained completely by topographic control. From B1-B2 there is approximately 50m of relief once compaction has occurred, which is the entire height of the main ridge in this area. as unit 5 is only 54m thick at its maximum it was ponded and restricted by this topography. The area of deposition is also very low for total % sand below, and is moderate for sand immediately below in unit 9. Therefore, the area was very compactible during loading. It appears that the southern channel was the main axis of sediment, with sand percentages being fairly high here. Sand is often found where the isopach is thinnest, once sediment made it over the initial barrier. Therefore, high concentrations of sand are found on the northern flanks of the southern high region around T1 and T4. Sand concentrations are also high around T17 and T13 on the flanks of minor high areas, suggesting sediment also came down the northern channel, with minor sands possibly coming down the middle channel too.

TOP UNIT 5 SURFACE - DEPOSITION OF UNIT 3 ISOPACH.

Maximum Unit 3 Thickness	No. of Depositional Sites	Uncompacted MLDS	No. of Uncompacted Matches	Compacted MLDS	No. of Compacted Matches	Topographic Control on Deposition	Deposition in Alternative Areas
24m *(Thin)*	7	12	3 (43%)	15	5 (71%)	B1, C1, E9.	C9-C10, D9-D10.

Other Areas of Deposition	**Uncompacted Relief**	**Compacted Relief**	Total % Sand Below	% Sand in Previous Unit.
C9-C10	Low, flat area behind high point at T5/T17	Compaction lowers the area, which remains flat.	Moderate (52-63%)	High (72-91%)
D9-D10	Edge of the flat area as described above, which slopes down to the SE corner where E9 is a MLDS.	Compaction lowers and steepens this slope area.	Low (49-60%)	High (65-84%)

General Observations

Sand concentrations again are best where the isopach to unit 3 is thin. Sediment appears to have come down the southern channel where sand has formed in three patches. Firstly, it has deposited on the initial downslope, followed by deposition on the upslope, and finally once it has made it over the main ridge to be deposited in the low of the SE corner. The middle channel also appears to have been operative, with high sand concentrations found in the T16-T2-T8 area, deposited on the southern flanks of the high region around T5 and T17. The high regions on the unit 5 surface almost appear to form natural levees for unit 3 deposition.

TOP UNIT 3 SURFACE - DEPOSITION OF UNIT 4 ISOPACH.

Maximum Unit 4 Thickness	No. of Depositional Sites	Uncompacted MLDS	No. of Uncompacted Matches	Compacted MLDS	No. of Compacted Matches	Topographic Control on Deposition	Deposition in Alternative Areas
12m *(Thin)*	6	12	5 (83%)	17	5 (83%)	B1-B2, C1-C2, D1.	A1.

Other Areas of Deposition	**Uncompacted Relief**	**Compacted Relief**	Total % Sand Below	% Sand in Previous Unit.
A1	Low area close to the large MLDS on the western side of the Arbroath region.	Compaction lowers the area, making it closer to the MLDS.	Low (52-56%)	Moderate (34-68%)

General Observations

Unit 4 is another difficult section to explain. Sand percentages tend to be higher where the isopach is thin. The thickest part of unit 4 which lies around T19 and T14, is generally mud-rich and fills a topographically low area. Unit 4 is only thin and therefore has little effect on the overall topographic expression of the Arbroath region. Sand generally appears to have been funnelled along the southern and middle channels, and have been deposited on upslopes and downslopes of the topography, with the majority being deposited on the upslopes as flow velocities are presumably slowed.

TOP UNIT 4 SURFACE - DEPOSITION OF UNIT 1 ISOPACH.

Maximum Unit 1 Thickness	No. of Depositional Sites	Uncompacted MLDS	No. of Uncompacted Matches	Compacted MLDS	No. of Compacted Matches	Topographic Control on Deposition	Deposition in Alternative Areas
36m *(Moderate)*	6	12	6 (100%)	14	6 (100%)	B1, C1-C2, D1, E7-E8.	-

General Observations

Topography is the main contributing factor to the deposition of unit 1, although compaction undoubtedly enhances the topographic variations in certain areas. The reason topography may form the main control to depositional patterns at this stage may be due to the fact that most areas have high sand percentages close to the depositional surface making early compaction more difficult and less significant than before. Unit 1 again shows widespread sand distribution, especially where the isopach is generally thinner. Sands appear to be found in the southern channel, especially deposited on the upslope to the high region around T1 and T4. Further thin sands (<6m) are found in the northern end of the northern channel around T15 and T5, where they have probably been trapped by the topography. Mud-rich areas appear to fill in topographically low areas, rather than forming levees.

TOP UNIT 1 SURFACE - DEPOSITION OF FORTIES ISOPACH.

Maximum Forties Thickness	No. of Depositional Sites	Uncompacted MLDS	No. of Uncompacted Matches	Compacted MLDS	No. of Compacted Matches	Topographic Control on Deposition	Deposition in Alternative Areas
8m *(V. Thin)*	18	11	8 (44%)	17	10 (56%)	C1-C3, D1-D3, E1.	B1, D4, E2-E3, B7-B10, C7-C9.

Other Areas of Deposition	**Uncompacted Relief**	**Compacted Relief**	Total % Sand Below	% Sand in Previous Unit.
B1	Low, flat area close to MLDS.	Area is lowered by compaction.	Moderate (56-63%)	High (72-90%)
D4	Low slope area of southern ridge, close to the MLDS.	Compaction lowers the slope.	V. Low (49-52%)	High (72-90%)
E2-E3	Similar low slope area as D4.	Compaction lowers and widens the slope area, making E2 a MLDS.	Low (49-56%)	Variable E2-E3 (45-81%)
B7-B10	High region around T17, and part of the northeast slope area from this high ridge.	Compaction lowers the ridge and smoothes the slopes.	Moderate (60-70%)	Variable B7-B10 (72-27%)
C7-C9	Minor low, circular area with the high located to the east in C10.	Compaction lowers the area, making C7-C8 a MLDS.	Low (<46-66%)	Variable C7-C9 (81-9%)

General Observations

Sand percentages are again higher where the isopach to the Forties unit is thin, keeping in mind that the unit is very thin anyway. Sand mainly comes down the middle channel of T20-T16-T2, but also overlaps with the southern channel. May just be the lateral off-setting of the southern channel due to previous sand flows along it. The isopach high area around T17 and T8 may form a small levee region, accentuating already slightly higher topography. However, generally mud-rich, isopach thick regions fill the topographically lowest regions in the Top unit 1 surface. These are possibly overbank deposits from the sand-rich turbidites, or they are later pelagic mud sedimentation.